frontiers | Research Topics

Imaging the immune response in inflammatory preclinical in vivo models

Edited by
Marco Erreni, Nick Devoogdt, Greetje Vande Velde and Roberto Weigert

Published in
Frontiers in Immunology
Frontiers in Oncology

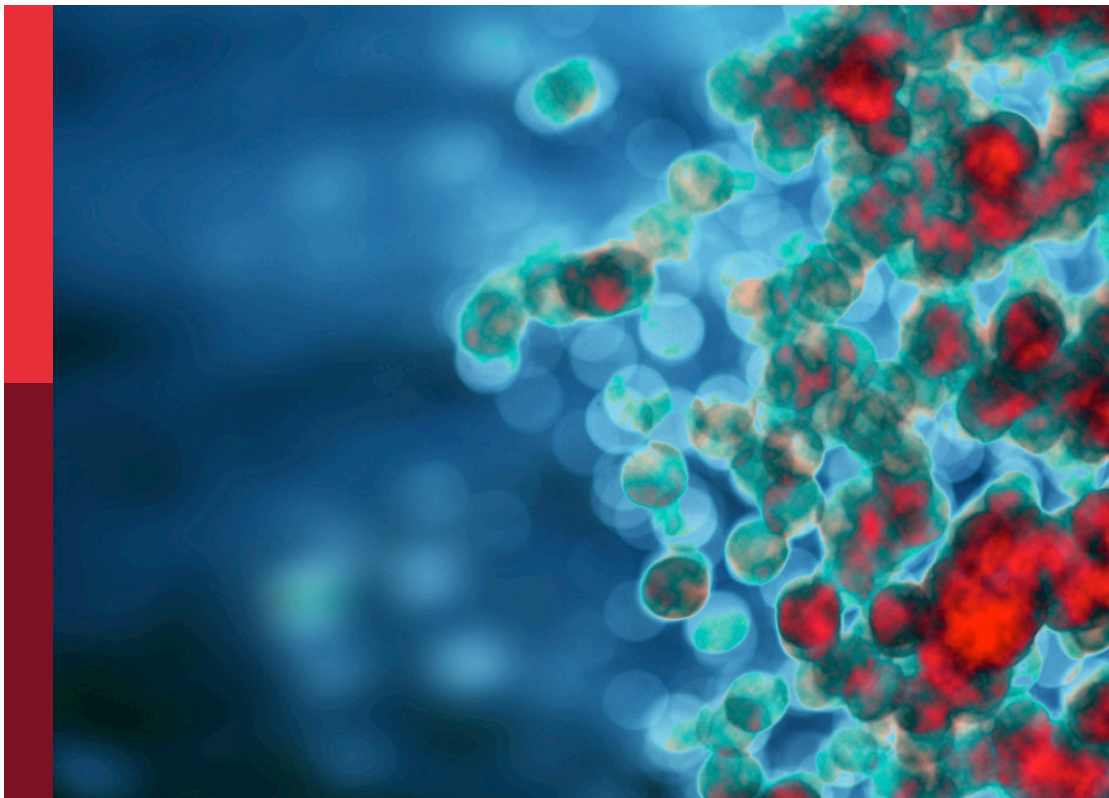

ISSN 1664-8714
ISBN 978-2-8325-2365-0
DOI 10.3389/978-2-8325-2365-0

About Frontiers

Frontiers is more than just an open access publisher of scholarly articles: it is a pioneering approach to the world of academia, radically improving the way scholarly research is managed. The grand vision of Frontiers is a world where all people have an equal opportunity to seek, share and generate knowledge. Frontiers provides immediate and permanent online open access to all its publications, but this alone is not enough to realize our grand goals.

Frontiers journal series

The Frontiers journal series is a multi-tier and interdisciplinary set of open-access, online journals, promising a paradigm shift from the current review, selection and dissemination processes in academic publishing. All Frontiers journals are driven by researchers for researchers; therefore, they constitute a service to the scholarly community. At the same time, the *Frontiers journal series* operates on a revolutionary invention, the tiered publishing system, initially addressing specific communities of scholars, and gradually climbing up to broader public understanding, thus serving the interests of the lay society, too.

Dedication to quality

Each Frontiers article is a landmark of the highest quality, thanks to genuinely collaborative interactions between authors and review editors, who include some of the world's best academicians. Research must be certified by peers before entering a stream of knowledge that may eventually reach the public - and shape society; therefore, Frontiers only applies the most rigorous and unbiased reviews. Frontiers revolutionizes research publishing by freely delivering the most outstanding research, evaluated with no bias from both the academic and social point of view. By applying the most advanced information technologies, Frontiers is catapulting scholarly publishing into a new generation.

What are Frontiers Research Topics?

Frontiers Research Topics are very popular trademarks of the *Frontiers journals series*: they are collections of at least ten articles, all centered on a particular subject. With their unique mix of varied contributions from Original Research to Review Articles, Frontiers Research Topics unify the most influential researchers, the latest key findings and historical advances in a hot research area.

Find out more on how to host your own Frontiers Research Topic or contribute to one as an author by contacting the Frontiers editorial office: frontiersin.org/about/contact

Imaging the immune response in inflammatory preclinical in vivo models

Topic editors

Marco Erreni — Humanitas Research Hospital, Italy
Nick Devoogdt — Université libre de Bruxelles, Belgium
Greetje Vande Velde — KU Leuven, Belgium
Roberto Weigert — Center for Cancer Research, National Cancer Institute (NIH), United States

Citation

Erreni, M., Devoogdt, N., Velde, G. V., Weigert, R., eds. (2023). *Imaging the immune response in inflammatory preclinical in vivo models*. Lausanne: Frontiers Media SA. doi: 10.3389/978-2-8325-2365-0

Table of contents

05 Editorial: Imaging the immune response in inflammatory preclinical *in vivo* models
M. Erreni, G. Vande Velde, R. Weigert and N. Devoogdt

08 Noninvasive Immuno-PET Imaging of CD8⁺ T Cell Behavior in Influenza A Virus-Infected Mice
Paul W. Rothlauf, Zeyang Li, Novalia Pishesha, Yushu Joy Xie, Andrew W. Woodham, Djenet Bousbaine, Stephen C. Kolifrath, Vincent L. Verschoor and Hidde L. Ploegh

20 Sinomenine Relieves Airway Remodeling By Inhibiting Epithelial-Mesenchymal Transition Through Downregulating TGF-β1 and Smad3 Expression *In Vitro* and *In Vivo*
Hongjuan He, Lihua Cao, Zheng Wang, Zhenzhen Wang, Jinxin Miao, Xiu-Min Li and Mingsan Miao

32 Imaging of Glioblastoma Tumor-Associated Myeloid Cells Using Nanobodies Targeting Signal Regulatory Protein Alpha
Karen De Vlaminck, Ema Romão, Janik Puttemans, Ana Rita Pombo Antunes, Daliya Kancheva, Isabelle Scheyltjens, Jo A. Van Ginderachter, Serge Muyldermans, Nick Devoogdt, Kiavash Movahedi and Geert Raes

46 The Colony Stimulating Factor-1 Receptor (CSF-1R)-Mediated Regulation of Microglia/Macrophages as a Target for Neurological Disorders (Glioma, Stroke)
Cristina Barca, Claudia Foray, Sven Hermann, Ulrich Herrlinger, Isabel Remory, Damya Laoui, Michael Schäfers, Oliver M. Grauer, Bastian Zinnhardt and Andreas H. Jacobs

58 Single-Domain Antibodies for Targeting, Detection, and *In Vivo* Imaging of Human CD4⁺ Cells
Bjoern Traenkle, Philipp D. Kaiser, Stefania Pezzana, Jennifer Richardson, Marius Gramlich, Teresa R. Wagner, Dominik Seyfried, Melissa Weldle, Stefanie Holz, Yana Parfyonova, Stefan Nueske, Armin M. Scholz, Anne Zeck, Meike Jakobi, Nicole Schneiderhan-Marra, Martin Schaller, Andreas Maurer, Cécile Gouttefangeas, Manfred Kneilling, Bernd J. Pichler, Dominik Sonanini and Ulrich Rothbauer

75 Shedding Structured Light on Molecular Immunity: The Past, Present and Future of Immune Cell Super Resolution Microscopy
Timothy M. Johanson, Christine R. Keenan and Rhys S. Allan

87 Radiolabeled Monoclonal Antibody Against Colony-Stimulating Factor 1 Receptor Specifically Distributes to the Spleen and Liver in Immunocompetent Mice
Stijn J. H. Waaijer, Frans V. Suurs, Cheei-Sing Hau, Kim Vrijland, Karin E. de Visser, Derk Jan A. de Groot, Elisabeth G. E. de Vries, Marjolijn N. Lub-de Hooge and Carolina P. Schröder

98 *In Vivo* Motility Patterns Displayed by Immune Cells Under Inflammatory Conditions
Diego Ulisse Pizzagalli, Alain Pulfer, Marcus Thelen, Rolf Krause and Santiago F. Gonzalez

111 Overload of the Temporomandibular Joints Accumulates γδ T Cells in a Mouse Model of Rheumatoid Arthritis: A Morphological and Histological Evaluation
Kohei Nagai, Takenobu Ishii, Tatsukuni Ohno and Yasushi Nishii

121 Exploiting Glutamine Consumption in Atherosclerotic Lesions by Positron Emission Tomography Tracer (2*S*,4*R*)-4-^{18}F-Fluoroglutamine
Senthil Palani, Maxwell W. G. Miner, Jenni Virta, Heidi Liljenbäck, Olli Eskola, Tiit Örd, Aarthi Ravindran, Minna U. Kaikkonen, Juhani Knuuti, Xiang-Guo Li, Antti Saraste and Anne Roivainen

131 Folate Receptor Beta for Macrophage Imaging in Rheumatoid Arthritis
Maarten M. Steinz, Aiarpi Ezdoglian, Fatemeh Khodadust, Carla F. M. Molthoff, Madduri Srinivasarao, Philip S. Low, Gerben J. C. Zwezerijnen, Maqsood Yaqub, Wissam Beaino, Albert D. Windhorst, Sander W. Tas, Gerrit Jansen and Conny J. van der Laken

141 PD-L1 Antibody Pharmacokinetics and Tumor Targeting in Mouse Models for Infectious Diseases
Gerwin G. W. Sandker, Gosse Adema, Janneke Molkenboer-Kuenen, Peter Wierstra, Johan Bussink, Sandra Heskamp and Erik H. J. G. Aarntzen

frontiers | Frontiers in Immunology

TYPE Editorial
PUBLISHED 24 April 2023
DOI 10.3389/fimmu.2023.1197819

OPEN ACCESS

EDITED AND REVIEWED BY
Pietro Ghezzi,
University of Urbino Carlo Bo, Italy

*CORRESPONDENCE
M. Erreni
marco.erreni@humanitasresearch.it

SPECIALTY SECTION
This article was submitted to Inflammation, a section of the journal Frontiers in Immunology

RECEIVED 31 March 2023
ACCEPTED 14 April 2023
PUBLISHED 24 April 2023

CITATION
Erreni M, Vande Velde G, Weigert R and Devoogdt N (2023) Editorial: Imaging the immune response in inflammatory preclinical *in vivo* models. *Front. Immunol.* 14:1197819. doi: 10.3389/fimmu.2023.1197819

Editorial: Imaging the immune response in inflammatory preclinical *in vivo* models

M. Erreni[1,2]*, G. Vande Velde[3], R. Weigert[4] and N. Devoogdt[5]

[1]Unit of Advanced Optical Microscopy, IRCCS Humanitas Research Hospital, Milan, Italy, [2]Department of Biomedical Sciences, Humanitas University, Milan, Italy, [3]Biomedical MRI/MoSAIC, Department of Imaging and Pathology, Faculty of Medicine, KU Leuven, Leuven, Belgium, [4]Laboratory of Cellular and Molecular Biology, Center for Cancer Research, National Cancer Institute, National Institutes of Health, Bethesda, MD, United States, [5]Medical Imaging Department, *In vivo* Cellular and Molecular Imaging Laboratory, Vrije Universiteit Brussel, Brussels, Belgium

KEYWORDS

imaging, inflammation, *in vivo* models, preclinical imaging, immune response

Editorial on the Research Topic
Imaging the immune response in inflammatory preclinical *in vivo* models

The immune response to pathological conditions is the result of a complex and coordinated activity of specialized cells, tissues and organs, aimed at promoting an effective host defense. Although *in vitro* models have been used to describe several aspects of the immune system, they often fail to reconstitute the dynamic complexity of *in vivo* multicellular systems. In the last decades, major breakthroughs in the fields of imaging and mouse engineering have opened the door to investigate such a complexity. Indeed, the possibility to select the appropriate imaging technique to address a specific biological question has made it possible to unveil novel aspects of the immune response at different levels of temporal and spatial resolution.

The aim of this Research Topic is to provide an overview of the different imaging technologies and their application to analyse immune responses in *in vivo* models.

Conventional histology and immunohistochemistry represent the techniques of choice to visualize the expression of inflammatory mediators in pathological tissues. He et al. demonstrated, by immunohistochemistry, Hematoxylin & Eosin and Masson staining that Sinomenin, a biologically active alkaloid isolated from the roots and stems of the plant *Sinomenium acutum*, suppresses epithelial to mesenchymal transition in a mouse model of ovalbumin-induced asthma.

Besides *ex vivo* techniques, a variety of non-invasive imaging methodologies were developed to study the biodistribution and tissue accumulation of targeting probes and drugs in preclinical models of disease. Positron Emission Tomography (PET) and Single Photon Emission Computed Tomography (SPECT) are the most widely used, due to their capability to provide information about the metabolic and molecular activity of the analysed tissue. Moreover, PET and SPECT are routinely used in patients, thus facilitating the translation of data from pre-clinical models to human clinical practice. De Vlaminck et al. and Sandker et al. provided examples of SPECT to study the pharmacokinetics of targeting molecules. De Vlaminck et al. generated nanobodies able to recognize the signal regulatory protein alpha (SIRPα) for the SPECT targeting of tumor-

associated myeloid cells in a mouse model of glioblastoma. They showed that the monovalent format of anti-SIRPα nanobodies has an improved tumor penetration compared to the bivalent counterpart and that myeloid cells infiltrated glioblastomas even in absence of blood-brain barrier permeabilization. Sandker et al. analyzed the effect of infectious stimuli in the pharmacokinetic and tumor targeting capability of an anti-PD-L1 antibody. They found that anti-PD-L1 antibody pharmacokinetics and tumor accumulation can be altered by a severe inflammatory response, thus requiring an appropriate modulation of the injected dose of the tracer.

Similarly, Rothlauf et al. applied PET and radiolabeled anti-CD8 nanobodies to track $CD8^+$ T cells infiltration in a mouse model of influenza A virus infection. They visualized $CD8^+$ T cells throughout the progression of the infection, showing that $CD8^+$ T cells initially accumulate in mesenteric lymph nodes, then migrate into the infected lungs, and finally exit the lungs as the mice recovered. Likewise, using non-invasive optical imaging and PET, Traenkle et al. generated anti-human CD4 nanobodies to visualize and quantify $CD4^+$ T cells in human tumor xenogratfs and in $CD4^+$ T cell-rich tissue in human CD4 knock-in mice. Waaijer et al. used PET to study, for the first time, the biodistribution of a CSF1R-binding monoclonal antibody. They demonstrated that anti-CSF1R monoclonal antibodies do not exclusively target tumor macrophages but preferably distribute to other organs with high macrophage infiltration, highlighting the need for more studies to enhance the understanding of macrophage-specific antibodies for their potential application as targeting agents in humans. The use of CSF1R targeting strategies in the context of neurological disorders was also reviewed by Barca et al. They revised the supporting evidence on the role of CSF1R in neurological disorders and the efficacy of CSF1R-inhibition as therapeutic strategy. In addition, they discussed the recent development of *in vivo* molecular imaging of CSF1R, with a specific focus on the translocator protein (TSPO)-PET as a CSFR1 inhibition therapy readout.

Macrophages represent an interesting target not only in tumors but also in the onset of other inflammatory disease. Steinz et al. reviewed the application of folate-based PET for macrophage targeting in rheumatoid arthritis. Radiolabeled folate interacts with folate receptor β expressed on macrophages and it is a useful tracer in both preclinical and clinical applications. Similarly, Palani et al. showed that the glutamine analog (2S,4*R*)-4-^{18}F-fluoroglutamine (^{18}F-FGln) can be used for PET of macrophage metabolic activity in a mouse model of atherosclerosis. They experimentally showed that ^{18}F-FGln PET is superior to ^{18}F-FDG PET in detecting inflamed atherosclerotic lesions in mice, paving the road for its clinical application.

Although PET and SPECT are useful to study the biodistribution of injected probes and the metabolic activity of diseased tissues, they do not provide anatomic information on the organs of interest. For this reason, PET and SPECT are usually combined with computed tomography (CT) or magnetic resonance imaging (MRI), thus linking accurate spatial localization with metabolic/molecular data. Examples of this combined application were reported by De Vlaminck et al., Traenkle et al., Palani et al. and Sandker et al. Moreover, dedicated microCT can be also used as a stand-alone technique to monitor structural changes in tissues. Nagai et al. applied microCT to visualise the morphological and histological properties of peripheral and temporomandibular joints (TMJ) in a mouse model of rheumatoid arthritis with or without the exposure to mechanical strain on the TMJ. 3D morphological evaluation by microCT revealed morphological changes in the posterior part of the mandibular condyle and signs of bone destruction in a mouse model of anti-collagen antibody-induced arthritis.

As shown by Traenkle et al., beside PET and SPECT, optical imaging can be used to monitor biological process in live animals. However, a drawback of this technique is that light scattering and absorption by tissues limit its applicability for non-invasive imaging at high spatial resolution. Less subjective to these limitations are techniques such as fluorescence-guided surgery and intravital microscopy, that have been developed for the visualization of surgically exposed organs, allowing the possibility to analyse biological processes at both cellular and subcellular level. Pizzagalli et al. discussed the investigation of the migratory patterns of immune cells in living animals by intravital microscopy. They described the morpho-dynamic properties associated with immune cell migration during immune responses and the computational methods employed for their quantification. Moreover, recent advances in super-resolution microscopy have enabled the analysis of biological events in living organisms beyond the light diffraction limits. In this context, Johanson et al. reviewed the usefulness of this technique to investigate immune cell function and molecular processes underlying inflammatory responses and to answer long-standing fundamental questions in this matter.

In conclusion, a variety of imaging methodologies, each with their distinct features and possible applications, are available for researchers to investigate the complexity of the immune response in living animals. Differently from conventional *ex vivo* imaging methods, that generally provide snapshot data from fixed samples, *in vivo* imaging approaches, such as intravital microscopy and whole-body imaging techniques (PET, SPECT, CT, MRI, etc.), have the great potential to add the temporal dimension to immunological investigations. The choice of the right imaging technique, or even better, the combination of appropriate imaging methodologies strictly depends on the biological questions asked, aimed at collecting as much information as possible from single experiments in animal disease models.

Author contributions

All authors have made a substantial, direct and intellectual contribution to the work. ME drafted the manuscript. The editors GVV, RW and ND provided critical revisions and approved the submitted manuscript.

Funding

This work was supported by the Associazione Italiana Ricerca Cancro (AIRC), AIRC 5x1000, 21147. ND received funding from the Strategic Research Programme SRP83 from the Vrije

Universiteit Brussel. RW research was supported by the NIH, NCI Center for Cancer Research Intramural Research Program (ZIA BC 011682). GVV received funding from the Flemish Research Foundation (FWO, G057721N).

Conflict of interest

Topic Editor DN holds several patents on probes for imaging of immune cells. He is co-founder and shareholder of the company AbScint that leverages new probes for immune cell imaging. He is in the management board of the IMI2 program Immune-Image where academics together with pharma companies and SMEs develop, preclinically evaluate and clinically test new tracers to imaging immune cells in cancer and inflammatory diseases. He is co-founder, shareholder and consultant for the company Precirix that develops therapeutic radiopharmaceuticals, and where nuclear imaging is a readout of anti-cancer immune responses. Finally, he is performing sponsored research for companies including Exevir, Esobiotech, Confo Therapeutics, Roche, Telix Pharma, Agenus, 121BIO, Complix, and Boehringer Ingelheim.

The remaining authors declare that the research was conducted in the absence of any commercial or financial relationships that could be construed as a potential conflict of interest.

Publisher's note

frontiers in Immunology

ORIGINAL RESEARCH
published: 03 November 2021
doi: 10.3389/fimmu.2021.777739

Noninvasive Immuno-PET Imaging of CD8$^+$ T Cell Behavior in Influenza A Virus-Infected Mice

Paul W. Rothlauf[1,2†], Zeyang Li[3†], Novalia Pishesha[3,4,5,6], Yushu Joy Xie[3], Andrew W. Woodham[3,7], Djenet Bousbaine[3], Stephen C. Kolifrath[3], Vincent L. Verschoor[3,8] and Hidde L. Ploegh[3,7]*

[1] Program in Virology, Harvard Medical School, Boston, MA, United States, [2] Department of Molecular Microbiology, Washington University School of Medicine, St. Louis, MO, United States, [3] Program in Cellular and Molecular Medicine, Boston Children's Hospital, Boston, MA, United States, [4] Society of Fellows, Harvard University, Cambridge, MA, United States, [5] Klarman Cell Observatory, Broad Institute of MIT and Harvard, Cambridge, MA, United States, [6] Department of Immunology and Infectious Diseases, Harvard School of Public Health, Boston, MA, United States, [7] Department of Pediatrics, Harvard Medical School, Boston, MA, United States, [8] Leiden Academic Centre for Drug Research, Leiden University, Leiden, Netherlands

OPEN ACCESS

Edited by:
Nick Devoogdt,
Free University of Brussels, Belgium

Reviewed by:
Nu Zhang,
The University of Texas Health Science Center at San Antonio, United States
Katayoun Ayasoufi,
Mayo Clinic, United States

***Correspondence:**
Hidde L. Ploegh
Hidde.Ploegh@childrens.harvard.edu

[†]These authors have contributed equally to this work and share first authorship

Specialty section:
This article was submitted to T Cell Biology, a section of the journal Frontiers in Immunology

Received: 15 September 2021
Accepted: 20 October 2021
Published: 03 November 2021

Citation:
Rothlauf PW, Li Z, Pishesha N, Xie YJ, Woodham AW, Bousbaine D, Kolifrath SC, Verschoor VL and Ploegh HL (2021) Noninvasive Immuno-PET Imaging of CD8$^+$ T Cell Behavior in Influenza A Virus-Infected Mice. Front. Immunol. 12:777739. doi: 10.3389/fimmu.2021.777739

Immuno-positron emission tomography (immuno-PET) is a noninvasive imaging method that enables tracking of immune cells in living animals. We used a nanobody that recognizes mouse CD8α and labeled it with ^{89}Zr to image mouse CD8$^+$ T cells in the course of an infection with influenza A virus (IAV). The CD8$^+$ signal showed a strong increase in the mediastinal lymph node (MLN) and thymus as early as 4 days post-infection (dpi), and as early as 6 dpi in the lungs. Over the course of the infection, CD8$^+$ T cells were at first distributed diffusely throughout the lungs and then accumulated more selectively in specific regions of the lungs. These distributions correlated with morbidity as mice reached the peak of weight loss over this interval. CD8$^+$ T cells obtained from control or IAV-infected mice showed a difference in their distribution and migration when comparing their fate upon labeling *ex vivo* with ^{89}Zr-labeled anti-CD8α nanobody and transfer into infected versus control animals. CD8$^+$ T cells from infected mice, upon transfer, appear to be trained to persist in the lungs, even of uninfected mice. Immuno-PET imaging thus allows noninvasive, dynamic monitoring of the immune response to infectious agents in living animals.

Keywords: immuno-PET, influenza A virus, CD8, T cells, imaging

INTRODUCTION

Influenza remains a serious disease, with an estimated 1 billion infections per year, some 290,000–650,000 of which are fatal (1). Influenza A virus (IAV), a segmented, negative-sense RNA virus in the family *Orthomyxoviridae*, causes seasonal epidemics. IAV can also cause pandemics, during which individuals have limited cross-protective immunity as a result of the virus's ability to reassort its segments with heterologous influenza strains (2, 3). Despite the development of antivirals and vaccines, influenza virus-associated deaths remain a major concern. A better understanding of the

clinical course of infection and the host's immunological response to the virus is crucial to improve vaccines and therapeutics against influenza viruses.

IAV, along with the related influenza B virus, causes a range of clinical manifestations, from mild self-limiting respiratory tract infections, to progressive and sometimes lethal pneumonia (4). Both the upper and lower respiratory tracts are sites of viral replication, with nascent virions spreading amongst epithelial cells of the upper respiratory tract and trachea in most non-fatal cases. Lower respiratory involvement and pneumonia, caused by the virus and/or secondary bacterial infections, are often seen in fatal cases (5).

Upon detecting the presence of IAV infection, the host immune system clears the viral infection using both innate and adaptive immune components (6). The rapid induction of innate defenses is critical for early protection and limits viral spread to host tissues, while adaptive immunity develops. Early stages of innate immunity include the rapid production of type I interferons (IFNs), cytokines, and chemokines through activation of pattern recognition receptors, which in turn attracts inflammatory cells to the airways to help clear the infection and prepare the host for the adaptive immune response (7). The adaptive immune response is activated when lung-resident dendritic cells sense cytokines and acquire debris from infected, dying cells, which induces their migration from the inflamed lungs to the lung-draining lymph nodes (DLNs). There, they display newly acquired viral antigen(s), processed to yield peptide-MHC complexes (8). Naïve T cells in the DLNs recognize these complexes, expand clonally, and then differentiate into IAV antigen-specific $CD8^+$ and $CD4^+$ effector T cells (9). Secondary lymphoid organs, such as DLNs and the spleen, provide the spatial organization and appropriate chemokine environment to prime the antiviral immune response by bringing together Th1 $CD4^+$ and naïve $CD8^+$ cells to generate influenza-specific $CD8^+$ cytotoxic T lymphocytes (CTLs). Virus-specific T lymphocytes then migrate to the site of infection in response to cytokines and chemokines, and B cells are primed to secrete neutralizing antibodies (10).

The virus itself causes extensive damage to and desquamation of the airway epithelium, but effector T cells also contribute to tissue damage directly by secreting granzymes and perforin, as well as by inducing FasL- and TRAIL-mediated apoptotic pathways (5, 11). CTL-induced tissue damage, however, is thought to be more extensive as a consequence of indirect mechanisms, such as by secretion of pro-inflammatory molecules that recruit other players to the site of infection, including IFNγ, macrophage inflammatory protein-1α, and CTL-derived tumor necrosis factor-α (12–18). Observing the spatiotemporal behavior of CTLs during IAV infection, ideally longitudinally and noninvasively, is essential to better understand the immunopathology induced by these cells and to eventually prevent collateral damage inflicted by T cells.

One technique used to visualize and track cells *in vivo* is positron emission tomography (PET), which is used to identify tumors in humans. PET scanning relies on detection of a radiotracer, such as ^{18}F-2-fluorodeoxyglucose, which is absorbed by tumor cells with high metabolic activity. Immuno-PET is a technique that uses radiolabeled antibodies, or antibody fragments, that target disease- or cell-specific antigens to track the distribution of that antigen (19, 20). We have used immuno-PET, more specifically using single domain antibody fragments (VHHs or nanobodies) derived from alpaca heavy chain-only antibodies, to track immune cell distribution and infiltration in graft-versus-host disease, as well as in models of cancer and the immune response to cancer therapies (21–23).

We used radiolabeled nanobodies to study the kinetics of $CD8^+$ T cell recruitment to the site of infection, using mouse-adapted IAV. We also identified the localization of $CD8^+$ T cells from IAV-infected and control mice upon transfer to assess cell-autonomous migratory behaviors. By transferring labeled $CD8^+$ T cells from IAV-infected mice into either healthy or IAV-infected recipients, we examined whether the inflamed environment of the infected lungs affects tissue-specific trafficking of both naïve and antigen-specific T cells. Prior studies have relied mostly on invasive techniques, such as tissue harvest, followed by flow cytometry to enumerate $CD8^+$ T cells in the organ of interest. While this provides insight into the local distribution of $CD8^+$ T cells, it does not provide information on changes in distribution or migration of $CD8^+$ T cells to peripheral tissues in the course of infection. We show that it is possible to noninvasively monitor the total population of $CD8^+$ T cells over the course of an IAV infection at millimeter spatial resolution. This approach provides a new means to track a $CD8^+$ T cell response noninvasively in a living animal.

MATERIALS AND METHODS

Synthesis of Peptide Probes for Sortase Reactions

Peptide GGGCGGSK(azide) with a free N-terminus and C-terminal amide was synthesized following standard solid phase synthesis protocols (24). All Fmoc amino acids were purchased from Chempep, Inc. Fmoc-Lys(azide)-OH was used as a building block to provide the bioorthogonal handle. Peptides were purified by reverse phase HPLC. Their identity was confirmed by LC-MS prior to maleimido-DFO coupling to the cysteine thiol. Peptides were further purified by reverse phase HPLC and their identity was confirmed again by LC-MS.

C-Terminal Sortagging and PEGylation

Ca^{2+}-independent heptamutant sortase A derived from *S. aureus* (10 μM final concentration, 10x stock in 50 mM Tris, pH 7.4, 150 mM NaCl) and probe (1 mM final concentration, 50x stock) were added to VHH-X118 (200 μM final concentration) in phosphate-buffered saline (PBS). The resulting mixture was incubated at 4°C overnight. Ni-NTA (0.5 ml) was added to the reaction mixture and incubated for 20 minutes to remove sortase and unreacted VHHs. The mixture was centrifuged and the supernatant was collected and purified by size exclusion chromatography (Superdex 75- GE Life Sciences), and analyzed by SDS-PAGE and LC-MS. PEGylated VHH-X118

was generated by reacting the bioorthogonal azide group with dibenzocyclooctyne DBCO-$(PEG)_{20}$ overnight. The end product was analyzed by SDS-PAGE to confirm efficient coupling.

Virus Quantification

IAV was quantified by flow cytometry, using a method adapted from one previously described (25). Briefly, confluent Madin-Darby canine kidney cells were infected in triplicate with 2-fold serial dilutions of IAV WSN/33 (in DMEM, 0.2% BSA) for 1 hour. The inoculum was removed and replaced with DMEM, 0.2% (w/v) BSA for 5 hours. Cells were washed with PBS, trypsinized, and fixed with 4% formaldehyde in PBS. Cells were stained with 1 μg/ml VHH62 (anti-IAV NP)-Alexa Fluor 647 under permeabilizing conditions. Fluorescence was quantified using a BD Accuri C6 Plus. The NP-positive population was determined by comparison with an uninfected control population (**Figure S1A**). Data were processed using the FlowJo software package (TreeStar Inc). A linear regression model was applied (**Figure S1B**). The slope of the line of best fit was used to determine the percentage of infected cells, which was multiplied by the number of cells per well to yield the number of viral particles per well.

Infection of Mice With IAV

Age-matched, 6-week old, female CD45.2 C57BL/6J mice (n≥3 in each group) were purchased from the Jackson Laboratory. Mice were anesthetized with isoflurane and infected by the intranasal route with 4 x 10^4 infectious units of IAV WSN/33 diluted in PBS. Control mice were similarly given an equal volume of PBS intranasally. Infection was tracked by monitoring daily weight loss. Mice were euthanized with CO_2 when weight loss exceeded 25% of initial body weight and/or animals displayed signs of severe distress, or if no weight was recovered 9 dpi.

Immuno-PET Imaging

IAV-infected and control mice were anesthetized using isoflurane and injected *via* the retro-orbital route with approximately 25 μCi of ^{89}Zr-VHH-X118-PEG_{20}. PET-CT procedures have been described in detail (21, 26). Briefly, approximately 24 h post-administration of ^{89}Zr-VHH-X118-PEG_{20}, mice were anesthetized using 2% isoflurane in O_2 at a flow rate of approximately 1 L/minute. Mice were imaged with a G8 PET-CT small-animal scanner (PerkinElmer). PET images were acquired over a 20 minute period, which was followed by approximately 2 minutes of CT acquisition. As a standard for absolute intensity, a fixed quantity of radioactivity was imaged using 5-fold serial dilutions of radioisotope in PCR strip tubes.

PET Quantification

We processed and quantified PET images using VivoQuant software. The CT scan was used as a guide to generate 3D regions of interest (ROIs) to represent regions corresponding to the lungs and MLN. ROIs were drawn for each image corresponding to the absence of CT signal in the ribcage, surrounding the heart as a means of identifying pulmonary space. We used preset CT values to view the area corresponding to the lungs, and preset CT intensities (-1400, 400) were used to generate the lung ROIs. For the MLN region, ROIs were generated by creating a spherical region with a 10-pixel diameter centered around the point of highest PET intensity of MLN. An additional ROI was drawn in the quadriceps muscle of the hind leg of each mouse, avoiding bones and LNs, which was subtracted as background. Once all ROIs were generated, statistical information for each ROI containing mean PET signal, was exported and processed. We normalized signal intensities to background signal for each mouse by using the ratio between PET signal in the lungs or MLN to PET signal in the quadriceps muscle. The level of significance was determined using a Student's t-test.

T Cell Purification

Mice were euthanized by asphyxiation with CO_2 and spleens were extracted by dissection. Spleens were homogenized into single-cell suspensions. Red blood cells were removed by hypotonic lysis. T cells were isolated from these splenocytes using the Dynabeads® Untouched™ Mouse T Cells Kit following the suppliers' recommended procedures. The lungs of day 9-infected CD45.2 C57BL/6J mice were extracted by dissection, and T cells were isolated using the Dynabeads® Untouched™ Mouse T Cells Kit with additional incubations with anti-CD326 and anti-CD31 antibodies to deplete epithelial and endothelial cells, respectively.

Flow Cytometry

Aside from virus quantification assays, all data were acquired on a Fortessa instrument (BD Biosciences) and analyzed using FlowJo software Cells obtained from the lungs and MLN of CD45.2 C57BL/6J mice were used for flow cytometry. Cells were resuspended in PBS (137 mM NaCl, 2.7 mM KCl, 10 mM Na_2HPO_4, 1.8 mM KH_2PO_4) with 2% (v/v) fetal bovine serum and passed through 40-μm cell strainers to obtain single-cell suspensions prior to antibody staining (30 minutes at 4°C). All antibodies were obtained from BioLegend (San Diego, CA). Student's t-test was applied for statistical analysis.

ELISpot Assay

96-well ELISpot plates (BD ELISPOT Mouse IFNγ ELISPOT Set, BD Biosciences, San Jose, CA) were coated with an IFNγ capture antibody (BD Biosciences) in PBS overnight at 4°C, followed by incubation with complete RPMI-1640 medium for 2 hours at room temperature (RT). Single cell suspensions from selected organs of IAV-infected and uninfected mice were prepared. Red blood cells were removed by hypotonic lysis. Quadruplicate ELISpot wells containing mononuclear cells, were supplemented with the IAV NP peptide (366-374; ASNENMETM) (2 μg/ml), to serve as a H2-D^b-restricted epitope from the Influenza A/PR/8/34 nucleoprotein (27, 28). As a control, medium without added IAV peptide was used. ELISpot plates were incubated at 37°C for 18 hours, washed and incubated with a biotinylated IFNγ detection antibody (BD Biosciences) for 2 hours, followed by incubation with a streptavidin-horse radish peroxidase (HRP) conjugate (BD Biosciences) for 1 hour at RT. ELISpot plates were developed with 3-amino-9-ethyl-carbazole substrate (BD ELISPOT AEC

Substrate Set) and dried. Spots were counted using an ImmunoSpot Analyzer.

Ex Vivo T Cell Activation

Splenocytes from CD45.2 C57BL/6J mice were cultured in plates pre-coated with anti-CD3 (5 μg/ml) and anti-CD28 (1 μg/ml) antibodies in complete RPMI-1640 medium supplemented with 250 ng/ml of mouse IL-2 produced in house. Following activation for 24 hours, cells were transferred to fresh dishes without anti-CD3 and anti-CD28 in complete RPMI-1640 supplemented with 250 ng/ml of mouse IL-2, followed by two additional days of culture. Cells were washed three times with PBS and cell numbers were determined prior to transfer experiments.

T Cell Transfer

Cells were labeled with non-PEGylated ^{89}Zr-VHH-X118 in PBS at 4°C for 20 minutes with constant agitation. Cells were then washed three times with PBS to remove unbound ^{89}Zr-VHH-X118. Labeled cells (6×10^6) were then transferred into the retro-orbital plexus of each CD45.1 C57BL/6J mouse. Images were acquired as previously described 1 and 24 h post-T cell transfer.

FACS

T cells purified from lungs of day 9-infected CD45.2 BL/6J mice were stained with FITC anti-mouse CD8 and Alexa700 anti-mouse CD45.2 antibodies (BioLegend). The CD8$^+$CD45.2$^+$ T cell population was sorted on a BD FACSAria III sorter.

Ethics Statement

All animal protocols were conducted in accordance with the Guide for the Care and Use of Laboratory Animals of the National Institutes of Health. All animals were maintained according to the guidelines of the Animal Resources Children's Hospital. These studies were approved by the Boston Children's Hospital Institutional Animal Care and Use Committee (protocol #16-12-3328). All infections and PET imaging procedures were performed under isoflurane anesthesia and all efforts were made to minimize suffering.

RESULTS

VHH Construct Design for Immuno-PET Imaging of CD8$^+$ T Cells

In order to follow CD8$^+$ T cells noninvasively over the course of IAV infection, we used a VHH specific for murine CD8α, VHH-X118 (21). We produced two versions of ^{89}Zr-labeled VHH-X118, both made *via* modification of the VHH's C-terminal sortase recognition motif (LPETG). This modification allows the use of a peptide containing an N-terminal GGGC sequence equipped with a radiometal chelator to serve as a nucleophile in a sortase A-mediated transpeptidation reaction (29). By incorporation of maleimido-desferrioxamine (DFO), we installed ^{89}Zr for PET imaging. We also generated a PEGylated version of ^{89}Zr-labeled VHH-X118 by using an azide-substituted lysine in the course of synthesis of the nucleophile to incorporate polyethylene glycol (PEG) moieties for *in vivo* injections, effectively reducing non-specific retention in the kidneys (**Figure 1**) (21). The agent used for *ex vivo* labeling of CD8$^+$ T cells prior to use in transfer experiments, as described below, did not include a PEG moiety.

CD8$^+$ T Cells Transiently Accumulate in the Lungs and Mediastinal Lymph Nodes (MLN) of IAV-Infected Mice, Correlating With Morbidity

To establish the whole-body distribution of CD8$^+$ T cells during IAV infection, we acquired CD8$^+$ PET images using ^{89}Zr-labeled VHH-X118, and in parallel, tracked weight loss after intranasal inoculation of CD45.2 C57BL/6J mice (n≥3 for each group) with a sub-lethal dose (4×10^4 infectious units) of influenza A/WSN/33 virus (H1N1). In uninfected mice, CD8$^+$ T cells were distributed in the cervical, axillary and brachial (lung draining), mediastinal (lung draining), popliteal, renal, iliac, and inguinal lymph nodes, as well as in the spleen, consistent with previous observations (21). PET signals in the organs of elimination (kidneys, liver and bladder) and the site of injection (retro-orbital plexus) are non-specific and common occurrences when using nanobodies as imaging agents (21, 30, 31). During the first week of IAV infection, mice experienced weight loss, paralleled by increases in PET signal in the mediastinal lymph node (MLN) and lungs (**Figure 2**). Attribution of PET signals to particular anatomical structures was confirmed by imaging dissected organs, including MLN, lungs, heart, and thymus (**Figure S2**). At 4 days post-infection (dpi), mice showed a striking increase in CD8$^+$ T cells in the area corresponding to the MLN and in the draining lymph nodes, as inferred from the PET signal. At the peak of infection (6 dpi) as determined by weight loss, a diffuse pattern of CD8 signal was present in the lungs, likely caused by CD8$^+$ T cell migration from secondary lymphoid organs towards particular foci of infection. This signal became more concentrated and localized in specific regions of the lungs over the course of the infection, starting at 9 dpi. The PET signal decreased around 18 dpi, when mice regained weight in the recovery phase, and finally disappeared from the lungs by 21 dpi.

Immuno-PET Shows Accumulation of CD8$^+$ T Cells in the Lungs and MLN of IAV-Infected Mice

In order to determine whether the PET signals observed in the lungs and MLN of mice over the course of infection constituted measurable significant increases, we quantified the PET signal from the animals in **Figure 2** using VivoQuant software. Specifically, we generated 3D regions of interest (ROIs) representing the lungs (**Figure 3A**; cyan), MLN (**Figure 3B**; cyan), and quadriceps muscle (control; green) to quantify the PET signal within the volume of the ROI. Mean intensity was calculated by dividing the PET signal by the volume of the ROI. This value was further normalized within each mouse to the intensity of the quadriceps muscle, in order to account for possible

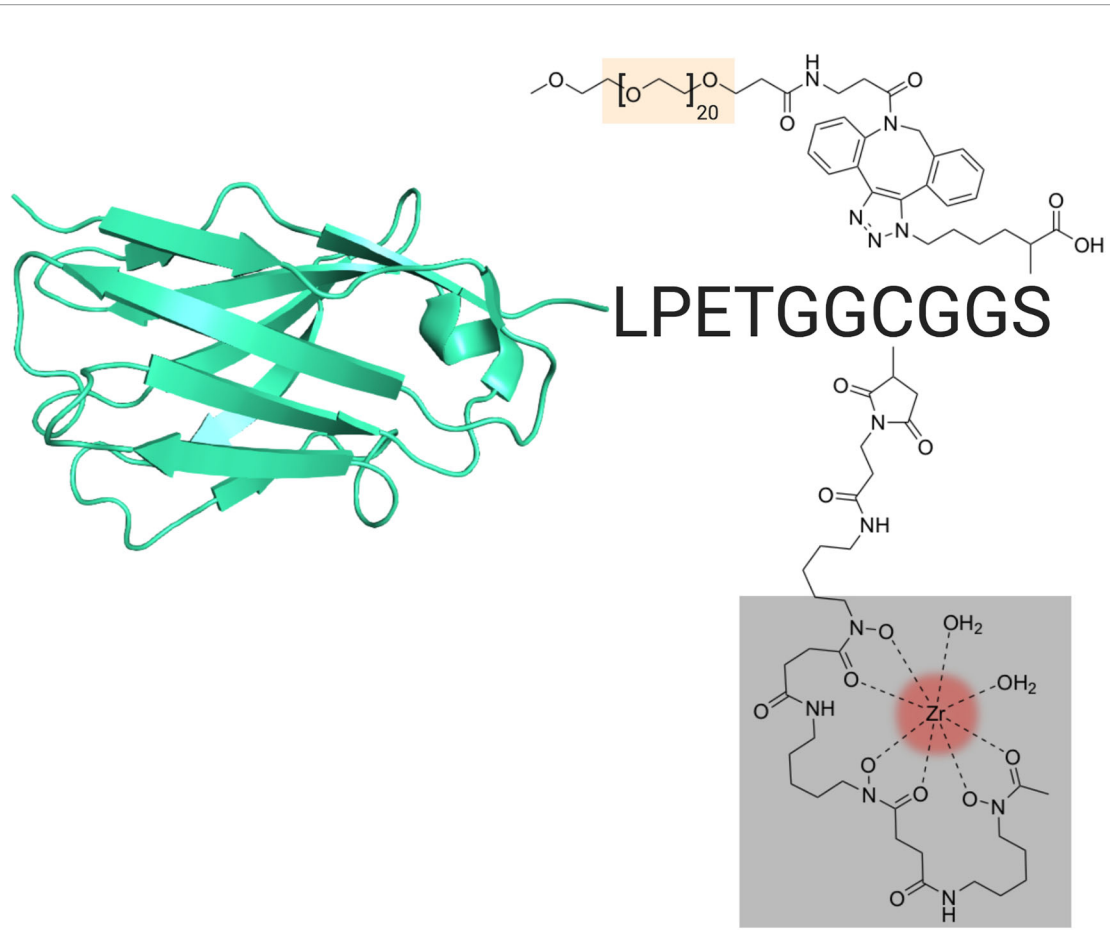

FIGURE 1 | VHH Construct and Design. Schematic of the VHH-X118 construct used to track $CD8^+$ T cells *in vivo*. A representative VHH structure (PDB: 3OGO) is shown covalently bound to the peptide probe LPETGGCGGS. Maleimido-DFO (grey), which was covalently linked to the peptide probe at the cysteine thiol, is shown chelating ^{89}Zr (red). A terminal, azide-substituted lysine was covalently modified with a PEG_{20} substrate (peach) for improved circulation.

variations in multiple experiments and across mice. CD8 signal intensity in the lungs increased during infection and remained elevated from days 6 through 12 of IAV infection. Lung signal decreased after day 12, as mice recovered from IAV infection. These results correlate with morbidity, as mice reached the peak of their weight loss in this interval (**Figure 2**, inset graphs). Similarly, we observed a trend towards an increase in CD8 signal intensity in the MLN beginning at 4 dpi, which reached significance ($P<0.05$) between days 9 and 15 of the infection, before eventually decreasing during the recovery phase of the infection (**Figures 3C, D**). An increase in CD8 signal intensity should be detectable in the MLN of infected mice prior to its appearance in the lungs, as T cells are activated in lymph nodes prior to migrating to the lungs in response to chemokines (32).

T Cells in Day 9-Infected Lungs Are Predominantly $CD8^+$ T_{EFF}/T_{EM} Cells

To characterize the population of infiltrating T cells at 9 dpi and uninfected mice, we performed flow cytometry on cells isolated from the lungs and MLN. The ratio of infiltrating $CD4^+$ versus $CD8^+$ T cells was determined by gating on the $CD3^+CD45^+$ population (**Figure 4A**). The number of infiltrating lymphocytes in the lungs of day 9-infected mice was significantly increased (**Figure 4C**), in agreement with the observed increase in PET signal. To better identify the T cell subset present in the infiltrating population and to establish the percentage of $CD44^+CD62L^+$ [central memory T cells (T_{CM})] and $CD44^+CD62L^-$ [effector T cells (T_{EFF}/T_{EM})] cells, we gated on either the $CD8^+$ or $CD4^+$ T cell population (**Figure 4B**). The majority of infiltrating $CD8^+$ and $CD4^+$ T cells in the lungs were $CD44^+CD62L^-$ (T_{EFF}/T_{EM}). No significant increase in $CD8^+CD44^+CD62L^+$(T_{CM}) was detected in the lungs of the infected animals (**Figure 4C**).

The Lung-Infiltrating Population Contains IAV-Specific T Cells

We next confirmed that IAV-specific T cell responses could be detected in the lungs, MLN, and spleen by using a peptide corresponding to the immunodominant H-$2D^b$-restricted IAV NP epitope, ASNENMETM, in an IFNγ ELISpot assay. As expected, we saw an increase in the number of IAV-specific $CD8^+$ T cells in the lungs, MLN, and spleen in infected mice (**Figure 4D**). We detected low levels of IFNγ-producing cells in

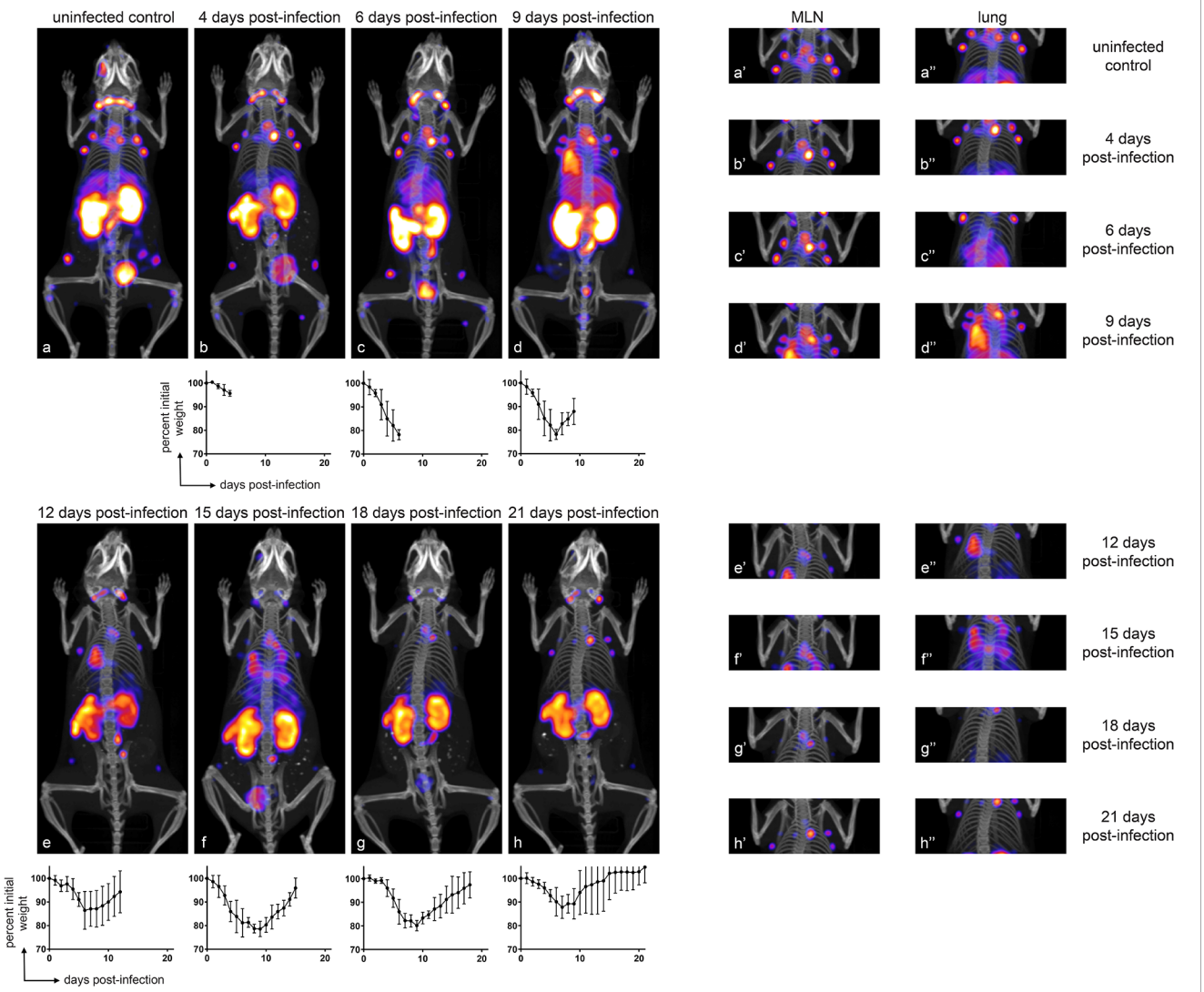

FIGURE 2 | $CD8^+$ T Cells Transiently Accumulate in the Lungs and MLN of IAV-Infected Mice, Correlating with Morbidity. Representative ($n \geq 3$) immuno-PET images of IAV WSN/33-infected mice (facing down) injected with ^{89}Zr-labeled VHH-X118-PEG_{20} on the indicated dpi. Graphs below immuno-PET images show percent initial weight for each day over the course of IAV infection for the cohort of animals. Insets to the right depict focused images of the MLN and lungs at the times indicated. Lower case letters link inset images to their corresponding full-body image, and single and double apostrophes indicate MLN and lung insets, respectively.

the media-only controls in the lungs from infected animals, presumably due to the persistence of antigen and/or previously activated IFNγ-producing T cells.

Distribution of Transferred $CD8^+$ T Cells Relies on the Mechanism of T Cell Activation and the Local Inflammatory Environment

Transfer of virus-specific $CD8^+$ T cells can clear IAV in a B cell-deficient mouse model (33). In such settings, the tissue distribution of donor $CD8^+$ T cells remains unclear. Does the inflamed environment of the lungs provide signals that direct and retain T cells? Do T cells instructed to deal with a pulmonary insult display lung homing properties, independent of whether the lungs are infected or not? In any case, little is known about the *in vivo* distribution of T cells immediately after transfer into recipients. We approached these questions by transfer of ^{89}Zr anti-CD8α-labeled $CD8^+$ T cells to trace their distribution in the recipients at 1 hour and 24 hours post-transfer, using whole-body immuno-PET imaging. T cells were harvested and purified from the lungs of IAV-infected mice 9 dpi, with additional negative selection steps to remove epithelial and endothelial cells, followed by cytofluorimetry to assess purity of the T cell population to be transferred. We likewise harvested splenocytes from uninfected control mice and purified $CD8^+$ T cells from them. These naïve T cells were then activated on plate-bound

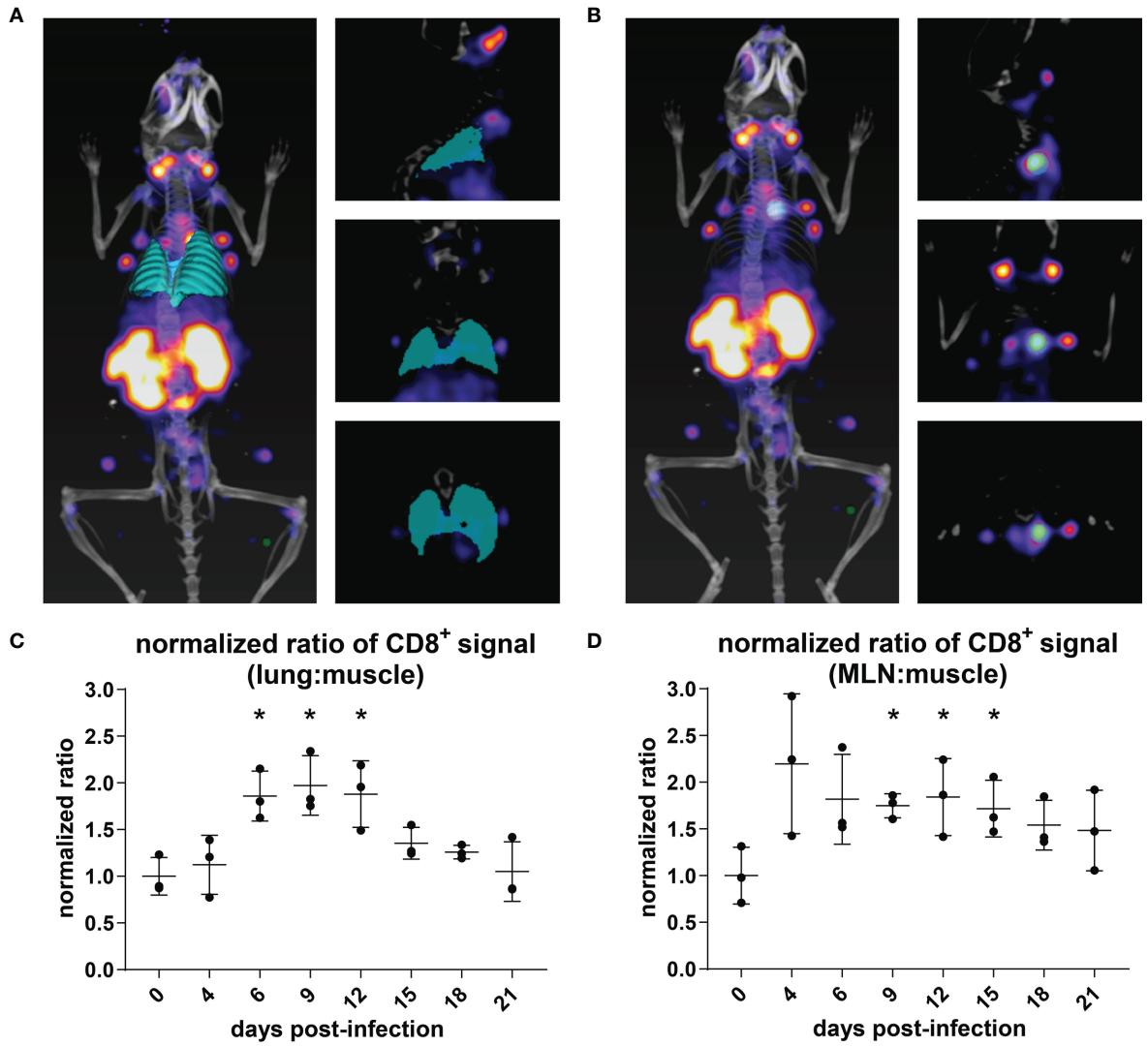

FIGURE 3 | Quantification of CD8$^+$ T Cell Immuno-PET Signal in the Lungs and MLN/Thymus. **(A, B)** The volume of the lungs (cyan) was determined using the VivoQuant 3D ROI tool in each mouse based on CT signal (white/grey) **(A)**. The volume of the MLN (cyan) was defined based on PET intensity **(B)**. In each mouse, PET intensity was normalized to background signal as defined by a ROI in the quadriceps muscle (green). Mice are shown facing down as 3D renderings (left) and in slices: frontal (top right), sagittal (middle right), and transverse (bottom right) ROI. **(C, D)** PET intensity from the lung ROI **(C)** for each day was normalized to the PET intensity of day 0, uninfected mice (n = 3). Student's t-tests were used to compare infected mice at each time point to uninfected mice. *P < 0.05.

anti-CD3 and anti-CD28, in medium supplemented with IL-2 (34). CD8$^+$ T cells from day 9-infected mice or activated CD8$^+$ T cells from control mice were labeled in suspension with ^{89}Zr-VHH-X118. Labeled cells were then transferred into either IAV-infected (4 dpi) or uninfected control mice *via* retro-orbital injection. PET images were acquired at 1 hour and 24 hours post-transfer (**Figure 5A**).

Upon transfer into day 4-infected recipient mice, *ex vivo* activated, control CD8$^+$ T cells initially localized to the lungs and spleen (**Figure 5B**, top panels). After 24 hours, the signal corresponding to CD8$^+$ T cells decreased in the lungs. Activated CD8$^+$ T cells generated from control splenocytes transferred into naïve mice localized mostly to the spleen and remained there after 24 hours. CD8$^+$ T cells from day 9-infected mice initially migrated to the lungs and spleen when transferred into day 4-infected and uninfected recipients, imaged 1 hour post-transfer (**Figure 5B**, bottom panels). After 24 hours, a signal corresponding to these CD8$^+$ T cells remained detectable in the lungs of day 4-infected mice and appeared to increase in intensity in the spleen and MLN. Uninfected mice also retained a signal corresponding to CD8$^+$ T cells from infected mice in their lungs 24 hours post-transfer, but to a lesser extent, probably due to the lack of an inflammatory environment. CD8$^+$ T cells harvested from day 9-infected mice did not initially populate the spleens of uninfected mice in large numbers, nor did they appear to migrate there over the 24 hour observation period.

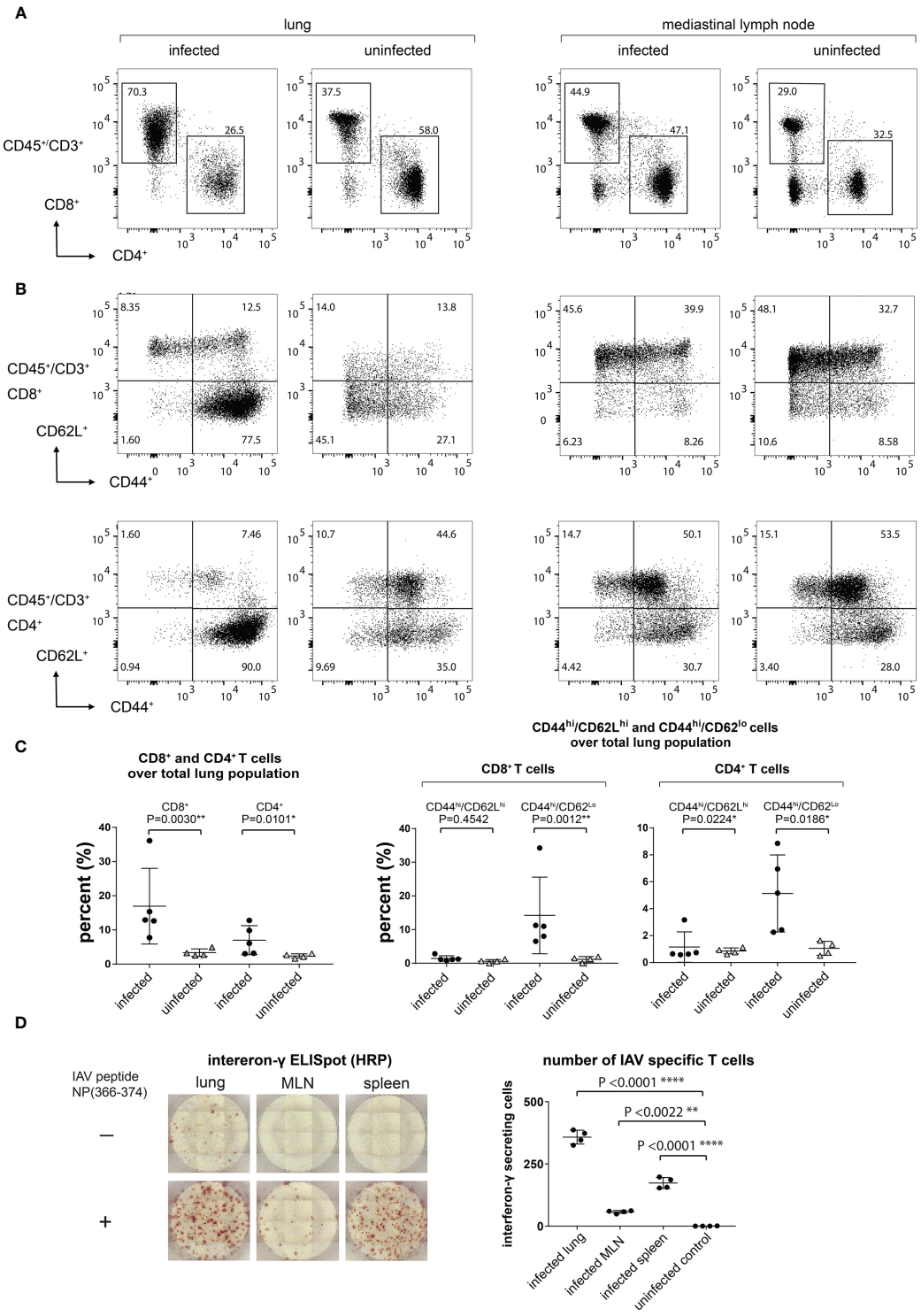

FIGURE 4 | Lung-Infiltrating Cells are Predominantly CD8$^+$ T_{EFF}/T_{EM} Cells, a Significant Amount of Which are IAV Specific. **(A)** The infiltrating T cells were gated on CD45$^+$CD3$^+$ and the ratio of CD4$^+$ and CD8$^+$ was determined. **(B)** CD8$^+$ and CD4$^+$ T_{EFF}/T_{EM} (CD44^{hi}CD62L^{lo}) and T_{CM} (CD44^{hi}CD62L^{hi}) were gated on CD45$^+$CD3$^+$CD4$^+$CD44$^+$CD62L$^-$ and CD45$^+$CD3$^+$CD8$^+$CD44$^+$CD62L$^+$. **(C)** Statistical analysis of data from **(A, B)**. **(D)** IAV-specific T cell responses in lungs, MLN, and spleen as determined by an ELISpot assay. Representative ELISpot wells are shown in the left panel and statistical analyses of lungs, MLN, and spleen IAV-specific T cells are shown in the right panel.

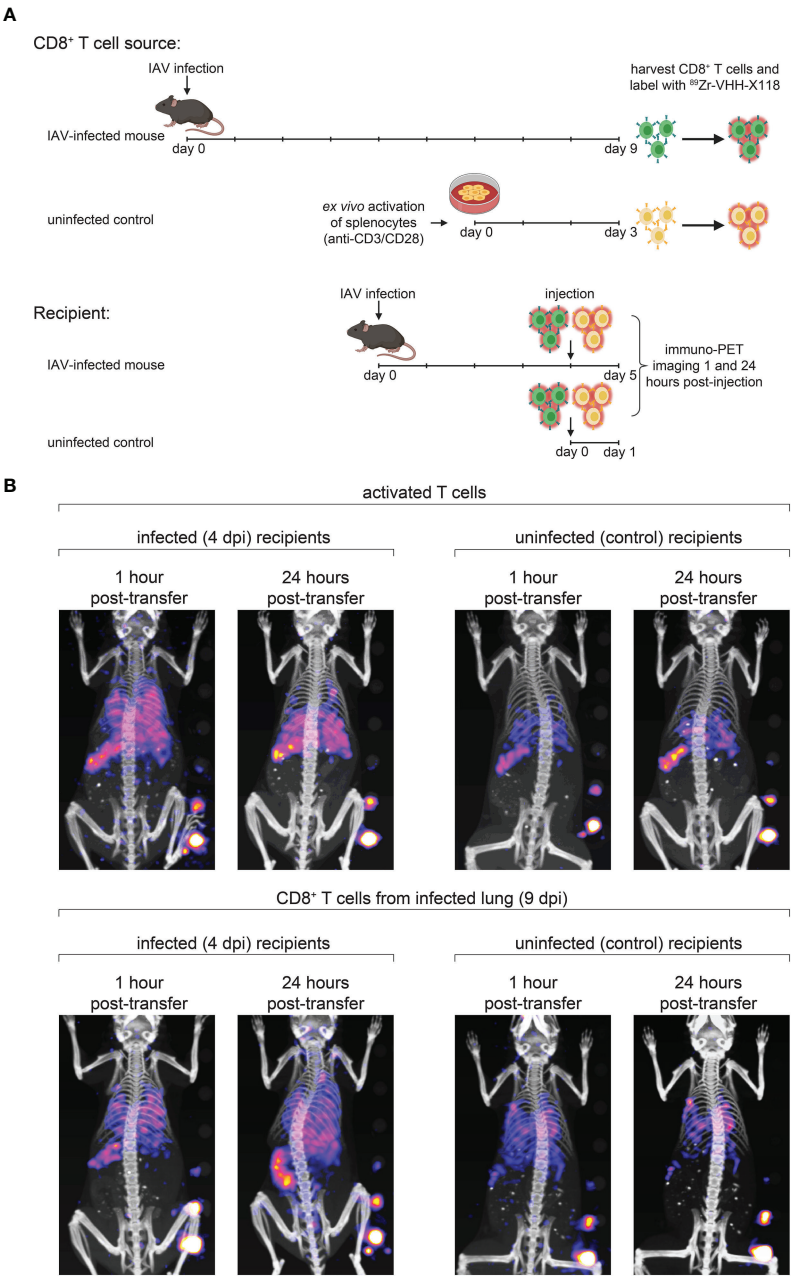

FIGURE 5 | Distribution of Transferred CD8$^+$ T Cells Relies on the Site of T Cell Maturation and Local Inflammatory Environment. **(A)** Schematic depicting CD8$^+$ T cell transfer experiments. Donor mice were infected with IAV WSN/33 and CD8$^+$ T cells were harvested from the lungs at 9 dpi. Harvested CD8$^+$ T cells were *ex vivo* labeled with ^{89}Zr-VHH-X118 and injected into day 4-infected or uninfected mice. As a control, CD8$^+$ T cells were purified from naïve splenocytes of uninfected mice, *ex vivo* activated, and injected into day 4-infected and uninfected mice. Mice were immuno-PET imaged 1 hour and 24 hours post-transfer. **(B)** Day 4-infected or uninfected recipient mice, shown face down, were immuno-PET imaged at the indicated times post-transfer of ^{89}Zr-labeled T cells from the indicated donor source. A standard with set amounts of radioactivity in 2-fold dilutions starting at 0.4 μCi is on the lower right side of each image. Data are representative of 2 experiments.

DISCUSSION

We determined the whole-body distribution of CD8$^+$ T cells in a living mouse in the course of infection with IAV. An increase in CD8$^+$ T cells was first detectable in lymph nodes, specifically the MLN, where CD8$^+$ T cells are activated by antigen presenting cells that present IAV-specific antigens (35). CD8$^+$ T cells then migrate to the lungs in response to chemotactic cues, where they can be detected diffusely, but in significant numbers at 6 dpi, when mice experience peak weight loss. At 9 dpi, CD8$^+$ T cells

showed more discrete sites of accumulation in the infected lungs. They remained there in elevated numbers until 12 dpi. $CD8^+$ T cells then left the lungs as mice recovered. The $CD8^+$ T cell signal remained elevated in the MLN throughout the infection, followed by a gradual decrease in signal strength as the infection waned.

Following viral infection, most pathogen-specific T cells undergo a process of contraction by apoptosis. A small fraction of the remaining antigen-specific T cells differentiate into memory cells (9). Effector memory T cells ($CD8^+CD44^+CD62L^-$) recirculate in the blood and non-lymphoid tissues. They protect the host against re-infection by their ability to kill cells infected with influenza virus and by the production of inflammatory cytokines at the site of infection (36). Central memory T cells ($CD8^+CD44^+CD62L^+$) take up residence in secondary lymphoid organs. They proliferate, differentiate, and migrate to new sites of infection (9). At 9 dpi with IAV, most $CD8^+$ T cells in the lungs are effector memory T cells.

As summarized in **Figure 6**, $CD8^+$ T cells obtained from IAV-infected mice (9 dpi), upon transfer, initially populate the lungs of both infected and uninfected mice. A CD8 signal remains detectable there after 24 hours. Lymphocyte function-associated antigen 1 (LFA-1) not only directs migration but also mediates retention of effector $CD8^+$ T cells in the lungs. LFA-1 interacts with intercellular adhesion molecules (ICAMs) on endothelial cells to allow leukocyte migration across the endothelium to sites of inflammation (37). Normal, healthy lung tissue supports retention of activated $CD8^+$ T cells. Indeed, ICAM-1, an LFA-1 ligand, is expressed in healthy lung tissue (38). In contrast, T cells activated *ex vivo* with anti-CD3 and anti-CD28 more transiently localized to the lungs of IAV-infected recipients, and did not populate the lungs of uninfected recipients in a manner that was detectable by immuno-PET imaging. This suggests that the inflamed status of the lungs provides signals, probably in the form of both soluble mediators and surface molecules, that allow retention of activated T cells, regardless of their specificity, whereas healthy lungs do not provide such cues. *Ex vivo* activated $CD8^+$ T cells initially populated the lungs of IAV-infected mice, presumably due to the pro-inflammatory signals resulting from infection. Signal is still detectable in the lungs 24 hours post-transfer, albeit of lesser intensity. We hypothesize that the absence of IAV antigens from control mice and the corresponding lack of continued engagement of the TCRs on transferred *ex vivo* activated T cells likely contribute to this phenotype. Further, the gene expression profiles of *ex vivo* activated and *in vivo* activated IAV-specific $CD8^+$ T cells likely differ, which may contribute to their ability to interact with lung-expressed retention ligands. It is also possible that IAV-specific $CD8^+$ T cells die upon transfer to uninfected recipients, which could explain why they appear to be retained in the lungs; however, it is unclear why antigen-specific $CD8^+$ T cells would die, while activated, non-specific T cells would retain the capacity to migrate post-transfer. These are subjects of future investigation.

In this study we show that ^{89}Zr-labeled single-domain antibody fragments can track the $CD8^+$ T cell response to IAV infection noninvasively in a living mouse. Nanobodies have several advantages for use in PET imaging when compared to intact Ig or Fab fragments. The small size of a nanobody (~12–16 kDa)

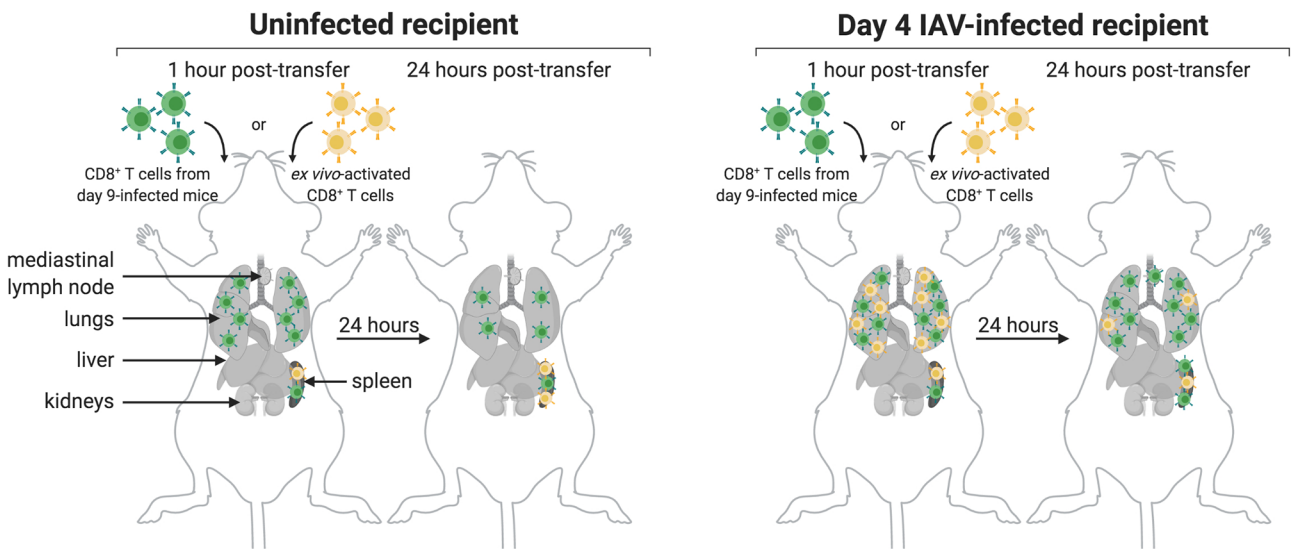

FIGURE 6 | Model of $CD8^+$ T Cell Transfer to Infected and Uninfected Mice. $CD8^+$ T cells transferred from day 9-infected mice (green) initially localize to the lungs and spleen of uninfected (left) and IAV-infected (right) mice. After 24 hours, these cells are retained in the lungs and spleen of both uninfected and infected mice, though retention is not as strong in the lungs of uninfected mice. Additionally, a subset of these cells migrates to the MLN of infected mice after 24 hours. Transferred *ex vivo* activated $CD8^+$ T cells (yellow) initially localize to the spleen of both uninfected and infected mice, and in both cases remain there after 24 hours. While these cells do not localize to the lungs of uninfected mice, they do transiently populate the lungs of infected mice; however, these cells are not retained in the lungs after 24 hours.

enables access to epitopes not available for binding to conventional Ig, provides improved tissue penetration, high stability, and rapid renal clearance from the body of unbound nanobodies (39–42). Further, nanobodies can be produced in high yield and in active form in bacteria (43). A possible drawback of nanobodies for *in vivo* use is their immunogenicity; while nanobodies are typically poorly immunogenic *in vivo*, this is not always the case. Even then, immunogenicity can often be modulated by modification of the framework regions of the construct (39, 40, 44, 45).

The platform used in this study is highly amenable to adaptation. Addition of a sortase recognition motif to the C-terminus of a nanobody enables rapid and efficient covalent modification of the nanobody. We used sortase to append a radiometal chelator to the nanobody of interest. Modification of this strategy is simple owing to the commercial availability of many different chelators with various functionalized handles. The sortase reaction also enabled us to append PEG_{20} to the nanobody of interest to increase circulatory half-life and decrease renal retention of the construct; PEGylation of a construct is not always required, and the size of the PEG moiety can be adjusted according to the needs of the experiment (43). The choice of available PET isotopes and their characteristic half-lives (^{68}Ga: ~60 min; ^{18}F: ~110 min; ^{64}Cu:~12 hrs; ^{89}Zr: ~3.3 days) sets differing observation windows, which can be matched to the immunological parameters of interest by the choice of a VHH of appropriate specificity.

We propose that immuno-PET can be used to study the immune response to any infection that induces $CD8^+$ T cells The signature advantage of this method is its noninvasiveness. More conventional methods require sacrificing the animals to enable organ retrieval by dissection. Additional VHHs can, of course, be developed against antigens from other animal models and can be used to track various immune cells. Because of this, we propose that immuno-PET can be utilized to monitor immune responses to vaccines and to garner a better understanding of their mechanisms of action.

DATA AVAILABILITY STATEMENT

The raw data supporting the conclusions of this article will be made available by the authors, without undue reservation.

ETHICS STATEMENT

The animal study was reviewed and approved by Boston Children's Hospital Institutional Animal Care and Use Committee.

AUTHOR CONTRIBUTIONS

PR, ZL, and HP contributed to conception and design of the study. Experiments were performed by PR and ZL with experimental assistance provided by NP, YX, AW, DB, SK, and VV. PR and ZL analyzed the data and performed statistical analyses with insight from NP and AW. PR, ZL, and HP drafted the manuscript with supportive feedback from NP, YX, AW, DB, SK, and VV. All authors contributed to the article and approved the submitted version.

ACKNOWLEDGMENTS

We thank the flow cytometry and sorting facility at Boston Children's Hospital for guidance and assistance. Some of the figures were created using BioRender.com.

SUPPLEMENTARY MATERIAL

The Supplementary Material for this article can be found online at: https://www.frontiersin.org/articles/10.3389/fimmu.2021.777739/full#supplementary-material

REFERENCES

1. Iuliano AD, Roguski KM, Chang HH, Muscatello DJ, Palekar R, Tempia S, et al. Estimates of Global Seasonal Influenza-Associated Respiratory Mortality: A Modelling Study. *Lancet* (2018) 391(10127):1285–300. doi: 10.1016/S0140-6736(17)33293-2
2. Belshe RB. The Origins of Pandemic Influenza–Lessons From the 1918 Virus. *N Engl J Med* (2005) 353(21):2209–11. doi: 10.1056/NEJMp058281
3. Eickhoff CS, Terry FE, Peng L, Meza KA, Sakala IG, Van Aartsen D, et al. Highly Conserved Influenza T Cell Epitopes Induce Broadly Protective Immunity. *Vaccine* (2019) 37(36):5371–81. doi: 10.1016/j.vaccine.2019.07.033
4. Knipe DM, Howley PM. *Fields Virology. 6th* Vol. 2. Philadelphia, PA: Wolters Kluwer/Lippincott Williams & Wilkins Health (2013).
5. Taubenberger JK, Morens DM. The Pathology of Influenza Virus Infections. *Annu Rev Pathol* (2008) 3:499–522. doi: 10.1146/annurev.pathmechdis.3.121806.154316
6. Chen X, Liu S, Goraya MU, Maarouf M, Huang S, Chen JL. Host Immune Response to Influenza A Virus Infection. *Front Immunol* (2018) 9:320. doi: 10.3389/fimmu.2018.00320
7. Iwasaki A, Pillai PS. Innate Immunity to Influenza Virus Infection. *Nat Rev Immunol* (2014) 14(5):315–28. doi: 10.1038/nri3665
8. Braciale TJ, Sun J, Kim TS. Regulating the Adaptive Immune Response to Respiratory Virus Infection. *Nat Rev Immunol* (2012) 12(4):295–305. doi: 10.1038/nri3166
9. Spitaels J, Roose K, Saelens X. In Fl Uenza and Memory T Cells: How to Awake the Force. *Vaccines (Basel)* (2016) 4(4). doi: 10.3390/vaccines4040033
10. Duan S, Thomas PG. Balancing Immune Protection and Immune Pathology by CD8(+) T-Cell Responses to Influenza Infection. *Front Immunol* (2016) 7:25. doi: 10.3389/fimmu.2016.00025
11. Hufford MM, Kim TS, Sun J, Braciale TJ. The Effector T Cell Response to Influenza Infection. *Curr Top Microbiol Immunol* (2015) 386:423–55. doi: 10.1007/82_2014_397
12. Wiley JA, Cerwenka A, Harkema JR, Dutton RW, Harmsen AG. Production of Interferon-Gamma by Influenza Hemagglutinin-Specific CD8 Effector T Cells Influences the Development of Pulmonary Immunopathology. *Am J Pathol* (2001) 158(1):119–30. doi: 10.1016/S0002-9440(10)63950-8
13. Cook DN, Beck MA, Coffman TM, Kirby SL, Sheridan JF, Pragnell IB, et al. Requirement of MIP-1 Alpha for an Inflammatory Response to Viral Infection. *Science* (1995) 269(5230):1583–5. doi: 10.1126/science.7667639
14. Damjanovic D, Divangahi M, Kugathasan K, Small CL, Zganiacz A, Brown EG, et al. Negative Regulation of Lung Inflammation and Immunopathology by TNF-Alpha During Acute Influenza Infection. *Am J Pathol* (2011) 179 (6):2963–76. doi: 10.1016/j.ajpath.2011.09.003
15. DeBerge MP, Ely KH, Enelow RI. Soluble, But Not Transmembrane, TNF-Alpha Is Required During Influenza Infection to Limit the Magnitude of Immune Responses and the Extent of Immunopathology. *J Immunol* (2014) 192(12):5839–51. doi: 10.4049/jimmunol.1302729

16. Hussell T, Pennycook A, Openshaw PJ. Inhibition of Tumor Necrosis Factor Reduces the Severity of Virus-Specific Lung Immunopathology. *Eur J Immunol* (2001) 31(9):2566–73. doi: 10.1002/1521-4141(200109)31:9<2566::AID-IMMU2566>3.0.CO;2-L
17. Menten P, Wuyts A, Van Damme J. Macrophage Inflammatory Protein-1. *Cytokine Growth Factor Rev* (2002) 13(6):455–81. doi: 10.1016/S1359-6101(02)00045-X
18. Peper RL, Van Campen H. Tumor Necrosis Factor as a Mediator of Inflammation in Influenza A Viral Pneumonia. *Microb Pathog* (1995) 19 (3):175–83. doi: 10.1006/mpat.1995.0056
19. Wright BD, Lapi SE. Designing the Magic Bullet? The Advancement of Immuno-PET Into Clinical Use. *J Nucl Med* (2013) 54(8):1171–4. doi: 10.2967/jnumed.113.126086
20. van Dongen GA, Visser GW, Lub-de Hooge MN, de Vries EG, Perk LR. Immuno-PET: A Navigator in Monoclonal Antibody Development and Applications. *Oncologist* (2007) 12(12):1379–89. doi: 10.1634/theoncologist.12-12-1379
21. Rashidian M, Ingram JR, Dougan M, Dongre A, Whang KA, LeGall C, et al. Predicting the Response to CTLA-4 Blockade by Longitudinal Noninvasive Monitoring of CD8 T Cells. *J Exp Med* (2017) 214(8):2243–55. doi: 10.1084/jem.20161950
22. Van Elssen C, Rashidian M, Vrbanac V, Wucherpfennig KW, Habre ZE, Sticht J, et al. Noninvasive Imaging of Human Immune Responses in a Human Xenograft Model of Graft-Versus-Host Disease. *J Nucl Med* (2017) 58 (6):1003–8. doi: 10.2967/jnumed.116.186007
23. Rashidian M, Keliher E, Dougan M, Juras PK, Cavallari M, Wojtkiewicz GR, et al. The Use of (18)F-2-Fluorodeoxyglucose (FDG) to Label Antibody Fragments for Immuno-PET of Pancreatic Cancer. *ACS Cent Sci* (2015) 1 (3):142–7. doi: 10.1021/acscentsci.5b00121
24. Guimaraes CP, Witte MD, Theile CS, Bozkurt G, Kundrat L, Blom AE, et al. Site-Specific C-Terminal and Internal Loop Labeling of Proteins Using Sortase-Mediated Reactions. *Nat Protoc* (2013) 8(9):1787–99. doi: 10.1038/nprot.2013.101
25. Schmidt FI, Hanke L, Morin B, Brewer R, Brusic V, Whelan SP, et al. Phenotypic Lentivirus Screens to Identify Functional Single Domain Antibodies. *Nat Microbiol* (2016) 1(8):16080. doi: 10.1038/nmicrobiol.2016.80
26. Rashidian M, Keliher EJ, Bilate AM, Duarte JN, Wojtkiewicz GR, Jacobsen JT, et al. Noninvasive Imaging of Immune Responses. *Proc Natl Acad Sci USA* (2015) 112(19):6146–51. doi: 10.1073/pnas.1502609112
27. Blachere NE, Orange DE, Gantman EC, Santomasso BD, Couture GC, Ramirez-Montagut T, et al. T Cells Presenting Viral Antigens or Autoantigens Induce Cytotoxic T Cell Anergy. *JCI Insight* (2017) 2(21). doi: 10.1172/jci.insight.96173
28. Rotzschke O, Falk K, Deres K, Schild H, Norda M, Metzger J, et al. Isolation and Analysis of Naturally Processed Viral Peptides as Recognized by Cytotoxic T Cells. *Nature* (1990) 348(6298):252–4. doi: 10.1038/348252a0
29. Antos JM, Ingram J, Fang T, Pishesha N, Truttmann MC, Ploegh HL. Site-Specific Protein Labeling *via* Sortase-Mediated Transpeptidation. *Curr Protoc Protein Sci* (2017) 89:15 3 1– 3 9. doi: 10.1002/cpps.38
30. Vegt E, de Jong M, Wetzels JF, Masereeuw R, Melis M, Oyen WJ, et al. Renal Toxicity of Radiolabeled Peptides and Antibody Fragments: Mechanisms, Impact on Radionuclide Therapy, and Strategies for Prevention. *J Nucl Med* (2010) 51(7):1049–58. doi: 10.2967/jnumed.110.075101
31. D'Huyvetter M, Xavier C, Caveliers V, Lahoutte T, Muyldermans S, Devoogdt N. Radiolabeled Nanobodies as Theranostic Tools in Targeted Radionuclide Therapy of Cancer. *Expert Opin Drug Delivery* (2014) 11(12):1939–54. doi: 10.1517/17425247.2014.941803
32. Lawrence CW, Braciale TJ. Activation, Differentiation, and Migration of Naive Virus-Specific CD8+ T Cells During Pulmonary Influenza Virus Infection. *J Immunol* (2004) 173(2):1209–18. doi: 10.4049/jimmunol.173.2.1209
33. Graham MB, Braciale TJ. Resistance to and Recovery From Lethal Influenza Virus Infection in B Lymphocyte-Deficient Mice. *J Exp Med* (1997) 186 (12):2063–8. doi: 10.1084/jem.186.12.2063
34. Xie YJ, Dougan M, Jailkhani N, Ingram J, Fang T, Kummer L, et al. Nanobody-Based CAR T Cells That Target the Tumor Microenvironment Inhibit the Growth of Solid Tumors in Immunocompetent Mice. *Proc Natl Acad Sci USA* (2019) 116(16):7624–31. doi: 10.1073/pnas.1817147116
35. Hamilton-Easton A, Eichelberger M. Virus-Specific Antigen Presentation by Different Subsets of Cells From Lung and Mediastinal Lymph Node Tissues of Influenza Virus-Infected Mice. *J Virol* (1995) 69(10):6359–66. doi: 10.1128/jvi.69.10.6359-6366.1995
36. Sallusto F, Lenig D, Forster R, Lipp M, Lanzavecchia A. Two Subsets of Memory T Lymphocytes With Distinct Homing Potentials and Effector Functions. *Nature* (1999) 401(6754):708–12. doi: 10.1038/44385
37. Smith A, Stanley P, Jones K, Svensson L, McDowall A, Hogg N. The Role of the Integrin LFA-1 in T-Lymphocyte Migration. *Immunol Rev* (2007) 218:135–46. doi: 10.1111/j.1600-065X.2007.00537.x
38. Dixon AE, Mandac JB, Martin PJ, Hackman RC, Madtes DK, Clark JG. Adherence of Adoptively Transferred Alloreactive Th1 Cells in Lung: Partial Dependence on LFA-1 and ICAM-1. *Am J Physiol Lung Cell Mol Physiol* (2000) 279(3):L583–91. doi: 10.1152/ajplung.2000.279.3.L583
39. Smolarek D, Bertrand O, Czerwinski M. Variable Fragments of Heavy Chain Antibodies (VHHs): A New Magic Bullet Molecule of Medicine? *Postepy Hig Med Dosw (Online)* (2012) 66:348–58. doi: 10.5604/17322693.1000334
40. Hassanzadeh-Ghassabeh G, Devoogdt N, De Pauw P, Vincke C, Muyldermans S. Nanobodies and Their Potential Applications. *Nanomed (Lond)* (2013) 8(6):1013–26. doi: 10.2217/nnm.13.86
41. Beltran Hernandez I, Rompen R, Rossin R, Xenaki KT, Katrukha EA, Nicolay K, et al. Imaging of Tumor Spheroids, Dual-Isotope SPECT, and Autoradiographic Analysis to Assess the Tumor Uptake and Distribution of Different Nanobodies. *Mol Imaging Biol* (2019) 21(6):1079–88. doi: 10.1007/s11307-019-01320-x
42. Debie P, Lafont C, Defrise M, Hansen I, van Willigen DM, van Leeuwen FWB, et al. Size and Affinity Kinetics of Nanobodies Influence Targeting and Penetration of Solid Tumours. *J Control Release* (2020) 317:34–42. doi: 10.1016/j.jconrel.2019.11.014
43. Harmand TJ, Islam A, Pishesha N, Ploegh HL. Nanobodies as *In Vivo*, Non-Invasive, Imaging Agents. *RSC Chem Biol* (2021) 2(3):685–701. doi: 10.1039/D1CB00023C
44. Vincke C, Loris R, Saerens D, Martinez-Rodriguez S, Muyldermans S, Conrath K. General Strategy to Humanize a Camelid Single-Domain Antibody and Identification of a Universal Humanized Nanobody Scaffold. *J Biol Chem* (2009) 284(5):3273–84. doi: 10.1074/jbc.M806889200
45. Vaneycken I, D'Huyvetter M, Hernot S, De Vos J, Xavier C, Devoogdt N, et al. Immuno-Imaging Using Nanobodies. *Curr Opin Biotechnol* (2011) 22(6):877–81. doi: 10.1016/j.copbio.2011.06.009

Conflict of Interest: The authors declare that the research was conducted in the absence of any commercial or financial relationships that could be construed as a potential conflict of interest.

Publisher's Note: All claims expressed in this article are solely those of the authors and do not necessarily represent those of their affiliated organizations, or those of the publisher, the editors and the reviewers. Any product that may be evaluated in this article, or claim that may be made by its manufacturer, is not guaranteed or endorsed by the publisher.

frontiers in Immunology

ORIGINAL RESEARCH
published: 05 November 2021
doi: 10.3389/fimmu.2021.736479

Sinomenine Relieves Airway Remodeling By Inhibiting Epithelial-Mesenchymal Transition Through Downregulating TGF-β1 and Smad3 Expression *In Vitro* and *In Vivo*

Hongjuan He[1], *Lihua Cao*[1], *Zheng Wang*[1], *Zhenzhen Wang*[1], *Jinxin Miao*[1], *Xiu-Min Li*[2]* *and Mingsan Miao*[1]*

[1] Academy of Chinese Medical Sciences, Henan University of Chinese Medicine, Zhengzhou, China, [2] Microbiology and Immunology, and Department of Otolaryngology, New York Medical College, New York, NY, United States

OPEN ACCESS

Edited by:
Roberto Weigert, National Cancer Institute, United States

Reviewed by:
Sutapa Sarkar, Stanford University, United States
Christina Stuelten, National Cancer Institute (NCI), United States

***Correspondence:**
Mingsan Miao
miaomingsan@hactcm.edu.cn
Xiu-Min Li
XiuMin_Li@NYMC.EDU

Specialty section:
This article was submitted to Inflammation, a section of the journal Frontiers in Immunology

Received: *05 July 2021*
Accepted: *14 October 2021*
Published: *05 November 2021*

Citation:
He H, Cao L, Wang Z, Wang Z, Miao J, Li X-M and Miao M (2021) Sinomenine Relieves Airway Remodeling By Inhibiting Epithelial-Mesenchymal Transition Through Downregulating TGF-β1 and Smad3 Expression In Vitro and In Vivo. Front. Immunol. 12:736479. doi: 10.3389/fimmu.2021.736479

Airway remodeling is associated with dysregulation of epithelial-mesenchymal transition (EMT) in patients with asthma. Sinomenine (Sin) is an effective, biologically active alkaloid that has been reported to suppress airway remodeling in mice with asthma. However, the molecular mechanisms behind this effect remain unclear. We aimed to explore the potential relationship between Sin and EMT in respiratory epithelial cells *in vitro* and *in vivo*. First, 16HBE cells were exposed to 100 μg/mL LPS and treated with 200 μg/mL Sin. Cell proliferation, migration, and wound healing assays were performed to evaluate EMT, and EMT-related markers were detected using Western blotting. Mice with OVA-induced asthma were administered 35 mg/kg or 75 mg/kg Sin. Airway inflammation and remodeling detection experiments were performed, and EMT-related factors and proteins in the TGF-β1 pathway were detected using IHC and Western blotting. We found that Sin suppressed cell migration but not proliferation in LPS-exposed 16HBE cells. Sin also inhibited MMP7, MMP9, and vimentin expression in 16HBE cells and respiratory epithelial cells from mice with asthma. Furthermore, it decreased OVA-specific IgE and IL-4 levels in serum, relieved airway remodeling, attenuated subepithelial collagen deposition, and downregulating TGF-β1and Smad3 expression in mice with asthma. Our results suggest that Sin suppresses EMT by inhibiting IL-4 and downregulating TGF-β1 and Smad3 expression.

Keywords: Sinomenine, airway remodeling, asthma, EMT, TGF-β1/Smad3 expression

INTRODUCTION

Asthma, a chronic inflammatory disease of the airways, is a common heterogeneous disease that affects approximately 300 million people worldwide, resulting in 250,000 deaths per year and billions of dollars in medical expenses (1, 2). Through the involvement of various immune and structural cells, including mast cells, eosinophils, and epithelial cells, it causes pathological changes

such as airway inflammation, mucus metaplasia, subepithelial fibrosis, airway hyper-responsiveness (AHR), and airway wall remodeling (3). Among these, airway inflammation and airway remodeling are the two main pathological features of asthma.

Airway remodeling refers to airway structural change that occurs in patients with asthma induced by persistent inflammation during injury and repair processes (4). It is characterized by airway wall thickening, subepithelial collagen deposition, and excessive mucus secretion (5). Airway remodeling largely causes airflow limitation and airway obstruction, endangering the lives of patients with severe asthma. Currently, most patients are well controlled and improved by well-established treatments, such as inhaled corticosteroids (ICS) and β2-adrenergic agonists. While these first-line treatments demonstrate potent anti-inflammatory effects, they are not very effective for treating airway remodeling (6). Unfortunately, approximately 10% of patients with asthma are poorly controlled, putting them at increased risk of hospitalization due to bronchial wall remodeling and airway constriction (7, 8). To prevent the progression of airway remodeling in the early stages and reduce disease severity, understanding the mechanism behind airway remodeling and identifying useful therapies are urgent (9).

Recently, it has been demonstrated that airway remodeling is associated with dysregulation of epithelial-mesenchymal transition (EMT) (10). EMT is a complex process related to tissue remodeling, in which epithelial cells gradually transform into mesenchymal-like cells through the loss of epithelial functionalities of cell-cell adhesion and polarity as well as gain of migration and invasion abilities (11, 12). During this process, biomarkers of epithelial cells, such as E-cadherin, are repressed, whereas mesenchymal markers, including vimentin, MMP7, MMP9, and alpha-smooth muscle actin (α-SMA), are upregulated. It is a novel clinical therapeutic target that is also activated in wound healing, cancer progression, and severe chronic airway diseases such as asthma and chronic obstructive pulmonary disease (COPD) (11). EMT occurs due to the stimulation of certain inflammatory factors and influence of various signaling pathways. In asthma, allergen-specific T cells are activated, and T helper type 2 (Th2) cytokines are secreted. Th17 cells are also known to modulate the disease. These cytokines interact with their receptors, activate their downstream transcription factors, increase EMT-related factors, and induce changes in airway thickness (13).

Chinese medicine has been widely used to treat bronchitis and bronchial asthma for thousands of years (14). Some traditional Chinese medicines (TCMs) have been found to inhibit airway remodeling and pulmonary fibrosis progression in asthma and COPD by targeting EMT (15, 16). Sinomenine (Sin) is an effective, biologically active alkaloid isolated from the roots and stems of the TCM Qingfengteng, also known as the climbing plant *Sinomenium acutum*. Sin has been found to demonstrate anti-inflammatory, immunosuppressive, and anti-arrhythmic effects. It was also reported to suppress collagen-induced arthritis by inhibiting Th17 factors and increasing numbers of Treg cells (17). While it has also been found to ameliorate airway remodeling in mice with asthma, the underlying molecular mechanism remains unclear (18). The aim of the present study was to explore the potential relationship between Sin and the EMT process in respiratory epithelial cells through *in vitro* and *in vivo* studies. It was found that Sin relieved airway remodeling by inhibiting EMT through downregulating the TGF-β1 and Smad3 expression.

MATERIALS AND METHODS

Cell Culture and EMT Induction

Human bronchial epithelial cells (16HBE) were purchased from ATCC (Manassas, VA, USA) and cultured in DMEM medium (Gibco, UK) with 10% FBS (Gibco, UK) at 37°C in a humidified incubator containing 5% CO_2. To induce EMT, the 16HBE cells were treated for 72 h with the following concentrations of LPS (Sigma-Aldrich, USA): 10, 20, 50, and 100 μg/mL. The cells were divided into four independent treatment groups: a control group, 100 μg/mL LPS group, 100 μg/mL LPS with 200 μg/mL Sin group, and 200 μg/mL Sin group.

Cell Viability and Proliferation Assays

The cell viabilities of 16HBE cells treated with Sin were evaluated using the cell counting kit-8 (CCK8) assay (Dojindo, Japan) (19). A total of 2 ×104 16HBE cells were cultured in 96-well plates overnight until complete adherence to the walls. The cells were then incubated with Sin at final concentrations of 0, 2, 10,20, 100, 200, 500, 1000, and 2000 μg/mL for 24 h. The media were removed, and the cells were incubated with 10% CCK8 solution (Dojindo, Kyushu, Japan) for 4 h. Absorbances at 450 nm were then measured.

For proliferation assay, a total of 1×10^4 cells per well were seeded in a 96-well plate, treated with the four abovementioned treatments with six replicates, and incubated for 0, 24, 48, and 72 h. The cells were then evaluated *via* CCK8 assay, as previously described.

Wound Healing Assay

Cell migration ability was evaluated using a previously described wound healing assay (20). After growing the 16HBE cells to 90% confluence in six-well plates, the cell layers were horizontally scraped using a sterile 10 μL pipette tip across the plate. The plates were then washed with DMEM to remove debris from the straight wound area. They were then incubated with the four abovementioned independent treatments in DMEM supplemented with 2% FBS. Images of six randomly chosen fields in each wound were captured using a light microscope at 100× magnification (0 and 24 h). The migration proportion of adjacent cells to the wound area was calculated using ImageJ software.

Migration Assay

A cell migration assay was carried out in 24-well Transwell chambers with an 8 μm pore polycarbonate membrane filter (Corning, NY, USA), as described elsewhere (21). A total of 6×10^4 16HBE cells were cultured in the upper wells with no more than 200 μL serum-free medium. The bottom chambers were

filled with 800 μL 10% FBS medium with the four abovementioned treatments. After incubation for 48 h, the migrated cells on the membrane filter were washed with phosphate buffered saline (PBS) solution, fixed with 4% paraformaldehyde for 30 min, and stained with 1% crystal violet (Amresco, Solon, OH) for 10 min. After washing and air drying, the cells were observed and photographed at 100× magnification using a microscope. The numbers of migrated cells were calculated based on six random fields per well using ImageJ software (National Institutes of Health, MD).

OVA-Induced Asthma Model

A total of 32 six-week-old female BALB/c mice were purchased from Beijing Weitong Lihua Laboratory Animal Technology Co., Ltd. (China), fed commercial diets, and maintained under an ambient temperature of 23 ± 3°C and 12 h light/dark cycle. All animal experiments complied with the ARRIVE guidelines, "British Animal (Scientific Procedure) Act of 1986", EU Directive 2010/63/EU, and related guidelines. All procedures described were approved by the Animal Welfare Ethics Committee of the Henan University of Chinese Medicine. The mice were randomly divided into four groups (8 mice per group): negative control, asthma, asthma with high-dose Sin (75 mg/kg), and asthma with low–dose Sin (35 mg/kg) groups.

Asthma was induced using ovalbumin (OVA, grade V, Sigma–Aldrich, USA) as previously described (9, 22). The mice were sensitized by intraperitoneal injection (i.p.) of 100 μg OVA emulsified in 2 mg Imject Alum Adjuvant (Thermo, USA) diluted in 200 μL PBS on days 0 and 7. Subsequently, the mice were intratracheally challenged with 100 μg OVA in 20 μL PBS on days 14, 17, and 20, followed by twice weekly challenges for four weeks. The control group was sensitized and challenged with PBS at the same time points. Sin was dissolved in 200 μL normal saline and intragastrically (i.g.) administered once daily from day 15–49. All mice were sacrificed 24 h after the final challenge.

Enzyme-Linked Immunosorbent Assay

The serum was collected and centrifuged for 15 min at 12000 rpm to examine the levels of immunoglobulin E (IgE) and other cytokines. OVA-specific IgE as well as levels of IL-4, IL-6, and IL-10 in the serum were measured using a mouse IgE ELISA development kit (Mabtech, USA) and a mouse ELISA kit (Mabtech), respectively.

Histological and Immunohistochemical Analysis

The left lung lobes were fixed in 4% paraformaldehyde and cut into 5 μm sections for histological examination and immunohistochemistry (IHC). To assess the degree of inflammation and airway remodeling, hematoxylin and eosin (H&E) staining was performed. The total area of the airway wall and the perimeter of the basement membrane (Wat/Pbm) were measured to evaluate airway remodeling (23). Masson's trichrome staining was performed to semi-quantitatively assess subepithelial collagen deposition (1, 10). The histological analyses were performed by two independent observers.

IHC was performed as previously reported (10). Briefly, the paraffin-fixed lung sections were permeabilized with 0.02% Triton X-100 (Sigma) in PBS and then blocked with 10% normal goat serum and 2% BSA in PBS. Then, the sections were incubated with primary antibodies overnight at 4°C, with MMP9 (Abways, 1:100), MMP7 (Abways, 1:100), vimentin (Abways, 1:100), TGF-β1 (Immunoway, 1:100), Smad2 (Abways, 1:100), Smad3 (Abways, 1:100) and p-Smad3 (S423/S425, Abclonal, 1:100); immunized with HRP-conjugated goat anti-rabbit IgG secondary antibodies; and visualized with diaminobenzidine (DAB). The sections were then counterstained, dehydrated, mounted on microscope slides, and imaged under a microscope. The expression levels were semi-quantitatively scored as previously reported (21).

Western Blotting

Total proteins from 16HBE cells or right lung tissues of mice were extracted using RIPA lysis buffer supplemented with 1% protease inhibitor (Roche Applied Science) and quantified using the BCA method. They were then diluted in 5× loading buffer, denatured, and separated *via* 10% SDS-polyacrylamide gel electrophoresis. An amount of 20 mg total protein was transferred to polyvinylidene difluoride membranes (Millipore, Billerica, MA, USA). Primary antibodies anti-MMP9 (1:1000 dilution, Abways), anti-MMP7 (1:1000 dilution, Abways), anti-vimentin (1:1000 dilution, Abways), TGF-β1 *(*Immunoway, 1:1000*)*, Smad3 (1:1000 dilution, Abways), GAPDH (1:5000 dilution, Abways), and secondary goat anti-rabbit antibody Abways, 1:10000*)* were used. The images were illuminated with enhanced chemiluminescence reagent (Epizyme, Shanghai, China) and visualized using an Amersham imager 600 (GE Healthcare, Freiburg, Germany). The gray values of the protein bands were calculated using ImageJ software.

Statistical Analysis

All experiments were performed at least in triplicate and all the values are expressed as mean ± standard error of mean (SEM). The differences among different groups were analyzed using one-way analysis of variance followed by Dunnett's Multiple Comparison Test. If the data were not normality distribution, non-parametric multiple comparison was applied to compare differences among different groups. All statistical analyses were performed using GraphPad Prism software (version 8.0; GraphPad Software Inc., San Diego, CA, USA). Statistical significance was set at $p < 0.05$.

RESULTS

Sin Inhibited Cell Migration but Not Proliferation in LPS-Exposed 16HBE Cells

Airway epithelial cells are the primary targets for the inhaled environmental allergens and can produce Th2 innate cytokines to trigger allergic reactions (24). The chronic exposure of repetitive environmental injury may lead to persistent activation of pathways involved in airway epithelial repair, such as epithelial to mesenchymal transition, changes in

progenitor cell migration and proliferation, and abnormal redifferentiation leading to airway remodeling (25). Lipopolysaccharide (LPS) produced by bacterial infections can exacerbate asthmatic inflammation and induce airway remodeling (26). LPS was reported to induce the proliferation, differentiation, and migration process of intestinal epithelial cell (27). In our study, we firstly suggested that LPS can promote the proliferation and migration ability of the human 16HBE cells. To explore the effect of Sin on airway remodeling, we evaluated its effect on the proliferation and migration ability induced by LPS. The viabilities of the HBE16 cells were not compromised when treated with doses of Sin less than 200 μg/mL (**Figure 1A**). The proliferation abilities of the 16HBE cells were significantly increased after stimulation with 100 μg/mL LPS. Sin did not significantly influence this effect (**Figure 1B**). However, Sin significantly inhibited LPS-induced cell motility as seen in the wound healing assay (**Figures 1C, D**). Moreover, it also inhibited LPS-induced cell migration (**Figures 1E, F**).

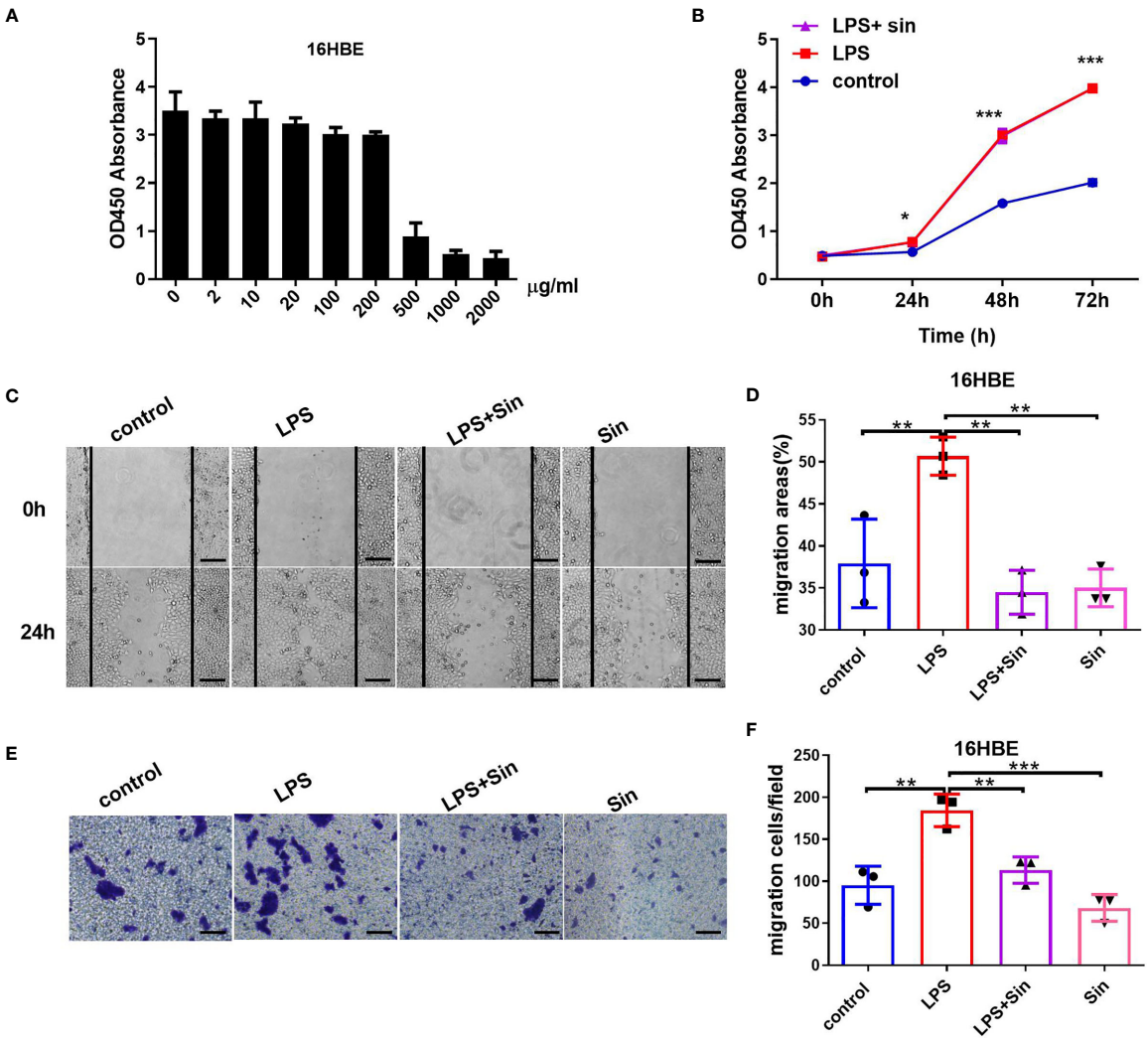

FIGURE 1 | Sin inhibited cell migration but not proliferation in LPS-exposed 16HBE cells. **(A)** A total of 2×10^4 16HBE cells were seeded in 96-well plates and stimulated with Sin at concentrations of 0, 2, 10, 20, 100, 200, 500, 1000, 2000 μg/mL for 24 h. Cell viability was analyzed using a CCK-8 assay. The OD450 values of the cells stimulated at different doses are shown in the Y-axis. **(B)** A total of 1×10^4 16HBE cells were seeded in 96-well plates and divided into three groups: 100 μg/mL LPS, 100 μg/mL LPS and 200 μg/mL Sin, control (untreated) group. Cell proliferation ability was analyzed using a CCK-8 assay. The OD450 values of the cells at 0, 24, 48, and 72 h were detected and shown by the ordinate. **(C)** The cell layers were horizontally scraped using a sterile 10 μL pipette tip upon reaching 90% confluence in six-well plates. Images of the wound areas were captured at 0 and 24 h after stimulation. **(D)** Migration area was measured to analyze cell migration. **(E)** A total of 6×10^4 HBE16 cells were seeded onto the upper wells with no more than 200 μL serum-free medium. The bottom chamber was filled with 800 μL 10% FBS medium with 100 μg/mL LPS, 100 μg/mL LPS with 200 μg/mL Sin, 200 μg/mL Sin, or 10% FBS medium. The migrated cells were observed and captured at 100× magnification after 48 h. **(F)** Numbers of migration cells were counted from 6 randomly chosen fields. Scale bar indicates 200 μm. The data are presented as mean ± SEM from three independent experiments. The one-way analysis of variance followed by Dunnett's Multiple Comparison Test was used. *$p < 0.05$. **$p < 0.01$. ***$p < 0.001$.

Sin Inhibited EMT in LPS-Exposed Human Airway Epithelial Cells

In order to further study the effect of Sin on EMT of 16HBE, we examined the EMT process induced by LPS exposure and detected the expression of EMT related biomarkers. Matrix metalloproteinase 9 (MMP9) was expressed by bronchial epithelium which may promote airway eosinophil infiltration and degrade the extracellular matrix (ECM)during the remodeling (18). MMP7 was identified to regulate wound repair process and was quickly upregulated after injury, which was associated with various mucosal immune processes (28). Upon evaluating EMT-related factors and MMPs at different concentrations of LPS we found that increasing concentrations of LPS increased the expression of the mesenchymal marker vimentin as well as matrix metalloproteinases MMP7 and MMP9 (**Figures 2A, C**). Additionally, Sin significantly suppressed the levels of vimentin, MMP7, and MMP9 in the 16HBE cells exposed to 100 μg/mL LPS (**Figures 2B, D**). These results suggested that Sin inhibited LPS-induced EMT in the airway epithelial cells.

Sin Relieved Th2 Airway Inflammation in Mice With OVA-Induced

Ovalbumin (OVA) is one of the most abundant glycoprotein allergens, which can induce IgE production and result in Th2 immune response in asthma (29). To further explore the relationship between Sin and airway remodeling, the OVA-induced asthmatic mice was established. The imbalance of Th1/Th2 is reported to cause airway inflammation –associated pathogenesis of asthma. Th2 cytokines, including interleukin–4, –5, –10, –13, were demonstrated to be involved in hyperresponsiveness and airway remodeling through activating EMT transformation (30). We detected the pharmacological effect of Sin on Th2 immune cytokines using an ELISA kit on the serum of the mice. We found that IL-4 concentrations were lower in the Sin-treated group than in the OVA group (**Figure 3A**). This indicates that Sin specifically suppressed IL-4 production. There were no significant differences in IL-10 and IL–6 concentrations (**Figures 3B, C**). Th2 allergic inflammation is classically characterized with the high levels of Th2 cytokines and immunoglobulin E (IgE) (31). In asthma

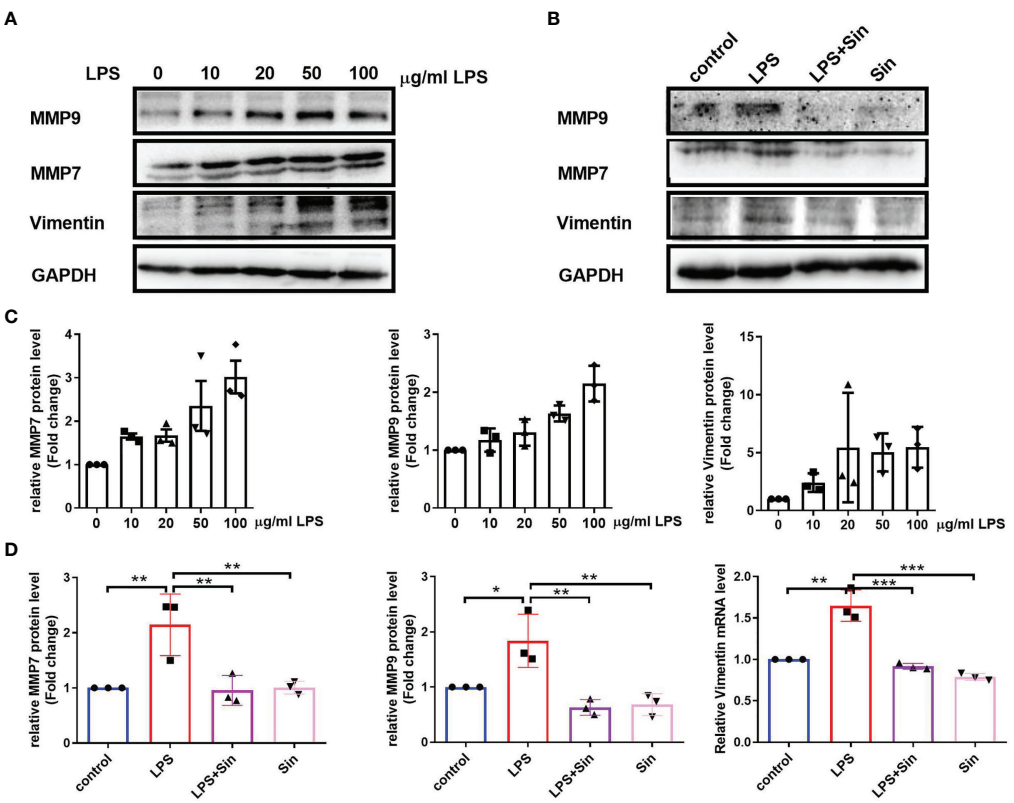

FIGURE 2 | Sin inhibited EMT in LPS-exposed human airway epithelial cells. **(A)** The 16HBE cells were seeded in a 6-well plate and stimulated with LPS at concentrations of 0, 10, 20, 50, 100 μg/mL for 72 h. Protein levels of MMP9, MMP7, and vimentin were determined using Western blotting. **(B)** The 16HBE cells were seeded in a 6-well plate and divided into four groups: control (untreated), LPS (100 μg/mL), LPS with Sin (100 μg/mL and 200 μg/mL, respectively), and sin (200 μg/mL) groups. The cells were incubated for 72 h to perform Western blotting. **(C, D)** Statistical analysis of the gray values of each protein normalized to GAPDH. The data are presented as mean ± SEM from three independent experiments. The one-way analysis of variance followed by Dunnett's Multiple Comparison Test was used. *$p < 0.05$. **$p < 0.01$. ***$p < 0.001$.

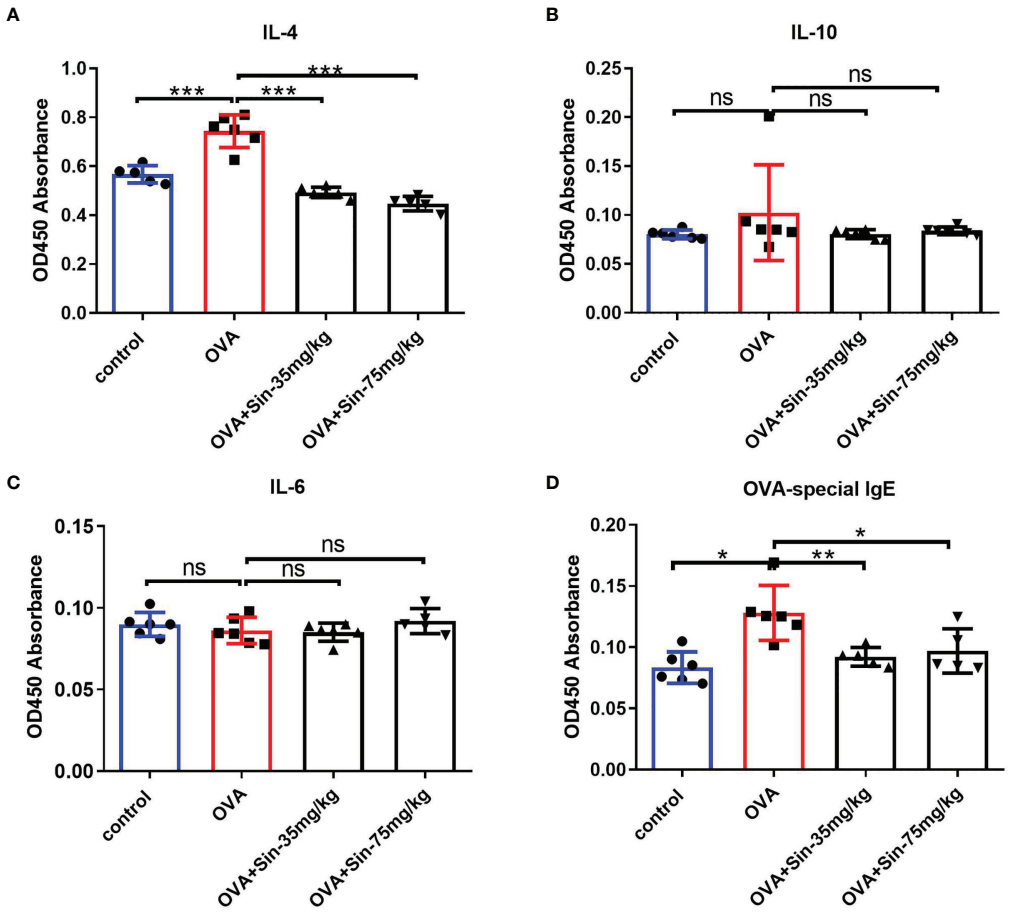

FIGURE 3 | Sin relieved Th2 airway inflammation in mice with OVA-induced asthma. **(A–C)**. IL-4, IL-6, and IL-10 expressions in serum were detected using ELISA on mice from control, model, and Sin-treated (35 mg/kg or 75 mg/kg) groups. OD450 absorbances are shown in the Y-axis. **(D)** OVA-specific IgE in the serum was detected using ELISA in the abovementioned group. The data are presented as mean ± SEM (n=5-6/group). The one-way analysis of variance followed by Dunnett's Multiple Comparison Test was used. *p < 0.05. **p < 0.01. ***p < 0.001. ns, no significant difference between the two groups.

patients, allergens is generally immunoreacted by high levels of IgE which was reported to mediate human allergic inflammation (32). Thus, we also examined the OVA-specific IgE level in mice. It is shown that IgE level was obviously decreased in Sin treated group compared to the OVA group (**Figure 3D**).

Sin Relieved the Airway Remodeling in Mice With OVA-Induced Asthma

Since airway remodeling is characterized by airway wall thickening, subepithelial collagen deposition, and excessive mucus secretion (5), we assessed the pathological changes caused by Sin on lung tissue sections. H&E staining revealed a significant reduction in bronchial inflammatory cell infiltration in the Sin group compared to the OVA group (**Figure 4A**). The wat/Pbm value in the OVA group was markedly increased compared to that in the control mice but obviously decreased in the treated groups. Masson staining showed that Sin remarkably relieved OVA-induced collagen deposition in asthmatic mice, as observed with the lower areas of blue-stained collagen fibers than in the OVA group (**Figure 4B**).

Sin Suppressed EMT in Mice With OVA-Induced Asthma

To examine the EMT process in mice with OVA-induced asthma, we evaluated the typical indications of EMT. Immunochemical staining of the lung sections showed that the levels of vimentin, MMP7, and MMP9 in the airway epithelial cells of the Sin-treated group were significantly lower than in the OVA group (**Figure 5A**). The Western blotting results also showed that Sin obviously suppressed the expressions of MMP7 and MMP9 in the lungs of the mice with asthma (**Figures 5B, C**). These results suggested that Sin suppressed EMT in the airway epithelial cells of mice.

Sin Suppressed the TGFβ-1 and Smad3 Expression in Airway Epithelial Cells

To assess the mechanism underlying the relieving effects of Sin on airway remodeling, we analyzed protein levels of components of the TGF-β1/Smad pathway. We found that the protein levels of TGF-β1 and Smad3 but not Smad2 or p-Smad3 were

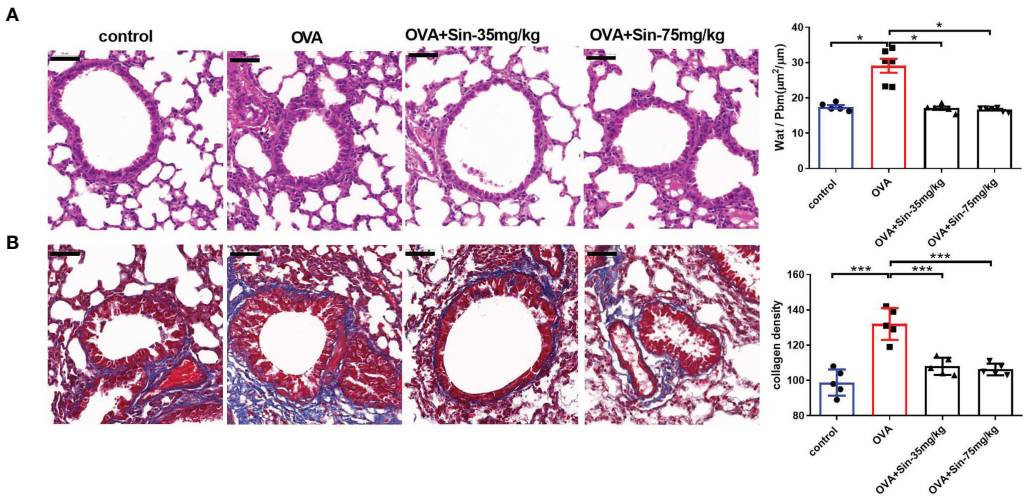

FIGURE 4 | Sin relieved airway remodeling and reduced collagen deposition in the lungs of mice with OVA-induced asthma. Scale bar indicates 50 μm. **(A)** Hematoxylin & eosin (H&E)-stained lung tissue specimen sections. The total area of the airway wall and the perimeter of the basement membrane (Wat/Pbm) were used to evaluate the airway remodeling. The Wat/Pbm values ($\mu m^2/\mu m$) are shown in Y-the axis. The non-parametric multiple comparison followed by Dunnett's Multiple Comparison Test was used. **(B)** Masson staining was conducted on sections of the lung bronchi tissue, in which collagen fibers are shown as blue. The subepithelial collagen density was quantified. The one-way analysis of variance followed by Dunnett's Multiple Comparison Test was used. The data are presented as mean ± SEM (n=5-6/group). *p < 0.05. ***p < 0.001.

significantly increased in the lung tissues of OVA-challenged mice compared to those in the control mice (**Figure 6A**). However, when the mice were treated with 35 mg/kg or 75 mg/kg Sin, these changes were markedly attenuated as seen in the results of the IHC (**Figure 6A**) and Western blotting (**Figures 6B, C**). These results suggested that it suppressed EMT through downregulating TGF-β1/Smad3 expression.

DISCUSSION

Airway remodeling is an airway structural change that is characterized by airway wall thickening, subepithelial collagen deposition, and excessive mucus secretion (5). The respiratory symptoms are largely caused by airway obstruction. Airway epithelial cells are the primary targets of inhaled environmental allergens, causing the production of Th2 innate cytokines that trigger allergic reactions (24). Chronic exposure to repetitive environmental injury may lead to persistent activation of pathways involved in airway epithelial repair, such as EMT, changes in progenitor cell migration and proliferation, and abnormal redifferentiation causing airway remodeling (25). However, it is still not clear whether environmental allergens cause the proliferation and migration of airway cells and their mechanisms. There are no reports on the effect of Sin on the changes in airway epithelial cell function caused by allergens. LPS produced by bacterial infections can exacerbate asthmatic inflammation and induce airway remodeling (26). It was also reported to induce proliferation, differentiation, and migration of intestinal epithelial cells (27). In our study, we firstly suggested that LPS can promote the proliferation and migration of human 16HBE cells. We found that Sin inhibited cell migration but not proliferation in LPS-induced 16HBE cells. These results suggest that Sin may inhibit cell migration and EMT in airway epithelial cells.

OVA, one of the most abundant glycoprotein allergens, induces IgE production and causes Th2 immune responses in patients with asthma (29). Furthermore, an imbalance in Th1/Th2 has been reported to cause airway inflammation-associated pathogenesis of asthma (30). To further explore the relationship between Sin and airway remodeling, a mouse model with OVA-induced asthma was established. We found that airway inflammatory cell infiltration was significantly increased in the lungs of the mice in this model. Additionally, severe airway remodeling and changes in collagen deposition were observed. To evaluate the therapeutic effects of Sin, we assessed the histological and morphological changes in their lungs.

Th2 allergic inflammation is classically characterized by high levels of Th2 cytokines and IgE (31). In patients with asthma, allergens generally react to high levels of IgE, causing human allergic inflammation (32). Thus, we examined the levels of Th2 cytokines and OVA-specific IgE in mice. Our results showed that Sin relieved Th2 inflammatory responses and suppressed levels of IL-4. In the human body, serum IgE concentration is very low. During an allergic response, the presence of IL-4 and IL-13 induces B cells to produce allergen-specific IgE (33). Once IgE is released into the circulation and attached to the allergic effector cells, an immediate hypersensitivity reaction occurs (34, 35). Thus, efforts to decrease IgE levels are considered very important for allergies. Furthermore, we also demonstrated that Sin regulated levels of OVA-specific IgE. Our results suggested that

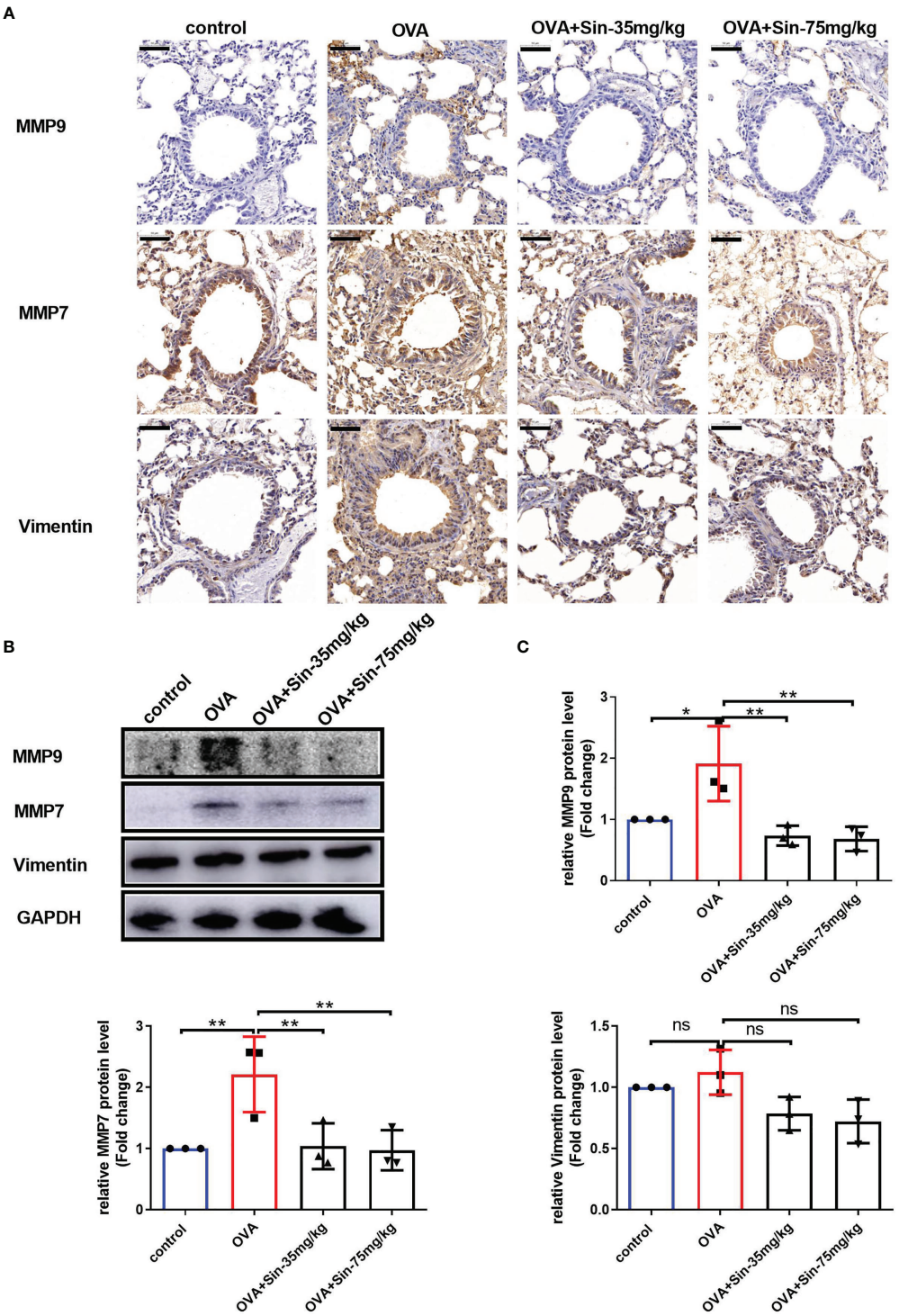

FIGURE 5 | Sin reduced the EMT of the airway epithelial cells in the lungs of the mice with OVA-induced asthma. **(A)** The protein levels of MMP9, MMP7, and vimentin were detected *via* immunohistochemistry. Scale bar indicates 50 μm. **(B)** The expressions of each protein were determined using Western blotting. **(C)** Statistical analysis of the gray values of each band normalized to GAPDH. The data are presented as mean ± SEM from three independent experiments. The one-way analysis of variance followed by Dunnett's Multiple Comparison Test was used. *$p < 0.05$. **$p < 0.01$. ns, no significant difference between the two groups.

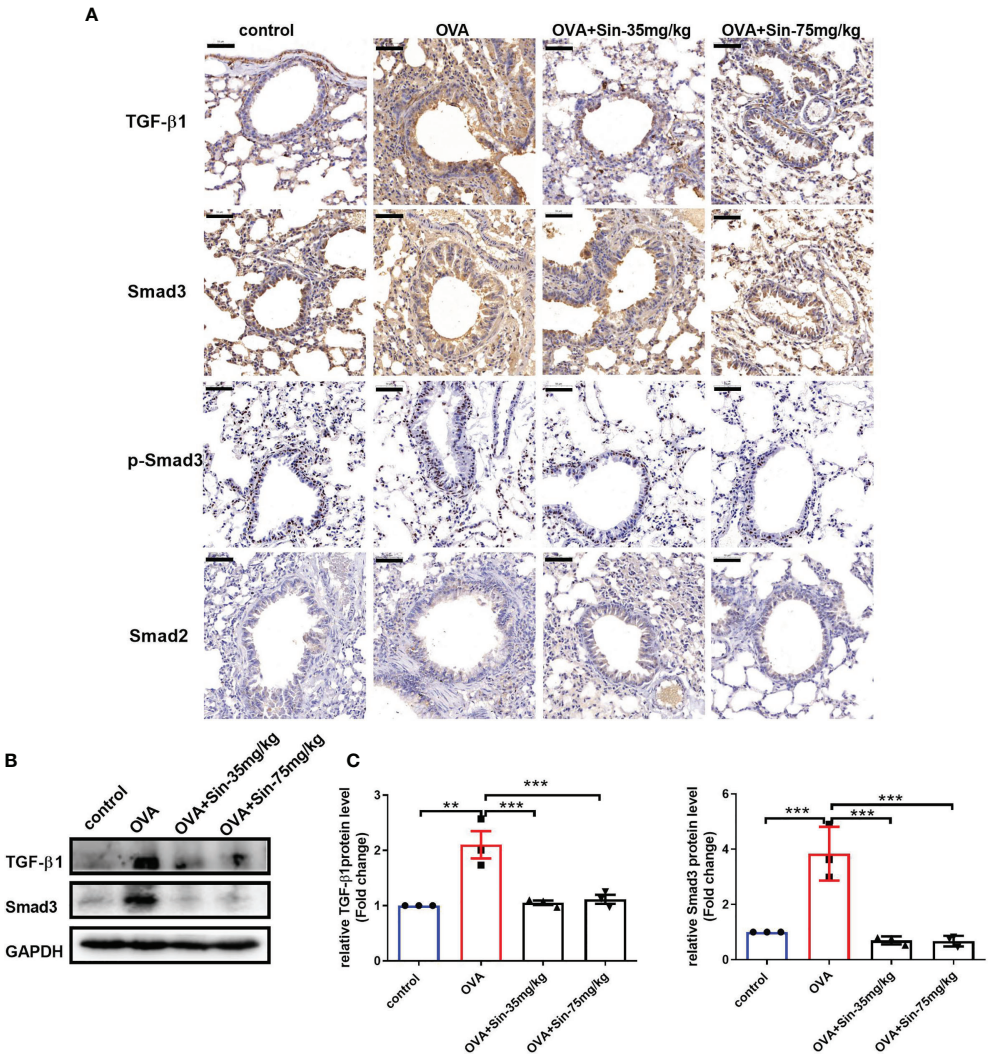

FIGURE 6 | Sin inhibited the TGF-β1/Smad3 expression in the lungs of mice with OVA-induced mice asthma. **(A)** Protein levels of TGF-β1, Smad3, p-Smad3 and Smad2 were detected using immunohistochemistry. Scale bar indicates 50 μm. **(B)** Protein levels of TGF-β1 and Smad3 in the lung tissue were determined by Western blotting. **(C)**, Statistical data of the gray values of each protein normalized to GAPDH. The data are presented as mean ± SEM from three independent experiments. The one-way analysis of variance followed by Dunnett's Multiple Comparison Test was used. **p < 0.01. ***p < 0.001. ns, no significant difference between the two groups.

Sin can effectively attenuate OVA-induced airway inflammation, airway thickness, and subepithelial collagen deposition.

It is generally believed that airway remodeling is caused by chronic exposure to an inflammatory environment, leading to repeated asthma attacks. Respiratory symptoms are mainly caused by changes in airway structure. However, the mechanism of how and when airway remodeling occurs is still unclear. A previous study has reported that airway remodeling may occur in the early stages of asthma and is associated with EMT dysfunction (10). The protective role of Sin against airway inflammation has also been reported, and its role in EMT in asthma is unclear. In our OVA-induced asthma model, the mesenchymal marker, vimentin, was increased.

To explore the relationship between Sin and EMT, we evaluated EMT-related factors and matrix metalloproteinases. Matrix metalloproteinase 9 (MMP9), which is expressed in the bronchial epithelium, promotes airway eosinophil infiltration and degrades the extracellular matrix (ECM) in remodeling (18). We also found that MMP9 levels were significantly increased in lung tissue and airway models. Our results demonstrated that Sin could inhibit MMP9 expression, suggesting that Sin may suppress the thickening of the airway wall. MMP7, which is associated with various mucosal processes, was identified to regulate the wound repair process and found to be quickly upregulated after injury (28). It attenuates ciliated epithelium cell differentiation and enhances wound closure and cell

migration, which are required for re-epithelialization after injury. The adhesion of cells to collagen is enhanced by MMP7 through indirect regulation of α2β1 integrin affinity (36). MMP7 has also been shown to induce EMT in various cancers (37, 38). However, the relationship between MMP7 and airway remodeling has not yet been studied. Our results showed that MMP7 expression was significantly increased in lung tissue and airway models. Moreover, MMP7 levels in the airway were significantly lower in the Sin group than in the OVA induced group. We also found that Sin significantly suppressed the levels of vimentin, MMP7, and MMP9 in LPS-induced 16HBE cells. These results indicate that Sin may inhibit collagen deposition and airway remodeling by regulating EMT.

TGF-β1 is a major inducer of EMT that is secreted by damaged or repairing epithelium. It has also been identified to be a main mediator of airway remodeling (39). Smad3 signaling is required for allergen-induced airway remodeling. It is suggested that airway remodeling is reduced in OVA-challenged Smad3-deficient mice (40). TGF-β1 induced EMT has also been implied in airway remodeling in lung allograft tissue (41).To gain insight into the mechanisms underlying the effects of Sin, we measured levels of several proteins in the TGF-β1/Smad pathway. We observed that TGF-β1 and Smad3 not Smad2 were increased in the lungs of OVA-induced mice. We also found that Sin inhibited the increases in the expressions of TGF-β1 and Smad3. Furthermore, Sin had been shown to attenuate renal fibrosis by increasing Nrf2 and mitigates profibrogenic signaling of TGF-β1/Smad (42). Sin was suggested to reduce TGF-β1-induced pSmad2/pSmad3 signaling in clear-cell renal carcinoma cells (43). p-Smad3-S423/S425 was also reported to be related to EMT. In our study, we did not observe the changes in p-Smad3, indicating that OVA may increase the expression of Smad3 without directly regulating its phosphorylation. There was also a synergic action between TGF-β1 and IL-4 in terms of induction of EMT, which can induce epithelial cells to the cell cycle together (44). IL-4 treatment leads to endogenous TGF-β1 release, which subsequently induces MMP7, MMP9, and vimentin expression (45, 46). Our results suggested that Sin may suppress MMP7, MMP9, and vimentin expression by inhibiting IL-4 and downregulating TGF-β1 and Smad3 expression.

Taken together, we demonstrated that Sin relieved airway remodeling by inhibiting EMT through downregulating TGF-β1 and Smad3 expression. However, there were some limitations to our study. Since we have not identified the direct target protein of Sin in the body, we evaluated the effects of Sin on EMT through histopathology, serology, and cell function experiments. More detailed basic and clinical studies are needed to evaluate the efficacy and mechanism of airway remodeling.

CONCLUSION

Sin suppressed cell migration but not proliferation and inhibited vimentin, MMP7, and MMP9 protein expression in 16HBE cells exposed to LPS. In an OVA-induced asthma mouse model, it decreased OVA-specific IgE and IL-4 levels in the serum, relieved airway remodeling, attenuated subepithelial collagen deposition and inhibited EMT process. Our results suggest that Sin relieves airway remodeling by inhibiting EMT through the IL-4 and downregulating TGF-β1 and Smad3 expression.

DATA AVAILABILITY STATEMENT

The raw data supporting the conclusions of this article will be made available by the authors, without undue reservation.

ETHICS STATEMENT

The animal study was reviewed and approved by the Animal Welfare Ethics Committee of the Henan University of Chinese Medicine.

AUTHOR CONTRIBUTIONS

Conception and design: HH and X-ML. Acquisition of data: HH, LC, and ZhengW. Analysis and interpretation of data: HH, LC, ZhengW, ZhenW, and JM. Manuscript writing: HH. Final approval of manuscript: HH, LC, ZhengW, ZhenW, JM, X-ML, and MM. All authors contributed to the article and approved the submitted version.

FUNDING

This work was financially supported by grants from Henan Province Scientific and Technological Project (212102310344,202102310472), Key scientific research projects of colleges and universities in Henan Province (20A360009), and Henan University of Traditional Chinese Medicine Doctoral Research Fund (RSBSJJ2018-12).

REFERENCES

1. Zhang F-Q, Han X-P, Zhang F, Ma X, Xiang D, Yang X-M, et al. Therapeutic Efficacy of a Co-Blockade of IL-13 and IL-25 on Airway Inflammation and Remodeling in a Mouse Model of Asthma. *Int Immunopharmacol* (2017) 46:133–40. doi: 10.1016/j.intimp.2017.03.005
2. Olin JT, Wechsler ME. Asthma: Pathogenesis and Novel Drugs for Treatment. *BMJ Clin Res* (2014) 349:g5517. doi: 10.1136/bmj.g5517
3. Lambrecht BN, Hammad H. The Immunology of Asthma. *Nat Immunol* (2015) 16(1):45–56. doi: 10.1038/ni.3049
4. Persinger RL, Poynter ME, Ckless K, Janssen-Heininger YMW. Molecular Mechanisms of Nitrogen Dioxide Induced Epithelial Injury in the Lung. *Mol Cell Biochem* (2002) 234-235(1):71–80. doi: 10.1023/A:1015973530559
5. Bullone M, Lavoie JP. The Equine Asthma Model of Airway Remodeling: From a Veterinary to a Human Perspective. *Cell Tissue Res* (2020) 380 (2):223–36. doi: 10.1007/s00441-019-03117-4

6. Berair R, Brightling CE. Asthma Therapy and Its Effect on Airway Remodelling. *Drugs* (2014) 74(12):1345–69. doi: 10.1007/s40265-014-0250-4
7. Braido F. Failure in Asthma Control: Reasons and Consequences. *Scientifica* (2013) 2013(6):549252. doi: 10.1155/2013/549252
8. Kang JY, Jo MR, Kang HH, Kim SK, Kim JW. Long-Term Azithromycin Ameliorates Not Only Airway Inflammation But Also Remodeling in a Murine Model of Chronic Asthma. *Pulmonary Pharmacol Ther* (2016) 36 (4):37–45. doi: 10.1016/j.pupt.2015.12.002
9. Liu T, Liu Y, Miller M, Cao L, Zhao J, Wu J, et al. Autophagy Plays a Role in FSTL1-Induced Epithelial Mesenchymal Transition and Airway Remodeling in Asthma. *Am J Physiol Lung Cell Mol Physiol* (2017) 313(1):L27–40. doi: 10.1152/ajplung.00510.2016
10. Yao L, Wang S, Wei P, Bao K, Hong M. Huangqi-Fangfeng Protects Against Allergic Airway Remodeling Through Inhibiting Epithelial–Mesenchymal Transition Process in Mice *via* Regulating Epithelial Derived TGF-β1. *Phytomedicine* (2019) 64(C):153076–6. doi: 10.1016/j.phymed.2019.153076
11. Liang X, He X, Li Y, Wang J, Wu D, Yuan X, et al. Lyn Regulates Epithelial-Mesenchymal Transition in CS-Exposed Model Through Smad2/3 Signaling. *Respir Res* (2019) 20(1):019–1166. doi: 10.1186/s12931-019-1166-z
12. Bartis D, Mise N, Mahida RY, Eickelberg O, Thickett DR. Epithelial-Mesenchymal Transition in Lung Development and Disease: Does It Exist and Is It Important? *Thorax* (2014) 69(8):760–5. doi: 10.1136/thoraxjnl-2013-204608
13. Liu QF, Chen FF, Liu F, Hong-Jia LI, Wen-Juan XU, Sun QJ, et al. IL-25 Induces Expression of Th2 Inflammatory Factor by Nuocyte in Asthma of Mouse. *Basic Clin Med* (2015) 35(11):1508–13.
14. Shan JJ, Zou JS, Xie T, Kang A, Zhou W, Xu JY, et al. Effects of Gancao on Pharmacokinetic Profiles of Platycodin D and Deapio-Platycodin D in Jiegeng. *J Ethnopharmacol* (2015) 170:50–6. doi: 10.1016/j.jep.2015.04.056
15. Gao Y, Yao LF, Zhao Y, Wei LM, Guo P, Yu M, et al. The Chinese Herbal Medicine Formula mKG Suppresses Pulmonary Fibrosis of Mice Induced by Bleomycin. *Int J Mol Sci* (2016) 17(2):238. doi: 10.3390/ijms17020238
16. Yu M, Jia HM, Cui FX, Yang Y, Zhao Y, Yang MH, et al. The Effect of Chinese Herbal Medicine Formula mKG on Allergic Asthma by Regulating Lung and Plasma Metabolic Alternations. *Int J Mol Sci* (2017) 18(3):602. doi: 10.3390/ijms18030602
17. Tong B, Yu J, Wang T, Dou Y, Wu X, Kong L, et al. Sinomenine Suppresses Collagen-Induced Arthritis by Reciprocal Modulation of Regulatory T Cells and Th17 Cells in Gut-Associated Lymphoid Tissues. *Mol Immunol* (2015) 65 (1):94–103. doi: 10.1016/j.molimm.2015.01.014
18. Işık S, Karaman M, Micili S, Çağlayan-Sözmen Ş., Bağrıyanık HA, Arıkan-Ayyıldız Z, et al. Sinomenine Ameliorates the Airway Remodelling, Apoptosis of Airway Epithelial Cells, and Th2 Immune Response in a Murine Model of Chronic Asthma. *Allergol Immunopathol* (2018) 46(1):67–75. doi: 10.1016/j.aller.2017.05.004
19. Bian W, An Y, Qu H, Yang Y, Yang J, Xu Y. Ally-Isatin Supresses Cell Viability, Induces Cell Cycle Arrest and Promotes Cell Apoptosis in Hepatocellular Carcinoma HepG2 Cells. *Fundam Clin Pharmacol* (2016) 30 (3):253–62. doi: 10.1111/fcp.12193
20. He H, Zhao X, Zhu Z, Du L, Chen E, Liu S, et al. MicroRNA-3191 Promotes Migration and Invasion by Downregulating TGFBR2 in Colorectal Cancer. *J Biochem Mol Toxicol* (2019) 33(6):15. doi: 10.1002/jbt.22308
21. He H, Chen E, Lei L, Yan B, Zhao X, Zhu Z, et al. Alteration of the Tumor Suppressor SARDH in Sporadic Colorectal Cancer: A Functional and Transcriptome Profiling-Based Study. *Mol Carcinog* (2019) 58(6):957–66. doi: 10.1002/mc.22984
22. Flanagan TW, Sebastian MN, Battaglia DM, Foster TP, Cormier SA, Nichols CD. 5-HT(2) Receptor Activation Alleviates Airway Inflammation and Structural Remodeling in a Chronic Mouse Asthma Model. *Life Sci* (2019) 236(116790):15. doi: 10.1016/j.lfs.2019.116790
23. Liu F, Shang YX. Sirtuin 6 Attenuates Epithelial-Mesenchymal Transition by Suppressing the TGF-β1/Smad3 Pathway and C-Jun in Asthma Models. *Int Immunopharmacol* (2020) 82(106333):106333. doi: 10.1016/j.intimp.2020.106333
24. Sheih A, Parks WC, Ziegler SF. GM-CSF Produced by the Airway Epithelium Is Required for Sensitization to Cockroach Allergen. *Mucosal Immunol* (2017) 10(3):705–15. doi: 10.1038/mi.2016.90
25. Ganesan S, Sajjan US. Repair and Remodeling of Airway Epithelium After Injury in Chronic Obstructive Pulmonary Disease. *Curr Respir Care Rep* (2013) 2(3):145–54. doi: 10.1007/s13665-013-0052-2
26. Kumari A, Singh DK, Dash D, Singh R. Intranasal Curcumin Protects Against LPS-Induced Airway Remodeling by Modulating Toll-Like Receptor-4 (TLR-4) and Matrixmetalloproteinase-9 (MMP-9) Expression *via* Affecting MAP Kinases in Mouse Model. *Inflammopharmacology* (2019) 27(4):731–48. doi: 10.1007/s10787-018-0544-3
27. Liu P, Xu L, Pu Y, Yi L, Chen J, Zhang X. Effects of Proanthocyanidin on Proliferation, Differentiation and Migration of LPS-Induced IEC-6 Cells. *J Environ* (2013) 30(12):1065–7.
28. Gharib SA, Altemeier WA, Van Winkle LS, Plopper CG, Schlesinger SY, Buell CA, et al. Matrix Metalloproteinase-7 Coordinates Airway Epithelial Injury Response and Differentiation of Ciliated Cells. *Am J Respir Cell Mol Biol* (2013) 48(3):390–6. doi: 10.1165/rcmb.2012-0083OC
29. Hwang HS, Kim JY, Park H, Jeong J, Hyun H, Yoon TJ, et al. Cleavage of the Terminal N-Acetylglucosamine of Egg-White Ovalbumin N-Glycans Significantly Reduces IgE Production and Th2 Cytokine Secretion. *Biochem Biophys Res Commun* (2014) 450(4):1247–54. doi: 10.1016/j.bbrc.2014.06.101
30. Huang C, Zhang Z, Wang L, Liu J, Gong X, Zhang C. ML-7 Attenuates Airway Inflammation and Remodeling *via* Inhibiting the Secretion of Th2 Cytokines in Mice Model of Asthma. *Mol Med Rep* (2018) 17(5):6293–300. doi: 10.3892/mmr.2018.8683
31. Kubo M. Innate and Adaptive Type 2 Immunity in Lung Allergic Inflammation. *Immunol Rev* (2017) 278(1):162–72. doi: 10.1111/imr.12557
32. Doyen V, Casset A, Divaret-Chauveau A, Khayath N, Peiffer G, Bonniaud P, et al. [Diagnosis of Allergy in Asthma]. *Rev Mal Respir* (2020) 37(3):243–56. doi: 10.1016/j.rmr.2019.07.014
33. Kelly BT, Grayson MH. Immunoglobulin E, What Is It Good for? *Ann Allergy Asthma Immunol Off Publ Am Coll Allergy Asthma Immunol* (2016) 116 (3):183–7. doi: 10.1016/j.anai.2015.10.026
34. Iweala OI, Burks AW. Food Allergy: Our Evolving Understanding of Its Pathogenesis, Prevention, and Treatment. *Curr Allergy Asthma Rep* (2016) 16 (5):37. doi: 10.1007/s11882-016-0616-7
35. Renz H, Allen KJ, Sicherer SH, Sampson HA, Lack G, Beyer K, et al. Food Allergy. *Nat Rev Dis Primers* (2018) 4:17098. doi: 10.1038/nrdp.2017.98
36. Chen P, Abacherli LE, Nadler ST, Wang Y, Li Q, Parks WC. MMP7 Shedding of Syndecan-1 Facilitates Re-Epithelialization by Affecting Alpha(2)Beta(1) Integrin Activation. *PloS One* (2009) 4(8):e6565. doi: 10.1371/journal.pone.0006565
37. Yang X, Du X, Sun L, Zhao X, Zhu J, Li G, et al. SULT2B1b Promotes Epithelial-Mesenchymal Transition Through Activation of the β-Catenin/MMP7 Pathway in Hepatocytes. *Biochem Biophys Res Commun* (2019) 510 (4):495–500. doi: 10.1016/j.bbrc.2019.01.034
38. Zhang Q, Liu S, Parajuli KR, Zhang W, Zhang K, Mo Z, et al. Interleukin-17 Promotes Prostate Cancer *via* MMP7-Induced Epithelial-to-Mesenchymal Transition. *Oncogene* (2017) 36(5):687–99. doi: 10.1038/onc.2016.240
39. Wei Y, Zhang Z, Wang F, Zhou S. Assessment of Tumor Growth Factor-β1 Neutralizing Antibody in the Treatment of Allergic Rhinitis and Asthma. *Exp Ther Med* (2018) 15(1):649–56.
40. Le AV, Cho JY, Miller M, McElwain S, Golgotiu K, Broide DH. Inhibition of Allergen-Induced Airway Remodeling in Smad 3-Deficient Mice. *J Immunol* (2007) 178(11):7310–6. doi: 10.4049/jimmunol.178.11.7310
41. Borthwick LA, Parker SM, Brougham KA, Johnson GE, Gorowiec MR, Ward C, et al. Epithelial to Mesenchymal Transition (EMT) and Airway Remodelling After Human Lung Transplantation. *Thorax* (2009) 64(9):770–7. doi: 10.1136/thx.2008.104133
42. Qin T, Yin S, Yang J, Zhang Q, Liu Y, Huang F, et al. Sinomenine Attenuates Renal Fibrosis Through Nrf2-Mediated Inhibition of Oxidative Stress and Tgfβ Signaling. *Toxicol Appl Pharmacol* (2016) 304:1–8. doi: 10.1016/j.taap.2016.05.009
43. Zhao B, Liu L, Mao J, Liu K, Fan W, Liu J, et al. Sinomenine Hydrochloride Attenuates the Proliferation, Migration, Invasiveness, Angiogenesis and Epithelial-Mesenchymal Transition of Clear-Cell Renal Cell Carcinoma Cells *via* Targeting Smad *In Vitro*. *BioMed Pharmacother* (2017) 96:1036–44. doi: 10.1016/j.biopha.2017.11.123
44. Zhou X, Spittau BR, Krieglstein K. Tgfβ Signalling Plays an Important Role in IL4-Induced Alternative Activation of Microglia. *J Neuroinflamm* (2012) 9 (1):1–14.

45. Wu Y, Tran T, Dwabe S, Sarkissyan M, Kim J, Nava M, et al. A83-01 Inhibits TGF-β-Induced Upregulation of Wnt3 and Epithelial to Mesenchymal Transition in HER2-Overexpressing Breast Cancer Cells. *Breast Cancer Res Treat* (2017) 163(3):449–60. doi: 10.1007/s10549-017-4211-y
46. Wang B, Liu T, Wu JC, Luo SZ, Chen R, Lu LG, et al. STAT3 Aggravates TGF-β1-Induced Hepatic Epithelial-to-Mesenchymal Transition and Migration. *BioMed Pharmacother* (2018) 98:214–21. doi: 10.1016/j.biopha.2017.12.035

Conflict of Interest: The authors declare that the research was conducted in the absence of any commercial or financial relationships that could be construed as a potential conflict of interest.

Publisher's Note: All claims expressed in this article are solely those of the authors and do not necessarily represent those of their affiliated organizations, or those of the publisher, the editors and the reviewers. Any product that may be evaluated in this article, or claim that may be made by its manufacturer, is not guaranteed or endorsed by the publisher.

frontiers in Immunology

ORIGINAL RESEARCH
published: 30 November 2021
doi: 10.3389/fimmu.2021.777524

Imaging of Glioblastoma Tumor-Associated Myeloid Cells Using Nanobodies Targeting Signal Regulatory Protein Alpha

Karen De Vlaminck[1,2,3†], Ema Romão[1†], Janik Puttemans[4†], Ana Rita Pombo Antunes[1,2†], Daliya Kancheva[1,2,3], Isabelle Scheyltjens[1,2,3], Jo A. Van Ginderachter[1,2], Serge Muyldermans[1], Nick Devoogdt[4‡], Kiavash Movahedi[1,2,3‡] and Geert Raes[1,2*‡]*

[1] Laboratory of Cellular and Molecular Immunology, Vrije Universiteit Brussel, Brussels, Belgium, [2] Myeloid Cell Immunology Lab, VIB Center for Inflammation Research, Brussels, Belgium, [3] Laboratory of Molecular and Cellular Therapy, Department of Biomedical Sciences, Vrije Universiteit Brussel, Brussels, Belgium, [4] In Vivo Cellular and Molecular Imaging Laboratory, Department of Medical Imaging, Vrije Universiteit Brussel, Brussels, Belgium

Glioblastoma (GBM) is the most common malignant primary brain tumor. Glioblastomas contain a large non-cancerous stromal compartment including various populations of tumor-associated macrophages and other myeloid cells, of which the presence was documented to correlate with malignancy and reduced survival. *Via* single-cell RNA sequencing of human GBM samples, only very low expression of PD-1, PD-L1 or PD-L2 could be detected, whereas the tumor micro-environment featured a marked expression of signal regulatory protein alpha (SIRPα), an inhibitory receptor present on myeloid cells, as well as its widely distributed counter-receptor CD47. CITE-Seq revealed that both SIRPα RNA and protein are prominently expressed on various populations of myeloid cells in GBM tumors, including both microglia- and monocyte-derived tumor-associated macrophages (TAMs). Similar findings were obtained in the mouse orthotopic GL261 GBM model, indicating that SIRPα is a potential target on GBM TAMs in mouse and human. A set of nanobodies, single-domain antibody fragments derived from camelid heavy chain-only antibodies, was generated against recombinant SIRPα and characterized in terms of affinity for the recombinant antigen and binding specificity on cells. Three selected nanobodies binding to mouse SIRPα were radiolabeled with ^{99m}Tc, injected in GL261 tumor-bearing mice and their biodistribution was evaluated using SPECT/CT imaging and radioactivity detection in dissected organs. Among these, Nb15 showed clear accumulation in peripheral organs such as spleen and liver, as well as a clear tumor uptake in comparison to a control non-targeting nanobody. A bivalent construct of Nb15 exhibited an increased accumulation in highly vascularized organs that express the target, such as spleen and liver, as compared to the monovalent format. However, penetration into the GL261 brain tumor fell back to levels detected with a

OPEN ACCESS

Edited by:
Alejandro López-Soto, University of Oviedo, Spain

Reviewed by:
Miguel Angel Morcillo, Centro de Investigaciones Energéticas, Medioambientales y Tecnológicas, Spain
Justin Lathia, Case Western Reserve University, United States
Lisa Sevenich, Georg Speyer Haus, Germany

***Correspondence:**
Geert Raes
Geert.Raes@vub.be
Kiavash Movahedi
Kiavash.Movahedi@vub.be

†These authors share first authorship

‡These authors share senior authorship

Specialty section:
This article was submitted to Cancer Immunity and Immunotherapy, a section of the journal Frontiers in Immunology

Received: *15 September 2021*
Accepted: *11 November 2021*
Published: *30 November 2021*

Citation:
De Vlaminck K, Romão E, Puttemans J, Pombo Antunes AR, Kancheva D, Scheyltjens I, Van Ginderachter JA, Muyldermans S, Devoogdt N, Movahedi K and Raes G (2021) Imaging of Glioblastoma Tumor-Associated Myeloid Cells Using Nanobodies Targeting Signal Regulatory Protein Alpha. Front. Immunol. 12:777524. doi: 10.3389/fimmu.2021.777524

non-targeting control nanobody. These results highlight the tumor penetration advantages of the small monovalent nanobody format and provide a qualitative proof-of-concept for using SIRPα-targeting nanobodies to noninvasively image myeloid cells in intracranial GBM tumors with high signal-to-noise ratios, even without blood-brain barrier permeabilization.

Keywords: signal regulatory protein alpha, glioblastoma, nanobodies (VHH), imaging, myeloid cell, SIRP alpha

INTRODUCTION

Glioblastoma (GBM) is the most prevalent and aggressive type of primary brain cancer. Standard treatment for GBM relies on surgical resection, radiotherapy and chemotherapy, but due to poor tissue accessibility, tumor invasiveness and rapid growth, patients relapse and the median survival is approximately two years following initial diagnosis. It is therefore imperative to find new diagnostic and therapeutic tools to tackle GBM (1). Over the last decade, immunotherapies such as the use of immune checkpoint inhibitors (ICIs), have revolutionized the field of cancer treatment (2). Cancer-immune cell interactions *via* so-called immune checkpoints, dampen anti-cancer immune responses and create an immuno-suppressive and pro-tumoral environment. Hence, the use of ICIs can promote anti-tumor immunity. Up to date, 7 ICIs that specifically focus on cytotoxic T cell activation have been clinically approved (3). Although these T-cell-centered ICIs have proven effective in so-called "hot" tumors such as melanoma and non-small cell lung carcinoma, which contain large proportions of cytotoxic T cells, only a minority of patients appears responsive to the treatment. Furthermore, they are of limited value in the treatment of non-T-cell inflamed "cold" tumors. Therefore, shifting the focus onto innate immune cells in order to boost anti-tumoral activity may provide complementary and synergistic potential for the treatment of tumors such as GBM, that, to date, only show very modest responses to the currently available ICIs (4, 5).

A potentially promising target is the SIRPα-CD47 axis (6). SIRPα is expressed by myeloid cells, including macrophages and dendritic cells, and binds to the ubiquitously expressed self-antigen CD47 (7). Their interaction serves as a "do not eat me" signal and avoids unwanted clearance of host cells. However, this mechanism is being exploited in the tumor microenvironment, as cancer cells overexpress CD47 to bypass macrophage-mediated phagocytic killing (8–10). Seminal pre-clinical mouse studies across many cancer types -including GBM- have shown that CD47-SIRPα interference significantly increases cancer cell engulfment (11–22). Consequently, several of such ICIs are currently being tested in clinical trials (23). Most studies are focusing on targeting CD47, using monoclonal antibodies. However, due to the ubiquitous expression of CD47, off-target adverse effects may arise. Secondly, as antibodies have a large molecular weight, their penetration capacity into brain tumors may be limited, for example in lowly vascularized hypoxic tumor regions or due to the presence of the blood-brain barrier (BBB). Therefore, specific targeting of SIRPα rather than CD47, and the use of smaller antigen-specific entities, may prove valuable in the context of GBM treatment.

Nanobodies are camelid-derived single-domain antibody fragments, which have emerged as promising tools for tumor targeting in both diagnostic and therapeutic settings (24–28). They are easily generated and retain high antigen specificity, but are smaller than monoclonal antibodies (29). Furthermore, preclinical studies have shown that nanobodies have superior tumor- and brain-penetrating capacity in comparison to monoclonal antibodies (30, 31).

In this study, we first confirm at single-cell resolution that SIRPα is a widely expressed target within the human and mouse GBM tumor microenvironment, with a high expression observed in tumor macrophages and certain dendritic cell (DC) subsets. Next, we generated SIRPα-specific nanobodies that bind the SIRPα$^+$ tumor myeloid populations and revealed that the monovalent nanobody format can efficiently target mouse GBM tumors *in vivo*.

MATERIALS AND METHODS

Expression, Purification and Quality Analysis of SIRPα Antigen

The gene encoding the ligand binding domain of mouse SIRPα (mSIRPα) (UniPROT ID P97797) was ordered at the company GenScript (Piscataway, USA) and cloned into the pHEN6 vector. *E. coli* bacteria (WK6 strain) transformed with the pHEN6-mSIRPα construct were inoculated in 5 mL of Luria-Bertani (LB) media supplemented with 100 μg mL^{-1} ampicillin (Sigma-Aldrich, St. Louis, USA), and were cultured overnight at 37°C, while shaking. On the next day, 1 mL of the bacterial suspension was transferred into 330 mL of fresh Terrific-broth (TB) media supplemented with 0.1% (w/v) glucose (Duchefa Biochemie, Haarlem, The Netherlands) and 100 μg mL^{-1} of ampicillin and cultured while shaking at 220 rpm and at 37°C for about 3 h until the OD_{600nm} reached 0.8. Isopropyl-β-D-thiolgalactopyranoside (IPTG) (Duchefa Biochemie, Haarlem, The Netherlands) was then added to the culture to a final concentration of 1 mM to induce the expression of the recombinant protein. The culture was incubated overnight at 28°C while shaking. The cells were harvested by centrifugation and the translocated recombinant periplasmic antigens were obtained *via* osmotic shock. Then periplasmic extracts underwent immobilized metal affinity chromatography (IMAC) using HisPur Ni-NTA resin (Thermo Fischer Scientific, Waltham, USA) as a capturing medium in a PD-10 column (GE-Healthcare, Chicago, USA) fitted with a

filter. After washing with 20 column volumes of phosphate buffered saline (PBS), the HisPur bound SIRPα antigens were eluted in five 1 mL fractions of 500 mM imidazole (Merck, Darmstadt, Germany) in PBS (pH 7.5). The eluate was further purified by size exclusion chromatography (SEC) using a Superdex S75 16/600 column on a ÄKTA Express System (GE-Healthcare, Chicago, USA) using PBS as a mobile phase. The concentration of the SIRPα antigen was determined by spectroscopy at 280 nm with Nanodrop using the theoretically calculated extinction coefficient (32). The purity of the SIRPα antigens was further examined using sodium dodecyl sulphate polyacrylamide gel electrophoresis (SDS-PAGE).

Generation and ELISA Screening of Nanobodies

Nanobodies were generated as previously described (33). An alpaca (*Vicugna pacos*) and two dromedaries (*Camelus dromedarius*) were immunized according to a six-week alternating schedule of weekly injections with 100 µg of recombinant antigen in Gerbu LQ 3000 adjuvant (GerbuBiotechnik GmbH, Heidelberg, Germany). Four days after the last immunization, 50 mL of anti-coagulated blood was collected from which plasma and peripheral blood lymphocytes were separated with Leucosep (Greiner Bio-One, Kremsünster, Austria) by density centrifugation. Total RNA was purified for the generation of cDNA by reverse transcription with oligo-dT primers. The generated cDNA was used as template in a two-step nested PCR that amplified the genes coding for the variable domains of the heavy-chain-only antibodies. The amplified pool of nanobody DNA fragments were ligated into a pMECS phagemid vector which were then transformed into *E. coli* TG1 electrocompetent cells. Using M13K07 helper phages, the nanobody libraries were expressed on phages. Enrichment for specific nanobody-phages was performed by 3 to 4 consecutive rounds of *in vitro* selection on recombinant antigen-coated wells of Nunc Maxisorp flat bottom microtiter plates (Thermo Fisher scientific). Clones were randomly selected from all rounds of panning of the different libraries and screened for binding on recombinant antigens using enzyme-linked immunoassays (ELISA).

Selected clones were sequenced and recloned into pHEN6 and pHEN25 plasmids for expression. The pMECS and pHEN6 vectors (to encode a C-terminal hexa-histidine (His6) tag respectively with or without an additional hemagglutinin (HA) tag) were used for expression of the monomeric version of the selected nanobodies, while the pHEN25 vector was used to obtain dimeric nanobodies. The pHEN25 expression vector is derived from the pHEN6 expression vector, where the nanobody amino-terminal glutamine is mutated to glutamic acid, followed by a fourteen amino acid long linker and a cysteine after the His6 tag, thereby allowing dimerization (24, 34).

For production, the pMECS-, pHEN6- and pHEN25-nanobody plasmids were transformed into a non-suppressor *E. coli* WK6 strain. The nanobodies were obtained *via* periplasmic extraction and subsequent purification by IMAC and SEC, as previously described. The concentration of the nanobodies was determined by spectroscopy at 280 nm with Nanodrop™ using the theoretically calculated extinction coefficient based on their amino acid sequence (32). The purity of all nanobodies was further examined using SDS-PAGE and western blot.

Flow Cytometry Nanobody Screening

Purified nanobodies were screened for their ability to bind the cognate natively expressed antigen on the cell surface of the RAW 264.7 cell line (American Type Culture Collection, Manassas, USA). One µg of each nanobody was incubated with 2 x 10^5 cells in DMEM (Gibco, Waltham, USA), supplemented with 10% FBS (Gibco), 300 mg mL^{-1} L-glutamine (Gibco), 100 U mL^{-1} penicillin and 100 mg mL^{-1} streptomycin (Gibco), at 4°C for 1 h. After incubation, the cells were washed three times with ice-cold PBS (pH 7.4) and then incubated with 1 µg of rat anti-mouse CD16/CD32 (clone 2.4G2, in house production) and 150 ng AF488 anti-mouse HA antibody (see **Supplementary Table 1**) prepared in ice-cold PBS (pH 7.4) and incubated for 30 min at 4°C in the dark. Finally, the cells were washed three more times, resuspended in 200 µL of ice-cold PBS (pH 7.4) and flow cytometry was performed on a FACS Canto II flow cytometer (BD Biosciences, San Jose, USA). As a negative control a nanobody against *Helicobacter pylori*'s outer-membrane adhesin BabA, i.e. Nb19, was used (35). APC anti-mouse CD172a (SIRPα) (clone P84, catalogue no. 144014, BioLegend, San Diego, USA) and APC rat IgG1 kappa isotype (clone RTK2071, catalogue no. 400412, BioLegend, San Diego, USA) antibodies were used as positive and negative controls for SIRPα expression detection on the RAW 264.7 cells. Data were analyzed using FlowJo 9.3.2 software (BD Biosciences). Based on forward and side scatter, cell debris and doublets were excluded, and the relative mean fluorescence intensity (ΔMFI) of AF488 was evaluated for each of the nanobodies compared to the anti-HA IgG.

Kinetic Antigen Binding Profiles

The kinetic affinity parameters of the SIRPα nanobodies were determined by surface plasmon resonance (SPR) using a Biacore-T200 device (GE-Healthcare, Chicago, USA). The recombinant antigen was immobilized *via* amino coupling chemistry on a CM5 chip Series S (GE-Healthcare, Chicago, USA) at a concentration of 10 µg mL^{-1}. The SPR measurements were performed at 25°C with HBS (20 mM HEPES pH 7.4, 150 mM NaCl, 0.005% Tween-20, 3.4 mM EDTA) as running buffer. The nanobodies were injected sequentially in 2-fold serial dilutions, from 500 to 1.95 nM. The rate kinetic constants were determined by a mathematical fitting of a 1:1 binding model using the Biacore Evaluation software, and the k_{off}/k_{on} ratio was used to determine the equilibrium dissociation constant (K_D).

In Vitro Radioligand Binding Assay

^{99m}Tc-labeled nanobodies were assessed for their ability to bind the cognate natively expressed antigen on the cell surface of the RAW 264.7 cell line (American Type Culture Collection, Manassas, USA). 5 x 10^4 RAW 264.7 cells/well were allowed to adhere overnight in DMEM (Gibco, Waltham, USA), supplemented with 10% FBS (Gibco), 300 mg mL^{-1}

L-glutamine (Gibco), 100 U mL^{-1} penicillin and 100 mg mL^{-1} streptomycin (Gibco). Cells were washed three times with ice-cold PBS (pH 7.4) and then incubated with 2 nM, 20 nM and 200 nM of ^{99m}Tc-labeled Nb19 (5-51-514 µCi resp.; n=2), monovalent Nb15 (5-55-554 µCi resp.; n=2) and bivalent Nb15 (5-49-492 µCi resp.; n=2) for 1 h at 4°C. Aspecific binding was assessed by adding a 100x molar excess of unlabeled Nb. After incubation, the cells were washed 3 times with ice-cold PBS to remove unbound Nb, and cells were detached using 1 M NaOH (Merck, Darmstadt, Germany) and counted for radioactivity using a Wizard2 γ-counter (PerkinElmer, Massachusetts, USA). Specific binding was calculated as $[\text{counts per minute}]_{\text{Unblocked}} - [\text{counts per minute}]_{\text{Blocked}}$.

Mouse Imaging and Biodistribution Studies

Stereotactic Intracerebral Tumor Cell Inoculation

The GL261 cell line (36) was cultured in DMEM F12 (Gibco, Waltham, USA) supplemented with 10% FBS, 300 mg mL^{-1} L-glutamine, 100 U mL^{-1} penicillin and 100 mg mL^{-1} streptomycin. For intracranial injection, cells were harvested *via* trypsinization, brought to a concentration of 1 x 10^5 cells mL^{-1} and injected in 7- to 10-week-old female C57BL/6J mice (Janvier) as previously described (37). Briefly, mice were anesthetized and immobilized in a stereotactic frame. A midline incision was made on the skin to expose the scalp and with a microdrill an injection burr hole was made. Then, very slowly, 5 x 10^5 cells were injected using a Hamilton syringe. Tumors were allowed to grow for 21 days.

Preparation of ^{99m}Tc-Labeled Nanobodies

Nanobodies were labeled with $[^{99m}Tc(H_2O)_3(CO)_3]^+$ at their His6-tag *via* tricarbonyl chemistry, as described previously (38). The ^{99m}Tc-labeled nanobodies were purified from the unbound $[^{99m}Tc(H_2O)_3(CO)_3]^+$ *via* NAP-5 SEC (Sephadex, GE-Healthcare, Chicago, USA), and filtered through a 0.22 µm filter (Millex, Millipore, Burlington, USA). The radiochemical purity of radiolabeled nanobodies was evaluated by instant thin layer chromatography-silica gel (iTLC-SG, Pall Corporation, Belgium).

In Vivo Biodistribution of Radiolabeled Nanobodies

Mice bearing intracranial GL261 tumors were intravenously injected with ^{99m}Tc-nanobodies (1-5-1.8 mCi; n=3). As a negative control, an anti-idiotypic nanobody targeting multiple myeloma, namely Nb R3B23, was used (25). Biodistribution analysis was performed as previously described (39). In brief, 1 h post-injection (p.i.), µSPECT/CT imaging was performed using a Vector$^+$ MILabs system (MILabs, The Netherlands). SPECT-images were obtained using a rat SPECT-collimator (1.5-mm pinholes) in spiral mode, nine positions for whole-body imaging and three positions for brain imaging. Image analysis was performed using a Medical Image Data Examiner (AMIDE) software (40). After imaging, the mice were killed, and organs and tumors were isolated and weighed. The radioactivity in each sample was measured using a Wizard2 γ-counter (PerkinElmer, Massachusetts, USA). Tracer uptake was expressed as % injected activity per gram organ (%IA/g). Statistical analyses were performed using one-way ANOVA.

Flow Cytometry Nanobody Binding on *Ex Vivo* Tumors

Tumor tissue was processed into single cell suspension as previously described (41). Thereto, at 21 days post tumor inoculation, mice were sacrificed and transcardially perfused with 20 mL of ice-cold PBS. Using a stereomicroscope, tumors were carefully dissected from the surrounding brain. They were cut into small pieces and incubated with enzyme mix (30 U mL^{-1} DNAse I (Roche), 10 U mL^{-1} collagenase type I (Worthington) and 400 U mL^{-1} collagenase type IV (Worthington), diluted in 1x HBSS (Gibco)), in a 1:3 ratio with RPMI (Gibco) for 20 min at 37°C. Subsequently, tumor tissue was crushed with a syringe plunger and heavily triturated using standard serological pipettes. The homogenized tissue was filtered twice over a 100 µm nylon filter and centrifuged (515 g, 5 min, 4°C). The pellet was resuspended in red blood cell lysis buffer (155 mM NH_4CL, 12 mM $NaHCO_3$ and 0.1 mM EDTA (Duchefa), dissolved in PBS). After 3 min, the lysis reaction was quenched by adding 9 mL of RPMI (Gibco), samples were centrifuged (450 g, 5 min, 4°C) and the pellet was resuspended in FACS buffer (2 mM EDTA, 2% heat-inactivated FCS (Gibco), dissolved in 1x HBSS). The cells were incubated for 15 min on ice with Zombie Aqua Fixable Live-Dead stain (BioLegend) at a 1:1000 concentration. Next, samples were washed, and incubated on ice for 1h with 5 µg of His6-tagged Nb15 or control Nb19. Samples were then washed again, blocked with rat anti-mouse CD16/CD32 (clone 2.4G2) for 15 min on ice and stained with fluorescently labeled antibodies for 30 min on ice. The antibodies that were used are listed in **Supplementary Table 1**. After a final wash step, flow cytometry was performed on a FACS Canto II flow cytometer and data was analyzed using FlowJo software.

Screening of SIRPα and CD47 Expression in Published Mouse and Human GBM Datasets

The expression matrices of single-cell RNA sequencing (scRNA-seq) of newly diagnosed (ND) human GBM tumors (patients ND1-6), of CITE-seq of newly diagnosed and recurrent (R) human GBM tumors (patients R2, R5 and ND8), and of CITE-seq of mouse GL261 tumors, previously generated in our lab (40), have been downloaded. The single cell data has been analyzed as previously described (40). Batch correction has been applied for the human ND-GBM scRNA-seq and for the human GBM Citeseq using harmony v1.0 with theta of 1 (theta is a diversity clustering penalty parameter with a default value of 2, higher theta resulting in a more aggressive correction). Unsupervised clustering has been performed using the Leiden algorithm. For the human ND-GBM scRNA-seq, the first 30 harmony-corrected PCA embeddings and resolution 0.25 were used for the clustering, yielding 13 clusters, which were annotated as cancer cells, myeloid cells, T cells, oligodendrocytes, endothelial cells and fibroblasts. The human GBM CITE-seq dataset was clustered using the first 30 harmony-corrected PCA embeddings and resolution 1. Artefact and doublets clusters were filtered out. For the clustering of the mouse GL261 CITE-seq, the first 30 PCA embeddings and resolution 1 were applied. Doublet

cells, co-expressing macrophage genes and markers of other cell types were manually removed.

To estimate the effect of sex on SIRPα expression in the myeloid compartment of the GBM tumors, we evaluated scRNAseq data from 6 female (ND1, ND6-8, R1-2) and 7 male (ND2-5, R3-5) GBM patients. The myeloid cells from these datasets were extracted (excluding mast cells), the expression was normalized per cell and the average SIRPα expression per patient was calculated.

RESULTS

The Immune Checkpoint SIRPα Is Highly Expressed by Tumor-Associated Myeloid Cells in Both Human and Mouse GBM

To evaluate the expression and distribution of SIRPα within the glioblastoma (GBM) microenvironment, we reanalyzed our recently published single-cell RNA sequencing (scRNA-seq) and cellular indexing of transcriptomes and epitopes sequencing (CITE-seq) datasets of human and mouse GBM (41). While scRNA-seq provides information about the transcriptome of individual cells, CITE-seq additionally uses a panel of barcoded antibodies which allows for the simultaneous quantification of both mRNA and cell surface protein expression (42). Unbiased scRNA-seq analysis of six newly diagnosed human GBM tumors revealed various cancer and stromal cell populations (**Figure 1A**). Based on known marker genes, we identified cancer cells, immune cells, oligodendrocytes and small clusters of fibroblasts and endothelial cells (**Figures 1A, B**). *SIRPα* expression was limited to tumor oligodendrocytes and myeloid cells, while its ligand, *CD47*, was ubiquitously expressed within the tumor microenvironment (**Figure 1C**). Results were consistent across all patients (**Figure 1D**). The expression of *SIRPG*, which also binds to CD47, was restricted to T cells (**Figure 1C**). Concerning prototypical immune checkpoints, expression of *CD274* (*PDL1*) and *PDCD1LG2* (*PDL2*), which encode ligands for *PDCD1* (*PD1*), expressed in tumor-infiltrating T cells, was virtually absent in the profiled human GBM tumors (**Figure 1C**). To assess whether *SIRPα* was differentially expressed in females *versus* males, we compared its expression in myeloid cells from newly diagnosed and recurrent patients, which showed no significant difference between males and females in this cohort of 13 patients (**Supplementary Figure 1**). To obtain a more detailed overview of *SIRPα* gene and protein expression in immune cells, we analyzed the $CD45^+$ compartment of 3 human GBM tumors *via* CITE-seq (41). Immune cell clusters were identified as previously described (41). Within the immune cell compartment, *SIRPα* was primarily expressed by dendritic cells (DCs), mainly the type 2 conventional (cDC2) subset, monocytes and tumor-associated macrophages (TAMs) (**Figures 1E, F**). As shown previously (41), TAMs in GBM tumors can be derived from microglia (Mg-TAMs) or monocytes (Mo-TAMs) (**Figure 1E**). Both subsets expressed *SIRPα* at comparable levels, and a close correlation between mRNA and protein expression was revealed (**Figure 1F**). To assess *SIRPα* expression in mouse GBM tumors, we reanalyzed the CITE-seq dataset from the $CD45^+$ fraction of orthotopic GL261 tumors (41). This yielded comparable results as in human tumors, with robust SIRPα gene and protein expression observed in TAMs and DCs, primarily cDC2s (**Figures 1G, H**).

Together, these results identified $SIRP\alpha^+$ myeloid cells -in particular cDC2s, monocytes and TAMs- as a potentially relevant target population in human GBM, and verify that mouse GBM functions as a good model system in this context.

mSIRPα Targeting Nanobodies Bind to Recombinant and Cell-Membrane mSIRPα *In Vitro*

Nanobodies were generated against the recombinant extracellular domain of mouse SIRPα (**Figure 2A**). ELISA screenings and sequencing of individual clones led to the identification of 17 individual nanobody clones binding to mouse SIRPα (mSIRPα), belonging to 14 clonally unrelated nanobody families, based on the sequence identity of the CDR3 (**Figure 2B**). Among these, 12 were able to bind to native murine SIRPα-expressing RAW 264.7 macrophages in flow cytometry (**Figures 2C, D**), with clones Nb15, Nb54 and Nb89 exhibiting the highest median fluorescence intensities (**Figure 2D**). Surface plasmon resonance (SPR) measurements of these 3 latter nanobody clones revealed binding affinities between 6,9 and 353,6 nM (**Figure 2E**). Epitope binning revealed that these 3 nanobodies did not compete with each other for antigen binding, except for a partial inhibition of each other's binding by Nb54 and Nb89, suggesting they mainly recognize non-overlapping epitopes on the antigen (**Supplementary Figure 2**).

Biodistribution Studies in the Mouse GL261 GBM Model Reveal Nb15 as a Prime Candidate for *In Vivo* Tumor Targeting of mSIRPα

To analyze their *in vivo* targeting potential, the 3 selected mSIRPα nanobodies, and a non-targeting control nanobody were labeled with ^{99m}Tc. All the ^{99m}Tc-labeled nanobodies had a radiochemical purity larger than 95%. Biodistribution and tumor targeting of ^{99m}Tc-nanobodies were assessed in mice bearing GL261 brain tumors, *via* micro-SPECT/CT at 1 hour post injection. Kidneys showed overall the highest signal irrespective of the nanobody, reflecting the fast filtration of unbound nanobody from the bloodstream, as is often observed for other nanobodies (44).

Among the tested anti-mSIRPα nanobodies, Nb15 exhibited the most profound tumor targeting potential as compared to the control nanobody (**Figure 3** and **Table 1**). Additionally, Nb15 showed high uptake in spleen, liver, lungs, thymus, lymph nodes and bone, while lower background signals were noted for other tissues (**Table 1** and **Supplementary Figure 3**). Signals detected in peripheral organs such as lungs and spleen were significantly lower for Nb89 and Nb54 as compared to Nb15. These data point to an inherently better *in vivo* targeting and imaging potential of

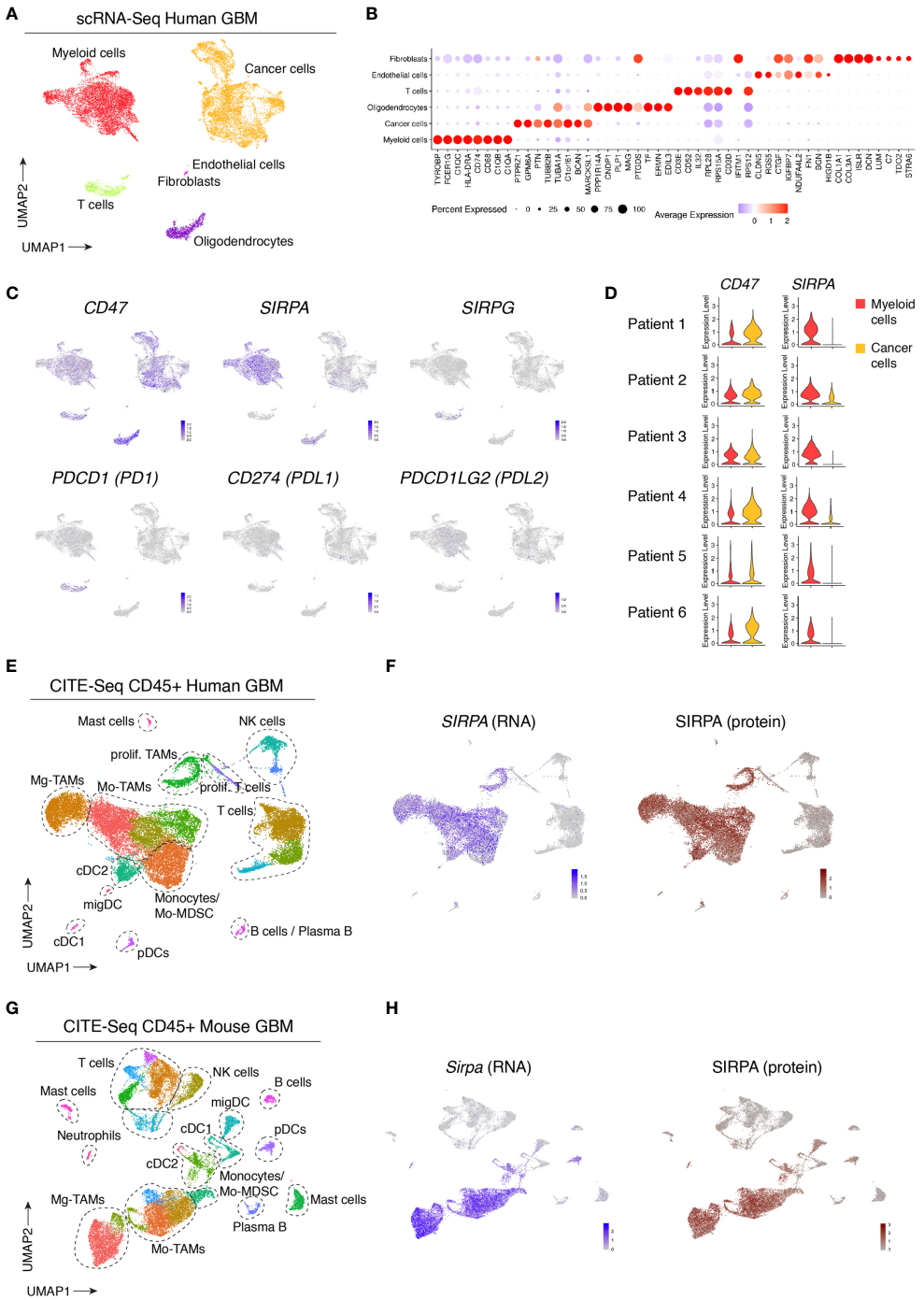

FIGURE 1 | Single-cell profiling of human and mouse GBM tumors reveals consistent SIRPα gene and protein expression in tumor-associated myeloid cells. **(A)** UMAP plot of 20033 cells isolated from n = 6 GBM tumors, visualizing the identified cell populations. **(B)** Dot plot, corresponding to the UMAP plot shown in **(A)**, visualizing the expression of key signature genes of the indicated cell populations. The dot size relates to the percentage of cells expressing the gene, while the color relates to its scaled average expression. **(C)** UMAP plots showing expression of the indicated genes. The color code and range of normalized counts are shown at the lower right on each plot. **(D)** Violin plots showing the expression of *CD47* and *SIRPA* on myeloid cells (red) and cancer cells (yellow) for each individual patient. **(E)** Gene expression-based UMAP plot of 25113 $CD45^+$ cells, isolated from n = 3 human GBM tumors and profiled with CITE-seq. **(F)** Feature plot showing *SIRPA* gene expression (blue) and SIRPA protein expression (brown) based on CITE-seq antibody staining (Antibody-Derived Tag or ADT signals), corresponding to the dataset shown in **(E)**. **(G)** Gene expression-based UMAP plot of 23926 $CD45^+$ cells isolated from orthotopic mouse GL261 tumors (n = 2 groups) and profile with CITE-seq. **(H)** Feature plot showing *Sirpa* gene expression (blue) and SIRPA protein expression (brown) in GL261 tumors based on CITE-seq antibody staining, corresponding to the dataset shown in **(G)**.

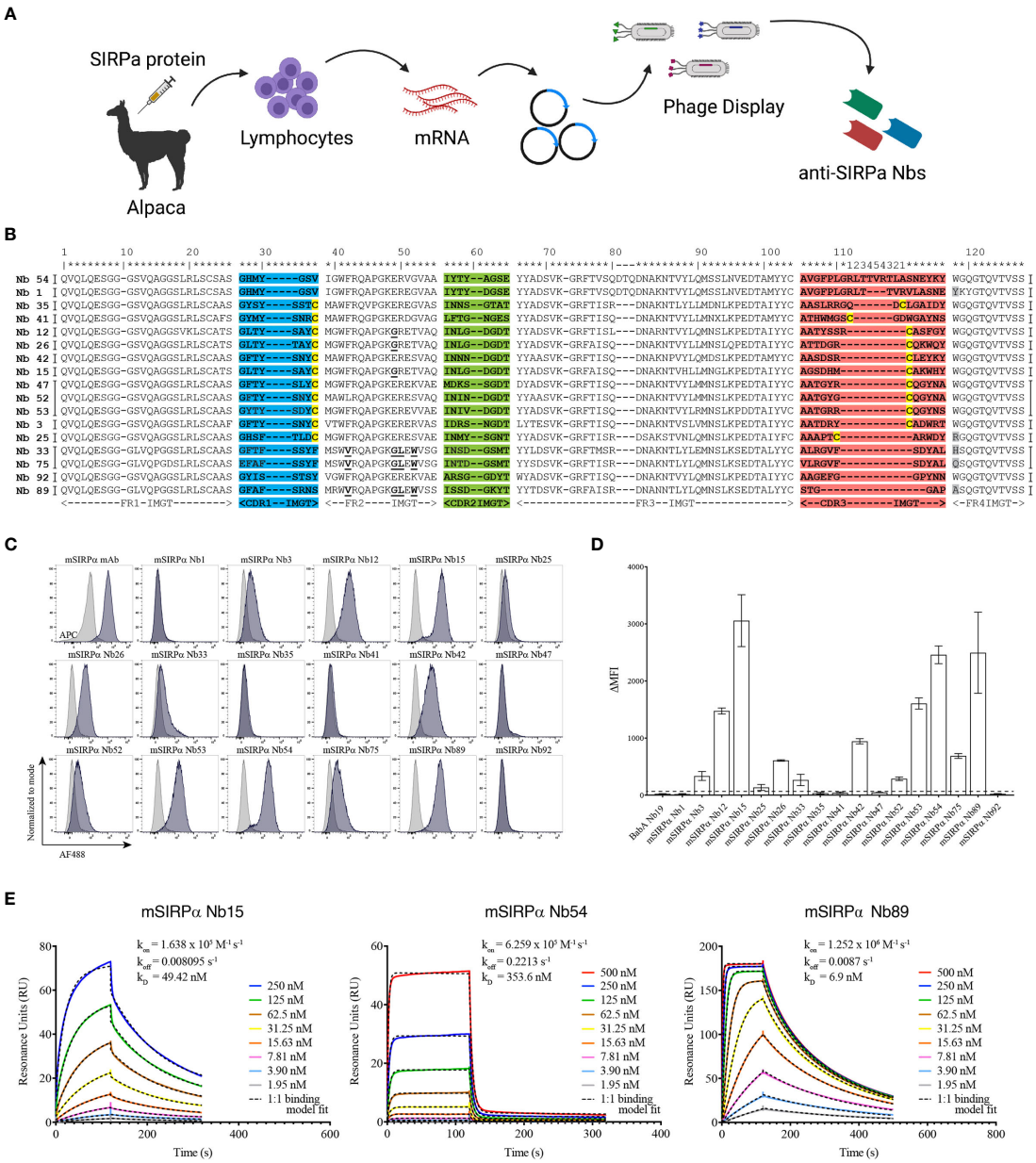

FIGURE 2 | Single-domain antibodies targeting SIRPα can be obtained following immunization with recombinant SIRPα protein. **(A)** Schematic representation of nanobody generation procedure. A camelid is immunized with recombinant SIRPα protein, the mRNA of peripheral blood lymphocytes is converted to cDNA and the region encoding the antigen binding domain of the camelid heavy chain-only antibodies is amplified by PCR and cloned in a phage display vector. Antigen-specific nanobodies are retrieved after phage display and panning on plastic coated SIRPα. **(B)** Amino acid sequence of mSIRPα nanobodies, with numbering according to the International ImMunoGeneTics – IMGT – information system http://www.imgt.org (43). The CDR1, CDR2 and CDR3 regions are colored in blue, green and red, respectively. The cysteine residues used as subfamily-hallmarks are highlighted in yellow. The amino acids which differ from the typical VHH hallmark residues in framework-2 are in bold and underlined. The amino acid at position 118 (Trp) is highly conserved, however, in nanobodies this amino acid is sometimes substituted, usually with Arg and highlighted here in grey. Each nanobody family is based on the sequence identity of the CDR3 region and nanobodies belonging to the same family are grouped, indicated by the vertical black lines on either side of the sequence (14 families in total). Asterixes on top are used to indicate amino acid positions. **(C)** Representative histogram plots of mSIRPα nanobodies binding to RAW 264.7 macrophages. Overlay of binding signals of mSIRPα nanobodies (blue) versus a non-targeting nanobody BabA Nb19 (grey). Note: the first plot shows binding of monoclonal antibody targeting mSIRPα (positive control, blue) and mouse IgG (isotype control, grey) **(D)** Median fluorescence intensity (the difference between the signal of the nanobody and the signal of the mouse anti-HA IgG) of the mSIRPα nanobodies binding to RAW 264.7. The dashed black line is defined by the triple ΔMFI value of the non-targeting nanobody (BabA Nb19) and it represents the threshold above which a nanobody is considered to bind specifically to its target. **(E)** Kinetic rate constants determination by SPR: the sensorgrams of different concentrations (as indicated in the inserts) of mSIRPα nanobodies binding to the recombinant antigen. Kinetics were measured with two-fold serially diluted nanobodies and the fitting of the binding curves was using a 1:1 binding mathematical model.

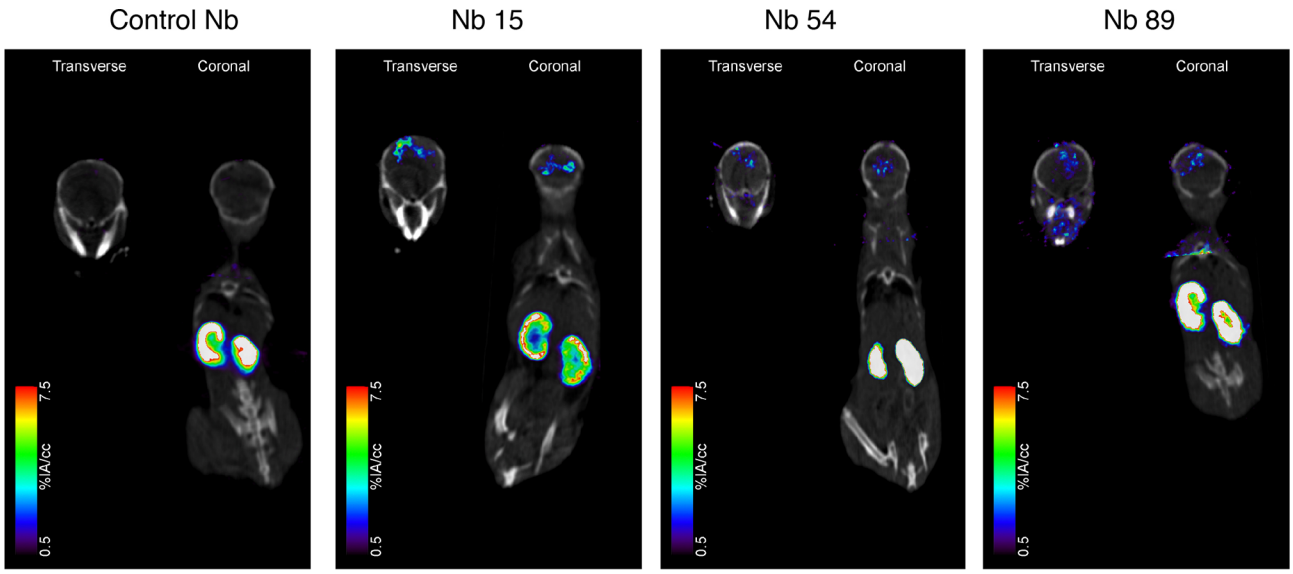

FIGURE 3 | Anti-SIRPα Nb15 targets mouse GL261 GBM tumors *in vivo*. Fused pinhole SPECT/micro-CT images of GL261 tumor-bearing mice injected with ^{99m}Tc-labeled "anti-SIRPα Nb clones 15, 54 and 89 or a non-targeting control Nb R3B23. Mice were imaged 1 hour post injection. Transverse and coronal views are shown, with slices chosen to pass through the brain tumor, without taking other organs into account. Slices that explicitly go through other organs are shown in **Supplementary Figure 3**. Results are representative of n = 3 mice for each group.

Nb15 as compared to Nb89 and Nb54. Hence, even without forced BBB permeabilization, Nb15 allowed us to clearly image mSIRPα in intracranial GBM tumors, exhibiting high signal-to-noise ratios (**Figure 3** and **Table 1**).

Nb15 Targets Monocytes and Tumor-Associated Macrophages From Mouse GBM Tumors

After identifying Nb15 as a suitable probe for *in vivo* imaging of mSIRPα in GBM tumors, we wanted to evaluate its binding capacity on the various populations of mSIRPα expressing tumor-infiltrating myeloid cells. Hereto, GL261 tumors were microdissected and processed into single-cell suspensions, whereupon Nb15 binding was assessed *via* flow cytometry. First, $CD45^+$ cells were selected followed by the exclusion of debris, dead cells and doublets (**Figure 4A**). Within the $CD45^+$ live single cells, the myeloid cells ($CD11b^+$) exhibited clear binding of Nb15, when compared to a control nanobody (**Figure 4B**). Within $CX3CR1^+$ $F4/80^+$ cells, we subgated on monocytes ($MHCII^-$ $Ly6B^+$), transitory TAMs ($MHCII^+$ $Ly6B^+$) and mature TAMs ($Ly6B^-$) (**Figure 4C**), using a previously described gating paradigm (41). Nb15 showed efficient binding to these different populations, in comparison to the control nanobody (**Figures 4D, E**). These results confirmed that Nb15 efficiently bound to $SIRP\alpha^+$ monocytes and TAMs in GL261 tumors.

TABLE 1 | Uptake values of ^{99m}Tc-labeled control Nb R3B23 or anti-SIRPα nanobodies in GL261 tumor-bearing mice based on dissection at 1 h 45 min post injection.

	Control Nb	Nb15	Nb54	Nb89
Blood	1.8055 ± 0.0315	1.3985 ± 0.3665	1.141 ± 0.3160	1.2375 ± 0.0335
Thymus	0.8435 ± 0.0225	1.3950 ± 0.5120	0.5000 ± 0.1000	0.6595 ± 0.0135
Heart	0.6850 ± 0.0320	1.2005 ± 0.2235	0.4745 ± 0.1315	0.6920 ± 0.0920
Lungs	0.8730 ± 0.7350	3.0315 ± 0.7025	1.0245 ± 0.2215	1.712 ± 0.0810
Liver	0.9150 ± 0.0090	3.0450 ± 0.5120	3.5060 ± 0.4880	4.3990 ± 0.0090
Spleen	0.7170 ± 0.0750	8.9050 ± 2.6080	1.7785 ± 0.2935	2.1655 ± 0.3385
Pancreas	0.4815 ± 0.0465	0.6945 ± 0.2005	0.3305 ± 0.0525	0.5070 ± 0.047
Left kidney	295.3835 ± 3.3245	269.206 ± 47.384	303.6065 ± 23.9875	265.543 ± 7.931
Right kidney	306.5695 ± 7.1735	283.6185 ± 28.0615	278.9795 ± 20.2255	283.552 ± 10.1700
Muscle	0.7640 ± 0.3150	0.3360 ± 0.0740	0.1720 ± 0.0220	0.3725 ± 0.0705
Bone	0.5565 ± 0.1745	1.8685 ± 0.0055	0.3855 ± 0.0345	0.8250 ± 0.0100
Lymph nodes	0.8680 ± 0.1360	1.5695 ± 0.4175	0.5885 ± 0.2035	0.9560 ± 0.1310
Brain	0.1355 ± 0.0265	0.4080 ± 0.3590	0.1165 ± 0.0535	0.1100 ± 0.0160
GL261 tumor	0.8080 ± 0.0260	1.7195 ± 0.2125	0.5010 ± 0.2290	0.6725 ± 0.0195

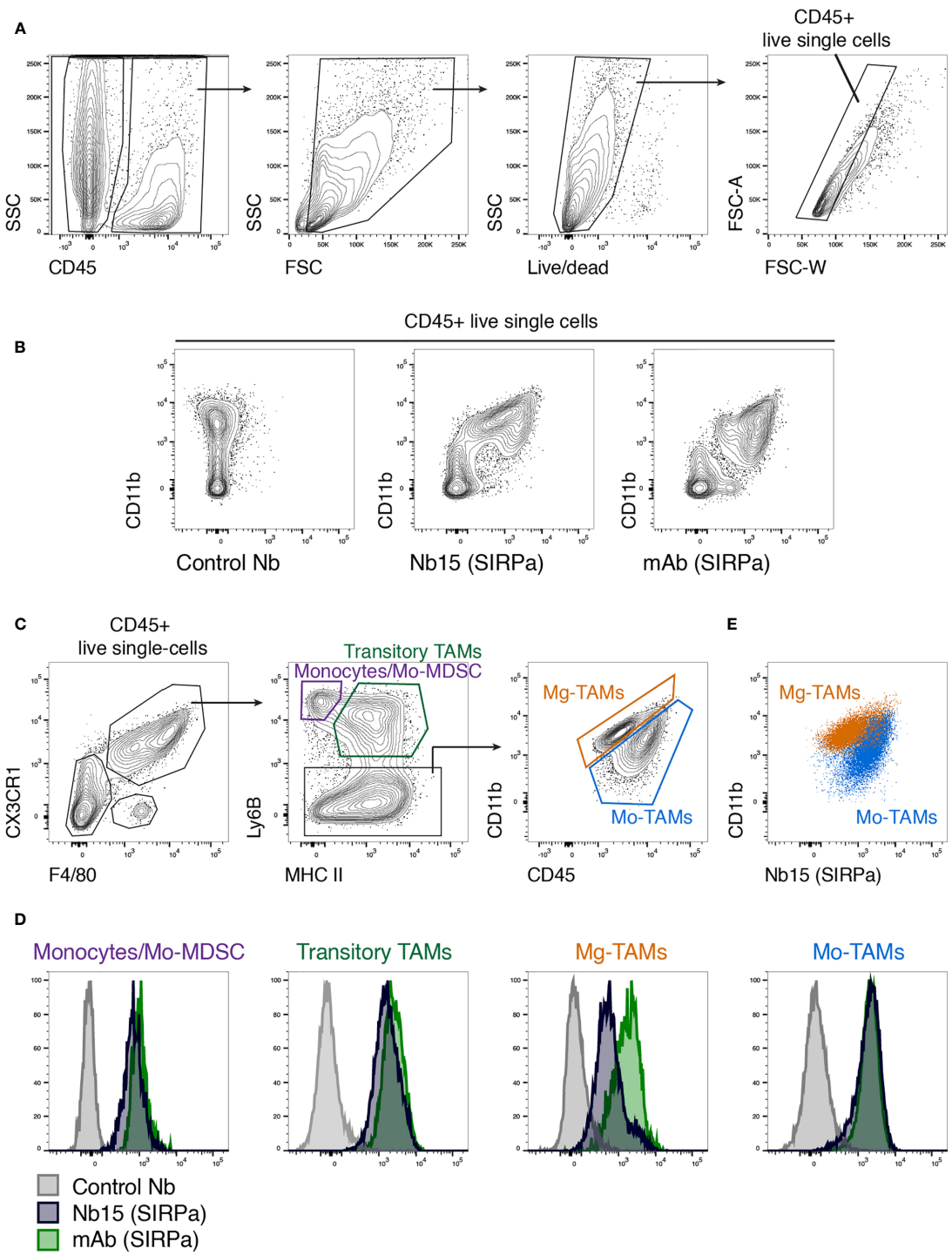

FIGURE 4 | *Ex vivo* staining confirms the specificity of anti-SIRPα Nb15 for tumor-associated monocytes and macrophages. **(A)** Single-cell suspensions were made from orthotopic GL261 tumors, followed by flow cytometric analysis. $CD45^+$ live single cells were gated as indicated. **(B)** Flow cytometry plots showing staining with CD11b in combination with either a non-targeting control nanobody, an anti-mSIRPα Nb15 or a commercially available monoclonal anti-mSIRPα antibody. Cells were pre-gated on $CD45^+$ live single cells. **(C)** Tumor-infiltrating monocyte and macrophage populations were gated based on their expression of CX3CR1, F4/80, Ly6B, MHC-II, CD11b and CD45, as indicated. Monocyte-derived or Mo-TAMs and microglia-derived or Mg-TAMs were distinguished based on their differential expression of CD11b versus CD45. **(D)** Histogram plots showing staining with a commercially available anti-mSIRPα mAb (green), anti-mSIRPα Nb15 (blue) or a non-targeting control Nb19 (grey) for the indicated populations [gated as shown in **(C)**]. **(E)** CD11b and anti-mSIRPα Nb15 staining in Mo-TAMs (blue) and Mg-TAMs (orange) were overlaid to reveal their differential expression. Results are representative of n = 4 mice.

Monovalent Nb15 Is the Preferred Format for *In Vivo* Tumor Imaging in Mice

The above-mentioned *in vitro, in vivo* and *ex vivo* data support that Nb15 could serve as a potent GBM tumor-targeting tool. Previous reports have shown that the binding capacity of nanobody constructs can significantly improve upon self-coupling, due to increased avidity (45). To examine this for Nb15, we created bivalent constructs (**Figure 5A**). *In vitro* characterization by surface plasmon resonance and radioligand binding assay, confirmed a robust binding capacity of both the monovalent and bivalent construct to the antigen (**Figure 5B** and **Supplementary Figure 4**). *In vivo* distribution, however, showed

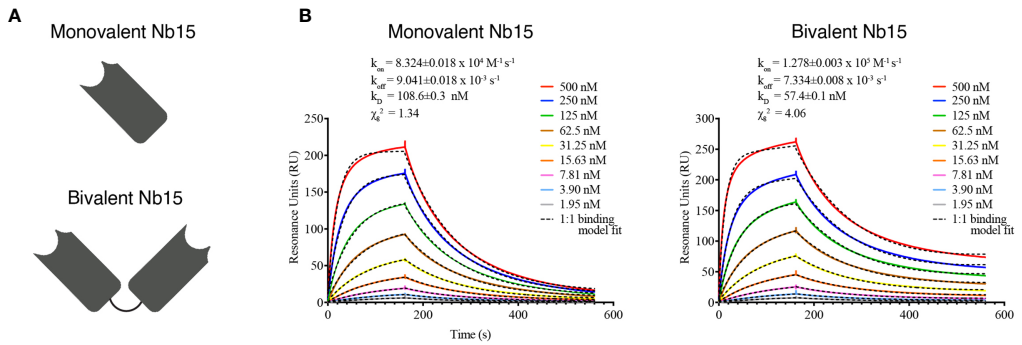

FIGURE 5 | Bivalent anti-SIRPα Nb15 binds SIRPα. **(A)** Schematic representation of mono- and bivalent anti-SIRPα Nb15. **(B)** Kinetic rate constants determination by SPR: the sensorgrams of different concentrations (2x serial dilution) of mono- and bivalent anti-SIRPα Nb15 binding to the recombinant antigen. Fitting of the binding curves was obtained by using a 1:1 mathematical model, for the mono- and bivalent constructs. Kinetic parameters are included as mean±SD.

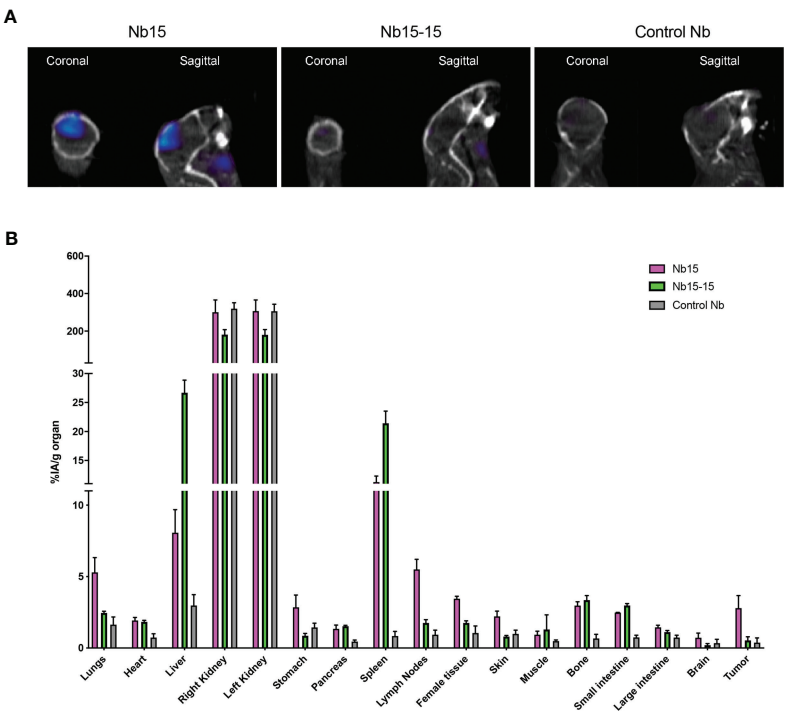

FIGURE 6 | Bivalent anti-SIRPα Nb15 exhibits impaired tumor targeting. **(A)** Fused pinhole SPECT/micro-CT images of GL261 tumor-bearing mice, inoculated with GL621 at the same time and randomized before injection of ^{99m}Tc-labeled monovalent or bivalent anti-SIRPα Nb15 or a non-targeting control Nb R3B23. Mice were imaged 1 hour post tracer injection. Coronal and sagittal views are shown. Images are representative of n = 3 mice for each group. Similar results were obtained for the different mice in each group. **(B)** *Ex vivo* radioactivity values measured in the indicated dissected organs at 1 hour 45 min post injection with ^{99m}Tc-labeled monovalent (magenta) or bivalent (green) anti-SIRPα Nb15 or non-targeting control Nb R3B23. Values are expressed as injected activity per gram (%IA/g). Results are represented as mean ± SEM of n = 3 mice for each group.

that the tumor targeting capacity of Nb15, was completely abolished by the creation of a bivalent construct (**Figure 6A**). Radioactivity measurements of brain, tumor and peripheral tissues, showed that tissue targeting of the bivalent construct was higher as compared to the monovalent construct in SIRPα$^+$ peripheral organs such as the liver and spleen. In the tumor, on the other hand, radioactivity dropped to similar background levels as with the control nanobody (**Figure 6B**). This reveals that small targeting moieties more efficiently penetrate GBM tumors.

DISCUSSION

Nanobodies as Efficient Tools for *In Vivo* Imaging of mSIRPα in GBM Tumors

In the present manuscript, we describe the generation and characterization of nanobodies against SIRPα, as targeting agents for SIRPα-positive glioblastoma (GBM)-infiltrating myeloid cells. Nanobodies isolated from immune libraries obtained after immunization with the recombinant ectodomain of SIRPα, were subjected to a cell binding screening using flow cytometry to determine their ability to bind the native form of the antigen. This revealed that 12 of the nanobodies could recognize murine macrophages expressing SIRPα. Among the 3 nanobodies exhibiting the highest median fluorescence intensities for binding to mouse SIRPα in flow cytometry, Nb15 was found to also target orthotopically implanted GL261 tumors *in vivo*, as shown *via* SPECT-CT imaging and biodistribution analysis of ^{99m}Tc-labeled nanobodies.

Most brain diseases and tumors structurally disrupt the BBB, consequently making it more permeable and easier to cross. GBMs, and in particular also in the GL261 murine GBM model used in this study, are known to display increased BBB disruption as they progress (46, 47). Importantly, Nb15 could target the GBM tumors even in the absence of additional BBB permeabilization. The nanobody format in this situation could be an advantage overcoming some of the limitations of the conventional antibodies, such as their slow diffusion through tissues and large size (150 kDa), even with a disrupted BBB that occurs in this type of disease and disease model. Nanobodies with their small size (15 kDa) and favorable pharmacokinetic properties could hypothetically have an easier path on their way to reach brain targets (48, 49). Moreover, there have already been reports of nanobodies passing the BBB, such as for example nanobodies targeting the prion protein (50), targeting Aβ fibrils associated with Alzheimer disease (51) or targeting tumor antigens associated with brain tumors (30, 31).

For Nb54 and Nb89, the accumulation in the GBM tumor did not significantly exceed that of the control nanobody. This difference in uptake was not correlated with the affinity for the target, since the affinity of Nb89 for mSIRPα as detected *via* SPR was even higher as compared to that of Nb15. It has been suggested that nanobodies with a basic pI could cross the BBB (52). However, this did not seem to be a factor here either, since Nb89 had an EXPASY calculated theoretical pI of higher than 9, as compared to below 7 for Nb15. The observation that Nb15 also showed high uptake in spleen, liver, lymph nodes, thymus, bone (marrow) and lungs, which are known macrophage resident "hot spots", indicates that the differences in GBM tumor targeting potential between these nanobodies was most likely related to an inherently better *in vivo* targeting and imaging potential of Nb15 as compared to Nb89 and Nb54. In particular for Nb54, its fast off-rate may contribute to a poor *in vivo* targeting. Possibly, the targeted epitope could be important for effective *in vivo* targeting of Nb15 to SIRPα on myeloid cells.

Possible Implications for Diagnostic Applications

Whole body preclinical SPECT/CT imaging using radiolabeled nanobodies targeting SIRPα as performed in the current study provides a proof of concept for *in vivo* targeting of SIRPα on GBM tumor-infiltrating myeloid cells and confirms the added value and favorable pharmacokinetics of monovalent nanobodies. Monovalent nanobodies offer a rapid targeting to antigen-positive organs, followed by fast clearance of non-targeting probes *via* the kidneys. This yields a high signal-to-noise contrast and limited off-target radiotoxicity, allowing high contrast imaging within 1 h post injection. Given that TAMs and the markers they express have been documented to correlate with malignancy and reduced survival in GBM patients (53), nanobody-based detection of SIRPα in GBM may entail prognostic value. Thereby, a high accumulation of radiolabeled nanobodies targeting SIRPα may correlate with the presence of a high amount of immune suppressive TAMs. Alternatively, a higher signal may correlate with higher expression of SIRPα per cell, reflecting a more immune suppressive environment, but potentially also rendering the TAMs more responsive to SIRPα-targeted therapies. As such, nuclear imaging of SIRPα may have value for disease monitoring or therapy guidance in GBM.

Besides whole body imaging, nanobodies also offer diagnostic possibilities for image-guided surgery (26). In our recently documented efforts to unravel the GBM immune landscape (41), multiplex immunohistochemistry revealed that (SIRPα expressing) TAMs are found throughout human GBM tumor tissue. Thus, an interesting perspective is that fluorescently labeled nanobodies targeting SIRPα could be evaluated for delineating tumors during surgery (26).

As a remark, while the current study provides a first qualitative indication that Nb15 can be used to target myeloid cells in a glioma model, proof that the method can also be used in a quantitative manner to track accumulation of SIPRα-expressing myeloid cells or to monitor upregulation of SIRPα expression has not been provided. This will need to be addressed in follow-up studies. Thereby, myeloid cell depletion strategies could help to evaluate whether the technique could be employed to quantify the abundance of myeloid cells in the glioma microenvironment. Corresponding IHC/IF of tumor area or *ex vivo* flow cytometry analysis of SIRPα expression could also be used to assess how well the radioactive signals from the tracer and the expression of the marker match.

Possible Implications for Therapeutic Applications

A significant body of evidence supports the targeting of the CD47-SIRPα immune checkpoint as a promising strategy against several hematological and solid tumors, especially when used in combination with other inhibitors targeting T-cell immune checkpoints, such as PD-L1-PD-1 (54–56). In GBM, preclinical data indicate that blocking the CD47-SIRPα axis can induce antitumor effects (13, 14, 57), although a combination with chemotherapy may be required to activate ER stress responses that promote tumor cell phagocytosis by professional antigen presenting cells (14). Moreover, Gholamin and colleagues have shown the promising therapeutic potential of targeting the CD47-SIRPα axis in patient-derived orthotopic xenograft models, where it reduces tumor growth in a variety of pediatric brain malignancies and inhibits metastasis (19). Accordingly, a number of immunological checkpoint inhibitors targeting the CD47-SIRPα axis are currently in clinical trials (58). So far, most efforts have been put on antibodies targeting CD47 or on Fc fusion proteins of the SIRPα ectodomain. However, a complication of effective targeting of the ubiquitously expressed CD47 with antibodies or fusion proteins containing an Fc is the occurrence of side effects such as anemia and thrombocytopenia. In this context, targeting of SIRPα, with its more confined expression pattern, may address some of these issues. And indeed, several anti-SIRPα antibodies are in active development in efforts to augment anti-tumor responses and overcome the significant off-target toxicities with anti-CD47 (56). Moreover, the nanobody format may bypass some of the safety concerns related to Fc-containing constructs. A direct therapeutic potential could be obtained if the nanobodies can modulate the CD47-SIRPα interaction, resulting in enhanced phagocytosis of cancer cells. The range of affinities detected for the identified nanobodies should in principle allow to interfere with the CD47-SIRPα interaction in a competitive manner, since the reported affinity for said interaction is in the sub-micromolar range (56).

In order to obtain sustained therapeutic effects, multivalency and lifetime extension of the nanobodies may be required, for example by genetically fusing the nanobody to a nanobody targeting serum albumin into a bispecific construct (59). Given the lower brain tumor uptake observed for bivalent nanobodies in this study, a sufficient level of accumulation in the tumor may be an attention point for multivalent and multispecific constructs. Of course, for therapeutic applications, the reduction in rapid tumor targeting for the bivalent constructs as detected here in the context of *in vivo* imaging, may be compensated for, by an increased accumulation in the tumor over time in case of life-time extended constructs (60). Of note, the size of multivalent and multispecific nanobody constructs is still smaller than full-sized antibodies, which may be beneficial for their brain targeting potential.

Next to counteracting the don't-eat-me signal, nanobodies targeting SIRPα could also be used to deplete tumor-promoting myeloid cells, which facilitate GBM development and protect it from therapeutic treatments (61). Thereto, these nanobodies could be labeled with therapeutic radionuclides such as ^{177}Lu, as we have shown before for nanobodies targeting mCD206 on tumor-associated macrophages (27). Alternatively, the nanobodies could be genetically coupled to an Fc-part that engenders antibody-dependent cellular cytotoxicity (ADCC), as we have documented for the depletion of tumor-infiltrating regulatory T cells (62). Of course, for such cell depletion approaches an important issue will be to avoid or at least minimize side-effects in peripheral organs where SIRPα is expressed, such as spleen, liver and lungs.

Overall, there is clear room for improvement and optimization of these nanobodies to increase their tumor targeting potential and protect the major antigen sinks (spleen, liver and lungs) to avoid possible side-toxicity effects. However, the notion that these nanobodies have reached their antigen in brain tumor-bearing mice is the first stepping stone towards further development. This is of particular importance given the high unmet medical need for brain pathologies at both diagnostic and therapeutic level.

DATA AVAILABILITY STATEMENT

All human and mouse scRNA-seq and CITE-seq datasets that we have used for this article can be accessed *via* our interactive webserver at www.brainimmuneatlas.org. All gene–cell count and cell annotation matrices can also be downloaded there. In addition, all mouse scRNA-seq and CITE-seq raw data, mouse gene–cell count matrices and human gene–cell count matrices have been deposited at GEO (NCBI) under accession number GSE163120. Raw sequencing reads of the human scRNA-seq and CITE-seq experiments have been deposited in the controlled access public repository European Genome-phenome Archive (EGA), under study accession number EGAS00001004871. Other data that support the findings of this study are available from the corresponding author upon request.

ETHICS STATEMENT

The animal study was reviewed and approved by "Ethische Commissie Dierproeven" at Vrije Universiteit Brussel.

AUTHOR CONTRIBUTIONS

KV, ER, JP, and AP performed experiments. KV, ER, JP, AP, DK, ND, and IS have analysed data. GR, ND, KM, SM, and JG designed experiments. KV, ER, GR, and KM wrote the manuscript text. All authors have critically reviewed, read and agreed to the published version of the manuscript.

FUNDING

This research project was realized with the support of Kom op tegen Kanker (project code ANI167) and a PhD scholarship grant from FWO to ER.

ACKNOWLEDGMENTS

We thank Jan De Jonge for technical assistance with nanobody production and purification, and Cindy Peleman with *in vivo* imaging experiments.

SUPPLEMENTARY MATERIAL

The Supplementary Material for this article can be found online at: https://www.frontiersin.org/articles/10.3389/fimmu.2021.777524/full#supplementary-material

REFERENCES

1. Jackson CM, Choi J, Lim M. Mechanisms of Immunotherapy Resistance: Lessons From Glioblastoma. *Nat Immunol* (2019) 20:1100–9. doi: 10.1038/s41590-019-0433-y
2. Galluzzi L, Chan TA, Kroemer G, Wolchok JD, López-Soto A. The Hallmarks of Successful Anticancer Immunotherapy. *Sci Transl Med* (2018) 10:eaat7807. doi: 10.1126/scitranslmed.aat7807
3. Vaddepally RK, Kharel P, Pandey R, Garje R, Chandra AB. Review of Indications of FDA-Approved Immune Checkpoint Inhibitors Per NCCN Guidelines With the Level of Evidence. *Cancers* (2020) 12:738. doi: 10.3390/cancers12030738
4. Brahm CG, van Linde ME, Enting RH, Schuur M, Otten RHJ, Heymans MW, et al. The Current Status of Immune Checkpoint Inhibitors in Neuro-Oncology: A Systematic Review. *Cancers* (2020) 12:586. doi: 10.3390/cancers12030586
5. Daubon T, Hemadou A, Romero Garmendia I, Saleh M. Glioblastoma Immune Landscape and the Potential of New Immunotherapies. *Front Immunol* (2020) 11:585616. doi: 10.3389/fimmu.2020.585616
6. Veillette A, Chen J. Sirpα–CD47 Immune Checkpoint Blockade in Anticancer Therapy. *Trends Immunol* (2018) 39:173–84. doi: 10.1016/j.it.2017.12.005
7. Barclay AN, Van Den Berg TK. The Interaction Between Signal Regulatory Protein Alpha (Sirpα) and CD47: Structure, Function, and Therapeutic Target. *Annu Rev Immunol* (2014) 32:25–50. doi: 10.1146/annurev-immunol-032713-120142
8. Jaiswal S, Jamieson CHM, Pang WW, Park CY, Chao MP, Majeti R, et al. CD47 Is Upregulated on Circulating Hematopoietic Stem Cells and Leukemia Cells to Avoid Phagocytosis. *Cell* (2009) 138:271–85. doi: 10.1016/j.cell.2009.05.046
9. Zhao H, Wang J, Kong X, Li E, Liu Y, Du X, et al. CD47 Promotes Tumor Invasion and Metastasis in Non-Small Cell Lung Cancer. *Sci Rep* (2016) 6:29719. doi: 10.1038/srep29719
10. Li Y, Lu S, Xu Y, Qiu C, Jin C, Wang Y, et al. Overexpression of CD47 Predicts Poor Prognosis and Promotes Cancer Cell Invasion in High-Grade Serous Ovarian Carcinoma. *Am J Transl Res* (2017) 9:2901–10.
11. Majeti R, Chao MP, Alizadeh AA, Pang WW, Jaiswal S, Gibbs KD, et al. CD47 Is an Adverse Prognostic Factor and Therapeutic Antibody Target on Human Acute Myeloid Leukemia Stem Cells. *Cell* (2009) 138:286–99. doi: 10.1016/j.cell.2009.05.045
12. Edris B, Weiskopf K, Volkmer AK, Volkmer JP, Willingham SB, Contreras-Trujillo H, et al. Antibody Therapy Targeting the CD47 Protein Is Effective in a Model of Aggressive Metastatic Leiomyosarcoma. *Proc Natl Acad Sci* (2012) 109:6656–61. doi: 10.1073/pnas.1121629109
13. von Roemeling CA, Wang Y, Qie Y, Yuan H, Zhao H, Liu X, et al. Therapeutic Modulation of Phagocytosis in Glioblastoma can Activate Both Innate and Adaptive Antitumour Immunity. *Nat Commun* (2020) 11:1508. doi: 10.1038/s41467-020-15129-8
14. Kim D, Wang J, Willingham SB, Martin R, Wernig G, Weissman IL. Anti-CD47 Antibodies Promote Phagocytosis and Inhibit the Growth of Human Myeloma Cells. *Leukemia* (2012) 26:2538–45. doi: 10.1038/leu.2012.141
15. Willingham SB, Volkmer JP, Gentles AJ, Sahoo D, Dalerba P, Mitra SS, et al. The CD47-Signal Regulatory Protein Alpha (SIRPa) Interaction Is a Therapeutic Target for Human Solid Tumors. *Proc Natl Acad Sci* (2012) 109:6662–7. doi: 10.1073/pnas.1121623109
16. Wang Y, Xu Z, Guo S, Zhang L, Sharma A, Robertson GP, et al. Intravenous Delivery of siRNA Targeting CD47 Effectively Inhibits Melanoma Tumor Growth and Lung Metastasis. *Mol Ther* (2013) 21:1919–29. doi: 10.1038/mt.2013.135
17. Weiskopf K, Jahchan NS, Schnorr PJ, Cristea S, Ring AM, Maute RL, et al. CD47-Blocking Immunotherapies Stimulate Macrophage-Mediated Destruction of Small-Cell Lung Cancer. *J Clin Invest* (2016) 126:2610–20. doi: 10.1172/JCI81603
18. Alvey CM, Spinler KR, Irianto J, Pfeifer CR, Hayes B, Xia Y, et al. SIRPA-Inhibited, Marrow-Derived Macrophages Engorge, Accumulate, and Differentiate in Antibody-Targeted Regression of Solid Tumors. *Curr Biol* (2017) 27:2065–77. doi: 10.1016/j.cub.2017.06.005
19. Gholamin S, Mitra SS, Feroze AH, Liu J, Kahn SA, Zhang M, et al. Disrupting the CD47-Sirpα Anti-Phagocytic Axis by a Humanized Anti-CD47 Antibody Is an Efficacious Treatment for Malignant Pediatric Brain Tumors. *Sci Transl Med* (2017) 9:eaaf2968. doi: 10.1126/scitranslmed.aaf2968
20. Wu L, Yu GT, Deng WW, Mao L, Yang LL, Ma SR, et al. Anti-CD47 Treatment Enhances Anti-Tumor T-Cell Immunity and Improves Immunosuppressive Environment in Head and Neck Squamous Cell Carcinoma. *Oncoimmunology* (2018) 7:e1397248. doi: 10.1080/2162402X.2017.1397248
21. Mohanty S, Yerneni K, Theruvath JL, Graef CM, Nejadnik H, Lenkov O, et al. Nanoparticle Enhanced MRI can Monitor Macrophage Response to CD47 mAb Immunotherapy in Osteosarcoma. *Cell Death Dis* (2019) 10:36. doi: 10.1038/s41419-018-1285-3
22. Hutter G, Theruvath J, Graef CM, Zhang M, Schoen MK, Manz EM, et al. Microglia Are Effector Cells of CD47-Sirpα Antiphagocytic Axis Disruption Against Glioblastoma. *Proc Natl Acad Sci* (2019) 116:997–1006. doi: 10.1073/pnas.1721434116
23. Chao MP, Takimoto CH, Feng DD, McKenna K, Gip P, Liu J, et al. Therapeutic Targeting of the Macrophage Immune Checkpoint CD47 in Myeloid Malignancies. *Front Oncol* (2020) 9:1380. doi: 10.3389/fonc.2019.01380
24. Massa S, Xavier C, De Vos J, Caveliers V, Lahoutte T, Muyldermans S, et al. Site-Specific Labeling of Cysteine-Tagged Camelid Single-Domain Antibody-Fragments for Use in Molecular Imaging. *Bioconjug Chem* (2014) 25:979–88. doi: 10.1021/bc500111t
25. Lemaire M, D'Huyvetter M, Lahoutte T, Van Valckenborgh E, Menu E, De Bruyne E, et al. Imaging and Radioimmunotherapy of Multiple Myeloma With Anti-Idiotypic Nanobodies. *Leukemia* (2014) 28:444–7. doi: 10.1038/leu.2013.292
26. Debie P, Devoogdt N, Hernot S. Targeted Nanobody-Based Molecular Tracers for Nuclear Imaging and Image-Guided Surgery. *Antibodies* (2019) 8:12. doi: 10.3390/antib8010012
27. Bolli E, D'Huyvetter M, Murgaski A, Berus D, Stangé G, Clappaert EJ, et al. Stromal-Targeting Radioimmunotherapy Mitigates the Progression of Therapy-Resistant Tumors. *J Control Release* (2019) 314:1–11. doi: 10.1016/j.jconrel.2019.10.024
28. Bolli E, Scherger M, Arnouk SM, Pombo Antunes AR, Straßburger D, Urschbach M, et al. Targeted Repolarization of Tumor-Associated Macrophages *via* Imidazoquinoline-Linked Nanobodies. *Adv Sci* (2021) 8:2004574. doi: 10.1002/advs.202004574
29. Muyldermans S. Nanobodies: Natural Single-Domain Antibodies. *Annu Rev Biochem* (2013) 82:775–97. doi: 10.1146/annurev-biochem-063011-092449
30. Debie P, Lafont C, Defrise M, Hansen I, van Willigen DM, van Leeuwen FWB, et al. Size and Affinity Kinetics of Nanobodies Influence Targeting and Penetration of Solid Tumours. *J Control Release* (2020) 317:34–42. doi: 10.1016/j.jconrel.2019.11.014
31. Puttemans J, Dekempeneer Y, Eersels JL, Hanssens H, Debie P, Keyaerts M, et al. Preclinical Targeted α- and β —Radionuclide Therapy in HER2-Positive Brain Metastasis Using Camelid Single-Domain Antibodies. *Cancers* (2020) 12:1017. doi: 10.3390/cancers12041017
32. Gasteiger E, Hoogland C, Gattiker A, Duvaud S, Wilkins MR, Appel RD, et al. Protein Identification and Analysis Tools on the ExPASy Server. In: JM Walker, editor. *The Proteomics Protocols Handbook Springer Protocol*

Handbooks. Totowa, NJ: Humana Press (2005). p. 571–607. doi: 10.1385/1-59259-890-0:571
33. Vincke C, Gutiérrez C, Wernery U, Devoogdt N, Hassanzadeh-Ghassabeh G, Muyldermans S. Generation of Single Domain Antibody Fragments Derived From Camelids and Generation of Manifold Constructs. In: P Chames, editor. *Antibody Engineering Methods in Molecular Biology (Methods and Protocols)*. Totowa, NJ: Humana Press (2012). p. 145–76. doi: 10.1007/978-1-61779-974-7_8
34. Conrath KE, Lauwereys M, Galleni M, Matagne A, Frère JM, Kinne J, et al. β-Lactamase Inhibitors Derived From Single-Domain Antibody Fragments Elicited in the Camelidae. *Antimicrob Agents Chemother* (2001) 45:2807–12. doi: 10.1128/AAC.45.10.2807-2812.2001
35. Subedi S, Moonens K, Romaõ E, Lo A, Vandenbussche G, Bugaytsova J, et al. Expression, Purification and X-Ray Crystallographic Analysis of the Helicobacter Pylori Blood Group Antigen-Binding Adhesin BabA. *Acta Crystallogr Sect F Struct Biol Commun* (2014) 70:1631–5. doi: 10.1107/S2053230X14023188
36. Ausmann JI, Shapiro WR, Rall DP. Studies on the Chemotherapy of Experimental Brain Tumors: Development of an Experimental Model. *Cancer Res* (1970) 30:2394–400.
37. Baumann BC, Dorsey JF, Benci JL, Joh DY, Kao GD. Stereotactic Intracranial Implantation and *In Vivo* Bioluminescent Imaging of Tumor Xenografts in a Mouse Model System of Glioblastoma Multiforme. *J Vis Exp* (2012) 67:e4089. doi: 10.3791/4089
38. Xavier C, Devoogdt N, Hernot S, Vaneycken I, D'Huyvetter M, De Vos J, et al. Site-Specific Labeling of His-Tagged Nanobodies With 99mtc: A Practical Guide. In: D Saerens, S Muyldermans, editors. *Single Domain Antibodies Methods in Molecular Biology (Methods and Protocols)*. Totowa, NJ: Humana Press (2012). p. 485–90. doi: 10.1007/978-1-61779-968-6_30
39. Vaneycken I, Govaert J, Vincke C, Caveliers V, Lahoutte T, De Baetselier P, et al. *In Vitro* Analysis and *In Vivo* Tumor Targeting of a Humanized, Grafted Nanobody in Mice Using Pinhole SPECT/micro-CT. *J Nucl Med* (2010) 51:1099–106. doi: 10.2967/jnumed.109.069823
40. Loening AM, Gambhir SS. AMIDE: A Free Software Tool for Multimodality Medical Image Analysis. *Mol Imaging* (2003) 2:131–7. doi: 10.1162/153535003322556877
41. Pombo Antunes AR, Scheyltjens I, Lodi F, Messiaen J, Antoranz A, Duerinck J, et al. Single-Cell Profiling of Myeloid Cells in Glioblastoma Across Species and Disease Stage Reveals Macrophage Competition and Specialization. *Nat Neurosci* (2021) 24:595–610. doi: 10.1038/s41593-020-00789-y
42. Stoeckius M, Hafemeister C, Stephenson W, Houck-Loomis B, Chattopadhyay PK, Swerdlow H, et al. Simultaneous Epitope and Transcriptome Measurement in Single Cells. *Nat Methods* (2017) 14:865–8. doi: 10.1038/nmeth.4380
43. Lefranc MP, Pommié C, Ruiz M, Giudicelli V, Foulquier E, Truong L, et al. IMGT Unique Numbering for Immunoglobulin and T Cell Receptor Constant Domains and Ig Superfamily V-Like Domains. *Dev Comp Immunol* (2003) 27:55–77. doi: 10.1016/s0145-305x(02)00039-3
44. Tchouate Gainkam LO, Caveliers V, Devoogdt N, Vanhove C, Xavier C, Boerman O, et al. Localization, Mechanism and Reduction of Renal Retention of Technetium-99m Labeled Epidermal Growth Factor Receptor-Specific Nanobody in Mice. *Contrast Media Mol Imaging* (2011) 6:85–92. doi: 10.1002/cmmi.408
45. Beirnaert E, Desmyter A, Spinelli S, Lauwereys M, Aarden L, Dreier T, et al. Bivalent Llama Single-Domain Antibody Fragments Against Tumor Necrosis Factor Have Picomolar Potencies Due to Intramolecular Interactions. *Front Immunol* (2017) 8:867. doi: 10.3389/fimmu.2017.00867
46. Leten C, Struys T, Dresselaers T, Himmelreich U. *In Vivo* and Ex Vivo Assessment of the Blood Brain Barrier Integrity in Different Glioblastoma Animal Models. *J Neurooncol* (2014) 119:297–306. doi: 10.1007/s11060-014-1514-2
47. Arvanitis CD, Ferraro GB, Jain RK. The Blood–Brain Barrier and Blood–Tumour Barrier in Brain Tumours and Metastases. *Nat Rev Cancer* (2020) 20:26–41. doi: 10.1038/s41568-019-0205-x
48. Pothin E, Lesuisse D, Lafaye P. Brain Delivery of Single-Domain Antibodies: A Focus on VHH and VNAR. *Pharmaceutics* (2020) 12:937. doi: 10.3390/pharmaceutics12100937
49. Bélanger K, Iqbal U, Tanha J, MacKenzie R, Moreno M, Stanimirovic D. Single-Domain Antibodies as Therapeutic and Imaging Agents for the Treatment of CNS Diseases. *Antibodies* (2019) 8:27. doi: 10.3390/antib8020027
50. Jones DR, Taylor WA, Bate C, David M, Tayebi M. A Camelid Anti-PrP Antibody Abrogates PrPSc Replication in Prion-Permissive Neuroblastoma Cell Lines. *PloS One* (2010) 5:e9804. doi: 10.1371/journal.pone.0009804
51. Kasturirangan S, Li L, Emadi S, Boddapati S, Schulz P, Sierks MR. Nanobody Specific for Oligomeric Beta-Amyloid Stabilizes Nontoxic Form. *Neurobiol Aging* (2012) 33:1320–8. doi: 10.1016/j.neurobiolaging.2010.09.020
52. Li T, Bourgeois JP, Celli S, Glacial F, Le Sourd AM, Mecheri S, et al. Cell-Penetrating Anti-GFAP VHH and Corresponding Fluorescent Fusion Protein VHH-GFP Spontaneously Cross the Blood-Brain Barrier and Specifically Recognize Astrocytes: Application to Brain Imaging. *FASEB J* (2012) 26:3969–79. doi: 10.1096/fj.11-201384
53. Ding P, Wang W, Wang J, Yang Z, Xue L. Expression of Tumor-Associated Macrophage in Progression of Human Glioma. *Cell Biochem Biophys* (2014) 70:1625–31. doi: 10.1007/s12013-014-0105-3
54. Matlung HL, Szilagyi K, Barclay NA, van den Berg TK. The CD47-Sirpα Signaling Axis as an Innate Immune Checkpoint in Cancer. *Immunol Rev* (2017) 276:145–64. doi: 10.1111/imr.12527
55. Weiskopf K. Cancer Immunotherapy Targeting the CD47/Sirpα Axis. *Eur J Cancer* (2017) 76:100–9. doi: 10.1016/j.ejca.2017.02.013
56. Jalil AAR, Andrechak JC, Discher DE. Macrophage Checkpoint Blockade: Results From Initial Clinical Trials, Binding Analyses, and CD47-Sirpα Structure-Function. *Antib Ther* (2020) 3:80–94. doi: 10.1093/abt/tbaa006
57. Li F, Lv B, Liu Y, Hua T, Han J, Sun C, et al. Blocking the CD47-Sirpα Axis by Delivery of Anti-CD47 Antibody Induces Antitumor Effects in Glioma and Glioma Stem Cells. *Oncoimmunology* (2018) 7:e1391973. doi: 10.1080/2162402X.2017.1391973
58. Hu J, Xiao Q, Dong M, Guo D, Wu X, Wang B. Glioblastoma Immunotherapy Targeting the Innate Immune Checkpoint CD47-Sirpα Axis. *Front Immunol* (2020) 11:593219. doi: 10.3389/fimmu.2020.593219
59. Sparkes A, De Baetselier P, Brys L, Cabrito I, Sterckx YGJ, Schoonooghe S, et al. Novel Half-Life Extended Anti-MIF Nanobodies Protect Against Endotoxic Shock. *FASEB J* (2018) 32:3411–22. doi: 10.1096/fj.201701189R
60. Tijink BM, Laeremans T, Budde M, Stigter-van Walsum M, Dreier T, de Haard HJ, et al. Improved Tumor Targeting of Anti-Epidermal Growth Factor Receptor Nanobodies Through Albumin Binding: Taking Advantage of Modular Nanobody Technology. *Mol Cancer Ther* (2008) 7:2288–97. doi: 10.1158/1535-7163.MCT-07-2384
61. Pombo Antunes AR, Scheyltjens I, Duerinck J, Neyns B, Movahedi K, Van Ginderachter JA. Understanding the Glioblastoma Immune Microenvironment as Basis for the Development of New Immunotherapeutic Strategies. *Elife* (2020) 9:e52176. doi: 10.7554/eLife.52176
62. Van Damme H, Dombrecht B, Kiss M, Roose H, Allen E, Van Overmeire E, et al. Therapeutic Depletion of CCR8+ Tumor-Infiltrating Regulatory T Cells Elicits Antitumor Immunity and Synergizes With Anti-PD-1 Therapy. *J Immunother Cancer* (2021) 9:e001749. doi: 10.1136/jitc-2020-001749

Conflict of Interest: The authors declare that the research was conducted in the absence of any commercial or financial relationships that could be construed as a potential conflict of interest.

Publisher's Note: All claims expressed in this article are solely those of the authors and do not necessarily represent those of their affiliated organizations, or those of the publisher, the editors and the reviewers. Any product that may be evaluated in this article, or claim that may be made by its manufacturer, is not guaranteed or endorsed by the publisher.

frontiers in Immunology

REVIEW
published: 07 December 2021
doi: 10.3389/fimmu.2021.787307

The Colony Stimulating Factor-1 Receptor (CSF-1R)-Mediated Regulation of Microglia/Macrophages as a Target for Neurological Disorders (Glioma, Stroke)

Cristina Barca[1], Claudia Foray[1], Sven Hermann[1], Ulrich Herrlinger[2,3], Isabel Remory[4], Damya Laoui[5,6], Michael Schäfers[1,7], Oliver M. Grauer[8], Bastian Zinnhardt[1,9†] and Andreas H. Jacobs[1,3,10*†]*

[1] European Institute for Molecular Imaging (EIMI), University of Münster, Münster, Germany, [2] Division of Clinical Neuro-Oncology, Department of Neurology, University Hospital Bonn, Bonn, Germany, [3] Centre of Integrated Oncology, University Hospital Bonn, Bonn, Germany, [4] In vivo Cellular and Molecular Imaging laboratory (ICMI), Vrije Universiteit Brussel (VUB), Brussels, Belgium, [5] Myeloid Cell Immunology Lab, VIB Center for Inflammation Research, Brussels, Belgium, [6] Lab of Cellular and Molecular Immunology, Vrije Universiteit Brussel, Brussels, Belgium, [7] Department of Nuclear Medicine, University Hospital Münster, Münster, Germany, [8] Department of Neurology with Institute of Translational Neurology, University Hospital Münster, Münster, Germany, [9] Biomarkers & Translational Technologies (BTT), Pharma Research & Early Development (pRED), F. Hoffmann-La Roche Ltd., Basel, Switzerland, [10] Department of Geriatrics and Neurology, Johanniter Hospital, Bonn, Germany

OPEN ACCESS

Edited by:
Marco Erreni,
Humanitas Research Hospital, Italy

Reviewed by:
Salvatore J Coniglio,
Kean University, United States
Cynthia Louis,
Walter and Eliza Hall Institute of Medical Research, Australia
Atay Vural,
Koç University, Turkey

***Correspondence:**
Andreas H. Jacobs
ahjacobs@uni-muenster.de
Cristina Barca
cristina.barca@uni-muenster.de

†These authors have contributed equally to this work

Specialty section:
This article was submitted to Inflammation, a section of the journal Frontiers in Immunology

Received: *30 September 2021*
Accepted: *17 November 2021*
Published: *07 December 2021*

Citation:
Barca C, Foray C, Hermann S, Herrlinger U, Remory I, Laoui D, Schäfers M, Grauer OM, Zinnhardt B and Jacobs AH (2021) The Colony Stimulating Factor-1 Receptor (CSF-1R)-Mediated Regulation of Microglia/Macrophages as a Target for Neurological Disorders (Glioma, Stroke). Front. Immunol. 12:787307. doi: 10.3389/fimmu.2021.787307

Immunomodulatory therapies have fueled interest in targeting microglial cells as part of the innate immune response after infection or injury. In this context, the colony-stimulating factor 1 (CSF-1) and its receptor (CSF-1R) have gained attention in various neurological conditions to deplete and reprogram the microglia/macrophages compartment. Published data in physiological conditions support the use of small-molecule inhibitors to study microglia/macrophages dynamics under inflammatory conditions and as a therapeutic strategy in pathologies where those cells support disease progression. However, preclinical and clinical data highlighted that the complexity of the spatiotemporal inflammatory response could limit their efficiency due to compensatory mechanisms, ultimately leading to therapy resistance. We review the current state-of-art in the field of CSF-1R inhibition in glioma and stroke and provide an overview of the fundamentals, ongoing research, potential developments of this promising therapeutic strategy and further application toward molecular imaging.

Keywords: colony stimulating factor-1 receptor, neuroinflammation, glioma, stroke, microglia/macrophages, positron emission tomography

INTRODUCTION

Inflammation is a biological process triggered by injuries, infections and damages suffered by the cells that disrupt tissue homeostasis. Together with the innate and adaptive immune responses, they are discussed as essential factors in the onset and progression of many neurological conditions (1). Therefore, the use of neuroprotective and immunomodulatory agents that curtail inflammation has become an essential area of research. The failure of clinically effective translation is partly due to the complexity of molecular alterations and the spatiotemporal functional dynamics of the different cellular players. Still, targeting specific inflammatory and immune pathways represents a promising therapeutic strategy in many neurological diseases requiring further investigations (1). One of the major players highly investigated is microglia (2–5). As part of the resident immune cells, microglia quickly activate after injury by producing chemokines, cytokines and other signalling molecules. These cells show evolving detrimental pro- and/or beneficial anti-inflammatory properties, worsening and/or promoting tissue repair, respectively (6, 7). Their spatiotemporal function and contribution to disease have been extensively investigated using different systems (genetic animal models, drug-based interventions) (8, 9). In this review, we focus on the pharmacological intervention employing the colony stimulating factor-1 receptor (CSF-1R) inhibitors, which stands as a powerful drug-based approach to study microglia dynamics under inflammatory conditions, with a promising translational value (10).

MICROGLIA

Microglial cells serve as regulators of homeostasis in the central nervous system and represent the first line of defence against infection and injury (11). They are long-living cells and have an intrinsic capacity for self-renewal (12, 13). Highly ramified, they continuously sense the local environment by extending and retracting their processes (14, 15). In case of injury or infection, microglia are highly dynamic cells capable of undergoing quick transcriptome changes depending on the type of signals sensed in their environment (15).

They play a significant role in neuronal plasticity and synaptic connections (14, 16). They shape neuronal networks and control synaptic pruning, serving an essential role in learning and memory. Furthermore, microglia secrete neurotrophic factors that affect synaptic plasticity and promote synapse formation, including insulin-like growth factor 1 (IGF-1), brain-derived neurotrophic factor (BDNF) and transforming growth factor (TGF)-β (17). Mice depleted of microglia showed deficits in learning tasks and significantly reduced synapse formation (16). It highlights the importance of microglia in activity-dependent plasticity, with proper neuron-microglia cross-talk essential for neural network landscape (18).

Microglia show region-dependent molecular and transcriptional heterogeneity in physiological conditions. Masuda et al. (19) reported the existence of ten microglia subtypes in the healthy mouse brain (19, 20). Ten clusters (C1-C10) were differentiated by their different gene expression profile, including C1-C6 to be embryonic microglia and C7-C10 to be postnatal microglia. Results indicated that *tmem119*, *Selplg* and *Slc2a5* markers were highly expressed in postnatal microglia compared to embryonic microglia, indicative of cell maturation. It was suggested that the four postnatal clusters might be related to different cell functions (19). Additional clusters were observed in inflammatory conditions, such as demyelinating and neurodegenerative diseases, suggesting that a pathological environment can trigger additional disease-specific microglial subpopulations (20, 21), displaying enriched disease-related genes. Moreover, some microglia clusters may also be depleted in neurodegenerative diseases (22).

A major limitation in tracking microglia-specific contributions to different pathological pathways is that they share many common features with bone marrow (BM)-derived macrophages, including morphologies, surface markers and other characteristics (23). That explains the frequent use of the terminology microglia/macrophages to describe this family of mononuclear myeloid cells. In response to infection or injury, peripheral myeloid cells (including macrophages, bone marrow-derived monocytes, etc.) are recruited to the injured tissue and exhibit similar morphology and expression patterns to microglia, forming a pool of indistinguishable activated myeloid cells (24). However, microglial cells do have a unique transcriptomic signature, and therefore they potentially exert different functions compared to macrophages. Microglia also show physiological differences: (i) resident microglia cells are long-lasting cells, (ii) they self-renew and (iii) they are not replaced by peripheral bone marrow-derived cells (17). Recently, Butovsky et al. described putative 89 markers for resident microglial cells (5), including *P2ry12*, *Tmem119*, *Olfml3*, *Hexb*, *Sall1*, etc., identified in gene-expression studies. Different genetic and pharmacological strategies have been implemented and are currently developed to investigate microglia/macrophages functions, including genetic ablation or inhibition of the previously reported markers. A promising approach includes inhibiting the colony stimulating factor-1 receptor by small molecule inhibitors since this receptor is almost exclusively expressed by microglial cells in a steady-state brain where it regulates their developmental functions, including survival, differentiation, and proliferation.

CSF-1R INHIBITION-INDUCED DEPLETION AND REPOPULATION IN PHYSIOLOGICAL CONDITIONS

The colony-stimulating factor-1 receptor (CSF-1R), also known as macrophage colony-stimulating factor (M-CSF) receptor, is a transmembrane tyrosine kinase receptor found at the cell surface of microglial cells, bone-marrow-derived macrophages, monocytes, and other cell types (osteoclasts, dendritic cells). The CSF-1/CSF-1R axis regulates cell survival, proliferation, differentiation, and functions of the mononuclear phagocytes (25, 26).

CSF-1R exists as an autoinhibited form and activates through dimerization and auto-phosphorylation of several tyrosine residues initiating a signalling cascade and the internalization of the receptor. The cascade is activated upon binding the endogenous CSF-1 or interleukin-34 (IL-34) and includes PI3K-AKT and AMPK pathways implicated in macrophages differentiation. Both cytokines promotes macrophages survival, differentiation and proliferation but show different ability to polarize macrophages (27). They share low primary sequence homology, but show similar folding/tertiary structure and interact with overlapping regions of CSF-1R (26). They exhibit different spatiotemporal patterns of expression and play complementary roles during development and adulthood. In the brain, CSF-1 is primarily expressed by the innate immune cells (astrocytes, microglia and oligodendrocytes) while IL-34 is secreted by neurons. IL-34 acts locally, not only on CSF-1R, but also on protein tyrosine phosphatase-z (PTP-z) and CD138, while CSF-1 is also found in the circulation and selective for CSF-1R (26). Furthermore, blocking of CSF-1 and IL-34 led to significant depletion in white and grey matters respectively, highlighting that those cytokines are differentially required for microglia maintenance in the different brain compartments (28). Accordingly, microglia are reduced by 30% in Csf1-null brains while reduced by 70% in IL-34-null brains but almost fully depleted in CSF-1R$^{-/-}$ deficient mice (29).

A low level of CSF-1 stimulates microglia survival and inhibits protein degradation, while increased CSF-1 expression, as observed in inflammatory conditions, was associated with cell proliferation and enhanced migration (26). Additionally, CSF-1R activates several regulators of multipotent progenitor cell differentiation, directing the cell fate toward monocyte/macrophages or granulocytes.

Many CSF-1R inhibitors have been developed (Dasatinib, PLX3397, PLX5622, Ki20227, PLX647, GW2580). Among them, PLX5622 (Plexxikon Inc.) is a potent inhibitor of the kinase activity (KI = 5.9 nM) showing high selectivity over other kinases (29, 30). X-ray crystal structure of the CSF-1R-PLX5622 complex shows that PLX5622 binds to the active site (pocket) of the CSF-1R by forming hydrogen bonds (30).

Under physiological conditions, CSF-1R inhibition causes a reversible depletion of the microglial population within a few days (29, 31). Roughly, around 50% of the microglia population is depleted within three days and over 90% after one week of treatment (29), with sustained effect over the month with continuous administration (29, 31). Elmore et al. (29) showed that depletion was induced *via* apoptosis (29) and did not result from the cell dedifferentiation into an intermediate cell type (32). Depletion did not have a discernible impact on baseline inflammation-related markers level (ROS, cytokines). However, investigations on the resistant Iba-1$^+$ cells in wild-type brains indicated that those cells displayed elevated inflammatory chemokines and proliferation marker and reduced homeostatic markers expression (13).

Elimination of CSF-1R$^+$ cells has no apparent long-lasting impact on neurological functions (29, 33, 34). Torres et al. (34) showed a transient alteration in spatial learning and memory after seven days of treatment (PLX3397) that vanished after 21 days, as previously reported by others (29). Additionally, no apparent effect on brain volume or blood-brain barrier integrity was observed under physiological conditions (29).

Besides, peripheral myeloid cells, including monocytes/macrophages, also express CSF-1R. Therefore, the depletion of microglia may affect the baseline peripheral immune response depending on the duration and way of administration. Otxoa-de-Amezaga et al. (35) observed a reduction in a minor subset of blood Ly6C$^-$ monocytes which are dependent on CSF-1R (35). A recent investigation reported that systemic PLX5622 treatment leads to broad myelosuppression and has long-term consequences even after drug withdrawal (36). CSF-1R inhibition significantly reduces CCR2$^+$ monocytes, F4/80$^+$ and MerTK$^+$ cells, T lymphocytes in bone marrow, and also spleen and blood cell populations (36).

PLX5622 treatment has minimal impact on neurons while its effect on astrocytes and oligodendrocytes is still controversial. Elmore et al. (29) observed a slight increase in GFAP and S100 markers (at mRNA and protein level) (29, 37) but no changes in cell number or morphology (29, 38) after short-term treatment. However, Torres et al. (34) indicated that GFAP$^+$ cells had thicker processes and higher intensity after seven days of treatment with PLX3397 (34). These results were consistent with Erblich et al. (39) that showed higher expression of GFAP and cell density in mice lacking CSF-1R (39).

Of interest, the action of drug-induced CSF-1R inhibition is reversible, meaning that withdrawal of the treatment allows the fast replenishment of the microglial population (40) from the resistant cells (13) without contribution from the bone marrow-derived cells. After near-complete depletion, repopulating microglia displayed enlarged cell bodies and a lack of ramifications within three days post-withdrawal (29, 40). After seven days, the microglia number increased by 160% of that in control mice, showing intermediate morphology and a cluster-like organization (13). By day 21 post-withdrawal, microglia returned to normal morphology and number (13, 40). Furthermore, Zhan et al. (41) indicated that PLX5622 withdrawal triggered the proliferation of the (Iba-1$^+$) microglial cells and non-microglial (Iba-1$^-$) cell populations within the first days of repopulation (13). They identified small subsets of Iba-1$^-$ DCX$^+$ and Iba-1$^-$ Olig2$^+$, markers of neurogenesis and oligodendrocytes, indicating that repopulation affects other resident cell types.

Comparison of gene expression indicated that BM-derived macrophages are highly different from steady-state microglia and, newly generated microglia after repopulation. Fewer differences were observed between control and newly repopulating microglial cells (32), indicating that repopulating microglia can keep most of their steady-state signature (13). However, morphologically, all three subtypes show similar cell body features. More detailed investigations revealed that repopulated microglial cells have a different transcriptome than resident microglia, showing upregulated cell-cycle (proliferation)-related gens Cdk1a and Mki67 and migration-related gene CD36 (32) but their impact on cell functionality has still to be investigated.

Additionally, Elmore et al. reported that control and newly repopulated microglia likely responded to lipopolysaccharide stimulation, indicating that both repopulated and steady-state microglia might also show similar reactivity and functional activity (42, 43). However, *ex vivo* analysis suggested that repopulated microglia showed reduced pro-inflammatory gene expression after stimulation to Toll-like receptor agonists (44), indicating that in some cases newly repopulated microglia might have attenuated pro-inflammatory activity, depending on the signalling molecules they sense.

Some depletion-repopulation paradigms in pathological conditions indicated that repopulation may resolve the activated microglial phenotypes and therefore, solve chronic microglia/macrophages-induced neuroinflammation (40, 45). Repopulation reduced almost half of the 46 genes overexpressed following neuronal lesion (40). Those genes were related to monocyte chemoattraction, endothelial transmigration of leukocytes and microglial proliferation, survival, phagocytic activity, and apoptotic pathway. It also resulted in the almost complete reversal of behavioural impairment observed with the elevated plus maze and Morris maze test. Similarly, (45) investigated the therapeutic effect of microglia depletion and repopulation during the chronic phase of experimental traumatic brain injury. They reported that short-term depletion followed by repopulation rescued microglia morphology, reduced neuroinflammation, oxidative stress, apoptosis and improved motor and cognitive functions (45).

On the other hand, there are also reports of absent therapeutic effects of microglia repopulation. In experimental autoimmune encephalomyelitis (EAE), drug withdrawal resulted in a rapid re-emergence of symptoms, leading eventually to peak scores comparable to those in control EAE mice, associated with an increase in microglia number 5-6 days after drug withdrawal (46). Moreover, the newly generated microglia triggered a degenerative inflammatory response upon their reappearance. Altogether, it seems that beneficial disease outcomes after CSF-1R inhibition-induced microglia repopulation are dependent on the disease model and therapy time window (46).

The Colony Stimulating Factor-1 Receptor in Glioma

Immunotherapies represent a promising approach for treating cancer. Despite favorable results obtained treating different tumor types (47–50), they have not proven to be efficient in glioma so far. Treatment failure is likely related to the extensive spatial and temporal heterogeneity of the glioma microenvironment (51) and the numerous immunosuppressive mechanisms the tumor exploits, such as immune surveillance evasion.

Microglia are part of the innate immune response and are responsible for the phagocytosis of abnormal cells. However, in the tumour microenvironment (TME), they acquire a pro-tumorigenic phenotype under the influence of the tumour cells. Similarly, tumour-associated macrophages (TAMs) are differentiated from monocytes precursors recruited from the systemic reservoirs to the tumour in response to cytokines and chemoattractants released by tumour cells, including the CSF-1 ligand (52), ultimately supporting the immunosuppressive environment (53, 54). In glioma, these cells are also known as glioma-associated microglia/macrophages (GAMM) and represent around 30-50% of the total tumour mass (55). Single-cell profiling indicated that microglia and TAMs differentially contribute to the glioma environment over time, with an early microglial and late TAM contribution (51). GAMM favour tumour progression by releasing pro-tumorigenic, pro-survival and growth factors (56). They promote escape from the tumour immune response by boosting glioma angiogenesis, growth and invasion (57), suppression of cytotoxic T cell functions and induction of an immunosuppressive regulatory T (T_{reg}) cell response (58). Additionally, GAMM has been associated with tumour progression and therapy resistance (59). Therefore, targeting GAMM may provide an important advantage over current standard therapy (60).

Efficient targeting of TAM using small molecule CSF-1R inhibitors was assessed in many tumour models, including solid tumours and breast cancers (61, 62). High levels of CSF-1 and CSF-1R have been observed in high-grade human glioma, supporting their pivotal role in tumour growth. The level of CSF-1 was correlated with tumorigenesis and increased GAMM density. Accordingly, targeting the CSF-1/CSF-1R axis may represent a potential therapeutic approach in glioma (63).

Significant reduction of TAM was achieved in different tumour models using CSF-1R inhibitors, partly due to the impaired recruitment and maturation of infiltrating monocytic TAMs precursors (64). While CSF-1R inhibition reduces the GAMM density, resistant cell populations were observed across different tumour types, including glioma (65, 66). Interestingly, Pyonteck et al. observed a substantial reduction in tumour growth, whereas Coniglio et al. reported a more subtle effect with decreased cell invasion and no effect on proliferation or survival, highlighting that CSF-1R inhibition therapeutic effects may depend on the glioma subtype (proneural vs mesenchymal). Nevertheless, the resistant TAM showed downregulated pro-tumorigenic markers expression, potentially slowing tumour progression in pancreatic cancer, cervical and mammary tumour and melanoma or improving the response to other treatments (67–69). In glioma models, CSF-1R inhibition delays recurrence and slightly prolonged overall survival (70) by altering the immune cell polarization state toward a less immunosuppressive phenotype (66). Different CSF-1R inhibitors and anti-CSF-1R antibodies have been tested in preclinical studies and clinical trials (71), to lower TAM burden, reprogram GAMM towards an anti-tumorigenic phenotype and stimulate the T-cells response (61). Despite promising results, they failed to show substantial efficacy across multiple tumor types (71) as well as in glioma (72, 73). Therapy resistance was predominantly associated with increased $Foxp3^+$ Treg influx in response to macrophage depletion (74) and enhanced recruitment of other pro-tumorigenic cell populations such as myeloid-derived suppressor cells (75, 76). Those studies highlighted the main role of the TME in supporting therapy resistance.

CSF-1R monotherapy falls short in providing therapeutic effects due to acquired resistance (66, 76, 77) (**Figure 1**). In experimental glioma models, CSF-1R inhibition significantly prolonged overall survival while recurrence was observed in a considerable subset of animals. Acquired resistance to long-term CSF-1R inhibition was correlated with increased insulin-like growth factor (IGF-1) signaling between macrophages and tumor cells, leading to aberrant activation of phosphatidylinositol 3-kinase (PI3K) signaling, therefore promoting tumor cell survival and invasion (77). Glioma recurrence was also associated with increased levels of granulocyte-macrophage (GM)-CSF and interferon (IFN)- γ, leading to TAM persistence (66). Other studies reported that upregulation of the T cell immune checkpoint molecules, such as programmed cell death 1 ligand (PD-L1) and cytotoxic T-lymphocyte-associated protein 4 (CTLA-4), should also be considered as a potential escape mechanism from CSF-1R monotherapy (67, 78). Antonios et al. (78) demonstrated that CSF-1R therapy indirectly promotes tumor-infiltrating lymphocytes (TILs) recruitment within the glioma microenvironment (78). TILs are an important cellular source of PD-L1 expression and therefore, their infiltration could promote immune escape and resistance mediated by the PD-1/PD-L1 axis. Altogether, resistance to CSF-1R monotherapy may be explained by the cellular heterogeneity of the tumor microenvironment beyond GAMM. Accordingly, single-agent therapy with CSF-1R inhibitor has demonstrated very modest results in glioblastoma clinical trials, showing no significant improvement of the progression-free survival of the patients (79, 80).

Accordingly, ongoing studies are currently combining CSF-1R therapy and immune-checkpoint inhibitors in different types of tumors (81). CSF-1R therapy in cancer seems to have mostly a synergistic effect and improve other treatments, such as adoptive cell transfer immuno-therapy or platinum-based chemotherapy in breast cancer models (82, 83). In glioma, CSF-1R inhibition was combined with ionizing radiation and potentiated the response of the tumour to irradiation, indicated by decreased irradiation-induced monocytes recruitment, reduced pro-tumorigenic TAMs and longer survival (84). CSF-1R inhibitors are also reported to enhance the anti-tumoral T-cell responses when combined with immune-checkpoint inhibitors like anti-PD-1 antibodies (70, 78, 85). In glioma, the combination of both therapies increased cytotoxic $CD8^+/CD4^+$ and $CD8^+/FoxP3^+$ T

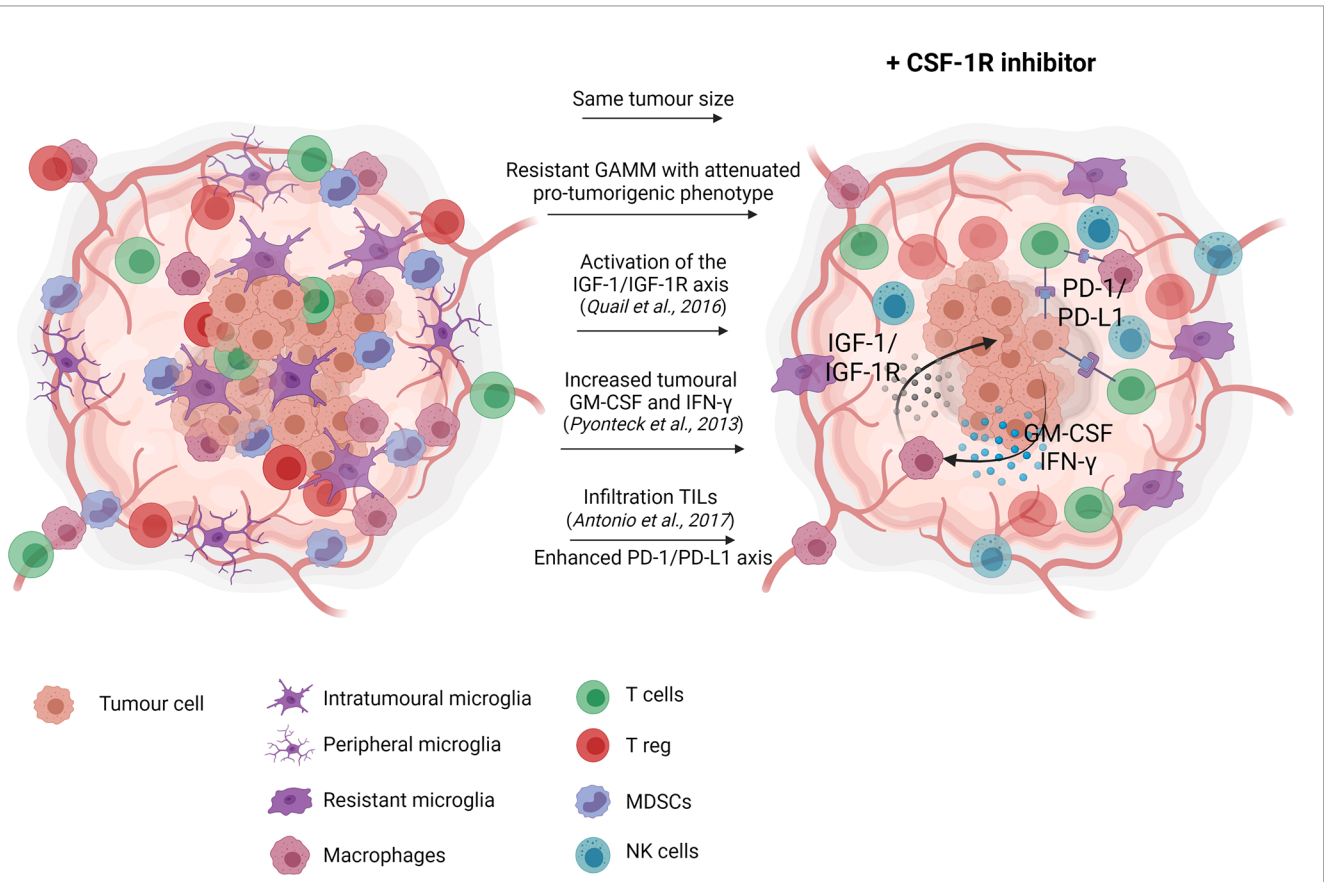

FIGURE 1 | CSF-1R inhibition monotherapy in glioma. In glioma models, CSF-1R inhibition delays recurrence, and therefore slightly prolong overall survival with no significant effect on tumour growth. Reported resistance mechanisms to CSF-1R inhibition include increased insulin-like growth factor (IGF-1) signaling between macrophages and tumor cells, ultimately promoting tumor cell survival and invasion (77), increased levels of granulocyte-macrophage (GM)-CSF and interferon (IFN)- γ, leading to TAM persistence (66) and increased tumor-associated lymphocytes infiltration favoring the immunosuppressive PD-1/PD-L1 signaling (78). Created with Biorender.com.

cell ratios, indicative of an enhanced anti-tumour activity (70), leading to longer-term surviving animals. Interestingly, Ali and colleagues investigated different combinatorial therapies, considering CSF-1R, PD-1 and other targets, in glioblastoma and highlighted the importance of the therapy-induced time-dependent changes in TME cells (86). Therefore, further preclinical and clinical research should combine CSF-1R inhibition with other therapies to enhance therapeutic effects and investigate the optimal therapy paradigm.

The Colony Stimulating Factor-1 Receptor in Stroke

Microglial cells play a significant role in initiating, maintaining, and resolving the inflammatory response after stroke. Microglia cells drastically change their morphology, gene expression, expression of inflammatory mediators, and surface molecule organization after detecting signs of injury such as intracellular calcium waves or ATP release. Based on the temporal changes of marker expression, microglial cells have potentially an early (beneficial) anti-inflammatory effect, while detrimental pro-inflammatory microglia seem to dominate at later stages (87). In experimental stroke, the level of anti-inflammatory markers peaked around day 4 post ischemia, while a wave of pro-inflammatory markers increased over the first two weeks, peaking around day 14 post ischemia (87).

PLX5622 and derivatives have been investigated in transient and permanent middle cerebral artery occlusion (MCAo) rodent models to understand how microglia depletion prior to stroke may affect disease outcomes. From the preventive studies, data confirmed that microglia might confer protection against injury at an early stage (**Figure 2A**). A 21-day PLX3397 microglia depletion prior to a transient middle cerebral artery occlusion (tMCAo) worsens disease outcomes, including increased brain injury, enhanced excitotoxicity and altered neuronal activity (89). Effect on brain injury/infarct size was also observed in a TBI mice model (90): depletion of microglia using PLX5622 (from 7 days before to 3 days after TBI) also increased the core size at day 3 (90).

In line with these findings, Wei Na Jin et al. (91) reported that uninterrupted PLX3397 treatment before and after MCAo exacerbated neurological deficits, brain inflammation (cytokine levels), cell death and leukocyte infiltration within the first days after ischemia (35, 91). Similarly, 35 reported continuous CSF-1R inhibition starting three weeks before ischemia increased the number of infiltrating neutrophils but reduced the numbers of monocytes (-40%), F4/80$^+$ macrophages (-80%) at day 4 post ischemia (35). Additionally, increased CD4$^+$T and NK cell counts correlated with a decrease of the corresponding leukocyte subsets in the spleen. Altogether, these studies suggest that the presence of CSF-1R$^+$ cells has beneficial effects within the first 3 days post ischemia, reducing neurological deficits, cell death, ROS levels, leukocytes infiltration, neuroinflammatory markers (such as pro-inflammatory cytokines IL-1α, IL-1β, IL-6 and TNF-α) and increasing levels of growth factors (IGF-1) in some cases. Additionally, CSF-1R depletion prior to and after MCAo reduces the pro-inflammatory astrocytic reactivity (including IL-1α, IL-1β, iNOS, TNF-α, IL-6) with no change in astrocytes number (35, 91). Interestingly, Li et al., (11) used the same paradigm in an intracerebral haemorrhagic model (ICH model) and found the opposite results (11). Altogether, these studies support a neuroprotective role of microglial cells within the first days after stroke, which may partially be explained by its phagocytic and inflammatory activity on infiltrating cells at early stages.

Recently, our group assessed the immunomodulatory effect of long-term PLX5622 administration in the post ischemic phase using *in vivo* multimodal imaging (88). We demonstrated that CSF-1R inhibition transiently decreased neuroinflammation within the infarct, while a sustained decrease was observed in the contralateral healthy tissue, correlating with Iba-1$^+$ (microglia/macrophages) dynamics. Interestingly, the decrease in activated microglia/macrophages number in remote areas such as the contralateral side may moderate the impact of spreading depression and ultimately global inflammation, as observed by the global decrease in pro- and anti-inflammatory markers expression in both hemispheres at late stage (**Figure 2B**). Moreover, long-term CSF-1R inhibition also affected homeostatic balance and tissue reperfusion, albeit transient, as indicated by diffusion- and perfusion-weighted MR imaging.

It is still unknown when and for how long microglia must be eliminated to enhance recovery: data may indicate that microglial activity is essential within the first days to reduce peripheral cell infiltration and cytotoxicity while it may become detrimental later on (87). Additionally, previous short-term CSF-1R inhibition studies in other disease models supported that PLX5622-induced microglia repopulation could reduce inflammatory cytokines expression, brain damage and resolve behavioural impairment. Altogether, those studies highlighted the importance of targeting microglia/macrophages within an optimal therapeutic time window to leverage their beneficial activity during the post ischemic phase. To date, no study on repopulation and/or short-term CSF-1R inhibition in stroke has been reported.

In Vivo Molecular Imaging of CSF-1R

In vivo assessment of CSF-1R inhibition therapy response and target engagement would benefit from developing imaging probes specifically targeting CSF-1R and/or microglial cells (**Figure 3**).

In this context, Horti et al. (92) developed the new radiotracer 11C-CPPC targeting the CSF-1R. Preclinical assessments seem to indicate high selectivity and binding specificity in animal models of acute LPS-induced neuroinflammation and post-mortem Alzheimer's disease human tissue (92) while others reported higher off-target binding and lower specificity (93). Therefore, other CSF-1R antagonist radioligands are currently investigated, potentially showing higher sensitivity and larger dynamic range in preclinical models (94). In addition, macrophage-targeted diagnostic tools are currently developed to visualize immune cell accumulation in a variety of inflammatory disease and assessed in the context of CSF-1R inhibition-induced

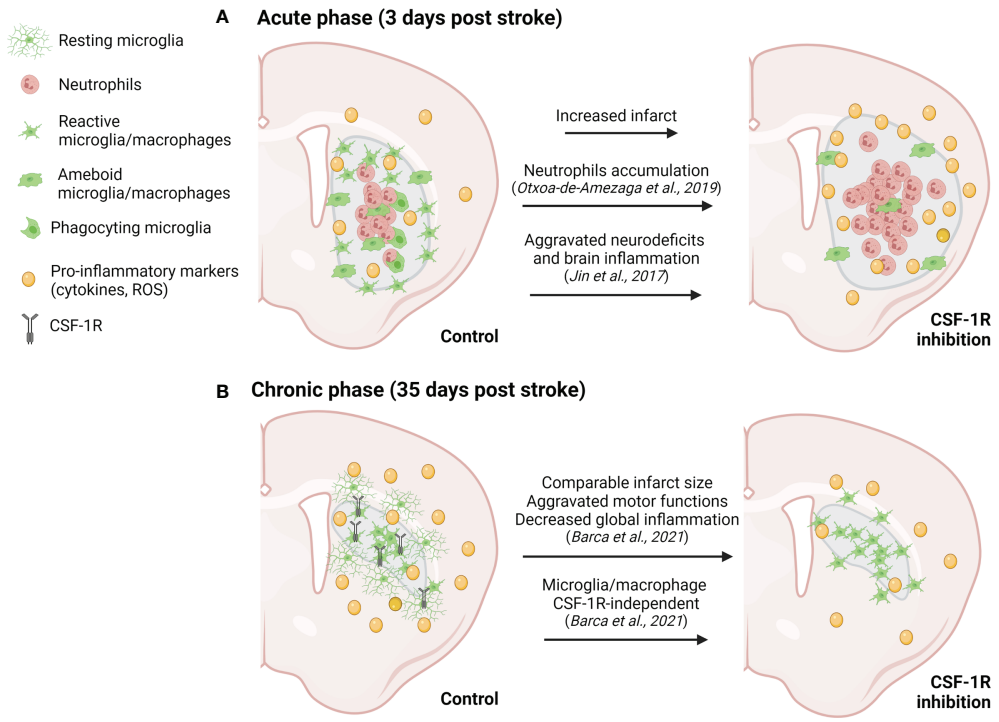

FIGURE 2 | CSF-1R inhibition monotherapy in stroke. **(A)** Previous studies on brain pre-conditioning reported the absence of microglial cells within the first days post ischemia (acute phase) worsened disease outcomes, including increased brain injury, peripheral infiltration and pro-inflammatory signaling, ultimately leading to aggravated neurodeficits. **(B)** Long-term treatment reveals the existence of an Iba-1$^+$ (microglia/macrophages) cell population resistant to CSF-1R inhibition while global expression of inflammation-related markers was decreased. Long-term CSF-1R inhibition starting right after surgery led to aggravated motor functions, partly explained by homeostatic imbalance and impaired infarct reperfusion (88). Created with Biorender.com.

microglia/macrophages depletion and other targeting immunotherapies (95).

The translocator protein (TSPO)-PET imaging has been widely used to study inflammation dynamics, immune cell activation and/or microgliosis in preclinical and clinical studies. Despite several well-known caveats, TSPO-PET imaging allows assessing global inflammation, visualizing areas of immune cell infiltration and defining tissue heterogeneity (96–98). Moreover, TSPO-PET has been used as a therapy readout in clinical trials in patients with primary glioblastoma or melanoma brain metastasis treated with chemoradiation or immunotherapy (NCT02431572). The validation of TSPO-PET tracers in clinical settings is necessary to improve the understanding of glioma-associated inflammation and microglia-targeting therapy resistance mechanisms. In a preclinical trial, seven days of CSF-1R inhibitor (PLX3397) in a non-human primate resulted in a significant reduction of 11C-PBR28 (TSPO) volumes of distribution by 46% from baseline, consistent with microglia depletion, which recovered after 12 days, supporting TSPO-PET as a CSF-1R inhibition therapy readout (99). However, the cellular sources of TSPO during or after treatment were not investigated. This finding encourages conducting back-translational studies to understand the biological mechanisms after CSF-1R therapy together with TSPO-PET imaging as a therapy readout.

Recently, our group reported the suitability of 18F-DPA-714 PET imaging, used as a biomarker of TSPO-dependent neuroinflammation and immune cell activation, to track the immunomodulatory effect of long-term PLX5622 administration in the post ischemic phase (88). We demonstrated that CSF-1R inhibition transiently decreased radiotracer uptake within the infarct, correlating with the dynamics of TSPO and microglia/macrophages *ex vivo*. Therefore, we supported the use of TSPO-PET imaging as a microglia-targeting therapy readout in stroke.

It should be noted that none of the TSPO radioligands is cell-specific or function-specific. Among the emerging targets, the purinergic metabotropic 12 receptor (P2Y12R) PET tracer is an attractive imaging biomarker to study microglial function (100, 101). P2Y12R expression is restricted to microglia in the CNS and absent on peripheral immune cells, involved in microglial chemotaxis and cytokine/chemokine signaling. In the inflammatory cascade, P2Y12R is downregulated in a pro-inflammatory environment and upregulated with exposure to anti-inflammatory stimuli, and therefore considered as a suitable biomarker for anti-inflammatory microglial cells (101). However, its temporal dynamics in an inflammatory environment remains not well understood (100): the specific role of P2Y12R seems to be disease- and stage-dependent. To our knowledge, only one P2Y12R-PET radioligand has been developed, the ethyl6-(3-(3-((5-chlorothiophen-2-yl)sulfonyl)

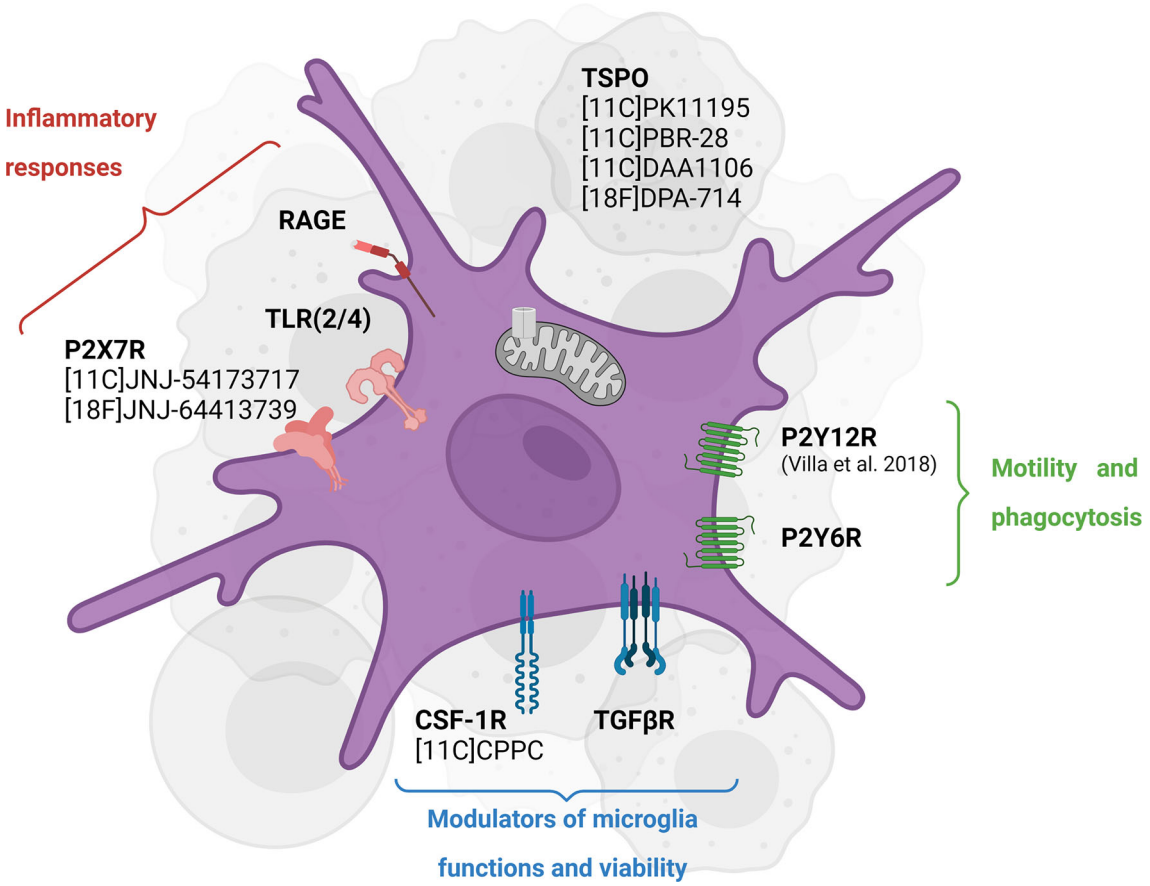

FIGURE 3 | Emerging targets for *in vivo* imaging of CSF-1R inhibition-induced microglial activity modulation. TSPO PET tracers have been widely used to assess neuroinflammation in different pathologies while they have shown some caveats, including inability to distinguish cellular sources of TSPO and phenotypes. Some of the newly investigated targets including P2X7R and P2Y12R highlight the different functions of microglial cells in an inflammatory environment. Created with Biorender.com.

11C-ureido)azetidin-1-yl)-5-cyano-2-methylnicotinate (101). While preliminary data looked promising, this tracer revealed low metabolic stability and lack of blood-brain barrier permeability. Further preclinical studies must assess other CNS-penetrant P2Y12R receptor PET radioligand and investigate the functional spatiotemporal role of P2Y12R.

As part of the same receptor family, the purinergic P2X7 receptor is found to be specifically upregulated in pro-inflammatory activated microglial cells in response to high ATP release. This receptor mediates cytokine and chemokines release, regulates T lymphocytes survival and differentiation (Di 102). A clinical trial investigated the blocking effect of JNJ-55308942 targeting the P2X7 receptor using the 18F-labelled analog in healthy volunteers (NCT03437590). The preliminary results in humans supported the use of the PET-tracer 18F-JNJ-54175446 to provide an insight into P2X7R in health and disease (103). In the context of CSF-1R inhibition, further studies may consider using this radioligand to assess (i) the spatiotemporal expression of P2X7 receptor in pathological conditions, (ii) the decrease in P2X7-expressing pro-inflammatory microglial cells following CSF-1R- and/or any microglia-targeting immunotherapy and (iii) the potential anti-inflammatory effect of microglia repopulation.

CONCLUSION REMARKS

Glioma and stroke are two complex pathological conditions, both inducing strong and chronic inflammatory and immunological responses following alterations of the immune balance. However, innate, and adaptive immune response differs in major aspects: origin, progression, and disease-induced phenotype. The comparison of both diseases represents a very interesting avenue of research as they represent the two extremes of neurological conditions. Stroke on the one hand with a strong pro-inflammatory stimulus (hypoxia, reperfusion) and on the other hand gliomas with a strong anti-inflammatory immunosuppressive microenvironment. The comparison thus supports evidence generation for the role of CSF-1R across neurological diseases.

CSF-1R inhibition studies demonstrate that many discernible subpopulations of microglial cells co-exist in the inflammatory

environment and are differentially sensitive to CSF-1R inhibition. In both glioma and ischemia, a resistant population of CSF-1R-independent microglia/macrophages were observed after long-term PLX5622 treatment. Their contribution to compensatory mechanisms or therapy resistance still needs further research. One line of investigation focuses on the enhanced communication with other immune players, triggering modulation of the peripheral immune cell infiltration or activation of resident cells. Still, numerous compensatory and resistance mechanisms seem to be implemented by immunological responses beyond microglia/macrophages cells, limiting the efficiency of CSF-1R inhibition as a monotherapy. Therefore, research supports its use as a combination therapy to synergize the therapeutic effects of other immunomodulatory approaches.

Recently, we validated the use of TSPO-PET in preclinical studies assessing the therapeutic effect of new microglia-targeting treatments. TSPO-PET employing 18F-DPA-714 allows visualization of microglia/macrophages depletion-repopulation and areas of immune cell infiltration. However, a better knowledge of the therapeutic effects on other immune cell populations after short-term or long-term CSF-1R inhibition would improve our understanding of the *in vivo* TSPO dynamics upon therapy. Advances in microglia-targeting immunotherapy should boost the development of microglia-specific PET radioligands. This could support further clinical trials for glioma and stroke patients, improve personalized management and understand the prognostic value of multimodal imaging in microglia-targeting therapeutic approaches.

AUTHOR CONTRIBUTIONS

All authors conceptualized and wrote this manuscript. All authors contributed to the article and approved the submitted version.

FUNDING

This work was partly funded by the Horizon 2020 Programme under grant agreement n°675417 (PET3D) and the Herbert-Worch-Stiftung. Additionally, this work was supported by a Collaboration Grant of the Medical Faculty of the University of Bonn between CIO UKB and Johanniter Hospital. This review was supported by the Immune-Image consortium. The Immune-Image project receives funding from the Innovative Medicines Initiative 2 Joint Undertaking (JU) under grant agreement No 831514 (Immune-Image). The JU receives support from the European Union's Horizon 2020 research and innovation programme and EFPIA.

ACKNOWLEDGMENTS

We thank all the members of the European Institute for Molecular Imaging (EIMI) for their support. Furthermore, we thank all the authors that contributed to the main recent studies and provided new insights into the field of CSF-1R inhibition. Figures were created with Biorender (www.biorender.com).

REFERENCES

1. Dokalis N, Prinz M. Resolution of Neuroinflammation: Mechanisms and Potential Therapeutic Option. *Semin Immunopathol* (2019) 41(6):699–709. doi: 10.1007/s00281-019-00764-1
2. Cherry JD, Olschowka JA, O'Banion MK. Neuroinflammation and M2 Microglia: The Good, the Bad, and the Inflamed. *J Neuroinflamm* (2014) 11:98–113. doi: 10.1186/1742-2094-11-98
3. Kanazawa M, Ninomiya I, Hatakeyama M, Takahashi T, Shimohata T. Microglia and Monocytes/Macrophages Polarization Reveal Novel Therapeutic Mechanism Against Stroke. *Int J Mol Sci* (2017) 18:2135–53. doi: 10.3390/ijms18102135
4. Gutmann DH, Kettenmann H. Microglia/Brain Macrophages as Central Drivers of Brain Tumor Pathobiology. *Neuron* (2019) 104:442–9. doi: 10.1016/j.neuron.2019.08.028
5. Butovsky O, Weiner HL. Microglial Signatures and Their Role in Health and Disease. *Nat Rev Neurosci* (2018) 19(10):622–35. doi: 10.1038/s41583-018-0057-5
6. Qin C, Zhou L-Q, Ma X-T, Hu Z-W, Yang S, Chen M, et al. Dual Functions of Microglia in Ischemic Stroke. *Neurosci Bull* (2019) 35(5):921–335. doi: 10.1007/s12264-019-00388-3
7. De Leo A, Ugolini A, Veglia F. Myeloid Cells in Glioblastoma Microenvironment. *Cells* (2020) 10(1):1–20. doi: 10.3390/cells10010018
8. Han J, Harris RA, Zhang X-M. An Updated Assessment of Microglia Depletion: Current Concepts and Future Directions. *Mol Brain* (2017) 10 (25):25–33. doi: 10.1186/s13041-017-0307-x
9. Green KN, Crapser JD, Hohsfield LA. To Kill a Microglia: A Case for CSF1R Inhibitors. *Trends Immunol* (2020) 41:771–845. doi: 10.1016/j.it.2020.07.001
10. Ries CH, Hoves S, Cannarile MA, Rüttinger D. CSF-1/CSF-1r Targeting Agents in Clinical Development for Cancer Therapy. *Curr Opin Pharmacol* (2015) 23:45–51. doi: 10.1016/j.coph.2015.05.008
11. Li Q, Barres BA. Microglia and Macrophages in Brain Homeostasis and Disease. *Nat Rev Immunol* (2018) 18(4):225–42. doi: 10.1038/nri.2017.125
12. Réu P, Khosravi A, Bernard S, Mold JE, Salehpour M, Alkass K, et al. The Lifespan and Turnover of Microglia in the Human Brain. *Cell Rep* (2017) 20 (4):779–84. doi: 10.1016/j.celrep.2017.07.004
13. Zhan L, Sohn PD, Zhou Y, Li Y, Gan L. A Mac2-Positive Progenitor-Like Microglial Population Survives Independent of CSF1R Signaling in Adult Mouse Brain. *BioRxiv* (2019) 9(e51796):1–225. doi: 10.1101/722090
14. Waisman A, Ginhoux F, Greter M, Bruttger J. Homeostasis of Microglia in the Adult Brain: Review of Novel Microglia Depletion Systems. *Trends Immunol* (2015) 36(10):625–36. doi: 10.1016/j.it.2015.08.005
15. Nimmerjahn A, Kirchhoff F, Helmchen F. Neuroscience: Resting Microglial Cells Are Highly Dynamic Surveillants of Brain Parenchyma *In Vivo*. *Science* (2005) 308(5726):1314–18. doi: 10.1126/science.1110647
16. Parkhurst CN, Yang G, Ninan I, Savas JN, Yates JR, Lafaille JJ, et al. Microglia Promote Learning-Dependent Synapse Formation Through Brain-Derived Neurotrophic Factor. *Cell* (2013) 155(7):1596–609. doi: 10.1016/j.cell.2013.11.030
17. Prinz M, Priller J. Microglia and Brain Macrophages in the Molecular Age: From Origin to Neuropsychiatric Disease. *Nat Rev Neurosci* (2014) 15:300–12. doi: 10.1038/nrn3722
18. Masuda T, Prinz M. Microglia: A Unique Versatile Cell in the Central Nervous System. *ACS Chem Neurosci* (2016) 7(4):428–34. doi: 10.1021/acschemneuro.5b00317
19. Masuda T, Sankowski R, Staszewski O, Böttcher C, Sagar LA, Scheiwe C, et al. Spatial and Temporal Heterogeneity of Mouse and Human Microglia at Single-Cell Resolution. *Nat* (2019) 566:388–92. doi: 10.1038/s41586-019-0924-x
20. Hammond TR, Dufort C, Dissing-Olesen L, Giera S, Young A, Wysoker A, et al. 'Single-Cell RNA Sequencing of Microglia Throughout the Mouse

Lifespan and in the Injured Brain Reveals Complex Cell-State Changes'. *Immunity* (2019) 50(1):253–71.e6. doi: 10.1016/j.immuni.2018.11.004
21. Mathys H, Davila-Velderrain J, Peng Z, Gao F, Mohammadi S, Young JZ, et al. Single-Cell Transcriptomic Analysis of Alzheimer's Disease. *Nature* (2019) 570(7761):332–37. doi: 10.1038/s41586-019-1195-2
22. Olah M, Menon V, Habib N, Taga MF, Ma Y, Yung CJ, et al. Single Cell RNA Sequencing of Human Microglia Uncovers a Subset Associated With Alzheimer's Disease. *Nat Commun* (2020) 11(1):6129–47. doi: 10.1038/s41467-020-19737-2
23. Roesch S, Rapp C, Dettling S, Herold-Mende C. When Immune Cells Turn Bad—Tumor-Associated Microglia/Macrophages in Glioma. *Int J Mol Sci* (2018) 19(2):436–56. doi: 10.3390/ijms19020436
24. Benakis C, Garcia-Bonilla L, Iadecola C, Anrather J. The Role of Microglia and Myeloid Immune Cells in Acute Cerebral Ischemia. *Front Cell Neurosci* (2015) 8:461(JAN). doi: 10.3389/fncel.2014.00461
25. Chitu V, Gokhan Ş, Nandi S, Mehler MF, Stanley ER. Emerging Roles for CSF-1 Receptor and Its Ligands in the Nervous System'. *Trends Neurosci* (2016) 39(6):378–93. doi: 10.1016/j.tins.2016.03.005
26. Stanley ER, Chitu V. CSF-1 Receptor Signaling in Myeloid Cells. *Cold Spring Harbor Perspect Biol* (2014) 6(6):a021857–a021857. doi: 10.1101/cshperspect.a021857
27. Boulakirba S, Pfeifer A, Mhaidly R, Obba S, Goulard M, Schmitt T, et al. IL-34 and CSF-1 Display an Equivalent Macrophage Differentiation Ability But a Different Polarization Potential. *Sci Rep* (2018) 8(1):1–11. doi: 10.1038/s41598-017-18433-4
28. Easley-Neal C, Foreman O, Sharma N, Zarrin AA, Weimer RM. CSF1R Ligands IL-34 and CSF1 Are Differentially Required for Microglia Development and Maintenance in White and Gray Matter Brain Regions. *Front Immunol* (2019) 10:2199(September). doi: 10.3389/fimmu.2019.02199
29. Elmore MRP, Najafi AR, Koike MA, Dagher NN, Spangenberg EE, Rice RA, et al. Colony-Stimulating Factor 1 Receptor Signaling Is Necessary for Microglia Viability, Unmasking a Microglia Progenitor Cell in the Adult Brain. *Neuron* (2014) 82(2):380–97. doi: 10.1016/j.neuron.2014.02.040
30. Spangenberg E, Severson PL, Hohsfield LA, Crapser J, Zhang J, Burton EA, et al. Sustained Microglial Depletion With CSF1R Inhibitor Impairs Parenchymal Plaque Development in an Alzheimer's Disease Model. *Nat Commun* (2019) 10(1):3758. doi: 10.1038/s41467-019-11674-z
31. Spangenberg E, Lee RJ, Najafi AR, Rice RA, Elmore MRP, Blurton-Jones M, et al. Eliminating Microglia in Alzheimer's Mice Prevents Neuronal Loss Without Modulating Amyloid-β Pathology. *Brain* (2016) 139(4):1265–81. doi: 10.1093/brain/aww016
32. Huang Y, Xu Z, Xiong S, Sun F, Qin G, Hu G, et al. Repopulated Microglia Are Solely Derived From the Proliferation of Residual Microglia After Acute Depletion. *Nat Neurosci* (2018) 21(4):530–40. doi: 10.1038/s41593-018-0090-8
33. Dagher NN, Najafi AR, Kayala KMN, Elmore MRP, White TE, Medeiros R, et al. Colony-Stimulating Factor 1 Receptor Inhibition Prevents Microglial Plaque Association and Improves Cognition in 3xtg-AD Mice'. *J Neuroinflamm* (2015) 12(1):1395. doi: 10.1186/s12974-015-0366-9
34. Torres L, Danver J, Ji K, Miyauchi JT, Chen D, Anderson ME, et al. Dynamic Microglial Modulation of Spatial Learning and Social Behavior. *Brain Behavior Immun* (2016) 55(July):6–16. doi: 10.1016/j.bbi.2015.09.001
35. Otxoa-de-Amezaga A, Miró-Mur F, Pedragosa J, Gallizioli M, Justicia C, Gaja-Capdevila N, et al. Microglial Cell Loss After Ischemic Stroke Favors Brain Neutrophil Accumulation. *Acta Neuropathol* (2019) 137(2):321–41. doi: 10.1007/s00401-018-1954-4
36. Lei F, Cui N, Zhou C, Chodosh J, Vavvas DG, Paschalis EI. CSF1R Inhibition by a Small-Molecule Inhibitor Is Not Microglia Specific; Affecting Hematopoiesis and the Function of Macrophages. *Proc Natl Acad Sci* (2020) 117(38):23336–38. doi: 10.1073/pnas.1922788117
37. Najafi AR, Crapser J, Jiang S, Ng W, Mortazavi A, West BL, et al. A Limited Capacity for Microglial Repopulation in the Adult Brain. *Glia* (2018) 66 (11):2385–96. doi: 10.1002/glia.23477
38. Bruttger J, Karram K, Wörtge S, Regen T, Marini F, Hoppmann N, et al. Genetic Cell Ablation Reveals Clusters of Local Self-Renewing Microglia in the Mammalian Central Nervous System. *Immunity* (2015) 43(1):92–106. doi: 10.1016/j.immuni.2015.06.012
39. Erblich B, Zhu L, Etgen AM, Dobrenis K, Pollard JW. Absence of Colony Stimulation Factor-1 Receptor Results in Loss of Microglia, Disrupted Brain Development and Olfactory Deficits'. Edited by Andreas Meisel. *PLoS One* (2011) 6(10):e263175. doi: 10.1371/journal.pone.0026317
40. Rice RA, Pham J, Lee RJ, Najafi AR, West BL, Green KN. Microglial Repopulation Resolves Inflammation and Promotes Brain Recovery After Injury. *Glia* (2017) 65(6):931–44. doi: 10.1002/glia.23135
41. Zhan LID, Krabbe G, Du F, Jones I, Reichert MC, TelpoukhovskaiaID M, et al. Proximal Recolonization by Self-Renewing Microglia Re-Establishes Microglial Homeostasis in the Adult Mouse Brain. *PLOS Biol* (2019) 17: e3000134. doi: 10.1371/journal.pbio.3000134
42. Elmore MRP, Lee RJ, West BL, Green KN. Characterizing Newly Repopulated Microglia in the Adult Mouse: Impacts on Animal Behavior, Cell Morphology, and Neuroinflammation'. Edited by Thomas Langmann. *PLoS One* (2015) 10(4):e01229125. doi: 10.1371/journal.pone.0122912
43. Elmore MRP, Hohsfield LA, Kramár E, Soreq L, Lee RJ, Pham ST, et al. 'Replacement of Microglia in the Aged Brain Reverses Cognitive, Synaptic, and Neuronal Deficits in Mice'. *Aging Cell* (2018) 17(6):e12832. doi: 10.1111/acel.12832
44. Coleman LG, Zou J, Crews FT. Microglial Depletion and Repopulation in Brain Slice Culture Normalizes Sensitized Proinflammatory Signaling. *J Neuroinflamm* (2020) 17(1):275. doi: 10.1186/s12974-019-1678-y
45. Henry RJ, Ritzel RM, Barrett JP, Doran SJ, Jiao Y, Leach JB, et al. Microglial Depletion With CSF1R Inhibitor During Chronic Phase of Experimental Traumatic Brain Injury Reduces Neurodegeneration and Neurological Deficits. *J Neurosci* (2020) 40(14):2960–74. doi: 10.1523/JNEUROSCI.2402-19.2020
46. Nissen JC, Thompson KK, West BL, Tsirka SE. Csf1R Inhibition Attenuates Experimental Autoimmune Encephalomyelitis and Promotes Recovery. *Exp Neurol* (2018) 307(September):24–36. doi: 10.1016/j.expneurol.2018.05.021
47. Schmid P, Adams S, Rugo HS, Schneeweiss A, Barrios CH, Iwata H, et al. Atezolizumab and Nab-Paclitaxel in Advanced Triple-Negative Breast Cancer. *N Engl J Med* (2018) 379(22):2108–21. doi: 10.1056/nejmoa1809615
48. Gandhi L, Rodríguez-Abreu D, Gadgeel S, Esteban E, Felip E, De Angelis F, et al. Pembrolizumab Plus Chemotherapy in Metastatic Non–Small-Cell Lung Cancer. *N Engl J Med* (2018) 378(22):2078–92. doi: 10.1056/nejmoa1801005
49. Iams WT, Porter J, Horn L. Immunotherapeutic Approaches for Small-Cell Lung Cancer. *Nat Rev Clin Oncol* (2020) 17(5):300–12. doi: 10.1038/s41571-019-0316-z
50. Ralli M, Botticelli A, Visconti IC, Angeletti D, Fiore M, Marchetti P, et al. Immunotherapy in the Treatment of Metastatic Melanoma: Current Knowledge and Future Directions. *J Immunol Res* (2020) 2020:1–12. doi: 10.1155/2020/9235638
51. Pombo Antunes AR, Scheyltjens I, Lodi F, Messiaen J, Antoranz A, Duerinck J, et al. Single-Cell Profiling of Myeloid Cells in Glioblastoma Across Species and Disease Stage Reveals Macrophage Competition and Specialization. *Nat Neurosci* (2021) 24(4):595–610. doi: 10.1038/s41593-020-00789-y
52. Guilliams M, Thierry GR, Bonnardel J, Bajenoff M. Establishment and Maintenance of the Macrophage Niche. *Immunity* (2020) 52(3):434–51. doi: 10.1016/j.immuni.2020.02.015
53. Xiang X, Wang J, Lu D, Xu X. Targeting Tumor-Associated Macrophages to Synergize Tumor Immunotherapy. *Signal Transduction Targeted Ther* (2021) 6(1):75–87. doi: 10.1038/s41392-021-00484-9
54. DeNardo DG, Ruffell B. Macrophages as Regulators of Tumour Immunity and Immunotherapy. *Nat Rev Immunol* (2019) 19(6):369–82. doi: 10.1038/s41577-019-0127-6
55. Komohara Y, Ohnishi K, Kuratsu J, Takeya M. Possible Involvement of the M2 Anti-Inflammatory Macrophage Phenotype in Growth of Human Gliomas. *J Pathol* (2008) 216(1):15–24. doi: 10.1002/path.2370
56. Quail DF, Joyce JA. The Microenvironmental Landscape of Brain Tumors. *Cancer Cell* (2017) 31(3):326–41. doi: 10.1016/j.ccell.2017.02.009
57. Dubinski D, Wölfer J, Hasselblatt M, Schneider-Hohendorf T, Bogdahn U, Stummer W, et al. CD4+ T Effector Memory Cell Dysfunction Is Associated With the Accumulation of Granulocytic Myeloid-Derived Suppressor Cells in Glioblastoma Patients. *Neuro-Oncology* (2016) 18(6):807–18. doi: 10.1093/neuonc/nov280
58. Ugel S, De Sanctis F, Mandruzzato S, Bronte V. Tumor-Induced Myeloid Deviation: When Myeloid-Derived Suppressor Cells Meet Tumor-Associated Macrophages. *J Clin Invest* (2015) 125(9):3365–76. doi: 10.1172/JCI80006

59. Ait Ssi S, Chraa D, El Azhary K, Sahraoui S, Olive D, Badou A. Prognostic Gene Expression Signature in Patients With Distinct Glioma Grades. *Front Immunol* (2021) 12:685213(September). doi: 10.3389/fimmu.2021.685213
60. Cassetta L, Pollard JW. Targeting Macrophages: Therapeutic Approaches in Cancer. *Nat Rev Drug Discov* (2018) 17(12):887–904. doi: 10.1038/nrd.2018.169
61. Ries CH, Cannarile MA, Hoves S, Benz J, Wartha K, Runza V, et al. Targeting Tumor-Associated Macrophages With Anti-CSF-1r Antibody Reveals a Strategy for Cancer Therapy. *Cancer Cell* (2014) 25(6):846–59. doi: 10.1016/j.ccr.2014.05.016
62. Laoui D, van Overmeire E, de Baetselier P, van Ginderachter J, Raes G. Functional Relationship Between Tumor-Associated Macrophages and Macrophage Colony-Stimulating Factor as Contributors to Cancer Progression. *Front Immunol* (2014) 5:489. doi: 10.3389/fimmu.2014.00489
63. De I, Steffen MD, Clark PA, Patros CJ, Sokn E, Bishop SM, et al. Microenvironment and Immunology CSF1 Overexpression Promotes High-Grade Glioma Formation Without Impacting the Polarization Status of Glioma-Associated Microglia and Macrophages. *Microenvironment Immunol* (2016) 76:2552–60. doi: 10.1158/0008-5472.CAN-15-2386
64. Overmeire EV, Stijlemans B, Heymann F, Keirsse J, Morias Y, Elkrim Y, et al. M-CSF and GM-CSF Receptor Signaling Differentially Regulate Monocyte Maturation and Macrophage Polarization in the Tumor Microenvironment. *Cancer Res* (2016) 76(1):35–42. doi: 10.1158/0008-5472.CAN-15-0869
65. Coniglio SJ, Eugenin E, Dobrenis K, Stanley ER, West BL, Symons MH, et al. Microglial Stimulation of Glioblastoma Invasion Involves Epidermal Growth Factor Receptor (EGFR) and Colony Stimulating Factor 1 Receptor (CSF-1r) Signaling. *Mol Med (Cambridge Mass.)* (2012) 18 (1):519–27. doi: 10.2119/molmed.2011.00217
66. Pyonteck SM, Akkari L, Schuhmacher AJ, Bowman RL, Sevenich L, Quail DF, et al. CSF-1r Inhibition Alters Macrophage Polarization and Blocks Glioma Progression. *Nat Med* (2013) 19(10):1264–72. doi: 10.1038/nm.3337
67. Zhu Y, Knolhoff BL, Meyer MA, Nywening TM, West BL, Luo J, et al. CSF1/CSF1R Blockade Reprograms Tumor-Infiltrating Macrophages and Improves Response to T-Cell Checkpoint Immunotherapy in Pancreatic Cancer Models. *Cancer Res* (2014) 74(18):5057–69. doi: 10.1158/0008-5472.CAN-13-3723
68. Strachan DC, Ruffell B, Oei Y, Bissell MJ, Coussens LM, Pryer N, et al. CSF1R Inhibition Delays Cervical and Mammary Tumor Growth in Murine Models by Attenuating the Turnover of Tumor-Associated Macrophages and Enhancing Infiltration by CD8+ T Cells. *OncoImmunology* (2013) 2(12): e26968. doi: 10.4161/onci.26968
69. Tham M, Khoo K, Yeo KP, Kato M, Prevost-Blondel A, Angeli V, et al. Macrophage Depletion Reduces Postsurgical Tumor Recurrence and Metastatic Growth in a Spontaneous Murine Model of Melanoma. *Oncotarget* (2015) 6(26):22857–68. doi: 10.18632/oncotarget.3127
70. Przystal JM, Becker H, Canjuga D, Tsiami F, Anderle N, Keller AL, et al. Targeting Csf1r Alone or in Combination With Pd1 in Experimental Glioma. *Cancers* (2021) 13(10):1–18. doi: 10.3390/cancers13102400
71. Zhao H, Wu L, Yan G, Chen Y, Zhou M, Wu Y, et al. Inflammation and Tumor Progression: Signaling Pathways and Targeted Intervention. *Signal Transduction Targeted Ther* (2021) 6:263–309. doi: 10.1038/s41392-021-00658-5
72. Bonelli S, Geeraerts X, Bolli E, Keirsse J, Kiss M, Antunes ARP, et al. Beyond the M-CSF Receptor - Novel Therapeutic Targets in Tumor-Associated Macrophages. *FEBS J* (2018) 285(4):777–87. doi: 10.1111/febs.14202
73. Butowski N, Colman H, De Groot JF, Omuro AM, Nayak L, Wen PY, et al. Orally Administered Colony Stimulating Factor 1 Receptor Inhibitor PLX3397 in Recurrent Glioblastoma: An Ivy Foundation Early Phase Clinical Trials Consortium Phase II Study. *Neuro-Oncology* (2016) 18 (4):557–64. doi: 10.1093/neuonc/nov245
74. Gyori D, Lim EL, Grant FM, Spensberger D, Roychoudhuri R, Shuttleworth SJ, et al. Compensation Between CSF1R+ Macrophages and Foxp3+ Treg Cells Drives Resistance to Tumor Immunotherapy. *JCI Insight* (2018) 3(11): e120631. doi: 10.1172/jci.insight.120631
75. Kumar V, Donthireddy L, Marvel D, Condamine T, Wang F, Lavilla-Alonso S, et al. Cancer-Associated Fibroblasts Neutralize the Anti-Tumor Effect of CSF1 Receptor Blockade by Inducing PMN-MDSC Infiltration of Tumors. *Cancer Cell* (2017) 32(5):654–68.e5. doi: 10.1016/j.ccell.2017.10.005
76. Quail DF, Joyce JA. Molecular Pathways: Deciphering Mechanisms of Resistance to Macrophage-Targeted Therapies. *Clin Cancer Res* (2017) 23 (4):876–45. doi: 10.1158/1078-0432.CCR-16-0133
77. Quail DF, Bowman RL, Akkari L, Quick ML, Schuhmacher AJ, Huse JT, et al. The Tumor Microenvironment Underlies Acquired Resistance to CSF-1r Inhibition in Gliomas. *Science* (2016) 352(6288):aad3018. doi: 10.1126/science.aad3018
78. Antonios JP, Soto H, Everson RG, Moughon D, Orpilla JR, Shin NP, et al. Immunosuppressive Tumor-Infltrating Myeloid Cells Mediate Adaptive Immune Resistance via a PD-1/PD-L1 Mechanism in Glioblastoma. *Neuro-Oncology* (2017) 19(6):796–807. doi: 10.1093/neuonc/now287
79. Lamb YN. Pexidartinib: First Approval. *Drugs* (2019) 79(16):1805–12. doi: 10.1007/s40265-019-01210-0
80. Shankarappa PS, Peer CJ, Odabas A, McCully CL, Garcia RC, Figg WD, et al. Cerebrospinal Fluid Penetration of the Colony-Stimulating Factor-1 Receptor (CSF-1r) Inhibitor, Pexidartinib. *Cancer Chemother Pharmacol* (2020) 85(5):1003–7. doi: 10.1007/s00280-020-04071-7
81. Benner B, Good L, Quiroga D, Schultz TE, Kassem M, Carson WE, et al. Pexidartinib, a Novel Small Molecule Csf-1r Inhibitor in Use for Tenosynovial Giant Cell Tumor: A Systematic Review of Pre-Clinical and Clinical Development. *Drug Design Dev Ther* (2020) 14:1693–704. doi: 10.2147/DDDT.S253232
82. Mok S, Koya RC, Tsui C, Xu J, Robert L, Wu L, et al. Inhibition of CSF-1 Receptor Improves the Antitumor Efficacy of Adoptive Cell Transfer Immunotherapy. *Cancer Res* (2014) 74(1):153–61. doi: 10.1158/0008-5472.CAN-13-1816
83. Salvagno C, Ciampricotti M, Tuit S, Hau CS, van Weverwijk A, Coffelt SB, et al. Therapeutic Targeting of Macrophages Enhances Chemotherapy Efficacy by Unleashing Type I Interferon Response. *Nat Cell Biol* (2019) 21(4):511–21. doi: 10.1038/s41556-019-0298-1
84. Stafford JH, Hirai T, Deng L, Chernikova SB, Urata K, West BL, et al. Colony Stimulating Factor 1 Receptor Inhibition Delays Recurrence of Glioblastoma After Radiation by Altering Myeloid Cell Recruitment and Polarization. *Neuro-Oncology* (2016) 18(6):797–806. doi: 10.1093/neuonc/nov272
85. Ding AS, Routkevitch D, Jackson C, Lim M. Targeting Myeloid Cells in Combination Treatments for Glioma and Other Tumors. *Front Immunol* (2019) 10:1715(July). doi: 10.3389/fimmu.2019.01715
86. Ali S, Borin TF, Piranlioglu R, Ara R, Lebedyeva I, Angara K, et al. Changes in the Tumor Microenvironment and Outcome for TME-Targeting Therapy in Glioblastoma: A Pilot Study'. Edited by Ilya Ulasov. *PLoS One* (2021) 16(2):e0246646. doi: 10.1371/journal.pone.0246646
87. Jiang CT, Wu WF, Deng YH, Ge JW. Modulators of Microglia Activation and Polarization in Ischemic Stroke (Review). *Mol Med Rep* (2020) 21 (5):2006–18. doi: 10.3892/mmr.2020.11003
88. Barca C, Kiliaan AJ, Foray C, Wachsmuth L, Hermann S, Faber C, et al. A Longitudinal PET/MR Imaging Study of Colony Stimulating Factor-1 Receptor-Mediated Microglia Depletion in Experimental Stroke'. *J Nucl Med* (2021) jnumed.121.262279. doi: 10.2967/jnumed.121.262279
89. Szalay G, Martinecz B, Lénárt N, Környei Z, Orsolits B, Judák L, et al. Microglia Protect Against Brain Injury and Their Selective Elimination Dysregulates Neuronal Network Activity After Stroke. *Nat Commun* (2016) 7(1):11499. doi: 10.1038/ncomms11499
90. Shinozaki Y, Shibata K, Yoshida K, Shigetomi E, Gachet C, Ikenaka K, et al. Transformation of Astrocytes to a Neuroprotective Phenotype by Microglia *via* P2Y 1 Receptor Downregulation. *Cell Rep* (2017) 19(6):1151–64. doi: 10.1016/j.celrep.2017.04.047
91. Jin W-N, Shi SX-Y, Li Z, Li M, Wood K, Gonzales RJ, et al. Depletion of Microglia Exacerbates Postischemic Inflammation and Brain Injury. *J Cereb Blood Flow & Metab* (2017) 37(6):2224–36. doi: 10.1177/0271678X17694185
92. Horti AG, Naik R, Foss CA, Minn I, Misheneva V, Du Y, et al. PET Imaging of Microglia by Targeting Macrophage Colony-Stimulating Factor 1 Receptor (CSF1R). *Proc Natl Acad Sci* (2019) 116(5):1686–91. doi: 10.1073/pnas.1812155116
93. Knight AC, Varlow C, Zi T, Liang SH, Josephson L, Schmidt K, et al. *In Vitro* Evaluation of [3H]CPPC as a Tool Radioligand for CSF-1r. *ACS Chem Neurosci* (2021) 12(6):998–1006. doi: 10.1021/acschemneuro.0c00802
94. Zhou X, Ji B, Seki C, Nagai Y, Minamimoto T, Fujinaga M, et al. PET Imaging of Colony-Stimulating Factor 1 Receptor: A Head-To-Head Comparison of a Novel Radioligand, 11c-GW2580, and 11C-CPPC, in Mouse Models of Acute and Chronic Neuroinflammation and a Rhesus

Monkey. *J Cereb Blood Flow Metab* (2021) 41(9):2410–22. doi: 10.1177/0271678X211004146
95. Mason CA, Kossatz S, Carter LM, Pirovano G, Brand C, Guru N, et al. An 89 Zr-HDL PET Tracer Monitors Response to a CSF1R Inhibitor. *J Nucl Med* (2020) 61(3):433–36. doi: 10.2967/jnumed.119.230466
96. Zinnhardt B, Pigeon H, Thézé B, Viel T, Wachsmuth L, Fricke IB, et al. Combined PET Imaging of the Inflammatory Tumor Microenvironment Identifies Margins of Unique Radiotracer Uptake. *Cancer Res* (2017) 77 (8):1831–41. doi: 10.1158/0008-5472.CAN-16-2628
97. Foray C, Valtorta S, Barca C, Winkeler A, Roll W, Müther M, et al. Imaging Temozolomide-Induced Changes in the Myeloid Glioma Microenvironment. *Theranostics* (2021) 11(5):2020–33. doi: 10.7150/thno.47269
98. Barca C, Foray C, Hermann S, Döring C, Schäfers M, Jacobs AH, et al. Characterization of the Inflammatory Post-Ischemic Tissue by Full Volumetric Analysis of a Multimodal Imaging Dataset. *NeuroImage* (2020) 222:117217. doi: 10.1016/j.neuroimage.2020.117217
99. Hillmer AT, Holden D, Fowles K, Nabulsi N, West BL, Carson RE, et al. Microglial Depletion and Activation: A [11c]PBR28 PET Study in Nonhuman Primates. *EJNMMI Res* (2017) 7(1):595. doi: 10.1186/s13550-017-0305-0
100. Walker DG, Tang TM, Mendsaikhan A, Tooyama I, Serrano GE, Sue LI, et al. Patterns of Expression of Purinergic Receptor P2RY12, a Putative Marker for Non-Activated Microglia, in Aged and Alzheimer's Disease Brains. *Int J Mol Sci* (2020) 21(2):678. doi: 10.3390/ijms21020678
101. Villa A, Klein B, Janssen B, Pedragosa J, Pepe G, Zinnhardt B, et al. Identification of New Molecular Targets for PET Imaging of the Microglial Anti-Inflammatory Activation State. *Theranostics* (2018) 8(19):5400–18. doi: 10.7150/thno.25572
102. Virgilio FD, Ben DD, Sarti AC, Giuliani AL, Falzoni S. The P2X7 Receptor in Infection and Inflammation. *Immunity* (2017) 47(1):15–31. doi: 10.1016/j.immuni.2017.06.020
103. Koole M, Schmidt ME, Hijzen A, Ravenstijn P, Vandermeulen C, Van Weehaeghe D, et al. 18f-JNJ-64413739, a Novel PET Ligand for the P2X7 Ion Channel: Radiation Dosimetry, Kinetic Modeling, Test-Retest Variability, and Occupancy of the P2X7 Antagonist JNJ-54175446. *J Nucl Med* (2019) 60 (5):683–90. doi: 10.2967/jnumed.118.216747

Conflict of Interest: The author BZ is currently employed by F. Hoffman-La Roche Ltd.

The remaining authors declare that the research was conducted in the absence of any commercial or financial relationships that could be construed as a potential conflict of interest.

Publisher's Note: All claims expressed in this article are solely those of the authors and do not necessarily represent those of their affiliated organizations, or those of the publisher, the editors and the reviewers. Any product that may be evaluated in this article, or claim that may be made by its manufacturer, is not guaranteed or endorsed by the publisher.

frontiers in Immunology

ORIGINAL RESEARCH
published: 09 December 2021
doi: 10.3389/fimmu.2021.799910

Single-Domain Antibodies for Targeting, Detection, and *In Vivo* Imaging of Human CD4$^+$ Cells

*Bjoern Traenkle[1], Philipp D. Kaiser[1], Stefania Pezzana[2], Jennifer Richardson[3], Marius Gramlich[1], Teresa R. Wagner[1,4], Dominik Seyfried[2,5], Melissa Weldle[4], Stefanie Holz[4], Yana Parfyonova[4], Stefan Nueske[6], Armin M. Scholz[6], Anne Zeck[1], Meike Jakobi[1], Nicole Schneiderhan-Marra[1], Martin Schaller[7], Andreas Maurer[2,8], Cécile Gouttefangeas[3,5,8], Manfred Kneilling[2,7,8], Bernd J. Pichler[2,5,8], Dominik Sonanini[2,9] and Ulrich Rothbauer[1,4,8]**

[1] NMI Natural and Medical Sciences Institute at the University of Tübingen, Reutlingen, Germany, [2] Werner Siemens Imaging Center, Department of Preclinical Imaging and Radiopharmacy, University of Tübingen, Tübingen, Germany, [3] Department of Immunology, Institute of Cell Biology, University of Tübingen, Tübingen, Germany, [4] Pharmaceutical Biotechnology, University of Tübingen, Tübingen, Germany, [5] German Cancer Consortium (DKTK) and German Cancer Research Center (DKFZ) partner site Tübingen, Tübingen, Germany, [6] Livestock Center of the Faculty of Veterinary Medicine, Ludwig Maximilians University Munich, Oberschleissheim, Germany, [7] Department of Dermatology, University of Tübingen, Tübingen, Germany, [8] Cluster of Excellence iFIT (EXC2180) "Image-Guided and Functionally Instructed Tumor Therapies," University of Tübingen, Tübingen, Germany, [9] Department of Medical Oncology and Pneumology, University of Tübingen, Tübingen, Germany

OPEN ACCESS

Edited by:
Marco Erreni,
Humanitas Research Hospital, Italy

Reviewed by:
Serge Muyldermans,
Vrije University Brussel, Belgium
Alexis Broisat,
Institut National de la Santé et de la Recherche Médicale (INSERM), France

***Correspondence:**
Ulrich Rothbauer
ulrich.rothbauer@uni-tuebingen.de
orcid.org/0000-0001-5923-8986

Specialty section:
This article was submitted to Cancer Immunity and Immunotherapy, a section of the journal Frontiers in Immunology

Received: 22 October 2021
Accepted: 17 November 2021
Published: 09 December 2021

Citation:
Traenkle B, Kaiser PD, Pezzana S, Richardson J, Gramlich M, Wagner TR, Seyfried D, Weldle M, Holz S, Parfyonova Y, Nueske S, Scholz AM, Zeck A, Jakobi M, Schneiderhan-Marra N, Schaller M, Maurer A, Gouttefangeas C, Kneilling M, Pichler BJ, Sonanini D and Rothbauer U (2021) Single-Domain Antibodies for Targeting, Detection, and In Vivo Imaging of Human CD4$^+$ Cells. Front. Immunol. 12:799910. doi: 10.3389/fimmu.2021.799910

The advancement of new immunotherapies necessitates appropriate probes to monitor the presence and distribution of distinct immune cell populations. Considering the key role of CD4$^+$ cells in regulating immunological processes, we generated novel single-domain antibodies [nanobodies (Nbs)] that specifically recognize human CD4. After in-depth analysis of their binding properties, recognized epitopes, and effects on T-cell proliferation, activation, and cytokine release, we selected CD4-specific Nbs that did not interfere with crucial T-cell processes *in vitro* and converted them into immune tracers for noninvasive molecular imaging. By optical imaging, we demonstrated the ability of a high-affinity CD4-Nb to specifically visualize CD4$^+$ cells *in vivo* using a xenograft model. Furthermore, quantitative high-resolution immune positron emission tomography (immunoPET)/MR of a human CD4 knock-in mouse model showed rapid accumulation of ^{64}Cu-radiolabeled CD4-Nb1 in CD4$^+$ T cell-rich tissues. We propose that the CD4-Nbs presented here could serve as versatile probes for stratifying patients and monitoring individual immune responses during personalized immunotherapy in both cancer and inflammatory diseases.

Keywords: CD4, nanobody, immune tracer, PET imaging, magnetic resonance imaging, immunotherapies

INTRODUCTION

In precision medicine, diagnostic classification of the disease-associated immune status should guide the selection of appropriate therapies. A comprehensive analysis of a patient's specific immune cell composition, activation state, and infiltration of affected tissue has been shown to be highly informative for patient stratification (1–3). In this context, CD4 is an important marker, as it is found on the surface of immune cells such as monocytes, macrophages, and dendritic cells and most

abundant on $CD4^+$ T cells (4, 5). $CD4^+$ T cells are a key determinant of the immune status due to their essential role in orchestrating immune responses in autoimmune diseases, immune-mediated inflammatory diseases (IMIDs), cancer, and chronic viral infections (6–13). Current diagnostic standards such as intra-cytoplasmic flow cytometry analysis (IC-FACS), immunohistochemistry, and *ex vivo* cytokine assays or RT-PCR analysis are exclusively invasive and therefore limited with respect to repetitive analyses over time (14–17). Considering the emerging role of infiltrating lymphocytes and the impact of $CD4^+$ T cells on the outcome of immunotherapies, novel approaches are needed to assess $CD4^+$ T cells more holistically (18). In this context, noninvasive imaging approaches offer a significant benefit compared to the current diagnostic standard. To date, radiolabeled antibodies have been applied to image $CD4^+$ cells in preclinical models (10, 19–21). Due to the recycling effect mediated by the neonatal Fc receptor, full-length antibodies have a long serum half-life, which requires long clearance times of several days before high-contrast images can be acquired (22). Additionally, effector function *via* the Fc region was shown to induce depletion or functional changes in $CD4^+$ cells including the induction of proliferation or cytokine release (23–25). Notably, also higher dosages of recombinant antibody fragments like Fab fragments or Cys-diabodies derived from the monoclonal anti-CD4 antibody GK1.5 were recently shown to decrease CD4 expression *in vivo* and inhibit proliferation and interferon (IFN)-γ production *in vitro* (24–26). These studies highlight the importance of carefully investigating $CD4^+$ cell-specific immunoprobes for their epitopes, binding properties, and functional effects.

During the last decade, antibody fragments derived from heavy-chain-only antibodies of camelids, referred to as VHHs or nanobodies (Nbs) (27), have emerged as versatile probes for molecular imaging [reviewed in (28)]. In combination with highly sensitive and/or quantitative whole-body molecular imaging techniques such as optical or radionuclide-based modalities, particularly positron emission tomography (PET), Nbs have been shown to bind their targets within several minutes of systemic application (29). Due to their great potential as highly specific imaging probes, numerous Nbs targeting immune- or tumor-specific cellular antigens are currently in preclinical development and even in clinical trials (28, 30, 31).

Here, we generated a set of human CD4 (hCD4)-specific Nbs. Following in-depth characterization of their binding properties, we selected candidates that did not affect T-cell proliferation, activation, or cytokine release and converted them into immune tracers for noninvasive optical and PET imaging. Using a mouse xenograft model and an hCD4 knock-in mouse model, we successfully demonstrated the capacity of these CD4-Nbs to visualize $CD4^+$ cells *in vivo*.

RESULTS

Generation of High-Affinity CD4 Nanobodies

To generate Nbs directed against hCD4, we immunized an alpaca (*Vicugna pacos*) with the recombinant extracellular portion of hCD4 following an 87-day immunization protocol. Subsequently, we generated a Nb phagemid library comprising ~4×10^7 clones that represent the full repertoire of variable heavy chains of heavy-chain antibodies (VHHs or Nbs) of the animal. We performed phage display using either passively adsorbed purified hCD4 or CHO and HEK293 cells stably expressing full-length hCD4 (CHO-hCD4 and HEK293-hCD4 cell lines, respectively). Following two cycles of phage display for each condition, we analyzed a total of 612 individual clones by whole-cell phage ELISA and identified 78 positive binders. Sequence analysis revealed 13 unique Nbs representing five different B-cell lineages according to their complementarity determining region (CDR) 3 (**Figure 1A**). One representative Nb of each lineage, termed CD4-Nb1–CD4-Nb5, was expressed in bacteria (*Escherichia coli)* and isolated with high purity using immobilized metal ion affinity chromatography (IMAC) followed by size exclusion chromatography (SEC) (**Figure 1B**). To test whether selected Nbs are capable of binding to full-length hCD4 localized at the plasma membrane of mammalian cells, we performed live-cell staining of CHO-hCD4 cells (**Figure 1C**, **Supplementary Figure 1**). Executed at 4°C, images showed a prominent staining of the plasma membrane, whereas at 37°C, the fluorescent signal was mainly localized throughout the cell body, presumably a consequence of endocytotic uptake of receptor-bound Nbs. CHO wild-type (wt) cells were not stained by any of the five CD4-Nbs at both temperatures (data not shown). CD4-Nb1 and CD4-Nb3, both identified by whole-cell panning, displayed strong staining of CHO-hCD4 cells. Of the Nbs derived from panning with recombinant hCD4, CD4-Nb2 also showed strong cellular staining, whereas staining with CD4-Nb4 revealed weak signals. CD4-Nb5 showed no staining under these conditions and was consequently excluded from further analyses (**Figure 1C**). To quantitatively assess binding affinities, we performed biolayer interferometry (BLI), measuring serial dilutions of Nbs on the biotinylated extracellular domain of hCD4 immobilized at the sensor tip. For CD4-Nb1 and CD4-Nb2, K_D values were determined to be ~5 and ~7 nM, respectively, while CD4-Nb3 and CD4-Nb4 displayed lower affinities of 75 and 135 nM, respectively (**Figure 1D**, **Table 1**, **Supplementary Figure 2A**). In addition, we determined corresponding EC_{50} values with full-length plasma membrane-located hCD4 on HEK293-hCD4 cells by flow cytometry. In accordance with cellular staining and biochemically determined affinities, these values revealed a strong functional binding for CD4-Nb1 and CD4-Nb2 with EC_{50} values in the subnanomolar range (~0.7 nM), whereas CD4-Nb3 and CD4-Nb4 displayed substantially lower cellular affinities (**Figure 1E**, **Table 1**, **Supplementary Figure 2B**). In summary, we generated four CD4-Nbs that bind isolated and cell-resident hCD4. While CD4-Nb3 and CD4-Nb4 appeared less affine, CD4-Nb1 and CD4-Nb2 displayed high affinities in the low nanomolar range.

Domain Mapping

Next, we applied chemo-enzymatic coupling using sortase A for site-directed functionalization of CD4-Nbs (32, 33). We thereby linked peptides conjugated to a single fluorophore to the C-terminus of CD4-Nbs, yielding a defined labeling ratio of 1:1 (34). Live-cell immunofluorescence imaging showed that all sortase-coupled CD4-Nbs retained their capability of binding

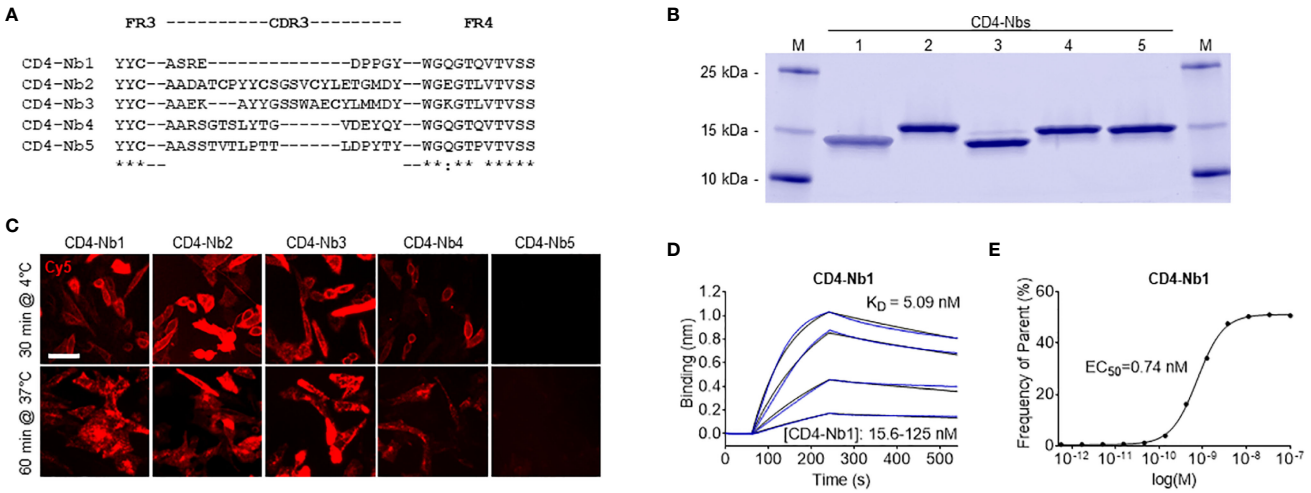

FIGURE 1 | Identification and characterization of nanobodies (Nbs) against human CD4 (hCD4). **(A)** Amino acid sequences of the complementarity determining region (CDR) 3 from unique CD4-Nbs selected after two rounds of biopanning are listed. **(B)** Recombinant expression and purification of CD4-Nbs using immobilized metal ion affinity chromatography (IMAC) and size exclusion chromatography (SEC). Coomassie-stained SDS-PAGE of 2 µg of purified Nbs is shown. **(C)** Representative images of live CHO-hCD4 cells stained with CD4-Nbs for 30 min at 4°C (top row) or 60 min at 37°C (bottom row); scale bar: 50 µm. **(D)** For biolayer interferometry (BLI)-based affinity measurements, biotinylated hCD4 was immobilized on streptavidin biosensors. Kinetic measurements were performed using four concentrations of purified Nbs ranging from 15.6 to 1,000 nM. As an example, the sensogram of CD4-Nb1 at indicated concentrations is shown. **(E)** EC_{50} determination by flow cytometry. Exemplarily shown for CD4-Nb1, the percentage of positively stained HEK293-hCD4 (frequency of parent) was plotted against indicated concentrations of CD4-Nbs.

TABLE 1 | Summary of affinities (k_D) and association (k_{on}) and dissociation constants (k_{off} and coefficient of determination R_2) determined by BLI (left side) and EC_{50} values of flow cytometry (right side).

	Dissociation constant K_D	k_{on} (10^5 M^{-1} s^{-1})	k_{off} (10^{-4} s^{-1})	R^2	EC_{50}
CD4-Nb1	5.1 nM	1.21 ± 0.022	6.13 ± 0.27	0.996	0.74 nM
CD4-Nb2	6.5 nM	1.22 ± 0.015	7.95 ± 0.18	0.998	0.73 nM
CD4-Nb3	75.3 nM	0.82 ± 0.026	61.8 ± 2.00	0.983	533 nM
CD4-Nb4	135 nM	1.18 ± 0.014	160 ± 0.97	0.998	7.36 µM

to cell-resident hCD4 of CHO-hCD4 cells (**Supplementary Figure 3A**). To localize the binding sites of the selected CD4-Nbs, we generated domain-deletion mutants of hCD4. Expression and correct surface localization of these mutants in CHO cells were confirmed by staining with antibody RPA-T4 binding to domain 1 of CD4. For mutants lacking domain 1, we introduced an N-terminal BC2 tag (35) to allow for live-cell surface detection with a fluorescently labeled bivBC2-Nb (34) (**Supplementary Figure 3B**). Transiently expressed domain-deletion mutants were then tested for binding of CF568-labeled CD4-Nbs by live-cell immunofluorescence imaging, including a non-specific fluorescently labeled green fluorescent protein (GFP)-binding Nb (GFP-Nb) as negative control. Based on these results, we allocated binding of CD4-Nb1 and CD4-Nb3 to domain 1, whereas CD4-Nb2 and CD4-Nb4 bind to domain 3 and/or 4 of hCD4 (**Figure 2A**, **Supplementary Figure 3C**).

To further examine combinatorial binding of the different CD4-Nbs, we performed an epitope binning analysis by BLI. Recombinant full-length hCD4 was immobilized at the sensor tip, and combinations of CD4-Nbs were allowed to bind consecutively (**Supplementary Figure 4**). Unsurprisingly, CD4-Nbs binding to different domains displayed combinatorial binding. Interestingly, a simultaneous binding was also detected for the combination of CD4-Nb1 and CD4-Nb3, suggesting that both CD4-Nbs bind to different epitopes within domain 1. In contrast, we did not observe simultaneous binding for CD4-Nb2 and CD4-Nb4, which might be due to close-by or overlapping epitopes at domain 3/4 for the latter Nb pair.

For a more precise epitope analysis, we conducted a hydrogen–deuterium exchange mass spectrometry (HDX-MS) analysis of hCD4 bound to CD4-Nb1, CD4-Nb2, or CD4-Nb3 (**Figures 2B–E**, **Supplementary Figure 5**). Due to its low affinity, CD4-Nb4 was not considered for HDX-MS analysis (data not shown). In accordance with our previous findings, binding of CD4-Nb1 and CD4-Nb3 protected sequences of domain 1 from HDX, whereas CD4-Nb2 protected sequences of domains 3 and 4 of hCD4 (**Figure 2B**). The results obtained for binding of CD4-Nb1 (**Figure 2C**) are similar to those obtained for CD4-Nb3 (**Figure 2D**) in that binding of either Nb reduced hydrogen exchange at amino acid (aa) residues from aa T17 to N73, albeit with a different extent of protection at individual sequence segments. For CD4-Nb1, the greatest protection from HDX

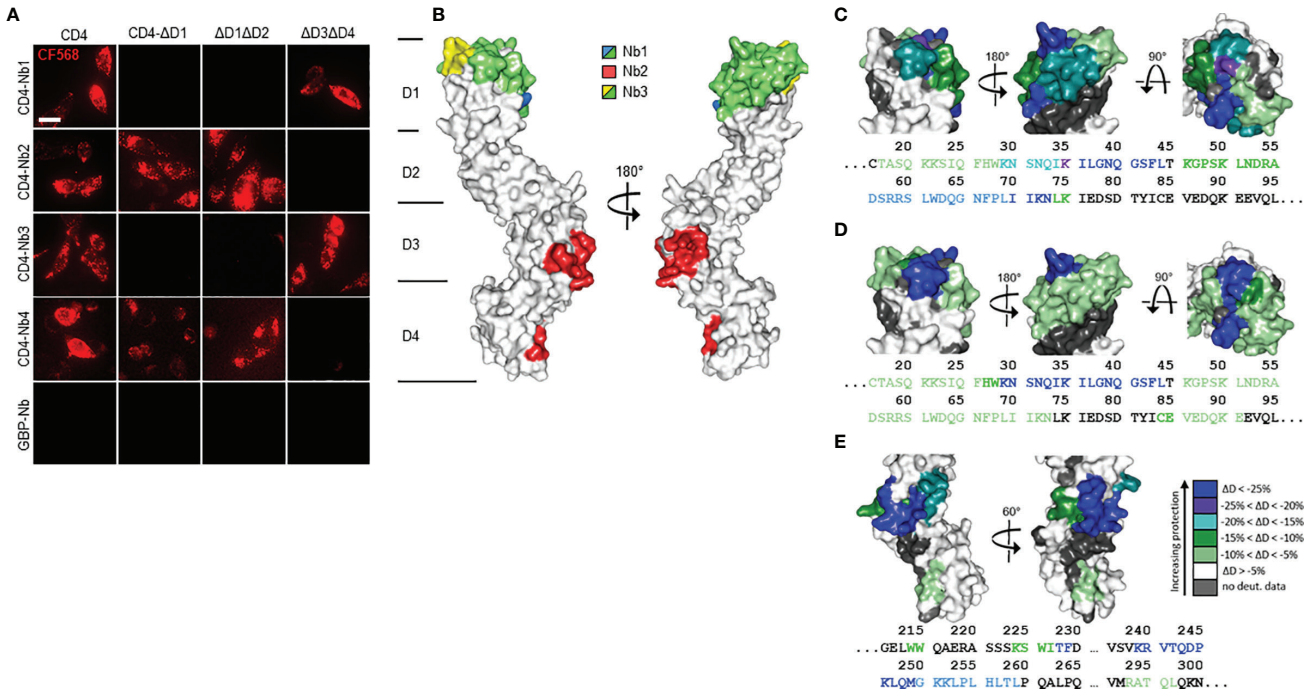

FIGURE 2 | Localization of CD4-nanobody (Nb) binding epitopes. **(A)** Representative images of live CHO cells expressing full-length or domain-deletion mutants of human CD4 (hCD4) stained with fluorescently labeled CD4-Nbs (CF568) are shown; scale bar 10 µm. **(B)** Surface structure model of hCD4 (PDBe 1wiq) (36) and the hydrogen-deuterium exchange mass spectrometry (HDX-MS) epitope mapping results of CD4-Nb1–3 are depicted. Different colors highlight the amino acid residues protected by CD4-Nb1 (blue), CD4-Nb2 (red), or CD4-Nb3 (yellow). Overlapping residues protected by both Nb1 and Nb3 are colored green. A more detailed surface map (%ΔD) of these specific regions is highlighted in **(C)** (CD4-Nb1), **(D)** (CD4-Nb3), and **(E)** (CD4-Nb2) with the corresponding CD4 amino acid sequence.

was observed for the sequence ranging from aa K35 to L44 corresponding to β strand C′ and C′′ of the immunoglobulin fold of domain 1 and residues aa K46–K75, comprising β strands D and E. In contrast, binding of CD4-Nb3 confers only a minor reduction in HDX within the latter sequence but additionally protects sequence aa C84–E91, which correspond to β strands G and F and their intermediate loop. For CD4-Nb2, we found protection of sequences aa W214–F229 (β strands C and C′) and aa K239–L259 (β strands C′′–E) and to a minor extent sequence aa R293–L296 as part of β strand A of domain 4 (**Figure 2E**). In summary, our HDX-MS analysis revealed that all three tested Nbs bind three dimensional epitopes within different parts of hCD4. It further provides an explanation how CD4-Nb1 and CD4-Nb3 can bind simultaneously to domain 1 of hCD4 and confirms that the epitope of CD4-Nb2 is mainly located at domain 3.

Binding of CD4-Nbs to Human Peripheral Blood Mononuclear Cells

Having demonstrated that all selected Nbs bind to recombinant and exogenously overexpressed cellular hCD4, we next examined their capability and specificity of binding to physiologically relevant levels of $CD4^+$ T cells within peripheral blood mononuclear cell (PBMC) samples. We costained human PBMCs from three donors with CD4-Nb1–CD4-Nb4 coupled to CF568 (100 nM for high-affine CD4-Nb1 and CD4-Nb2; 1,000 nM for low-affine CD4-Nb3 and CD4-Nb4) in combination with an anti-CD3 antibody and analyzed the percentage of double-positive cells ($CD3^+CD4^+$) by flow cytometry (**Figure 3**, **Supplementary Figure 6**). Compared to staining with an anti-CD4 antibody used as a positive control, all CD4-Nbs stained a similar percentage of $CD4^+$ T cells for all tested donors, while the non-specific GFP-Nb yielded a negligible percentage of double-positive cells even at the highest concentration (1,000 nM) (**Table 2**). Our analysis further revealed that, as observed with a conventional anti-CD4 antibody, the CD4-Nbs stain a substantial proportion of $CD3^-$ cells, indicating that all selected candidates are also able to recognize cells such as monocytes, macrophages, or dendritic cells that express lower levels of CD4 (**Figure 3**).

Impact of CD4-Nbs on Activation, Proliferation, and Cytokine Release of $CD4^+$ T and Immune Cells

In view of the envisioned application as clinical imaging tracer, we next evaluated the potential of the Nbs to be further developed into clinically approved binding molecules. Since CD4-Nb2 and CD4-Nb3 contain a number of cysteine residues in their CDR3, we excluded them at this stage because such non-canonical unpaired cysteines are often associated with expression

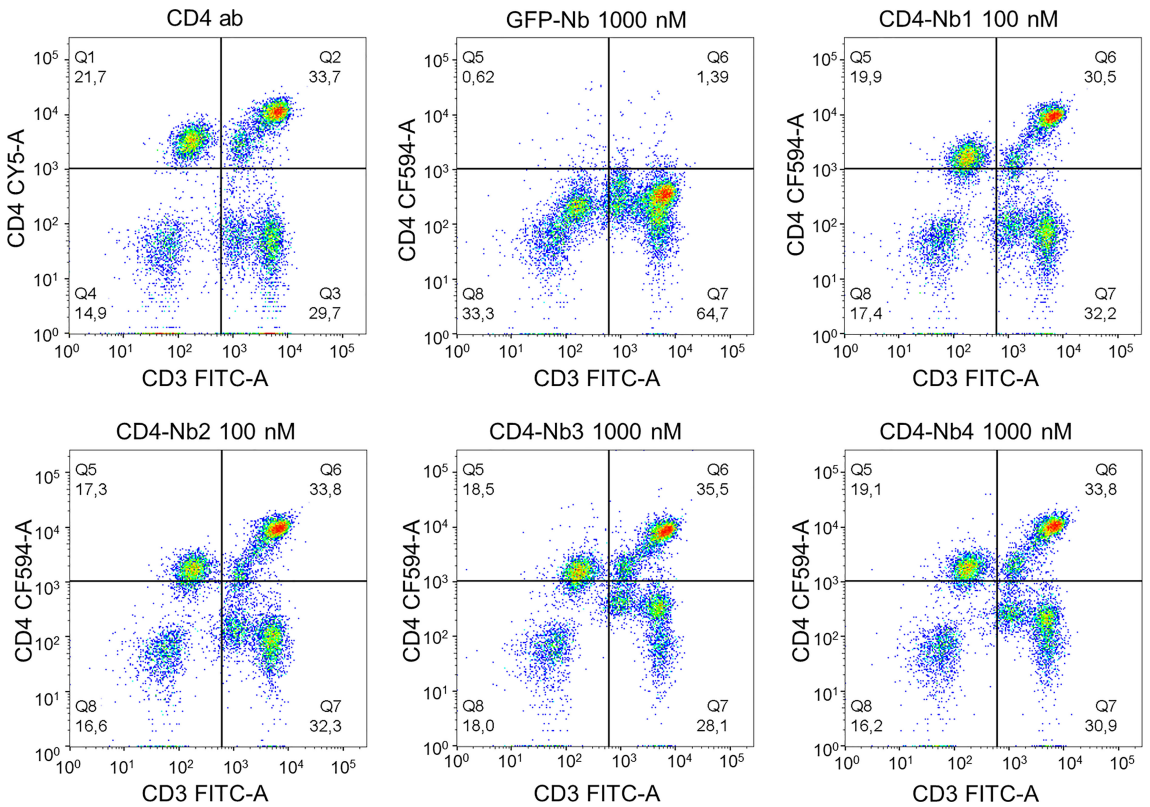

FIGURE 3 | Flow cytometry analysis of human peripheral blood mononuclear cells (PBMCs) stained with fluorescently labeled CD4-nanobodies (Nbs). Schematic representation of the final gating step for $CD3^+CD4^+$ double-positive cells derived from donor 1.

problems and a higher tendency to form aggregates in downstream production (37, 38). With CD4-Nb1 and CD4-Nb4, we pursued two candidates that do not contain non-canonical cysteines and also cover a broad affinity spectrum. For these two Nbs and a non-specific GFP-Nb as a control, we then examined their influence on $CD4^+$ T-cell activation, proliferation, and cytokine release. To rule out adverse effects of bacterial endotoxins in the Nb preparations, we first removed endotoxins by depletion chromatography, resulting in Food and Drug Administration (FDA)-acceptable endotoxin levels of <0.25 EU per mg. Typically, Nb-based radiotracers are applied at serum concentrations between 0.01 and 0.2 μM in (pre)clinical imaging (39, 40). To investigate the effects of Nbs at the expected, but also at a 10-fold increased concentration and consequently elongated serum retention times that might occur during *in vivo* (pre)clinical imaging, we treated carboxyfluorescein succinimidyl ester (CFSE)-labeled human PBMCs from three preselected healthy donors with three Nbs at concentrations ranging from 0.05 from 5 μM for 1 h at 37°C. Subsequently, cells were washed to remove Nbs and stimulated with an antigenic [cognate major histocompatibility complex (MHC)II peptides] or a non-antigenic stimulus (phytohemagglutinin, PHA-L) and analyzed after 4, 6, and 8 days by flow cytometry with the gating strategy shown in **Supplementary Figure 7A**. According to the highly similar CFSE intensity profiles observed, the total number of cell divisions was not affected by the different Nb treatments (exemplarily shown for one of three donors on day 6; **Supplementary Figure 7A**). For samples of the same donor and time point, no substantial differences in the percentage of proliferated cells were observed between mock incubation and individual Nb treatments.

For both stimuli, the average percentage of proliferated cells increased over time in all donors tested, with no clear differences between conditions (**Figure 4A**). As a quantitative measure of T-cell activation, we also determined the cell surface induction of a very early activation marker (CD69) and of the interleukin (IL)-2 receptor α chain (CD25) on $CD4^+$ T cells (**Figure 4B**). Among samples of the same donor and stimulation, we found highly similar activation profiles for all Nb treatments. While the percentage of $CD4^+CD25^+$ cells steadily increased over time for MHCII peptide stimulation, for the PHA-stimulated condition, the percentage of positive cells was similarly high at all times of analysis. Importantly, regardless of the differences between donors, the individual Nb treatments from the same donor did not result in significant differences in the percentage of $CD4^+CD25^+$ or $CD4^+CD69^+$ cells for either stimulation at any point in the analysis.

Next, we analyzed cytokine expression of $CD4^+$ T cells by intracellular cytokine staining after restimulation with cognate MHCII peptides. The corresponding gating strategy is shown in

TABLE 2 | Percentage of double-positive cells of three donors, stained with CD4-Nb1 or CD4-Nb2 (100 nM), or CD4-Nb3 or CD4-Nb4 (1,000 nM), compared to anti-CD4 antibody and negative control Nb (GFP-Nb, 1,000 nM).

		Frequency $CD3^+$ $CD4^+$ (%)		
	c (nM)	Donor 1	Donor 2	Donor 3
Anti-CD4 antibody	~1	33.7	27.0	*24.3*
CD4-Nb1	100	30.5	29.2	22.7
CD4-Nb2	100	33.8	25.6	18.4
CD4-Nb3	1,000	35.5	26.5	20.4
CD4-Nb4	1,000	33.8	26.9	23.9
GFP-Nb	1,000	1.4	0.3	1.0

Supplementary Figure 7B. Samples of the same donor treated with different Nbs had highly similar percentages of cytokine [tumor necrosis factor (TNF), IFN-γ, or IL-2] or activation marker (CD154)-positive cells without stimulation and upon stimulation with MHCII peptides (**Figure 4C**). Overall, exposure to CD4-Nbs did not affect the proliferation, activation, or cytokine production of $CD4^+$ T cells. In addition, we analyzed potential effects of CD4-Nbs on the release of cytokines from full-blood samples of three further donors. Upon stimulation with lipopolysaccharide (LPS) or PHA–L, we determined the serum concentrations with a panel of pro- and anti-inflammatory cytokines (**Supplementary Table 2**). Although there was significant inter-donor variation for some cytokines, Nb treatment did not result in significant differences in either stimulated or unstimulated samples (**Supplementary Figure 8**).

CD4-Nbs for *In Vivo* Imaging

For optical *in vivo* imaging, we labeled CD4-Nbs with the fluorophore Cy5.5 (CD4-Nb-Cy5.5) by sortase-mediated attachment of an azide group followed by click-chemistry addition of dibenzocyclooctyne (DBCO)-Cy5.5. First, we tested potential cross-reactivity of the four Cy5.5-labeled CD4-Nbs to murine $CD4^+$ lymphocytes. Notably, flow cytometric analysis showed that none of the selected CD4-Nbs bound murine $CD4^+$

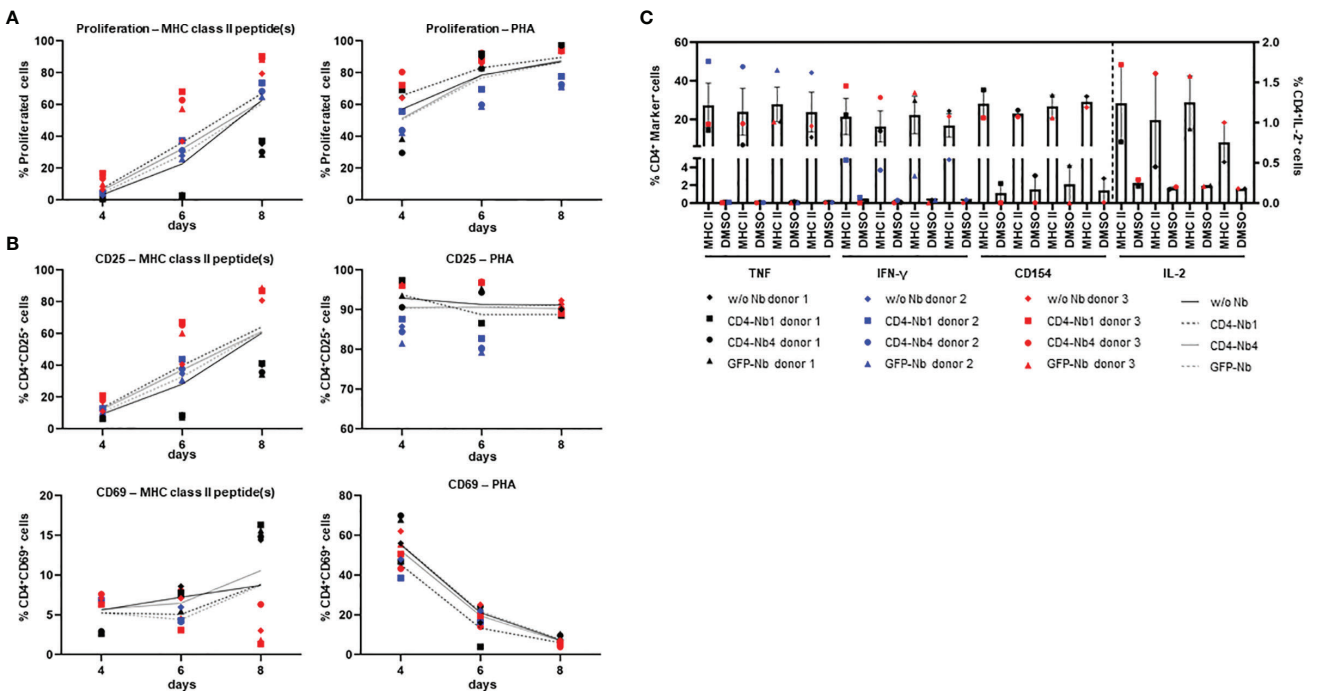

FIGURE 4 | Impact of CD4-nanobodies (Nbs) on activation, proliferation, and cytokine release of T cells. Cells were stained with carboxyfluorescein succinimidyl ester (CFSE), treated with 5 μM Nbs or without for 1 h (one replicate each), washed, stimulated with 5 μg/ml MHCII peptides, 10 μg/ml PHA or not stimulated, and cultured for 12 days. **(A)** Cells were analyzed by flow cytometry for proliferation (CFSE-low/negative fraction) and activation (CD25 and CD69) on days 4, 6, and 8. Proliferation of $CD4^+$ cells after stimulation with MHCII peptide(s) (left) or PHA (right). **(B)** Activation markers on $CD4^+$ cells. Top: CD25 expression after stimulation with MHCII peptide(s) (left) or PHA (right); Bottom: CD69 expression after stimulation with MHCII peptide(s) (left) or PHA (right). Mean percentages of all three donors are shown as plain or dotted lines. **(C)** Cytokine and activation marker expression of $CD4^+$ cells—TNF, IFN-γ, CD154 (left y-axis), or IL-2 (right y-axis). Cells were restimulated on day 12 with MHCII peptide(s) or dimethyl sulfoxide (DMSO) (background) for 14 h in the presence of Golgi Stop and brefeldin A and analyzed by flow cytometry. Error bars display SEM. Gating strategy is shown in **Supplementary Figure 6**; all percentages are given within $CD4^+$ T cells.

cells, suggesting exclusive binding to hCD4. Moreover, low-affine binding CD4-Nb4 bound neither mouse nor human CD4$^+$ cells at the concentration used here (0.75 µg/ml, ~49 nM) (**Supplementary Figure 9**). Consequently, we focused on CD4-Nb1 as the most promising candidate and CD4-Nb4 as a candidate with a high off-target rate, both of which we further analyzed for their *in vivo* target specificity and dynamic distribution using a murine xenograft model.

To establish hCD4-expressing tumors, NOD SCID gamma (NSG) mice were inoculated subcutaneously with CD4$^+$ T-cell leukemia HPB-ALL cells (41). After 2–3 weeks, mice bearing HPB-ALL xenografts were intravenously (i.v.) injected with 5 µg of CD4-Nb1-Cy5.5, CD4-Nb4-Cy5.5, or a control Nb (GFP-Nb-Cy5.5) and non-invasively *in vivo* investigated by optical imaging (OI) in intervals over the course of 24 h (**Figure 5A**, **Supplementary Figure 10A**). The Cy5.5 signal intensity (SI) of the control Nb peaked within 10–20 minutes and rapidly declined thereafter to approximately the half and a quarter of maximum level at 2 and 24 h, respectively (**Figure 5B**, **Supplementary Figure 10B**). While the SI of the low-affinity CD4-Nb4-Cy5.5 did not exceed the SI of the control Nb at any time (**Supplementary Figure 10B**), CD4-Nb1-Cy5.5 reached its maximum SI within the HPB-ALL xenograft of ~1.8-fold above the control Nb at 30 min and slowly declined to ~90% and ~80% of maximum after 2 and 4 h, respectively (**Figure 5B**). Based on the differences in the SI between CD4-Nb1-Cy5.5 and GFP-Nb-Cy5.5, we observed constant high target accumulation and specificity between 30 and 480 min post injection (**Figure 5B**). After 24 h, mice were euthanized, and the presence of fluorophore-labeled CD4-Nbs within the explanted tumors was analyzed by OI (**Figure 5C**, **Supplementary Figure 10C**). Compared to control, tumors from mice injected with CD4–Nb1–Cy5.5 had ~4-fold higher Cy5.5 SI, indicating a good signal-to-background ratio for this Nb-derived fluorescently labeled immunoprobe even at later time points. To confirm CD4-specific targeting of CD4-Nb1 within the xenograft, we additionally performed *ex vivo* immunofluorescence of HPB-ALL tumors at 2 and 24 h post injection (**Supplementary Figure S11**). At the early time point, when the *in vivo* OI signal peaked, CD4-Nb1 was widely distributed throughout the whole tumor, whereas no Cy5.5 signal was detected in the GFP-Nb-injected mice (**Supplementary Figures 11A, B**). Semiquantitative analysis at the single-cell level revealed intense CD4-Nb1 binding at the surface of HBP-ALL cells that correlated with the CD4 antibody signal and internalization of CD4-Nb1 in some cells (**Supplementary Figure 11C**). In contrast, no binding was observed upon administration of unrelated GFP-Nb (**Supplementary Figure 11D**). At 24 h post injection, we observed regions of strongly internalized CD4-Nb1 (**Supplementary Figures 11E, G**), but also regions showing a low residual CD4-Nb1 uptake (**Supplementary Figures 11E, H**).

The OI data from the xenograft model clearly indicates that the high-affinity CD4-Nb1 but not CD4-Nb4 is suitable to specifically visualize CD4$^+$ cells *in vivo* within a short period

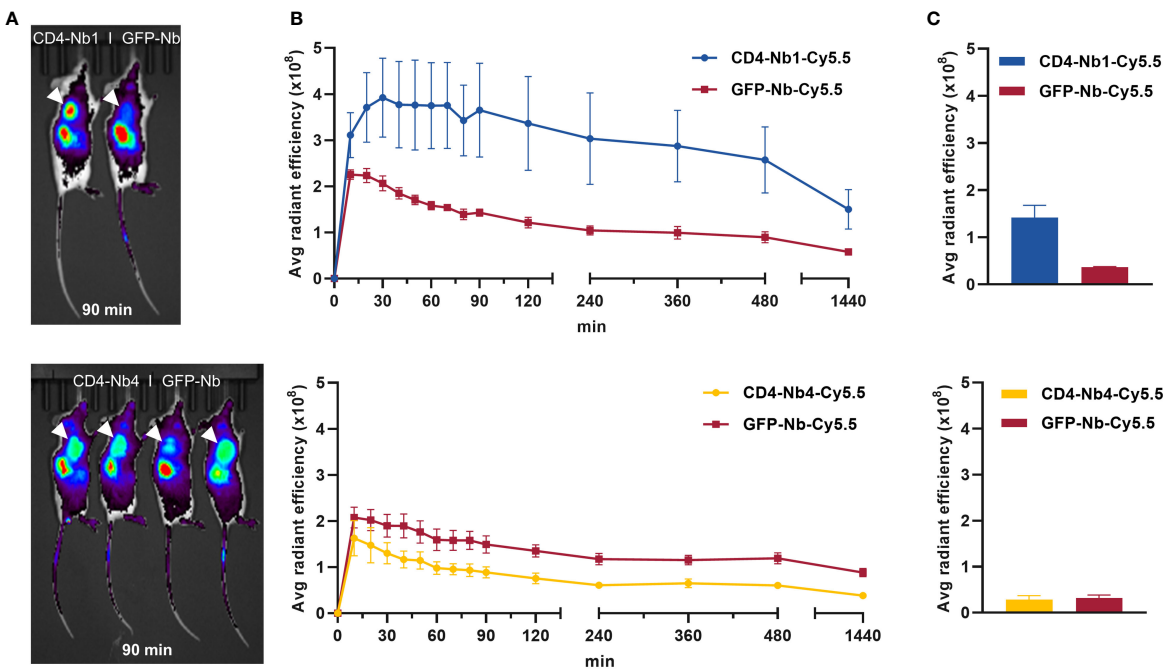

FIGURE 5 | *In vivo* optical imaging (OI) with CD4-Nbs-Cy5.5. Here, 5 µg of CD4-Nbs-Cy5.5 (top) or CD4-Nb4-Cy5.5 (bottom) or GFP-Nb-Cy5.5 (top and bottom) were administered intravenously (i.v.) to subcutaneously human CD4$^+$ HPB-ALL-bearing NSG mice, and tumor biodistribution was monitored by repetitive OI measurements over the course of 24h **(A)** Acquired images of each measurement time point of one representative mouse injected with CD4-Nbs-Cy5.5 (left) or GFP-Nb-Cy5.5 (right, ctrl). Red circles and white arrows indicate the tumor localization at the right upper flank. **(B)** Quantification of the fluorescence signal from the tumors (n = 4 per group, arithmetic mean of the average radiant efficiency ± SEM) determined at indicated time points. **(C)** After the last imaging time point, tumors were explanted for *ex vivo* OI, confirming increased accumulation of CD4-Nb1-Cy5.5 compared to the GFP-Nb-Cy5.5 (n = 2 per group, arithmetic mean ± SEM).

(30–120 min) after administration. Considering that this model does not reflect the natural distribution of $CD4^+$ T cells in an organism, we continued with a model that allowed us to visualize the physiological composition of $CD4^+$ immune cells. Thus, we employed a humanized CD4 murine knock-in model (hCD4KI) in which the extracellular fraction of the mouse CD4 antigen was replaced by the hCD4 while normal immunological function and T-cell distribution is restored (42).

^{64}Cu-CD4-Nb1 Specifically Accumulates in $CD4^+$ T Cell-Rich Organs

To generate immunoPET compatible tracers, CD4-Nb1 and GFP-Nb were labeled with the PET isotope ^{64}Cu using a copper-chelating BCN-NODAGA group added to our azide-coupled Nbs. Radiolabeling yielded high radiochemical purity (≥95%) and specific binding of ^{64}Cu-hCD4-Nb1 to CD4-expressing HBP-ALL cells (46.5% ± 5.6%) *in vitro* that was ~30 times higher than the non-specific binding to CD4-negative DHL cells or of the radiolabeled ^{64}Cu-GFP-Nb control (**Supplementary Figure 12A**).

Subsequently, we injected ^{64}Cu-CD4-Nb1 i.v. in hCD4KI and wt C57BL/6 mice and performed PET/MRI repetitively over 24 h. In two of the hCD4KI animals, we additionally followed tracer biodistribution over the first 90 min by dynamic PET (**Supplementary Figure 12B**). As expected for small-sized immunotracers, after an initial uptake peak within the first 10 min, ^{64}Cu-CD4-Nb1 is rapidly cleared from the blood, lung, and liver *via* renal elimination. In comparison to wild type, mice carrying the hCD4 antigen on T cells showed an increased tracer accumulation in lymph nodes, thymus, liver, and spleen (**Figure 6A**). In these organs, which are known to harbor high numbers of $CD4^+$ T cells (43), discrimination of $CD4^+$-specific signal from organ background was optimal 3 h post injection (**Figure 6B**). Here, lymph nodes yielded a ~3-fold, spleen a ~2.5-fold, and liver a ~1.4-fold higher ^{64}Cu-CD4-Nb1 accumulation in hCD4KI mice compared to wt littermates (**Figure 6B**). In contrast, we observed similar uptake levels for blood, muscle, lung, and kidney in both groups (**Supplementary Figure 12C**). Analyzing *ex vivo* biodistribution 24 h post tracer injection confirmed persistent accumulation of ^{64}Cu-CD4-Nb1 in lymph nodes and spleen of hCD4-expressing mice, although the limited number of animals per group did not allow statistical analysis (**Supplementary Figure 12D**). In summary, these results demonstrate that CD4-Nb1 is capable of visualizing and monitoring $CD4^+$ T cells in both optical and PET-based imaging.

DISCUSSION

Given the important role of CD4 as a marker for a variety of immune cells including monocytes, macrophages, dendritic cells, and $CD4^+$ T cells, detailed monitoring of this marker is proving to be extremely important for the diagnosis and concomitant therapeutic monitoring of a variety of diseases. Several mouse studies and early clinical trials have already indicated the value of noninvasive imaging of $CD4^+$ cells in rheumatoid arthritis (20), colitis (21), allogeneic stem cell transplantation (44), organ transplant rejection (45), acquired immunodeficiency disease (10), and in the context of cancer immunotherapies (46), using radiolabeled full-length antibodies or fragments thereof. However, biological activity, particularly $CD4^+$ T-cell depletion, and long-term systemic retention of full-length antibodies limit their development into clinically applied immunoprobes (20, 24, 47, 48).

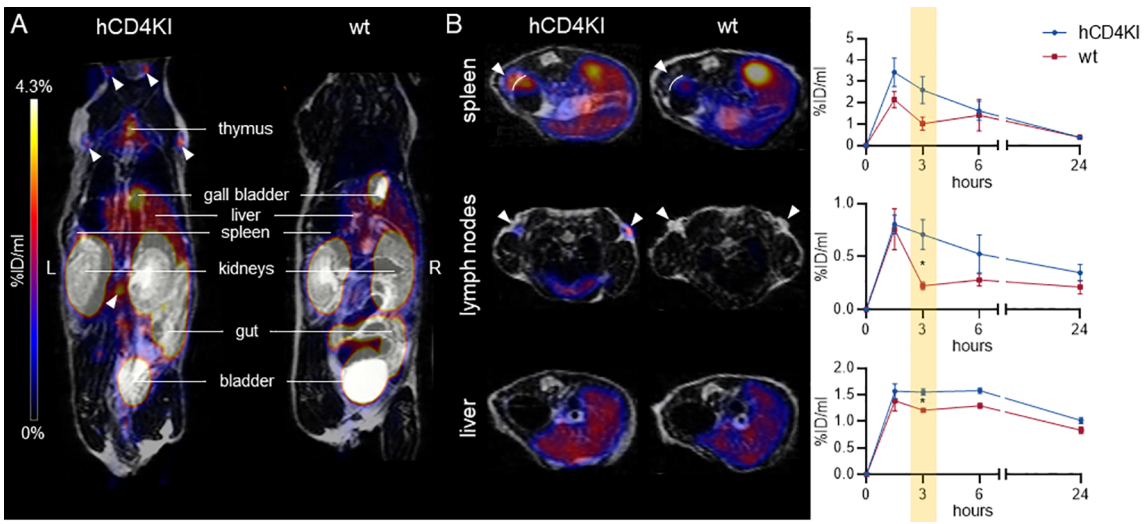

FIGURE 6 | ^{64}Cu-CD4-Nb1 specifically accumulates in $CD4^+$ T cell-rich organs. **(A)** Representative maximum intensity projection PET/MR images of human CD4 knock-in (hCD4KI) and wild-type (wt) C57BL/6 mice 3 h post intravenous (i.v.) injection of ^{64}Cu-CD4-Nb1. White arrows indicate localization of lymph nodes. **(B)** Exemplary transversal PET/MR images of spleen, lymph nodes, and liver (3 h post injection) and dynamic organ uptake quantification of ^{64}Cu-CD4-Nb1 over 24 h [n = 3 per group, arithmetic mean of the % injected dose per ml (%ID/ml) ± SEM, unpaired t-test of the 3-h time point, * $p < 0.05$]. White arrows indicate the target organ.

The aim of this study was to develop hCD4-specific Nbs as novel *in vivo* imaging probes to overcome the limitations of previous noninvasive imaging approaches. To identify binders that recognize the cellular exposed CD4, we employed two screening strategies where we selected Nbs either against adsorbed recombinant CD4 or against hCD4-expressing cells. Interestingly, both panning strategies proved successful, as demonstrated by the selection of two Nbs each that efficiently bind cell-resident CD4. Combining different biochemical analyses including epitope binning, cellular imaging, and HDX-MS, we were able to elucidate in detail the detected domains, as well as the three-dimensional epitopes addressed by the individual Nbs, and thus identified two candidates, CD4-Nb1 and CD4-Nb3, that can simultaneously bind to different segments within domain 1, while CD4-Nb2 has been shown to bind to domain 3 of CD4.

Notably, for most Nbs currently being developed for *in vivo* imaging purposes, detailed information about their epitopes is not available (49–55). There are only few examples such as the anti-HER2-specific Nb 2Rs15d, where the precise epitope was elucidated by complex crystallization (56) and that was successfully applied in a phase I study for clinical imaging (39). However, for CD4-specific Nbs, this knowledge is all the more important because epitope-specific targeting of $CD4^+$ T-cell functions has far-reaching implications. This is true especially for cancer treatment, as $CD4^+$ T cells have opposing effects on tumor growth and response to immunotherapies, crucially depending on the CD4 effector cell differentiation and tumor entity (57, 58). In this context, it was shown that domain 1 of CD4 mediates transient interaction of the CD4 receptor and the MHCII complex (59–61), while T-cell activation is abrogated when T-cell receptor (TCR) and CD4 colocalization is blocked *via* domain 3 (62). To further elucidate a possible impact on immunomodulation, we analyzed the effect of CD4-Nb1 and CD4-Nb4 targeting two different domains on $CD4^+$ Tcell proliferation and cytokine expression. Notably, neither CD4-Nb1 nor CD4-Nb4 affected the behavior of endogenous $CD4^+$ T-cells *in vitro* or induced increased cytokine levels in whole blood samples when employed at concentrations that are intended for molecular imaging purposes in patients. From these data, it can be concluded that these Nbs are mostly biologically inert and thus might be beneficial compared to full-length antibodies (24) or other antibody fragments such as the anti-CD4 Cys-diabody, which was recently reported to inhibit the proliferation of $CD4^+$ cells and IFN-γ production *in vitro* (26).

Following our initial intention to generate immune tracer for *in vivo* imaging, we performed a site-directed labeling approach employing C-terminal sortagging to conjugate an azide group, which can be universally used to attach a multitude of detectable moieties by straightforward DBCO-mediated click chemistry (49). For the fluorescent and radiolabeled CD4-Nb1, we observed rapid recruitment and sustained targeting of $CD4^+$ cells in a xenograft and hCD4 knock-in mouse model. Using a quantitative high-resolution PET/MR imaging approach, our radiolabeled ^{64}Cu-CD4-Nb1 allowed visualizing T cell-rich organs with high sensitivity. Beyond immune organs including lymph nodes, thymus, and spleen, we could detect enhanced CD4-Nb1 uptake in liver. At this point, we cannot distinguish whether this is due to the presence of $CD4^+$ cells or non-specific elimination occurring through this organ. Consequently, further experiments are needed to analyze whether CD4-Nbs lacking the Fc region are advantageous compared to larger antibody formats, which have a higher tendency to accumulate non-specifically in the spleen and liver due to Fcγ receptor-mediated uptake. However, to further modify serum retention times in order to improve specific tissue targeting, CD4-Nbs could easily be modified, as shown by the addition of an albumin-binding fragment (63) or PEGylation (49).

Considering the translation of the CD4-Nb1 for clinical imaging, additional aspects such as potential immunogenicity have to be assessed. Due to their high homology to the human type 3 VH domain, Nbs were described as weakly immunogenic in humans (64), and several strategies are available to humanize Nbs by exchanging a small number of aa residues in the framework regions (65). Moreover, a recent study of two Nbs in phase II clinical trials for PET imaging reported that very few patients developed low levels of anti-drug antibodies after prolonged administration of Nbs (66), indicating that monomeric Nbs present a low immunogenicity risk profile. In addition, long-term kidney retention of radiolabeled Nbs, mediated primarily by the endocytic receptor megalin (67), can cause undesirable nephrotoxicity and interfere with imaging of molecular targets near the kidneys. However, this can be overcome by targeted engineering of Nbs, e.g., removal of charged aa tags or simultaneous administration of positively charged components that interact with megalin receptors (68, 69). Of note, compared to other radiolabeled Nbs used for preclinical imaging of similar targets (49), CD4-Nb1 showed relatively low renal accumulation. However, as the molecular reasons for this are unclear at this stage, further studies are needed to gain deeper insight into this phenomenon.

In summary, this study demonstrates for the first time the generation and detailed characterization of Nbs specific for hCD4 and their comprehensive experimental evaluation *in vitro* and *in vivo*. In particular, CD4-Nb1 turned out as a promising candidate for a noninvasive whole-body study of $CD4^+$ cells in mice. Considering the increasing importance of advanced molecular imaging in clinical practice, we anticipate that this Nb-based immunotracer could become a highly versatile tool as a novel theranostic to accompany the clinical translation of emerging immunotherapies.

MATERIALS AND METHODS

Nanobody Library Generation

Alpaca immunization and Nb library construction were carried out as described previously (70, 71). Animal immunization has been approved by the government of Upper Bavaria (Permit number: 55.2-1-54-2532.0-80-14). In brief, an alpaca (*Vicugna pacos*) was immunized with the purified extracellular domains of

hCD4 (aa26-390) recombinantly produced in HEK293 cells (antibodies-online GmbH, Germany). After initial priming with 1 mg, the animal received six boost injections with 0.5 mg hCD4 each, every second week. Then, 87 days after initial immunization, ~100 ml of blood were collected and lymphocytes were isolated by Ficoll gradient centrifugation using Lymphocyte Separation Medium (PAA Laboratories GmbH). Total RNA was extracted using TRIzol (Life Technologies), and mRNA was transcribed into cDNA using the First-Strand cDNA Synthesis Kit (GE Healthcare). The Nb repertoire was isolated in three subsequent PCR reactions using the following primer combinations: 1) CALL001 and CALL002; 2) forward primer set FR1-1, FR1-2, FR1-3, FR1-4, and reverse primer CALL002; and 3) forward primer FR1-ext1 and FR1-ext2 and reverse primer set FR4-1, FR4-2, FR4-3, FR4-4, FR4-5, and FR4-6 introducing SfiI and NotI restriction sites. The Nb library was subcloned into the SfiI/NotI sites of the pHEN4 phagemid vector (72).

Nanobody Screening

For the selection of CD4-specific Nbs, two consecutive phage enrichment rounds were performed, both with immobilized recombinant antigen and CHO-hCD4 cells. *E. coli* TG1 cells comprising the hCD4-Nb library in pHEN4 were infected with the M13K07 helper phage to generate Nb-presenting phages. For each round, 1×10^{11} phages of the hCD4-Nb library were applied on immunotubes coated with hCD4 (10 µg/ml). In each selection round, extensive blocking of antigen and phages was performed with 5% milk or bovine serum albumin (BSA) in phosphate-buffered saline containing 0.05% (v/v) Tween 20 PBS-T, and with increasing panning rounds, PBS-T washing stringency was increased. Bound phages were eluted in 100 mM triethylamine (TEA; pH 10.0), followed by immediate neutralization with 1 M Tris/HCl pH 7.4. For cell-based panning, 2×10^6 CHO-hCD4 or HEK293-hCD4 cells were non-enzymatically detached using dissociation buffer (Gibco) and suspended in 5% fetal bovine serum (FBS) in PBS. Antigen-expressing cells were incubated with 1×10^{11} phages under constant mixing at 4°C for 3 h. Cells were washed 3× with 5% FBS in PBS. Cell lines were alternated between panning rounds. Phages were eluted with 75 mM citric acid buffer at pH 2.3 for 5 min. To deplete non-CD4-specific phages, eluted phages were incubated 3× with 1×10^7 wt cells. Exponentially growing *E. coli* TG1 cells were infected with eluted phages from both panning strategies and spread on selection plates for the following panning rounds. Antigen-specific enrichment for each round was monitored by counting colony-forming units (CFUs).

Whole-Cell Phage ELISA

Polystyrene Costar 96-well cell culture plates (Corning) were coated with poly-L-lysine (Sigma Aldrich) and washed once with H_2O. CHO-wt and CHO-hCD4 were plated at 2×10^4 cells per well in 100 µl and grown to confluency overnight. Next day, 70 µl of phage supernatant was added to the culture medium of each cell type and incubated at 4°C for 3 h. Cells were washed 5× with 5% FBS in PBS. M13-horseradish peroxidase (HRP)-labeled antibody (Progen) was added at a concentration of 0.5 ng/ml for 1 h, washed 3× with 5% FBS in PBS. One-Step Ultra TMB 32048 ELISA Substrate [Thermo Fisher Scientific (TFS)] was added and incubated until color change was visible, and the reaction was stopped by addition of 100 µl of 1 M H_2SO_4. Detection occurred at 450 nm at a Pherastar plate reader, and phage ELISA-positive clones were defined by a 2-fold signal above wt control cells.

Expression Constructs

The cDNA of hCD4 (UniProtKB-P01730) was amplified from hCD4-mOrange plasmid DNA (hCD4-mOrange was a gift from Sergi Padilla Parra; addgene plasmid #110192; http://n2t.net/addgene:110192; RRID : Addgene_110192) by PCR using forward primer hCD4 fwd and reverse primer hCD4 rev and introduced into BamHI and XhoI sites of a pcDNA3.1 vector variant [pcDNA3.1(+)IRES GFP, a gift from Kathleen_L Collins; addgene plasmid #51406; http://n2t.net/addgene:51406; RRID : Addgene_51406]. We replaced the neomycin resistance gene (NeoR) with the cDNA for Blasticidin S deaminase (bsd), amplified with forward primer bsd fwd and reverse primer bsd rev, by integration into the XmaI and BssHII sites of the vector. CD4 domain deletion mutants were generated using the Q5 Site-Directed Mutagenesis Kit (NEB) according to the manufacturer's protocol. For mutants lacking domain 1 of hCD4, we introduced an N-terminal BC2-tag (35). For the generation of plasmid pcDNA3.1_CD4_ΔD1_IRES-eGFP, we used forward primer ΔD1 fwd and reverse primer ΔD1 rev; for pcDNA3.1_CD4_ΔD1ΔD2_IRES-eGFP, forward primer ΔD1ΔD2 fwd and reverse primer ΔD1ΔD2 rev; for pcDNA3.1_CD4_ΔD3ΔD4_IRES-EGFP, forward primer ΔD3ΔD4 fwd and reverse primer ΔD3ΔD4 rev. For bacterial expression of Nbs, sequences were cloned into the pHEN6 vector (73), thereby adding a C-terminal sortase tag LPETG followed by 6× His-tag for IMAC purification as described previously (34). For protein production of the extracellular domains 1-4 of hCD4 in Expi293 cells, corresponding cDNA was amplified from plasmid DNA containing full-length hCD4 cDNA (addgene plasmid #110192) using forward primer CD4-D1-4 f and reverse primer CD4-D1-4 r. A 6× His tag was introduced by the reverse primer. Esp3I and EcoRI restriction sites were used to introduce the cDNA into a pcDNA3.4 expression vector with the signal peptide MGWTLVFLFLLSVTAGVHS from the antibody JF5 (74).

Cell Culture, Transfection, Stable Cell Line Generation

HEK293T and CHO-K1 cells were obtained from ATCC (CCL-61, LGC Standards GmbH, Germany). As this study does not include cell line-specific analysis, cells were used without additional authentication. Cells were cultivated according to standard protocols. Briefly, growth media containing Dulbecco's modified Eagle's medium (DMEM) (HEK293) or DMEM/F12 (CHO) [both high glucose, pyruvate (TFS)] supplemented with 10% (v/v) FBS, L-glutamine, and penicillin/streptomycin (P/S; all from TFS) were used for cultivation. Cells were passaged using 0.05% trypsin-EDTA (TFS) and were cultivated at 37°C and 5% CO_2 atmosphere in a humidified chamber. Plasmid DNA was transfected using Lipofectamine

2000 (TFS) according to the manufacturer's protocol. For the generation of the stable HEK293-hCD4 and CHO-hCD4 cell line, 24 h post transfection, cells were subjected to a 2-week selection period using 5 µg/ml Blasticidin S (Sigma Aldrich) followed by single cell separation. Individual clones were analyzed by live-cell fluorescence microscopy regarding their level and uniformity of GFP and CD4 expression.

Protein Expression and Purification

CD4-specific Nbs were expressed and purified as previously published (71, 75). Extracellular fragment of hCD4 comprising domains 1–4 of hCD4 and a C-terminal His6-tag was expressed in Expi293 cells according to the manufacturer's protocol (TFS). Cell supernatant was harvested by centrifugation 4 days after transfection, sterile filtered and purified according to previously described protocols (76). For quality control, all purified proteins were analyzed *via* sodium dodecyl sulfate-polyacrylamide gel electrophoresis (SDS-PAGE) according to standard procedures. Therefore, protein samples were denaturized (5 min, 95°C) in 2× SDS sample buffer containing 60 mM Tris/HCl, pH 6.8; 2% (w/v) SDS; 5% (v/v) 2-mercaptoethanol, 10% (v/v) glycerol, 0.02% bromphenole blue. All proteins were visualized by InstantBlue Coomassie (Expedeon) staining. For immunoblotting, proteins were transferred to a nitrocellulose membrane (Bio-Rad Laboratories) and detection was performed using anti-His primary antibody (Penta-His Antibody, #34660, Qiagen) followed by donkey anti-mouse secondary antibody labeled with Alexa Fluor 647 (Invitrogen) using a Typhoon Trio scanner (GE Healthcare, excitation 633 nm, emission filter settings 670 nm BP 30).

Live-Cell Immunofluorescence

CHO-hCD4 and CHO wt cells transiently expressing CD4 domain-deletion mutants were plated at ~10,000 cells per well of a µClear 96-well plate (Greiner Bio One, cat. #655090) and cultivated at standard conditions. Next day, medium was replaced by live-cell visualization medium DMEMgfp-2 (Evrogen, cat. #MC102) supplemented with 10% FBS, 2 mM L-glutamine, 2 µg/ml Hoechst 33258 (Sigma Aldrich) for nuclear staining and fluorescently labeled or unlabeled CD4-Nbs at concentrations between 1 and 100 nM. Unlabeled CD4-Nbs were visualized by addition of 2.5 µg/ml anti-VHH secondary Cy5 AffiniPure Goat Anti-Alpaca IgG (Jackson ImmunoResearch). Images were acquired with a MetaXpress Micro XL system (Molecular Devices) at ×20 or ×40 magnification.

Biolayer Interferometry

To determine the binding affinity of purified Nbs to recombinant hCD4, biolayer interferometry (BLItz, ForteBio) was performed. First, CD4 was biotinylated by 3-fold molar excess of biotin-N-hydroxysuccinimide ester. CD4 was then immobilized at single-use streptavidin biosensors (SA) according to manufacturer's protocols. For each Nb, we executed four association/dissociation runs with concentrations appropriate for the affinities of the respective Nbs (overall between 15.6 nM and 1 µM). As a reference run, PBS was used instead of Nb in the association step. As a negative control, the GFP-Nb (500 nM) was applied in the binding studies. Recorded sensograms were analyzed using the BLItzPro software, and dissociation constants (K_D) were calculated based on global fits. For the epitope competition analysis, two consecutive application steps were performed, with a short dissociation period of 30 s after the first association.

Peripheral Blood Mononuclear Cell Isolation, Freezing, and Thawing

Fresh blood, buffy coats, or mononuclear blood cell concentrates were obtained from healthy volunteers at the Department of Immunology or from the ZKT Tübingen gGmbH. Participants gave informed consent, and the studies were approved by the ethical review committee of the University of Tübingen, projects 156/2012B01 and 713/2018BO2. Blood products were diluted with PBS 1× (homemade from 10× stock solution, Lonza, Switzerland), and PBMCs were isolated by density gradient centrifugation with Biocoll separation solution (Biochrom, Germany). PBMCs were washed twice with PBS 1×, counted with an NC-250 cell counter (Chemometec, Denmark), and resuspended in heat-inactivated (h.i.) FBS (Capricorn Scientific, Germany) containing 10% dimethyl sulfoxide (DMSO; Merck). Cells were immediately transferred into a -80°C freezer in a freezing container (Mr. Frosty; TFS). After at least 24 h, frozen cells were transferred into a liquid nitrogen tank and were kept frozen until use. For the experiments, cells were thawed in Iscove´s Modified Dulbecco´s Medium (IMDM) (+L-Glutamin + 25 mM HEPES; Life Technologies) supplemented with 2.5% h.i. human serum (HS; PanBiotech, Germany), 1× P/S (Sigma-Aldrich), and 50 µm β-mercaptoethanol (β-ME; Merck), washed once, counted, and used for downstream assays.

Affinity Determination by Flow Cytometry

For cell-based affinity determination, HEK293-hCD4 cells were detached using enzyme-free cell dissociation buffer (Gibco) and resuspended in FACS buffer (PBS containing 5% FBS). For each staining condition, 200,000 cells were incubated with suitable dilution series of CD4-Nbs at 4°C for 30 min. Cells were washed two times, and for detection of Cy5 AffiniPure Goat Anti-Alpaca IgG, VHH domain (Jackson ImmunoResearch) was applied for 15 min. PBMCs (Department of Immunology/ZKT Tübingen gGmbH, Germany) were freshly thawed and resuspended in FACS buffer. For each sample, 200,000 cells were incubated with suitable concentrations of CD4-Nbs coupled to CF568 in combination with 1:500 dilution of anti-CD3-FITC (BD Biosciences) at 4°C for 30 min. For control staining, PE/Cy5-labeled anti-hCD4 antibody (RPA-T4, BioLegend) was used. After two washing steps, samples were resuspended in 200 µl FACS buffer and analyzed with a BD FACSMelody Cell Sorter. Final data analysis was performed *via* FlowJo10® software (BD Biosciences).

Sortase Labeling of Nanobodies

Sortase A pentamutant (eSrtA) in pET29 was a gift from David Liu (Addgene plasmid # 75144) and was expressed and purified as described (77). CF568-coupled peptide H-Gly-Gly-Gly-Doa-

Lys-NH_2 (sortase substrate) was custom-synthesized by Intavis AG. For the click chemistry, a peptide H-Gly-Gly-Gly-propyl-azide was synthesized. In brief, for sortase coupling 50 µM Nb, 250 µM sortase peptide dissolved in sortase buffer (50 mM Tris, pH 7.5, and 150 mM NaCl) and 10 µM sortase were mixed in coupling buffer (sortase buffer with 10 mM $CaCl_2$) and incubated for 4 h at 4°C. Uncoupled Nb and sortase were depleted by IMAC. Unbound excess of unreacted sortase peptide was removed using Zeba Spin Desalting Columns (TFS, cat. #89890). Azide-coupled Nbs were labeled by strain-promoted azide-alkyne cycloaddition (SPAAC) click chemistry reaction with 2-fold molar excess of DBCO-Cy5.5 (Jena Bioscience) for 2 h at 25°C. Excess DBCO-Cy5.5 was subsequently removed by dialysis (GeBAflex-tube, 6-8 kDa, Scienova). Finally, to remove untagged Nb (side product of the sortase reaction), we used hydrophobic interaction chromatography (HIC; HiTrap Butyl-S FF, Cytiva). Binding of DBCO-Cy5.5-coupled Nb occurred in 50 mM H_2NaPO_4, 1.5 M $(NH4)_2SO_4$, pH7.2. Elution took place with 50 mM H_2NaPO_4, pH 7.2. Dye-labeled protein fractions were analyzed by SDS-PAGE followed by fluorescent scanning on a Typhoon Trio (GE-Healthcare; CF568: excitation 532 nm, emission filter settings 580 nm BP 30; Cy5.5: excitation 633 nm, emission filter settings 670 nm BP 30; 546) and subsequent Coomassie staining. Identity and purity of final products were determined by liquid chromatography-mass spectrometry (LC-MS) (CD4-Nbs-CF568, >60%; CD4-Nb1-Cy5.5, ~94%; CD4-Nb4-Cy5.5, ~99%; GBP-Cy5.5, ~94%; CD4-Nb1-3, ~99%; bivGFP-Nb, ~99%).

Hydrogen–Deuterium Exchange

CD4 Deuteration Kinetics and Epitope Elucidation

On the basis of the affinity constants of 5.1 nM (CD4-Nb1), 6.5 nM (CD4-Nb2), and 75.3 nM (CD4-Nb3) (predetermined by BLI analysis), the molar ratio of antigen to Nb was calculated, ensuring 90% complex formation according to Kochert et al. (78). CD4 (5 µl, 65.5 µM) was preincubated with CD4-specific Nbs (5 µl; 60.3, 67.4, and 143.1 µM for Nb1, Nb2, and Nb3, respectively) for 10 min at 25°C. Deuteration samples containing CD4 only were preincubated with PBS instead of the Nbs. HDX of the preincubated samples was initiated by 1:10 dilution with PBS (pH 7.4) prepared with D_2O, leading to a final concentration of 90% D_2O. After 5- and 50-min incubation at 25°C, aliquots of 20 µl were taken and quenched by adding 20 µl ice-cold quenching solution (0.2 M TCEP with 1.5% formic acid and 4 M guanidine HCl in 100 mM ammonium formate solution pH 2.2), resulting in a final pH of 2.5. Quenched samples were immediately snap-frozen.

Immobilized pepsin (TFS) was prepared using 60 µl of 50% slurry (in ammonium formate solution pH 2.5) that was then centrifuged (1,000 × g for 3 min at 0°C). The supernatant was discarded. Prior to each analysis, samples were thawed and added to the pepsin beads. After digestion for 2 min in a water ice bath, samples were separated from the beads by centrifugation at 1,000 × g for 30 s at 0°C using a 0.22-µm filter (Merck, Millipore) and immediately analyzed by LC-MS. Undeuterated control samples for each complex and CD4 alone were prepared under the same conditions using H_2O instead of D_2O. Additionally, each Nb was digested without addition of CD4 to generate a list of peptic peptides deriving from the Nb. The HDX experiments of the CD4-Nb complexes were performed in triplicate. The back-exchange of the method as determined using a standard peptide mixture of 14 synthetic peptides was 24%.

Chromatography and Mass Spectrometry

HDX samples were analyzed as described previously (75).

HDX Data Analysis

A peptic peptide list was generated in a preliminary LC-MS/MS experiment as described previously (75). For data-based search, no enzyme selectivity was applied; furthermore, identified peptides were manually evaluated to exclude peptides originated through cleavage after arginine, histidine, lysine, proline, and the residue after proline (79). Additionally, a separate list of peptides for each Nb was generated, and peptides overlapping in mass, retention time, and charge with the antigen digest were manually removed. Analysis of the deuterated samples was performed in MS mode only, and HDExaminer v2.5.0 (Sierra Analytics, USA) was used to calculate the deuterium uptake (centroid mass shift). HDX could be determined for peptides covering 87%–88% of the CD4 sequence (**Supplementary Figure 11**). The calculated percentages of deuterium uptake of each peptide between CD4-Nb and CD4-only were compared. Any peptide with uptake reduction of 5% or greater upon Nb binding was considered protected. All relevant HDX parameters are shown in **Supplementary Table S3** as recommended (80).

Endotoxin Determination and Removal

The concentration of bacterial endotoxins was determined with Pierce LAL Chromogenic Endotoxin Quantitation Kit (TFS), and removal occurred using EndoTrap HD 1 ml (Lionex) according to the manufacturer's protocols.

Synthetic Peptides

The following human leukocyte antigen (HLA)-class II peptides were used for the stimulations: MHCII pool (HCMVA pp65 aa 109-123 MSIYVYALPLKMLNI, HCMV pp65 aa 366-382 HPTFTSQYRIQGKLEYR, EBVB9 EBNA2 aa 276-290 PRSPTVFYNIPPMPL, EBVB9 EBNA1 aa 514-527 KTSLYNLRRGTALA, EBV BXLF2 aa 126-140 LEKQLFYYIGTMLPNTRPHS, EBV BRLF1 aa 119-133 DRFFIQAPSNRVMIP, EBVB9 EBNA3 aa 381-395 PIFIRRLHRLLLMRA, EBVB9 GP350 aa 167-181 STNITAVVRAQGLDV, IABAN HEMA aa 306-318 PKYVKQNTLKLAT) or CMVpp65 aa 510-524 YQEFFWDANDIYRIF. All peptides were synthesized and dissolved in water 10% DMSO as previously described (purity ≥80%) and were kindly provided by S. Stevanović (81).

Stimulation and Cultivation of Peripheral Blood Mononuclear Cells

PBMCs from donors previously screened for *ex vivo* $CD4^+$ T-cell reactivities against MHCII peptides were thawed and rested in T-cell medium (TCM; IMDM + 1× P/S + 50 µM β-ME + 10% h.i.

HS) containing 1 µg/ml DNase I (Sigma-Aldrich) at a concentration of 2–3 × 10^6 cells/ml for 3 h at 37°C and 7.5% CO_2. After resting, cells were washed once and counted, and up to 1 × 10^8 cells were labeled with 1.5–2 µM carboxyfluorescein succinimidyl ester (CFSE; BioLegend, USA) in 1 ml PBS 1× for 20 min according to the manufacturer's protocol. The cells were washed twice in medium containing 10% FBS after CFSE labeling and incubated with 5, 0.5, or 0.05 µM of CD4-Nb1, CD4-Nb4, or a control Nb for 1 h at 37°C in serum-free IMDM medium. Concentrations and duration were chosen to mimic the expected approximate concentration and serum retention time during clinical application. After incubation, cells were washed twice and counted, and each condition was separated into three parts and seeded in a 48-well cell culture plate (1.6–2.5 × 10^6 cells/well in triplicate). Cells were stimulated with either 10 µg/ml PHA-L (Sigma-Aldrich) or 5 µg/ml MHCII peptide(s) or left unstimulated and cultured at 37°C and 7.5% CO_2. Then, 2 ng/ml recombinant human IL-2 (R&D, USA) were added on days 3, 5, and 7. One-third of the culture on day 4, one half of the culture on days 6 and 8, and the remaining cells on day 12 were harvested, counted, and stained for flow cytometry analyses. For donor 1, the proliferation/activation status and cytokine production were analyzed in two different experiments, whereas for donors 2 and 3, cells from a single experiment were used for the three assays.

Assessment of T-Cell Proliferation and Activation

Cells from days 4, 6, and 8 were transferred into a 96-well round-bottom plate and washed twice with FACS buffer [PBS + 0.02% sodium azide (Roth, Germany) + 2 mM EDTA (Sigma-Aldrich) + 2% h.i. FBS]. Extracellular staining was performed with CD4 APC-Cy7 (RPA-T4; BD Biosciences), CD8 BV605 (RPA-T8; BioLegend), the dead cell marker Zombie Aqua (BioLegend), CD25 PE-Cy7 (BC96; BioLegend), CD69 PE (FN50; BD Biosciences) and incubated for 20 min at 4°C. All antibodies were used at pretested optimal concentrations. Cells were washed twice with FACS buffer. Approximately 500,000 cells were acquired on the same day using an LSRFortessaTM SORP (BD Biosciences, USA) equipped with the DIVA Software (Version 6, BD Biosciences, USA). The percentage of proliferating $CD4^+$ cells was determined by assessment of CFSE-negative cells and activation by the percentage of $CD69^+$ or $CD25^+$.

Assessment of T-Cell Function by Intracellular Cytokine Staining

On day 12, the MHCII peptide(s)-stimulated and cultured cells were transferred into a 96-well round-bottom plate (0.5–1 × 10^6 cells/well) and restimulated using 10 µg/ml of the same peptide (s), 10 µg/ml staphylococcal enterotoxin B (SEB; Sigma-Aldrich; positive control), or 10% DMSO (negative control). Protein transport inhibitors brefeldin A (10 µg/ml; Sigma-Aldrich) and Golgi Stop (BD Biosciences) were added at the same time as the stimuli. After 14-h stimulation at 37°C and 7.5% CO_2, cells were stained extracellularly with the fluorescently labeled antibodies CD4 APC-Cy7, CD8 BV605, and Zombie Aqua and incubated for 20 min at 4°C. Afterward, cells were washed once, fixed, and permeabilized using the BD Cytofix/Cytoperm solution (BD Biosciences) according to the manufacturer's instructions; stained intracellularly with TNF Pacific Blue (Mab11), IL-2 PE-Cy7 (MQ1-17H12), IFN-γ Alexa Fluor 700 (4S.B7), and CD154 APC (2431) antibodies (all BioLegend) (82); and washed twice. Approximately 500,000 cells were acquired on the same day using an LSRFortessaTM SORP (BD Biosciences, USA) equipped with the DIVA Software (Version 6; BD Biosciences). All flow cytometry analyses were performed with FlowJo version 10.6.2; gating strategies are shown in **Supplementary Figure 6**. Statistical analyses were performed with GraphPad Prism version 9.0.0.

Full Blood Stimulation and Cytokine Release Assay

Here, 100 µl of lithium-heparin blood was incubated for 1 h at 37°C and 7.5% CO_2. The blood was stimulated with 5 µM Nb (CD4-Nb1, CD4-Nb4, or control Nb), 100 ng/ml LPS (Invivogen, USA), or 2 µg/ml PHA-L in a final volume of 250 µl (serum-free IMDM medium) or left unstimulated for 24 h at 37°C and 7.5% CO_2. After two centrifugations, supernatant was collected without transferring erythrocytes. The supernatants were frozen at -80°C until cytokine measurements. Levels of IL-1β, IL-1Ra, IL-4, IL-6, IL-8, IL-10, IL-12p70, IL-13, granulocyte-macrophage colony-stimulating factor (GM-CSF), IFN-γ, macrophage chemotactic protein (MCP)-1, macrophage inflammatory protein (MIP)-1β, TNFα, and vascular endothelial growth factor (VEGF) were determined using a set of in-house-developed Luminex-based sandwich immunoassays each consisting of commercially available capture and detection antibodies and calibrator proteins. All assays were thoroughly validated ahead of the study with respect to accuracy, precision, parallelism, robustness, specificity, and sensitivity (83, 84). Samples were diluted at least 1:4 or higher. After incubation of the prediluted samples or calibrator protein with the capture coated microspheres, beads were washed and incubated with biotinylated detection antibodies. Streptavidin-phycoerythrin was added after an additional washing step for visualization. For control purposes, calibrators and quality control samples were included on each microtiter plate. All measurements were performed on a Luminex FlexMap® 3D analyzer system using Luminex xPONENT® 4.2 software (Luminex, USA). For data analysis, MasterPlex QT, version 5.0, was employed. Standard curve and quality control samples were evaluated according to internal criteria adapted to the Westgard Rules (85) to ensure proper assay performance.

Analysis of Cross-Species Reactivity Binding to Mouse $CD4^+$ Cells by Flow Cytometry

Murine $CD4^+$ cells were isolated from spleen and lymph nodes of C57BL/6N mice by positive selection over CD4 magnetic microbeads (Miltenyi Biotech, Germany). Human $CD4^+$ cells were extracted from blood using StraightFrom® Whole Blood CD4 MicroBeads (Miltenyi Biotech). Single-cell suspensions were incubated with 0.75 µg/ml of CD4-Nbs-Cy5.5 (~47–60

nM) or GFP-Nb-Cy5.5 (~51 nM) in 1% FPS/PBS at 4°C for 20 min and subsequently analyzed on an LSR-II cytometer (BD Biosciences).

Optical Imaging of CD4-Expressing HPB-ALL Tumors

Human T-cell leukemia HPB-ALL cells (German Collection of Microorganisms and Cell Cultures GmbH, DSMZ, Braunschweig, Germany) were cultured in RPMI-1640 supplemented with 10% FBS and 1% P/S. Here, 10^7 HPB-ALL cells were injected subcutaneously in the right upper flank of 7-week-old NSG (NOD.Cg-*Prkdc*^{scid} *Il2rg*^{tm1WjI}/SzJ; Charles River Laboratories, Sulzfeld, Germany) mice, and tumor growth was monitored for 2–3 weeks. When tumors reached a diameter of ~7 mm, 5 µg of CD4-Nbs-Cy5.5 or control Nb (GFP-Nb-Cy5.5) were administered into the tail vein of two mice each. Optical imaging (OI) was performed repetitively in short-term isoflurane anesthesia over a period of 24 h using the IVIS Spectrum *In Vivo* Imaging System (PerkinElmer, Waltham, MA, USA). Four days after the first Nb administration, the CD4-Nbs-Cy5.5 groups received the GFP-Nb-Cy5.5 (and *vice versa*), and tumor biodistribution was analyzed identically by OI over 24 h. After the last imaging time point, animals were sacrificed and tumors were explanted for *ex vivo* OI analysis. Data were analyzed with Living Image 4.4 software (PerkinElmer). The fluorescence intensities were quantified by drawing regions of interest around the tumor borders and were expressed as average radiant efficiency (photons/s)/(µW/cm^2) subtracted by the background fluorescence signal before Nb injection to eliminate potential residual signal from the previous Nb application. All mouse experiments were performed according to the German Animal Protection Law and were approved by the local authorities (Regierungspräsidium Tübingen).

Immunofluorescence Staining of Explanted Xenograft Tumors

Freshly frozen 5-µm sections of hCD4-Nb1-Cy5.5-containing mouse tumors were analyzed using an LSM 800 laser scanning microscope (Zeiss). Afterward, the sections were fixed with perjodate-lysine-paraformaldehyde, blocked using donkey serum, and stained with primary rabbit-anti-CD4 antibody (Cell Marque, USA). Bound antibody was visualized using donkey-anti-rabbit-Cy3 secondary antibody (Dianova, Germany). YO-PRO-1 (Invitrogen, USA) was used for nuclear staining. Acquired images of the same areas were manually overlaid.

Radiolabeling With NODAGA and ^{64}Cu

All procedures for conjugation and radiolabeling with ^{64}Cu were performed using metal-free equipment and Chelex 100 (Sigma-Aldrich) pretreated buffers. Azide-modified Nbs (100 µg) were treated with 4 µl of 5 mM EDTA in 250 mM sodium acetate buffer (pH 6) for 30 min at room temperature (RT). The protein was reacted with 15 molar equivalents of BCN-NODAGA (CheMatech, Dijon, France) in 250 mM sodium acetate pH 6 for 30 min at RT followed by incubation at 4°C for 18 h. Excess of chelator was removed by ultrafiltration (Amicon Ultra 0.5 ml, 3 kDa MWCO, Merck Millipore) using the same buffer. [^{64}Cu]$CuCl_2$ (150 MBq in 0.1 M HCl) was neutralized by addition of 1.5 volumes of 0.5 M ammonium acetate solution (pH 6), resulting in a pH of 5.5. To this solution, 50 µg of conjugate was added and incubated at 42°C for 60 min. Then, 1 µl of 20% diethylenetriaminepentaacetic acid (DTPA) solution was added to quench the labeling reaction. Complete incorporation of the radioisotope was confirmed after each radiosynthesis by thin-layer chromatography (iTLC-SA; Agilent Technologies; mobile phase 0.1 M citric acid pH 5) and high-performance size exclusion chromatography (HPSEC; BioSep SEC-s2000, 300 × 7.8 mm, Phenomenex; mobile phase DPBS with 0.5 mM EDTA). All radiolabeled preparations used for *in vivo* PET imaging had radiochemical purities of ≥97% (iTLC) and ≥94% (HPSEC).

In Vitro Radioimmunoassay

Here, 10^7 HPB-ALL or DHL cells were incubated in triplicate with 1 ng (3 MBq/µg) of radiolabeled ^{64}Cu-CD4-Nb1 or ^{64}Cu-GFP-Nb for 1 h at 37°C and washed twice with PBS/2% FCS. The remaining cell-bound radioactivity was measured using a Wizard² 2480 gamma counter (PerkinElmer Inc., Waltham, MA, USA) and quantified as percentage of total added activity.

PET/MRI

Human CD4 knock-in (hCD4KI, genOway, Lyon, France) and wt C57BL/6J mice (Charles River) were injected intravenously with 5 µg (~15 MBq) of ^{64}Cu-CD4-Nb1. During the scans, mice were anesthetized with 1.5% isoflurane in 100% oxygen and warmed by water-filled heating mats. Ten-minute static PET scans were performed after 1.5, 3, 6, and 24 h in a dedicated small-animal Inveon microPET scanner (Siemens Healthineers, Knoxville, TN, USA; acquisition time: 600 s). For anatomical information, sequential T2 TurboRARE MR images were acquired immediately after the PET scans on a small animal 7 T ClinScan magnetic resonance scanner (Bruker BioSpin GmbH, Rheinstetten, Germany). Dynamic PET data of the first 90 min post injection were gained in two mice and divided into 10-min frames. After attenuation correction by a cobalt-57 point source, PET images were reconstructed using an ordered subset expectation maximization (OSEM3D) algorithm and analyzed with Inveon Research Workplace (Siemens Preclinical Solutions). The volumes of interest of each organ were drawn based on the anatomical MRI to acquire corresponding PET tracer uptake. The resulting values were decay-corrected and presented as percentage of injected dose per volume (%ID/ml). *Ex vivo* γ-counting was conducted after the last imaging time point by measuring the weight and radioactivity of each organ. For quantification, standardized aliquots of the injected radiotracer were added to the measurement.

Analyses and Statistics

Data analysis of the flow cytometry data was performed with the FlowJo Software Version 10.6.2 (FlowJo LLT, USA), and graph preparation and statistical analysis were performed using the GraphPad Prism Software (Version 8.3.0 or higher).

DATA AVAILABILITY STATEMENT

The original contributions presented in the study are included in the article/**Supplementary Material**. Further inquiries can be directed to the corresponding author.

ETHICS STATEMENT

The animal study was reviewed and approved by Regierungspräsidium Tübingen Konrad-Adenauer-Straße 20 72072 Tübingen.

AUTHOR CONTRIBUTIONS

BT, MK, DSo, BP, and UR designed the study. SN and AS immunized the animal. PK, SH, and YP performed Nb selection. PK, BT, MW, TW, and AM performed biochemical characterization and functionalization of Nbs. MG and AZ performed HDX-MS analysis. AZ and MG performed HDX-MS experiments. JR, CG, MJ, and NS-M analyzed the Nb effects on T-cell proliferation and cytokine expression. DSe, AM, and SP radiolabeled the Nbs. SP and DSo performed *in vivo* imaging. MS performed staining of xenograft cryosections. BT, JR, CG, MK, BP, DSo, and UR drafted the article. MK, BP, and UR supervised the study. All authors contributed to the article and approved the submitted version.

FUNDING

This work received financial support from the State Ministry of Baden-Wuerttemberg for Economic Affairs, Labour and Tourism (Grant: Predictive diagnostics of immune-associated diseases for personalized medicine. FKZ: 35-4223.10/8). We acknowlegde support by Open Access Publishing Fund of University of Tuebingen.

ACKNOWLEDGMENTS

The authors thank Sandra Maier and Ulrich Kratzer (both Natural and Medical Sciences Institute) for technical support with MS analyses and Birgit Fehrenbacher (Department of Dermatology, University of Tuebingen) for technical support with imaging of xenograft cryosections.

SUPPLEMENTARY MATERIAL

The Supplementary Material for this article can be found online at: https://www.frontiersin.org/articles/10.3389/fimmu.2021.799910/full#supplementary-material

REFERENCES

1. Delhalle S, Bode SFN, Balling R, Ollert M, He FQ. A Roadmap Towards Personalized Immunology. *NPJ Syst Biol Appl* (2018) 4:9. doi: 10.1038/s41540-017-0045-9
2. Rossi JF, Ceballos P, Lu ZY. Immune Precision Medicine for Cancer: A Novel Insight Based on the Efficiency of Immune Effector Cells. *Cancer Commun (Lond)* (2019) 39(1):34. doi: 10.1186/s40880-019-0379-3
3. Scheuenpflug J. Precision Medicine in Oncology and Immuno-Oncology: Where We Stand and Where We're Headed. *BioMed Hub* (2017) 2(Suppl 1):79–86. doi: 10.1159/000481878
4. Collman R, Godfrey B, Cutilli J, Rhodes A, Hassan NF, Sweet R, et al. Macrophage-Tropic Strains of Human Immunodeficiency Virus Type 1 Utilize the CD4 Receptor. *J Virol* (1990) 64(9):4468–76. doi: 10.1128/JVI.64.9.4468-4476.1990
5. Claeys E, Vermeire K. The CD4 Receptor: An Indispensable Protein in T Cell Activation and A Promising Target for Immunosuppression. *Arch Microbiol Immunol* (2019) 3(3):133–50. doi: 10.26502/ami.93650036
6. Chitnis T. The Role of CD4 T Cells in the Pathogenesis of Multiple Sclerosis. *Int Rev Neurobiol* (2007) 79:43–72. doi: 10.1016/S0074-7742(07)79003-7
7. Goverman J. Autoimmune T Cell Responses in the Central Nervous System. *Nat Rev Immunol* (2009) 9(6):393–407. doi: 10.1038/nri2550
8. Becker W, Emmrich F, Horneff G, Burmester G, Seiler F, Schwarz A, et al. Imaging Rheumatoid Arthritis Specifically With Technetium 99m CD4-Specific (T-Helper Lymphocytes) Antibodies. *Eur J Nucl Med* (1990) 17(3-4):156–9. doi: 10.1007/BF00811445
9. Borst J, Ahrends T, Babala N, Melief CJM, Kastenmuller W. CD4(+) T Cell Help in Cancer Immunology and Immunotherapy. *Nat Rev Immunol* (2018) 18(10):635–47. doi: 10.1038/s41577-018-0044-0
10. Di Mascio M, Paik CH, Carrasquillo JA, Maeng JS, Jang BS, Shin IS, et al. Noninvasive *In Vivo* Imaging of CD4 Cells in Simian-Human Immunodeficiency Virus (SHIV)-Infected Nonhuman Primates. *Blood* (2009) 114(2):328–37. doi: 10.1182/blood-2008-12-192203
11. Byrareddy SN, Arthos J, Cicala C, Villinger F, Ortiz KT, Little D, et al. Sustained Virologic Control in SIV+ Macaques After Antiretroviral and Alpha4beta7 Antibody Therapy. *Science* (2016) 354(6309):197–202. doi: 10.1126/science.aag1276
12. Aubert RD, Kamphorst AO, Sarkar S, Vezys V, Ha SJ, Barber DL, et al. Antigen-Specific CD4 T-Cell Help Rescues Exhausted CD8 T Cells During Chronic Viral Infection. *Proc Natl Acad Sci USA* (2011) 108(52):21182–7. doi: 10.1073/pnas.1118450109
13. Penaloza-MacMaster P, Barber DL, Wherry EJ, Provine NM, Teigler JE, Parenteau L, et al. Vaccine-Elicited CD4 T Cells Induce Immunopathology After Chronic LCMV Infection. *Science* (2015) 347(6219):278–82. doi: 10.1126/science.aaa2148
14. Mousset CM, Hobo W, Woestenenk R, Preijers F, Dolstra H, van der Waart AB. Comprehensive Phenotyping of T Cells Using Flow Cytometry. *Cytometry A* (2019) 95(6):647–54. doi: 10.1002/cyto.a.23724
15. Doan M, Vorobjev I, Rees P, Filby A, Wolkenhauer O, Goldfeld AE, et al. Diagnostic Potential of Imaging Flow Cytometry. *Trends Biotechnol* (2018) 36(7):649–52. doi: 10.1016/j.tibtech.2017.12.008
16. Hartmann FJ, Babdor J, Gherardini PF, Amir ED, Jones K, Sahaf B, et al. Comprehensive Immune Monitoring of Clinical Trials to Advance Human Immunotherapy. *Cell Rep* (2019) 28(3):819–831 e4. doi: 10.1016/j.celrep.2019.06.049
17. Matos LL, Trufelli DC, de Matos MG, da Silva Pinhal MA. Immunohistochemistry as an Important Tool in Biomarkers Detection and Clinical Practice. *Biomark Insights* (2010) 5:9–20. doi: 10.4137/bmi.s2185
18. Tay RE, Richardson EK, Toh HC. Revisiting the Role of CD4(+) T Cells in Cancer Immunotherapy-New Insights Into Old Paradigms. *Cancer Gene Ther* (2021) 28(1-2):5–17. doi: 10.1038/s41417-020-0183-x
19. Rubin RH, Baltimore D, Chen BK, Wilkinson RA, Fischman AJ. *In Vivo* Tissue Distribution of CD4 Lymphocytes in Mice Determined by Radioimmunoscintigraphy With an 111In-Labeled Anti-CD4 Monoclonal Antibody. *Proc Natl Acad Sci USA* (1996) 93(15):7460–3. doi: 10.1073/pnas.93.15.7460
20. Steinhoff K, Pierer M, Siegert J, Pigla U, Laub R, Hesse S, et al. Visualizing Inflammation Activity in Rheumatoid Arthritis With Tc-99 M Anti-CD4-mAb Fragment Scintigraphy. *Nucl Med Biol* (2014) 41(4):350–4. doi: 10.1016/j.nucmedbio.2013.12.018

21. Kanwar B, Gao DW, Hwang AB, Grenert JP, Williams SP, Franc B, et al. *In Vivo* Imaging of Mucosal CD4+ T Cells Using Single Photon Emission Computed Tomography in a Murine Model of Colitis. *J Immunol Methods* (2008) 329(1-2):21–30. doi: 10.1016/j.jim.2007.09.008
22. Dammes N, Peer D. Monoclonal Antibody-Based Molecular Imaging Strategies and Theranostic Opportunities. *Theranostics* (2020) 10(2):938–55. doi: 10.7150/thno.37443
23. Dialynas DP, Wilde DB, Marrack P, Pierres A, Wall KA, Havran W, et al. Characterization of the Murine Antigenic Determinant, Designated L3T4a, Recognized by Monoclonal Antibody GK1.5: Expression of L3T4a by Functional T Cell Clones Appears to Correlate Primarily With Class II MHC Antigen-Reactivity. *Immunol Rev* (1983) 74:29–56. doi: 10.1111/j.1600-065x.1983.tb01083.x
24. Wilde DB, Marrack P, Kappler J, Dialynas DP, Fitch FW. Evidence Implicating L3T4 in Class II MHC Antigen Reactivity; Monoclonal Antibody GK1.5 (Anti-L3T4a) Blocks Class II MHC Antigen-Specific Proliferation, Release of Lymphokines, and Binding by Cloned Murine Helper T Lymphocyte Lines. *J Immunol* (1983) 131(5):2178–83.
25. Haque S, Saizawa K, Rojo J, Janeway CAJr. The Influence of Valence on the Functional Activities of Monoclonal Anti-L3T4 Antibodies. Discrimination of Signaling From Other Effects. *J Immunol* (1987) 139(10):3207–12.
26. Freise AC, Zettlitz KA, Salazar FB, Lu X, Tavare R, Wu AM. ImmunoPET Imaging of Murine CD4(+) T Cells Using Anti-CD4 Cys-Diabody: Effects of Protein Dose on T Cell Function and Imaging. *Mol Imaging Biol* (2017) 19 (4):599–609. doi: 10.1007/s11307-016-1032-z
27. Hamers-Casterman C, Atarhouch T, Muyldermans S, Robinson G, Hamers C, Songa EB, et al. Naturally Occurring Antibodies Devoid of Light Chains. *Nature* (1993) 363(6428):446–8. doi: 10.1038/363446a0
28. Lecocq Q, De Vlaeminck Y, Hanssens H, D'Huyvetter M, Raes G, Goyvaerts C, et al. Theranostics in Immuno-Oncology Using Nanobody Derivatives. *Theranostics* (2019) 9(25):7772–91. doi: 10.7150/thno.34941
29. Chakravarty R, Goel S, Cai W. Nanobody: The "Magic Bullet" for Molecular Imaging? *Theranostics* (2014) 4(4):386–98. doi: 10.7150/thno.8006
30. Yang EY, Shah K. Nanobodies: Next Generation of Cancer Diagnostics and Therapeutics. *Front Oncol* (2020) 10:1182. doi: 10.3389/fonc.2020.01182
31. Chanier T, Chames P. Nanobody Engineering: Toward Next Generation Immunotherapies and Immunoimaging of Cancer. *Antibodies (Basel)* (2019) 8(1):13. doi: 10.3390/antib8010013
32. Popp MWL, Ploegh HL. Making and Breaking Peptide Bonds: Protein Engineering Using Sortase. *Angew Chem Int Edition* (2011) 50(22):5024–32. doi: 10.1002/anie.201008267
33. Massa S, Vikani N, Betti C, Ballet S, Vanderhaegen S, Steyaert J, et al. Sortase A-Mediated Site-Specific Labeling of Camelid Single-Domain Antibody-Fragments: A Versatile Strategy for Multiple Molecular Imaging Modalities. *Contrast Media Mol Imaging* (2016) 11(5):328–39. doi: 10.1002/cmmi.1696
34. Virant D, Traenkle B, Maier J, Kaiser PD, Bodenhofer M, Schmees C, et al. A Peptide Tag-Specific Nanobody Enables High-Quality Labeling for dSTORM Imaging. *Nat Commun* (2018) 9(1):930. doi: 10.1038/s41467-018-03191-2
35. Braun MB, Traenkle B, Koch PA, Emele F, Weiss F, Poetz O, et al. Peptides in Headlock–a Novel High-Affinity and Versatile Peptide-Binding Nanobody for Proteomics and Microscopy. *Sci Rep* (2016) 6:19211. doi: 10.1038/srep19211
36. Wu H, Kwong PD, Hendrickson WA. Dimeric Association and Segmental Variability in the Structure of Human CD4. *Nature* (1997) 387(6632):527–30. doi: 10.1038/387527a0
37. Raybould MIJ, Marks C, Krawczyk K, Taddese B, Nowak J, Lewis AP, et al. Five Computational Developability Guidelines for Therapeutic Antibody Profiling. *Proc Natl Acad Sci USA* (2019) 116(10):4025–30. doi: 10.1073/pnas.1810576116
38. Xu Y, Wang D, Mason B, Rossomando T, Li N, Liu D, et al. Structure, Heterogeneity and Developability Assessment of Therapeutic Antibodies. *MAbs* (2019) 11(2):239–64. doi: 10.1080/19420862.2018.1553476
39. Keyaerts M, Xavier C, Heemskerk J, Devoogdt N, Everaert H, Ackaert C, et al. Phase I Study of 68Ga-HER2-Nanobody for PET/CT Assessment of HER2 Expression in Breast Carcinoma. *J Nucl Med* (2016) 57(1):27–33. doi: 10.2967/jnumed.115.162024
40. Xavier C, Vaneycken I, D'Huyvetter M, Heemskerk J, Keyaerts M, Vincke C, et al. Synthesis, Preclinical Validation, Dosimetry, and Toxicity of 68Ga-NOTA-Anti-HER2 Nanobodies for iPET Imaging of HER2 Receptor Expression in Cancer. *J Nucl Med* (2013) 54(5):776–84. doi: 10.2967/jnumed.112.111021
41. Masuda S, Kumano K, Suzuki T, Tomita T, Iwatsubo T, Natsugari H, et al. Dual Antitumor Mechanisms of Notch Signaling Inhibitor in a T-Cell Acute Lymphoblastic Leukemia Xenograft Model. *Cancer Sci* (2009) 100(12):2444–50. doi: 10.1111/j.1349-7006.2009.01328.x
42. Killeen N, Sawada S, Littman DR. Regulated Expression of Human CD4 Rescues Helper T Cell Development in Mice Lacking Expression of Endogenous CD4. *EMBO J* (1993) 12(4):1547–53. doi: 10.1002/j.1460-2075.1993.tb05798.x
43. Sckisel GD, Mirsoian A, Minnar CM, Crittenden M, Curti B, Chen JQ, et al. Differential Phenotypes of Memory CD4 and CD8 T Cells in the Spleen and Peripheral Tissues Following Immunostimulatory Therapy. *J Immunother Cancer* (2017) 5:33. doi: 10.1186/s40425-017-0235-4
44. Tavare R, McCracken MN, Zettlitz KA, Salazar FB, Olafsen T, Witte ON, et al. Immuno-PET of Murine T Cell Reconstitution Postadoptive Stem Cell Transplantation Using Anti-CD4 and Anti-CD8 Cys-Diabodies. *J Nucl Med* (2015) 56(8):1258–64. doi: 10.2967/jnumed.114.153338
45. Li H, Chen Y, Jin Q, Wu Y, Deng C, Gai Y, et al. Noninvasive Radionuclide Molecular Imaging of the CD4-Positive T Lymphocytes in Acute Cardiac Rejection. *Mol Pharm* (2021) 18(3):1317–26. doi: 10.1021/acs.molpharmaceut.0c01155
46. Kristensen LK, Frohlich C, Christensen C, Melander MC, Poulsen TT, Galler GR, et al. CD4(+) and CD8a(+) PET Imaging Predicts Response to Novel PD-1 Checkpoint Inhibitor: Studies of Sym021 in Syngeneic Mouse Cancer Models. *Theranostics* (2019) 9(26):8221–38. doi: 10.7150/thno.37513
47. Choy EH, Panayi GS, Emery P, Madden S, Breedveld FC, Kraan MC, et al. Repeat-Cycle Study of High-Dose Intravenous 4162W94 Anti-CD4 Humanized Monoclonal Antibody in Rheumatoid Arthritis. A Randomized Placebo-Controlled Trial. *Rheumatol (Oxford)* (2002) 41(10):1142–8. doi: 10.1093/rheumatology/41.10.1142
48. Moreland LW, Pratt PW, Mayes MD, Postlethwaite A, Weisman MH, Schnitzer T, et al. Double-Blind, Placebo-Controlled Multicenter Trial Using Chimeric Monoclonal Anti-CD4 Antibody, cM-T412, in Rheumatoid Arthritis Patients Receiving Concomitant Methotrexate. *Arthritis Rheum* (1995) 38(11):1581–8. doi: 10.1002/art.1780381109
49. Rashidian M, Ingram JR, Dougan M, Dongre A, Whang KA, LeGall C, et al. Predicting the Response to CTLA-4 Blockade by Longitudinal Noninvasive Monitoring of CD8 T Cells. *J Exp Med* (2017) 214(8):2243–55. doi: 10.1084/jem.20161950
50. Huang L, Gainkam LO, Caveliers V, Vanhove C, Keyaerts M, De Baetselier P, et al. SPECT Imaging With 99mtc-Labeled EGFR-Specific Nanobody for *In Vivo* Monitoring of EGFR Expression. *Mol Imaging Biol* (2008) 10(3):167–75. doi: 10.1007/s11307-008-0133-8
51. Roovers RC, Laeremans T, Huang L, De Taeye S, Verkleij AJ, Revets H, et al. Efficient Inhibition of EGFR Signaling and of Tumour Growth by Antagonistic Anti-EFGR Nanobodies. *Cancer Immunol Immunother* (2007) 56(3):303–17. doi: 10.1007/s00262-006-0180-4
52. Evazalipour M, D'Huyvetter M, Tehrani BS, Abolhassani M, Omidfar K, Abdoli S, et al. Generation and Characterization of Nanobodies Targeting PSMA for Molecular Imaging of Prostate Cancer. *Contrast Media Mol Imaging* (2014) 9(3):211–20. doi: 10.1002/cmmi.1558
53. Blykers A, Schoonooghe S, Xavier C, D'Hoe K, Laoui D, D'Huyvetter M, et al. PET Imaging of Macrophage Mannose Receptor-Expressing Macrophages in Tumor Stroma Using 18f-Radiolabeled Camelid Single-Domain Antibody Fragments. *J Nucl Med* (2015) 56(8):1265–71. doi: 10.2967/jnumed.115.156828
54. Bala G, Baudhuin H, Remory I, Gillis K, Debie P, Krasniqi A, et al. Evaluation of [(99m)Tc]Radiolabeled Macrophage Mannose Receptor-Specific Nanobodies for Targeting of Atherosclerotic Lesions in Mice. *Mol Imaging Biol* (2018) 20(2):260–7. doi: 10.1007/s11307-017-1117-3
55. Jailkhani N, Ingram JR, Rashidian M, Rickelt S, Tian C, Mak H, et al. Noninvasive Imaging of Tumor Progression, Metastasis, and Fibrosis Using a Nanobody Targeting the Extracellular Matrix. *Proc Natl Acad Sci USA* (2019) 116(28):14181–90. doi: 10.1073/pnas.1817442116
56. D'Huyvetter M, De Vos J, Xavier C, Pruszynski M, Sterckx YGJ, Massa S, et al. (131)I-Labeled Anti-HER2 Camelid sdAb as a Theranostic Tool in Cancer

Treatment. *Clin Cancer Res* (2017) 23(21):6616–28. doi: 10.1158/1078-0432.CCR-17-0310
57. Bruni D, Angell HK, Galon J. The Immune Contexture and Immunoscore in Cancer Prognosis and Therapeutic Efficacy. *Nat Rev Cancer* (2020) 20 (11):662–80. doi: 10.1038/s41568-020-0285-7
58. Accogli T, Bruchard M, Vegran F. Modulation of CD4 T Cell Response According to Tumor Cytokine Microenvironment. *Cancers (Basel)* (2021) 13 (3):373. doi: 10.3390/cancers13030373
59. Sakihama T, Smolyar A, Reinherz EL. Oligomerization of CD4 Is Required for Stable Binding to Class II Major Histocompatibility Complex Proteins But Not for Interaction With Human Immunodeficiency Virus Gp120. *Proc Natl Acad Sci USA* (1995) 92(14):6444–8. doi: 10.1073/pnas.92.14.6444
60. Jonsson P, Southcombe JH, Santos AM, Huo J, Fernandes RA, McColl J, et al. Remarkably Low Affinity of CD4/peptide-Major Histocompatibility Complex Class II Protein Interactions. *Proc Natl Acad Sci USA* (2016) 113(20):5682–7. doi: 10.1073/pnas.1513918113
61. Cruikshank WW, Greenstein JL, Theodore AC, Center DM. Lymphocyte Chemoattractant Factor Induces CD4-Dependent Intracytoplasmic Signaling in Lymphocytes. *J Immunol* (1991) 146(9):2928–34.
62. Vignali DA, Vignali KM. Profound Enhancement of T Cell Activation Mediated by the Interaction Between the TCR and the D3 Domain of CD4. *J Immunol* (1999) 162(3):1431–9.
63. Tijink BM, Laeremans T, Budde M, Stigter-van Walsum M, Dreier T, de Haard HJ, et al. Improved Tumor Targeting of Anti-Epidermal Growth Factor Receptor Nanobodies Through Albumin Binding: Taking Advantage of Modular Nanobody Technology. *Mol Cancer Ther* (2008) 7(8):2288–97. doi: 10.1158/1535-7163.MCT-07-2384
64. Muyldermans S, Baral TN, Retamozzo VC, De Baetselier P, De Genst E, Kinne J, et al. Camelid Immunoglobulins and Nanobody Technology. *Vet Immunol Immunopathol* (2009) 128(1-3):178–83. doi: 10.1016/j.vetimm.2008.10.299
65. Vincke C, Loris R, Saerens D, Martinez-Rodriguez S, Muyldermans S, Conrath K. General Strategy to Humanize a Camelid Single-Domain Antibody and Identification of a Universal Humanized Nanobody Scaffold. *J Biol Chem* (2009) 284(5):3273–84. doi: 10.1074/jbc.M806889200
66. Ackaert C, Smiejkowska N, Xavier C, Sterckx YGJ, Denies S, Stijlemans B, et al. Immunogenicity Risk Profile of Nanobodies. *Front Immunol* (2021) 12:632687. doi: 10.3389/fimmu.2021.632687
67. Gainkam LO, Caveliers V, Devoogdt N, Vanhove C, Xavier C, Boerman O, et al. Localization, Mechanism and Reduction of Renal Retention of Technetium-99m Labeled Epidermal Growth Factor Receptor-Specific Nanobody in Mice. *Contrast Media Mol Imaging* (2011) 6(2):85–92. doi: 10.1002/cmmi.408
68. D'Huyvetter M, Vincke C, Xavier C, Aerts A, Impens N, Baatout S, et al. Targeted Radionuclide Therapy With A 177Lu-Labeled Anti-HER2 Nanobody. *Theranostics* (2014) 4(7):708–20. doi: 10.7150/thno.8156
69. de Jong M, Barone R, Krenning E, Bernard B, Melis M, Visser T, et al. Megalin Is Essential for Renal Proximal Tubule Reabsorption of (111)In-DTPA-Octreotide. *J Nucl Med* (2005) 46(10):1696–700.
70. Traenkle B, Emele F, Anton R, Poetz O, Haeussler RS, Maier J, et al. Monitoring Interactions and Dynamics of Endogenous Beta-Catenin With Intracellular Nanobodies in Living Cells. *Mol Cell Proteomics* (2015) 14 (3):707–23. doi: 10.1074/mcp.M114.044016
71. Maier J, Traenkle B, Rothbauer U. Real-Time Analysis of Epithelial-Mesenchymal Transition Using Fluorescent Single-Domain Antibodies. *Sci Rep* (2015) 5:13402. doi: 10.1038/srep13402
72. Arbabi Ghahroudi M, Desmyter A, Wyns L, Hamers R, Muyldermans S. Selection and Identification of Single Domain Antibody Fragments From Camel Heavy-Chain Antibodies. *FEBS Lett* (1997) 414(3):521–6. doi: 10.1016/S0014-5793(97)01062-4
73. Rothbauer U, Zolghadr K, Muyldermans S, Schepers A, Cardoso MC, Leonhardt H. A Versatile Nanotrap for Biochemical and Functional Studies With Fluorescent Fusion Proteins. *Mol Cell Proteomics* (2008) 7(2):282–9. doi: 10.1074/mcp.M700342-MCP200
74. Davies G, Rolle AM, Maurer A, Spycher PR, Schillinger C, Solouk-Saran D, et al. Towards Translational ImmunoPET/MR Imaging of Invasive Pulmonary Aspergillosis: The Humanised Monoclonal Antibody JF5 Detects Aspergillus Lung Infections *In Vivo*. *Theranostics* (2017) 7 (14):3398–414. doi: 10.7150/thno.20919
75. Wagner TR, Ostertag E, Kaiser PD, Gramlich M, Ruetalo N, Junker D, et al. NeutrobodyPlex-Monitoring SARS-CoV-2 Neutralizing Immune Responses Using Nanobodies. *EMBO Rep* (2021) 22(5):e52325. doi: 10.15252/embr.202052325
76. Becker M, Strengert M, Junker D, Kaiser PD, Kerrinnes T, Traenkle B, et al. Exploring Beyond Clinical Routine SARS-CoV-2 Serology Using MultiCoV-Ab to Evaluate Endemic Coronavirus Cross-Reactivity. *Nat Commun* (2021) 12(1):1152. doi: 10.1038/s41467-021-20973-3
77. Chen I, Dorr BM, Liu DR. A General Strategy for the Evolution of Bond-Forming Enzymes Using Yeast Display. *Proc Natl Acad Sci USA* (2011) 108 (28):11399–404. doi: 10.1073/pnas.1101046108
78. Kochert BA, Iacob RE, Wales TE, Makriyannis A, Engen JR. Hydrogen-Deuterium Exchange Mass Spectrometry to Study Protein Complexes. *Methods Mol Biol* (2018) 1764:153–71. doi: 10.1007/978-1-4939-7759-8_10
79. Hamuro Y, Coales SJ. Optimization of Feasibility Stage for Hydrogen/Deuterium Exchange Mass Spectrometry. *J Am Soc Mass Spectrom* (2018) 29(3):623–9. doi: 10.1007/s13361-017-1860-3
80. Masson GR, Burke JE, Ahn NG, Anand GS, Borchers C, Brier S, et al. Recommendations for Performing, Interpreting and Reporting Hydrogen Deuterium Exchange Mass Spectrometry (HDX-MS) Experiments. *Nat Methods* (2019) 16(7):595–602. doi: 10.1038/s41592-019-0459-y
81. Loffler MW, Nussbaum B, Jager G, Jurmeister PS, Budczies J, Pereira PL, et al. A Non-Interventional Clinical Trial Assessing Immune Responses After Radiofrequency Ablation of Liver Metastases From Colorectal Cancer. *Front Immunol* (2019) 10:2526. doi: 10.3389/fimmu.2019.02526
82. Widenmeyer M, Griesemann H, Stevanovic S, Feyerabend S, Klein R, Attig S, et al. Promiscuous Survivin Peptide Induces Robust CD4+ T-Cell Responses in the Majority of Vaccinated Cancer Patients. *Int J Cancer* (2012) 131(1):140–9. doi: 10.1002/ijc.26365
83. EMEA. *Guideline on Bioanalytical Method Validation*. European Medicines Agency; Comittee for Medicinal Products for Human Use. London (CHMP (2013).
84. FDA. *Bioanalytical Method Validation: Guidance for Industry*. Silver Spring, Rockville: U.S. Department of Health and Human Services, Food and Drug Administration, Center for Drug Evaluation and Research, Center for Veterinary Medicine.
85. Westgard JO, Barry PL, Hunt MR, Groth T. A Multi-Rule Shewhart Chart for Quality Control in Clinical Chemistry. *Clin Chem* (1981) 27(3):493–501. doi: 10.1093/clinchem/27.3.493

Conflict of Interest: DSo, MK, BP, BT, PK, and UR are named as inventors on a patent application claiming the use of the described nanobodies for diagnosis and therapeutics filed by the Natural and Medical Sciences Institute and the Werner Siemens Imaging Center.

The remaining authors declare that the research was conducted in the absence of any commercial or financial relationships that could be construed as a potential conflict of interest.

Publisher's Note: All claims expressed in this article are solely those of the authors and do not necessarily represent those of their affiliated organizations, or those of the publisher, the editors and the reviewers. Any product that may be evaluated in this article, or claim that may be made by its manufacturer, is not guaranteed or endorsed by the publisher.

frontiers in Immunology

REVIEW
published: 15 December 2021
doi: 10.3389/fimmu.2021.754200

Shedding Structured Light on Molecular Immunity: The Past, Present and Future of Immune Cell Super Resolution Microscopy

Timothy M. Johanson[1,2]*, *Christine R. Keenan*[1,2] *and Rhys S. Allan*[1,2]

[1] The Walter and Eliza Hall Institute of Medical Research, Parkville, VIC, Australia, [2] Department of Medical Biology, The University of Melbourne, Parkville, VIC, Australia

In the two decades since the invention of laser-based super resolution microscopy this family of technologies has revolutionised the way life is viewed and understood. Its unparalleled resolution, speed, and accessibility makes super resolution imaging particularly useful in examining the highly complex and dynamic immune system. Here we introduce the super resolution technologies and studies that have already fundamentally changed our understanding of a number of central immunological processes and highlight other immunological puzzles only addressable in super resolution.

Keywords: super resolution microscopy, immune cells, immune cell activation, recombination, single molecule microscopy

OPEN ACCESS

Edited by:
Greetje Vande Velde, KU Leuven, Belgium

Reviewed by:
Andrey Shaw, Genentech, Inc., United States
Laura Patrussi, University of Siena, Italy

***Correspondence:**
Timothy M. Johanson
johanson@wehi.edu.au

Specialty section:
This article was submitted to T Cell Biology, a section of the journal Frontiers in Immunology

Received: *06 August 2021*
Accepted: *23 November 2021*
Published: *15 December 2021*

Citation:
Johanson TM, Keenan CR and Allan RS (2021) Shedding Structured Light on Molecular Immunity: The Past, Present and Future of Immune Cell Super Resolution Microscopy. Front. Immunol. 12:754200. doi: 10.3389/fimmu.2021.754200

INTRODUCTION

Microscopy has a long history of enabling immunological discoveries. After likely being observed by the 'father of microscopy' A. van Leeuwenhoek in 1687 in human saliva (1), the first definitive description of leukocytes came in 1749 when Joseph Lietaud and Jean-Baptiste de Senac observed human "globuli albicantes" and "globules blanc", respectively (2, 3). Roughly a hundred years later the first suggestions of immune cell function were observed when leukocytes were seen exiting the vasculature of a frog's tongue in response to injury (4) and 'attacking' a rose thorn stuck into a sea star larva (1).

Unbeknownst to these microscopy pioneers their ability to observe microscopic structures was limited not only by the strength of light (be it sun or candle) but also the nature of light itself. When light passes through an aperture, such as a microscope objective, it diffracts. How widely it diffracts is dependent on the size of the aperture and the wavelength of the light. Visible light has wavelengths from 400-700 nm. The smaller the aperture or the longer the wavelength of the light the greater the diffraction. When this diffracted light hits a surface, such as the sample, it forms a ripple like pattern, known as an Airy disc (**Figure 1**). The size of the Airy disc is dependent on the extent of diffraction, and importantly sets a limit on the resolution of the microscope. Put simply, only illuminated objects that are laterally separated by more than the radius on the disc, or approximately half the wavelength of the illuminating light, can be discerned. This resolution limit is known as the diffraction limit.

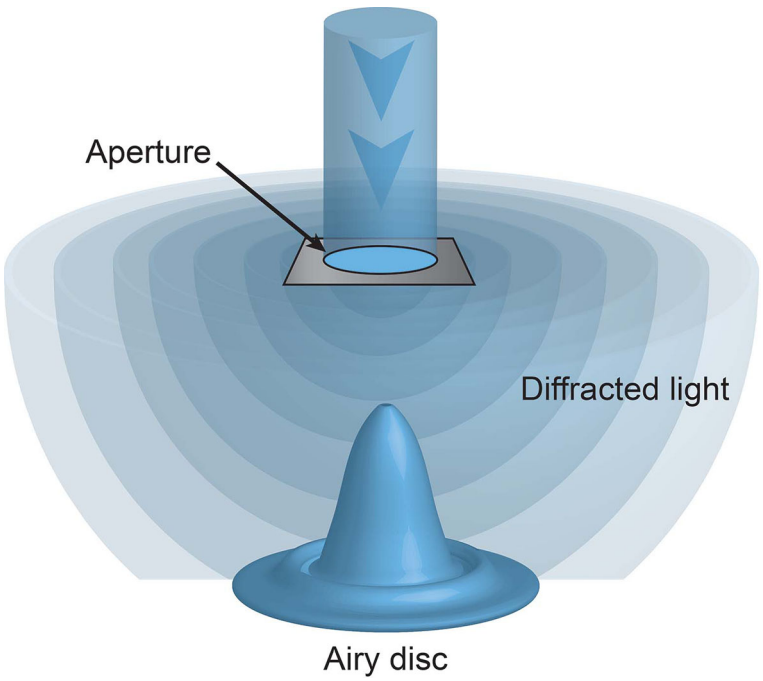

FIGURE 1 | The diffraction limit. Light passing through an aperture diffracts. When hitting a surface this light forms a ripple like pattern of illumination, with a central focus of intensity surrounded by concentric rings, known as an Airy disc. No objects laterally separated by less than the radius of this disc can be discriminated.

The diffraction limit restricted all forms of light microscopy, including laser microscopy (albeit with a shorter and more defined wavelength), for hundreds of years, until the invention of revolutionary super resolution imaging technologies (5, 6). By structuring the excitation light (**Box 1**) or by using modified laser beams to 'switch off' select fluorophores in an illuminated sample (**Box 2**) these pioneering super resolution technologies were able to break the diffraction limit and increase resolution to ~100 nm. Following these breakthrough technologies has a been procession of Nobel Prize winning super resolution imaging technologies that have improved potential resolution to as little as ~20 nm, not only in fixed samples but in highly dynamic live cells and tissues.

The ability to observe and record the behaviour of immune cells, both individually and in tissues, at super resolution has enabled the interrogation of numerous long-standing cellular immunological questions (7). However, while individual cells have been observable for hundreds of years, it was only the super resolution revolution that allowed the thorough examination of single molecules. It is arguably at this molecular level, at which single RNA transcripts (8, 9), individual gene loci (10), chemokines (11), actin filaments (12) and transcription factors (13), among others, can be visually disentangled, that super resolution imaging holds its greatest utility.

Here we focus on four central immunological processes; two of which super resolution microscopy has already fundamentally changed the way they are understood (immune cell danger detection and activation) and two which these technologies

BOX 1 | Structural Illumination Microscopy (SIM) (5) uses moveable diffraction gratings inserted into the excitation beam path creating a striped pattern of illumination. By acquiring multiple images with this known pattern of structured illumination it is possible to omit out-of-focus signal to create a super resolution image. SIM can be used to image live cells.

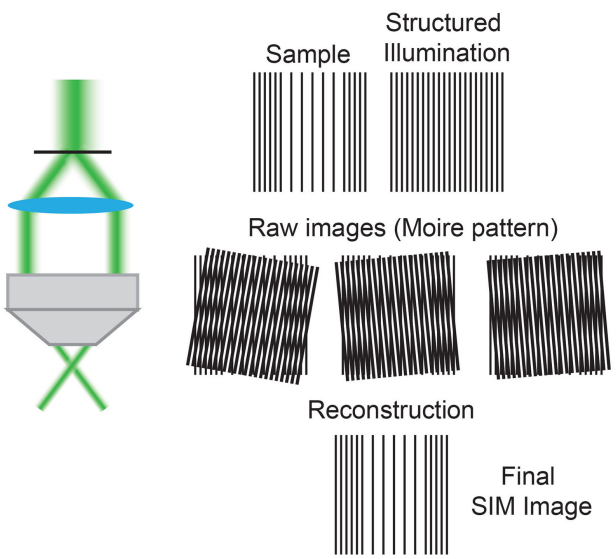

BOX 2 | Stimulated Emission Depletion (STED) (6) microscopy relies on the interplay between two laser pulses, the first to excite fluorophores at the focal spot, and the second a modified depleting beam that reversibly de-excites any fluorophores surrounding the focal spot. Thus, only the excited fluorophores in the focal spot emit light, allowing features smaller than the diffraction limit to be visualised. STED can be used in live cells.

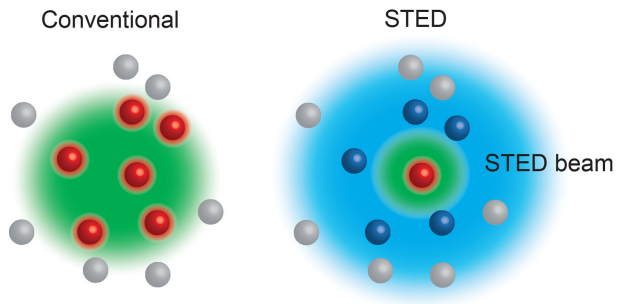

have the currently unrealised potential to answer key, longstanding molecular immunological questions (recombination and lineage decisions). In doing so we also provide introductions to the technologies that have profoundly altered the way not only the immune system, but all life is seen.

Super Resolution Imaging of Immune Cell Receptors

The ability of immune cells to detect and respond to danger signals is fundamental in immune function. While the receptors involved differ across immune cells types (14) the distribution of these receptors, and other co-stimulatory molecules, is critically important to appropriate activation.

For many years it was thought that receptors, such as B cell receptor (BCR) on B cells, T cell receptor (TCR) on T cells and Toll like receptors (TLRs) on macrophages, were evenly distributed across their respective cell surfaces only to aggregate upon activation (15). However, despite electron microscopy results suggesting the non-random distribution of immunoglobulin molecules on resting B cells (16) as early as 1975, it was not until the advent of super-resolution imaging technologies that it was explicitly shown that many, if not all, receptors cluster within the plasma membrane in the steady state (17–19).

For example, in a seminal work using PALM imaging (**Box 3**) the TCR and a key T cell signalling adaptor molecule, Linker for Activation of T cells (Lat), were shown to reside in clusters upon the plasma membrane, termed protein islands (21). In more recent technically and visually stunning expansions of the characterisation of TCR distribution it was shown that these TCR islands are found across the whole live T cell membrane in culture (22) and in the lymph node (23).

Using other variants of SMLM (**Box 3**) other immune signalling molecules have also been shown to form clusters in the steady state including; CD4 and Lck on T cells (24–26), IgM, IgG and IgD on B cells (27–29), IgE on mast cells (30), TLR4 (31–33), signal regulatory protein α, Fc gamma receptor I and II on human macrophages (34), β2 integrins on human neutrophils (35) and NKG2D on NK cells (36).

The majority of these studies revealed not only the pre-activation clustering of these signalling molecules, but a consistent activation induced redistribution of these clusters. Interestingly, evidence from STORM, PALM and FLIM/FRET (**Box 4**) imaging of T and B cell membranes reveals this redistribution to be a concatenation, but not coalescence, of these clusters (21, 38, 39) (**Figure 2**). This concatenation of protein islands, as opposed to a complete merging, is thought to play an important regulatory function. As such, it is thought that signalling occurs only at the boundaries of clusters that contain distinct compositions of important signalling molecules. For example, in B cells IgM and CD45 are found together on an

BOX 3 | Single Molecule Localisation Microscopy (SMLM), including Stochastic Optical Reconstruction Microscopy (STORM) (20) and Photo-Activated Localization Microscopy (PALM) (17), use a low power beam to activate a small proportion of reversibly photoactivatable molecules within an illuminated area before a higher power illuminating beam records the molecules position and photobleaches them. As only a small proportion of the total fluorescent molecules are activated in each cycle the centre of mass of individual molecules can be determined in each image (a process that would be impossible if all molecules fluoresced simultaneously) before being collated into a final super resolution image. These compiled images can achieve ~25 nm resolution. PALM generally use genetically encoded photo-switchable fluorescent proteins, while STORM uses conventional synthetic dyes. Both can be used in live cells.

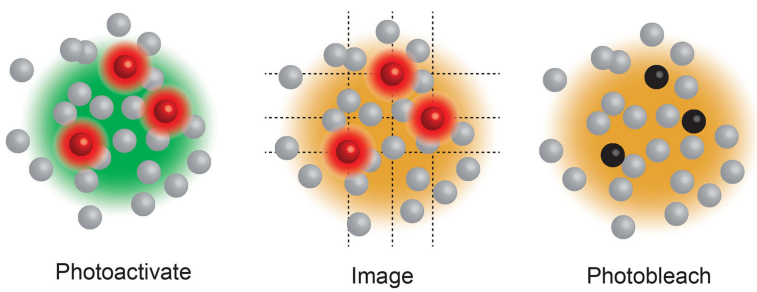

BOX 4 | Fluorescence-lifetime imaging microscopy (FLIM) (37) images the decay rate of fluorescence of a tagged donor molecule of interest after excitation. This rate of decay is impacted by the proximity of an acceptor molecule. The closer the molecules of interest, the faster the decay. As such, FLIM-FRET techniques provide high temporal resolution of tagged protein-protein interactions in live cells.

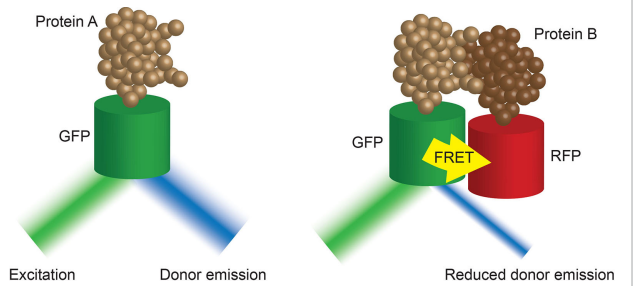

island separated from islands containing Lyn and CD19 (40, 41). This is important as Lyn is required for some forms of signalling *via* IgM (42, 43). Thus, the two islands must come together, and exchange components, during activation, however, if complete coalescence of the islands was allowed dysregulated activation could result.

It has been known for over a decade that the network of cortical actin just under the cell membrane plays a critical role in the separation of protein islands (44, 45). However, it was the application of super resolution imaging technologies that allowed elucidation of the underlying molecular mechanism of control. As such, STORM imaging has shown that treatment of B cells with an actin-depolymerizing compound (latrunculin A) increases the proximity of the aforementioned IgM and IgD containing islands (28) and the lateral mobility of BCR and CD19 containing islands (27, 46, 47).

Immune Cell Activation at Super Resolution

Once a danger signal is detected, immune cells undergo dramatic cellular and molecular changes in order to play their part in the immune response. In addition to revealing previously unseen mechanisms of immune cell danger detection, super resolution imaging has also added to our understanding of the molecular changes during immune cell activation.

Some immune cells, such as cytotoxic T cells and natural killer (NK) cells, respond to activation with the release of lytic granules at a synapse between them and their target cell. These granules are designed to induce apopotosis in the target cell. Unsurprisingly, given their lethality, the formation, trafficking and release of these modified lysosomes is tightly controlled. The ability of sub-diffraction limit imaging to visually untangle the dense, intricate and highly dynamic network of cortical actin and lytic granules underlying the synapse and the plasma membrane in general has revolutionised our understanding of immune cell killing (48).

For example, in recent years a number of super-resolution imaging technologies, including 3D-SIM (49), STED (50, 51), SMLM and TIRF (**Box 5**) (53, 54), and Lattice light sheet microscopy (**Box 6**) (12, 56) have all been used to observe the rapid and intricate movement of actin and lytic granules towards, and within, the immune synapse of both T and NK cells. As such, it was revealed that upon activation the network of actin that normally forms a mesh too dense for lytic granules to traverse dilates or dissolves at the immune synapse allowing microtubule-guided granule release (**Figure 3**) This process takes approximately one or thirty minutes in T and NK cells, respectively (50, 54, 57).

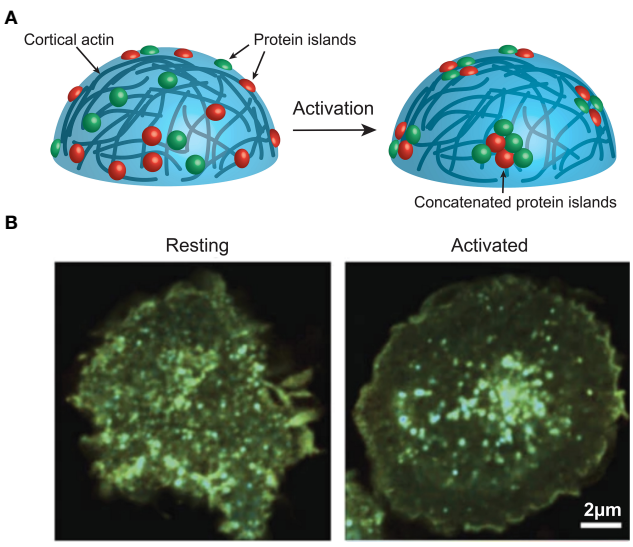

FIGURE 2 | **(A)** Activation induces actin-mediated concatenation of cell surface protein islands on the surface of immune cells to facilitate signalling. **(B)** FRET imaging data from Ma et al. (38), showing CD3z clustering on a Jurkat cell before and after activation. Image used under the terms of the Creative Commons licence.

BOX 5 | Total internal reflection fluorescence microscopy (TIRF). When light encounters the interface of two transparent materials with different refractive indices (such as a live cell and a cover slip, as below), it will most often be both diffracted and reflected. However, at a certain angle of incidence the light will be totally reflected in a phenomenon called total internal reflection. Total internal reflection creates an electromagnetic field that passes through the interface between the two materials to form an evanescent wave. TIRF imaging (52) exploits this evanescence to excite fluorophores only in close proximity to the interface to achieve sub-diffraction limit axial resolution.

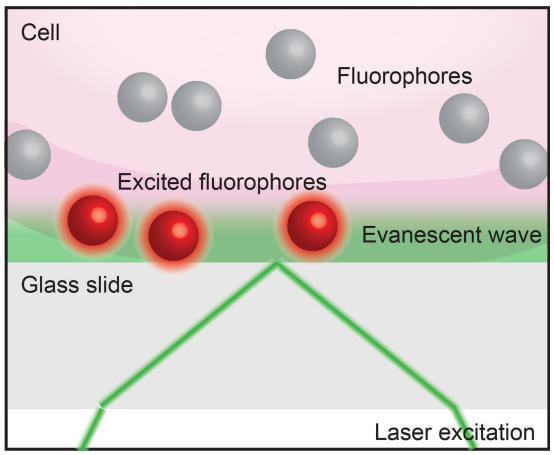

BOX 6 | Lattice light sheet fluorescence microscopy (55) uses a combination of techniques from light sheet, Bessel beam and structural illumination microscopy (SIM). As such, it uses a two-dimensional lattice of non-diffracting Bessel beam light sheets that are spaced such that they cause destructive interference and removal of the 'out of field' illumination which hampers traditional Bessel beam light sheet microscopy. This allows lattice light sheet microscopy to achieve unparalleled resolution and penetrance, while minimising phototoxicity.

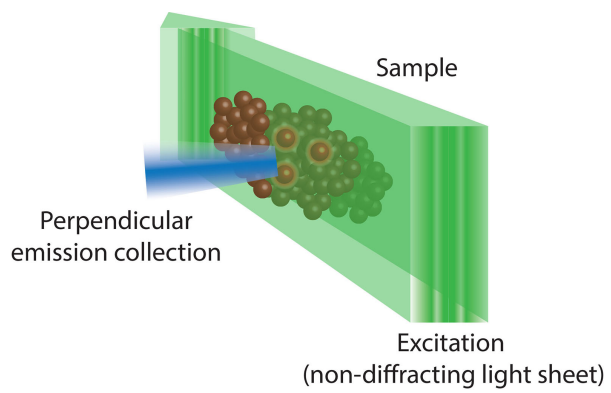

Furthermore, not only is the intricate actin network important for facilitating degranulation, it also appears to play an important role in regulating the number of granules released. This control is critically important as it minimises healthy by-stander cell killing (58) and potentially also influences the number of target cells an individual cytotoxic lymphocyte can kill (59). Recent imaging studies have shown that T and NK cells do not release their entire granule payload during initial degranulation. In fact, they may release as little as one tenth of their total granules (60, 61). Actin likely regulates degranulation *via* two mechanisms; one, it limits the transport of granules to the immune synapse (60) and two, TIRF imaging recently observed the reformation of the dense actin network underlying the immune synapse soon after degranulation, restricting further granule release (12).

While cytotoxic lymphocytes respond to activation with the direct killing of target cells, B lymphocytes direct killing *via* the mass production of specific antibodies. This requires transformation into 'antibody factories', including dramatic increases in cell size, proliferation and RNA synthesis (62). The process also involves the spreading of chromatin from its naïve location, predominantly at the nuclear periphery, to a more dispersed configuration. This chromatin spreading is thought to promote transcription factor binding and gene expression important in the transformation to antibody secreting cells (63, 64).

While super resolution investigations confirmed chromatin spreading (13, 65), the ability to visualise the chromatin fibre to <20 nm resolution revealed that not only do the fibres spread within the nucleus, they also decompact, meaning there is more accessible DNA between normally tightly compacted nucleosomes. These processes were shown to be regulated independently, and furthermore it was chromatin decompaction, not spreading, that was important in regulating transcription factor binding (13). By inserting a fluorescent Halo-Tag downstream of two transcription factors, CTCF and JunD, almost unimaginably detailed three-dimensional single molecule tracking revealed the binding and diffusion behaviours of these factors during their DNA interrogations. As such, in a naïve B cell JunD collides with DNA roughly 130 times before finding a suitable and accessible binding site. This search time is roughly halved upon B cell activation (13). This was elegantly shown to be independent of chromatin spreading and reliant upon nucleosome decompaction using drug treatment or energy depletion, respectively (13). The dwell or residence times of CTCF determined by single molecule tracking was confirmed using FRAP imaging (**Box 7**).

These studies are examples of how super resolution imaging has already fundamentally changed our understanding of central immunological processes, in this case by revealing the molecular underpinnings of immune cell activation. While earlier technologies did elude to many of these mechanisms, the fact that actin fibres, nucleosomes and indeed protein islands (22) are frequently separated by less that 200 nm means they can only be meaningfully visualised, and thus more completely understood, in super resolution.

THE FUTURE OF SUPER RESOLUTION IN MOLECULAR IMMUNOLOGY

The works outlined thus far highlight the impact of super resolution imaging on our understanding of immune cell

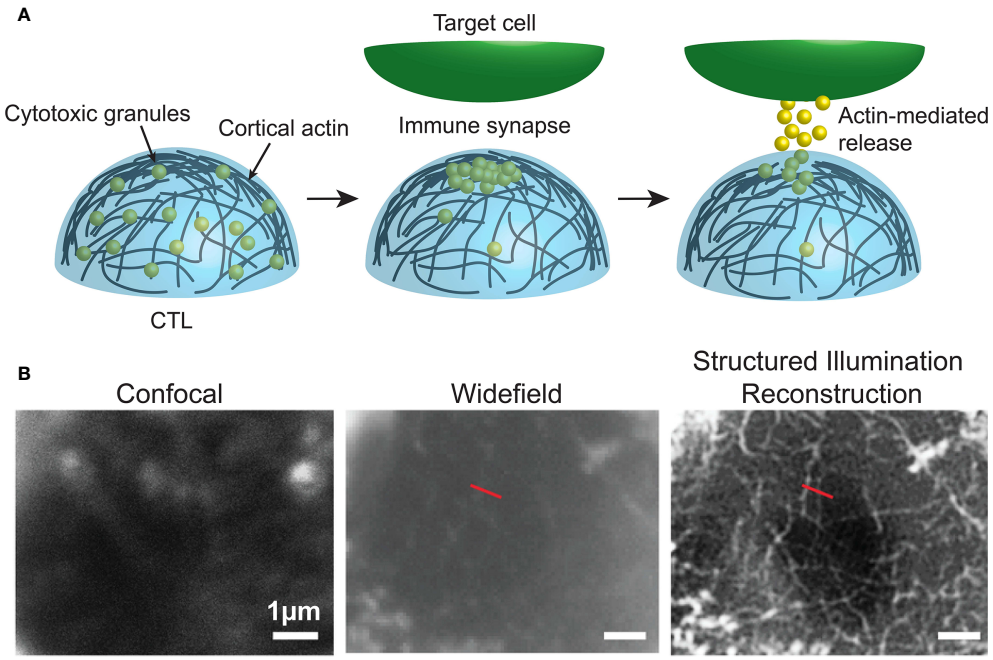

FIGURE 3 | **(A)** Dynamic cortical actin regulates the accumulation and release of cytotoxic granules at the immune synapse of cytotoxic immune cells. **(B)** Data from Brown et al. (57), comparing F-actin (white) at human NK cell synapses using confocal, widefield and structured illumination reconstruction imaging. Image used under the terms of the Creative Commons licence.

function. While these explorations have already yielded fruit, below we outline two incompletely understood, but essential, molecular immune processes in which super resolution imaging has the potential to answer longstanding questions.

Antigen Receptor Recombination

Recombination of the antigen receptor genes (*Igh, Igk and Igl* in B cells and *Tcrg*, *Tcrd*, *Tcrb* and *Tcra* in T cells) is key to generating a wide antigen receptor repertoire. The tightly controlled process involves removal of the intervening DNA between genes from three segment pools, known as variable (V), diversity (D) and joining (J). The result is in an exon that encodes the antigen-binding domain of an antigen receptor. Recombination relies on a series of remarkable genomic manoeuvres, including relocalisation of the antigen receptor gene from the periphery to the centre of the nucleus (67, 68), removal of genomic domain boundaries within the gene (69) and a contraction of the gene to bring linearly distant V regions into close physical proximity with the D-J region for recombination (68, 70–72). These processes have been extensively examined using molecular and genetic manipulations, but also imaging technologies. For example, DNA FISH has been used to quantify the nuclear position and contraction of the Igh locus in B cell progenitors (67).

While these studies have added to our understanding of antigen receptor recombination there are still significant gaps

BOX 7 | Fluorescence recovery after photobleaching (FRAP) (66) measures the recovery of local photodestruction of a tagged molecule via diffusion to determine the molecules dynamics within the local molecular environment.

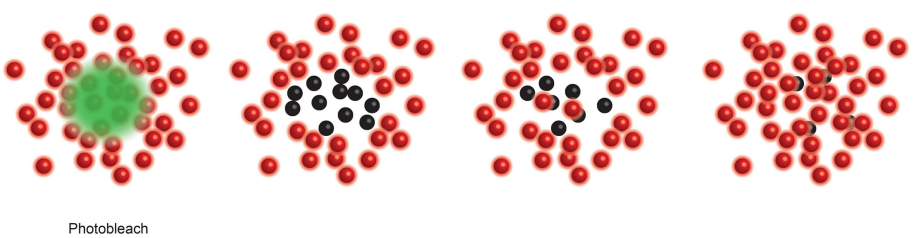

in our knowledge of the process. For example, while locus contraction brings the V region into proximity with the D-J region, how the V region that will ultimately form part of the functional exon is 'selected' from numerous candidates within the distal region is unclear. Diffusion fitting a fractional Langevin motion model (73) within the viscoelastic nuclear environment is currently the best explanation of how this process may work (74, 75).

Recent super resolution imaging breakthrough technologies provide an opportunity to reveal the mechanics of this long-standing immunological puzzle. These technologies, including ORCA and Hi-M (**Box 8**) (80, 81), leverage the development of complex pools of synthetic fluorescently labelled oligonucleotides (OligoPaint) alongside sequential super resolution STORM imaging to reveal the nanoscale configuration of genomic regions. In visually stellar works building on super resolution examinations of chromosome scale genome organisation (83–85), both ORCA and Hi-M have been used to visualise the nanoscale (2-15 kB resolution) organisation of specific genomic regions (up to 700 kB in size) within individual cells of whole *Drosophila* embryo sections. These works revealed previously undetectable relationships between genome organisation, epigenetic states and transcription (80, 81).

Given the unprecedented resolution, throughput and applicability of these new super resolution technologies it is conceivable that they could be used to examine the nanoscale genome organisation of antigen receptor loci in thousands of adaptive immune cell progenitors of any species. Taking mouse *Igh* as an example 700 probes would be sufficient to cover the entirety of the expansive 2 million base pair locus at a 3 kb resolution. Given the 113 V_H region gene segments are mostly separated from each other by at least 5 kb (86), 3 kb resolution would be sufficient to reveal the location of all V_H gene segments, along with the rest of the locus, within thousands of individual cells. While fixation required by sequential imaging prohibits a live view of the recombination process, a compilation analysis from the thousands of single cells could reveal an unparalleled view of the local genomic environment in which recombination occurs (80, 84, 87). This could reveal patterns of order, indicative of stable, consistent position or interactions, or disorder, potentially revealing regions undergoing random diffusion. For example, it could be that locus contraction consistently brings particular regions into physical proximity, relative to all others. Alternatively, it could be that the entire locus diffuses with minimal physical constraints and no discernible patterns of interaction. Either way these breakthrough super resolution technologies could enable a greater understanding of the role of diffusion and physical proximity during recombination.

As for live imaging, the fixation required for ORCA and Hi-M would also obstruct downstream examination of the physiological impacts of the visualised genomic organisation. For example, even if as hypothesised the distal V_H gene segments are revealed to contract to, then diffuse near, the D-J region, the ultimately selected segment could not be confirmed within fixed cells. However, here it is worth remembering that the near universal applicability of these technologies mean they can not only expand our understanding of steady state conditions, but also be applied to the genetic and molecular manipulation systems used previously to understand recombination. Thus, perturbations to antigen receptor loci genomic organisation could be re-examined using these novel technologies validating and expanding previous conclusions.

Immune Cell Lineage Decisions

Immune cells make up arguably the most diverse cellular system in complex organisms. This diversity requires numerous lineage decisions as an immune cell differentiates from a haematopoietic stem cell. Be they step-wise and absolute or fluid and continuous (88), these decisions are directed by transcription factors (89). Some of these factors as so influential that the expression of a single transcription factor gene can alter a cells lineage fate (90, 91). The cellular consequences of these lineage decisions have been well explored, in part using imaging (7). However, the molecular events underlying immune cell lineage decisions remain largely unexplored.

Recent application of cutting-edge super resolution imaging technologies in other systems have demonstrated the power of these technologies to reveal molecular insights into transcriptional regulation, and thus potentially lineage decisions. For example, in a recent technical masterpiece single molecule tracking combined with target loci locking microscopy was used to reveal the single molecule resolution, real time kinetics of transcription and its regulators in mouse embryonic stem cells (92). As such, phage genome sequences that can be recognised by fluorescently tagged phage coat proteins were engineered into the 3' UTR of two pluripotency transcription factor genes (**Box 8**). This allowed single molecule visualisation of nascent mRNA. In the same cells, RNA polymerase II or other transcriptional regulatory factors (Sox2, Cdk9, Brd4 or Mediator) were fluorescently labelled. This allowed a phenomenally detailed examination of the relationship between the numbers, dynamics and positioning of these factors relative to transcription, revealing hierarchical, highly dynamic (2-10 second turnover) but relatively small clusters (<20 molecules) of all factors at sites of transcription.

As mentioned above single molecule tracking has been previously performed in immune cells (13). However, these experiments were not in the context of lineage decisions or concurrent with transcriptional visualisation. Here we outline experiments applying the visualisation systems used in *Drosophila* transcriptional regulation to immune cell lineage decisions. While ultimately these experiments could be conducted in genetically engineered primary cells, there are numerous *in vitro* systems in which immune cells can be induced to make lineage decisions. For example, the monocytic cell line THP-1 can be induced to differentiate into M1 or M2 macrophages by treatment with propidium monoazide (93).

BOX 8 | While visualisation of total RNA or DNA is relatively trivial, identification of specific RNA species or DNA regions within the vast cellular pool of both is far from it (76). The visualisation of RNA is most frequently used to identify transcriptional activity based upon concentrations of specific RNA species. For many years, RNA Fluorescence *In Situ* Hybridization (FISH) (77) was the method of choice. However, the number of different RNA species detected was limited by fluorescence spectra. Recent multiplexing technologies resolved this issue using sequential imaging allowing visualisation of over a thousand RNA species in a single cell (8, 9). While FISH requires sample fixation, there are a number of imaging technologies that allow visualisation of RNA in live cells. These utilise small molecule fluorescent dyes (molecular beacons, nanoflares and dye aptamers) or fluorescent proteins fused to RNA aptamer binding proteins (MS2, PP7 or pumilio1) or single stranded RNA-binding Cas9 (rCas9) (78). The aptamer strategies require genetic engineering of the RNA of interest to insert aptamer sequences while beacons, nanoflares and rCas9 bind native RNA species. Similar to RNA visualisation, DNA FISH (79) has traditionally been the method used to view locus position within fixed cells, with the same spectral constraints. Recent technological advances have allowed both sequential imaging in fixed cells [ORCA (80), Hi-M (81)] and imaging DNA in live cells (10, 82). Similar to the multiplexed RNA-FISH technologies the DNA sequential imaging technologies use successive rounds of imaging separated by fluorescent stranddisplacement to reveal the location of, and relationship between, numerous regions of DNA. Imaging DNA regions of interest in live cells currently relies upon the binding of tagged and catalytically dead Cas9 (dCas9) to these loci. This creates challenges in delivering sufficient guide RNAs to target labelled dCas9 to the regions of interest. One recent solution includes the development of molecular assembly strategies that allow the introduction of up to 36 guide RNAs into a single cell providing sufficient guide to visualise non-repetitive DNA regions in live cells (10).

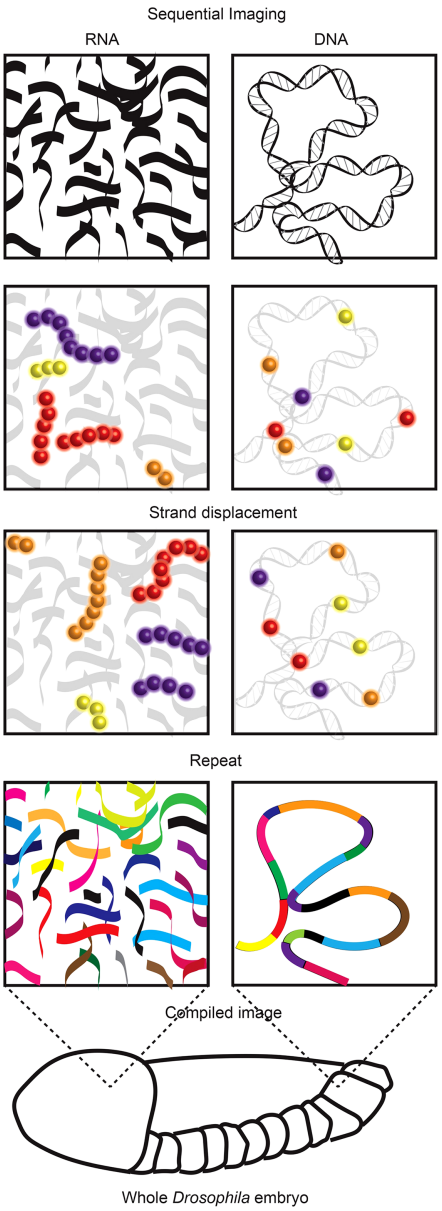

Within this system expression of lineage defining transcription factors, such as STAT1, 3 or 6, could be visualised (94). When the expression of these transcription factors is first detected the locus could be target locked and the relationship between transcription and single molecules of select regulatory factors could be examined. This could reveal how single molecules can regulate expression of these lineage defining transcription factors, and thus influence the fate of the immune lineage.

One obvious weakness of this methodology is the inability to visualise regulatory events prior to transcription initiation. Many of these events are likely just as lineage defining as those after transcription begins. As previously outlined, there are a number of technologies that allow visualisation of specific loci in cells (**Box 8**), however, none have yet been combined with live single molecule tracking of regulatory factors and transcription. Like so many recent molecular technologies one recent breakthrough in visualising loci in live cells utilises catalytically dead Cas9 (dCas9). As such, in a system known as Chimeric Array of gRNA Oligonucleotides (CARGO), numerous guide RNAs are introduced into the cell to guide fluorescently tagged dCas9 to a locus of interest (10) (**Box 8**). While the presence of dCas9 was shown not to dramatically impact local genome organisation (10), it is likely that dCas9 will obstruct other regulatory factors at sites of interest. Thus, other methods of visualising loci of interest prior to transcription will be required if the regulatory events prior to transcription are to be studied at the nanoscale.

While there is still work to be done, recent developments in super resolution imaging have revealed the behaviours of lineage defining molecules, be it transcriptional regulators or genomic loci, in almost unimaginable detail. If, or perhaps when, they are ultimately applied to immune cells, these single molecule scale technologies will provide an unprecedented view of entire antigen receptor gene loci and potentially allow us to watch as a single transcriptional regulator changes the fate of an entire lineage.

CONCLUSION

In the two decades since the invention of laser-based super resolution imaging, scientists have used these technologies to continue the long tradition of using microscopy to understand the immune system.

However, while impactful, all of these discoveries have been made using *in vitro* systems. This is because *in vivo* super resolution technologies still face major technological hurdles. The solution will likely come by emulating current high-resolution *in vivo* imaging systems. These high-resolution systems, such as confocal microscopy, have used surgically implanted windows (95, 96) or simply exteriorized, though still living, organs and tissues in reveal important insights into immune cells *in vivo*. Among many insights, high-resolution imaging has revealed distinct waves of cancer-induced immune cell infiltrates (97) and the role of neutrophils (98, 99), macrophages (100) and dendritic cells (101) in combatting, but also at times inadvertently aiding, cancer progression. Furthermore, the speed of high-resolution imaging technologies has allowed the imaging of interactions between immune cell types in real time. For example, using intravital microscopy in exteriorized lymph nodes of anesthetized mice, Mempel et al. tracked how cytotoxic T cells interacted with antigen-presenting B cells in the presence or absence of regulatory T cells in real time (102). Other examples include interactions between NK cells and dendritic cells (103), macrophages and dendritic cells (104), macrophages and cytotoxic T cells (105), among many others (106).

Finally, and perhaps most clinically relevant, high-resolution *in vivo* imaging has allowed tracking of the immune cell response to drug treatment. For example, Hawkins et al. imaged the retraction of T cell leukaemia in the calvarium of the mouse skull upon dexamethasone treatment (95), while Lohela et al. imaged the reduction in macrophages and dendritic cells in the mouse mammary gland during anti-colony stimulating factor 1 treatment (107).

Expanding these types of studies to super-resolution imaging has significant further challenges. These include scattering of structured light by dynamic tissues (108) to balancing excitation power to detect nanoscale structures while avoiding lethal phototoxicity. However, new technologies continue to push these boundaries (80, 81), often by combining the strengths of existing systems, such as lattice light sheet microscopy and adaptive optics (109). Currently the financial and technical thresholds of these technologies mean they are not widely available; however, excitingly, it is likely that immunologists will soon be able to use these and other, as yet unimagined, technologies to explore nanoscale structures within living tissues. Thus, the future of super resolution imaging is bright and will continue to shed (structured) light on molecular immunology well into the future.

AUTHOR CONTRIBUTIONS

TJ, CK and RA wrote the manuscript. All authors contributed to the article and approved the submitted version.

FUNDING

This work was supported by grants and fellowships from the National Health and Medical Research Council of Australia (TJ #1124081, RA and TJ #1049307, #1100451, CK #1125436). This study was made possible through Victorian State Government Operational Infrastructure Support and Australian Government NHMRC Independent Research Institute Infrastructure Support scheme. The funders had no role in the decision to publish or preparation of the manuscript.

REFERENCES

1. Gordon S. *Phagocytosis: The Host*. Elsevier Science (1999).
2. Lieutaud J. *Elementa Physiologiae*. Detournes, Amsterdam (1749).
3. Senac JB. *D. Traite De La Structure Du Coeur, De Son Action, Et De Ses Maladies*. France: Jacque Vincent (1749).
4. Waller A. Microscopic Observations on the Perforation of the Capillaries by the Corpuscles of the Blood, and Oil - the Origin of Mucus and Pus-Globules. *London Edinburgh Phil Mag J Sci* (1847) 29:397–405. doi: 10.1080/14786444608645527
5. Gustafsson MGL. Surpassing the Lateral Resolution Limit by a Factor of Two Using Structured Illumination Microscopy. *J Microscopy* (2000) 198:82–7. doi: 10.1046/j.1365-2818.2000.00710.x
6. Klar TA, Jakobs S, Dyba M, Egner A, Hell SW. Fluorescence Microscopy With Diffraction Resolution Barrier Broken by Stimulated Emission. *Proc Natl Acad Sci* (2000) 97:8206–10. doi: 10.1073/pnas.97.15.8206
7. Hawkins ED. Advanced Microscopy and Imaging Techniques in Immunology and Cell Biology. *Immunol Cell Biol* (2017) 95:499–500. doi: 10.1038/icb.2017.34
8. Xiao L, Guo J. Multiplexed Single-Cell *in Situ* RNA Analysis by Reiterative Hybridization. *Analytical Methods* (2015) 7:7290–5. doi: 10.1039/C5AY00500K
9. Chen KH, Boettiger AN, Moffitt JR, Wang S, Zhuang X. RNA Imaging. Spatially Resolved, Highly Multiplexed RNA Profiling in Single Cells. *Science* (2015) 348:aaa6090. doi: 10.1126/science.aaa6090
10. Gu B, Swigut T, Spencley A, Bauer MR, Chung M, Meyer T, et al. Transcription-Coupled Changes in Nuclear Mobility of Mammalian Cis-Regulatory Elements. *Science* (2018) 359:1050–5. doi: 10.1126/science.aao3136
11. Miller H, Cosgrove J, Wollman AJM, Taylor E, Zhou Z, O'Toole PJ, et al. High-Speed Single-Molecule Tracking of CXCL13 in the B-Follicle. *Front Immunol* (2018) 9:1073. doi: 10.3389/fimmu.2018.01073
12. Ritter AT, Kapnick SM, Murugesan S, Schwartzberg PL, Griffiths GM, Lippincott-Schwartz J. Cortical Actin Recovery at the Immunological Synapse Leads to Termination of Lytic Granule Secretion in Cytotoxic T Lymphocytes. *Proc Natl Acad Sci USA* (2017) 114:E6585–94. doi: 10.1073/pnas.1710751114
13. Kieffer-Kwon KR, Nimura K, Rao SSP, Xu J, Jung S, Pekowska A, et al. Myc Regulates Chromatin Decompaction and Nuclear Architecture During B Cell Activation. *Mol Cell* (2017) 67:566–78.e510. doi: 10.1016/j.molcel.2017.07.013
14. Mosser DM, Edwards JP. Exploring the Full Spectrum of Macrophage Activation. *Nat Rev Immunol* (2008) 8:958–69. doi: 10.1038/nri2448
15. Pierce SK, Liu W. The Tipping Points in the Initiation of B Cell Signalling: How Small Changes Make Big Differences. *Nat Rev Immunol* (2010) 10:767–77. doi: 10.1038/nri2853
16. Abbas AK, Ault KA, Karnovsky MJ, Unanue ER. Non-Random Distribution of Surface Immunoglobulins on Murine B Lymphocytes. *J Immunol* (1975) 114:1197–204.
17. Betzig E, Patterson GH, Sougrat R, Lindwasser OW, Olenych S, Bonifacino JS, et al. Imaging Intracellular Fluorescent Proteins at Nanometer Resolution. *Science* (2006) 313:1642–5. doi: 10.1126/science.1127344
18. van Zanten TS, Cambi A, Garcia-Parajo MF. A Nanometer Scale Optical View on the Compartmentalization of Cell Membranes. *Biochim Biophys Acta* (2010) 1798:777–87. doi: 10.1016/j.bbamem.2009.09.012
19. Stone MB, Shelby SA, Veatch SL. Super-Resolution Microscopy: Shedding Light on the Cellular Plasma Membrane. *Chem Rev* (2017) 117:7457–77. doi: 10.1021/acs.chemrev.6b00716
20. Rust MJ, Bates M, Zhuang X. Sub-Diffraction-Limit Imaging by Stochastic Optical Reconstruction Microscopy (STORM). *Nat Methods* (2006) 3:793–5. doi: 10.1038/nmeth929
21. Lillemeier BF, Pfeiffer JR, Surviladze Z, Wilson BS, Davis MM. Plasma Membrane-Associated Proteins Are Clustered Into Islands Attached to the Cytoskeleton. *Proc Natl Acad Sci USA* (2006) 103:18992–7. doi: 10.1073/pnas.0609009103
22. Carr AR, Ponjavic A, Basu S, McColl J, Santos AM, Davis S, et al. Three-Dimensional Super-Resolution in Eukaryotic Cells Using the Double-Helix Point Spread Function. *Biophys J* (2017) 112:1444–54. doi: 10.1016/j.bpj.2017.02.023
23. Hu YS, Cang H, Lillemeier BF. Superresolution Imaging Reveals Nanometer- and Micrometer-Scale Spatial Distributions of T-Cell Receptors in Lymph Nodes. *Proc Natl Acad Sci* (2016) 113:7201–6. doi: 10.1073/pnas.1512331113
24. Rossy J, Owen DM, Williamson DJ, Yang Z, Gaus K. Conformational States of the Kinase Lck Regulate Clustering in Early T Cell Signaling. *Nat Immunol* (2013) 14:82–9. doi: 10.1038/ni.2488
25. Roh KH, Lillemeier BF, Wang F, Davis MM. The Coreceptor CD4 Is Expressed in Distinct Nanoclusters and Does Not Colocalize With T-Cell Receptor and Active Protein Tyrosine Kinase P56lck. *Proc Natl Acad Sci USA* (2015) 112:E1604–13. doi: 10.1073/pnas.1503532112
26. Lukes T, Glatzova D, Kvicalova Z, Levet F, Benda A, Letschert S, et al. Quantifying Protein Densities on Cell Membranes Using Super-Resolution Optical Fluctuation Imaging. *Nat Commun* (2017) 8:1731. doi: 10.1038/s41467-017-01857-x
27. Mattila PK, Feest C, Depoil D, Treanor B, Montaner B, Otipoby KL, et al. The Actin and Tetraspanin Networks Organize Receptor Nanoclusters to Regulate B Cell Receptor-Mediated Signaling. *Immunity* (2013) 38:461–74. doi: 10.1016/j.immuni.2012.11.019
28. Maity PC, Blount A, Jumaa H, Ronneberger O, Lillemeier BF, Reth M. B Cell Antigen Receptors of the IgM and IgD Classes Are Clustered in Different Protein Islands That Are Altered During B Cell Activation. *Sci Signal* (2015) 8:ra93. doi: 10.1126/scisignal.2005887
29. Lee J, Sengupta P, Brzostowski J, Lippincott-Schwartz J, Pierce SK. The Nanoscale Spatial Organization of B-Cell Receptors on Immunoglobulin M- and G-Expressing Human B-Cells. *Mol Biol Cell* (2017) 28:511–23. doi: 10.1091/mbc.E16-06-0452
30. Shelby SA, Holowka D, Baird B, Veatch SL. Distinct Stages of Stimulated FcepsilonRI Receptor Clustering and Immobilization Are Identified Through Superresolution Imaging. *Biophys J* (2013) 105:2343–54. doi: 10.1016/j.bpj.2013.09.049
31. Aaron JS, Carson BD, Timlin JA. Characterization of Differential Toll-Like Receptor Responses Below the Optical Diffraction Limit. *Small* (2012) 8:3041–9. doi: 10.1002/smll.201200106
32. Kruger CL, Zeuner MT, Cottrell GS, Widera D, Heilemann M. Quantitative Single-Molecule Imaging of TLR4 Reveals Ligand-Specific Receptor Dimerization. *Sci Signal* (2017) 10. doi: 10.1126/scisignal.aan1308
33. Neumann J, Ziegler K, Gelleri M, Frohlich-Nowoisky J, Liu F, Bellinghausen I, et al. Nanoscale Distribution of TLR4 on Primary Human Macrophages Stimulated With LPS and ATI. *Nanoscale* (2019) 11:9769–79. doi: 10.1039/c9nr00943d
34. Lopes FB, Balint S, Valvo S, Felce JH, Hessel EM, Dustin ML, et al. Membrane Nanoclusters of FcgammaRI Segregate From Inhibitory SIRPalpha Upon Activation of Human Macrophages. *J Cell Biol* (2017) 216:1123–41. doi: 10.1083/jcb.201608094
35. Fan Z, McArdle S, Marki A, Mikulski Z, Gutierrez E, Engelhardt B, et al. Neutrophil Recruitment Limited by High-Affinity Bent Beta2 Integrin Binding Ligand in Cis. *Nat Commun* (2016) 7:12658. doi: 10.1038/ncomms12658
36. Balint S, Lopes FB, Davis DM. A Nanoscale Reorganization of the IL-15 Receptor Is Triggered by NKG2D in a Ligand-Dependent Manner. *Sci Signal* (2018) 11. doi: 10.1126/scisignal.aal3606
37. Lakowicz JR, Szmacinski H, Nowaczyk K, Berndt KW, Johnson M. Fluorescence Lifetime Imaging. *Anal Biochem* (1992) 202:316–30. doi: 10.1016/0003-2697(92)90112-k
38. Ma Y, Pandzic E, Nicovich PR, Yamamoto Y, Kwiatek J, Pageon SV, et al. An Intermolecular FRET Sensor Detects the Dynamics of T Cell Receptor Clustering. *Nat Commun* (2017) 8:15100. doi: 10.1038/ncomms15100
39. Sherman E, Barr V, Manley S, Patterson G, Balagopalan L, Akpan I, et al. Functional Nanoscale Organization of Signaling Molecules Downstream of the T Cell Antigen Receptor. *Immunity* (2011) 35:705–20. doi: 10.1016/j.immuni.2011.10.004
40. Klasener K, Maity PC, Hobeika E, Yang J, Reth M. B Cell Activation Involves Nanoscale Receptor Reorganizations and Inside-Out Signaling by Syk. *Elife* (2014) 3:e02069. doi: 10.7554/eLife.02069
41. Stone MB, Shelby SA, Nunez MF, Wisser K, Veatch SL. Protein Sorting by Lipid Phase-Like Domains Supports Emergent Signaling Function in B Lymphocyte Plasma Membranes. *Elife* (2017) 6. doi: 10.7554/eLife.19891

42. Avalos AM, Bilate AM, Witte MD, Tai AK, He J, Frushicheva MP, et al. Monovalent Engagement of the BCR Activates Ovalbumin-Specific Transnuclear B Cells. *J Exp Med* (2014) 211:365–79. doi: 10.1084/jem.20131603
43. Volkmann C, Brings N, Becker M, Hobeika E, Yang J, Reth M. Molecular Requirements of the B-Cell Antigen Receptor for Sensing Monovalent Antigens. *EMBO J* (2016) 35:2371–81. doi: 10.15252/embj.201694177
44. Kusumi A, Ike H, Nakada C, Murase K, Fujiwara T. Single-Molecule Tracking of Membrane Molecules: Plasma Membrane Compartmentalization and Dynamic Assembly of Raft-Philic Signaling Molecules. *Semin Immunol* (2005) 17:3–21. doi: 10.1016/j.smim.2004.09.004
45. Gowrishankar K, Ghosh S, Saha S, Mayor S, Rao M. Active Remodeling of Cortical Actin Regulates Spatiotemporal Organization of Cell Surface Molecules. *Cell* (2012) 149:1353–67. doi: 10.1016/j.cell.2012.05.008
46. Treanor B, Depoil D, Gonzalez-Granja A, Barral P, Weber M, Dushek O, et al. The Membrane Skeleton Controls Diffusion Dynamics and Signaling Through the B Cell Receptor. *Immunity* (2010) 32:187–99. doi: 10.1016/j.immuni.2009.12.005
47. Freeman SA, Jaumouille V, Choi K, Hsu BE, Wong HS, Abraham L, et al. Toll-Like Receptor Ligands Sensitize B-Cell Receptor Signalling by Reducing Actin-Dependent Spatial Confinement of the Receptor. *Nat Commun* (2015) 6:6168. doi: 10.1038/ncomms7168
48. Hammer JA, Wang JC, Saeed M, Pedrosa AT. Origin, Organization, Dynamics, and Function of Actin and Actomyosin Networks at the T Cell Immunological Synapse. *Annu Rev Immunol* (2019) 37:201–24. doi: 10.1146/annurev-immunol-042718-041341
49. Jang JH, Huang Y, Zheng P, Jo MC, Bertolet G, Zhu MX, et al. Imaging of Cell-Cell Communication in a Vertical Orientation Reveals High-Resolution Structure of Immunological Synapse and Novel PD-1 Dynamics. *J Immunol* (2015) 195:1320–30. doi: 10.4049/jimmunol.1403143
50. Rak GD, Mace EM, Banerjee PP, Svitkina T, Orange JS. Natural Killer Cell Lytic Granule Secretion Occurs Through a Pervasive Actin Network at the Immune Synapse. *PloS Biol* (2011) 9:e1001151. doi: 10.1371/journal.pbio.1001151
51. Fritzsche M, Fernandes RA, Chang VT, Colin-York H, Clausen MP, Felce JH, et al. Cytoskeletal Actin Dynamics Shape a Ramifying Actin Network Underpinning Immunological Synapse Formation. *Sci Adv* (2017) 3:e1603032. doi: 10.1126/sciadv.1603032
52. Ambrose EJ. A Surface Contact Microscope for the Study of Cell Movements. *Nature* (1956) 178:1194. doi: 10.1038/1781194a0
53. Ashdown GW, Burn GL, Williamson DJ, Pandzic E, Peters R, Holden M, et al. Live-Cell Super-Resolution Reveals F-Actin and Plasma Membrane Dynamics at the T Cell Synapse. *Biophys J* (2017) 112:1703–13. doi: 10.1016/j.bpj.2017.01.038
54. Carisey AF, Mace EM, Saeed MB, Davis DM, Orange JS. Nanoscale Dynamism of Actin Enables Secretory Function in Cytolytic Cells. *Curr Biol* (2018) 28:489–502.e489. doi: 10.1016/j.cub.2017.12.044
55. Chen BC, Legant WR, Wang K, Shao L, Milkie DE, Davidson MW, et al. Lattice Light-Sheet Microscopy: Imaging Molecules to Embryos at High Spatiotemporal Resolution. *Science* (2014) 346:1257998. doi: 10.1126/science.1257998
56. Ritter AT, Asano Y, Stinchcombe JC, Dieckmann NM, Chen BC, Gawden-Bone C, et al. Actin Depletion Initiates Events Leading to Granule Secretion at the Immunological Synapse. *Immunity* (2015) 42:864–76. doi: 10.1016/j.immuni.2015.04.013
57. Brown AC, Oddos S, Dobbie IM, Alakoskela JM, Parton RM, Eissmann P, et al. Remodelling of Cortical Actin Where Lytic Granules Dock at Natural Killer Cell Immune Synapses Revealed by Super-Resolution Microscopy. *PloS Biol* (2011) 9:e1001152. doi: 10.1371/journal.pbio.1001152
58. Hsu HT, Mace EM, Carisey AF, Viswanath DI, Christakou AE, Wiklund M, et al. NK Cells Converge Lytic Granules to Promote Cytotoxicity and Prevent Bystander Killing. *J Cell Biol* (2016) 215:875–89. doi: 10.1083/jcb.201604136
59. Bhat R, Watzl C. Serial Killing of Tumor Cells by Human Natural Killer Cells–Enhancement by Therapeutic Antibodies. *PloS One* (2007) 2:e326. doi: 10.1371/journal.pone.0000326
60. Ming M, Schirra C, Becherer U, Stevens DR, Rettig J. Behavior and Properties of Mature Lytic Granules at the Immunological Synapse of Human Cytotoxic T Lymphocytes. *PloS One* (2015) 10:e0135994. doi: 10.1371/journal.pone.0135994
61. Gwalani LA, Orange JS. Single Degranulations in NK Cells Can Mediate Target Cell Killing. *J Immunol* (2018) 200:3231–43. doi: 10.4049/jimmunol.1701500
62. Pogo BG, Allfrey VG, Mirsky AE. RNA Synthesis and Histone Acetylation During the Course of Gene Activation in Lymphocytes. *Proc Natl Acad Sci USA* (1966) 55:805–12. doi: 10.1073/pnas.55.4.805
63. Fowler T, Garruss AS, Ghosh A, De S, Becker KG, Wood WH, et al. Divergence of Transcriptional Landscape Occurs Early in B Cell Activation. *Epigenet Chromatin* (2015) 8:20. doi: 10.1186/s13072-015-0012-x
64. Zhang Y, Fear DJ, Willis-Owen SA, Cookson WO, Moffatt MF. Global Gene Regulation During Activation of Immunoglobulin Class Switching in Human B Cells. *Sci Rep* (2016) 6:37988. doi: 10.1038/srep37988
65. Morrish RB, Hermes M, Metz J, Stone N, Pagliara S, Chahwan R, et al. Single Cell Imaging of Nuclear Architecture Changes. *Front Cell Dev Biol* (2019) 7:141. doi: 10.3389/fcell.2019.00141
66. Axelrod D, Koppel DE, Schlessinger J, Elson E, Webb WW. Mobility Measurement by Analysis of Fluorescence Photobleaching Recovery Kinetics. *Biophys J* (1976) 16:1055–69. doi: 10.1016/S0006-3495(76)85755-4
67. Fuxa M, Skok J, Souabni A, Salvagiotto G, Roldan E, Busslinger M. Pax5 Induces V-To-DJ Rearrangements and Locus Contraction of the Immunoglobulin Heavy-Chain Gene. *Genes Dev* (2004) 18:411–22. doi: 10.1101/gad.291504
68. Kosak ST, Skok JA, Medina KL, Riblet R, Le Beau MM, Fisher AG, et al. Subnuclear Compartmentalization of Immunoglobulin Loci During Lymphocyte Development. *Science* (2002) 296:158–62. doi: 10.1126/science.1068768
69. Johanson TM, Chan WF, Keenan CR, Allan RS. Genome Organization in Immune Cells: Unique Challenges. *Nat Rev Immunol* (2019) 19:448–56. doi: 10.1038/s41577-019-0155-2
70. Roldan E, Fuxa M, Chong W, Martinez D, Novatchkova M, Busslinger M, et al. Locus 'Decontraction' and Centromeric Recruitment Contribute to Allelic Exclusion of the Immunoglobulin Heavy-Chain Gene. *Nat Immunol* (2005) 6:31–41. doi: 10.1038/ni1150
71. Sayegh CE, Jhunjhunwala S, Riblet R, Murre C. Visualization of Looping Involving the Immunoglobulin Heavy-Chain Locus in Developing B Cells. *Genes Dev* (2005) 19:322–7. doi: 10.1101/gad.1254305
72. Skok JA, Gisler R, Novatchkova M, Farmer D, de Laat W, Busslinger M. Reversible Contraction by Looping of the Tcra and Tcrb Loci in Rearranging Thymocytes. *Nat Immunol* (2007) 8:378–87. doi: 10.1038/ni1448
73. Lutz E. Fractional Langevin Equation. *Phys Rev E* (2001) 64:51106. doi: 10.1103/PhysRevE.64.051106
74. Jain S, Ba Z, Zhang Y, Dai HQ, Alt FW. CTCF-Binding Elements Mediate Accessibility of RAG Substrates During Chromatin Scanning. *Cell* (2018) 174:102–116 e114. doi: 10.1016/j.cell.2018.04.035
75. Lucas JS, Zhang Y, Dudko OK, Murre C. 3D Trajectories Adopted by Coding and Regulatory DNA Elements: First-Passage Times for Genomic Interactions. *Cell* (2014) 158:339–52. doi: 10.1016/j.cell.2014.05.036
76. Weiss LE, Naor T, Shechtman Y. Observing DNA in Live Cells. *Biochem Soc Trans* (2018) 46:729–40. doi: 10.1042/BST20170301
77. Bauman JG, Wiegant J, Borst P, van Duijn P. A New Method for Fluorescence Microscopical Localization of Specific DNA Sequences by *in Situ* Hybridization of Fluorochromelabelled RNA. *Exp Cell Res* (1980) 128:485–90. doi: 10.1016/0014-4827(80)90087-7
78. Specht EA, Braselmann E, Palmer AE. A Critical and Comparative Review of Fluorescent Tools for Live-Cell Imaging. *Annu Rev Physiol* (2017) 79:93–117. doi: 10.1146/annurev-physiol-022516-034055
79. Langer-Safer PR, Levine M, Ward DC. Immunological Method for Mapping Genes on Drosophila Polytene Chromosomes. *Proc Natl Acad Sci USA* (1982) 79:4381–5. doi: 10.1073/pnas.79.14.4381
80. Mateo LJ, Murphy SE, Hafner A, Cinquini IS, Walker CA, Boettiger AN. Visualizing DNA Folding and RNA in Embryos at Single-Cell Resolution. *Nature* (2019) 568:49–54. doi: 10.1038/s41586-019-1035-4
81. Cardozo Gizzi AM, Cattoni DI, Fiche JB, Espinola SM, Gurgo J, Messina O, et al. Microscopy-Based Chromosome Conformation Capture Enables Simultaneous Visualization of Genome Organization and Transcription in Intact Organisms. *Mol Cell* (2019) 74:212–22.e215. doi: 10.1016/j.molcel.2019.01.011

82. Chen B, Gilbert LA, Cimini BA, Schnitzbauer J, Zhang W, Li GW, et al. Dynamic Imaging of Genomic Loci in Living Human Cells by an Optimized CRISPR/Cas System. *Cell* (2013) 155:1479–91. doi: 10.1016/j.cell.2013.12.001
83. Nir G, Farabella I, Perez Estrada C, Ebeling CG, Beliveau BJ, Sasaki HM, et al. Walking Along Chromosomes With Super-Resolution Imaging, Contact Maps, and Integrative Modeling. *PloS Genet* (2018) 14:e1007872. doi: 10.1371/journal.pgen.1007872
84. Bintu B, Mateo LJ, Su JH, Sinnott-Armstrong NA, Parker M, Kinrot S, et al. Super-Resolution Chromatin Tracing Reveals Domains and Cooperative Interactions in Single Cells. *Science* (2018) 362(6413):eaau1783. doi: 10.1126/science.aau1783
85. Wang S, Su JH, Beliveau BJ, Bintu B, Moffitt JR, Wu CT, et al. Spatial Organization of Chromatin Domains and Compartments in Single Chromosomes. *Science* (2016) 353:598–602. doi: 10.1126/science.aaf8084
86. Proudhon C, Hao B, Raviram R, Chaumeil J, Skok JA. Long-Range Regulation of V(D)J Recombination. *Adv Immunol* (2015) 128:123–82. doi: 10.1016/bs.ai.2015.07.003
87. Finn EH, Pegoraro G, Brandao HB, Valton AL, Oomen ME, Dekker J, et al. Extensive Heterogeneity and Intrinsic Variation in Spatial Genome Organization. *Cell* (2019) 176:1502–15.e1510. doi: 10.1016/j.cell.2019.01.020
88. Brown G, Ceredig R. *Cell Lineage Choice During Haematopoiesis: A Commemorative Issue in Honor of Professor Antonius Rolink*. MDPI AG (2018).
89. Stadhouders R, Filion GJ, Graf T. Transcription Factors and 3D Genome Conformation in Cell-Fate Decisions. *Nature* (2019) 569:345–54. doi: 10.1038/s41586-019-1182-7
90. Rothenberg EV. The Chromatin Landscape and Transcription Factors in T Cell Programming. *Trends Immunol* (2014) 35:195–204. doi: 10.1016/j.it.2014.03.001
91. Nutt SL, Taubenheim N, Hasbold J, Corcoran LM, Hodgkin PD. The Genetic Network Controlling Plasma Cell Differentiation. *Semin Immunol* (2011) 23:341–9. doi: 10.1016/j.smim.2011.08.010
92. Li J, Dong A, Saydaminova K, Chang H, Wang G, Ochiai H, et al. Single-Molecule Nanoscopy Elucidates RNA Polymerase II Transcription at Single Genes in Live Cells. *Cell* (2019) 178:491–506.e428. doi: 10.1016/j.cell.2019.05.029
93. Gatto F, Cagliani R, Catelani T, Guarnieri D, Moglianetti M, Pompa PP, et al. PMA-Induced THP-1 Macrophage Differentiation Is Not Impaired by Citrate-Coated Platinum Nanoparticles. *Nanomaterials (Basel)* (2017) 7 (10):332. doi: 10.3390/nano7100332
94. Li H, Jiang T, Li MQ, Zheng XL, Zhao GJ. Transcriptional Regulation of Macrophages Polarization by MicroRNAs. *Front Immunol* (2018) 9:1175. doi: 10.3389/fimmu.2018.01175
95. Hawkins ED, Duarte D, Akinduro O, Khorshed RA, Passaro D, Nowicka M, et al. T-Cell Acute Leukaemia Exhibits Dynamic Interactions With Bone Marrow Microenvironments. *Nature* (2016) 538:518–22. doi: 10.1038/nature19801
96. Schietinger A, Arina A, Liu RB, Wells S, Huang J, Engels B, et al. Longitudinal Confocal Microscopy Imaging of Solid Tumor Destruction Following Adoptive T Cell Transfer. *Oncoimmunology* (2013) 2:e26677. doi: 10.4161/onci.26677
97. Headley MB, Bins A, Nip A, Roberts EW, Looney MR, Gerard A, et al. Visualization of Immediate Immune Responses to Pioneer Metastatic Cells in the Lung. *Nature* (2016) 531:513–7. doi: 10.1038/nature16985
98. Cools-Lartigue J, Spicer J, McDonald B, Gowing S, Chow S, Giannias B, et al. Neutrophil Extracellular Traps Sequester Circulating Tumor Cells and Promote Metastasis. *J Clin Invest* (2013) 123(8):3446–58. doi: 10.1172/JCI67484
99. Spicer JD, McDonald B, Cools-Lartigue JJ, Chow SC, Giannias B, Kubes P, et al. Neutrophils Promote Liver Metastasis *via* Mac-1-Mediated Interactions With Circulating Tumor Cells. *Cancer Res* (2012) 72:3919–27. doi: 10.1158/0008-5472.CAN-11-2393
100. Harney AS, Arwert EN, Entenberg D, Wang Y, Guo P, Qian BZ, et al. Real-Time Imaging Reveals Local, Transient Vascular Permeability, and Tumor Cell Intravasation Stimulated by TIE2hi Macrophage-Derived VEGFA. *Cancer Discov* (2015) 5:932–43. doi: 10.1158/2159-8290.CD-15-0012
101. Roberts EW, Broz ML, Binnewies M, Headley MB, Nelson AE, Wolf DM, et al. Critical Role for CD103(+)/CD141(+) Dendritic Cells Bearing CCR7 for Tumor Antigen Trafficking and Priming of T Cell Immunity in Melanoma. *Cancer Cell* (2016) 30:324–36. doi: 10.1016/j.ccell.2016.06.003
102. Mempel TR, Pittet MJ, Khazaie K, Weninger W, Weissleder R, von Boehmer H, et al. Regulatory T Cells Reversibly Suppress Cytotoxic T Cell Function Independent of Effector Differentiation. *Immunity* (2006) 25:129–41. doi: 10.1016/j.immuni.2006.04.015
103. Mingozzi F, Spreafico R, Gorletta T, Cigni C, Di Gioia M, Caccia M, et al. Prolonged Contact With Dendritic Cells Turns Lymph Node-Resident NK Cells Into Anti-Tumor Effectors. *EMBO Mol Med* (2016) 8:1039–51. doi: 10.15252/emmm.201506164
104. Moalli F, Proulx ST, Schwendener R, Detmar M, Schlapbach C, Stein JV. Intravital and Whole-Organ Imaging Reveals Capture of Melanoma-Derived Antigen by Lymph Node Subcapsular Macrophages Leading to Widespread Deposition on Follicular Dendritic Cells. *Front Immunol* (2015) 6:114. doi: 10.3389/fimmu.2015.00114
105. Mrass P, Takano H, Ng LG, Daxini S, Lasaro MO, Iparraguirre A, et al. Random Migration Precedes Stable Target Cell Interactions of Tumor-Infiltrating T Cells. *J Exp Med* (2006) 203:2749–61. doi: 10.1084/jem.20060710
106. Torcellan T, Stolp J, Chtanova T. Imaging Sheds Light on Immune Cell Migration and Function in Cancer. *Front Immunol* (2017) 8:309. doi: 10.3389/fimmu.2017.00309
107. Lohela M, Casbon AJ, Olow A, Bonham L, Branstetter D, Weng N, et al. Intravital Imaging Reveals Distinct Responses of Depleting Dynamic Tumor-Associated Macrophage and Dendritic Cell Subpopulations. *Proc Natl Acad Sci USA* (2014) 111:E5086–95. doi: 10.1073/pnas.1419899111
108. Vicidomini G, Bianchini P, Diaspro A. STED Super-Resolved Microscopy. *Nat Methods* (2018) 15:173–82. doi: 10.1038/nmeth.4593
109. Liu TL, Upadhyayula S, Milkie DE, Singh V, Wang K, Swinburne IA, et al. Observing the Cell in Its Native State: Imaging Subcellular Dynamics in Multicellular Organisms. *Science* (2018) 360(6386):eaaq1392. doi: 10.1126/science.aaq1392

Conflict of Interest: The authors declare that the research was conducted in the absence of any commercial or financial relationships that could be construed as a potential conflict of interest.

frontiers in Oncology

ORIGINAL RESEARCH
published: 16 December 2021
doi: 10.3389/fonc.2021.786191

Radiolabeled Monoclonal Antibody Against Colony-Stimulating Factor 1 Receptor Specifically Distributes to the Spleen and Liver in Immunocompetent Mice

*Stijn J. H. Waaijer[1], Frans V. Suurs[1], Cheei-Sing Hau[2], Kim Vrijland[2], Karin E. de Visser[2,3], Derk Jan A. de Groot[1], Elisabeth G. E. de Vries[1], Marjolijn N. Lub-de Hooge[4,5] and Carolina P. Schröder[1]**

[1] Department of Medical Oncology, University Medical Center Groningen, University of Groningen, Groningen, Netherlands, [2] Division of Tumor Biology & Immunology, Oncode Institute, Netherlands Cancer Institute, Amsterdam, Netherlands, [3] Department of Immunohematology and Blood Transfusion, Leiden University Medical Center, Leiden, Netherlands, [4] Department of Clinical Pharmacy and Pharmacology, University Medical Center Groningen, University of Groningen, Groningen, Netherlands, [5] Department of Nuclear Medicine and Molecular Imaging, University Medical Center Groningen, University of Groningen, Groningen, Netherlands

OPEN ACCESS

Edited by:
Nick Devoogdt,
Free University of Brussels, Belgium

Reviewed by:
Andreas Maurer,
University of Tübingen, Germany
Guus Van Dongen,
Amsterdam University Medical Center, Netherlands

***Correspondence:**
Carolina P. Schröder
c.p.schroder@umcg.nl

Specialty section:
This article was submitted to Cancer Immunity and Immunotherapy, a section of the journal Frontiers in Oncology

Received: *29 September 2021*
Accepted: *10 November 2021*
Published: *16 December 2021*

Citation:
Waaijer SJH, Suurs FV, Hau C-S, Vrijland K, de Visser KE, de Groot DJA, de Vries EGE, Lub-de Hooge MN and Schröder CP (2021) Radiolabeled Monoclonal Antibody Against Colony-Stimulating Factor 1 Receptor Specifically Distributes to the Spleen and Liver in Immunocompetent Mice. Front. Oncol. 11:786191. doi: 10.3389/fonc.2021.786191

Macrophages can promote tumor development. Preclinically, targeting macrophages by colony-stimulating factor 1 (CSF1)/CSF1 receptor (CSF1R) monoclonal antibodies (mAbs) enhances conventional therapeutics in combination treatments. The physiological distribution and tumor uptake of CSF1R mAbs are unknown. Therefore, we radiolabeled a murine CSF1R mAb and preclinically visualized its biodistribution by PET. CSF1R mAb was conjugated to *N*-succinyl-desferrioxamine (*N*-suc-DFO) and subsequently radiolabeled with zirconium-89 (^{89}Zr). Optimal protein antibody dose was first determined in non-tumor-bearing mice to assess physiological distribution. Next, biodistribution of optimal protein dose and ^{89}Zr-labeled isotype control was compared with PET and *ex vivo* biodistribution after 24 and 72 h in mammary tumor-bearing mice. Tissue autoradiography and immunohistochemistry determined radioactivity distribution and tissue macrophage presence, respectively. [^{89}Zr]Zr-DFO-*N*-suc-CSF1R-mAb optimal protein dose was 10 mg/kg, with blood pool levels of 10 ± 2% injected dose per gram tissue (ID/g) and spleen and liver uptake of 17 ± 4 and 11 ± 4%ID/g at 72 h. In contrast, 0.4 mg/kg of [^{89}Zr]Zr-DFO-*N*-suc-CSF1R mAb was eliminated from circulation within 24 h; spleen and liver uptake was 126 ± 44% and 34 ± 7%ID/g, respectively. Tumor-bearing mice showed higher uptake of [^{89}Zr]Zr-DFO-*N*-suc-CSF1R-mAb in the liver, lymphoid tissues, duodenum, and ileum, but not in the tumor than did ^{89}Zr-labeled control at 72 h. Immunohistochemistry and autoradiography showed that ^{89}Zr was localized to macrophages within lymphoid tissues. Following [^{89}Zr]Zr-DFO-*N*-suc-CSF1R-mAb administration, tumor macrophages were almost absent, whereas isotype-group tumors contained over 500 cells/mm^2. We hypothesize that intratumoral macrophage depletion by [^{89}Zr]Zr-DFO-*N*-suc-CSF1R-mAb precluded tumor uptake higher than

^{89}Zr-labeled control. Translation of molecular imaging of macrophage-targeting therapeutics to humans may support macrophage-directed therapeutic development.

Keywords: positron emission tomography (PET), antibody immunotherapy, noninvasive imaging in animal models, pharmacokinetics/pharmacodynamics (PKPD), tumor-associated macrophage (TAM)

INTRODUCTION

The tumor microenvironment comprises several cell types, including fibroblasts and many different immune cells. Recently, macrophages gained attention as an important part of the intratumoral immune cell compartment. A high number of tumor-associated macrophages (TAMs) correlate with a higher tumor grade and a worse prognosis for patients with several cancer types (1–4).

In various preclinical mouse tumor models, TAMs have been targeted with small molecules or antibodies, resulting in depletion, repolarization, activation, or inhibition of recruitment to the tumor (5–12). These strategies synergized with antitumor effects of cancer therapies, including immune checkpoint inhibitors, chemotherapy, and radiotherapy (5–14). Especially in preclinical models of mammary tumors, strong synergistic antitumor effects were seen when treatment modalities were combined with targeting TAMs (9–11, 13, 14). One of these preclinical models is the *K14cre;Cdh1$^{F/F}$;Trp53$^{F/F}$* (KEP) mouse model for spontaneous mammary tumorigenesis. Mammary tumors arising in KEP mice resemble human invasive lobular carcinomas (15) and are strongly infiltrated with macrophages (11). Targeting TAMs by inhibiting their survival in the KEP model provoked a type 1 interferon response, which enhanced the efficacy of platinum-based chemotherapies (11).

One of the major routes for targeting TAMs is inhibition of the colony-stimulating factor-1 (CSF1; CD115)–CSF1 receptor (CSF1R) axis. The CSF1–CSF1R axis is a crucial macrophage survival and differentiation pathway (16). Multiple monoclonal antibodies (mAbs) targeting CSF1R have been developed to disrupt the immunosuppressive tumor microenvironment and are evaluated in early clinical trials. They generally appear tolerable, but monotherapy efficacy is still limited (1, 17). Macrophage targeting as an adjunct to potentiate chemo-, immuno-, or radiotherapy may be more successful. However, insight into the whole-body distribution and tumor uptake of CSF1R mAbs is lacking.

Breast cancer is thought to be relatively insensitive to immunotherapy than other tumor types, which is why combination strategies to improve efficacy are potentially relevant (18). Non-invasive imaging of CSF1R mAb biodistribution could provide information regarding physiological distribution and tumor targeting and thereby support the rational design of combination strategies that include macrophage targeting for breast cancer (19–21). Choosing a preclinical model reflecting the complexity of the tumor immune microenvironment and its components is thereby essential to mimic the human setting.

Therefore, in the present study, we studied the biodistribution of a radiolabeled CSF1R mAb that targets murine CSF1R. To enable radiolabeling, we conjugated the CSF1R mAb with *N*-succinyl (*N*-suc) desferrioxamine (DFO) followed by coupling to PET isotope zirconium-89 (^{89}Zr). Thus, its behavior in a mouse model bearing an orthotopically transplanted KEP tumor can be studied. We tested the impact of protein dose on [^{89}Zr]Zr-DFO-*N*-suc-CSF1R-mAb pharmacokinetics. Furthermore, with complementary *ex vivo* techniques including autoradiography and immunohistochemistry, mAb localization and the presence of tissue macrophages were assessed.

MATERIALS AND METHODS

Antibody Conjugation and Labeling

Anti-mouse CSF1R mAb (rat IgG2a; clone AFS98) and rat IgG2a isotype control (clone 2A3) were obtained from BioXCell. Antibodies were conjugated with tetrafluorophenol-*N*-succinyl-DFO B-Fe (TFP-*N*-suc-DFO-Fe; ABX). To improve conjugation efficiency, antibodies were concentrated using Vivaspin 2, 10-kDa centrifugal concentrators (Sartorius). The pH was adjusted to 9.5 using 0.1 M of Na_2CO_3, followed by a sevenfold molar excess of TFP-*N*-suc-DFO-Fe. After a 1-h incubation at room temperature with mild agitation, conjugation efficiency was determined using a Waters size-exclusion high-performance liquid chromatography (SE HPLC) system. This SE HPLC system is equipped with a dual-wavelength absorbance detector (280 versus 430 nm), and TSK-gel SW column G3000SWXL 5 μm, 7.8 mm (Joint Analytical Systems) using phosphate-buffered saline (PBS; 9.0 mM of sodium phosphate, 1.3 mM of potassium phosphate, 140 mM of sodium chloride, pH 7.4; UMCG; flow 0.7 ml/min) as mobile phase. On average, four molecules of TFP-*N*-suc-DFO-Fe were conjugated to one antibody molecule CSF1R mAb or IgG2a. Next, pH was adjusted to 4.5 using 0.25 M of H_2SO_4, and a 50-fold molar excess EDTA was added to remove Fe during 90 min of incubation at 37°C with mild agitation. The reaction mixture was purified using a PD Minitrap G-25 (GE Healthcare) according to manufacturer's gravity protocol to deplete unbound TFP-*N*-suc-DFO and EDTA. After purification, protein concentration and purity were assessed by UV-Vis spectrophotometry (Cary 60 Agilent) and SE HPLC, respectively.

Thus, obtained purified intermediates DFO-*N*-suc-CSF1R-mAb and DFO-*N*-suc-IgG2a were radiolabeled with [^{89}Zr]Zr-oxalate (Perkin Elmer) as described before (22). Radiochemical purity was assessed by a trichloroacetic acid precipitation assay (23), and antibody purity was assessed by SE HPLC using an absorbance detector (280 nm) and in-line radioactivity detector (23).

CSF1R Binding Assay

Maintained immunoreactivity of DFO-*N*-suc-CSF1R-mAb to CSF1R extracellular domain was determined using an ELISA.

A Nunc 96-well polystyrene conical bottom microwell plate (Thermo Fisher Scientific) was coated overnight at 4°C with 1 µg/ml of recombinant mouse CSF1R protein (Sino Biological) in a 100 µl of 0.05 M Na_2CO_3 solution, pH 9.6. Next, wells were washed three times with 0.05% polysorbate 20/PBS. The aspecific binding was blocked with a 0.5% bovine serum albumin (BSA; Sigma-Aldrich)/0.05% polysorbate 20/PBS for 2 h. Subsequently, the plate was incubated at room temperature with 100 µl concentration series of parental CSF1R mAb or DFO-*N*-suc-CSF1R-mAb ranging from 0.001 to 20 nM. After 1-h incubation, wells were washed three times and incubated with peroxidase-conjugated rabbit anti-rat polyclonal Ab (P0450; Dako) for 30 min at room temperature. Finally, wells were washed three times and incubated for 5 min with 3,3′,5,5′–tetramethylbenzidine (SureBlue Reserve; Seracare) followed by 1 M of hydrochloric acid to stop the reaction. Absorbance was measured at 450 nm in a microplate reader.

Animal Experiments

All animal experiments were approved by both the Institutional Animal Care and Use Committee of the University of Groningen and the Netherlands Cancer Institute. Food and water were provided *ad libitum*. Female FVB/N mice of 10–12 weeks of age (Janvier Labs) were studied. Mammary tumors from the KEP mouse model for spontaneous mammary tumorigenesis were collected to be implanted in FVB/N female mice (11, 15). In short, KEP tumors were collected in ice-cold PBS, cut into small pieces, and resuspended in DMEM F12 containing 60% fetal calf serum (FCS) and 20% dimethyl sulfoxide and stored at −150°C. KEP tumor pieces (1 × 1 mm) were placed into the mammary fat pad of FVB/N female mice. Tumor growth was monitored twice weekly by palpation and caliper measurements. The radiolabeled antibody was retro-orbitally injected when tumors reached a size of 200 to 400 mm^3. Mice were allocated randomly to antibody groups. Antibody doses comprised 0.4 mg/kg (10 µg, 0.067 nmol) of ^{89}Zr-labeled antibody, and at higher doses, an unlabeled unconjugated antibody of up to 4 mg/kg (100 µg, 0.67 nmol) or 10 mg/kg (250 µg, 1.67 nmol) was added. Mice were anesthetized during microPET scanning with isoflurane/oxygen inhalation (5% induction, 2.5% maintenance). Details regarding antibody dose, number of animals, microPET scans, and time of biodistribution are included in the figure legends.

MicroPET Scanning and *Ex Vivo* Biodistribution

All microPET scans were executed in a Focus 200 rodent scanner (CTI Siemens). Mice were kept warm on heating mats. A transmission scan of 515 s was obtained using a ^{57}Co point source for tissue attenuation. The reconstruction of microPET scans was performed as previously described (24). After reconstruction, images were interpolated with trilinear interpolation using PMOD software (version 3.7, PMOD Technologies LLC). Coronal microPET images or maximal intensity projection images were used for display. Volumes of interest (VOIs) of the whole tumor were drawn based on biodistribution tumor weight. For the heart, a 92-mm^3 ellipsoid VOI in the coronal plane was drawn. Furthermore, representative VOIs were drawn for the spleen and liver and subsequently quantified. Data are expressed as the mean standardized uptake value (SUV_{mean}).

For all *ex vivo* biodistribution studies, the tumor, whole blood, and organs of interest were retrieved and weighed. Whole blood was collected in sodium heparin tubes (BD) and was fractionated by centrifugal force to obtain plasma. Samples, together with radiolabeled antibody standards, were counted in a calibrated well-type g-counter (LKB Instruments). Antibody uptake is expressed as the percentage injected dose per gram of tissue (%ID/g).

Ex Vivo Autoradiography and Immunohistochemistry

Organs of interest, including tumors, were fixed in formalin (4% paraformaldehyde/PBS) overnight, followed by paraffin embedding. Sections measuring 4 µm were subsequently exposed overnight to a phosphor screen (PerkinElmer) in an X-ray cassette. Signal was detected with a Cyclone Storage Phosphor System (PerkinElmer). Slides used for *ex vivo* autoradiography were deparaffinized. After that, they were stained with H&E and digitalized with NanoZoomer and NDP software (Hamamatsu). Subsequent slides were stained for murine pan-macrophage marker F4/80 with a rat anti-mouse F4/80 mAb (CI:A3; Bio-Rad) by immunohistochemistry. For antigen retrieval, slides were incubated for 15 min at 95°C in citrate buffer (10 mM, pH 6). The primary antibody was used in a 1:250 dilution for overnight incubation at 4°C. This incubation was followed by a rabbit anti-rat (1:100; P0450; Dako) and a peroxidase-conjugated goat anti-rabbit polyclonal Ab (1:100; P0448; Dako). Peroxidase activity was visualized by the addition of 3,3′-diaminobenzidine. Strong membrane staining above background noise was considered positive and was identified with both the combined and DAB-only view (QuPath 0.1.2). Positive cell identification was determined unblinded. Tumoral F4/80 staining was quantified by counting positive cells in three representative fields containing both epithelial and stromal tumoral tissue and expressed as the average number of cells per mm^2.

Statistical Analysis

Statistical analyses were performed using GraphPad Prism 7.02. Unless otherwise stated, data are presented as mean ± SD. Unpaired t-test served to test differences between two groups. p-Values ≤0.05 were considered significant.

RESULTS

In Vitro Characterization of [^{89}Zr]Zr-DFO-*N*-suc-CSF1R-mAb

CSF1R-mAb binds specifically to CSF1R, while IgG2a does not show binding (**Figure 1A**). The intermediate DFO-N-suc-CSF1R-mAb maintained binding to CSF1R comparable to unconjugated CSF1R-mAb in the ELISA-based binding assay (**Figure 1B**). We successfully radiolabeled CSF1R-mAb and

IgG2a ^{89}Zr at a specific activity of 60-75 MBq/nmol. Radiochemical purity exceeded 95%, and high molecular weight species were below 5% (**Figure 1C**).

Biodistribution of 0.4 mg/kg of [^{89}Zr]Zr-DFO-*N*-suc-CSF1R-mAb in Non-Tumor-Bearing FVB/N Mice

PET imaging in non-tumor-bearing mice revealed low blood pool levels of [^{89}Zr]Zr-DFO-*N*-suc-CSF1R-mAb with SUV_{mean} of 0.3 ± 0.04 at 24 h and 0.2 ± 0.04 at 72 h after injection (**Figures 2A, B**). Spleen uptake showed a mean SUV_{mean} of 5.6 ± 1.1 at 24 h and 5.8 ± 1.0 at 72 h (**Figure 2B**). Similar high uptake was observed in the liver with SUV_{mean} of 5.4 ± 0.5 and 4.8 ± 0.7 at 24 and 72 h, respectively (**Figure 2B**). High uptake in the spleen and liver, with spleen uptake at 72 h after injection of 115 ± 23%ID/g and liver uptake of 31 ± 5%ID/g, was confirmed by *ex vivo* biodistribution (**Figure 2C**). Also, *ex vivo* biodistribution showed uptake in the mesenteric and axillary lymph nodes, duodenum, ileum, and bone marrow (**Figure 2C**). Autoradiography at 72 h showed a ^{89}Zr distribution pattern for the spleen overlapping with the macrophage containing red pulp and for the mesenteric lymph nodes overlapping with the macrophage containing non-follicular regions (**Figure 2D**). For the ileum, no specific ^{89}Zr distribution pattern was observed, except for some slightly elevated aspecific uptake in regions showing autolysis (**Figure 2D**). Thus, 0.4 mg/kg of [^{89}Zr]Zr-DFO-*N*-suc-CSF1R-mAb was distributed quickly to the spleen and liver, with macrophage-specific localization in lymphoid organs.

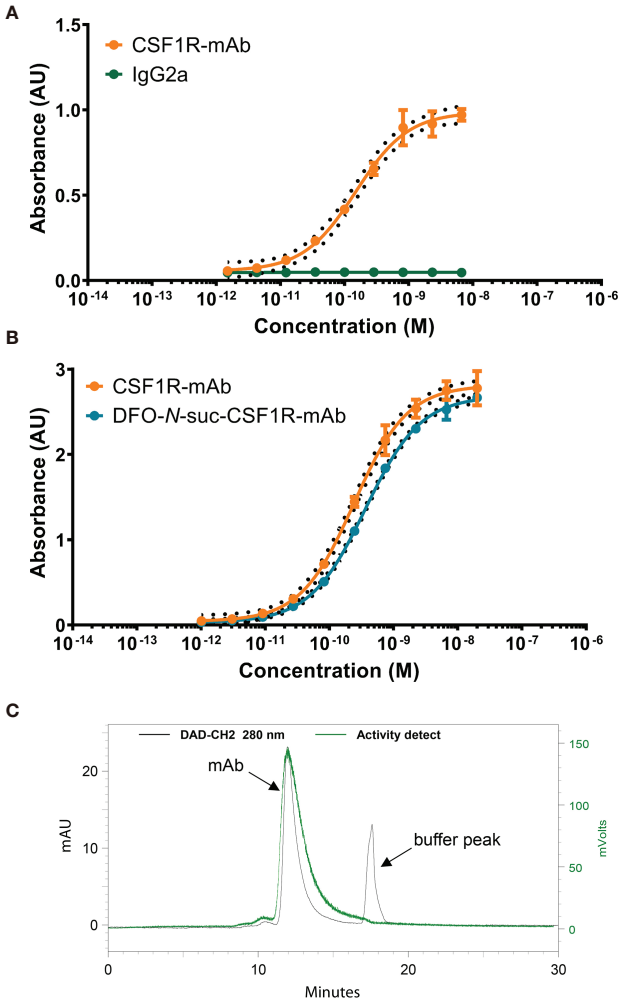

FIGURE 1 | *In vitro* characteristics of CSF1R mAb, DFO-*N*-suc-conjugated, and ^{89}Zr-labeled mAb. **(A)** Representative binding curve of CSF1R mAb and IgG2a binding to mouse CSF1R recombinant protein. **(B)** Representative binding curve of DFO-*N*-suc-CSF1R-mAb and CSF1R mAb binding to mouse CSF1R recombinant protein. **(C)** Representative SE HPLC of [^{89}Zr]Zr-DFO-*N*-suc-CSF1R-mAb 280-nm signal (black) with the radiochemical signal overlay (green). mAb, monoclonal antibody; AU, absorbance unit; CSF1, colony-stimulating factor 1; CSF1R, colony-stimulating factor 1 receptor; SE HPLC, size-exclusion high-performance liquid chromatography.

Biodistribution of 4 mg/kg of [^{89}Zr]Zr-DFO-*N*-suc-CSF1R-mAb in Non-Tumor-Bearing FVB/N Mice

MicroPET imaging 24 h after 4 mg/kg of [^{89}Zr]Zr-DFO-*N*-suc-CSF1R-mAb administration revealed a higher SUV_{mean} of 1.9 ± 0.3 in the blood pool (**Figures 3A, B**) and 11.2 ± 1.8%ID/g by *ex vivo* biodistribution (**Figure 3C**). Again no [^{89}Zr]Zr-DFO-*N*-suc-CSF1R-mAb was present in the blood pool 72 h after injection, as shown by PET with a SUV_{mean} of 0.2 ± 0.04 and by *ex vivo* biodistribution 0.4 ± 0.2%ID/g (**Figures 3B, C**). Also for the 4 mg/kg dose after 24 and 72 h, there was clear spleen and liver uptake (**Figure 3A**), but uptake was lower compared with that of the 0.4 mg/kg group at both time points (**Figures 2B** and **3B**). *Ex vivo* biodistribution was in line with microPET findings (**Figure 3C**). *Ex vivo* biodistribution at 24 h after radiolabeled antibody administration further revealed enriched [^{89}Zr]Zr-DFO-*N*-suc-CSF1R-mAb in plasma over whole blood levels (**Figure 3C**). In short, this demonstrates that 4 mg/kg of [^{89}Zr]Zr-DFO-*N*-suc-CSF1R-mAb marginally increased circulating levels and visualized the spleen and liver.

Biodistribution of 10 mg/kg of [^{89}Zr]Zr-DFO-*N*-suc-CSF1R-mAb in Non-Tumor-Bearing FVB/N Mice

After administration of 10 mg/kg of [^{89}Zr]Zr-DFO-*N*-suc-CSF1R-mAb, microPET visualized blood pool as well as the liver and spleen (**Figure 4A**). Blood pool levels at 24 and 72 h showed a SUV_{mean} of 2.8 ± 0.4 and 1.8 ± 0.2, respectively (**Figure 4B**). Spleen SUV_{mean} was 1.3 ± 0.2 at 24 h and 1.5 ± 0.02 at 72 h after radiolabeled antibody administration (**Figure 4B**). Liver SUV_{mean} was 2.6 ± 0.3 at 24 h and 2.4 ± 0.1 at 72 h. *Ex vivo* biodistribution confirmed PET results, with a high presence in blood pool and high uptake in the liver and spleen 24 and 72 h after radiolabeled antibody administration (**Figure 4C**). *Ex vivo* biodistribution showed for the liver, spleen, duodenum, and ileum no change in uptake between 24 and 72 h after radiolabeled antibody administration (**Figure 4C**).

Comparing all three dose groups, *ex vivo* biodistribution of [^{89}Zr]Zr-DFO-*N*-suc-CSF1R-mAb showed a clear dose-dependent increase in blood levels (**Supplementary Figures 1A, B**), with the lowest dose rapidly eliminating from circulation and distributing

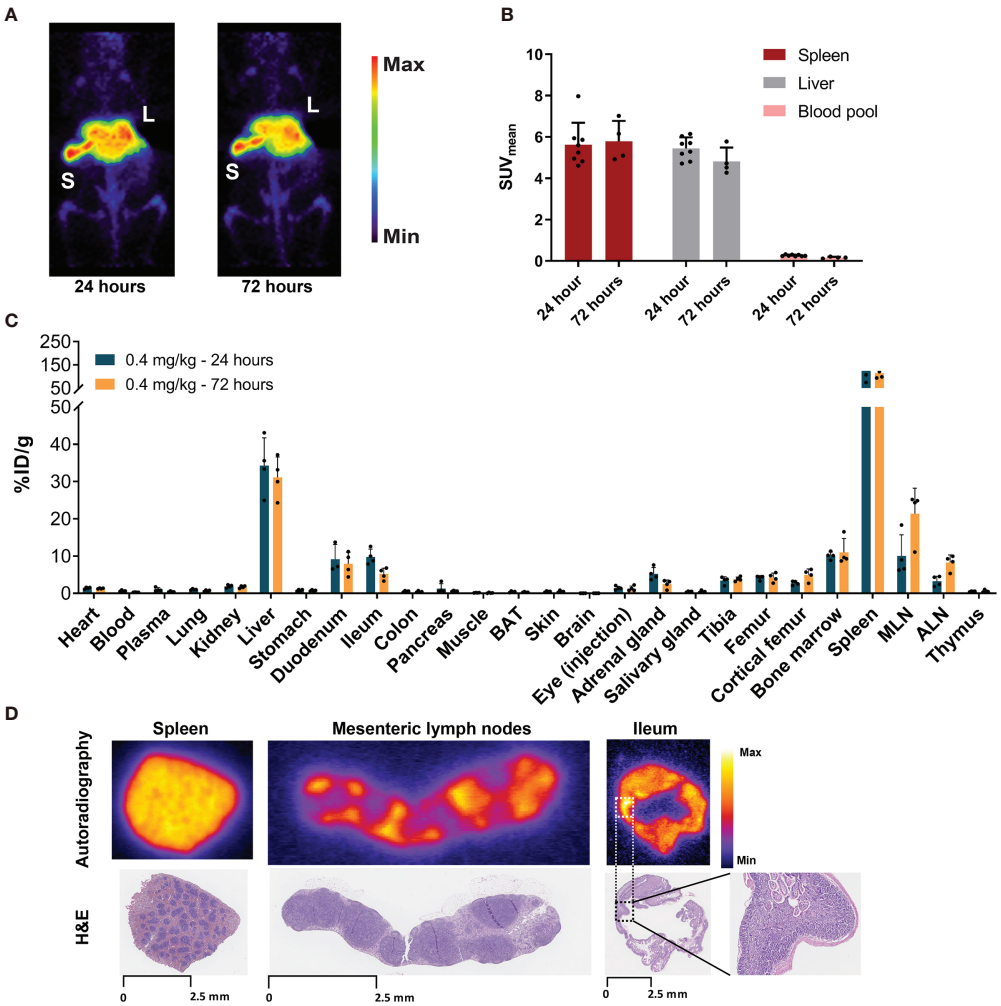

FIGURE 2 | Biodistribution of 0.4 mg/kg of [^{89}Zr]Zr-DFO-*N*-suc-CSF1R-mAb in non-tumor-bearing FVB/N mice. **(A)** Representative maximal intensity projection PET images of non-tumor-bearing FVB/N mice 24 and 72 h after intravenous administration of 0.4 mg/kg of [^{89}Zr]Zr-DFO-*N*-suc-CSF1R-mAb. **(B)** PET quantification of spleen, liver, and blood pool at 24 (n = 8) and 72 (n = 4) h after [^{89}Zr]Zr-DFO-*N*-suc-CSF1R-mAb administration. Data are represented as mean SUV_{mean} ± SD. **(C)** *Ex vivo* biodistribution at 24 (n = 4) and 72 (n = 4) h after administration of 0.4 mg/kg of [^{89}Zr]Zr-DFO-*N*-suc-CSF1R-mAb intravenously. **(D)** *Ex vivo* autoradiography of spleen, mesenteric lymph node, and ileum tissue (upper panel) and matching H&E staining on the same tissue slide. Spleen, mesenteric lymph node, and ileum were exposed to different phosphor plates. Ileum magnification depicting autolysis. L, liver; S, spleen; BAT, brown adipose tissue; MLN, mesenteric lymph nodes; ALN, axillary lymph nodes; %ID/g, percentage injected dose per gram of tissue.

predominantly to the liver and spleen. Increasing the antibody protein dose decreased uptake in the spleen and liver and increased blood levels of [^{89}Zr]Zr-DFO-*N*-suc-CSF1R-mAb at 24 h (**Supplementary Figure 1A**) and 72 h (**Supplementary Figure 1B**). Increasing antibody protein dose trended to a dose-dependent decrease in duodenum and ileum uptake (**Supplementary Figures 1A, B**).

Uptake of [^{89}Zr]Zr-DFO-*N*-suc-CSF1R-mAb and [^{89}Zr]Zr-DFO-*N*-suc-IgG2a in KEP Tumor-Bearing FVB/N Mice

As 10 mg/kg of [^{89}Zr]Zr-DFO-*N*-suc-CSF1R-mAb showed blood pool levels up to 72 h, thereby allowing sufficient time for circulating antibody to potentially reach the tumor, we compared the biodistribution of 10 mg/kg of [^{89}Zr]Zr-DFO-*N*-suc-CSF1R-mAb and 10 mg/kg of isotype control [^{89}Zr]Zr-DFO-*N*-suc-IgG2a in orthotopic KEP tumor-bearing FVB/N mice. The tumor, liver, and heart region, representing the blood pool, showed visual uptake by microPET with both radiolabeled antibodies (**Figure 5A**). The spleen was only visualized following [^{89}Zr]Zr-DFO-*N*-suc-CSF1R-mAb administration (**Figure 5A**). At 72 h after [^{89}Zr]Zr-DFO-*N*-suc-IgG2a administration, there was a higher presence in tumor and blood pool and less in the liver and spleen than for [^{89}Zr]Zr-DFO-*N*-suc-CSF1R-mAb (**Figures 5B–E**). When corrected for blood pool levels, tumor SUV_{mean} was similar for both radiolabeled antibodies (data not shown). This was confirmed by *ex vivo* biodistribution, which also showed no specific tumor uptake of [^{89}Zr]Zr-DFO-*N*-suc-

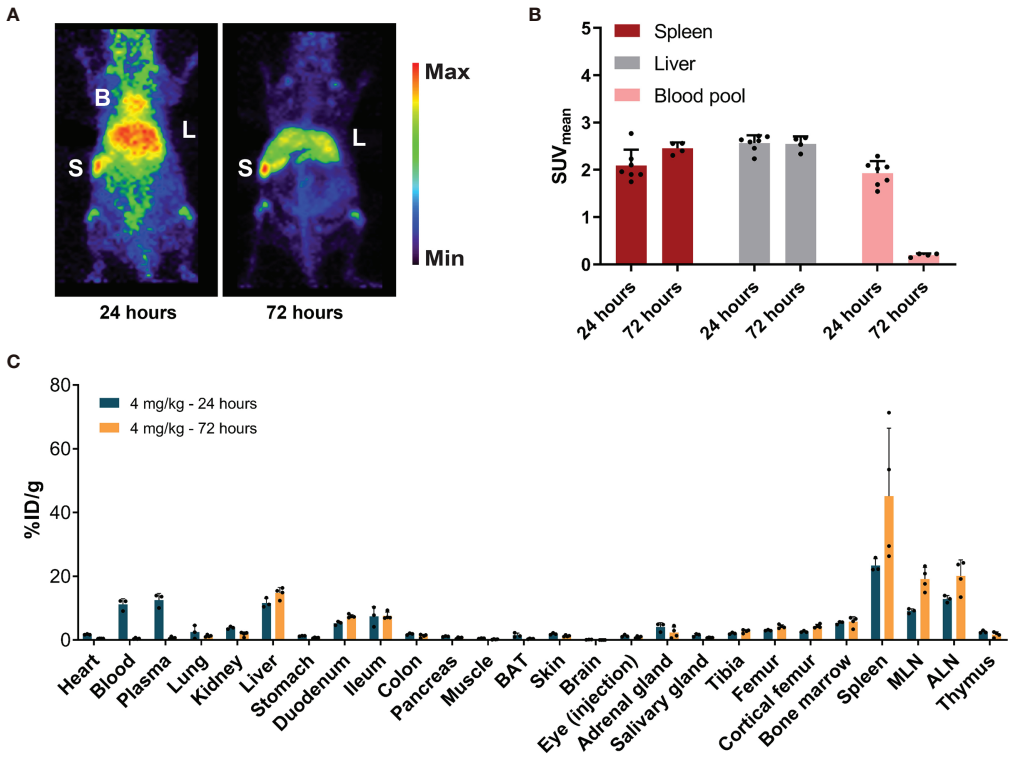

FIGURE 3 | Biodistribution of 4 mg/kg of [^{89}Zr]Zr-DFO-*N*-suc-CSF1R-mAb in non-tumor-bearing FVB/N mice. **(A)** Representative maximal intensity projection PET images of non-tumor-bearing FVB/N mice 24 and 72 h after administration of 4 mg/kg of [^{89}Zr]Zr-DFO-*N*-suc-CSF1R-mAb intravenously. **(B)** PET quantification of spleen, liver, and blood pool at 24 (n = 7) and 72 (n = 4) h after [^{89}Zr]Zr-DFO-*N*-suc-CSF1R-mAb administration. Data are presented as mean + SD. **(C)** *Ex vivo* biodistribution at 24 (n = 4) and 72 (n = 4) h after administration of 4 mg/kg of [^{89}Zr]Zr-DFO-*N*-suc-CSF1R-mAb intravenously. Data are expressed as mean + SD. B, blood pool; L, liver; S, spleen; SUV_{mean}, mean standardized uptake value; BAT, brown adipose tissue; MLN, mesenteric lymph nodes; ALN, axillary lymph nodes; %ID/g, percentage injected dose per gram of tissue.

CSF1R-mAb (**Figure 5F**). *Ex vivo* analyses showed at 72 h higher uptake of [^{89}Zr]Zr-DFO-*N*-suc-CSF1R-mAb than [^{89}Zr]Zr-DFO-*N*-suc-IgG2 in primary and secondary lymphoid tissues. These included the spleen, mesenteric lymph nodes, axillary lymph nodes, thymus, and bone marrow (**Figure 5F**). In addition, specific uptake of [^{89}Zr]Zr-DFO-*N*-suc-CSF1R-mAb was observed in the liver, duodenum, and ileum (**Figure 5F**). Ten-fold fewer macrophages were observed in tumors from mice that received 10 mg/kg of [^{89}Zr]Zr-DFO-*N*-suc-CSF1R-mAb (47 ± 77 per mm^2) compared with [^{89}Zr]Zr-DFO-*N*-suc-IgG2a (525 ± 111 per mm^2) as assessed by immunohistochemistry (**Figures 5G, H**). Staining of a mesenteric lymph node of a mouse treated with 10 mg/kg of [^{89}Zr]Zr-DFO-*N*-suc-CSF1R-mAb without primary antibody showed no signal, indicating no interference of the CSF1R mAb with immunohistochemical staining (**Supplementary Figure 2**).

DISCUSSION

This is the first molecular imaging study to analyze the biodistribution of a CSF1R mAb. A low protein dose of [^{89}Zr]Zr-DFO-*N*-suc-CSF1R-mAb resulted within 24 h in antibody elimination from the blood pool due to distribution to CSF1R-rich organs, such as the liver, spleen, lymph nodes, duodenum, and ileum. Increasing the protein dose up to 10 mg/kg resulted in circulating antibody levels up to 72 h. There was CSF1R-specific uptake by macrophages in the spleen and liver but not in the tumor with [^{89}Zr]Zr-DFO-*N*-suc-CSF1R-mAb most likely due to antibody-mediated depletion of intratumoral macrophages.

Macrophages are widely spread across many organs in which they are involved in tissue homeostasis. Many different tissue-resident macrophages express CSF1R, such as Kupffer cells in the liver, red pulp macrophages in the spleen, and macrophages in the intestine (25–27). Besides, macrophages can have tumor-promoting characteristics in the tumor microenvironment (5–12). The CSF1R mAb has to reach the tumor to deplete these protumor macrophages. This study demonstrates that [^{89}Zr]Zr-DFO-*N*-suc-CSF1R-mAb is not exclusively targeting tumor macrophages but preferably distributes to other organs with high macrophage presence such as the liver and spleen, removing the antibody from circulation. Due to the therapeutic effects of the high dose required to establish circulating antibody, imaging macrophages in other organs seems not possible with this approach. The low number of intratumoral macrophages observed in our study after 10 mg/kg of [^{89}Zr]Zr-DFO-*N*-suc-CSF1R-mAb administration can explain the lack of specific

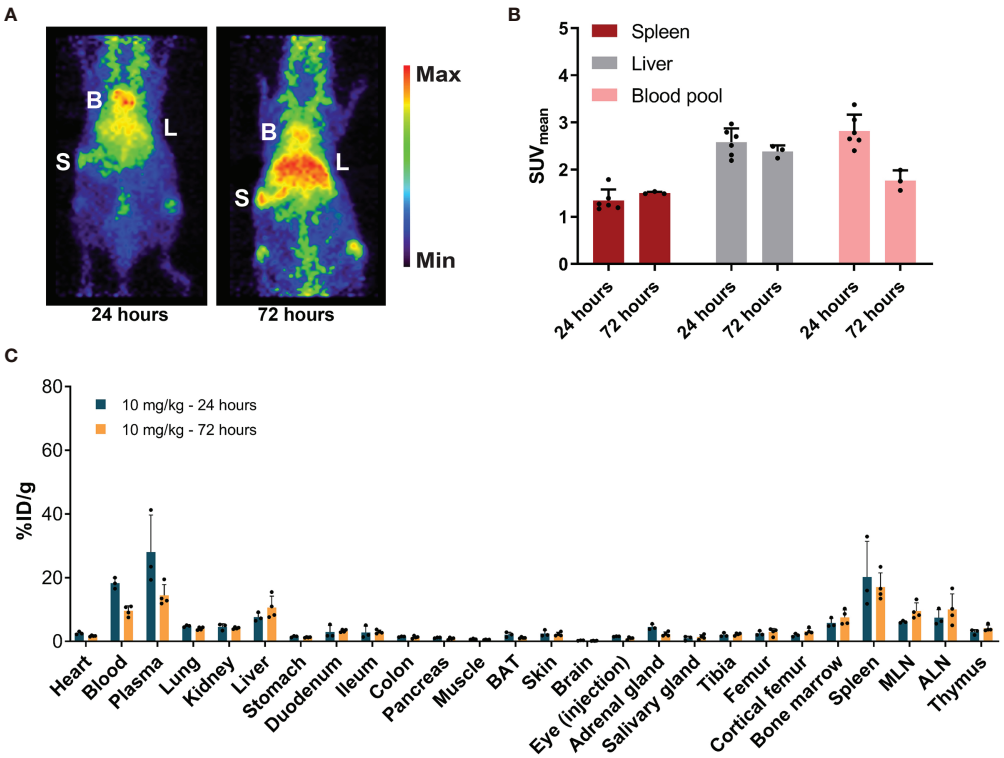

FIGURE 4 | Biodistribution of 10 mg/kg of [^{89}Zr]Zr-DFO-*N*-suc-CSF1R-mAb in non-tumor-bearing FVB/N mice. **(A)** Representative maximal intensity projection PET images of non-tumor-bearing FVB/N mice 24 and 72 h after intravenous administration of 10 mg/kg of [^{89}Zr]Zr-DFO-*N*-suc-CSF1R-mAb. B, blood pool; L, liver; S, spleen. **(B)** PET quantification of spleen, liver, and blood pool at 24 (n = 6) and 72 (n = 3) h after [^{89}Zr]Zr-DFO-N-suc-CSF1R-mAb administration. Data are presented as mean SUV_{mean} ± SD. **(C)** *Ex vivo* biodistribution at 24 (n = 3) and 72 (n = 4) h after administration of 10 mg/kg of [^{89}Zr]Zr-DFO-*N*-suc-CSF1R-mAb. Data are expressed as mean + SD. B, blood pool; L, liver; S, spleen; SUV_{mean}, mean standardized uptake value; BAT, brown adipose tissue; MLN, mesenteric lymph nodes; ALN, axillary lymph nodes; %ID/g, percentage injected dose per gram of tissue.

tumor uptake of [^{89}Zr]Zr-DFO-*N*-suc-CSF1R-mAb. [^{89}Zr]Zr-DFO-*N*-suc-CSF1R-mAb still reached the tumor, and due to the relatively high protein dose, CSF1R-positive macrophages were already eliminated within the 72-h exposure. Although macrophage depletion at 24 h after antibody administration could not be assessed in this study, future studies with macrophage-targeting agents might want to address macrophage depletion or reprogramming at multiple time points during treatment course. This might help to better understand their *in vivo* behavior and streamline drug development. CSF1R single antibody activity on the tumor microenvironment in this tumor model was also reported earlier (11). In this study, 225-mm^3 KEP tumors were treated with 60 mg/kg of CSF1R mAb intraperitoneally loading dose and 30 mg/kg intraperitoneally once per week, corresponding to 1.5 and 0.75 mg based on a 25-g mouse (11). CSF1R mAb-treated tumors showed less tumoral macrophages as compared with control treatment as assessed by immunohistochemistry and flow cytometry (11). In that study, CSF1R mAb alone, however, did not demonstrate antitumor effects, whereas the combination with cisplatin showed synergistic antitumor effects (11).

Similar to our study, using single-photon emission CT (SPECT) isotope indium-111 (^{111}In)-labeled antibody targeting the pan-mouse macrophage marker F4/80, antibody tumor uptake did not differ from isotype control in a human breast cancer cell line MDA-MD-231 xenograft (28). When corrected for blood pool levels, tumor uptake was higher for ^{111}In-labeled anti-F4/80 than isotype control. However, this was only tested at a low protein dose of 10 µg (~0.4 mg/kg) and, thus, a major difference in elimination half-life. This tracer was studied in an immunodeficient severe combined immunodeficiency (SCID)/beige mouse model with an impaired immune system to allow the engraftment of a human breast cancer xenograft. The impaired immune system and a xenograft tumor make it challenging to translate these results into an immunocompetent model. Noteworthy, F4/80 has no human macrophage equivalent and is therefore not a drug target. Another SPECT study in mice used a radiolabeled antibody against a different macrophage marker, namely, CD206. In that study, biodistribution was determined as early at 24 h after ^{125}I-labeled tracer administration reporting whole blood pool levels of 10%ID/g (29). Of interest, in that study, specific tumor uptake was observed. We did not use a CD206-mAb, as CD206 showed low expression by the TAMs in our model (11).

By *ex vivo* biodistribution in our study, high specific uptake was observed in the duodenum and ileum. This uptake could be explained by the presence of an abundant number of macrophages in the lamina propria of the murine small intestine (26). PET allowed us to

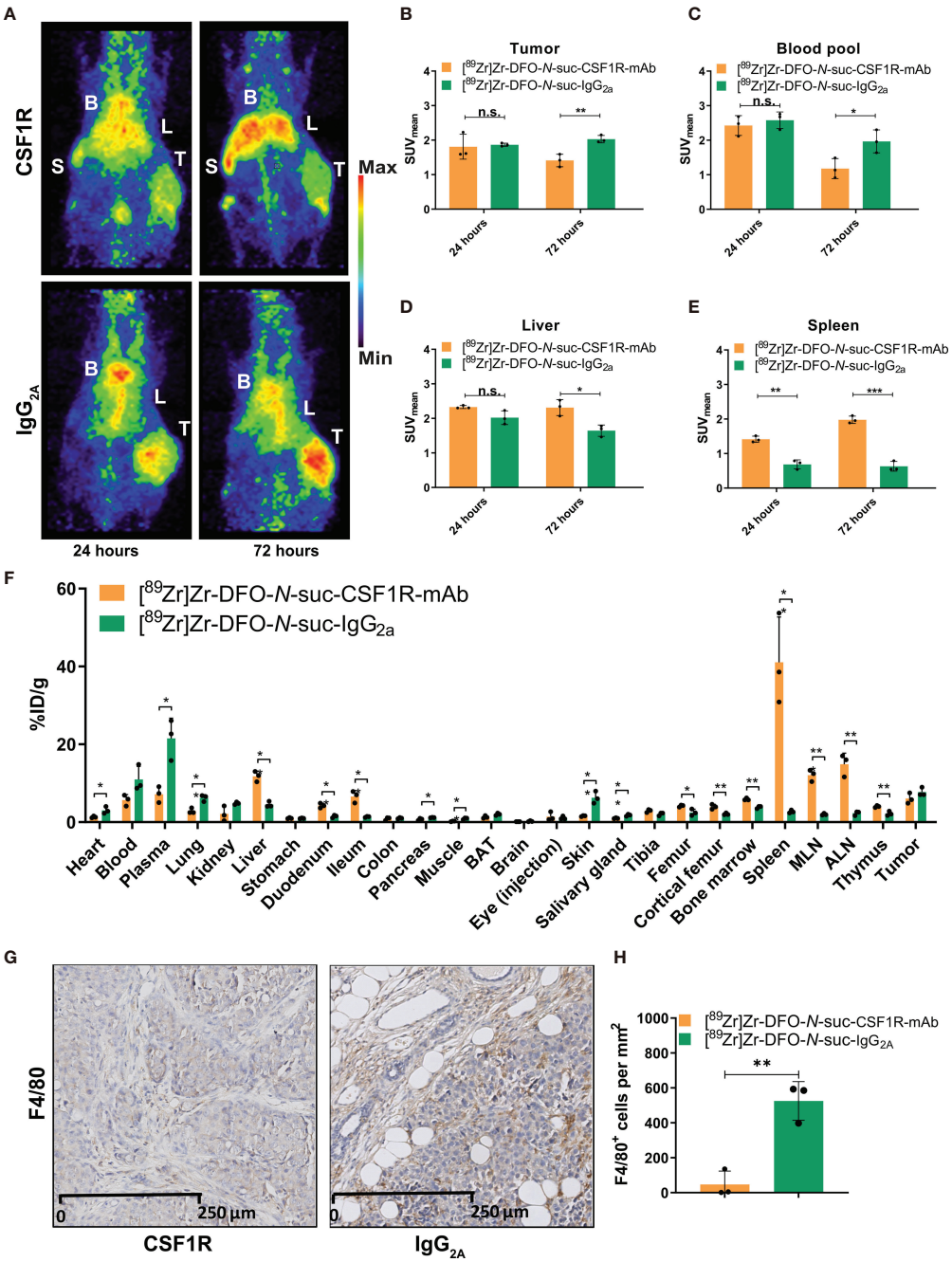

FIGURE 5 | Biodistribution of 10 mg/kg of [^{89}Zr]Zr-DFO-*N*-suc-CSF1R-mAb and [^{89}Zr]Zr-DFO-*N*-suc-IgG2a antibody in KEP tumor-bearing FVB/N mice. **(A)** Representative maximal intensity projection PET images of KEP tumor-bearing FVB/N mice 24 and 72 h after intravenous administration of 10 mg/kg of [^{89}Zr]Zr-DFO-*N*-suc-CSF1R-mAb or [^{89}Zr]Zr-DFO-*N*-suc-IgG2a antibody. PET quantification of **(B)** tumor, **(C)** blood pool, **(D)** liver, and **(E)** spleen at 24 (n = 3) and 72 (n = 3) h after [^{89}Zr]Zr-DFO-*N*-suc-CSF1R-mAb or [^{89}Zr]Zr-DFO-*N*-suc-IgG2a antibody administration. Data are presented as mean + SD. **(F)** *Ex vivo* biodistribution at 72 h after administration of 10 mg/kg of [^{89}Zr]Zr-DFO-*N*-suc-CSF1R-mAb (n = 3) or [^{89}Zr]Zr-DFO-*N*-suc-IgG2a (n = 3) antibody. Data are expressed as mean + SD. **(G)** Representative immunohistochemistry of F4/80 in KEP tumors of FVB/N mice at 72 h after administration of [^{89}Zr]Zr-DFO-*N*-suc-CSF1R-mAb or [^{89}Zr]Zr-DFO-*N*-suc-IgG2a intravenously. **(H)** Quantification of tumoral F4/80 immunohistochemistry. *$p \leq 0.05$; **$p \leq 0.01$; ***$p \leq 0.001$ (unpaired t-test). B, blood pool; L, liver; S, spleen; T, tumor; SUV_{mean}, mean standardized uptake value; BAT, brown adipose tissue; MLN, mesenteric lymph nodes; ALN, axillary lymph nodes; %ID/g, percentage injected dose per gram of tissue. n.s., not significant.

demonstrate the uptake in the liver, spleen, and blood over time. Nevertheless, PET was unable to detect clear uptake in lymph nodes and the intestine, possibly related to the detection limit of the camera. Gastrointestinal specificity is in line with specific duodenum uptake observed with *ex vivo* biodistribution in a study using ^{111}In-labeled F4/80 mAb (28).

In our study at a dose of 0.4 mg/kg, low blood pool levels of CSF1R mAb were observed at 24 h post-administration. The extensive availability of the CSF1R target as a macrophage marker in organs such as the liver and spleen might act as an antibody sink. Besides CSF1R-mediated clearance to the liver and spleen, it cannot be excluded that interaction between the IgG_{2a} backbone of the CSF1R mAb and mouse Fc-receptor partially impacted distribution to the spleen and liver at lower antibody dose levels. For future studies, distribution of IgG_{2a} control at all dose levels might be considered. Similarly to our study, ^{111}In-labeled F4/80-mAb demonstrated low blood pool levels and high uptake in the liver and spleen at 24 h post-injection of a 10-μg tracer (28). In that study, increasing the protein dose by 10-fold only slightly increased blood pool levels of ^{111}In-F4/80-mAb. Besides, SPECT visualized the kidneys at 24 h post 100-μg tracer administration, which questions the tracer's *in vivo* stability.

Similar to our findings, fast serum clearance of free CSF1 mAb was observed in a clinical trial with pharmacokinetic analysis of healthy volunteers of a clinical mAb binding CSF1. This trial suggested target-mediated drug disposition as the mechanism responsible for the decline of free CSF1 mAb in serum at low doses up to 5 mg/kg (30). In oncology, many CSF1/CSF1R-targeting drugs are in clinical trials, often in combination with immune checkpoint blockade (1). In early-phase clinical trials in patients with advanced cancer, elevation of liver enzymes has been observed with the CSF1 mAb AMG 820 and the CSF1R mAb MCS110 (31, 32). This increase could be related to the depletion of CSF1R-positive Kupffer cells without any actual liver tissue damage, as seen in cynomolgus macaques treated with a CSF1 mAb (33). In turn, this could be linked to our observation of high liver uptake of [^{89}Zr]Zr-DFO-*N*-suc-CSF1R-mAb. The observed decrease in liver uptake upon higher CSF1R-mAb dose could be a result of antigen saturation at the target site, the depletion of Kupffer cells in the liver, or a combination.

As targeting the CSF1–CSF1R axis can result in a potential pan-macrophage depletion, reprogramming or activating TAMs more specifically to a more antitumor role may elicit additional benefits. An example is targeting the macrophage receptor with collagenous structure (MARCO). This scavenging receptor is constitutively expressed by subpopulations of macrophages, particularly those of the spleen's marginal zone and lymph node medulla and by residential peritoneal macrophages (34). MARCO expression on liver macrophages showed conflicting results, with both absence and higher immunohistochemical MARCO expression on peritumoral macrophages compared with intratumoral macrophages of hepatocellular carcinoma (34–36). MARCO is expressed by TAMs in human breast cancer and correlated with poor clinical outcome (37, 38). Anti-MARCO mAb arrested tumor growth and lowered metastasis in a mouse 4T1 mammary carcinoma model by reprogramming TAMs (36). No clinical trials for MARCO targeting therapy are described. Biodistribution of such novel therapeutics is still unknown, and future studies may provide more insight in TAM biology and support the development of drugs selectively targeting TAMs. In addition, treatment with anti-MARCO mAb could be followed up by imaging macrophage surface markers to study pharmacodynamics.

Our study highlights the need for more biodistribution studies to enhance our understanding of macrophage-targeting antibodies. These studies likely need to address dose, timing, antibody format, and physiological expression of the target to get a comprehensive overview of the pharmacokinetic and pharmacodynamic properties of macrophage-targeting drug. Once such features are identified in the preclinical setting, clinical imaging studies should consider these in their trial design. Studying CSF1R-targeting antibody biodistribution in humans may support elucidating the role of CSF1R-positive macrophages in healthy tissues as well as breast cancer treatment and optimizing (combination) targeting strategies.

DATA AVAILABILITY STATEMENT

The original contributions presented in the study are included in the article/**Supplementary Material**. Further inquiries can be directed to the corresponding author.

ETHICS STATEMENT

The animal study was reviewed and approved by Institutional Animal Care and Use Committee of the University of Groningen and the Netherlands Cancer Institute.

AUTHOR CONTRIBUTIONS

Study concept and design: SW, KV, and CS. Acquisition of data: SW, FS, CH, and KV. Analysis and interpretation of data: all authors. Study supervision: KV, CS, ML, and EV. Writing, review, and revision of the manuscript: all authors. All authors contributed to the article and approved the submitted version.

ACKNOWLEDGMENTS

We thank Linda Pot-de Jong for assistance with immunohistochemical staining procedures. We thank the Mouse Clinic for Cancer and Aging (MCCA) Intervention Unit at the NKI.

SUPPLEMENTARY MATERIAL

The Supplementary Material for this article can be found online at: https://www.frontiersin.org/articles/10.3389/fonc.2021.786191/full#supplementary-material

REFERENCES

1. Qiu SQ, Waaijer SJH, Zwager MC, de Vries EGE, van der Vegt B, Schröder CP. Tumor-Associated Macrophages in Breast Cancer: Innocent Bystander or Important Player? *Cancer Treat Rev* (2018) 70:178–89. doi: 10.1016/j.ctrv.2018.08.010
2. Zhang QW, Liu L, Gong CY, Shi HS, Zeng YH, Wang XZ, et al. Prognostic Significance of Tumor-Associated Macrophages in Solid Tumor: A Meta-Analysis of the Literature. *PLoS One* (2012) 7:e50946. doi: 10.1371/journal.pone.0050946
3. Gentles AJ, Newman AM, Liu CL, Bratman SV, Feng W, Kim D, et al. The Prognostic Landscape of Genes and Infiltrating Immune Cells Across Human Cancers. *Nat Med* (2015) 21:938–45. doi: 10.1038/nm.3909
4. Bense RD, Sotiriou C, Piccart-Gebhart MJ, Haanen J, van Vugt M, de Vries EGE, et al. Relevance of Tumor-Infiltrating Immune Cell Composition and Functionality for Disease Outcome in Breast Cancer. *J Natl Cancer Inst* (2017) 109:djw192. doi: 10.1093/jnci/djw192
5. Engblom C, Pfirschke C, Pittet MJ. The Role of Myeloid Cells in Cancer Therapies. *Nat Rev Cancer* (2016) 16:447–62. doi: 10.1038/nrc.2016.54
6. Coffelt SB, de Visser KE. Immune-Mediated Mechanisms Influencing the Efficacy of Anticancer Therapies. *Trends Immunol* (2015) 36:198–216. doi: 10.1016/j.it.2015.02.006
7. DeNardo DG, Ruffell B. Macrophages as Regulators of Tumour Immunity and Immunotherapy. *Nat Rev Immunol* (2019) 19:369–82. doi: 10.1038/s41577-019-0127-6
8. Zhu Y, Knolhoff BL, Meyer MA, Nywening TM, West BL, Luo J, et al. CSF1/CSF1R Blockade Reprograms Tumor-Infiltrating Macrophages and Improves Response to T-Cell Checkpoint Immunotherapy in Pancreatic Cancer Models. *Cancer Res* (2014) 74:5057–69. doi: 10.1158/0008-5472.CAN-13-3723
9. DeNardo DG, Brennan DJ, Rexhepaj E, Ruffell B, Shiao SL, Madden SF, et al. Leukocyte Complexity Predicts Breast Cancer Survival and Functionally Regulates Response to Chemotherapy. *Cancer Discov* (2011) 1:54–67. doi: 10.1158/2159-8274.CD-10-0028
10. Ruffell B, Chang-Strachan D, Chan V, Rosenbusch A, Ho CM, Pryer N, et al. Macrophage IL-10 Blocks CD8+ T Cell-Dependent Responses to Chemotherapy by Suppressing IL-12 Expression in Intratumoral Dendritic Cells. *Cancer Cell* (2014) 26:623–37. doi: 10.1016/j.ccell.2014.09.006
11. Salvagno C, Ciampricotti M, Tuit S, Hau CS, van Weverwijk A, Coffelt SB, et al. Therapeutic Targeting of Macrophages Enhances Chemotherapy Efficacy by Unleashing Type I Interferon Response. *Nat Cell Biol* (2019) 21:511–21. doi: 10.1038/s41556-019-0298-1
12. Pathria P, Louis TL, Varner JA. Targeting Tumor-Associated Macrophages in Cancer. *Trends Immunol* (2019) 40:310–27. doi: 10.1016/j.it.2019.02.003
13. Shiao SL, Ruffell B, DeNardo DG, Faddegon BA, Park CC, Coussens LM. Th2-Polarized CD4(+) T Cells and Macrophages Limit Efficacy of Radiotherapy. *Cancer Immunol Res* (2015) 3:518–25. doi: 10.1158/2326-6066.CIR-14-0232
14. Guerriero JL, Sotayo A, Ponichtera HE, Castrillon JA, Pourzia AL, Schad S, et al. Class IIa HDAC Inhibition Reduces Breast Tumours and Metastases Through Anti-Tumour Macrophages. *Nature* (2017) 543:428–32. doi: 10.1038/nature21409
15. Derksen PW, Liu X, Saridin F, van der Gulden H, Zevenhoven J, Evers B, et al. Somatic Inactivation of E-Cadherin and P53 in Mice Leads to Metastatic Lobular Mammary Carcinoma Through Induction of Anoikis Resistance and Angiogenesis. *Cancer Cell* (2006) 10:437–49. doi: 10.1016/j.ccr.2006.09.013
16. Chitu V, Stanley ER. Colony-Stimulating Factor-1 in Immunity and Inflammation. *Curr Opin Immunol* (2006) 18:39–48. doi: 10.1016/j.coi.2005.11.006
17. Cannarile MA, Weisser M, Jacob W, Jegg AM, Ries CH, Ruttinger D. Colony-Stimulating Factor 1 Receptor (CSF1R) Inhibitors in Cancer Therapy. *J Immunother Cancer* (2017) 5:53. doi: 10.1186/s40425-017-0257-y
18. Esteva FJ, Hubbard-Lucey VM, Tang J, Pusztai L. Immunotherapy and Targeted Therapy Combinations in Metastatic Breast Cancer. *Lancet Oncol* (2019) 20:e175–86. doi: 10.1016/S1470-2045(19)30026-9
19. Waaijer SJH, Kok IC, Eisses B, Schröder CP, Jalving M, Brouwers AH, et al. Molecular Imaging in Cancer Drug Development. *J Nucl Med* (2018) 59:726–32. doi: 10.2967/jnumed.116.188045
20. van der Veen EL, Bensch F, Glaudemans A, Lub-de Hooge MN, de Vries EGE. Molecular Imaging to Enlighten Cancer Immunotherapies and Underlying Involved Processes. *Cancer Treat Rev* (2018) 70:232–44. doi: 10.1016/j.ctrv.2018.09.007
21. de Vries EGE, Kist de Ruijter L, Lub-de Hooge MN, Dierckx RA, Elias SG, Oosting SF. Integrating Molecular Nuclear Imaging in Clinical Research to Improve Anticancer Therapy. *Nat Rev Clin Oncol* (2019) 16:241–55. doi: 10.1038/s41571-018-0123-y
22. Verel I, Visser GW, Boellaard R, Stigter-van Walsum M, Snow GB, van Dongen GA. ^{89}Zr Immuno-PET: Comprehensive Procedures for the Production of ^{89}Zr-Labeled Monoclonal Antibodies. *J Nucl Med* (2003) 44:1271–81.
23. Nagengast WB, de Vries EG, Hospers GA, Mulder NH, de Jong JR, Hollema H, et al. *In Vivo* VEGF Imaging With Radiolabeled Bevacizumab in a Human Ovarian Tumor Xenograft. *J Nucl Med* (2007) 48:1313–9. doi: 10.2967/jnumed.107.041301
24. Warnders FJ, Waaijer SJH, Pool M, Lub-de Hooge MN, Friedrich M, Terwisscha van Scheltinga AG, et al. Biodistribution and PET Imaging of Labeled Bispecific T Cell-Engaging Antibody Targeting EpCAM. *J Nucl Med* (2016) 57:812–7. doi: 10.2967/jnumed.107.041301
25. Sauter KA, Pridans C, Sehgal A, Tsai YT, Bradford BM, Raza S, et al. Pleiotropic Effects of Extended Blockade of CSF1R Signaling in Adult Mice. *J Leukoc Biol* (2014) 96:265–74. doi: 10.1189/jlb.2A0114-006R
26. Sehgal A, Donaldson DS, Pridans C, Sauter KA, Hume DA, Mabbott NA. The Role of CSF1R-Dependent Macrophages in Control of the Intestinal Stem-Cell Niche. *Nat Commun* (2018) 9:1272. doi: 10.1038/s41467-018-03638-6
27. Gordon S, Pluddemann A. Tissue Macrophages: Heterogeneity and Functions. *BMC Biol* (2017) 15:53. doi: 10.1186/s12915-017-0392-4
28. Terry SY, Boerman OC, Gerrits D, Franssen GM, Metselaar JM, Lehmann S, et al. ^{111}In-Anti-F4/80-A3-1 Antibody: A Novel Tracer to Image Macrophages. *Eur J Nucl Med Mol Imaging* (2015) 42:1430–8. doi: 10.1007/s00259-015-3084-8
29. Zhang C, Yu X, Gao L, Zhao Y, Lai J, Lu D, et al. Noninvasive Imaging of CD206-Positive M2 Macrophages as an Early Biomarker for Post-Chemotherapy Tumor Relapse and Lymph Node Metastasis. *Theranostics* (2017) 7:4276–88. doi: 10.7150/thno.20999
30. Pognan F, Couttet P, Demin I, Jaitner B, Pang Y, Roubenoff R, et al. Colony-Stimulating Factor-1 Antibody Lacnotuzumab in a Phase 1 Healthy Volunteer Study and Mechanistic Investigation of Safety Outcomes. *J Pharmacol Exp Ther* (2019) 369:428–42. doi: 10.1124/jpet.118.254128
31. Papadopoulos KP, Gluck L, Martin LP, Olszanski AJ, Tolcher AW, Ngarmchamnanrith G, et al. First-In-Human Study of AMG 820, a Monoclonal Anti-Colony-Stimulating Factor 1 Receptor Antibody, in Patients With Advanced Solid Tumors. *Clin Cancer Res* (2017) 23:5703–10. doi: 10.1158/1078-0432.CCR-16-3261
32. Calvo A JH, Sebastian M, Naing A, Bang Y-J, Martin M. Phase Ib/II Study of Lacnotuzumab (MCS110) Combined With Spartalizumab (PDR001) in Patients (Pts) With Advanced Tumors. *J Clin Oncol* (2018) 36 (15_suppl):3014. doi: 10.1200/JCO.2018.36.15_suppl.3014
33. Radi ZA, Koza-Taylor PH, Bell RR, Obert LA, Runnels HA, Beebe JS, et al. Increased Serum Enzyme Levels Associated With Kupffer Cell Reduction With No Signs of Hepatic or Skeletal Muscle Injury. *Am J Pathol* (2011) 179:240–7. doi: 10.1016/j.ajpath.2011.03.029
34. Elomaa O, Kangas M, Sahlberg C, Tuukkanen J, Sormunen R, Liakka A, et al. Cloning of a Novel Bacteria-Binding Receptor Structurally Related to Scavenger Receptors and Expressed in a Subset of Macrophages. *Cell* (1995) 80:603–9. doi: 10.1016/0092-8674(95)90514-6
35. Maler MD, Nielsen PJ, Stichling N, Cohen I, Ruzsics Z, Wood C, et al. Key Role of the Scavenger Receptor MARCO in Mediating Adenovirus Infection and Subsequent Innate Responses of Macrophages. *mBio* (2017) 8:e00670–17. doi: 10.1128/mBio.00670-17
36. Sun H, Song J, Weng C, Xu J, Huang M, Huang Q, et al. Association of Decreased Expression of the Macrophage Scavenger Receptor MARCO With Tumor Progression and Poor Prognosis in Human Hepatocellular Carcinoma. *J Gastroenterol Hepatol* (2017) 32:1107–14. doi: 10.1111/jgh.13633
37. Georgoudaki A-M, Prokopec KE, Boura VF, Hellqvist E, Sohn S, Ostling J, et al. Reprogramming Tumor-Associated Macrophages by Antibody Targeting Inhibits Cancer Progression and Metastasis. *Cell Rep* (2016) 15:2000–11. doi: 10.1016/j.celrep.2016.04.084
38. Bergamaschi A, Tagliabue E, Sorlie T, Naume B, Triulzi T, Orlandi R, et al. Extracellular Matrix Signature Identifies Breast Cancer Subgroups With Different Clinical Outcome. *J Pathol* (2008) 214:357–67. doi: 10.1002/path.2278

Conflict of Interest: EV reports institutional financial support for her advisory role from Daiichi Sankyo, Merck, NSABP, Pfizer, Sanofi, and Synthon and institutional financial support for clinical trials or contracted research from Amgen, AstraZeneca, Bayer, Chugai Pharma, CytomX Therapeutics, G1 Therapeutics, Genentech, Nordic Nanovector, Radius Health, Roche, Synthon, and Servier. CS reports receiving unrestricted research grants from Novartis, Roche, Genentech, Pfizer, SNS Oncology, and G1 Therapeutics that were made available to UMCG. KdV reports receiving research grants from Roche and is a consultant for Third Rock Ventures.

The remaining authors declare that the research was conducted in the absence of any commercial or financial relationships that could be construed as a potential conflict of interest.

Publisher's Note: All claims expressed in this article are solely those of the authors and do not necessarily represent those of their affiliated organizations, or those of the publisher, the editors and the reviewers. Any product that may be evaluated in this article, or claim that may be made by its manufacturer, is not guaranteed or endorsed by the publisher.

frontiers in Immunology

REVIEW
published: 03 January 2022
doi: 10.3389/fimmu.2021.804159

In Vivo Motility Patterns Displayed by Immune Cells Under Inflammatory Conditions

Diego Ulisse Pizzagalli[1,2†], Alain Pulfer[1,3†], Marcus Thelen[1], Rolf Krause[2] and Santiago F. Gonzalez[1]*

[1] Istituto di Ricerca in Biomedicina (IRB), Università della Svizzera italiana, Bellinzona, Switzerland, [2] Euler institute, Università della Svizzera italiana, Lugano-Viganello, Switzerland, [3] Department of Information Technology and Electrical Engineering, Swiss Federal Institute of Technology Zurich (ETHZ) Zürich, Zürich, Switzerland

The migration of immune cells plays a key role in inflammation. This is evident in the fact that inflammatory stimuli elicit a broad range of migration patterns in immune cells. Since these patterns are pivotal for initiating the immune response, their dysregulation is associated with life-threatening conditions including organ failure, chronic inflammation, autoimmunity, and cancer, amongst others. Over the last two decades, thanks to advancements in the intravital microscopy technology, it has become possible to visualize cell migration in living organisms with unprecedented resolution, helping to deconstruct hitherto unexplored aspects of the immune response associated with the dynamism of cells. However, a comprehensive classification of the main motility patterns of immune cells observed *in vivo*, along with their relevance to the inflammatory process, is still lacking. In this review we defined cell actions as motility patterns displayed by immune cells, which are associated with a specific role during the immune response. In this regard, we summarize the main actions performed by immune cells during intravital microscopy studies. For each of these actions, we provide a consensus name, a definition based on morphodynamic properties, and the biological contexts in which it was reported. Moreover, we provide an overview of the computational methods that were employed for the quantification, fostering an interdisciplinary approach to study the immune system from imaging data.

Keywords: cell actions, computer vision, inflammation, intravital imaging, leukocytes, motility patterns

OPEN ACCESS

Edited by:
Marco Erreni,
Humanitas Research Hospital, Italy

Reviewed by:
Masaru Ishii,
Osaka University, Japan
Pedro Elias Marques,
KU Leuven, Belgium

***Correspondence:**
Santiago F. Gonzalez
santiago.gonzalez@irb.usi.ch

[†]These authors have contributed equally to this work

Specialty section:
This article was submitted to Inflammation, a section of the journal Frontiers in Immunology

Received: *28 October 2021*
Accepted: *26 November 2021*
Published: *03 January 2022*

Citation:
Pizzagalli DU, Pulfer A, Thelen M, Krause R and Gonzalez SF (2022) In Vivo Motility Patterns Displayed by Immune Cells Under Inflammatory Conditions. Front. Immunol. 12:804159. doi: 10.3389/fimmu.2021.804159

INTRODUCTION

Inflammation is a highly dynamic process that involves changes in cell behavior both at the site of the insult as well as at distant organs (1, 2). Immune cells are key players in this process, as they relocate into inflamed tissues, and secrete mediators of inflammation that orchestrate a cascade of immune reactions (3–7).

Over the last two decades, intravital microscopy (MP-IVM) techniques have consolidated the *in vivo* analysis of the immune response. Videos acquired *via* MP-IVM capture the behavior of immune cells, including their migratory and interaction patterns, in organs of living organisms (8–11). However, the quantification of these videos remains challenging. This is due to a range of factors, such

as the complexity of the *in vivo* environment, which includes a multitude of cell types and anatomical structures (12) or the high plasticity and dynamism of the migration patterns displayed by immune cells, which change over time. Moreover, numerous technical artifacts introduced by the intravital imaging procedure also affect the analysis to a large extent (13).

The recently established image-based systems biology paradigm offers a unique opportunity to study cell behavior *in vivo*, as it combines imaging data and computational methods (14). Analogously, recently developed computer vision methods for action recognition (AR) have enabled the analysis of the complex behavior of humans associated with specific actions such as walking, jumping, etc. (15). This is a particularly challenging task, as human actions may be hierarchical in their nature, composed of multiple actors, or captured by different imaging modalities (15). Interestingly, these three challenges are shared with the quantification of the immune cell behavior in intravital movies, as they display different morphodynamics, undergo cell-to-cell interactions, and can be imaged in different anatomical regions. Hence, in line with AR, we define cell actions as motility patterns associated with relevant biological functions to dissect leukocyte behavior.

To this end, we collected and reported from the literature a list of actions displayed by immune cells in different organs during key inflammatory processes. A summary of the diseases, organs, and studies included in this review is reported in **Table 1**. Moreover, we provide a consensus definition for each action and its biological relevance during inflammation. Lastly, we report the computational methods currently available for the detection and quantification of each reviewed action.

TABLE 1 | Summary of the actions described in different inflammatory conditions, organs, and cell types.

Condition	Organ	Cell type	Reported actions
Acute inflammation	Kidney	Monocytes	Patrolling (16)
		Monocytes Neutrophils	Contact formation (16)
Chronic inflammation	Liver	NKT	Directed (17) Patrolling (17) Swarming (17)
Hypersensitivity	Lymphatics	T	Arrested (18) Patrolling (18) Swarming (18)
		T DCs	Contact formation (18)
		DCs	Arrested (18) Patrolling (18)
Induced/Sterile inflammation	Vasculature	Monocytes	Patrolling (19–21)
		Neutrophils	Directed (22) Arresting (22)
	LN	NK	Contact formation (23) Patrolling (23, 24)
		T cells	Contact formation (23)
		NKs B	Contact formation (24)
		B	Arrested (25)
		T	Arrested (26) Patrolling (27)
		T DCs	Contact formation (27–31)
	Skin	Neutrophils	Directed (32) Swarming (32)
	Lung	Eosinophils	Directed (33)
	Kidney	Monocytes	Patrolling (16)
	CNS	Monocytes	Patrolling (34)
	Liver	Neutrophils	Directed (35) Swarming (35)
Infection	Spleen	Neutrophils	Directed (36) Patrolling (36)
		DCs	Swarming (36)
		T	Arrested (36)
		Monocytes	Swarming (36)
	Skin	Neutrophils	Directed (37) Swarming (38, 39)
		Eosinophils Macrophages	Contact formation (40)
		Eosinophils	Arrested (40) Directed (40)
	Lung	Neutrophils	Patrolling (38) Swarming (38)
	LN	Neutrophils	Arrested (41) Directed (41) Swarming (42)
		NKs DCs	Contact formation (43)
		NKs	Arrested (43)
Injury	Skin	Neutrophils	Directed (44, 45) Swarming (44, 45)
Steady state	Vasculature	Monocytes	Patrolling (19, 20)
	Skin	Eosinophils	Patrolling (40)
		Eosinophils Macrophages	Contact formation (40)
	LN	T	Patrolling (46, 47)
	Lung	Eosinophils	Patrolling (33)
Tumor	Lungs	Monocytes	Patrolling (49)
	Ovary	T	Directed (50)
Vaccination	LN	Neutrophils	Arrested (51) Directed (51) Patrolling (51) Swarming (51)
	Vasculature	Monocytes	Patrolling (52)

INTRAVITAL IMAGING WORKFLOW

The application of MP-IVM for the imaging of multiple cells during the inflammatory process involves the following steps.

Cell labeling

Different methods are available, including the adoptive transfer of cells from transgenic animals expressing a fluorophore-tagged protein, *in vitro* labeling with fluorescent dies, or the injection of fluorescently labeled antibodies that specifically bind to the cells of interest. Available optical probes for MP-IVM and fluorescent proteins are comprehensively reviewed elsewhere (53, 54) and are beyond the scope of this work.

Surgery

The next step to perform a MP-IVM protocol is to select the proper surgical model, to enable the exposure and immobilization of the targeted organ (**Figure 1A**) (8, 9, 55). Although this typically requires minimally invasive surgery, more advanced surgical setups can be employed for long-term imaging of internal organs, including gut (56), brain and spinal cord (57), primary tumors and metastasis (58, 59) amongst others (60–63).

Image Acquisition

Once surgery is completed, the anesthetized animal is transported to the microscope where image acquisition is performed. The fluorophores present in the sample are excited, and the resulting emitted fluorescence is acquired. A number of microscopy platforms are available for intravital imaging of the immune system (11, 64). Amongst these, multiphoton microscopy (MP-IVM) allows for deeper tissue penetration (by reducing scattering and autofluorescence) and prolonged acquisition time (by significantly reducing photodamage) (65, 66). This is achieved by employing a pulsed laser that emits excitation photons in the near-infrared range (NIR). The simultaneous absorption of multiple photons by a single fluorophore leads to the emission of one photon with higher energy. Finally, emitted photons are collected with detectors such as high-sensitivity photomultipliers (**Figure 1B**) (67).

4D imaging data (time lapses of 3D z-stacks) are obtained at different time points by sliding the excitation point throughout the sample on a focal plane and repeating this process by moving the focal plane along the z-axis. One drawback of this process is the reduced acquisition speed of MP-IVM. Conversely, other technologies such as resonant scanners or spinning disk confocal microscopy may be employed to capture rapid biological processes such as short-lived interactions or morphological changes (68).

Data Analysis

The standard pipeline to analyze IVM videos consists of tracking the cells in the field of view, then computing motility measures from the cell trajectories (**Figure 1C**) (69, 70). Computer vision stands as a promising approach to automatically performing cell tracking (71). However, to date, a series of limitations hamper the accuracy of state-of-the-art automatic tracking algorithms when applied to immune cells observed *via* MP-IVM. For example, the high plasticity of the immune cells might yield to double tracking errors (69). Additionally, the high cell density associated with biological processes such as swarm formation hinder the distinction of individual cells. Lastly, technical artifacts introduced by the intravital imaging, such as varying signal-to-noise ratio across space and time, might affect the overall experimental readout (72, 73).

Therefore, to obtain insightful results, manual tracking and editing of automatically generated tracks are still required. Indeed, manual tracking significantly minimizes tracking errors and improves the accuracy of motility measures used to quantify cell migration and interaction (13). However, these procedures are time-consuming and prone to bias from each individual researcher.

Common Measures of Cell Motility

A variety of measures formerly used to study particle dynamics in physics have been adopted by image analysts to study cell

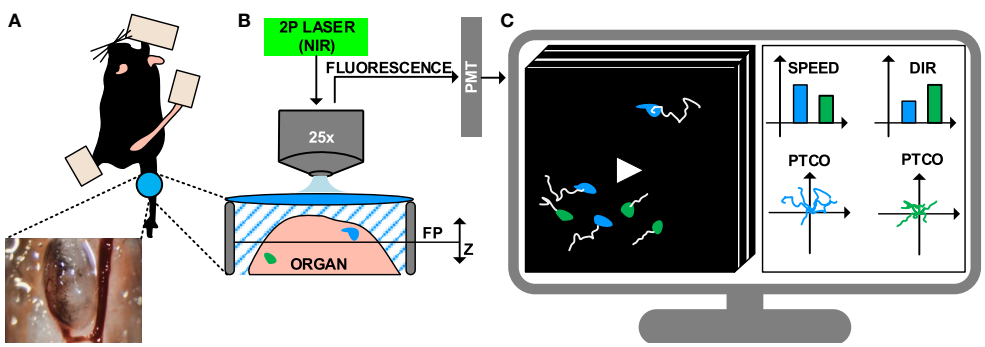

FIGURE 1 | Intravital imaging of the immune system under inflammatory conditions. **(A)** Representation of the surgical model used to perform intravital imaging in the murine popliteal lymph node, including a minimally invasive surgery and imaging through a transparent window. **(B)** Example of intravital imaging setup based on 2-photon microscopy, including a pulsed laser with near-infrared (NIR) emission wavelengths and photomultipliers (PMT) for fluorescence detection. **(C)** 4D videos (3D z-stacks over time) capturing cell motility are acquired and visualized on a computer. Cells are tracked (white lines) to compute metrics such as speed, directionality (dir), and plotting of tracks with a common origin (PTCO).

motility in different experimental setups, including intravital imaging (69, 70). Amongst these, speed and confinement ratio (also known as directionality, or meandering index) are the most common parameters when performing MP-IVM analysis of immune cells. Speed is defined as the ratio between the track length and the track duration, while the confinement ratio is defined as the distance between the first and the last point of the trajectory (displacement) divided by the total length of the track followed by a cell. This parameter tends to 1 for straight tracks, but decreases to 0 for circular tracks.

The aforementioned measures can be computed either on entire tracks (*track-based*) or on track fragments (*step-based)* (51). Track-based measures describe the overall motility of a cell for the entire period of observation. An important limitation in the application of these measures is that tracking errors can compromise the readout. Additionally, a cell whose behavior varies over time is represented by a single average value, yielding to an information loss. By contrast, step-based measures are computed amongst adjacent time points only, or on a temporal window, limiting the temporal propagation of errors. Moreover, step-based measures further allow the quantification of instantaneous changes in cell behavior, which may occur over time, rather than taking an average value of the entire track. If cells cannot be tracked for long periods of time, a step-based measure may represent the only possible choice for quantification.

More advanced measurements to evaluate the directionality of cells have also been defined. For example, the mean squared displacement analysis (MSD) evaluates the diffusivity of a particle by comparing it with the expected motion of a random walk. This measure can be represented by plotting the squared displacement over consecutive time steps, resulting in a straight line for a randomly diffusive process. Conversely, plots above this line refer to super diffusive, or directed, processes, while plots below it indicate a confined motion (74). The motility coefficient, expressed in μm^2/min, is a diffusivity measure derived from the MSD (70). This coefficient considers the square of the cell displacement over time, which can be inferred as the slope of the MSD plot and can be used to compare migratory modes of different cells. In addition, the distribution of the turning angles can be evaluated to assess how much a cell deviates from its previous path. Following this analysis, narrow distribution centered on small angles are indicative of straight trajectories (75).

ACTIONS PERFORMED BY INDIVIDUAL CELLS

Patrolling

Patrolling, also referred as scanning (76) or stochastic migration (46, 77), is an action associated with random-like movement characterized by long tracks in a confined area, which results in low directionality (**Figures 2A, B**) (19). The speed of patrolling cells varies according to the cell type, conditions, and anatomical site. For instance, monocytes exhibited a speed of 36 μm/min in the endothelium of carotid arteries and 9 μm/min in the mesenteric venules (52), while B cells exhibited a speed of 6 um/min in the lymph node follicles.

Patrolling cells are found in different biological processes occurring both at steady state and under inflammatory conditions.

Maximization of antigen encountering in steady state conditions

Patrolling cells are capable of monitoring large areas and promptly responding to specific antigens. For example, monocytes display a patrolling behavior while monitoring the endothelium of blood vessels (**Figures 2C, i**) (19). Upon activation, these cells promote the recruitment of immune cells locally *via* paracrine secretion of proinflammatory cytokines (16, 19, 20, 34, 52), and transient interactions (21). Similarly, a population of neutrophils were described with a patrolling behavior within the lumen of blood vessels. This was and associated with an increased capacity of these cells for being recruited to the inflammation site (78, 79). More recently, tissue-resident eosinophils have also been reported to display a patrolling behavior in different organs (33, 40).

In the LN, patrolling B cells continuously survey subcapsular macrophages and follicular dendritic cells in order to identify antigens that are either presented on a cell surface or suspended in the environment (80). Moreover, within the germinal centers (GC), patrolling B cells exhibited a probing, dendritic morphology that conferred them a larger surface area and therefore a greater opportunity for antigen encountering (**Figures 2C, ii**) (80). In addition, patrolling of T cells was also reported as a strategy to maximize the encountering of antigen presenting cells (APCs) (46, 77, 81) and avoid obstacles in densely packed microenvironments (82). Finally, Bajenoff and colleagues reported that the apparently random movement associated with the patrolling of T cells in the LN is indeed reflecting the complex network of fibroblastic reticular cells (47).

Patrolling under inflammatory conditions

NK cells were reported to maintain a patrolling behavior during priming (26), and while searching for cognate targets and transformed cells (**Figure 2C, iii**) (24), suggesting that the patrolling pattern is an efficient strategy for sensing and integrating cytokine signals under inflammatory conditions (26). Similarly, T cells displayed a patrolling behavior in the LN, to integrate signals from multiple APCs. Upon the encountering of APCs this behavior was maintained if the affinity was low, or switched to the formation of local clusters in case of high affinity (83).

Moreover, within the tumor microenvironment, patrolling monocytes were also associated with immune surveillance, promptly detecting tumor material, establishing interactions with metastasizing cells, and promoting recruitment and activation of natural killer (NK) cells in lung carcinoma (49).

Directed Migration

Directed migration is associated with cells displacing along straight trajectories. These cells typically exhibit long tracks with high confinement ratio and possibly high speed (**Figures 2D, E**) depending on the cell type, the conditions, and the microenvironment.

In inflammatory contexts, cells undergo directional migration in response to chemotactic cues and inflammatory signals, as well as when influenced by anatomical structures. Generally, directional migration is described as a strategy to rapidly reach a specific target,

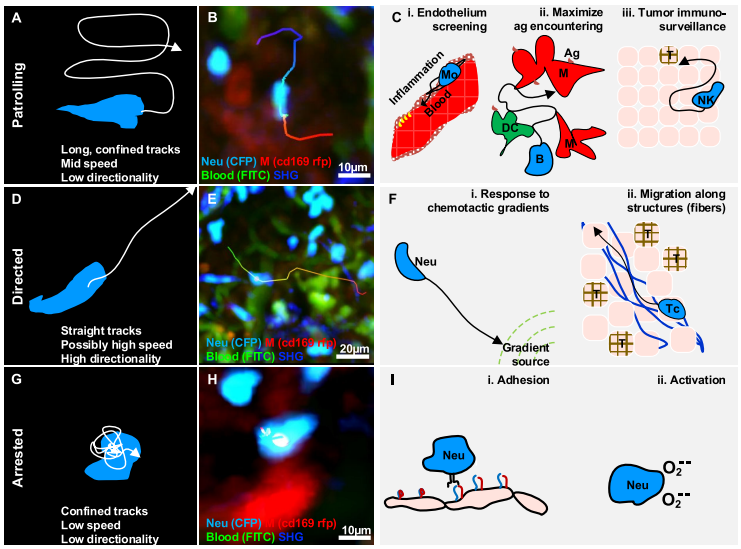

FIGURE 2 | Gallery of actions displayed by individual immune cells. **(A)** Illustration of a patrolling cell, with the characteristic long track in a confined area, which is associated with mid-speed and low directionality (high confinement). **(B)** MP-IVM micrograph showing a patrolling neutrophil (light blue) migrating between macrophages (red) in the subcapsular sinus of a lymph node following infection. **(C)** Illustration of biological cases of patrolling behavior, including **(i)** a monocyte (Mo) screening the endothelium of blood vessels, **(ii)** a B cell surveying antigen-presenting cells in the lymph nodes (M: macrophages, DC: dendritic cells), and **(iii)** a natural killer (NK) cell during immune-surveillance in tumor microenvironments (T). **(D)** Illustration of a cell migrating directionally, with the characteristic straight tracks associated with high directionality and possibly high speed. **(E)** MP-IVM micrograph showing a neutrophil (light blue) exhibiting directed migration towards the subcapsular sinus area of a lymph node following infection. **(F)** Illustration of biological cases of directed migration including **(i)** a neutrophil (Neu) directed towards the source of a chemotactic gradient, and **(ii)** a T cell (Tc) moving with directed migration while following collagen fibers (blue structures) in the tumor microenvironment (T). **(G)** Illustration of an arrested cell with the characteristic folded track, which is associated with a low speed and high confinement. **(H)** MP-IVM micrograph showing a neutrophil (light blue) arresting in the proximity of a macrophage (red) in the subcapsular sinus area of a lymph node following infection. **(I)** Illustration of biological cases of arresting including **(i)** a neutrophil (Neu) during an adhesive interaction with an epithelial cell layer, and **(ii)** a neutrophil arresting during the production of reactive oxygen species.

which also plays important roles in recruitment, tissue repair, cleaning, and antigen presentation (84, 85). Amongst the different biological context where cells display this action we can find:

Response to Chemotactic Gradients

One of the best-characterized processes associated with directional migration is chemotaxis, which involves the polarization and displacement of cells towards the source of a chemotactic gradient (**Figures 2F, i**). For instance, neutrophils perform directed migration towards injured, infected, or inflamed areas (35, 37, 44, 86, 87), where their presence is relevant for tissue repairing, microbial clearing (88), amplification of the inflammatory response (89), and shaping of the adaptive immune response (90). In addition, macrophages perform directed migration in interstitial tissue in response to bacterial infection or tissue injury (91).

Influence of Anatomical Structures on the Directed Migration

Tissue architecture can influence cell movements, conferring properties of directed migration. The most compelling example is the transportation of cells *via* the bloodstream (92, 93). More recently, transportation of immune cells *via* lymphatics (94, 95) was also reported and associated with a strategy for rapidly reaching lymphoid tissues (84). Moreover, the architecture of the LN was reported to influence the recruitment of B and T cells, which displayed directional migration to relocate precisely in their respective areas (96). Finally, directed migration of immune cells was also associated with the architecture of tumor microenvironments. For instance, CD8+ T cells exhibited a directed migration pattern along collagen fibers in a model of ovarian carcinoma (50) (**Figures 2F, ii**).

Arresting

Arresting is an action associated with cells that typically display confined trajectories and a speed below a predefined threshold (96) (**Figures 2G, H**). However, the migration of immune cells typically involves alternating cycles of "stop-and-go" (97). Hence, to define a cell as arrested, we consider that it should be tracked for longer than the duration of the stop-and-go cycle.

During the inflammatory process, motile cells change their behavior to arresting in order to perform a variety of functions, including signaling, killing, and activation.

Cell Activation and Signaling

Effective intracellular communication requires arresting. Notably, both B cells and T cells undergo an arresting phase prior to interacting with DC during priming (98). This step is essential to maximize the contact duration and to induce signaling.

In neutrophils, arresting was associated with the oxidative burst (38), a state in which reactive oxygen species are generated.

This occurs both during phagocytosis and in response to soluble antigens. In contrast, Beuneu and colleagues (26) reported that NK cells do not arrest while being activated by DC. However, NK cells were reported to arrest in the medullary part of the LN (99) following influenza vaccination. Although the arrested NK cells were forming stable contacts with macrophages, this behavior was not associated with NK-mediated lysis. Therefore, it may suggest an alternative activation pattern.

Killing

The formation of stable contacts between a cytotoxic cell and its target is one of the best-characterized biological processes during which cytotoxic cells arrest. For instance, $CD8^+$ T cells arrest during the formation of the cytotoxic synapses with target cells and resume their migration after killing the target (48, 100).

Adhesive Interactions During Recruitment

During recruitment from the blood stream, several types of leukocytes form adhesive interactions with stromal cells, leading to a decrease in motility and eventually to their arrest (22, 96) (**Figure 2I**). This process has been extensively revised (4, 101) and coincides with findings showing, that T cells interacting with lymphatic capillaries were commonly arrested (18).

ACTIONS PERFORMED BY TWO OR MORE CELLS

Studies of cell migration have typically been performed by quantifying the motility of individual cells. Collective migration patterns, meanwhile, are more difficult to interpret (69) but they remain necessary for understanding complex biological processes such as inflammation. Indeed, Mayor and colleagues argue that considering cells as part of supracellular entities allows the quantification of migration at a higher scale (102).

Contact Formation

Contact formation is an action characterized by the absence of space between two or more cells (103) (**Figures 3A, B**). Indeed, during contact formation, the distance between membranes of cells decreases up to a distance of 15 nm to 100 nm (104). Cells forming contacts may exhibit an arrested behavior or maintain a patrolling behavior according to the duration and the type of contact.

Cellular contacts are a form of cell-to-cell communication that enables the formation of clusters between the proteins on the surface of distinct cells (**Figures 3A–C**) (105, 106), and the delivery of highly localized signals (40). Although contacts are continuously formed and disrupted between migratory and resident cells in physiological conditions, certain contacts of immune cells are important for the inflammatory processes (99, 107) due to their involvement in the modulation of the immune response.

Immunological Synapses

One of the best-characterized cases of contact formation between immune cells is the immune synapse that occurs between DC and T cells (**Figures 3C, i**). This process can occur either in lymphoid organs such as the LN (28), or non-lymphoid organs such as the lymphatic capillaries of the ear skin (18), and is pivotal for immunity and tolerance (29). DC play a crucial role in initiating the immune cell response as they scan the surrounding

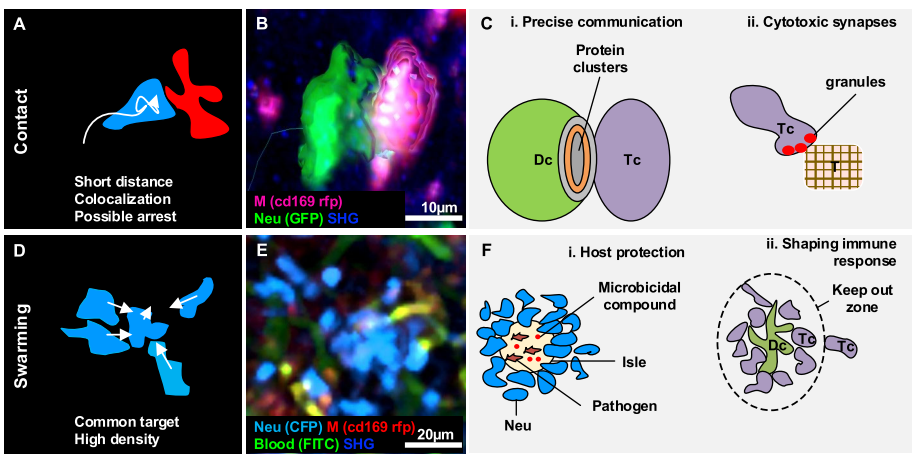

FIGURE 3 | Gallery of actions displayed by two or a collectivity of cells. **(A)** Illustration of the morphodynamics of contact formation between two cells, characterized by a low distance and the possible overlap of colors. **(B)** MP-IVM micrograph showing a neutrophil (green) establishing contact with a macrophage (violet). 3D reconstructions are shown to highlight the shape of the cells during the formation of the contacts. **(C)** Illustration of biological cases of contact formation including **(i)** a T cell (Tc) forming an immunological synapse with a dendritic cell (Dc) with a cluster of proteins in the contact area, and **(ii)** a T cell (Tc) accumulating cytotoxic granules in contact with a tumor cell (T). **(D)** Illustration of the morphodynamics of swarm formation, characterized by cells moving towards a common target, resulting in the accumulation of cells in a confined area (high density). **(E)** MP-IVM micrograph showing a neutrophil swarm (light blue) following infection in the subcapsular area of a lymph node. **(F)** Illustration of biological cases including **(i)** a swarm of neutrophil (Neu) to contain pathogens in an isle enriched with microbicidal compounds, and **(ii)** a swarm of T cell (Tc) accumulating around an antigen-presenting dendritic cell (Dc) to prevent the other Tc from interacting with the Dc.

environment in search of antigens to capture and present to naive T cells (108). The interaction between T cells and DC follow a series of steps characterized by a varying contact duration. At first, T cells engage many short-lived contacts with the surrounding DC, reducing their overall motility due to the multiple interactions (25). Upon successful encountering of a DC presenting the antigen specific for the T cell receptor, long-term stable contacts occur, and T cells remain arrested, which leads to their activation. Finally, the T cell recover its motility and proliferate. This process has been observed in an OT-I model, where a comparison between antigen-specific $CD8^+$ T cells and polyclonal $CD8^+$ T cells revealed that antigen-specific cells significantly decreased their speed in response to the formation of stable interactions with DC (109). By contrast, polyclonal $CD8^+$ T cells maintained a constant speed (109). This finding is in agreement with the T-DC model, where different phases of the T cell-DC interaction were associated with different contact durations (28), and highlights the importance of contact duration for efficient cell activation (30).

Moreover, some studies reported that NK cells maintained a motile behavior during the formation of short-term (1 – 3 min) contacts with DC, by recognizing cytokines on the surface of DC in addition to soluble signals (23, 43). This suggested an efficient strategy to sense and integrate cytokine signals from multiple DC (23). However, other *in vivo* studies have reported the formation of stable contacts with macrophages during the activation of these cells (99), in accordance with previous studies performed *in vitro* (110, 111).

Cytotoxic Synapses and Lysis

Cytotoxic T leukocytes (CTL) can establish cytotoxic synapses with target cells, which eventually leads to the lysis of the target (112). Cytotoxic synapses formed by $CD8^+$ T cells (**Figures 3C, ii**), rely on a shared molecular mechanism with $CD4^+$ T cell immunological synapses (112). However, $CD8^+$ T cell synapses appear to be more stable and efficient in killing the target (113). Two known killing mechanisms involve the binding of Fas death ligand to Fas death receptor, resulting in the induction of apoptotic death by caspase activation (114). The second mechanism involves calcium-dependent release of perforin and granzymes, yielding to the activation of alternative apoptotic pathways (114). The latter mechanism was reported to be faster since it does not require specific receptors to be activated (112). Common targets of CTL are virus-infected or transformed cells. Moreover, CTL killing efficiency was reported to be affected by the affinity for its ligand (25, 112).

NK cells are also able to form contacts to lyse target cells through degranulation of lytic enzymes. Within the LN, NK has been observed to form contacts with B cells to eliminate major histocompatibility complexes mismatched targets (24). Additionally, in the context of tumor microenvironment, NK-mediated lysis was reported to occur either by establishing contacts of long duration with a single NK or *via* multiple short contacts with several NK (26).

Swarming

Swarming is an action that involves a collectivity of cells clustering in a defined space or moving towards a common target in a coordinated manner, giving rise to a swarm (**Figures 3D, E**) (42). Swarms have been classified according to their size and duration (42). Transient swarms with fewer than 150 cells are reported to last up to 40 minutes. Larger swarms can include more than 300 cells and can persist for hours (42).

The swarming process has been primarily described in neutrophils, which form cell aggregates in inflamed and injured tissues. Notably, duration and swarm size were positively correlated with the severity of the tissue damage or infection, with extended lesions massively recruiting neutrophils involved in swarms that persisted for days (32, 115). Cell death, known to induce recruitment of phagocytic cells (51, 116, 117), is regarded as one of the triggers of swarming.

Swarming is associated with two key biological functions, host protection and tissue remodeling.

Host Protection

Swarm formation was reported in infection models as a strategy to contain pathogens and protect the host (118). To this end, swarms lead to the confinement of pathogens in isles where microbicidal compounds concentrate (**Figures 3F, i**) (115). Accordingly, neutrophil swarming was observed to contain bacteria spread (39) and limit the growth of fungi *in vivo* (119). Eosinophils were also observed performing swarms throughout the parenchyma in the lungs in different infection models. Amongst these, during parasitic infections, swarms of eosinophils were maintained for several days (120).

Tissue Remodeling and Shaping the Immune Response

Neutrophil swarming was also reported in the context of sterile inflammation. Sterile photo burning (87) and needle damage (44) caused neutrophils to form abrupt and long-lasting clusters of large dimensions, suggesting a role in tissue remodeling and repair.

Additionally, the formation of swarms can alter the cellular structure of immune organs. For instance, swarms formed by neutrophils were reported to disrupt the network of resident SCS macrophages in parasitic infection models (41, 115, 121). Considering that SCS macrophages are important for containing the spread of pathogens (122, 123) and for activating the adaptive immunity (86, 122), the alteration of this cell layer by swarms might influence the overall immune response. Interestingly, other cell types, such as NK cells, were also observed to form swarms in the SCS area of the LN and to interact with resident $CD11b^+$ cells. The accumulation of NK cells in the SCS area was linked to the function of promoting self-activation by the encountering of specific APC (124). Other cell types such as T cells were reported to form swarms around APC following immunization. Since most of the interactions in the swarms were maintained over time (108), it has been proposed that swarms may keep newly arrived T cells at the boundaries of the swarm, limiting their interaction with DC (**Figures 3F, ii**) (108). Finally, swarming of invariant natural killer T cells was associated with a reduced level of fibrosis in a model of steatohepatitis (17), suggesting a further role of swarming in tissue remodeling under inflammatory conditions.

METHODS TO DETECT AND QUANTIFY CELL ACTIONS

Due to the difficulties associated with the processing and quantification of IVM movies (125), computational methods have become essential for the analysis of cell motility *in vivo*. A variety of software and methods were applied to detect and quantify cell actions. A summary of these methods, including how to use them and how to interpret the computed numerical values is presented in **Table 2**.

Quantification of Patrolling Cells

To quantify the patrolling behavior, coefficients that evaluate the displacement over time, such as the directionality and the motility index are typically used. These coefficients are larger than the ones displayed by arrested cells, but lower than the values displayed by directional cells (18, 126, 127). Additionally, the previously mentioned MSD analysis can be used to distinguish patrolling cells from arrested or directed cells, as they display a random-like migratory pattern. However, several studies demonstrated that the movement of cells *in vivo* is not stochastic, but rather influenced by alternative parameters such as the interaction with stromal cells, amongst others (70). Therefore, we suggest to complement the MSD analysis with other parameters, such as the angle or speed distribution, which would provide additional insights on the migratory mode.

Quantification of Directed Cells

Directional migration can be inferred by plotting the trajectories of the analyzed cells with a common origin, resulting in tracks

TABLE 2 | Software and tools to quantify cell actions.

Action	Tools	How to use	How to interpret	Requires surfaces	Requires tracking
Patrolling	Imaris	After having tracked each cell, use the Filter tool to select tracks according to Track Length and Track Straightness.	High Track Length, and mid–low Track Straightness are indicative of patrolling	no	Yes
	Icy, QuantEV	Launch the QuantEV plugin (track processor) and select tracks according to the confinement ratio distribution	A confinement ratio distribution skewed towards the right indicates patrolling	no	yes
	Fiji. Trajectory classifier	Run the Trajectory classifier for TrackMate plugin, analyze the tracks	Patrolling cells are typically classified as "subdiffusive".	no	yes
Directed	Microsoft Excel, Matlab, Imaris	Import into Microsoft Excel, Matlab, or a similar program the standard track measures, such as Track Duration and Track Straightness from Imaris. Exclude short tracks (i.e., < 300s) or add a rule to compute normalized Track Straightness.	Track Straightness is close to 1 indicates directed migration	optional	yes
	Icy, QuantEV	Launch the QuantEV plugin (track processor) and select tracks whose	A confinement ratio distribution skewed towards the left indicates directed migration	no	yes
	Fiji, Trajectory classifier	Run the Trajectory classifier for TrackMate plugin, analyze the tracks.	Directed cells are typically classified as "directed/active motion".	no	yes
Arresting	Imaris, Arrest Coefficient XT	Select the cells of interest, launch the plugin, and define a speed threshold to consider a cell arrested. The plugin computes the arrest coefficient and counts the number of stops for each cell.	Values of the arrest coefficient close to 1 indicate arresting	optional	yes
	Icy, QuantEV	Launch the QuantEV plugin (track processor) and select tracks whose lifetime is sufficiently high.	Total path length of arrested cells is typically low.	no	yes
Contact formation	Imaris, Kiss and Run XT	Launch the plugin, define a distance threshold to detect a contact (i.e., 2 μm) and select two surfaces (i.e., two types of cells) to compute contact number and duration for each single cell.	The plugin automatically reports the number and the duration of contacts which can be used to discriminate between short- and long-lived interactions	yes	optional
	Imaris, Colocalization, Matlab	To detect contacts between cells of different color, launch the Coloc functionality to create an imaging channel specific to the contacts. Create a surface on this new channel and export the number of surfaces to count contacts. Smoothing can be applied to enhance contact detection with minimal overlap.	Contacts are associated with regions having a high brightness intensity in the created colocalization channel	no	no
Swarming	Matlab/R, etc.	Import cell tracks, compute the distance over time vs. a common target.	If multiple cells display a reduction of the distance over time towards a common target, this might recall a swarming behavior.	no	yes
	Matlab/R, etc.	Import cell tracks and compute a density map based on the emitted fluorescence, or a velocity map based on optical flow	Swarming is associated with regions having high density and convergent velocity tensors	no	yes
	Imaris	Reconstruct a surface on all the cell of interest with large smoothing (> expected cell diameter), divide the surface volume by the typical cell volume to overestimate cells in the swarm, and apply smoothing to fill gaps.	Swarming is associated with large areas or volumes of the reconstructed surfaces. A growing behavior can be inferred by plotting the surface area or volume over time	yes	no

with a strong preferential migration direction (45, 51, 63). More quantitatively, one of the parameters that better characterizes directed migration is the confinement ratio, which presents high values for highly directional cells (69). However, the confinement ratio of different tracks is comparable only if they have similar track durations. Otherwise, normalizing the trajectories for their duration is often required. Another measure typically used for predicting directed migration is the distribution of the turning angles (36). Following this analysis, a skewing toward small angles would indicate that a cell trajectory does not deviate abruptly from its established path. In addition, the MSD analysis could also indicate directional migration recalling super diffusivity (36, 44).

When analyzing the overall motility of a cell population, directional migration can be inferred by evaluating the distance over time of all the cells with respect to a reference point or region. The chosen reference point should ideally represent a common target (32, 41, 51, 115) towards which the distance decreases or increases.

Quantification of Arresting Cells

An arrested cell is typically detected by evaluating the arrest coefficient (69). This coefficient measures the amount of time in which a cell migrates with a speed below a defined threshold (typically 2 μm/min) (31). However, the value of the arrest coefficient depends on the track duration. Therefore, tracks (or track fragments) with similar duration should be compared; otherwise, normalization strategies are required for comparative studies (i.e., dividing the arrest coefficient by the track duration). The confinement ratio used to predict the directionality of a trajectory is also used to detect arrested cells, which typically display low values (31).

Quantification of Contacts

Contacts are typically detected by evaluating the distance between cells. Such a distance can be computed either between the centroids of the cells (75), or reconstructed surfaces (i.e. between the closest points of two cells) (13). In the first case, a contact is detected when the distance is less than a threshold, which is equal to the expected cell diameter. However, errors may be introduced when cells with a non-convex shape are analyzed. In the second case, the distance threshold is preferably small, up to the spatial resolution of the microscope (i.e., 1 μm). This allows to detect contacts between cells of arbitrary shapes. However, the distance between the membranes of two cells forming a contact is on average lower than the spatial resolution of fluorescent microscopes used in intravital imaging (0.2 μm – 0.3 μm) (128). Moreover, an accurate reconstruction of cell surfaces might be hampered by the presence of cell-to-cell contacts themselves (13). For these reasons, cell-to-cell contacts are still annotated manually (18). More robust approaches inferred contact formation from time series, such as the trajectories of the individual cells or the changes in cell speed (27). Moreover, spatial colocalization of two distinct fluorophores can be used to highlight overlapping cells without the need for surface reconstruction (27) nor the computation of spatial distances between cells.

Contact dynamics can be quantified by computing for each cell the contact duration and the number of contacts. This ultimately allows one to distinguish between transient and long-lasting contacts.

Quantification of Cell Swarms

To quantify swarm dynamics in the case of localized tissue damage or infection, the distance between the affected region and each cell at different time points can be computed. Cells whose distance over time falls below a defined threshold are considered part of a forming swarm (32, 41, 44, 51, 63).

Alternatively, when the swarm coordinates are not known, the increase of fluorescence intensity over time in different areas can be computed. In turn, surface and volumetric reconstruction enable the monitoring of the swarm growth over time by encompassing the fluorescence intensity emitted by the forming swarm (41, 45, 51). This provides insights into the different stages of the process, including initiation, growth, stabilization (41) and whether the swarm is transient or persistent (119). Furthermore, dividing the measured surface or volume by the mean volume or area of cells leads to an estimate of the number of swarming cells (41).

Swarming can be also inferred from the trajectories and speed of cells. Indeed, color coding the cell trajectories for their instantaneous cell speed can help to locate transient and persistent swarms (39). Similarly, representing a heatmap of the cell velocities and densities generates a spatiotemporal visualization that accounts for both migratory and clustering dynamics (38).

CONCLUDING REMARKS

In line with the computer vision community, we considered distinct motility patterns displayed by cells as elementary actions (129, 130), which are the building blocks of several biological processes. This approach is relevant to dissecting the complex dynamics of inflammation, as it provides a link between identifiable morpho-phenotypes and the underlying cellular function. Moreover, by detecting the occurrence of each action over time, it is possible to quantify the dynamic behavior of immune cells in response to different stimuli.

Another advantage of decomposing cell motility in elementary actions is that these can be quantified from tracks of short duration (tracklets) or short image sequences using instantaneous measures. However, a longer imaging time can lead to more accurate results for actions such as swarming, which can persist for up to several hours.

In this review, the visual approach adopted to classify each action further aims to facilitate the interpretation of intravital microscopy data for immunologists and imaging specialists. The described measurements and definitions are provided to help researchers in differentiating between distinct cellular actions from a motility perspective. These are, however, intended only as guidelines rather than absolute discriminatory factors, as no consensus definition and numerical characterization exists thus far. In fact, to identify cell actions, it might be necessary to adopt

a gating strategy that considers the combination of several motility parameters (51). Future advancements in this direction will require further characterization of cell motility based on the function, cell type, and organ.

In conclusion, the development of computer vision methods for cellular action recognition represents a promising methodology for deciphering biological processes occurring *in vivo* from imaging data.

INCLUSION CRITERIA

This review includes studies that reported specific motility patterns of immune cells, which were observed under inflammatory conditions *in vivo*. The included imaging modalities were MP-IVM, spinning disk, laser scanning confocal, and epifluorescence microscopy. All the definitions of cell actions used in this work were inferred from the original studies. In most cases, the authors explicitly named the migratory patterns displayed by the imaged cells. Indeed, directed migration, arresting, contact formation and swarming (or clustering) are well-characterized processes that were typically referred to using a direct name. In these cases, we did not perform re-analysis of the data. In the case of patrolling instead, studies referred to it either with the same term, or a similar nomenclature (i.e., scanning, undirected migration, random migration), or provided measurements whose values were indicative of this motility pattern.

AUTHOR CONTRIBUTIONS

DP and AP reviewed the literature and wrote the manuscript. MT and RK corrected the manuscript. SG supervised and wrote the manuscript. All authors contributed to the article and approved the submitted version.

FUNDING

This work was supported by the Swiss National Foundation (SNF) grants, 176124, SystemsX.ch (2013/124), Biolink (189699).

REFERENCES

1. Luster AD, Alon R, von Andrian UH. Immune Cell Migration in Inflammation: Present and Future Therapeutic Targets. *Nat Immunol* (2005) 6:1182–90. doi: 10.1038/ni1275
2. BB MD. Systemic Response to Inflammation. *Nutr Rev* (2008) 65:S170–2. doi: 10.1111/j.1753-4887.2007.tb00357.x
3. Voisin MB, Nourshargh S. Neutrophil Transmigration: Emergence of an Adhesive Cascade Within Venular Walls. *J Innate Immun* (2013) 5:336–47. doi: 10.1159/000346659
4. Ley K, Laudanna C, Cybulsky MI, Nourshargh S. Getting to the Site of Inflammation: The Leukocyte Adhesion Cascade Updated. *Nat Rev Immunol* (2007) 7:678–89. doi: 10.1038/nri2156
5. Teixidó J, Hidalgo A, Fagerholm S. Editorial: Leukocyte Trafficking in Homeostasis and Disease. *Front Immunol* (2019) 10:2560. doi: 10.3389/fimmu.2019.02560
6. Nowarski R, Gagliani N, Huber S, Flavell RA. Innate Immune Cells in Inflammation and Cancer. *Cancer Immunol Res* (2013) 1:77–84. doi: 10.1158/2326-6066.CIR-13-0081
7. Barton GM. A Calculated Response: Control of Inflammation by the Innate Immune System. *J Clin Invest* (2008) 118:413–20. doi: 10.1172/JCI34431
8. Pittet MJ, Garris CS, Arlauckas SP, Weissleder R. Recording the Wild Lives of Immune Cells. *Sci Immunol* (2018) 3:eaaq0491. doi: 10.1126/sciimmunol.aaq0491
9. Stein JV, Gonzalez SF F, Gonzalez S, Gonzalez SF. Dynamic Intravital Imaging of Cell-Cell Interactions in the Lymph Node. *J Allergy Clin Immunol* (2017) 139:12–20. doi: 10.1016/j.jaci.2016.11.008
10. Cahalan MD, Parker I, Wei SH, Miller MJ. Two-Photon Tissue Imaging: Seeing the Immune System in a Fresh Light. *Nat Rev Immunol* (2002) 2:872–80. doi: 10.1038/nri935
11. Sumen C, Mempel TR, Mazo IB, Von Andrian UH. Intravital Microscopy: Visualizing Immunity in Context. *Immunity* (2004) 21:315–29. doi: 10.1016/j.immuni.2004.08.006
12. SenGupta S, Parent CA, Bear JE. The Principles of Directed Cell Migration. *Nat Rev Mol Cell Biol* (2021) 22. doi: 10.1038/s41580-021-00366-6
13. Pizzagalli DU, Farsakoglu Y, Palomino-Segura M, Palladino E, Sintes J, Marangoni F, et al. Leukocyte Tracking Database, a Collection of Immune Cell Tracks From Intravital 2-Photon Microscopy Videos. *Sci Data* (2018) 5:180129. doi: 10.1038/sdata.2018.129
14. Figge MT, Murphy RF. Image-Based Systems Biology. *Cytometry A* (2015) 87:459–61. doi: 10.1002/cyto.a.22663
15. Poppe R. A Survey on Vision-Based Human Action Recognition. *Image Vis Comput* (2010) 28:976–90. doi: 10.1016/j.imavis.2009.11.014
16. Finsterbusch M, Hall P, Li A, Devi S, Westhorpe CLV, Kitching AR, et al. Patrolling Monocytes Promote Intravascular Neutrophil Activation and Glomerular Injury in the Acutely Inflamed Glomerulus. *Proc Natl Acad Sci* (2016) 113:E5172–81. doi: 10.1073/pnas.1606253113
17. Wang H, Li L, Li Y, Li Y, Sha Y, Wen S, et al. Intravital Imaging of Interactions Between iNKT and Kupffer Cells to Clear Free Lipids During Steatohepatitis. *Theranostics* (2021) 11:2149–69. doi: 10.7150/thno.51369
18. Hunter MC, Teijeira A, Montecchi R, Russo E, Runge P, Kiefer F, et al. Dendritic Cells and T Cells Interact Within Murine Afferent Lymphatic Capillaries. *Front Immunol* (2019) 10:520. doi: 10.3389/fimmu.2019.00520
19. Auffray C, Fogg D, Garfa M, Elain G, Join-Lambert O, Kayal S, et al. Monitoring of Blood Vessels and Tissues by a Population of Monocytes With Patrolling Behavior. *Science (80-)* (2007) 317:666–70. doi: 10.1126/science.1142883
20. Carlin LM, Stamatiades EG, Auffray C, Hanna RN, Glover L, Vizcay-Barrena G, et al. Nr4a1-Dependent Ly6Clow Monocytes Monitor Endothelial Cells and Orchestrate Their Disposal. *Cell* (2013) 153:362–75. doi: 10.1016/j.cell.2013.03.010
21. Westhorpe CLV, Ursula Norman M, Hall P, Snelgrove SL, Finsterbusch M, Li A, et al. Effector CD4+ T Cells Recognize Intravascular Antigen Presented by Patrolling Monocytes. *Nat Commun* (2018) 9. doi: 10.1038/s41467-018-03181-4
22. Phillipson M, Heit B, Colarusso P, Liu L, Ballantyne CM, Kubes P. Intraluminal Crawling of Neutrophils to Emigration Sites: A Molecularly Distinct Process From Adhesion in the Recruitment Cascade. *J Exp Med* (2006) 203:2569–75. doi: 10.1084/jem.20060925
23. Deguine J, Bousso P. Dynamics of NK Cell Interactions *In Vivo*. *Immunol Rev* (2013) 251:154–9. doi: 10.1111/imr.12015
24. Garrod KR, Wei SH, Parker I, Cahalan MD. Natural Killer Cells Actively Patrol Peripheral Lymph Nodes Forming Stable Conjugates to Eliminate MHC-Mismatched Targets. *Proc Natl Acad Sci* (2007) 104:12081–6. doi: 10.1073/pnas.0702867104
25. Mempel TR, Pittet MJ, Khazaie K, Weninger W, Weissleder R, von Boehmer H, et al. Regulatory T Cells Reversibly Suppress Cytotoxic T Cell Function Independent of Effector Differentiation. *Immunity* (2006) 25:129–41. doi: 10.1016/j.immuni.2006.04.015

26. Beuneu H, Deguine J, Breart B, Mandelboim O, Di Santo JP, Bousso P. Dynamic Behavior of NK Cells During Activation in Lymph Nodes. *Blood* (2009) 114:3227–34. doi: 10.1182/blood-2009-06-228759
27. Miller MJ, Hejazi AS, Wei SH, Cahalan MD, Parker I. T Cell Repertoire Scanning is Promoted by Dynamic Dendritic Cell Behavior and Random T Cell Motility in the Lymph Node. *Proc Natl Acad Sci USA* (2004) 101:998–1003. doi: 10.1073/pnas.0306407101
28. Mempel TR, Henrickson SE, von Andrian UH. T-Cell Priming by Dendritic Cells in Lymph Nodes Occurs in Three Distinct Phases. *Nature* (2004) 427:154–9. doi: 10.1038/nature02238
29. Shakhar G, Lindquist RL, Skokos D, Dudziak D, Huang JH, Nussenzweig MC, et al. Stable T Cell-Dendritic Cell Interactions Precede the Development of Both Tolerance and Immunity *In Vivo*. *Nat Immunol* (2005) 6:707–14. doi: 10.1038/ni1210
30. Celli S, Lemaître F, Bousso P. Real-Time Manipulation of T Cell-Dendritic Cell Interactions *In Vivo* Reveals the Importance of Prolonged Contacts for CD4+ T Cell Activation. *Immunity* (2007) 27:625–34. doi: 10.1016/j.immuni.2007.08.018
31. Hugues S, Fetler L, Bonifaz L, Helft J, Amblard F, Amigorena S. Distinct T Cell Dynamics in Lymph Nodes During the Induction of Tolerance and Immunity. *Nat Immunol* (2004) 5:1235–42. doi: 10.1038/ni1134
32. Lämmermann T, Afonso PV, Angermann BR, Wang JM, Kastenmüller W, Parent CA, et al. Neutrophil Swarms Require LTB4 and Integrins at Sites of Cell Death *In Vivo*. *Nature* (2013) 498:371–5. doi: 10.1038/nature12175
33. Chojnacki A, Wojcik K, Petri B, Aulakh G, Jacobsen EA, LeSuer WE, et al. Intravital Imaging Allows Real-Time Characterization of Tissue Resident Eosinophils. *Commun Biol* (2019) 2:181. doi: 10.1038/S42003-019-0425-3
34. Audoy-Remus J, Richard J-F, Soulet D, Zhou H, Kubes P, Vallieres L. Rod-Shaped Monocytes Patrol the Brain Vasculature and Give Rise to Perivascular Macrophages Under the Influence of Proinflammatory Cytokines and Angiopoietin-2. *J Neurosci* (2008) 28:10187–99. doi: 10.1523/JNEUROSCI.3510-08.2008
35. McDonald B, Pittman K, Menezes GB, Hirota SA, Slaba I, Waterhouse CCM, et al. Intravascular Danger Signals Guide Neutrophils to Sites of Sterile Inflammation. *Science (80-)* (2010) 330:362–6. doi: 10.1126/science.1195491
36. Waite JC, Leiner I, Lauer P, Rae CS, Barbet G, Zheng H, et al. Dynamic Imaging of the Effector Immune Response to Listeria Infection *In Vivo*. *PLoS Pathog* (2011) 7:1–16. doi: 10.1371/journal.ppat.1001326
37. Peters NC, Egen JG, Secundino N, Debrabant A, Kimblin N, Kamhawi S, et al. *In Vivo* Imaging Reveals an Essential Role for Neutrophils in Leishmaniasis Transmitted by Sand Flies. *Science (80-)* (2008) 321:970–4. doi: 10.1126/science.1159194
38. Kreisel D, Nava RG, Li W, Zinselmeyer BH, Wang B, Lai J, et al. *In Vivo* Two-Photon Imaging Reveals Monocyte-Dependent Neutrophil Extravasation During Pulmonary Inflammation. *Proc Natl Acad Sci* (2010) 107:18073–8. doi: 10.1073/pnas.1008737107
39. Kienle K, Glaser KM, Eickhoff S, Mihlan M, Knöpper K, Reátegui E, et al. Neutrophils Self-Limit Swarming to Contain Bacterial Growth *In Vivo*. *Science (80-)* (2021) 372(6548):eabe7729. doi: 10.1126/science.abe7729
40. Lee SH, Chaves MM, Kamenyeva O, Gazzinelli-Guimaraes PH, Kang BH, Pessenda G, et al. M2-Like, Dermal Macrophages are Maintained *via* IL-4/CCL24 Mediated Cooperative Interaction With Eosinophils in Cutaneous Leishmaniasis. *Sci Immunol* (2020) 5(46):eaaz4415. doi: 10.1126/SCIIMMUNOL.AAZ4415
41. Chtanova T, Schaeffer M, Han S-J, van Dooren GG, Nollmann M, Herzmark P, et al. Dynamics of Neutrophil Migration in Lymph Nodes During Infection. *Immunity* (2008) 29:487–96. doi: 10.1016/j.immuni.2008.07.012
42. Chtanova T, Schaeffer M, Han SJ, van Dooren GG, Nollmann M, Herzmark P, et al. Dynamics of Neutrophil Migration in Lymph Nodes During Infection (DOI:10.1016/J.Immuni.2008.07.012). *Immunity* (2008) 29:487–96. doi: 10.1016/j.immuni.2008.09.007
43. Bajénoff M, Breart B, Huang AYC, Qi H, Cazareth J, Braud VM, et al. Natural Killer Cell Behavior in Lymph Nodes Revealed by Static and Real-Time Imaging. *J Exp Med* (2006) 203:619–31. doi: 10.1084/jem.20051474
44. Ng LG, Qin JS, Roediger B, Wang Y, Jain R, Cavanagh LL, et al. Visualizing the Neutrophil Response to Sterile Tissue Injury in Mouse Dermis Reveals a Three-Phase Cascade of Events. *J Invest Dermatol* (2011) 131:2058–68. doi: 10.1038/jid.2011.179
45. Park SA, Choe YH, Park E, Hyun YM. Real-Time Dynamics of Neutrophil Clustering in Response to Phototoxicity-Induced Cell Death and Tissue Damage in Mouse Ear Dermis. *Cell Adhes Migr* (2018) 6918:1–8. doi: 10.1080/19336918.2018.1471322
46. Miller MJ, Wei SH, Cahalan MD, Parker I. Autonomous T Cell Trafficking Examined *In Vivo* With Intravital Two-Photon Microscopy. *Proc Natl Acad Sci USA* (2003) 100:2604–9. doi: 10.1073/pnas.2628040100
47. Bajénoff M, Egen JG, Koo LY, Laugier JP, Brau F, Glaichenhaus N, et al. Stromal Cell Networks Regulate Lymphocyte Entry, Migration, and Territoriality in Lymph Nodes. *Immunity* (2006) 25:989–1001. doi: 10.1016/j.immuni.2006.10.011
48. Boissonnas A, Fetler L, Zeelenberg IS, Hugues S, Amigorena S. *In Vivo* Imaging of Cytotoxic T Cell Infiltration and Elimination of a Solid Tumor. *J Exp Med* (2007) 204:345–56. doi: 10.1084/jem.20061890
49. Hanna RN, Cekic C, Sag D, Tacke R, Thomas GD, Nowyhed H, et al. Patrolling Monocytes Control Tumor Metastasis to the Lung. *Science (80-)* (2015) 350:985–90. doi: 10.1126/science.aac9407
50. Bougherara H, Mansuet-Lupo A, Alifano M, Ngô C, Damotte D, Le Frère-Belda M-A, et al. Real-Time Imaging of Resident T Cells in Human Lung and Ovarian Carcinomas Reveals How Different Tumor Microenvironments Control T Lymphocyte Migration. *Front Immunol* (2015) 6:500. doi: 10.3389/fimmu.2015.00500
51. Pizzagalli DU, Latino I, Pulfer A, Palomino-Segura M, Virgilio T, Farsakoglu Y, et al. Characterization of the Dynamic Behavior of Neutrophils Following Influenza Vaccination. *Front Immunol* (2019) 10:2621. doi: 10.3389/fimmu.2019.02621
52. Buscher K, Marcovecchio P, Hedrick CC, Ley K. Patrolling Mechanics of Non-Classical Monocytes in Vascular Inflammation. *Front Cardiovasc Med* (2017) 4:80. doi: 10.3389/fcvm.2017.00080
53. Ricard C, Arroyo ED, He CX, Portera-Cailliau C, Lepousez G, Canepari M, et al. Two-Photon Probes for *In Vivo* Multicolor Microscopy of the Structure and Signals of Brain Cells. *Brain Struct Funct* (2018) 223:3011–43. doi: 10.1007/s00429-018-1678-1
54. Shaner NC, Steinbach PA, Tsien RY. A Guide to Choosing Fluorescent Proteins. *Nat Methods* (2005) 2:905–9. doi: 10.1038/nmeth819
55. Secklehner J, Celso C, Carlin LM. Intravital Microscopy in Historic and Contemporary Immunology. *Immunol Cell Biol* (2017) 95:506–13. doi: 10.1038/icb.2017.25
56. Rakhilin N, Garrett A, Eom CY, Chavez KR, Small DM, Daniel AR, et al. An Intravital Window to Image the Colon in Real Time. *Nat Commun* (2019) 10 (1). doi: 10.1038/s41467-019-13699-w
57. Jahromi NH, Tardent H, Enzmann G, Deutsch U, Kawakami N, Bittner S, et al. A Novel Cervical Spinal Cord Window Preparation Allows for Two-Photon Imaging of T-Cell Interactions With the Cervical Spinal Cord Microvasculature During Experimental Autoimmune Encephalomyelitis. *Front Immunol* (2017) 8:406. doi: 10.3389/fimmu.2017.00406
58. Zhang W, Karschnia P, von Mücke-Heim IA, Mulazzani M, Zhou X, Blobner J, et al. *In Vivo* Two-Photon Characterization of Tumor-Associated Macrophages and Microglia (TAM/M) and CX3CR1 During Different Steps of Brain Metastasis Formation From Lung Cancer. *Neoplasia (United States)* (2021) 23:1089–100. doi: 10.1016/j.neo.2021.09.001
59. Mulazzani M, Fräßle SP, von Mücke-Heim I, Langer S, Zhou X, Ishikawa-Ankerhold H, et al. Long-Term *In Vivo* Microscopy of CAR T Cell Dynamics During Eradication of CNS Lymphoma in Mice. *Proc Natl Acad Sci USA* (2019) 116:24275–84. doi: 10.1073/pnas.1903854116
60. Dunn KW, Sutton TA. Functional Studies in Living Animals Using Multiphoton Microscopy. *ILAR J* (2008) 49:66–77. doi: 10.1093/ilar.49.1.66
61. Soulet D, Lamontagne-Proulx J, Aubé B, Davalos D. Multiphoton Intravital Microscopy in Small Animals: Motion Artefact Challenges and Technical Solutions. *J Microsc* (2020) 278:3–17. doi: 10.1111/jmi.12880
62. Vaghela R, Arkudas A, Horch RE, Hessenauer M. Actually Seeing What Is Going on – Intravital Microscopy in Tissue Engineering. *Front Bioeng Biotechnol* (2021) 9:627462. doi: 10.3389/fbioe.2021.627462
63. Phillipson M, Kubes P. The Neutrophil in Vascular Inflammation. *Nat Med* (2011) 17:1381–90. doi: 10.1038/nm.2514

64. Marques PE, Oliveira AG, Chang L, Paula-Neto HA, Menezes GB. Understanding Liver Immunology Using Intravital Microscopy. *J Hepatol* (2015) 63:733–42. doi: 10.1016/j.jhep.2015.05.027
65. Zipfel WR, Williams RM, Webb WW. Nonlinear Magic: Multiphoton Microscopy in the Biosciences. *Nat Biotechnol* (2003) 21:1369–77. doi: 10.1038/nbt899
66. Helmchen F, Denk W. Deep Tissue Two-Photon Microscopy. *Nat Methods* (2005) 2:932–40. doi: 10.1038/nmeth818
67. Modi MN, Daie K, Turner GC, Podgorski K. Two-Photon Imaging With Silicon Photomultipliers. *Opt Express* (2019) 27:35830. doi: 10.1364/OE.27.035830
68. Jorch SK, Deppermann C. Intravital Imaging Allows Organ-Specific Insights Into Immune Functions. *Front Cell Dev Biol* (2021) 9:623906. doi: 10.3389/fcell.2021.623906
69. Beltman JB, Marée AFM, de Boer RJ, M Marée AF, de Boer RJ, Marée AFM, et al. Analysing Immune Cell Migration. *Nat Rev Immunol* (2009) 9:789–98. doi: 10.1038/nri2638
70. Cahalan MD, Parker I. Choreography of Cell Motility and Interaction Dynamics Imaged by Two-Photon Microscopy in Lymphoid Organs. *Annu Rev Immunol* (2008) 26:585–626. doi: 10.1146/annurev.immunol.24.021605.090620
71. Ulman VV, Maška M, Magnusson KEGG, Ronneberger O, Haubold C, Harder N, et al. An Objective Comparison of Cell-Tracking Algorithms. *Nat Methods* (2017) 14:1141. doi: 10.1038/nmeth.4473
72. Vladymyrov M, Haghayegh Jahromi N, Kaba E, Engelhardt B, Ariga A. VivoFollow 2: Distortion-Free Multiphoton Intravital Imaging. *Front Phys* (2020) 7:222. doi: 10.3389/fphy.2019.00222
73. Pizzagalli DU, Thelen M, Gonzalez SF, Krause R. Semi-Supervised Machine Learning Facilitates Cell Colocalization and Tracking in Intravital Microscopy. *BioRxiv* (2019). doi: 10.1101/829838
74. Loosley AJ, O'Brien XM, Reichner JS, Tang JX. Describing Directional Cell Migration With a Characteristic Directionality Time. *PloS One* (2015) 10: e0127425. doi: 10.1371/journal.pone.0127425
75. Beltman JB, Henrickson SE, von Andrian UH, de Boer RJ, Marée AFM. Towards Estimating the True Duration of Dendritic Cell Interactions With T Cells. *J Immunol Methods* (2009) 347:54–69. doi: 10.1016/j.jim.2009.05.013
76. Schienstock D, Mueller SN. Moving Beyond Velocity: Opportunities and Challenges to Quantify Immune Cell Behavior. *Immunol Rev* (2021) 1–14. doi: 10.1111/imr.13038
77. Wei SH, Parker I, Miller MJ, Cahalan MD. A Stochastic View of Lymphocyte Motility and Trafficking Within the Lymph Node. *Immunol Rev* (2003) 195:136–59. doi: 10.1034/j.1600-065X.2003.00076.x
78. Kolaczkowska E, Kubes P. Neutrophil Recruitment and Function in Health and Inflammation. *Nat Rev Immunol* (2013) 13:159–75. doi: 10.1038/nri3399
79. Nourshargh S, Alon R. Leukocyte Migration Into Inflamed Tissues. *Immunity* (2014) 41:694–707. doi: 10.1016/j.immuni.2014.10.008
80. Cyster JG, Allen CDC. B Cell Responses: Cell Interaction Dynamics and Decisions. *Cell* (2019) 177:524–40. doi: 10.1016/j.cell.2019.03.016
81. Miller MJ, Wei SH, Parker I, Cahalan MD. Two-Photon Imaging of Lymphocyte Motility and Antigen Response in Intact Lymph Node. *Science (80-)* (2002) 296:1869–73. doi: 10.1126/science.1070051
82. Katakai T, Kinashi T. Microenvironmental Control of High-Speed Interstitial T Cell Migration in the Lymph Node. *Front Immunol* (2016) 7:194. doi: 10.3389/fimmu.2016.00194
83. Moreau HD, Bousso P. Visualizing How T Cells Collect Activation Signals *In Vivo*. *Curr Opin Immunol* (2014) 26:56–62. doi: 10.1016/j.coi.2013.10.013
84. Arasa J, Collado-Diaz V, Kritikos I, Medina-Sanchez JD, Friess MC, Sigmund EC, et al. Upregulation of VCAM-1 in Lymphatic Collectors Supports Dendritic Cell Entry and Rapid Migration to Lymph Nodes in Inflammation. *J Exp Med* (2021) 218:e20201413. doi: 10.1084/jem.20201413
85. Singer AJ, Clark RA. Cutaneous Wound Healing. *N Engl J Med* (1999) 341:738–46. doi: 10.1056/NEJM199909023411006
86. Chatziandreou N, Farsakoglu Y, Palomino-Segura M, D'Antuono R, Pizzagalli DU, Sallusto F, et al. Macrophage Death Following Influenza Vaccination Initiates the Inflammatory Response That Promotes Dendritic Cell Function in the Draining Lymph Node. *Cell Rep* (2017) 18:2427–40. doi: 10.1016/j.celrep.2017.02.026
87. Kamenyeva O, Boularan C, Kabat J, Cheung GYC, Cicala C, Yeh AJ, et al. Neutrophil Recruitment to Lymph Nodes Limits Local Humoral Response to Staphylococcus Aureus. *PloS Pathog* (2015) 11:e1004827. doi: 10.1371/journal.ppat.1004827
88. de Oliveira S, Rosowski EE, Huttenlocher A. Neutrophil Migration in Infection and Wound Repair: Going Forward in Reverse. *Nat Rev Immunol* (2016) 16:378–91. doi: 10.1038/nri.2016.49
89. Mayadas TN, Cullere X, Lowell CA. The Multifaceted Functions of Neutrophils. *Annu Rev Pathol Mech Dis* (2014) 9:181–218. doi: 10.1146/annurev-pathol-020712-164023
90. Leliefeld PHC, Koenderman L, Pillay J. How Neutrophils Shape Adaptive Immune Responses. *Front Immunol* (2015) 6:471. doi: 10.3389/fimmu.2015.00471
91. Zhang Y, Bai X-T, Zhu K-Y, Jin Y, Deng M, Le H-Y, et al. *In Vivo* Interstitial Migration of Primitive Macrophages Mediated by JNK-Matrix Metalloproteinase 13 Signaling in Response to Acute Injury. *J Immunol* (2008) 181:2155–64. doi: 10.4049/jimmunol.181.3.2155
92. Zinselmeyer BH, Lynch JN, Zhang X, Aoshi T, Miller MJ. Video-Rate Two-Photon Imaging of Mouse Footpad - A Promising Model for Studying Leukocyte Recruitment Dynamics During Inflammation. *Inflamm Res* (2008) 57:93–6. doi: 10.1007/s00011-007-7195-y
93. De Filippo K, Rankin SM. The Secretive Life of Neutrophils Revealed by Intravital Microscopy. *Front Cell Dev Biol* (2020) 8:603230. doi: 10.3389/fcell.2020.603230
94. Hampton HR, Chtanova T. Lymphatic Migration of Immune Cells. *Front Immunol* (2019) 10:1168. doi: 10.3389/fimmu.2019.01168
95. Lindquist RL, Shakhar G, Dudziak D, Wardemann H, Eisenreich T, Dustin ML, et al. Visualizing Dendritic Cell Networks *In Vivo*. *Nat Immunol* (2004) 5:1243–50. doi: 10.1038/ni1139
96. Friedl P, Weigelin B. Interstitial Leukocyte Migration and Immune Function. *Nat Immunol* (2008) 9:960–9. doi: 10.1038/ni.f.212
97. Hallett MB. editor. "Biophysics of leukocytes: neutrophil chemotaxis, characteristics, and mechanisms". In: *The Neutrophil: Cellular Biochemistry and Physiology*. Boston, MA: CRC Press (1989).
98. Qi H, Cannons JL, Klauschen F, Schwartzberg PL, Germain RN. SAP-Controlled T–B Cell Interactions Underlie Germinal Centre Formation. *Nature* (2008) 455:764–9. doi: 10.1038/nature07345
99. Farsakoglu Y, Palomino-Segura M, Latino I, Zanaga S, Chatziandreou N, Pizzagalli DU, et al. Influenza Vaccination Induces NK-Cell-Mediated Type-II IFN Response That Regulates Humoral Immunity in an IL-6-Dependent Manner. *Cell Rep* (2019) 26:2307–15.e5. doi: 10.1016/j.celrep.2019.01.104
100. Kawakami N, Flügel A. Knocking at the Brain's Door: Intravital Two-Photon Imaging of Autoreactive T Cell Interactions With CNS Structures. *Semin Immunopathol* (2010) 32:275–87. doi: 10.1007/s00281-010-0216-x
101. Xu N, Lei X, Liu L. Tracking Neutrophil Intraluminal Crawling, Transendothelial Migration and Chemotaxis in Tissue by Intravital Video Microscopy. *J Vis Exp* (2011) 55. doi: 10.3791/3296
102. Shellard A, Mayor R. Supracellular Migration - Beyond Collective Cell Migration. *J Cell Sci* (2019) 132:345–56. doi: 10.1242/jcs.226142
103. Mrass P, Takano H, Ng LG, Daxini S, Lasaro MO, Iparraguirre A, et al. Random Migration Precedes Stable Target Cell Interactions of Tumor-Infiltrating T Cells. *J Exp Med* (2006) 203:2749–61. doi: 10.1084/jem.20060710
104. Krummel MF, Cahalan MD. The Immunological Synapse: A Dynamic Platform for Local Signaling. *J Clin Immunol* (2010) 30:364–72. doi: 10.1007/s10875-010-9393-6
105. Dustin ML, Chakraborty AK, Shaw AS. Understanding the Structure and Function of the Immunological Synapse. *Cold Spring Harb Perspect Biol* (2010) 2:a002311–a002311. doi: 10.1101/cshperspect.a002311
106. Monks CRF, Freiberg BA, Kupfer H, Sciaky N, Kupfer A. Three-Dimensional Segregation of Supramolecular Activation Clusters in T Cells. *Nature* (1998) 395:82–6. doi: 10.1038/25764
107. Xie J, Tato CM, Davis MM. How the Immune System Talks to Itself: The Varied Role of Synapses. *Immunol Rev* (2013) 251:65–79. doi: 10.1111/imr.12017
108. Bousso P, Robey E. Dynamics of CD8+ T Cell Priming by Dendritic Cells in Intact Lymph Nodes. *Nat Immunol* (2003) 4:579–85. doi: 10.1038/ni928
109. Kitano M, Yamazaki C, Takumi A, Ikeno T, Hemmi H, Takahashi N, et al. Imaging of the Cross-Presenting Dendritic Cell Subsets in the Skin-Draining

Lymph Node. *Proc Natl Acad Sci* (2016) 113:1044–9. doi: 10.1073/pnas.1513607113
110. Brilot F, Strowig T, Roberts SM, Arrey F, Münz C. NK Cell Survival Mediated Through the Regulatory Synapse With Human DCs Requires IL-15rα. *J Clin Invest* (2007) 117:3316–29. doi: 10.1172/JCI31751
111. Borg C, Jalil A, Laderach D, Maruyama K, Wakasugi H, Charrier S, et al. NK Cell Activation by Dendritic Cells (DCs) Requires the Formation of a Synapse Leading to IL-12 Polarization in DCs. *Blood* (2004) 104:3267–75. doi: 10.1182/blood-2004-01-0380
112. Dustin ML, Long EO. Cytotoxic Immunological Synapses. *Immunol Rev* (2010) 235:24–34. doi: 10.1111/j.0105-2896.2010.00904.x
113. Beal AM, Anikeeva N, Varma R, Cameron TO, Vasiliver-Shamis G, Norris PJ, et al. Kinetics of Early T Cell Receptor Signaling Regulate the Pathway of Lytic Granule Delivery to the Secretory Domain. *Immunity* (2009) 31:632–42. doi: 10.1016/j.immuni.2009.09.004
114. Trapani JA, Smyth MJ. Functional Significance of the Perforin/Granzyme Cell Death Pathway. *Nat Rev Immunol* (2002) 2:735–47. doi: 10.1038/nri911
115. Kienle K, Lämmermann T. Neutrophil Swarming: An Essential Process of the Neutrophil Tissue Response. *Immunol Rev* (2016) 273:76–93. doi: 10.1111/imr.12458
116. Gregory CD, Pound JD. Cell Death in the Neighbourhood: Direct Microenvironmental Effects of Apoptosis in Normal and Neoplastic Tissues. *J Pathol* (2011) 223:178–95. doi: 10.1002/path.2792
117. Ravichandran KS. Find-Me and Eat-Me Signals in Apoptotic Cell Clearance: Progress and Conundrums. *J Exp Med* (2010) 207:1807–17. doi: 10.1084/jem.20101157
118. Shannon JG, Bosio CF, Hinnebusch BJ. Dermal Neutrophil, Macrophage and Dendritic Cell Responses to Yersinia Pestis Transmitted by Fleas. *PloS Pathog* (2015) 11:1–19. doi: 10.1371/journal.ppat.1004734
119. Alex H, Scherer A, Kreuzburg S, Abers MS, Zerbe CS, Dinauer MC, et al. Neutrophil Swarming Delays the Growth of Clusters of Pathogenic Fungi. *Nat Commun* (2020) 11:2031. doi: 10.1038/s41467-020-15834-4
120. Nguyen WNT, Jacobsen EA, Finney CAM, Colarusso P, Patel KD. Intravital Imaging of Eosinophils: Unwrapping the Enigma. *J Leukoc Biol* (2020) 108:83–91. doi: 10.1002/JLB.3HR0220-396R
121. Coombes JL, Charsar BA, Han S-J, Halkias J, Chan SW, Koshy AA, et al. Motile Invaded Neutrophils in the Small Intestine of Toxoplasma Gondii-Infected Mice Reveal a Potential Mechanism for Parasite Spread. *Proc Natl Acad Sci* (2013) 110:E1913–22. doi: 10.1073/pnas.1220272110
122. Louie DAP, Liao S. Lymph Node Subcapsular Sinus Macrophages as the Frontline of Lymphatic Immune Defense. *Front Immunol* (2019) 10:347. doi: 10.3389/fimmu.2019.00347
123. Moseman EA, Iannacone M, Bosurgi L, Tonti E, Chevrier N, Tumanov A, et al. Von Andrian UH. B Cell Maintenance of Subcapsular Sinus Macrophages Protects Against a Fatal Viral Infection Independent of Adaptive Immunity. *Immunity* (2012) 36:415–26. doi: 10.1016/j.immuni.2012.01.013
124. Coombes JL, Han S-J, van Rooijen N, Raulet DH, Robey EA. Infection-Induced Regulation of Natural Killer Cells by Macrophages and Collagen at the Lymph Node Subcapsular Sinus. *Cell Rep* (2012) 2:124–35. doi: 10.1016/j.celrep.2012.06.001
125. Pizzagalli DU, Farsakoglu Y, Palomino-Segura M, Palladino E, Sintes J, Marangoni F, et al. Leukocyte Tracking Database, a Collection of Immune Cell Tracks From Intravital 2-Photon Microscopy Videos. *Sci Data* (2018) 5:1–13. doi: 10.1038/sdata.2018.129
126. Selmeczi D, Mosler S, Hagedorn PH, Larsen NB, Flyvbjerg H. Cell Motility as Persistent Random Motion: Theories From Experiments. *Biophys J* (2005) 89:912–31. doi: 10.1529/biophysj.105.061150
127. Teijeira A, Hunter MC, Russo E, Proulx ST, Frei T, Debes GF, et al. T Cell Migration From Inflamed Skin to Draining Lymph Nodes Requires Intralymphatic Crawling Supported by ICAM-1/LFA-1 Interactions. *Cell Rep* (2017) 18:857–65. doi: 10.1016/j.celrep.2016.12.078
128. Doi A, Oketani R, Nawa Y, Fujita K. High-Resolution Imaging in Two-Photon Excitation Microscopy Using *In Situ* Estimations of the Point Spread Function. *BioMed Opt Express* (2018) 9:202–13. doi: 10.1364/boe.9.000202
129. Nguyen NT, Phung DQ, Venkatesh S, Bui H. Learning and Detecting Activities From Movement Trajectories Using the Hierarchical Hidden Markov Model. In: *Proceedings - 2005 IEEE Computer Society Conference on Computer Vision and Pattern Recognition, CVPR 2005*. June 2005, San Diego, CA, USA (2005). doi: 10.1109/CVPR.2005.203
130. Cyrille B, Renaud P, Laurent M. "Human Activity Recognition in the Semantic Simplex of Elementary Actions". In: Xie X, Jones MW, Tam GKL. *Proceedings of the British Machine Vision Conference (BMVC)*. BMVA Press (2015). pp. 118.1–118.12. doi: 10.5244/c.29.118

Conflict of Interest: The authors declare that the research was conducted in the absence of any commercial or financial relationships that could be construed as a potential conflict of interest.

frontiers in Immunology

ORIGINAL RESEARCH
published: 05 January 2022
doi: 10.3389/fimmu.2021.753754

Overload of the Temporomandibular Joints Accumulates γδ T Cells in a Mouse Model of Rheumatoid Arthritis: A Morphological and Histological Evaluation

Kohei Nagai[1†], *Takenobu Ishii*[1*†], *Tatsukuni Ohno*[2,3] *and Yasushi Nishii*[1]

[1] Department of Orthodontics, Tokyo Dental College, Tokyo, Japan, [2] Oral Health Science Center, Tokyo Dental College, Tokyo, Japan, [3] Tokyo Dental College Research Branding Project, Tokyo Dental College, Tokyo, Japan

Recently, it has been reported that γδ T cells are associated with the pathology of rheumatoid arthritis (RA). However, there are many uncertainties about their relationship. In this study, we investigated the morphological and histological properties of peripheral as well as temporomandibular joints (TMJ) in a mouse model of rheumatoid arthritis with and without exposure to mechanical strain on the TMJ. Collagen antibody-induced arthritis (CAIA) was induced by administering collagen type II antibody and lipopolysaccharide to male DBA/1JNCrlj mice at 9–12 weeks of age, and mechanical stress (MS) was applied to the mandibular condyle. After 14 days, 3D morphological evaluation by micro-CT, histological staining (Hematoxylin Eosin, Safranin O, and Tartrate-Resistant Acid Phosphatase staining), and immunohistochemical staining (ADAMTS-5 antibody, CD3 antibody, CD45 antibody, RORγt antibody, γδ T cell receptor antibody) were performed. The lower jawbone was collected. The mandibular condyle showed a rough change in the surface of the mandibular condyle based on three-dimensional analysis by micro-CT imaging. Histological examination revealed bone and cartilage destruction, such as a decrease in chondrocyte layer width and an increase in the number of osteoclasts in the mandibular condyle. Then, immune-histological staining revealed accumulation of T and γδ T cells in the subchondral bone. The temporomandibular joint is less sensitive to the onset of RA, but it has been suggested that it is exacerbated by mechanical stimulation. Additionally, the involvement of γδ T cells was suggested as the etiology of rheumatoid arthritis.

Keywords: temporomandibular joint, rheumatoid arthritis, CAIA, mechanical stress, γδ T cell

OPEN ACCESS

Edited by:
Marco Erreni,
Humanitas Research Hospital, Italy

Reviewed by:
Stephanie Finzel,
University of Freiburg, Germany
Jianhai Chen,
Shenzhen Institutes of Advanced Technology (CAS), China

****Correspondence:***
Takenobu Ishii
ishiit@tdc.ac.jp

[†]These authors have contributed equally to this work

Specialty section:
This article was submitted to Inflammation, a section of the journal Frontiers in Immunology

Received: *05 August 2021*
Accepted: *08 December 2021*
Published: *05 January 2022*

Citation:
Nagai K, Ishii T, Ohno T and Nishii Y (2022) Overload of the Temporomandibular Joints Accumulates γδ T Cells in a Mouse Model of Rheumatoid Arthritis: A Morphological and Histological Evaluation. Front. Immunol. 12:753754. doi: 10.3389/fimmu.2021.753754

INTRODUCTION

Rheumatoid arthritis (RA) is an autoimmune disease with a 1% prevalence worldwide. Chronic inflammation of the joints and synovial hyperplasia, known as pannus, are observed, as well as cartilage and bone destruction by inflammatory cytokines. The detailed causes of RA have not yet been fully elucidated (1). However, the involvement of γδ T cells has recently been reported as one

of the causes of autoimmune rheumatoid diseases. It is thought that γδ T cells in RA patients exhibit functional characteristics similar to helper T cells, such as antigen presentation and assistance in antibody production (2). The most common sites of RA are the metacarpophalangeal joints, metatarsophalangeal joints, proximal interphalangeal joints, wrists, and shoulder, knee or ankle joints (3). Reports on the involvement of the TMJ are rather heterogeneous and range between 4-85% of RA patients (4–6). Therefore, the morbidity range is wide. However, unlike RA in the limb joints, the pathogenetic mechanism of RA in the TMJ (TMJ-RA) is still unknown.

TMJ-RA first causes degradation of proteoglycan and softening and degeneration of the mandibular condylar cartilage, followed by the destruction of the subchondral bone and bone resorption by osteoclasts (4). Inflammatory cells, such as macrophages, infiltrate the synovial tissue and form pannus. They then release a chemical mediator, destroying the joint and causing pain (4, 5). In particular, tumor necrosis factor alpha (TNF-α), interleukin 1 beta (IL-1β), and IL-6 are associated with RA etiology (6–8). They cause excessive production and secretion of proteolytic enzymes such as matrix metalloproteinase (MMP) and "a disintegrin and metalloproteinase with thrombospondin motifs" (ADAMTS) in synovial fibroblasts and deform the mandibular condyle cartilage. These degenerative changes can cause joint dysfunction, fibrous and bony ankylosis, occlusal-facial malformations, and occlusal inconsistencies. Therefore, early diagnosis and treatment are required (9).

Several animal RA models have been established for analysis (10). In particular, collagen-induced arthritis (CIA) and collagen antibody-induced arthritis (CAIA) mice share many morphological similarities with human RA, such as the production of autoantibodies to Type II collagen (11), and are, therefore, often used as RA models. However, most studies have focused on the knee and hind limb joints, and TMJ-RA has not yet been reported in detail. RA models and human RA clinical symptoms suggest that limb joint RA is exacerbated by overloading (12, 13). Further, it has been reported that overloading the mandibular condyle also causes osteoarthritis-like cartilage resorption (14).

Unlike the joints of the extremities, made of hyaline cartilage that is constantly loaded, the TMJ contains fibrocartilage, a tissue that is loaded only during functions such as mastication (15). Therefore, the TMJ may be more vulnerable to overload than the limb joints. In this study, we devised a method for overloading by pushing the mandibular condyle posteriorly according to this hypothesis.

Therefore, the purpose of this study was to clarify the effect of load on the TMJ on the onset of RA by using the CAIA mouse model and elucidate the causes of TMJ-RA.

MATERIALS AND METHODS

Mice

Animal experiments were approved by the Ethics Committee of Tokyo Dental College (Ethics Application Number: 203102). Male DBA/1JNCrlj mice were bred till 7–8 weeks of age (Charles River, Yokohama, Japan) under standard environmental conditions and were given free access to solid feed and tap water. The mice in the experiment were divided into a control group [N= 5], mechanical stress [MS] group [N= 5], CAIA group [N=5], and CAIA MS group [N=5]. The mice were anesthetized, and a metal plate (product number: 21700BZZ00197000, TOMY INTERNATIONAL INC., Tokyo) was bonded to the posterior surface of the maxillary portal teeth with dental composite resin to a basal thickness of 2 mm to induce an imbalanced occlusion. After anesthesia, the control and CAIA groups did not wear the device. Fourteen days after the commencement of the experiment, after induction of anesthesia with an inhalant anesthetic (sevoflurane), the mice were euthanized by an intraperitoneal overdose of 150 mg/kg pentobarbital sodium, and samples were collected (**Figures 1A–C**).

CAIA Production

Mice aged 9–12 weeks (N=10) were injected intraperitoneally with 1.5 mg of Arthrogen-CIA® Arthritogenic Monoclonal Antibody Cocktail (Condrex Inc, WA, USA). Three days after antibody administration, 25 μg of LPS (Lipopolysaccharide) was injected intraperitoneally to induce CAIA (CAIA and CAIA MS group) (10, 16). The control and MS groups were injected intraperitoneally with phosphate-buffered saline (PBS).

Evaluation of Arthritis

The severity of arthritis was blindly scored on a scale of 0 to 4 as follows: 1 (mild swelling confined to the ankle or tarsal joint), 2 (mild swelling extending to the center of the foot), 3 (moderate swelling over the metatarsal joints), and 4 (severe swelling including the ankles, feet, and fingers). The scores of all four feet were summed to generate an arthritis score with a maximum value of 16 (17).

Evaluation of Inflammation by Histological Staining of the Knee Joint

The mice were euthanized 14 days after the injection of the anti-Type II collagen antibody, and the knee joints were fixed with 10% formaldehyde (Wako Pure Chemical Corporation, Japan) for 2 days. The knee joints were then decalcified in 10% ethylenediaminetetraacetic acid [EDTA (MUTO PURE CHEMICALS CO, LTD. Japan)] at 4°C for 30 days and embedded in paraffin. The knee joint tissues were sliced into 4 μm sections and subjected to hematoxylin and eosin (HE) and Safranin O staining to evaluate the morphological changes in the femur and tibia and the staining of proteoglycans in the chondrocyte layer.

Measurement of Inflammatory Cytokines in Blood

All mice were standardized by restricting their eating and drinking for three hours prior to blood collection. Blood was collected using a 5 mm Goldenrod Animal Lancet (MEDI Point NY, USA) and bled using the submandibular bleeding method. Blood was collected in BD Microtina microcentrifuge tubes (365967 Fisher

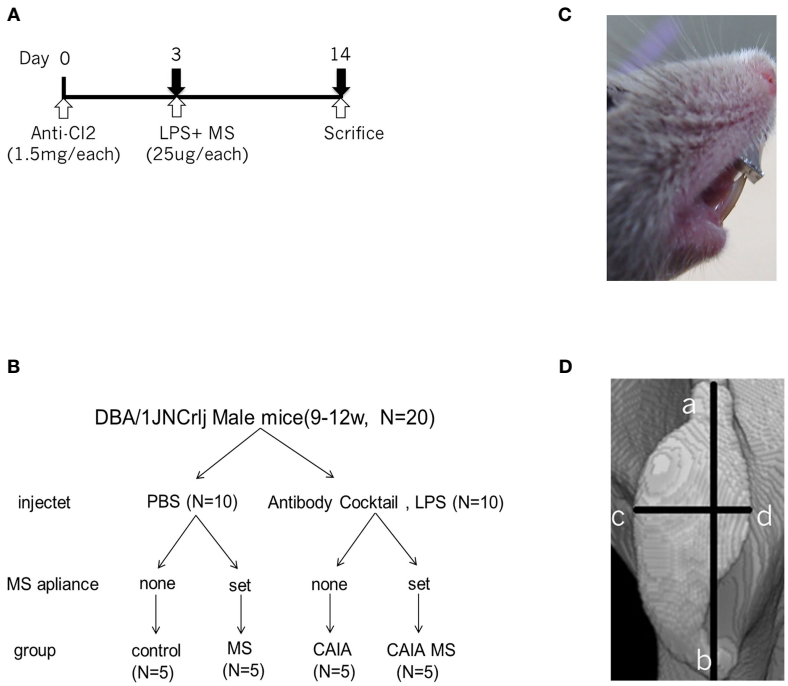

FIGURE 1 | Experimental method. **(A)** Experimental time schedule. **(B)** Details of the treatments among the groups. **(C)** Mechanical stress application to the mandibular condyle. **(D)** Linear measurement diagram of the mandibular condyle. The major length **(a, b)** and width **(c, d)** of the mandibular condyle: a is the anterior point, b the rearmost point, and c and d are the innermost and outermost points, respectively.

Scientific Pittsburgh, PA, USA) with a coagulant accelerator and serum separator and allowed to coagulate at 4°C for 30 mins. It was then centrifuged at 13,000 rpm for 10 mins, and the serum was collected and stored at -20°C. The Mouse IL-1β/IL-1F2 Immunoassay ELISA kit (Catalog Number MLB00C Quantikine ®ELISA MN, USA), Mouse IL-6 ELISA kit (Catalog Number KE10007 Proteintech IL, USA), and Mouse TNF-α Immunoassay ELISA kit (Catalog Number MTA00B Quantikine ®ELISA MN, USA) were used to evaluate the serum IL-1β, IL-6, and TNF-α levels in mice. The assay was performed in the control and CAIA groups (n=5).

Morphological Evaluation by Micro-Computed Tomography

The dimensions of bone destruction were measured and analyzed using microcomputer tomography (μCT) imaging after euthanasia (R mCT, RIGAKU, Tokyo, Japan). The sample was irradiated with X-rays with a tube voltage of 90 kV and a tube current of 150 mA. The shooting time was 2 mins, the shooting magnification was 10 times, and the voxel size was 20 × 20 × 20 μm. For evaluation, μCT images were constructed three-dimensionally using the bone structure analysis software TRI/3D-BON (Ratoc System Engineering Co. Ltd., Japan), and the mandibular condyle length and width were measured (18) (**Figure 1D**). The percentage of the crude area was calculated using the ImageJ software (National Institutes of Health, Bethesda, MD, USA) from the ratio of the number of pixels in the crude area of the mandibular condyle to the number of pixels in the entire mandibular condyle image. The area of interest reached from the crown of the mandibular condyle to the rearmost part (19).

Histopathological Analysis of the Mandibular Condyle

After euthanasia, the heads were fixed with 10% formaldehyde for 2 days. They were then decalcified in 10% EDTA at 4°C for 30 days and embedded in paraffin. The TMJ tissues were sliced into 4 μm sections. The TMJ was stained with HE staining to evaluate mandibular condyle morphology and measure the average TMJ condylar cartilage cell layer thickness in the mid-coronal portion of the mandibular condylar head of five mice in each group. Additionally, the staining of proteoglycans in the mandibular condyle was evaluated by staining with Safranin O. Tartrate-resistant acid phosphatase (TRAP) staining was then performed to evaluate osteoclast differentiation in the subchondral bone. TRAP activity was measured according to the method given by Shirakura M et al. (20), and TRAP-positive cells with three or more nuclei were counted as osteoclasts using a TRAP staining kit (Sigma, St. Louis, MO, USA).

Evaluation of Immunohistochemistry of the Mandibular Condyle

After deparaffinizing the sections of each group, we performed antigen retrieval with the agent ImmunoSaver Antigen Retriever (Electron Microscopic Sciences, Hatfield, PA) and blocking with 1% bovine serum albumin. Immunofluorescence staining was

performed using ADAMTS (a disintegrin and metalloproteinase with thrombospondin motifs); -5 rabbit polyclonal antibody (abcam, Cambridge, MA, USA), CD (cluster of differentiation) 3 rabbit polyclonal antibody (my biosource Inc., CA, USA), CD45 rat monoclonal antibody (my biosource Inc., CA, USA), RORγt (related orphan receptor gamma t) American hamster monoclonal antibody (BioLegend, CA, USA), and γδ TCR (T cell receptor) mouse monoclonal antibody (Alexa Fluor 546 is added as a fluorescent label) (Santa Cruz Biotechnology, TX, USA) were used as the primary antibodies. Secondary antibodies were Alexa Fluor 546 Donkey Anti-Rabbit IgG (Thermo Fisher Scientific, US) to detect ADAMTS-5 and CD45, Alexa Fluor 647 Goat Anti-Rat IgG (Thermo Fisher Scientific, US) to detect CD3, and Alexa Fluor 488 goat Anti-Rabbit IgG (BioLegend, CA, USA) to detect RORγt. Nuclear staining was performed using stain solution Hoechst 33342 (Thermo Fisher Scientific, US). The number of cells was measured using the ImageJ software.

Statistical Analysis

SPSS 17.0 (SPSS Inc. CHI, USA) was used for statistical analyses. For in-group comparisons, multiple comparisons were performed using the Tukey-Kramer test. For comparisons with the control group, multiple comparisons were performed using Dunnett's test. Comparisons between two groups were made using Student's t-test. The level of significance was set at $P < 0.05$ (*).

RESULTS

Evaluation of Arthritis in CAIA

All mice injected with the collagen antibody cocktail developed inflammatory arthritis after LPS administration. The arthritis score was 0 in the control group and 12 in the CAIA group on the 6th day of administration, and thereafter, maintained a stable score of about 14 until sacrifice (**Figures 2A, B**). The localization of inflammatory cells in knee arthritis and their effect on the chondrocyte layer were investigated using HE and Safranin O staining. As a result, compared with the control group, in the CAIA group, infiltration of inflammatory cells was observed in the synovial membrane, and a defect in the surface layer of the femur and cartilage erosion due to loss of proteoglycan in the chondrocyte layer in the chondrocyte layer was observed (**Figure 2C**). In the CAIA group, the systemic concentration of the pro-inflammatory cytokine IL1-β increased approximately

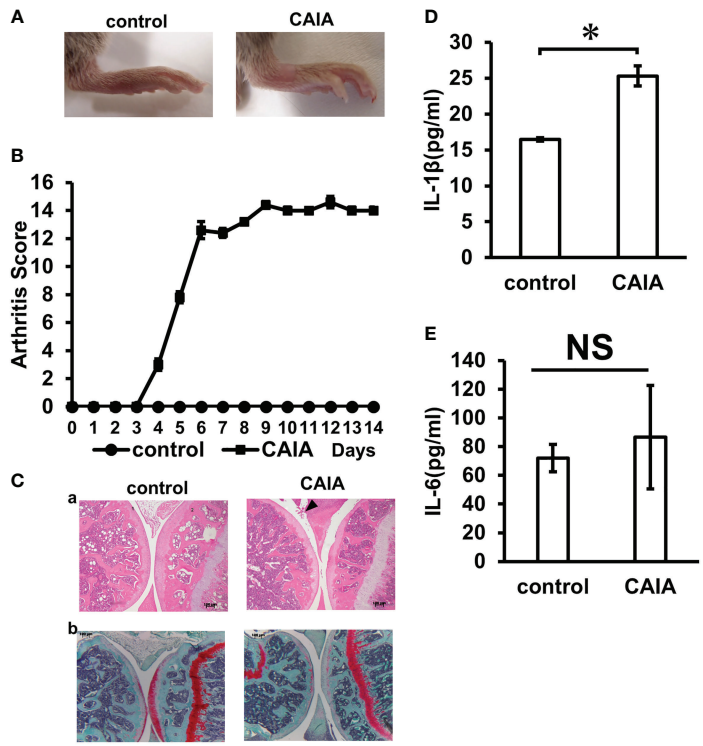

FIGURE 2 | Inflammation evaluation. **(A)** Clinical photographs of hind legs of the control group and CAIA group mice. Swelling of the ankle was observed in the CAIA group. (Score 3) **(B)** Clinical severity of arthritis in control group and CAIA group after collagen antibody cocktail injection. Severity of arthritis in each foot was scored from 0 (no swelling) to 4 (erythema and severe swelling of the entire tarsal joint), and the total of 4 feet (0–16). In the CAIA group, the score was about 12 on day 6 of antibody administration. *$P < 0.05$. **(C)** Histological analysis of the hind paw of each group on day 14. The knee joint was stained with hematoxylin and eosin **(a)** and Safranin O **(b)** (1: tibia, 2: femur). Arrows indicate increased inflammatory cells. (scale bar: 100 μm) **(D)** Blood IL-1β levels (pg/ml) in the control and CAIA groups. In the CAIA group, the IL-β concentration was 24.5 (pg/ml) *$P < 0.05$. **(E)** Blood IL-6 levels (pg/ml) in the control and CAIA groups. There was no significant (NS) difference between the control group and the CAIA group. NS, not significant.

1.5-fold compared to the control group (**Figure 2D**). The systemic concentration of the pro-inflammatory cytokine IL-6 levels was not significantly different between the control and CAIA groups (**Figure 2E**). The systemic concentration of the pro-inflammatory cytokine TNF-alpha levels was below the detectable limit.

Evaluation of Mandibular Condyle Morphology in μCT

A morphological evaluation of the mandibular condyle was performed using μCT. The mandibular condyle length and width were measured as shown in **Figure 1D**, but no significant change was found in the width diameter of each group (**Figures 3A, D**). The morphological evaluation of each group revealed changes in the posterior part of the mandibular condyle and signs of bone destruction in the CAIA MS group (**Figures 3B, D**). Moreover, the crude area increased approximately 1.5-fold in the CAIA MS group compared with the control group (**Figures 3C, D**).

Histological Evaluation of Mandibular Condyle Morphology

The mandibular condyle HE staining showed no clear morphological changes in each group compared to the control group [**Figures 4A (a–d)**]. In the HE staining, the CAIA group did not show abnormal synovial proliferation or accumulation of inflammatory cells [**Figure 4A (c)**]. In the CAIA MS group, accumulation of inflammatory cells in the TMJ cavity was observed [**Figure 4A (d)**, **Figure 4B**]. Additionally, the mean TMJ condyle cartilage cell layer thickness in the CAIA MS group was significantly thinner than that in the control group (**Figure 4C**). Further, Safranin O staining showed decreased staining of proteoglycans in the MS and CAIA MS groups compared to the control group [**Figures 4A (e–h)**]. The number of TRAP-positive cells in the subchondral bone was higher in each group compared with the control group. The number of TRAP-positive cells in the subchondral bone was higher in each group compared with the control group. Furthermore, it was also higher in the CAIA MS group compared to the MS group and CAIA group [**Figures 4A (i–l)**]. The total number of osteoclasts measured by TRAP-positive cell counting increased significantly in all experimental groups compared to the control group, especially in the CAIA MS group, in which the number of osteoclasts increased by approximately 2-fold compared to the control group (**Figure 4D**). Finally, the expression of ADAMTS-5, a chondrocyte-destroying enzyme, was also higher in the chondrocyte layer of the CAIA MS group [**Figures 4A (m–p)**].

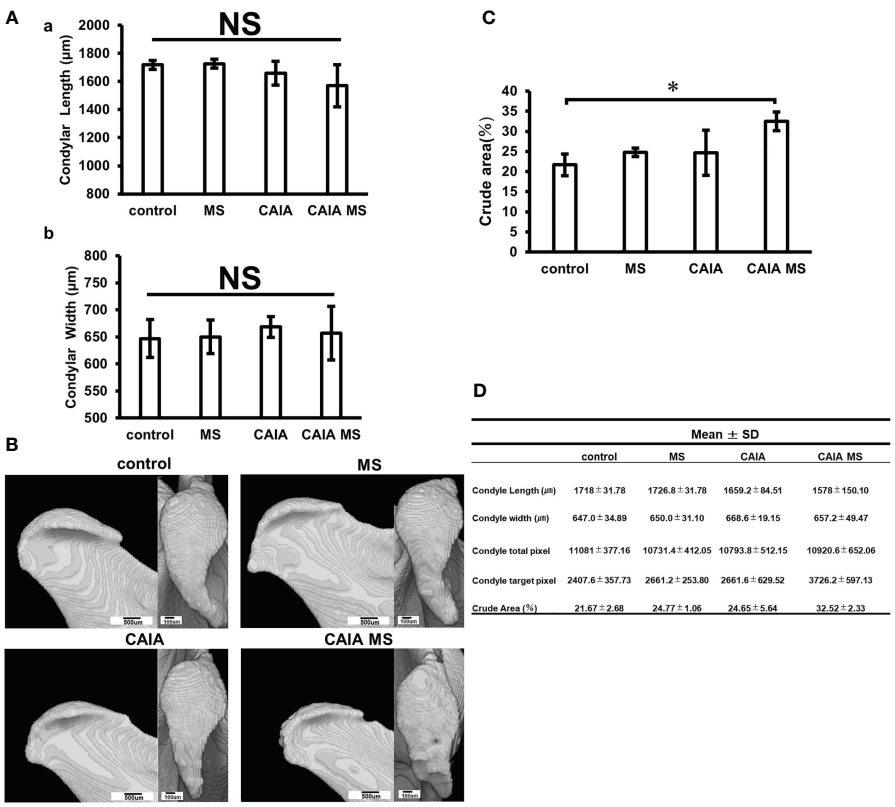

FIGURE 3 | Evaluation of mandibular condyle morphology in micro-CT. **(A) (a)** Mandibular condyle length of each group; **(b)** Mandibular condyle width of each group. There was no significant difference in change in either. **(B)** Mandibular condyle lateral (scale bar: 500 μm) and superior (scale bar: 100 μm) morphology of each group. The arrow indicates crude area. **(C)** Percentage of crude area mandibular condyle in each group. The crude area was larger in the CAIA MS group. *$p < 0.05$. **(D)** Details about mandibular width and length diameters, whole and target pixels, and crude area are shown. NS, not significant.

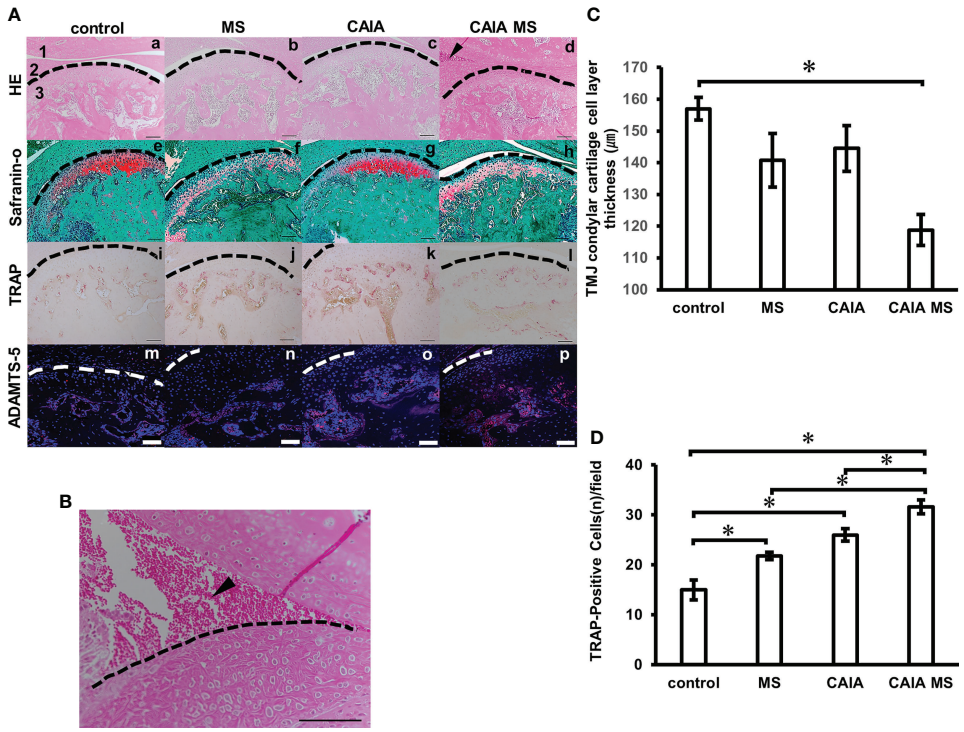

FIGURE 4 | Histological evaluation of mandibular condyle morphology. **(A) (a–d)** Representative hematoxylin and eosin staining with histological examination performed in each experimental group. Arrow indicates areas of inflammatory cell accumulation (1: mandibular fossa, 2: articular disc, 3: mandibular condyle). No major bone loss or other changes were observed. **(e–h)** Representative Safranin O staining. The Safranin O staining property is reduced by the addition of mechanical stress. **(i–l)** Representative TRAP staining. **(m–p)** Expression of ADAMTS-5 in the mandibular condyle (scale bar: 100 μm; red: ADAMTS-5, blue: cell nuclei). Enzyme expression in the chondrocyte layer was observed in all groups. **(B)** Inflammatory cell accumulation findings in the superior articular space of the temporomandibular joint in the CAIA MS group. Arrow indicates area of inflammatory cell accumulation. (scale bar: 100 μm) **(C)** TMJ cartilage cell layer thickness diameter assessment by HE staining. *P < 0.05. **(D)** Number of TRAP-positive osteoclasts. The number of cells with three or more nuclei within a fixed measurement frame (450 μm × 900 μm) was counted. The CAIA MS group showed an average of 31.6 cells. *P < 0.05.

Lymphocyte Expression in TMJ Assessed by Immunofluorescent Staining

The expression of lymphocytes was confirmed by immunofluorescence staining. Accumulated B cell expression was observed in the subchondral bone of each group. Accumulated T cell expression was hardly observed in the control and MS groups. However, in the CAIA and CAIA MS groups, the expression of accumulated T cells in the subchondral bone was observed (**Figures 5A, B**). There was no significant difference in the expression of B cells in each group (**Figure 5C**). The numbers of T cells in the CAIA MS group were approximately 2-fold higher than that in the control group (**Figures 5C, D**).

Expression of γδ Tcells and Th17 Cells in TMJ Assessed by Immunofluorescent Staining

There was little expression of γδ T cells and Th17 cells in the control and MS groups. However, in the CAIA and CAIA MS group, γδ T cells were mostly expressed in the subchondral bone (**Figures 6A, B**). The number of γδ T cells in the CAIA MS group was approximately 6-fold higher than that in the control group and Th17 expression was approximately 3-fold higher in the CAIA MS group than in the control group (**Figures 6C, D**).

DISCUSSION

Creating a CAIA Mouse Model

In this experiment, CAIA was developed based on the report by Nandakumar et al. (16). In general, because of the action of female hormones, female mice may not be suitable for accurate studies on bone metabolism or joint inflammation and bone tissue destruction; therefore, male mice were used in this experiment (21, 22). CAIA was used because it shares many morphological similarities with human RA, including the production of autoantibodies to Type II collagen. The CAIA group showed a significant increase in the arthritis score and swelling of the limb joints compared with the control group. Furthermore, HE staining showed inflammatory cell proliferation in the knee joint space. Additionally, Safranin O staining showed a decrease in proteoglycans. This is consistent with a report that the CAIA model causes extensive infiltration of subsynovial tissue by inflammatory cells, cell infiltration into the

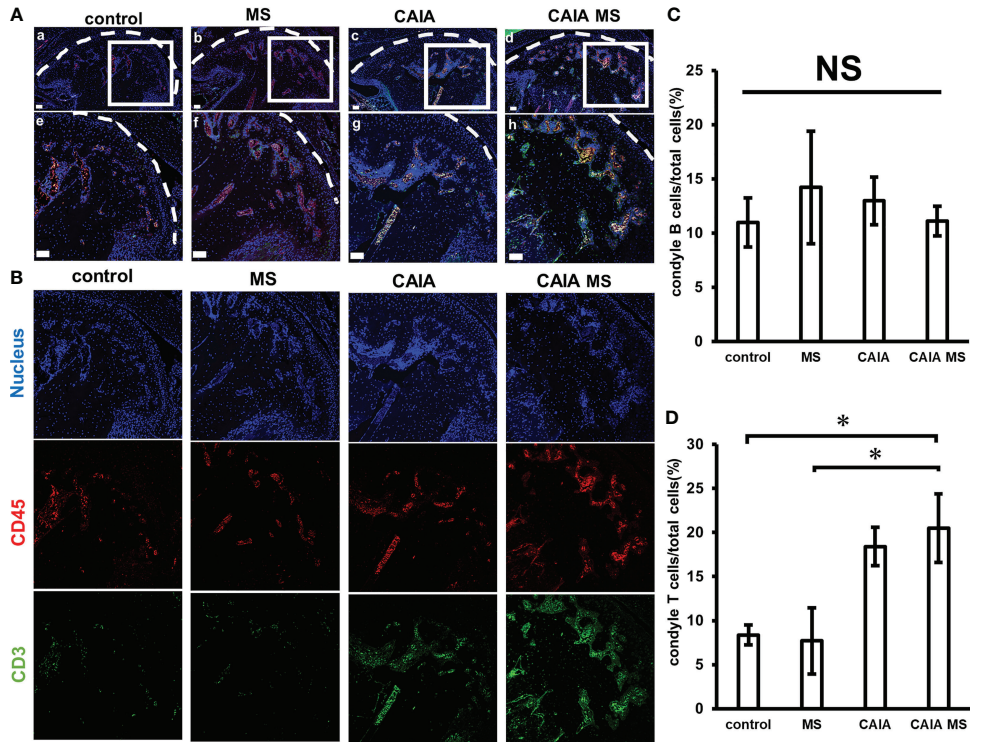

FIGURE 5 | Expression of T cells and B cells in the mandibular condyle by immunofluorescence staining. **(A)** Expression of mandibular condyle B cells and T cells **(a–d)** low magnification, and **(e–h)** high magnification. (scale bar: 50 μm; red: B cells, green: T cells, blue: cell nuclei). T cells and B cells are expression in the subchondral bone of each group. **(B)** Expression of B cells and T cells in the mandibular condyle by immunofluorescence staining. Representative images of 20x are shown in blue for nucleus, red for CD45, and green for CD3 for each group. **(C)** Number of B cells in the mandibular condyle vs. the total number of cells (percentage). *P < 0.05 **(D)** Number of T cells in the mandibular condyle vs. the total number of cells (percentage). *P < 0.05. NS, not significant.

joint space, and significant cartilage destruction (10). Furthermore, there was an increase in the concentration of IL-1β in the blood. However, there was no significant difference in IL-6 concentration, and TNF-α concentration was below the detection limit. This may be because the concentration of these cytokines has been reported to decrease with prolonged rearing in RA model mice (7, 23). These results confirmed the existence of systemic arthritis inflammation and proved that the CAIA mouse model was correctly generated.

Effects of Excessive MS on the Mandibular Condyle in the CAIA Mouse Model

In the RA model, limb joints showed swelling, erythema, and synovial proliferation, but clinical signs in the TMJ are generally unclear; therefore, attempts to investigate the RA model of the TMJ have been made recently. In a study using a cartilage proteoglycan (PG)-induced arthritis (PGIA) mouse model, increased ADAMTS in the TMJ was observed; therefore, structural damage was only observed in the TMJ of mice with severe arthritis symptoms (24). In another study using the K/BxN model of spontaneous inflammation, increased expression of vascular endothelial growth factor and IL-17 and decreased expression of osteoprotegerin were observed in the limb joints, but not in the TMJ (25). In the same study with the K/BxN mouse model, the enlargement of the upper joint cavity in arthritic mice was confirmed by Magnetic Resonance Imaging, and only cartilage detachment of the TMJ surface was observed (26). In the present study, although the CAIA group showed increased osteoclast differentiation, there was no significant thinning of the chondrocyte layer or localization of lymphocytes. These results suggest that the TMJ is a less primary target for inflammation than the peripheral joints in the RA model. However, in the CAIA MS group, ADAMTS-5 was strongly expressed, the chondrocyte layer was thinned, and lymphocytes increased in expression. Therefore, it can be inferred that the overloading of the TMJ might be a factor in the development of TMJ-RA. Functional occlusal loading on the TMJ (by forced unilateral or anterior occlusion) has been shown to worsen of TMJ arthritis (27, 28). Therefore, overloading the mandibular condyle may accelerate the degeneration of the mandibular condyle cartilage, and overloading the TMJ may be an important factor for the development of inflammation in the TMJ in the RA model.

The metal plate device used in the present study as a method of applying MS to the mandibular condyle applied excessive MS to the TMJ, demonstrating that it can induce TMJ-arthritis in CAIA mice. It has been reported that TMJ osteoarthritis-like changes occurred when a resin block was attached to a mouse's

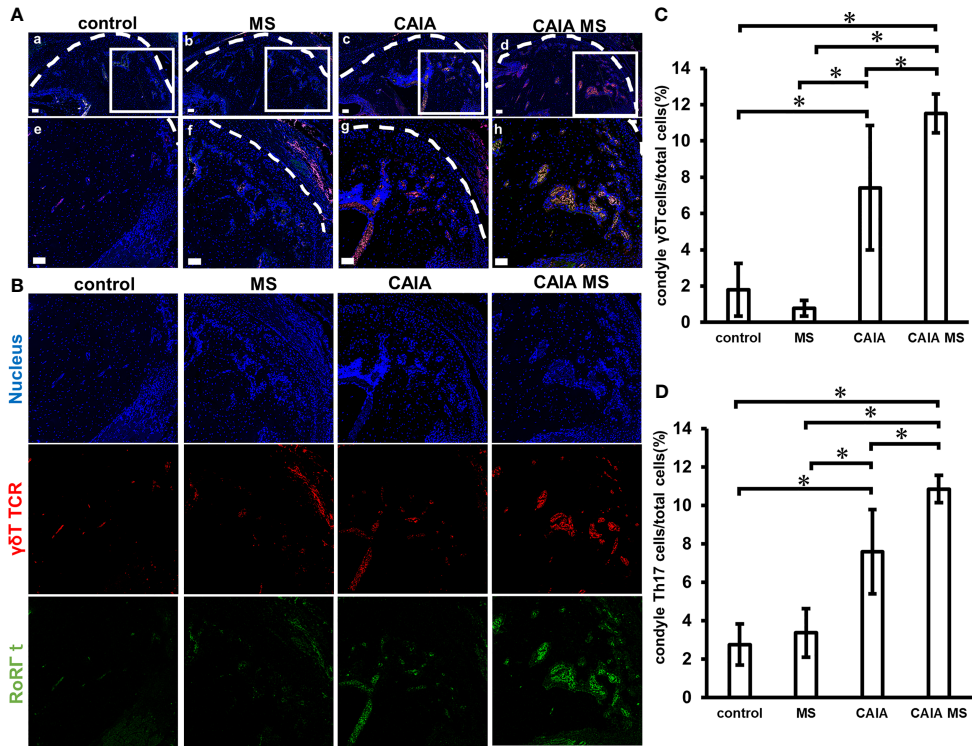

FIGURE 6 | Expression of γδ T and Th17 cells in mandibular condyle by immunofluorescence staining. **(A)** Expression of mandibular condyle γ δT and Th17 cells **(a–d)** Low magnification, and **(e–h)** high magnification. (scale bar: 50 μm; red: γ δT cells, green: Th17 cells blue: cell nuclei) γδ T and Th17 cells are mostly expressed in the subchondral bone of the CAIA MS group. **(B)** Expression of Th17 cells and γδT cells in the mandibular condyle by immunofluorescence staining. Representative images of 20x are shown in blue for nucleus, red for γδTCR, and green for RoRγt for each group. **(C)** Number of γ δT cells in the mandibular condyle vs. the total number of cells (percentage). *P < 0.05 **(D)** Number of Th17 cells in the mandibular condyle vs. the total number of cells (percentage). *P < 0.05.

maxillary horn teeth and the mandible was pushed backward (20). Therefore, we designed a similar device for the mouse model. Unlike the TMJ, which is composed of hyaline cartilage, the mandibular condyle cartilage is composed of fibrocartilage derived from periosteal tissue, so the size and characteristics of the tissue are adjusted to adapt to changes in load (29). As the device we used in this study used a metal plate for the occlusal part, it did not wear because of occlusion, and its thickness remained constant during the device wearing period. Therefore, as it can be regarded that a stable overload was applied to the mandibular condyle, this method is considered very useful for establishing a load on the TMJ in mice.

Among all the experimental groups examined in this study, TMJ-arthritis showed worsening of pathology in the group that combined excessive MS and systemic inflammation (CAIA MS group). Therefore, we confirmed that excessive MS worsens the pathology of the TMJ in CAIA mice.

Involvement of γδ T Cells in The Mandibular Condyle in CAIA Mouse Model

The CAIA mouse model is not affected by lymphocytes when inflammation develops. However, exacerbation of arthritis due to Type II collagen-reactive T cells in limb joints has been reported in CAIA (30, 31). In this study, T cell expression was observed in the subchondral bone of the CAIA MS group. Co-staining of γδ T cells and Th17 cells revealed an increase in Th17 cells and the expression of γδ T cells, which are the least abundant of all T cells. It has been previously reported that Th17 produces IL-17 and is associated with RA (1). γδ T cells produce IL-17 and are known to be an important factor in cancer research (32, 33). IL-17 is a cytokine that is mainly produced by Th17 and induces the expression of various pro-inflammatory cytokines and chemokines in a wide variety of cells (34). γδ T cells have also been shown to be associated with RA (2). It has been reported that the number of IL-17-producing cells in mouse femoral bone marrow also increases in CAIA mice (35). Furthermore, it has been reported that Vγ4/Vδ4 + γδ T cells, one of the γδ T cell subsets, produce IL-17, with localization in the synovial membrane and peripheral blood in CIA mice (36). However, because there is no report that γδ T cells are involved in TMJ-RA, we investigated this and found that they were involved. Therefore, the application of MS increases the number of T cells in TMJ-RA. Among them, Th17 and γδ T cells would be increased. Therefore, it was suggested that this could be exacerbated by IL-17 production.

However, this experiment could not clarify why γδ T cells show increased localization in the TMJ. Isopentenyl pyrophosphate (IPP) is a factor that activates γδ T cells (37). However, IPP is an intermediate product of the intracellular

mevalonate pathway, which is difficult to quantify and has not been identified. Therefore, further research on quantification methods is needed.

Conclusion

The TMJ is less susceptible to inflammation in RA. However, MS exacerbates the disease. The findings suggested that γδ T cells are involved in an RA-mouse model of TMJ arthritis as a causal factor. Future scientific studies should check whether these effects are also identifiable in humans and whether γδ T cells play a similar role in humans. If this is confirmed, the γδ T cells might represent a new therapeutic target.

DATA AVAILABILITY STATEMENT

The original contributions presented in the study are included in the article/supplementary material. Further inquiries can be directed to the corresponding author.

ETHICS STATEMENT

The animal study was reviewed and approved by the Ethics Committee of Tokyo Dental College (Ethics Application Number: 203102).

AUTHOR CONTRIBUTIONS

KN along with TI designed and performed the experiments and conducted data analysis. KN wrote the manuscript. TO provided the RORγt antibodies. TI and YN contributed in manuscript editing. Both authors read and approved the final manuscript. All authors contributed to the article and approved the submitted version.

FUNDING

The work was supported by the Department of Orthodontics, Tokyo Dental College.

REFERENCES

1. Smolen JS, Aletaha D, McInnes IB. Rheumatoid Arthritis. *Lancet* (2016) 388:2023–38. doi: 10.1016/S0140-6736(16)30173-8
2. Bank I. The Role of Gamma Delta T Cells in Autoimmune Rheumatic Diseases. *Cells* (2020) 9:462. doi: 10.3390/cells9020462
3. Szkudlarek M, Terslev L, Wakefield RJ, Backhaus M, Balint PV, Bruyn GAV, et al. Summary Findings of a Systematic Literature Review of the Ultrasound Assessment of Bone Erosions in Rheumatoid Arthritis. *J Rheumatol* (2016) 43:12–21. doi: 10.3899/jrheum.141416
4. Liu W-W, Xu Z-M, Li Z-Q, Zhang Y, Han B. RANKL, OPG and CTR mRNA Expression in the Temporomandibular Joint in Rheumatoid Arthritis. *Exp Ther Med* (2015) 10:895–900. doi: 10.3892/etm.2015.2629
5. Strand V, Kavanaugh AF. The Role of Interleukin-1 in Bone Resorption in Rheumatoid Arthritis. *Rheumatol (Oxf)* (2004) 43(Suppl 3):10–6. doi: 10.1093/rheumatology/keh202
6. Ahmed N, Petersson A, Catrina AI, Mustafa H, Alstergren P. Tumor Necrosis Factor Mediates Temporomandibular Joint Bone Tissue Resorption in Rheumatoid Arthritis. *Acta Odontol Scand* (2015) 73:232–40. doi: 10.3109/00016357.2014.994561
7. Kagari T, Doi H, Shimozato T. The Importance of IL-1 Beta and TNF-Alpha, and the Noninvolvement of IL-6, in the Development of Monoclonal Antibody-Induced Arthritis. *J Immunol* (2002) 169:1459–66. doi: 10.4049/jimmunol.169.3.1459
8. Nie H, Zheng Y, Li R, Guo TB, He D, Fang L, et al. Phosphorylation of FOXP3 Controls Regulatory T Cell Function and Is Inhibited by TNF-α in Rheumatoid Arthritis. *Nat Med* (2013) 19:322–8. doi: 10.1038/nm.3085
9. Lin Y-C, Hsu M-L, Yang J-S, Liang T-H, Chou S-L, Lin H-Y. Temporomandibular Joint Disorders in Patients With Rheumatoid Arthritis. *J Chin Med Assoc* (2007) 70:527–34. doi: 10.1016/S1726-4901(08)70055-8
10. Caplazi P, Baca M, Barck K, Carano RAD, DeVoss J, Lee WP, et al. Mouse Models of Rheumatoid Arthritis. *Vet Pathol* (2015) 52:819–26. doi: 10.1177/0300985815588612
11. Terato K, Hasty KA, Reife RA, Cremer MA, Kang AH, Stuart JM. Induction of Arthritis With Monoclonal Antibodies to Collagen. *J Immunol* (1992) 148:2103–8.
12. Cambré I, Gaublomme D, Burssens A, Jacques P, Schryvers N, De Muynck A, et al. Mechanical Strain Determines the Site-Specific Localization of Inflammation and Tissue Damage in Arthritis. *Nat Commun* (2018) 9:4613. doi: 10.1038/s41467-018-06933-4
13. Koh JH, Jung SM, Lee JJ, Kang KY, Kwok S-K, Park S-H, et al. Radiographic Structural Damage Is Worse in the Dominant Than the Non-Dominant Hand in Individuals With Early Rheumatoid Arthritis. *PLoS One* (2015) 10:e0135409. doi: 10.1371/journal.pone.0135409
14. Ikeda Y, Yonemitsu I, Takei M, Shibata S, Ono T. Mechanical Loading Leads to Osteoarthritis-Like Changes in the Hypofunctional Temporomandibular Joint in Rats. *Arch Oral Biol* (2014) 59:1368–76. doi: 10.1016/j.archoralbio.2014.08.010
15. Ghassemi Nejad S, Kobezda T, Tar I, Szekanecz Z. Development of Temporomandibular Joint Arthritis: The Use of Animal Models. *Joint Bone Spine* (2017) 84:145–51. doi: 10.1016/j.jbspin.2016.05.016
16. Nandakumar KS, Holmdahl R. Efficient Promotion of Collagen Antibody Induced Arthritis (CAIA) Using Four Monoclonal Antibodies Specific for the Major Epitopes Recognized in Both Collagen Induced Arthritis and Rheumatoid Arthritis. *J Immunol Methods* (2005) 304:126–36. doi: 10.1016/j.jim.2005.06.017
17. Bonnefoy F, Daoui A, Valmary-Degano S, Toussirot E, Saas P, Perruche S. Apoptotic Cell Infusion Treats Ongoing Collagen-Induced Arthritis, Even in the Presence of Methotrexate, and Is Synergic With Anti-TNF Therapy. *Arthritis Res Ther* (2016) 18:184. doi: 10.1186/s13075-016-1084-0
18. Crossman J, Alzaheri N, Abdallah MN, Tamimi F, Flood P, Alhadainy H, et al. Low Intensity Pulsed Ultrasound Increases Mandibular Height and Col-II and VEGF Expression in Arthritic Mice. *Arch Oral Biol* (2019) 104:112–8. doi: 10.1016/j.archoralbio.2019.05.032
19. Katsumata Y, Kanzaki H, Honda Y, Tanaka T, Yamaguchi Y, Itohiya K, et al. Single Local Injection of Epigallocatechin Gallate-Modified Gelatin Attenuates Bone Resorption and Orthodontic Tooth Movement in Mice. *Polymers (Basel)* (2018) 10:1384. doi: 10.3390/polym10121384
20. Shirakura M, Tanimoto K, Eguchi H, Miyauchi M, Nakamura H, Hiyama K, et al. Activation of the Hypoxia-Inducible Factor-1 in Overloaded Temporomandibular Joint, and Induction of Osteoclastogenesis. *Biochem Biophys Res Commun* (2010) 393:800–5. doi: 10.1016/j.bbrc.2010.02.086
21. Yoneda T, Ishimaru N, Arakaki R, Kobayashi M, Izawa T, Moriyama K, et al. Estrogen Deficiency Accelerates Murine Autoimmune Arthritis Associated With Receptor Activator of Nuclear Factor-Kappa B Ligand-Mediated Osteoclastogenesis. *Endocrinology* (2004) 145:2384–91. doi: 10.1210/en.2003-1536
22. Sekiguchi Y, Mano H, Nakatani S, Shimizu J, Wada M. Effects of the Sri Lankan Medicinal Plant, Salacia Reticulata, in Rheumatoid Arthritis. *Genes Nutr* (2010) 5:89–96. doi: 10.1007/s12263-009-0144-3

23. Macías I, García-Pérez S, Ruiz-Tudela M, Medina F, Chozas N, Girón-González JA. Modification of Pro- and Antiinflammatory Cytokines and Vascular-Related Molecules by Tumor Necrosis Factor-A Blockade in Patients With Rheumatoid Arthritis. *J Rheumatol* (2005) 32:2102–8.
24. Ghassemi-Nejad S, Kobezda T, Rauch TA, Matesz C, Glant TT, Mikecz K. Osteoarthritis-Like Damage of Cartilage in the Temporomandibular Joints in Mice With Autoimmune Inflammatory Arthritis. *Osteoarthr Cartil* (2011) 19:458–65. doi: 10.1016/j.joca.2011.01.012
25. Safi S, Frommholz D, Reimann S, Götz W, Bourauel C, Neumann A-L, et al. Comparative Study on Serum-Induced Arthritis in the Temporomandibular and Limb Joint of Mice. *Int J Rheum Dis* (2019) 22:636–45. doi: 10.1111/1756-185X.13486
26. Kuchler-Bopp S, Mariotte A, Strub M, Po C, De Cauwer A, Schulz G, et al. Temporomandibular Joint Damage in K/BxN Arthritic Mice. *Int J Oral Sci* (2020) 12:5. doi: 10.1038/s41368-019-0072-z
27. Liu Y-D, Liao L-F, Zhang H-Y, Lu L, Jiao K, Zhang M, et al. Reducing Dietary Loading Decreases Mouse Temporomandibular Joint Degradation Induced by Anterior Crossbite Prosthesis. *Osteoarthr Cartil* (2014) 22:302–12. doi: 10.1016/j.joca.2013.11.014
28. Liu Y-D, Yang H-X, Liao L-F, Jiao K, Zhang H-Y, Lu L, et al. Systemic Administration of Strontium or NBD Peptide Ameliorates Early Stage Cartilage Degradation of Mouse Mandibular Condyles. *Osteoarthr Cartil* (2016) 24:178–87. doi: 10.1016/j.joca.2015.07.022
29. Robinson JL, Cass K, Aronson R, Choi T, Xu M, Buttenbaum R, et al. Sex Differences in the Estrogen-Dependent Regulation of Temporomandibular Joint Remodeling in Altered Loading. *Osteoarthr Cartil* (2017) 25:533–43. doi: 10.1016/j.joca.2016.11.008
30. Nandakumar KS, Bäcklund J, Vestberg M, Holmdahl R. Collagen Type II (CII)-Specific Antibodies Induce Arthritis in the Absence of T or B Cells But the Arthritis Progression is Enhanced by CII-Reactive T Cells. *Arthritis Res Ther* (2004) 6:R544–50. doi: 10.1186/ar1217
31. Mitamura M, Nakano N, Yonekawa T, Shan L, Kaise T, Kobayashi T, et al. T Cells Are Involved in the Development of Arthritis Induced by Anti-Type II Collagen Antibody. *Int Immunopharmacol* (2007) 7:1360–8. doi: 10.1016/j.intimp.2007.05.021
32. Zou C, Zhao P, Xiao Z, Han X, Fu F, Fu L. γδ T Cells in Cancer Immunotherapy. *Oncotarget* (2017) 8:8900–9. doi: 10.18632/oncotarget.13051
33. Holers VM, Banda NK. Complement in the Initiation and Evolution of Rheumatoid Arthritis. *Front Immunol* (2018) 9:1057. doi: 10.3389/fimmu.2018.01057
34. Weaver CT, Hatton RD, Mangan PR, Harrington LE. IL-17 Family Cytokines and the Expanding Diversity of Effector T Cell Lineages. *Annu Rev Immunol* (2007) 25:821–52. doi: 10.1146/annurev.immunol.25.022106.141557
35. Grahnemo L, Andersson A, Nurkkala-Karlsson M, Stubelius A, Lagerquist MK, Svensson MND, et al. Trabecular Bone Loss in Collagen Antibody-Induced Arthritis. *Arthritis Res Ther* (2015) 17:189. doi: 10.1186/s13075-015-0703-5
36. Roark CL, French JD, Taylor MA, Bendele AM, Born WK, O'brien RL. γδ T Cells Clonally Expand, Produce IL-17, and Are Pathogenic in Collagen-Induced Arthritis. *J Immunol* (2007) 179:5576–83. doi: 10.4049/jimmunol.179.8.5576
37. Wang R-N, Wen Q, He W-T, Yang J-H, Zhou C-Y, Xiong W-J, et al. Optimized Protocols for γδ T Cell Expansion and Lentiviral Transduction. *Mol Med Rep* (2019) 19:1471–80. doi: 10.3892/mmr.2019.9831

Conflict of Interest: The authors declare that the research was conducted in the absence of any commercial or financial relationships that could be construed as a potential conflict of interest.

Publisher's Note: All claims expressed in this article are solely those of the authors and do not necessarily represent those of their affiliated organizations, or those of the publisher, the editors and the reviewers. Any product that may be evaluated in this article, or claim that may be made by its manufacturer, is not guaranteed or endorsed by the publisher.

frontiers in Immunology

ORIGINAL RESEARCH
published: 25 January 2022
doi: 10.3389/fimmu.2022.821423

Exploiting Glutamine Consumption in Atherosclerotic Lesions by Positron Emission Tomography Tracer (2*S*,4*R*)-4-^{18}F-Fluoroglutamine

Senthil Palani[1], Maxwell W. G. Miner[1], Jenni Virta[1], Heidi Liljenbäck[1,2], Olli Eskola[1], Tiit Örd[3], Aarthi Ravindran[3], Minna U. Kaikkonen[3], Juhani Knuuti[1,4,5], Xiang-Guo Li[1,5], Antti Saraste[1,6] and Anne Roivainen[1,2,4,5]**

[1] Turku PET Centre, University of Turku, Turku, Finland, [2] Turku Center for Disease Modeling, University of Turku, Turku, Finland, [3] A.I. Virtanen Institute for Molecular Sciences, University of Eastern Finland, Kuopio, Finland, [4] Turku PET Centre, Turku University Hospital, Turku, Finland, [5] InFLAMES Research Flagship Center, University of Turku, Turku, Finland, [6] Heart Center, Turku University Hospital and University of Turku, Turku, Finland

OPEN ACCESS

Edited by:
Nick Devoogdt,
Free University of Brussels, Belgium

Reviewed by:
Alexis Broisat,
Institut National de la Santé et de la Recherche Médicale (INSERM), France
Ismaheel Lawal,
University of Pretoria, South Africa

***Correspondence:**
Anne Roivainen
anne.roivainen@utu.fi
Senthil Palani
palsen@utu.fi

Specialty section:
This article was submitted to Inflammation, a section of the journal Frontiers in Immunology

Received: 24 November 2021
Accepted: 03 January 2022
Published: 25 January 2022

Citation:
Palani S, Miner MWG, Virta J, Liljenbäck H, Eskola O, Örd T, Ravindran A, Kaikkonen MU, Knuuti J, Li X-G, Saraste A and Roivainen A (2022) Exploiting Glutamine Consumption in Atherosclerotic Lesions by Positron Emission Tomography Tracer (2S,4R)-4-^{18}F-Fluoroglutamine. Front. Immunol. 13:821423. doi: 10.3389/fimmu.2022.821423

Increased glutamine metabolism by macrophages is associated with development of atherosclerotic lesions. Positron emission tomography/computed tomography (PET/CT) with a glutamine analog (2S,4*R*)-4-^{18}F-fluoroglutamine (^{18}F-FGln) allows quantification of glutamine consumption *in vivo*. Here, we investigated uptake of ^{18}F-FGln by atherosclerotic lesions in mice and compared the results with those obtained using the glucose analog 2-deoxy-2-^{18}F-fluoro-*D*-glucose (^{18}F-FDG). Uptake of ^{18}F-FGln and ^{18}F-FDG by healthy control mice (C57BL/6JRj) and atherosclerotic low-density lipoprotein receptor-deficient mice expressing only apolipoprotein B100 (LDLR$^{-/-}$ApoB$^{100/100}$) was investigated. The mice were injected intravenously with ^{18}F-FGln or ^{18}F-FDG for *in vivo* PET/CT imaging. After sacrifice at 70 minutes post-injection, tracer uptake was analyzed by gamma counting of excised tissues and by autoradiography of aorta cryosections, together with histological and immunohistochemical analyses. We found that myocardial uptake of ^{18}F-FGln was low. PET/CT detected lesions in the aortic arch, with a target-to-background ratio (SUV_{max}, aortic arch/SUV_{mean}, blood) of 1.95 ± 0.42 (mean ± standard deviation). Gamma counting revealed that aortic uptake of ^{18}F-FGln by LDLR$^{-/-}$ApoB$^{100/100}$ mice (standardized uptake value [SUV], 0.35 ± 0.06) was significantly higher than that by healthy controls (0.20 ± 0.08, $P = 0.03$). More detailed analysis by autoradiography revealed that the plaque-to-healthy vessel wall ratio of ^{18}F-FGln (2.90 ± 0.42) was significantly higher than that of ^{18}F-FDG (1.93 ± 0.22, $P = 0.004$). Immunohistochemical staining confirmed that ^{18}F-FGln uptake in plaques co-localized with glutamine transporter SLC7A7-positive macrophages. Collectively these data show that the ^{18}F-FGln PET tracer detects inflamed atherosclerotic lesions. Thus, exploiting glutamine consumption using ^{18}F-FGln PET may have translational relevance for studying atherosclerotic inflammation.

Keywords: atherosclerosis, ^{18}F-fluoroglutamine, PET/CT, macrophages, inflammation

INTRODUCTION

Atherosclerosis is a chronic inflammatory disease characterized by inflammation and accumulation of macrophages. Macrophages are highly plastic cells that play an important role during inflammation and propagation of plaques, and during the resolution of atherosclerosis (1). The vulnerability of atherosclerotic plaques to rupture correlates with the number of pro-inflammatory macrophages, whereas plaque stability correlates with the number of inflammation-resolving macrophages (2). These vital roles, together with their plasticity, make macrophages attractive targets for diagnosis and for therapy aimed at preventing or halting existing atherosclerosis.

Pro-inflammatory stimuli such as lipopolysaccharides (LPS) (3, 4) or oxidized low-density lipoprotein (5, 6) increase glycolytic capacity and glucose uptake by macrophages, phenomena that may be associated with a high risk phenotype for atherosclerotic plaques (7). This high glycolytic capacity of macrophages has been utilized to identify atherosclerotic inflammation by positron emission tomography (PET) using glucose analog 2-deoxy-2-^{18}F-fluoro-*D*-glucose (^{18}F-FDG) (3, 8). High glucose uptake, however, is not only a key hallmark of pro-inflammatory macrophages; it is also a common attribute of anti-inflammatory macrophages (3, 9, 10) along with all other glucose-metabolizing cells. The normally high physiological glucose uptake of myocardial cells further complicates the accurate assessment and quantification of increases in ^{18}F-FDG uptake due to local inflammation. Therefore, using ^{18}F-FDG PET alone as a tool to detect macrophages associated with atherosclerotic inflammation has its limitations and better tools are required for assessing the heterogeneity of macrophage activation and disease characterization.

Glutamine is an abundant amino acid and nutrient source that plays a role in exercise recovery, wound healing, metabolism, and promoting the growth of cancer cells (11). Glutamine is transported to cells by many membrane-bound solute carrier-type transporters (SLCs) (12). Experimental studies show that glutamine is required for polarization of macrophages, and that differently polarized macrophages show changes in glutamine metabolism (4, 13). A recent study demonstrated that combined assessment of 2-deoxyglucose and glutamine metabolism improved the *ex vivo* identification of macrophage polarization states (10). Furthermore, accumulation of these substrates showed different patterns in atherosclerotic lesions. However, the *in vivo* significance of glutamine uptake in atherosclerosis remains to be studied. The glutamine analog (2*S*,4*R*)-4-^{18}F-fluoroglutamine (^{18}F-FGln) allows quantification of glutamine consumption *in vivo* by PET. Recently, we and others showed that ^{18}F-FGln is taken up preferentially by glioma cells compared with healthy brain tissue, making it feasible for *in vivo* imaging of enhanced glutamine uptake by PET (14, 15).

Here, we investigated uptake of ^{18}F-FGln by inflamed atherosclerotic lesions in mice and compared the results with those obtained using ^{18}F-FDG. First, we evaluated uptake of intravenously (i.v) administered ^{18}F-FGln or ^{18}F-FDG to detect atherosclerotic lesions using PET/CT imaging. Second, we used a gamma counter to measure the radioactivity of the administered tracer in excised tissues. Finally, we used digital autoradiography and immunohistochemistry of tissue cryosections to assess tracer accumulation in the atherosclerotic aorta and its localization in macrophage-rich lesions.

MATERIALS AND METHODS

Chemicals and Reagents

The tosylated precursor for ^{18}F-FGln synthesis and the non-radioactive reference compound FGln were provided by the Organic Synthesis Core Facility at Memorial Sloan Kettering Cancer Center, New York, NY, USA. The cassettes for ^{18}F-FDG synthesis were purchased from GE Healthcare (Waukesha, WI, USA).

Radiosynthesis and *In Vivo* Stability Analysis

The chemical structures of ^{18}F-FGln and ^{18}F-FDG are shown in **Supplementary Figure 1**. ^{18}F-FGln was prepared according to a published method (16), with some modifications to fit into the radiosynthesis device as described in our previous work (14). Quality control of the obtained ^{18}F-FGln was performed using high-performance liquid chromatography (HPLC). ^{18}F-FDG was prepared in-house using a fully automated cassette-based system and a FASTLab® radiosynthesis device (17). The synthesis procedure was compliant with Good Manufacturing Practices. Quality control of ^{18}F-FDG before release of each batch was performed using HPLC and thin-layer chromatography.

To assess the *in vivo* stability of ^{18}F-FGln, blood samples were taken at the end of PET/CT imaging. Whole-blood was weighed and radioactivity measured (Triathler 3″; Hidex, Turku, Finland) before being centrifuged at 700 ×*g* at 4°C for 5 minutes to separate the plasma. All results were decay-corrected to the corresponding animals' time of sacrifice. A plasma sample was then weighed and radioactivity measured before a subsample was precipitated with 2.4 volumes of methanol, followed by vortexing and centrifugation at 11,000 ×*g* for 10 minutes. The radioactivity of the separated supernatant and resulting precipitated protein pellet was measured. The precipitated plasma supernatants were further analyzed using established HPLC methods (18) to measure the fraction of intact ^{18}F-FGln.

Mouse Model

To induce atherosclerosis, low-density lipoprotein receptor-deficient male mice expressing only apolipoprotein B100 (LDLR$^{-/-}$ApoB$^{100/100}$, strain #003000 with C57BL/6J background; Jackson Laboratory, Bar Harbor, ME, USA) were fed with a high-fat diet (HFD; 0.2% total cholesterol; TD 88137; Envigo, Madison, WI, USA) starting at the age of 2 months; this diet was maintained for 3–5 months. C57BL/6JRj male mice (7 months old; Central Animal Laboratory of the University of Turku) fed a regular chow diet were used as healthy controls. In total, 12 LDLR$^{-/-}$ApoB$^{100/100}$ (45.4 ± 2.4 g) and 12 healthy control mice (31.7 ± 3.9 g) were studied (**Table 1**). The mice had access to food and water *ad libitum* throughout the study,

TABLE 1 | Characteristics of the investigated animals.

	$LDLR^{-/-}ApoB^{100/100}$ atherosclerotic mice	C57BL/6JRj control mice
Age, months	5–7	6
High-fat diet, months	3–5	ND
Male animals, no.	12	12
Weight, g	45.4 ± 2.4*	31.7 ± 3.9*
In vivo ^{18}F-FGln PET/CT, no.	4	4
In vivo ^{18}F-FDG PET/CT, no.	4	4
Ex vivo ^{18}F-FGln gamma counting, no.	5	5
Ex vivo ^{18}F-FGln autoradiography, no.	5	5
Ex vivo ^{18}F-FDG autoradiography, no.	5	4
^{18}F-FGln metabolite analysis, no.	4	7
Injected ^{18}F-FGln (MBq/mice)	14.5 ± 1.1*	14.4 ± 0.5*
Injected ^{18}F-FDG (MBq/mice)	13.7 ± 1.2*	14.2 ± 0.3*

*$LDLR^{-/-}ApoB^{100/100}$, low-density lipoprotein receptor-deficient mice expressing only apolipoprotein B100; ND, not done; no., number of investigated animals. *Values are presented as the mean ± SD.*

which was conducted at the Central Animal Laboratory of the University of Turku. All animal experiments were approved by the National Project Authorization Board of Finland (license numbers: ESAVI/4567/2018 and ESAVI/11751/2021) and were carried out in compliance with European Union Directive 2010/63/EU.

PET/CT Imaging

Mice were fasted for 3–4 hours, anesthetized with isoflurane (4–5% induction, 1.5–2.5% maintenance), and placed on a dedicated heating pad in the PET/CT scanner (Inveon Multimodality; Siemens Medical Solutions, Knoxville, TN, USA). The mice received i.v. ^{18}F-FDG (13.9 ± 0.9 MBq) or ^{18}F-FGln (14.5 ± 0.8 MBq) *via* a tail vein cannula for the 60 minute dynamic PET imaging. For anatomical reference, an iodinated intravascular contrast agent (100 µL eXIATM160XL; Binitio Biomedical, Ottawa, ON, Canada) was i.v. injected immediately after PET imaging, and a 10 minute high-resolution CT was performed. PET/CT images were analyzed using Carimas 2.10 software (Turku PET Centre, Turku, Finland; www.turkupetcentre.fi/carimas/). The regions of interest (ROI) in the aortic arch, vena cava (representing blood), and myocardium were defined using contrast-enhanced CT as an anatomical reference, as previously described (18). The myocardial ROI was consistently defined at the same site for all mice tested. The results were expressed as standardized uptake values (SUVs), which were normalized to the injected radioactivity dose and animal body weight. The maximum target-to-background ratio (TBR) at 40–60 minutes post-injection was calculated as follows: $SUV_{max,\ aortic\ arch}/SUV_{mean,\ blood}$ according to the established method (19).

Ex Vivo Biodistribution

At 70 minutes post-injection, mice were placed under deep anesthesia, and blood samples were obtained by cardiac puncture. The mice were euthanized by cervical dislocation, and tissues were dissected and weighed. Radioactivity was measured using a γ-counter (Triathler 3″; Hidex, Turku, Finland). The gamma counting was performed on the entire aorta, extending from the aortic arch to the iliac artery bifurcation. After compensating for the remaining radioactivity in the tail and cannula, the results were expressed as SUVs, which is calculated as radioactivity concentration (becquerel per gram of tissue) normalized for injected radioactivity dose and animal body weight.

Autoradiography, Histology, and Immunostaining

Following *ex vivo* gamma counting of excised tissues, the aorta was embedded in optimal cutting temperature compound, frozen at −70°C, and cut into 20 and 8 µm cryosections. The quantitative digital autoradiography analysis of tracer distribution was done using 20 µm cryosections, as previously described (20). The sections were exposed to a Fuji Imaging Plate BAS-TR2025 (Fuji, Tokyo, Japan) for at least 4 hours and then scanned by a Fuji Analyzer BAS-5000. After scanning, sections were stored at −70°C until staining with hematoxylin–eosin (H&E). They were then scanned with a digital slide scanner (Pannoramic 250 Flash; 3DHISTECH, Ltd., Budapest, Hungary). Tina 2.1 software (Ravtest Isotopenmessgeräte, GmbH, Straubenhardt, Germany) was used to analyze the autoradiographs. Uptake of ^{18}F-FDG and ^{18}F-FGln was normalized to the injected radioactivity dose per unit of body mass and corrected for radioactivity decay. Data were expressed as photostimulated luminescence per square millimeter (Normalized PSL/mm^2).

Consecutive 8 µm sections were used to investigate co-localization of ^{18}F-FGln in Mac-3-positive macrophages and glutamine transporter (SLC7A7 [solute carrier family 7, member 7])-positive macrophages. Briefly, sections were incubated with an anti-mouse Mac-3 antibody (1:1,000; catalog number: 550292; BD Biosciences, Franklin Lakes, NJ, USA) and an anti-SLC7A7 antibody (1:1,000; catalog number: PA5-113527; Thermo Fisher Scientific, Waltham, MA, USA), followed by development of a color reaction using 3.3′-diaminobenzidine (Bright-DAB, BS04-110; ImmunoLogic, Duiven, the Netherlands).

Collected mouse hearts were preserved overnight at room temperature in 10% formalin, followed by dehydration in 70% ethanol. Hearts were embedded in paraffin prior to histological characterization of atherosclerotic lesions at the level of the aortic root.

Sections (6 μm thick) were cut transversely at the level of the coronary ostia, and consecutive sections were stained with modified Movat's pentachrome or with the anti-mouse Mac-3 antibody to detect macrophages (20, 21). Furthermore, to detect SLC family glutamine transporters, sections were stained with anti-SLC1A5 (1:500; NBP1-59732; Novus Biologicals, Centennial, CO, USA), anti-SCL3A2 (1:500; sc-390154; Santa Cruz Biotechnology, Dallas, TX, USA), and anti-SLC7A7 (1:500; PA5-113527; Thermo Fisher Scientific, Waltham, MA, USA)) antibodies, followed by development of a color reaction using 3.3′-diaminobenzidine.

Statistical Analysis

Results are presented as the mean ± standard deviation (SD). Normality was examined by a Shapiro–Wilk test, and equality of variances was tested with an F test. For normally distributed datasets, a two-tailed unpaired Student's *t* test in Microsoft Excel was used to analyze differences between the groups. *P*-values <0.05 were considered statistically significant.

RESULTS

In Vivo Stability of ^{18}F-FGln

^{18}F-FGln was prepared as previously reported, with comparable yield and purity (14). Seventy minutes after ^{18}F-FGln administration, all measured parameters of metabolism in both control and diseased groups of mice were very similar. On average (n = 11), red blood cell uptake of the radioactivity was 46.8% ± 1.5. When analyzing plasma samples, an average (n = 11) of 24.6% ± 4.4 of the radioactivity was bound to proteins after approximately 70 minutes post-injection. HPLC analysis of precipitated plasma supernatant indicated that the amount of intact ^{18}F-FGln in plasma was 78.2% ± 4.0 (**Supplementary Figure 2**).

^{18}F-FGln Accumulates in Inflamed Atherosclerotic Lesions in Mice

The *in vivo* PET/CT imaging studies of atherosclerotic mice revealed that myocardial uptake of ^{18}F-FGln (SUV_{mean} 0.43 ± 0.06, n = 4) was significantly lower than that of ^{18}F-FDG (SUV_{mean} 10.84 ± 1.10, n = 4, P < 0.0001; **Figures 1A, B**). PET/CT images

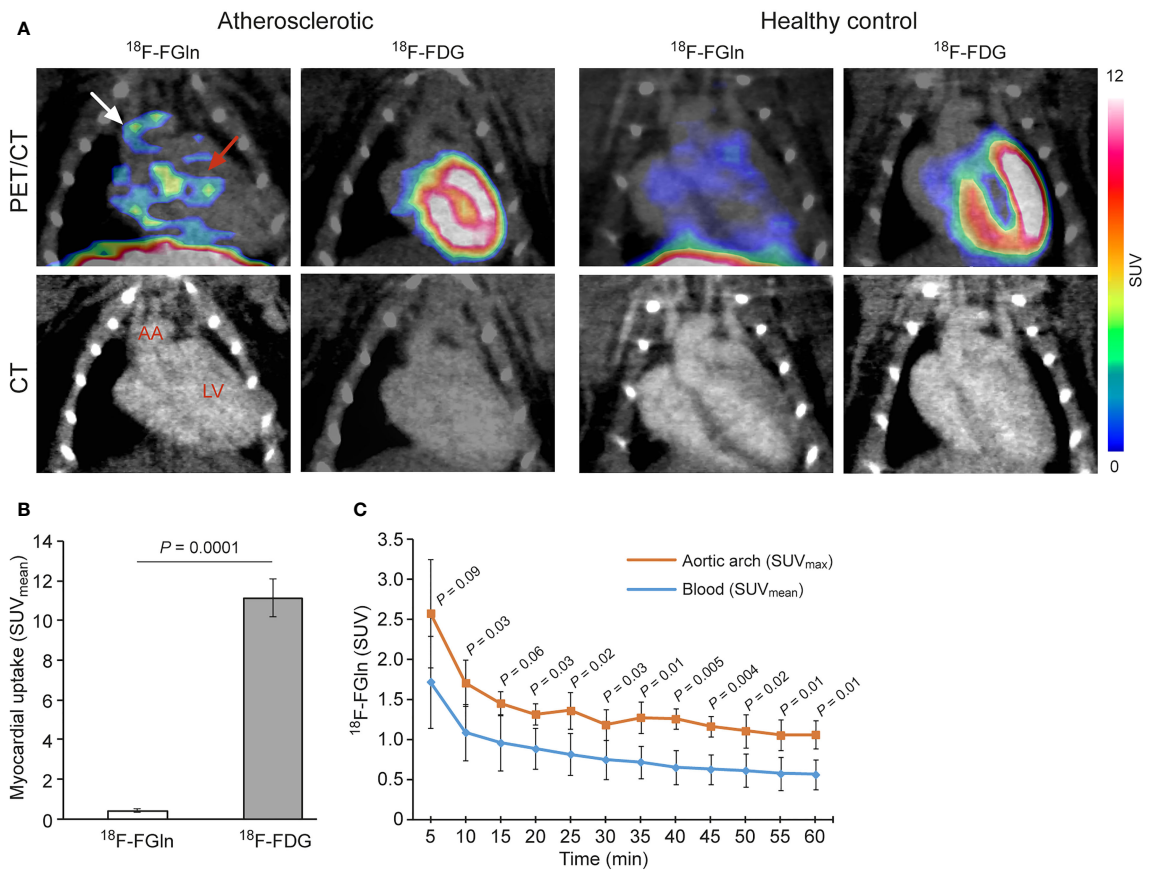

FIGURE 1 | **(A)** Representative coronal PET/CT images of atherosclerotic and control mice administered with ^{18}F-FGln or ^{18}F-FDG. White arrow indicate the aortic arch (AA), and pink arrow indicates the myocardium. LV, left ventricle. **(B)** PET quantification of the myocardium, showing a significant difference between the tracers. **(C)** ^{18}F-FGln time-activity curves in the AA and blood (vena cava) of atherosclerotic mice show a statistically significant difference (n = 4). Values are presented as the mean ± SD (n = 4). *P*-values were calculated using a two-tailed unpaired Student's *t* test.

showed ^{18}F-FGln uptake by the aortic arch of atherosclerotic mice, whereas ^{18}F-FDG was not detectable. The time-activity curve of ^{18}F-FGln in the atherosclerotic aortic arch (SUV_{max}) was higher than that in blood (SUV_{mean}; **Figure 1C**). For comparison, all SUV_{max} and SUV_{mean} time-activity curves of ^{18}F-FGln in the aortic arch and blood of atherosclerotic mice are shown in **Supplementary Figure 3**. The average TBR of ^{18}F-FGln in the aortic arch of atherosclerotic mice (1.95 ± 0.42) tended to be higher than that in healthy control mice (1.44 ± 0.10, n = 4, P = 0.09). There was no difference in the TBR of ^{18}F-FDG in the aortic arch of atherosclerotic mice (2.77 ± 0.71) and that of healthy control mice (2.74 ± 0.77, n = 4, P = 0.96).

Ex vivo gamma counting showed that uptake of ^{18}F-FGln in the whole aorta of atherosclerotic mice (SUV 0.35 ± 0.06) was significantly higher than that in healthy controls (SUV 0.20 ± 0.08, n = 5, P = 0.03; **Table 2**). In both mouse strains, the highest radioactivity concentration was observed in pancreas, and the difference in this organ between LDLR$^{-/-}$ApoB$^{100/100}$ and C57BL/6JRj mice was statistically significant (P = 0.004). The lowest uptake of ^{18}F-FGln was observed in brain, brown adipose tissue and white adipose tissue, respectively.

Macrophages in Atherosclerotic Plaques Express Glutamine Transporters

Two types of samples were taken from each mouse: 1) the aorta, which extended from the aortic arch to the iliac artery bifurcation, was frozen for longitudinal cryosections, 2) paraffin-embedded aortic root was cut into cross-sections at the level of the left coronary artery ostium. According to histological and Mac-3 macrophage staining of aortic roots and aortas, the LDLR$^{-/-}$ApoB$^{100/100}$ mice had prominent, macrophage-rich atherosclerotic lesions, while C57Bl/6JRj mice had no signs of atherosclerosis (**Figures 2**, **3** and **Supplementary Figures 4**, **5**).

Immunostaining of aortic root sections from atherosclerotic mice showed that plaque regions were enriched with Mac-3-positive macrophages. Furthermore, SLC1A5, SLC3A2, and SLC7A7 glutamine transporters were expressed in atherosclerotic lesions, but with unique expression profiles. SLC1A5 was expressed predominantly in aortic valve leaflets, whereas SLC3A2 was expressed in atherosclerotic lesions. Expression of SLC7A7 was prominent in both the aortic valve and atherosclerotic lesions. Noticeably, SLC7A7-positive cells co-localized with Mac-3-positive macrophages (**Figure 2**). However, in control aortic roots without plaques, minimal staining with either Mac-3 or glutamine transporter antibodies was visible (**Supplementary Figure 4**).

^{18}F-FGln Uptake Is Associated With SLC7A7-Positive Macrophage-Rich Lesions in Atherosclerotic Mice

To further elucidate the localization of ^{18}F-FGln and ^{18}F-FDG uptake in the aortas of atherosclerotic mice, we compared autoradiographs with histological and immunohistochemical staining. The results revealed that uptake of both ^{18}F-FGln and ^{18}F-FDG co-localized with Mac-3-positive macrophage-rich lesions. Notably, those macrophages were also positive for SLC7A7 (**Figure 3A**). Furthermore, detailed analysis of ^{18}F-FGln uptake in atherosclerotic aortas showed that plaque regions had higher uptake of ^{18}F-FGln (PSL/mm^2 89.05 ± 18.09, n = 5) than the vessel wall (PSL/mm^2 34.60 ± 5.23, P = 0.002) or adventitia (PSL/mm^2 35.48 ± 10.34, P = 0.001). There was no difference in uptake of ^{18}F-FGln between the vessel wall and adventitia in either the atherosclerotic or control groups (**Figure 3B**). Furthermore, the average plaque-to-healthy vessel wall ratio of ^{18}F-FGln (2.90 ± 0.42) was significantly higher than that of ^{18}F-FDG (1.93 ± 0.22, n = 5, P = 0.004; **Figure 3C**).

TABLE 2 | *Ex vivo* biodistribution of ^{18}F-FGln at 70 minutes post-injection into mice (expressed as SUV).

Tissue	LDLR$^{-/-}$ApoB$^{100/100}$ atherosclerotic mice (n = 5)	C57BL/6JRj control mice (n = 5)	P-value
Aorta	0.35 ± 0.06	0.20 ± 0.08	0.03
Brown adipose tissue	0.29 ± 0.03	0.48 ± 0.09	0.04
Bone (skull)	4.07 ± 1.56	4.62 ± 0.36	0.38
Bone + marrow (femur)	3.06 ± 1.18	3.48 ± 0.18	0.36
Blood	0.52 ± 0.10	0.51 ± 0.02	0.86
Brain	0.27 ± 0.08	0.29 ± 0.02	0.66
Heart	0.78 ± 0.18	0.96 ± 0.15	0.10
Intestine, small (empty)	2.71 ± 1.50	2.92 ± 0.49	0.94
Intestine, large (empty)	0.93 ± 0.30	1.30 ± 0.20	0.05
Kidney	2.29 ± 0.92	2.41 ± 0.31	0.74
Lungs	0.85 ± 0.22	1.07 ± 0.26	0.40
Liver	1.20 ± 0.24	1.90 ± 0.14	0.0001
Lymph nodes	0.94 ± 0.30	1.28 ± 0.11	0.06
Muscle	0.67 ± 0.28	0.91 ± 0.06	0.14
Pancreas	2.64 ± 0.62	4.77 ± 0.90	0.004
Plasma	0.60 ± 0.11	0.61 ± 0.02	0.86
Spleen	1.04 ± 0.37	1.38 ± 0.16	0.06
Stomach	1.05 ± 0.24	1.34 ± 0.20	0.04
Thymus	0.90 ± 0.38	0.94 ± 0.09	0.95
White adipose tissue	0.08 ± 0.04	0.09 ± 0.01	0.69

SUV, standardized uptake value, which is calculated as radioactivity concentration (becquerel per gram of tissue) normalized for injected radioactivity dose and animal body weight. Values are presented as the mean ± SD. P-values were calculated using a two-tailed unpaired Student's t test.

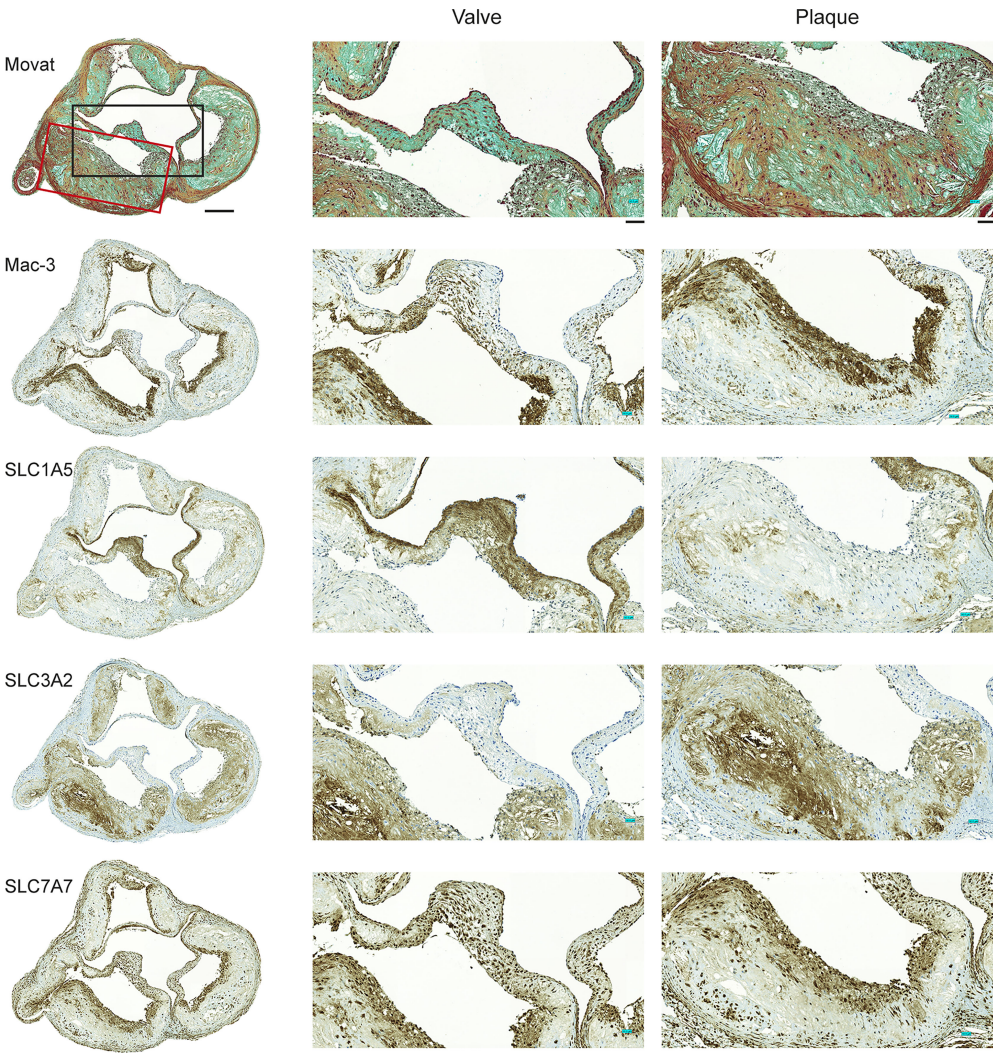

FIGURE 2 | Expression of Mac-3 and glutamine transporters by mouse aortic plaque macrophages. Movat's pentachrome staining of the aortic root demonstrates that atherosclerotic plaques were composed mostly of a fibrous cap and a necrotic region. Immunostaining of adjacent sections shows that Mac-3-positive macrophages are also positive for glutamine transporters SLC1A5, SLC3A2, and SLC7A7. Higher magnifications of the valve and plaque vessel regions are shown in the black and red rectangular boxes, respectively. Expression of SLC1A5 is prominent in the aortic valve region but not in the vessel plaque region. Expression of SLC3A2 is absent from the valve region but present in the vessel plaque region. Expression of SLC7A7 is clear in both the valve and vessel plaque regions. Scale bar = 200 μm; zoomed region scale bar = 50 μm.

However, there was no clear tracer uptake by control aorta (**Supplementary Figure 5**).

DISCUSSION

Imaging of atherosclerotic lesions with ^{18}F-FDG may be difficult due to physiological uptake by the myocardium and because non-inflammatory cells may consume large amounts of glucose during inflammation. Uptake of ^{18}F-FGln, a glutamine analog that is used for PET imaging of cancer (22–26) correlates with upregulation of alanine-serine-cysteine transporter 2 (ASCT2), a sodium-dependent neutral amino acid transporter of glutamine (27); as such, it detects lesions more sensitively than ^{18}F-FDG (23). Recently, we and others showed that uptake of ^{18}F-FGln by gliomas is higher than that by healthy brain tissue (14, 15).

In addition to cancers, glutamine metabolism is altered in some inflammatory conditions. A study by Tavakoli and co-workers showed a difference in the uptake of glutamine and 2-deoxyglucose by *in vitro*-polarized macrophages (10). Macrophages polarized with IL-4 ($M\Phi_{IL\text{-}4}$) show higher uptake of glutamine than macrophages polarized with interferon-gamma and tumor necrosis factor alpha ($M\Phi_{INF\text{-}\gamma\ +\ TNF\text{-}\alpha}$), or unstimulated macrophages ($M\Phi_0$). In the same study, an *ex vivo* experiment with ^{14}C-glutamine showed uptake by macrophage-rich atherosclerotic lesions in the aortas of mice.

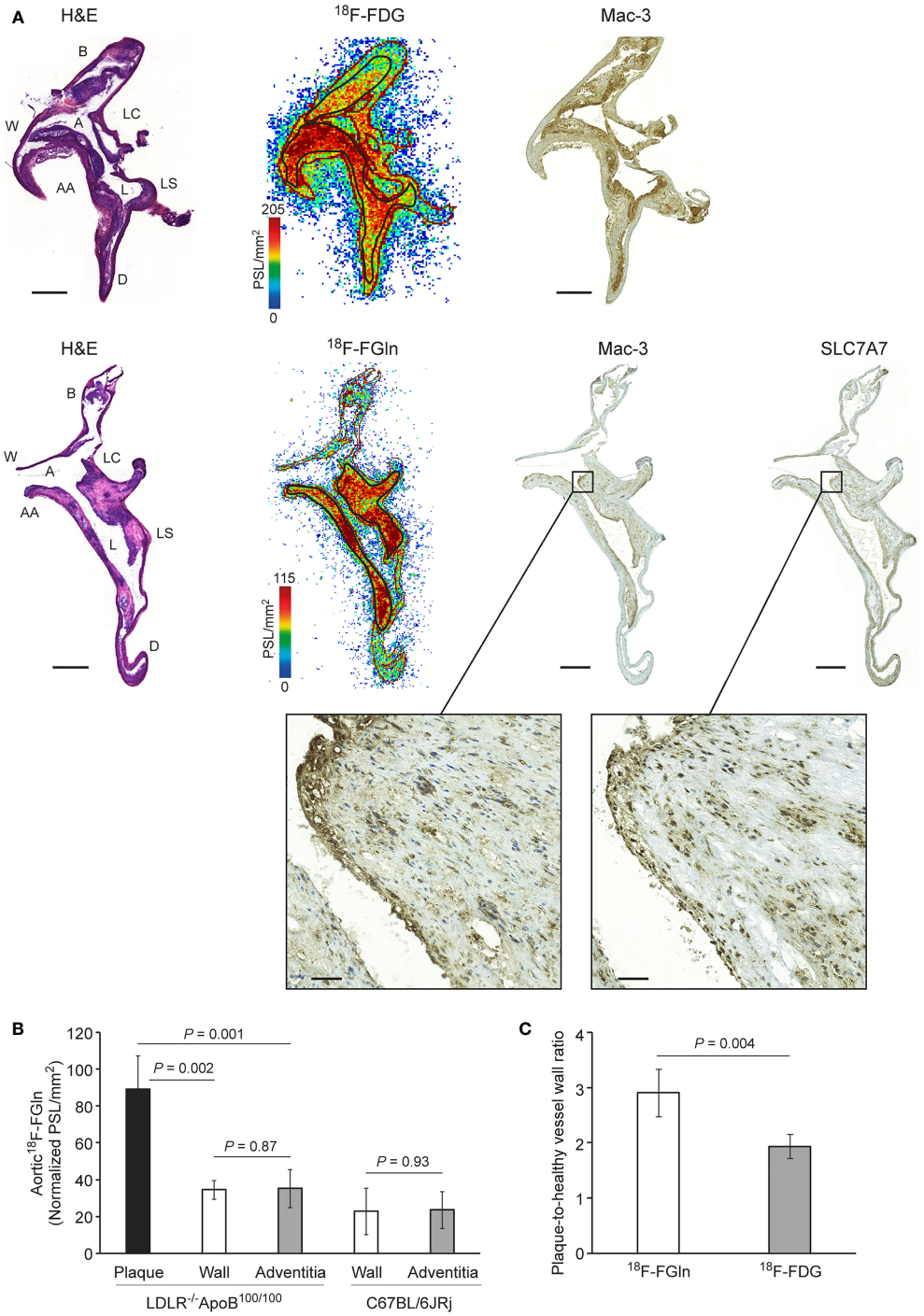

FIGURE 3 | **(A)** Representative images showing hematoxylin–eosin (H&E) staining, autoradiographs, Mac-3 macrophage staining, and SLC7A7 glutamine transporter staining in consecutive aorta cryosections from atherosclerotic mice. Black rectangles denote the plaque region shown at higher magnification. Scale bar = 500 µm; zoomed region scale bar = 50 µm. A, arch; AA, ascending aorta; B, brachiocephalic artery; D, descending thoracic aorta; L, lesion; LC, left common carotid artery; LS, left subclavian artery; W, vessel wall. **(B)** Quantification of ^{18}F-FGln *ex vivo* autoradiography data showing differences in tracer uptake between plaques, vessel wall, and adventitia in LDLR$^{-/-}$ApoB$^{100/100}$ atherosclerotic and C67BL/6JRj healthy control mice aortas. Values are expressed as the mean ± SD (n = 5). **(C)** Quantification of autoradiography data showing a significant difference between the tracers (n = 5). Values are expressed as the mean ± SD. P-values were calculated using a two-tailed unpaired Student's t test.

Here, we report for the first time that after i.v. administration, ^{18}F-FGln accumulates in inflamed atherosclerotic lesions in mice, which, combined with low myocardial uptake, facilitates visualization of aortic arch lesions *in vivo* by PET/CT. The myocardial uptake of ^{18}F-FGln was 25-fold lower than that of ^{18}F-FDG (**Figure 1B**). Uptake of tracers by inflamed lesions was further confirmed by a more detailed analysis using *ex vivo* digital autoradiography of aorta sections, which showed a higher plaque-to-healthy vessel wall ratio for ^{18}F-FGln than for ^{18}F-FDG (**Figure 3C**). Immunohistochemical staining confirmed that uptake of ^{18}F-FGln accumulated in plaques rich in Mac-3 and SLC7A7-positive cells. However, our results do not preclude that other cell types and glutamine transporters could be responsible for part of ^{18}F-FGln uptake in atherosclerotic lesions.

To assess the *in vivo* stability of ^{18}F-FGln, blood samples were collected 70 minutes after radiopharmaceutical administration and subjected to multiple assays. Very little difference was observed between control and disease populations with respect to red blood cell uptake, plasma protein binding, and the purity of the plasma fraction. Based on HPLC analysis, an average of 78.2% of plasma radioactivity detected 70 minutes post-injection was derived from intact ^{18}F-FGln, indicating good *in vivo* stability.

Furthermore, immunostaining of aortic roots showed that atherosclerotic plaques were rich in macrophages (Mac-3), and that not all of the glutamine transporters are expressed uniformly in the plaque region. In line with previous studies, we observed that expression of SLC1A5 and SLC3A2 in the plaque region was not ubiquitous (10). However, we noticed that SLC7A7 expression was universal in macrophages in plaques of the aortic root, which supports the possibility that SLC7A7 is the prominent glutamine transporter in macrophage-rich plaques of the atherosclerotic aorta. Interestingly, a previous study has reported that downregulating SLC7A7 in human macrophages by using small interfering RNA triggers an inflammatory phenotype (28) suggesting SLC7A7 contribution in macrophage polarization

When we compared the plaque-to-healthy vessel wall ratio of ^{18}F-FGln (2.90 ± 0.42) with that of other tracers using a similar protocol for detection of atherosclerotic lesions, we found that it was higher than that of ^{18}F-FDG (1.93 ± 0.22), ^{18}F-FOL (2.6 ± 0.58), ^{68}Ga-FOL (2.44 ± 0.15), and ^{68}Ga-NODAGA-exendin-4 (1.6 ± 0.10) (19, 29, 30).

We acknowledge that this study has some limitations. It should be noted that because the size of atherosclerotic plaques in mice is small in relation to the spatial resolution of PET scanner, spill over from adjacent tissue with low tracer uptake is likely to artificially reduce the measured uptake in small lesions. We did not perform ^{18}F-FGln blocking studies *in vivo* or *in vitro*. Furthermore, we did not illustrate how glutamine consumption changes in a plaque regression model. *In vitro* blocking studies might provide insight into the specific solute carrier transporter involved in transport of glutamine during atherosclerotic inflammation. Further studies should determine whether blocking one transporter in the family might decrease uptake of glutamine, or whether blocking allows other transporters in the family to take over and compensate for any loss of glutamine uptake.

A study suggested that combined imaging of glucose and glutamine metabolism is a potential approach to better discriminate macrophage subtypes in atherosclerotic lesions with higher ratio of glutamine to 2-deoxyglucose representing the predominance of an anti-inflammatory macrophage population (10). Our autoradiography results indicate that indeed, both ^{18}F-FDG and ^{18}F-FGln accumulate in atherosclerotic lesions showing relatively similar distribution in macrophage-rich areas. However, we were not able to compare uptake of these tracers directly in the same atherosclerotic lesions due to limited ^{18}F-FDG signal in PET images and the use of same radionuclide precluding dual tracer autoradiography. Given the feasibility of detecting atherosclerotic lesions with ^{18}F-FGln, evaluation of the ratio of glutamine to 2-deoxyglucose seems a feasible approach in future studies.

The results presented herein provide preclinical evidence that ^{18}F-FGln is taken up by inflamed atherosclerotic lesions in mice. Further studies using ^{18}F-FGln in different atherosclerotic settings and models would strengthen data supporting the translational use of ^{18}F-FGln as a tracer to image atherosclerotic inflammation.

DATA AVAILABILITY STATEMENT

The raw data supporting the conclusions of this article may be made available by the authors upon a reasonable request. Requests will be evaluated by authors. Requests to access the datasets should be directed to Anne Roivainen, anne.roivainen@utu.fi.

ETHICS STATEMENT

The animal study was reviewed and approved by National Project Authorization Board of Finland (license numbers: ESAVI/4567/2018 and ESAVI/11751/2021).

AUTHOR CONTRIBUTIONS

SP acquired and analyzed the data, prepared figures, and wrote the first draft of the manuscript. MM, JV, HL, OE, TÖ, ARa, and MK acquired and analyzed the data. JK, X-GL, AS and ARo designed and supervised the work. All authors contributed to the writing and approved the submitted version of the manuscript.

FUNDING

The study was financially supported by grants from the Academy of Finland (decision numbers: 314554, 314556, 335973, and 335975), the Sigrid Jusélius Foundation, the Jane and Aatos Erkko Foundation, and the Finnish Foundation for Cardiovascular

Research. This research was supported by InFLAMES Flagship Programme of the Academy of Finland (decision number: 337530).

ACKNOWLEDGMENTS

The authors thank Ass. Prof. Riku Klén, Aake Honkaniemi, Erica Nyman, Marja-Riitta Kajaala (Histology Core Facility of the Institute of Biomedicine, University of Turku, Finland), and Timo Kattelus for technical assistance. We thank Prof. Jason Lewis and Dr. Ouathek Ouerfelli at the Memorial Sloan Kettering Cancer Center for providing the ^{18}F-FGln precursor. The ^{18}F-FGln precursor tosylate and cold ^{19}F-FGln standard were synthesized by the Organic Synthesis Core Facility at Memorial Sloan Kettering Cancer Center, New York. Funding for the Core Facility is provided by grant NCI R50 CA243895-01 and by an NCI P30 CA008748-53 Core Grant.

SUPPLEMENTARY MATERIAL

The Supplementary Material for this article can be found online at: https://www.frontiersin.org/articles/10.3389/fimmu.2022.821423/full#supplementary-material

REFERENCES

1. Tavakoli S, Vashist A, Sadeghi MM. Molecular Imaging of Plaque Vulnerability. *J Nucl Cardiol* (2014) 21:1112–28. doi: 10.1007/s12350-014-9959-4
2. Chinetti-Gbaguidi G, Colin S, Staels B. Macrophage Subsets in Atherosclerosis. *Nat Rev Cardiol* (2015) 12:10–7. doi: 10.1038/nrcardio.2014.173
3. Tavakoli S, Zamora D, Ullevig S, Asmis R. Bioenergetic Profiles Diverge During Macrophage Polarization: Implications for the Interpretation of ^{18}F-FDG PET Imaging of Atherosclerosis. *J Nucl Med* (2013) 54:1661–7. doi: 10.2967/jnumed.112.119099
4. Tannahill GM, Curtis AM, Adamik J, Palsson-Mcdermott EM, McGettrick AF, Goel G, et al. Succinate is an Inflammatory Signal That Induces IL-1β Through HIF-1α. *Nature* (2013) 496:238–42. doi: 10.1038/nature11986
5. Lee SJ, Quach CHT, Jung KH, Paik JY, Lee JH, Park JW, et al. Oxidized Low-Density Lipoprotein Stimulates Macrophage ^{18}F-FDG Uptake *via* Hypoxia-Inducible Factor-1α Activation Through Nox2-Dependent Reactive Oxygen Species Generation. *J Nucl Med* (2014) 55:1699–705. doi: 10.2967/jnumed.114.139428
6. Ogawa M, Nakamura S, Saito Y, Kosugi M, Magata Y. What can be Seen by ^{18}F-FDG PET in Atherosclerosis Imaging? The Effect of Foam Cell Formation on ^{18}F-FDG Uptake to Macrophages *In Vitro*. *J Nucl Med* (2012) 53:55–8. doi: 10.2967/jnumed.111.092866
7. Tomas L, Edsfeldt A, Mollet IG, Matic LP, Prehn C, Adamski J, et al. Altered Metabolism Distinguishes High-Risk From Stable Carotid Atherosclerotic Plaques. *Eur Heart J* (2018) 39:2301–10. doi: 10.1093/eurheartj/ehy124
8. Sadeghi MM. ^{18}F-FDG PET and Vascular Inflammation: Time to Refine the Paradigm? *J Nucl Cardiol* (2015) 22:319–24. doi: 10.1007/s12350-014-9917-1
9. Folco EJ, Sheikine Y, Rocha VZ, Christen T, Shvartz E, Sukhova GK, et al. Hypoxia But Not Inflammation Augments Glucose Uptake in Human Macrophages: Implications for Imaging Atherosclerosis With ^{18}fluorine-Labeled 2-Deoxy-D-Glucose Positron Emission Tomography. *J Am Coll Cardiol* (2011) 58:603–14. doi: 10.1016/j.jacc.2011.03.044
10. Tavakoli S, Downs K, Short JD, Nguyen HN, Lai Y, Jerabek PA, et al. Characterization of Macrophage Polarization States Using Combined Measurement of 2-Deoxyglucose and Glutamine Accumulation: Implications for Imaging of Atherosclerosis. *Arterioscler Thromb Vasc Biol* (2017) 37:1840–8. doi: 10.1161/ATVBAHA.117.308848
11. Rajagopalan KN, DeBerardinis RJ. Role of Glutamine in Cancer: Therapeutic and Imaging Implications. *J Nucl Med* (2011) 52:1005–8. doi: 10.2967/jnumed.110.084244
12. Bhutia YD, Ganapathy V. Glutamine Transporters in Mammalian Cells and Their Functions in Physiology and Cancer. *Biochim Biophys Acta - Mol Cell Res* (2016) 1863:2531–9. doi: 10.1016/j.bbamcr.2015.12.017
13. Jha AK, Huang SCC, Sergushichev A, Lampropoulou V, Ivanova Y, Loginicheva E, et al. Network Integration of Parallel Metabolic and Transcriptional Data Reveals Metabolic Modules That Regulate Macrophage Polarization. *Immunity* (2015) 42:419–30. doi: 10.1016/j.immuni.2015.02.005
14. Miner MW, Liljenbäck H, Virta J, Merisaari J, Oikonen V, Westermarck J, et al. (2S, 4R)-4-[^{18}F]Fluoroglutamine for *In Vivo* PET Imaging of Glioma Xenografts in Mice: An Evaluation of Multiple Pharmacokinetic Models. *Mol Imaging Biol* (2020) 22:969–78. doi: 10.1007/s11307-020-01472-1
15. Venneti S, Dunphy MP, Zhang H, Pitter KL, Zanzonico P, Campos C, et al. Glutamine-Based PET Imaging Facilitates Enhanced Metabolic Evaluation of Gliomas *In Vivo*. *Sci Transl Med* (2015) 7:274ra17. doi: 10.1126/scitranslmed.aaa1009
16. Lieberman BP, Ploessl K, Wang L, Qu W, Zha Z, Wise DR, et al. PET Imaging of Glutaminolysis in Tumors by ^{18}F-(2S,4R)4- Fluoroglutamine. *J Nucl Med* (2011) 52:1947–55. doi: 10.2967/jnumed.111.093815
17. Long JZ, Jacobson MS, Hung JC. Comparison of Fastlab ^{18}F-FDG Production Using Phosphate and Citrate Buffer Cassettes. *J Nucl Med Technol* (2013) 41:32–4. doi: 10.2967/jnmt.112.112649
18. Zhou R, Pantel AR, Li S, Lieberman BP, Ploessl K, Choi H, et al. ^{18}F(2S,4R)4-Fluoroglutamine PET Detects Glutamine Pool Size Changes in Triple-Negative Breast Cancer in Response to Glutaminase Inhibition. *Cancer Res* (2017) 77:1476–84. doi: 10.1158/0008-5472.CAN-16-1945
19. Bucerius J, Hyafil F, Verberne JH, Slart AJHR, Lindner O, Sciagra R, et al. Position Paper of the Cardiovascular Committee of the European Association of Nuclear Medicine (EANM) on PET Imaging of Atherosclerosis. *Eur J Nucl Med Mol Imaging* (2016) 43:780–92. doi: 10.1007/s00259-015-3259-3
20. Silvola JMU, Li XG, Virta J, Marjamäki P, Liljenbäck H, Hytönen JP, et al. Aluminum Fluoride-18 Labeled Folate Enables *In Vivo* Detection of Atherosclerotic Plaque Inflammation by Positron Emission Tomography. *Sci Rep* (2018) 8:9720. doi: 10.1038/s41598-018-27618-4
21. Silvola JMU, Saraste A, Laitinen I, Savisto N, Laine VJO, Heinonen SE, et al. Effects of Age, Diet, and Type 2 Diabetes on the Development and FDG Uptake of Atherosclerotic Plaques. *JACC Cardiovasc Imaging* (2011) 4:1294–301. doi: 10.1016/j.jcmg.2011.07.009
22. Dunphy MPS, Harding JJ, Venneti S, Zhang H, Burnazi EM, Bromberg J, et al. *In Vivo* PET Assay of Tumor Glutamine Flux and Metabolism: in-Human Trial of ^{18}F-(2S,4R)-4-Fluoroglutamine. *Radiology* (2018) 287:667–75. doi: 10.1148/radiol.2017162610
23. Liu F, Xu X, Zhu H, Zhang Y, Yang J, Zhang L, et al. PET Imaging of ^{18}F-(2S,4R)4-Fluoroglutamine Accumulation in Breast Cancer: From Xenografts to Patients. *Mol Pharm* (2018) 15:3448–55. doi: 10.1021/acs.molpharmaceut.8b00430
24. Valtorta S, Toscani D, Chiu M, Sartori A, Coliva A, Brevi A, et al. [^{18}F](2S,4R)-4-Fluoroglutamine as a New Positron Emission Tomography Tracer in Myeloma. *Front Oncol* (2021) 11:760732. doi: 10.3389/fonc.2021.760732
25. Miner MWG, Liljenbäck H, Virta J, Helin S, Eskola O, Elo P, et al. Comparison of: (2S,4R)-4-[^{18}F]Fluoroglutamine, [^{11}C]Methionine, and 2-Deoxy-2-[^{18}F]Fluoro-D-Glucose and Two Small-Animal PET/CT Systems Imaging Rat Gliomas. *Front Oncol* (2021) 11:730358. doi: 10.3389/fonc.2021.730358
26. Viswanath V, Zhou R, Lee H, Li S, Cragin A, Doot RK, et al. Kinetic Modeling of ^{18}F-(2S,4R)4-Fluoroglutamine in Mouse Models of Breast Cancer to Estimate Glutamine Pool Size as an Indicator of Tumor Glutamine Metabolism. *J Nucl Med* (2021) 62:1154–62. doi: 10.2967/jnumed.120.250977
27. Hassanein M, Hight MR, Buck JR, Tantawy MN, Nickels ML, Hoeksema MD, et al. Preclinical Evaluation of 4-[^{18}F]Fluoroglutamine PET to Assess ASCT2 Expression in Lung Cancer. *Mol Imaging Biol* (2016) 18:18–23. doi: 10.1007/s11307-015-0862-4
28. Rotoli BM, Barilli A, Visigalli R, Ingoglia F, Milioli M, Lascia M, et al. Downregulation of SLC7A7 Triggers an Inflammatory Phenotype in Human

Macrophages and Airway Epithelial Cells. *Front Immunol* (2018) 9:508. doi: 10.3389/fimmu.2018.00508

29. Moisio O, Palani S, Virta J, Elo P, Liljenbäck H, Tolvanen T, et al. Radiosynthesis and Preclinical Evaluation of [^{68}Ga]Ga-NOTA-Folate for PET Imaging of Folate Receptor β-Positive Macrophages. *Sci Rep* (2020) 10:13593. doi: 10.1038/s41598-020-70394-3
30. Ståhle M, Hellberg S, Virta J, Liljenbäck H, Metsälä O, Li XG, et al. Evaluation of Glucagon-Like Peptide-1 Receptor Expression in Nondiabetic and Diabetic Atherosclerotic Mice Using PET Tracer ^{68}Ga-NODAGA-Exendin-4. *Am J Physiol - Endocrinol Metab* (2021) 320:E989–98. doi: 10.1152/AJPENDO.00465.2020

Conflict of Interest: The authors declare that the research was conducted in the absence of any commercial or financial relationships that could be construed as a potential conflict of interest.

Publisher's Note: All claims expressed in this article are solely those of the authors and do not necessarily represent those of their affiliated organizations, or those of the publisher, the editors and the reviewers. Any product that may be evaluated in this article, or claim that may be made by its manufacturer, is not guaranteed or endorsed by the publisher.

frontiers in Immunology

REVIEW
published: 02 February 2022
doi: 10.3389/fimmu.2022.819163

Folate Receptor Beta for Macrophage Imaging in Rheumatoid Arthritis

*Maarten M. Steinz[1], Aiarpi Ezdoglian[1], Fatemeh Khodadust[1], Carla F. M. Molthoff[2], Madduri Srinivasarao[3], Philip S. Low[3], Gerben J. C. Zwezerijnen[2], Maqsood Yaqub[2], Wissam Beaino[2], Albert D. Windhorst[2], Sander W. Tas[4], Gerrit Jansen[1] and Conny J. van der Laken[1]**

[1] Department of Rheumatology and Clinical Immunology, Amsterdam University Medical Center, VU University Medical Center (VUmc), Amsterdam, Netherlands, [2] Department of Radiology & Nuclear Medicine, Amsterdam University Medical Center, VU, Amsterdam, Netherlands, [3] Department of Chemistry, Purdue University, West Lafayette, IN, United States, [4] Department of Rheumatology and Clinical Immunology, Amsterdam University Medical Center, AMC, Amsterdam, Netherlands

OPEN ACCESS

Edited by:
Marco Erreni,
Humanitas Research Hospital, Italy

Reviewed by:
Venkatesh Chelvam,
Indian Institute of Technology Indore, India
Fengying Sun,
Jilin University, China
Hannes Stockinger,
Medical University of Vienna, Austria

***Correspondence:**
Conny J. van der Laken
j.vanderlaken@amsterdamumc.nl

Specialty section:
This article was submitted to Inflammation, a section of the journal Frontiers in Immunology

Received: 20 November 2021
Accepted: 11 January 2022
Published: 02 February 2022

Citation:
Steinz MM, Ezdoglian A, Khodadust F, Molthoff CFM, Srinivasarao M, Low PS, Zwezerijnen GJC, Yaqub M, Beaino W, Windhorst AD, Tas SW, Jansen G and van der Laken CJ (2022) Folate Receptor Beta for Macrophage Imaging in Rheumatoid Arthritis. Front. Immunol. 13:819163. doi: 10.3389/fimmu.2022.819163

Non-invasive imaging modalities constitute an increasingly important tool in diagnostic and therapy response monitoring of patients with autoimmune diseases, including rheumatoid arthritis (RA). In particular, macrophage imaging with positron emission tomography (PET) using novel radiotracers based on differential expression of plasma membrane proteins and functioning of cellular processes may be suited for this. Over the past decade, selective expression of folate receptor β (FRβ), a glycosylphosphatidylinositol-anchored plasma membrane protein, on myeloid cells has emerged as an attractive target for macrophage imaging by exploiting the high binding affinity of folate-based PET tracers. This work discusses molecular, biochemical and functional properties of FRβ, describes the preclinical development of a folate-PET tracer and the evaluation of this tracer in a translational model of arthritis for diagnostics and therapy-response monitoring, and finally the first clinical application of the folate-PET tracer in RA patients with active disease. Consequently, folate-based PET tracers hold great promise for macrophage imaging in a variety of (chronic) inflammatory (autoimmune) diseases beyond RA.

Keywords: PET imaging, folate receptor beta, rheumatoid arthritis, macrophage, antigen-induced arthritis

1 THE ROLE OF FOLATE RECEPTOR BETA FOR PET IMAGING IN ARTHRITIS

1.1 Synovial Macrophages as Biomarkers for RA Disease Activity Assessment

Rheumatoid arthritis (RA) is an autoimmune disease of the joints characterized by the infiltration of various immune cells in the synovium amongst which macrophages play an important role (1, 2). Macrophages impact on other immune cells and inflammatory processes *via* the release of proinflammatory cytokines (e.g. TNFα) and chemokines, which may promote activation of

T cells and other immune cells, trigger endothelial cell activation and (pathological) angiogenesis, and induce osteoclast activation (3, 4). Synovial tissue analysis has pointed out that the (activated) synovial macrophage is a key biomarker for disease activity assessment from the early disease onwards and for monitoring of therapeutic efficacy at later stages of the disease (5, 6). The basic synovial joint architecture of the healthy joint is comprised of a double layered structure (synovial lining) which holds tissue resident macrophages, and underneath a vascularized sub-lining layer of connective tissue (7). In the early stages of RA, infiltration of immune cells is observed in combination with activation of resident macrophages present in the synovial lining layer (2). Established RA is marked by progressive macrophage infiltration in the synovium (~10-20 layers) (8). In fact, macrophages represent one of the most prominent cell types present in the synovium during early stage and also established RA (2, 9, 10), being responsive to treatment (6), and thus underscoring their exploitation as a biomarker for the assessment of RA disease through positron emission tomography (PET) imaging.

The importance of macrophages as key player in the pathogenesis of RA has been explored in both preclinical and clinical studies. It has for example been shown in animal models of arthritis that depletion of macrophages significantly decreases the severity of the disease (11, 12). Also, in RA patients, macrophage infiltration in the RA synovium has been found to significantly correlate with disease severity (e.g. with changes in disease activity score (DAS) and composite change index) (5, 6, 13). In addition, recent in depth cellular and molecular analyses of RA synovial tissues revealed that RA patients could be stratified in 3 pathology groups based on the presence of specific immune cell types (14–16). These 3 pathotypes were designated *diffuse-myeloid* (characterized by predominantly myeloid cell infiltration, notably macrophages), *lympho-myeloid* (predominantly B-cell infiltration), and *pauci-immune* (low immune cell infiltration) (14). Remarkably, a higher diffuse-myeloid gene expression profile, thus characterized by macrophage infiltration, was associated with a higher DAS 28-ESR and a larger DAS 28-ESR reduction after treatment with disease modifying anti-rheumatic drugs (DMARDs) (14), again underscoring the importance of the synovial macrophage as biomarker for RA disease activity.

Although it is well recognized that macrophages play an important role in the pathology of RA, they can exert both pro- and anti-inflammatory roles associated with their polarization (17). The synovial cytokine milieu, in particular granulocyte-macrophage colony-stimulating factor (GM-CSF) and macrophage colony-stimulating-factor (M-CSF), constitutes the driving force in skewing macrophages to the M1-type pro-inflammatory phenotype and the M2-type anti-inflammatory macrophage, respectively (9, 18–20). M1 and M2 represent the extremes of macrophage polarization and have been characterized based on differences in their transcriptome, secretome and proteome profiles (19–22). Several (membrane) marker proteins are commonly used to classify M1 (e.g. CD80, TNFα, iNOS) and M2 (e.g. CD163, IL-10, Arginase) macrophage subpopulations, and have been associated to an inflammatory or remission state of RA. For example, macrophage subpopulations were found associated with RA disease remission such as synovial tissue macrophages that are MerTK positive (MerTKpos), lymphatic vessel endothelial hyaluronan receptor 1 positive (LYVE1pos) and have a high expression of Folate Receptor (FR) beta (FRβ-high) (23). In the context of this review, FRβ expression has long been recognized on macrophages that are triggered by inflammatory stimuli and on activated macrophages in inflamed joints of RA patients (24, 25). In ex-vivo M-CSF skewed monocyte-derived macrophages, FRβ is differentially expressed on M2-type macrophages (26–28). However, in inflamed RA synovium, these FRβ-expressing M2-macrophages can produce pro-inflammatory cytokines when exposed to either pro-inflammatory stimuli (i.e. lipo-polysaccharide (LPS) + interferon-γ (IFNγ) (19) or an RA synovial microenvironment with anti-citrullinated protein antibodies or complex IgGs (29, 30). Together, FRβ is a bona fide marker on synovial macrophage subpopulations, even though its exact role in function in either pro- and anti-inflammatory macrophages needs to be defined in greater detail. FRβ expression on (activated) macrophages in RA has initiated research aimed at therapeutic targeting as well disease monitoring with imaging modalities (31, 32), which will be discussed in the next sections.

1.2 Folate Receptors: Function, Structure and Targeting

Human FRs are high affinity binding proteins for folates (folic acid and reduced folate cofactors) which are essential vitamins necessary for single carbon transfer reactions in amino acid biosynthesis (e.g. conversion of homocysteine into methionine) and for *de novo* purine and thymidylate biosynthesis (33–35). There are four types of FRs: FR-alpha (FRα), FR-beta (FRβ), FR-gamma (FRγ) and FR-delta (FRδ) (**Figure 1A**). Of those, FRα, FRβ and FRδ are glycosylphosphatidylinositol (GPI) membrane anchored, whereas FRγ is a secreted form (mainly from hematopoietic cells) because of a lack of an efficient signal for GPI modification (36–39). FRα is expressed on normal epithelial cells (e.g. kidney, spleen and lung tissue) (40) and tumor tissues like ovarian, breast (41), pancreatic and lung carcinomas (42, 43). FRβ is selectively expressed on cells of the myeloid lineage (44, 45) and is upregulated on activated macrophages in active RA disease (24, 25) wherein its expression is regulated by PU.1 transcription factor (46). The FRδ gene was originally identified being highly homologous mouse folate binding protein 3 (Folbp3) (47), but does not harbor folate binding capacity (48). FRδ (and splice variants thereof) is expressed on regulatory T cells and has a proposed function in immune regulation (49).

Macrophage FRβ is a valid target for folate-based imaging (**Figure 1B**), along with other FRβ targeting approaches (**Figure 1C**) by (drug-conjugated) monoclonal antibodies, folate-conjugated drugs, CAR T cells and folate antagonists (25, 31, 34, 50, 51). FRβ contains a binding pocket for folic acid where binding of folic acid is facilitated by a conformational change in two regions of the receptor, in particular the region

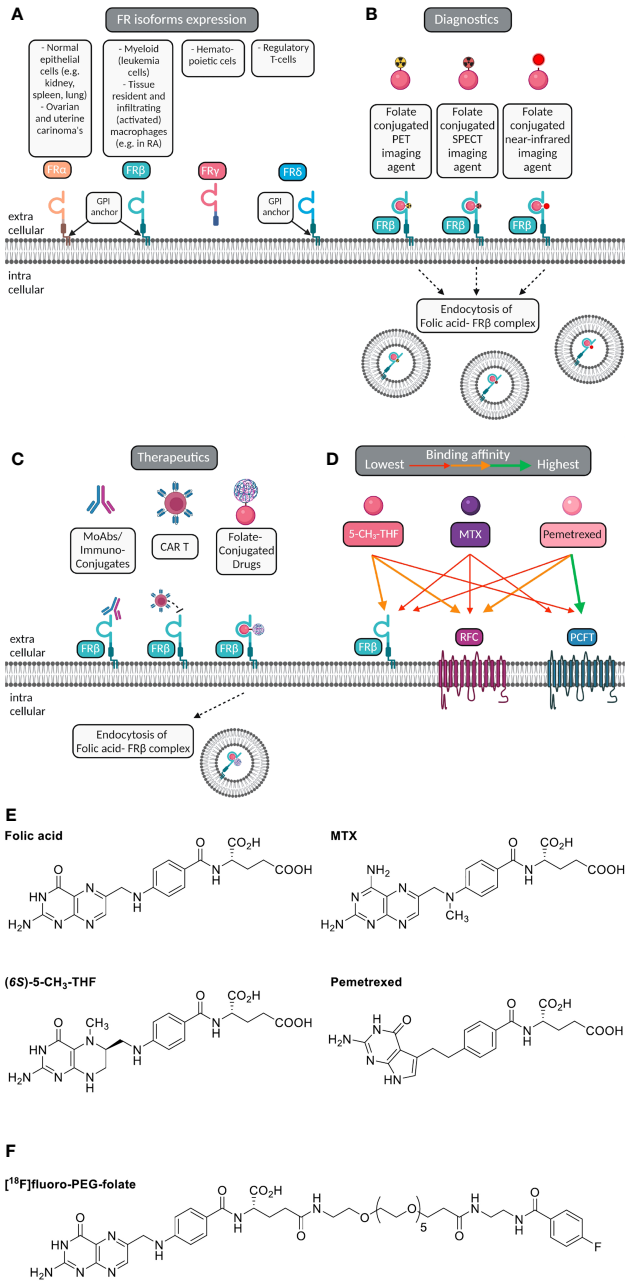

FIGURE 1 | Macrophage FRβ for folate-based imaging and therapeutic targeting. **(A)** Folate receptor isoforms FRα, FRβ, FRγ and FRδ, their GPI-membrane anchoring (except FRγ), and cell/tissue expression. **(B)** Selective expression of FRβ (cyanin), a glycosylphosphatidylinositol-anchored plasma membrane protein, on myeloid cells (e.g. macrophages) constitutes a suitable target for imaging of inflammatory disease, including RA. Folate (pink ellipse) is coupled to a radioactive isotope (for PET or SPECT) or near infrared fluorescent dye (for optical imaging). Following high affinity binding to FRβ, these imaging agents may stay membrane bound or potentially internalized *via* endocytosis. **(C)** Macrophage FRβ can also be subject to therapeutic targeting to ameliorate inflammation. This can be achieved by (drug-conjugated) monoclonal antibodies, folate-conjugated drugs, CAR-T cells targeted towards FRβ and with small molecule folate antagonists. **(D)** Folic acid, the primary circulating plasma folate form 5-CH_3-THF, and folate antagonist therapeutic drugs MTX or PMX can bind to FRβ or one of the two other folate carriers expressed on macrophages, i.e. RFC/SLC19A1 and PCFT/SLC46A1. The binding affinity of 5-CH_3-THF, MTX and PMX varies for FRβ, RFC and PCFT, respectively, as indicated by colored arrows. For example, 5-CH_3-THF binding affinity to FRβ > MTX and PMX. MTX transport is facilitated by all three folate carriers, but with slightly higher affinities for RFC and PCFT. PMX displays the highest affinity to PCFT, moderate affinity to RFC and the lowest affinity for FRβ. **(E)** Chemical structures of folic acid, (*6S*)-5CH_3-THF, methotrexate (MTX) and pemetrexed (PMX) illustrating the shared pterin moiety which is captured in the folic acid binding cleft of FRβ. **(F)** Chemical structure of [^{18}F]fluoro-PEG-Folate, the folate PET imaging agent for high-affinity binding to FRβ on macrophages and utilization for diagnostics and therapy response monitoring.

connecting beta strand 1 and 2 and the region of alpha helix 1 (52). Like folic acid, folate antagonist therapeutic drugs such as methotrexate (MTX, the anchor drug in RA treatment) (53, 54) and pemetrexed (PMX) (55) share a pterin moiety in their structure which can bind in the hydrophobic region of the binding pocket of FRβ (52) (**Figure 1D**). FRα and FRβ share high affinity binding of folic acid with Kd's in the low nanomolar range (0.1-1 nM) (36). Structure activity testing disclosed anti-folate structures with FRα and FRβ affinities close to folic acid, 2-3 orders of magnitude lower affinities for MTX than folic acid and intermediate affinities for PMX (25, 56).

In order to elicit therapeutic activity against macrophages, a folate antagonist should compete with FRβ binding of the primary circulating reduced folate in plasma, 5-methyltetrahydrofolate (5-CH_3-THF) (25). Also FRβ functions as one of three transport proteins for folates and antifolates, the two others are the reduced folate carrier (RFC, SLC19A1) and proton-coupled folate transporter (PCFT, SLC46A1) (57) (**Figure 1E**). The expression of these 3 folate transporters does vary between polarized macrophages; in *ex vivo* skewed monocytes to M1-type macrophages by GM-CSF and M2-type macrophage by M-CSF, RFC gene expression is differentially higher in M1-type macrophages, whereas FRβ and PCFT expression are markedly higher in M2-type macrophages (27, 28). Given that FRα/β also retain a high affinity binding profile for folate conjugates, this allowed the design of folate conjugates which could serve as folate based imaging agents like [^{18}F]fluoro-PEG-folate (**Figure 1F**) (58–60).

1.3 PET Imaging of Macrophages

Over the past decade, non-invasive molecular imaging techniques that assess RA disease activity using macrophage PET imaging have been developed (31, 58, 61–63). Disease activity assessment of RA is currently performed clinically through calculation of the DAS, which takes into account the number of swollen and tender joints, the erythrocyte sedimentation rate (ESR) and the visual analogue score (VAS) (1). However, the DAS score contains subjective elements and is limited to the sensitivity and specificity of clinical assessment of tenderness and swelling of the joints (64). To make further steps in improvement of diagnostics and monitoring of disease activity, objective tools such as macrophage (whole body) PET imaging may offer new opportunities for early diagnosis and early determination of the treatment outcome. Early diagnosis (even before clinical diagnosis) and effective, personalized treatment may ultimately result in prevention of (progression of) joint damage (1).

Initially, imaging studies were performed for FRα-expressing tumors with folate-SPECT tracer [^{99}Tc]EC20 (48). By serendipity, imaging of a cancer patient who had an arthritic comorbidity showed a positive scan of the inflamed knee joint due to infiltration of FRβ-positive macrophages (65). This was the start of exploration of arthritis imaging by FRβ targeting. The easy accessibility as GPI-linked plasma membrane protein and its myeloid cell specific expression constitutes FRβ a suitable target for macrophage imaging. [^{99}Tc]EC20 proved its suitability in visualizing FRβ-positive macrophages in inflamed joints of arthritic rats (66) and RA patients (67). These findings encouraged the development of folate-based PET tracer which would provide a higher sensitivity and spatial resolution compared to scintigraphy.

The original synthesis of folate-based PET tracers relied on chemistry linking folic acid with an spacer moiety (polyethylene glycol) as a precursor molecule to which the PET isotope is coupled (68). This approach was adopted in studies by Gent et al. (58) and Kularatne et al. (59) to synthesize [^{18}F]fluoro-PEG-folate (**Figure 1F**). Assessment of FR binding affinity for fluoro-PEG-folate in a [^{3}H]folic acid competition assay showed that the unlabeled tracer had a 2-fold lower affinity than for folic acid, but a 2.5-fold higher affinity than for the circulating plasma folate 5CH_3-THF (58). After fulfilling this important criterium of high affinity binding and outcompeting binding of circulating plasma 5-CH_3-THF, next [^{18}F]fluoro-PEG-folate was examined further for *in vivo* PET–based monitoring of disease activity and therapy response in a preclinical model of RA (see section 2).

2 FOLATE RECEPTOR β-TARGETED IMAGING IN THE ANTIGEN-INDUCED ARTHRITIS MODEL

2.1 The Antigen-Induced Arthritis Model

In the preclinical assessment of FRβ as a macrophage target for PET imaging of arthritis, Chandrupatla et al. established a pre-clinical rat model of arthritis with sustained macrophage infiltration in the joints (69). In this model arthritis is induced through immunization with methylated bovine serum albumin (mBSA) in complete Freund's adjuvant (CFA) and custom Bordetella pertussis antigen (CBP) following one or repeated intra-articular (i.a.) injections with mBSA in one knee of the rat (leaving the contralateral knee as control), after which synovial inflammation accompanied by an increase in knee thickness occurs over 3 days (**Figures 2A, B**) (69). This antigen-induced arthritis model was selected for PET imaging of molecular markers in arthritis and therapeutic evaluations due to several reasons; (i) the model is mono-articular, and hence the contra-lateral and other joints can serve as control, (ii) the model is relatively mild and is not accompanied by severe bone destruction or polyarticular involvement, (iii) the model is also reminiscent of human RA featuring macrophage infiltration (71, 72) (**Figure 2C**) and moderate systemic inflammation manifested by modest macrophage infiltration in the liver and spleen (70), (iv) macrophage infiltration can be sustained by repeated mBSA injections, which is a good condition for therapeutic monitoring (69), and (v) the larger size of the rat allows injecting more radioactivity and the larger knee size of the rat (compared to a mouse) is advantageous given the spatial resolution of most PET scanners. This model therefore allows for studying if [^{18}F]fluoro-PEG-folate is a suitable tracer for objective macrophage imaging in arthritis affected joints and for longitudinally studying the effect of anti-rheumatic drugs on joint macrophage infiltration (58, 62, 70).

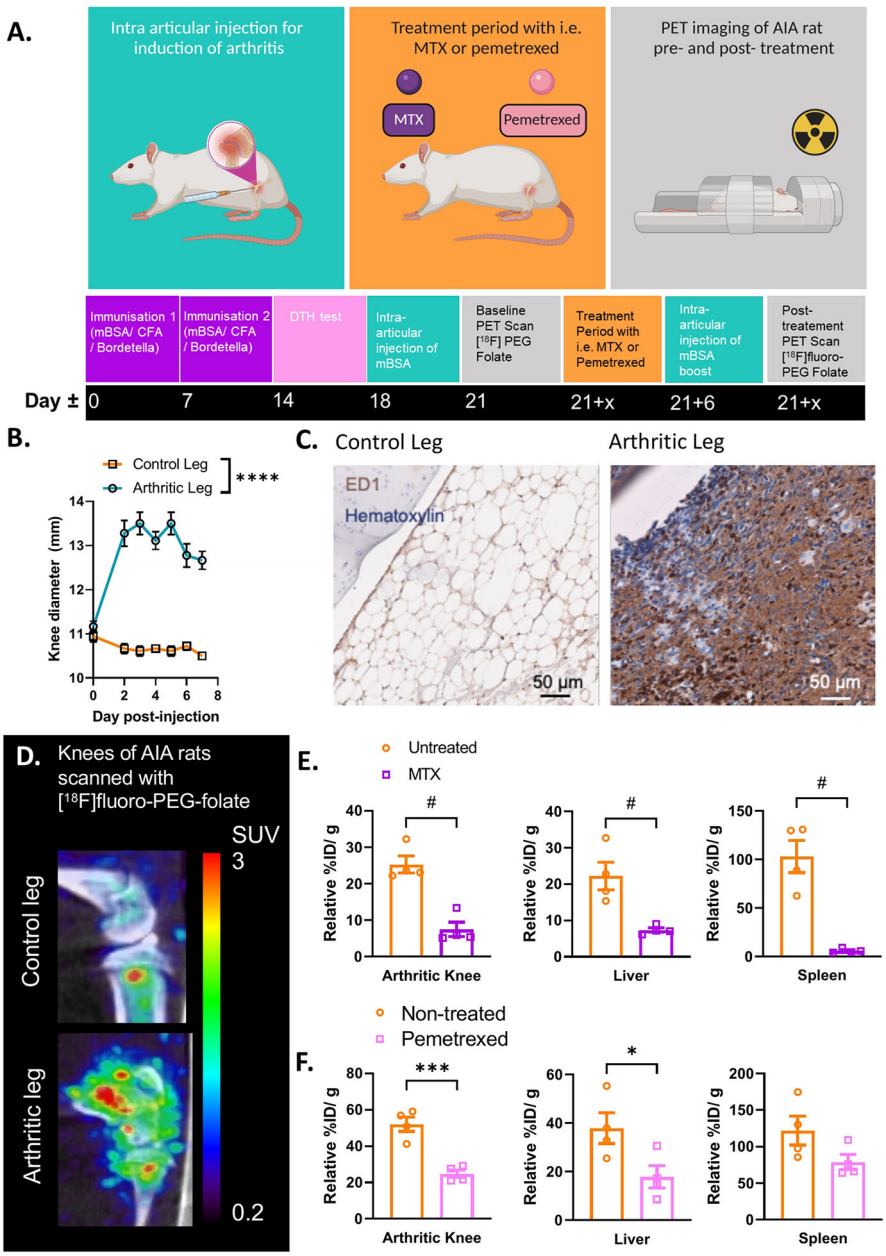

FIGURE 2 | Antigen induced arthritis (AIA) rat model used in preclinical studies for PET imaging with [^{18}F]fluoro-PEG-folate tracer. **(A)** Schematic representation of the preclinical set up of the experiment: starting at day 0 and day 7 with an immunization of the rat with an emulsion of Complete Freund's Adjuvant, Custom Bordetella Pertussis and methylated BSA (mBSA). Immunization status is checked at day 14 with a delayed type hypersensitivity (DTH) test through injection of mBSA in the ear. Around day 18, an intra-articular (i.a.) injection is given in one of the knees with mBSA. During the whole duration of the experiment or after i.a. injection, the rat can be treated with FRβ-targeted folate antagonist such as MTX or PMX. A baseline (/pre-treatment) PET scan and post-treatment PET scan with [^{18}F]fluoro-PEG-folate have been used to monitor the effect of antifolate therapy. **(B)** After 1-3 days post i.a. injection a significant swelling of the knee diameter is seen in the arthritis-affected leg (****$p < 0.0001$, two-way ANOVA, N = 9 rats/group, paired samples). **(C)** Representative image of macrophage infiltration in the synovium of the arthritic leg as detected by immunohistochemical (IHC) DAB-staining of rat knee tissue with ED-1 antibody (HM3029, Hycult Biotech) (scale bar = 50µm). **(D)** Illustrative image of increased [^{18}F]fluoro-PEG-folate uptake in the arthritic knee (lower panel, arthritic leg) vs. the non-arthritic, contra-lateral knee (upper panel, control leg) of an AIA rat. Both images are scaled to the same standard uptake value based on the injected dose (in MBq/ml) of the tracer and the body weight of the animal (in g.). **(E)** Biodistribution of [^{18}F]fluoro-PEG-folate in the arthritic knee, liver and spleen of non-treated and MTX-treated AIA rats. Data were corrected for blood %ID/g. **(F)** Biodistribution of [^{18}F]fluoro-PEG-folate in the arthritic knee, liver and spleen of non-treated and PMX-treated AIA rats. Data were corrected for blood %ID/g. Statistics for images E-F were performed in Graph-Pad Prism version 9, $^{\#}p < 0.01$, Mann-Whitney U test for non-parametric divided data, *$p < 0.05$, ***$p < 0.001$, unpaired T-TEST for parametric divided data, N = 4 rats/group. All results described in Figure 2 were derived (and reanalyzed were indicated) from own research (58, 62, 69, 70).

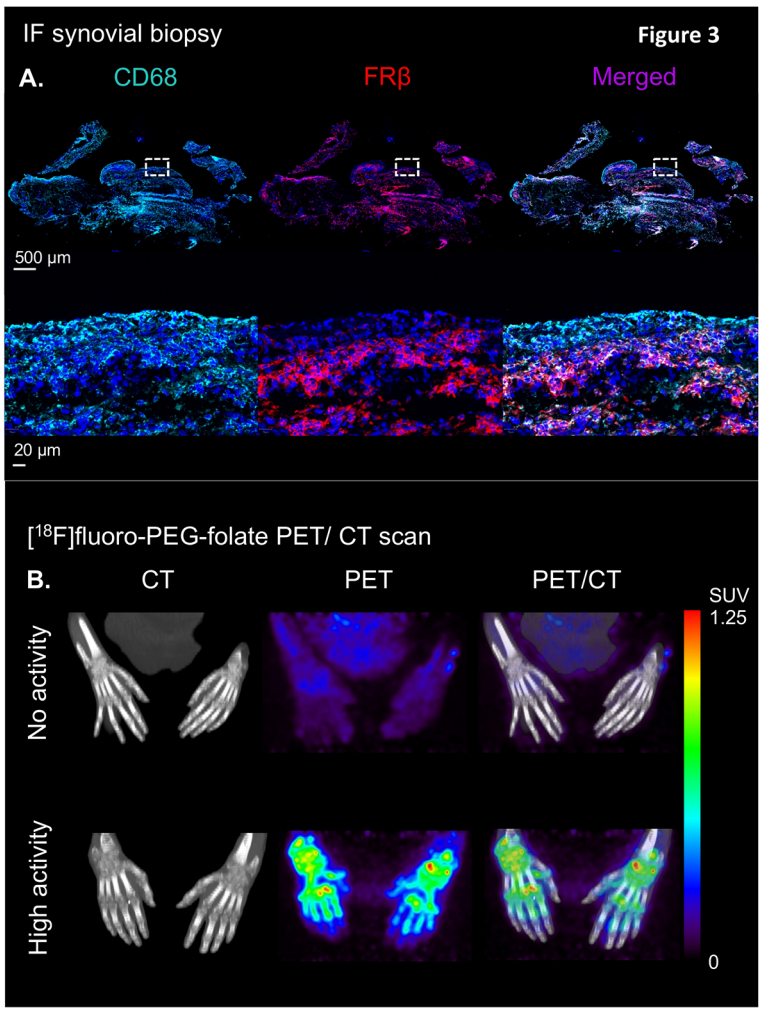

FIGURE 3 | Illustration of the clinical validation of the [^{18}F]fluoro-PEG-folate tracer in patients with rheumatoid arthritis. **(A)** *Upper panel* showing an illustrative example of immunofluorescent staining of CD68 (left), FRβ (middle) and CD68 + FRβ merged staining in a synovial knee biopsy of an RA patient with active disease. *Lower panel* depicts marked expression of CD68- and FRβ-positive macrophages in both synovial lining and sublining (see the zoomed view of the dashed marked box in the upper panel of the RA synovial tissue. **(B)** Representative example of high specific uptake of [^{18}F]fluoro-PEG-folate in the hand joints of a patient with high RA disease activity vs. marginal uptake in the hand joints of a RA patient with low disease activity in the hands. Both images are scaled to the same standard uptake value based on the injected dose (in MBq/ml) of the tracer and the body weight of the patient (in kg.). All representative images of Figure 3 were derived from own research (25, 61).

2.2 FRβ-Targeted Macrophage PET Imaging in Arthritic Rats

Initially, imaging for FRβ in preclinical arthritis models and RA patients was performed with the SPECT tracer [^{99m}Tc]EC20 (66, 67). It has only been up until recently that the [^{18}F]-PEG-folate tracer has been tested pre-clinically in a model of arthritis (i.e. the AIA model). Gent et al. showed that in arthritic rats scanned with [^{18}F]fluoro-PEG-folate had a ~50% increased tracer uptake in the arthritic knee compared to the contralateral uninflamed knee joint (58) (see illustrative image **Figure 2D**). Gent et al. also showed that the [^{18}F]fluoro-PEG-folate tracer specifically targeted folate receptors since blocking of this receptor with unlabeled glucosamine-folate significantly abolished [^{18}F]fluoro-PEG-folate uptake in the arthritic knees (58).

Treatment of arthritic rats with different dosages of the folate antagonist MTX significantly reduced (~2-4 fold) tracer uptake in the arthritic knee compared to the arthritic knee of untreated rats (62, 70) (**Figure 2E**). Consistently, histological analysis demonstrated that macrophage infiltration was also ~2-4 fold reduced in the arthritic knee as well as in the liver and spleen following MTX therapy (70). Involvement of liver and spleen point to systemic inflammation in the arthritic rat model, which is suppressed by MTX treatment (70). This is in line with the systemic character of RA in patients (73). Similar results were

obtained after treatment of arthritic rats with the second-generation folate antagonist pemetrexed (PMX)/Alimta (74). [^{18}F]fluoro-PEG-folate uptake in the arthritic knee, liver and spleen of PMX treated rats was reduced ~2.2; 3.2 and 1.6-fold, respectively compared to untreated rats (**Figure 2F**). PMX was originally developed to overcome MTX resistance in cancer chemotherapy (55) by harboring more efficient transport properties *via* RFC, PCFT and FR than MTX (**Figure 1C**). PMX has shown anti-arthritic effects by suppressing cytokine production in activated T cells of RA patients (75), experimental arthritis models (74) and polarized macrophages *in vitro* (28). Together, these preclinical studies demonstrate the suitability and feasibility of macrophage PET with [^{18}F]fluoro-PEG-folate for arthritis disease monitoring and therapy response monitoring thereby supporting clinical studies in RA. Preclinical animal studies also revealed that [^{18}F]fluoro-PEG-folate may provide improved arthritis imaging compared to an established macrophage translocator protein (TSPO) tracer *(R)*-[^{11}C]PK11195 (58) as a 2.3-fold higher arthritic knee over blood ratios was observed for [^{18}F]fluoro-PEG-folate than for (*R*)-[^{11}C]PK11195.

3 CLINICAL EVALUATION OF FOLATE PET IMAGING IN RA PATIENTS

3.1 First Clinical Study With [^{18}F]fluoro-PEG-Folate in RA Patients

Immuno-histochemical and immuno-fluorescent analysis of FRβ expression in RA synovial biopsies showed marked expression of double CD68 and FRβ-positive macrophages in both lining and sublining of RA synovial tissue (representative example shown in **Figure 3A**) (25), thus encouraging further clinical evaluation of the [^{18}F]fluoro-PEG-folate PET tracer. The first clinical evaluation of the [^{18}F]fluoro-PEG-folate PET tracer for arthritis was performed by Verweij et al. in RA patients (61). This study showed uptake of the [^{18}F]fluoro PEG folate PET tracer in clinically active joints (**Figure 3B**). Although the absolute tracer uptake of [^{18}F]fluoro-PEG-folate in arthritic joints was ~ 2.5-fold lower than for the previously investigated macrophage tracer (*R*)-[^{11}C]-PK11195, the target-to-background ratios of [^{18}F]fluoro-PEG-folate PET-CT were significantly higher (3.5 ± 2.2 versus 1.7 ± 0.6; $p<0.02$; n=6 patients) (61). This was a relevant improvement regarding clinical application of macrophage PET imaging in RA, since PK11195 (first generation TSPO) imaging in RA is limited by relatively high background uptake in bone marrow and peri-articular tissues (e.g. muscle) (76). As a consequence, more subtle arthritis activity can easily be missed, which is particularly relevant for early disease assessment and highly sensitive monitoring of therapeutic efficacy. Both clinically and sub-clinically inflamed joints were imaged by folate PET-CT with lower false positive and false negative findings (as compared to clinical findings) than PK11195 PET-CT (61). This holds promise for [^{18}F]fluoro-PEG-folate PET-CT in terms of potential predictive value in clinical RA diagnosis and development of relapse in established disease, since previous studies with PK11195 PET-CT already demonstrated predictive value for these clinical applications (76, 77), which thus may be further improved using [^{18}F]fluoro-PEG-folate whole body PET-CT. Our preliminary data also point at the potential [^{18}F]fluoro-PEG-folate PET-CT to monitor treatment efficacy of anti-rheumatic drugs including of anti-folates (70). [^{18}F]fluoro-PEG-folate binding affinity towards FRβ outweighs methotrexate by at least 2–3 orders of magnitude (26, 58). If, additionally, a safe time window of 7 days is applied between last methotrexate administration and [^{18}F]fluoro-PEG-folate, no blockade of [^{18}F]fluoro-PEG-folate binding in arthritic joints of RA patients by anti-folates (61).

3.2 Future Perspectives

Given the fact that macrophage PET imaging with FRβ has shown clinical feasibility in RA patients, future challenges will be to use folate PET tracers for detection of disease activity in early stage RA and monitoring/prediction of the therapy response of targeted synthetic or biological DMARDs in joints and other sides affected by systemic inflammation. Furthermore, many other inflammatory diseases with macrophage involvement, e.g. idiopathic pulmonary fibrosis, systemic lupus erythematosus, scleroderma, psoriasis, ulcerative colitis, Crohn's disease (78, 79), giant cell arteritis (80), cardiovascular diseases (81, 82) and tumor associated macrophages in oncology (43) may benefit from folate PET imaging to detect and monitor disease activity. Recently, also folate PET imaging of lung macrophages in COVID-19 was advocated to identify patients at risk of a severe or even lethal disease (83). Steps forward in the folate-linker chemistry also allow for more rapid synthesis of alternative folate tracers from precursor molecules, e.g. [^{18}F]folate-PEG-NOTA-Al (84), which are promising but warrant further (pre)clinical evaluation. Beyond PET tracers, there is also increasing interest in the development of folate near- infrared/optical imaging agents for FRβ targeting in oncology and inflammatory diseases (85, 86). Altogether, FRβ remains a reputable target for continued research and (pre)clinical testing of imaging and therapeutic agents in a wide range of pathological conditions.

AUTHOR CONTRIBUTIONS

MS, AE, GJ, and CL: conceptual design, drafting of the article, critical scientific revision and approval of final version. MS: design and scientific translation of the reviewed literature to all figures. MS, FK, CM, PL, GZ, MY, WB, AW, ST, GJ and CL: critical revision and approval of the final version. All authors contributed to the article and approved the submitted version.

FUNDING

The work of this review was supported in part by grant from the Center for Translationational Molecular Medicine (CTMM TRACER), the Dutch Rheumatism Fund (ReumaNederland,

NRF 09-01-404), Cancer Center Amsterdam, and EU-Marie Curie ARCAID program.

ACKNOWLEDGMENTS

The authors greatly appreciate the technical assistance of Elise Mantel, Maxime Schreurs, Mariska Verlaan, Yik Kan, Martien Mooijer, Rolf van Kooii and Esther Kooijman at the laboratories of the Amsterdam University Medical Center and Nuclear Medicine Laboratories. Furthermore, we would like to thank Michiel Stork and René Raeven at Intravacc (Bilthoven) for kindly providing CBP for the AIA animal model, and Guus van Dongen, Daniëlle Vugts and Marc Huisman for their advice regarding the (AIA) animal PET experiments. Illustrations were created as original figures specific for this review by using BioRender.com.

REFERENCES

1. Smolen JS, Aletaha D, Barton A, Burmester GR, Emery P, Firestein GS, et al. Rheumatoid Arthritis. *Nat Rev Dis Primers* (2018) 4:18001. doi: 10.1038/nrdp.2018.1
2. Boutet MA, Courties G, Nerviani A, Le Goff B, Apparailly F, Pitzalis C, et al. Novel Insights Into Macrophage Diversity in Rheumatoid Arthritis Synovium. *Autoimmun Rev* (2021) 20(3):102758. doi: 10.1016/j.autrev.2021.102758
3. Brennan FM, McInnes IB. Evidence That Cytokines Play a Role in Rheumatoid Arthritis. *J Clin Invest* (2008) 118(11):3537–45. doi: 10.1172/JCI36389
4. McInnes IB, Schett G. Cytokines in the Pathogenesis of Rheumatoid Arthritis. *Nat Rev Immunol* (2007) 7(6):429–42. doi: 10.1038/nri2094
5. Jahangier ZN, Jacobs JW, Kraan MC, Wenting MJ, Smeets TJ, Bijlsma JW, et al. Pretreatment Macrophage Infiltration of the Synovium Predicts the Clinical Effect of Both Radiation Synovectomy and Intra-Articular Glucocorticoids. *Ann Rheumatic Dis* (2006) 65(10):1286–92. doi: 10.1136/ard.2005.042333
6. Haringman JJ, Gerlag DM, Zwinderman AH, Smeets TJ, Kraan MC, Baeten D, et al. Synovial Tissue Macrophages: A Sensitive Biomarker for Response to Treatment in Patients With Rheumatoid Arthritis. *Ann Rheumatic Dis* (2005) 64(6):834–8. doi: 10.1136/ard.2004.029751
7. Smith MD. The Normal Synovium. *Open Rheumatol J* (2011) 5:100–6. doi: 10.2174/1874312901105010100
8. Orr C, Vieira-Sousa E, Boyle DL, Buch MH, Buckley CD, Canete JD, et al. Synovial Tissue Research: A State-of-the-Art Review. *Nat Rev Rheumatol* (2017) 13(8):463–75. doi: 10.1038/nrrheum.2017.115
9. Hamilton JA, Tak PP. The Dynamics of Macrophage Lineage Populations in Inflammatory and Autoimmune Diseases. *Arthritis Rheum* (2009) 60(5):1210–21. doi: 10.1002/art.24505
10. Kennedy A, Fearon U, Veale DJ, Godson C. Macrophages in Synovial Inflammation. *Front Immunol* (2011) 2:52. doi: 10.3389/fimmu.2011.00052
11. Zhang Q, Yuan R, Li C, Wei W, Shen W, Cui Y, et al. Macrophage Depletion With Clodronate-Containing Liposomes Affects the Incidence and Development of Rheumatoid Arthritis. *Z Rheumatol* (2019) 78(10):996–1003. doi: 10.1007/s00393-018-0563-x
12. Li J, Hsu HC, Yang P, Wu Q, Li H, Edgington LE, et al. Treatment of Arthritis by Macrophage Depletion and Immunomodulation: Testing an Apoptosis-Mediated Therapy in a Humanized Death Receptor Mouse Model. *Arthritis Rheum* (2012) 64(4):1098–109. doi: 10.1002/art.33423
13. Bresnihan B, Pontifex E, Thurlings RM, Vinkenoog M, El-Gabalawy H, Fearon U, et al. Synovial Tissue Sublining CD68 Expression Is a Biomarker of Therapeutic Response in Rheumatoid Arthritis Clinical Trials: Consistency Across Centers. *J Rheumatol* (2009) 36(8):1800–2. doi: 10.3899/jrheum.090348
14. Humby F, Lewis M, Ramamoorthi N, Hackney JA, Barnes MR, Bombardieri M, et al. Synovial Cellular and Molecular Signatures Stratify Clinical Response to csDMARD Therapy and Predict Radiographic Progression in Early Rheumatoid Arthritis Patients. *Ann Rheumatic Dis* (2019) 78(6):761–72. doi: 10.1136/annrheumdis-2018-214539
15. Pitzalis C, Kelly S, Humby F. New Learnings on the Pathophysiology of RA From Synovial Biopsies. *Curr Opin Rheumatol* (2013) 25(3):334–44. doi: 10.1097/BOR.0b013e32835fd8eb
16. Dennis G Jr, Holweg CT, Kummerfeld SK, Choy DF, Setiadi AF, Hackney JA, et al. Synovial Phenotypes in Rheumatoid Arthritis Correlate With Response to Biologic Therapeutics. *Arthritis Res Ther* (2014) 16(2):R90. doi: 10.1186/ar4555
17. Ross EA, Devitt A, Johnson JR. Macrophages: The Good, the Bad, and the Gluttony. *Front Immunol* (2021) 12:708186. doi: 10.3389/fimmu.2021.708186
18. Wang N, Liang H, Zen K. Molecular Mechanisms That Influence the Macrophage M1-M2 Polarization Balance. *Front Immunol* (2014) 5:614. doi: 10.3389/fimmu.2014.00614
19. Ohradanova-Repic A, Machacek C, Charvet C, Lager F, Le Roux D, Platzer R, et al. Extracellular Purine Metabolism Is the Switchboard of Immunosuppressive Macrophages and a Novel Target to Treat Diseases With Macrophage Imbalances. *Front Immunol* (2018) 9:852. doi: 10.3389/fimmu.2018.00852
20. Fuentelsaz-Romero S, Cuervo A, Estrada-Capetillo L, Celis R, Garcia-Campos R, Ramirez J, et al. GM-CSF Expression and Macrophage Polarization in Joints of Undifferentiated Arthritis Patients Evolving to Rheumatoid Arthritis or Psoriatic Arthritis. *Front Immunol* (2020) 11:613975. doi: 10.3389/fimmu.2020.613975
21. Smiljanovic B, Grutzkau A, Sorensen T, Grun JR, Vogl T, Bonin M, et al. Synovial Tissue Transcriptomes of Long-Standing Rheumatoid Arthritis Are Dominated by Activated Macrophages That Reflect Microbial Stimulation. *Sci Rep* (2020) 10(1):7907. doi: 10.1038/s41598-020-64431-4
22. Navegantes KC, de Souza Gomes R, Pereira PAT, Czaikoski PG, Azevedo CHM, Monteiro MC. Immune Modulation of Some Autoimmune Diseases: The Critical Role of Macrophages and Neutrophils in the Innate and Adaptive Immunity. *J Transl Med* (2017) 15(1):36. doi: 10.1186/s12967-017-1141-8
23. Alivernini S, MacDonald L, Elmesmari A, Finlay S, Tolusso B, Gigante MR, et al. Distinct Synovial Tissue Macrophage Subsets Regulate Inflammation and Remission in Rheumatoid Arthritis. *Nat Med* (2020) 26(8):1295–306. doi: 10.1038/s41591-020-0939-8
24. Xia W, Hilgenbrink AR, Matteson EL, Lockwood MB, Cheng JX, Low PS. A Functional Folate Receptor Is Induced During Macrophage Activation and Can Be Used to Target Drugs to Activated Macrophages. *Blood* (2009) 113(2):438–46. doi: 10.1182/blood-2008-04-150789
25. van der Heijden JW, Oerlemans R, Dijkmans BA, Qi H, van der Laken CJ, Lems WF, et al. Folate Receptor Beta as a Potential Delivery Route for Novel Folate Antagonists to Macrophages in the Synovial Tissue of Rheumatoid Arthritis Patients. *Arthritis Rheum* (2009) 60(1):12–21. doi: 10.1002/art.24219
26. Puig-Kroger A, Sierra-Filardi E, Dominguez-Soto A, Samaniego R, Corcuera MT, Gomez-Aguado F, et al. Folate Receptor Beta Is Expressed by Tumor-Associated Macrophages and Constitutes a Marker for M2 Anti-Inflammatory/Regulatory Macrophages. *Cancer Res* (2009) 69(24):9395–403. doi: 10.1158/0008-5472.CAN-09-2050
27. Municio C, Soler Palacios B, Estrada-Capetillo L, Benguria A, Dopazo A, Garcia-Lorenzo E, et al. Methotrexate Selectively Targets Human Proinflammatory Macrophages Through a Thymidylate Synthase/P53 Axis. *Ann Rheumatic Dis* (2016) 75(12):2157–65. doi: 10.1136/annrheumdis-2015-208736
28. Fuentelsaz-Romero S, Barrio-Alonso C, García Campos R, Torres Torresano M, Muller IB, Triguero-Martínez A, et al. The Macrophage Reprogramming Ability of Antifolates Reveals Soluble CD14 as a Potential Biomarker for Methotrexate Response in Rheumatoid Arthritis. *Front Immunol* (2021) 12(4580). doi: 10.3389/fimmu.2021.776879
29. Vogelpoel LT, Hansen IS, Rispens T, Muller FJ, van Capel TM, Turina MC, et al. Fc Gamma Receptor-TLR Cross-Talk Elicits Pro-Inflammatory Cytokine Production by Human M2 Macrophages. *Nat Commun* (2014) 5:5444. doi: 10.1038/ncomms6444
30. Clavel C, Ceccato L, Anquetil F, Serre G, Sebbag M. Among Human Macrophages Polarised to Different Phenotypes, the M-CSF-Oriented Cells Present the Highest Pro-Inflammatory Response to the Rheumatoid Arthritis-

Specific Immune Complexes Containing ACPA. *Ann Rheumatic Dis* (2016) 75(12):2184–91. doi: 10.1136/annrheumdis-2015-208887
31. Chandrupatla D, Molthoff CFM, Lammertsma AA, van der Laken CJ, Jansen G. The Folate Receptor Beta as a Macrophage-Mediated Imaging and Therapeutic Target in Rheumatoid Arthritis. *Drug Deliv Transl Res* (2019) 9 (1):366–78. doi: 10.1007/s13346-018-0589-2
32. Lu YJ, Wheeler LW2nd, Chu H, Kleindl PJ, Pugh M, You F, et al. Targeting Folate Receptor Beta on Monocytes/Macrophages Renders Rapid Inflammation Resolution Independent of Root Causes. *Cell Rep Med* (2021) 2(10):100422. doi: 10.1016/j.xcrm.2021.100422
33. Ducker GS, Rabinowitz JD. One-Carbon Metabolism in Health and Disease. *Cell Metab* (2017) 25(1):27–42. doi: 10.1016/j.cmet.2016.08.009
34. Frigerio B, Bizzoni C, Jansen G, Leamon CP, Peters GJ, Low PS, et al. Folate Receptors and Transporters: Biological Role and Diagnostic/Therapeutic Targets in Cancer and Other Diseases. *J Exp Clin Cancer Res* (2019) 38 (1):125. doi: 10.1186/s13046-019-1123-1
35. Dekhne AS, Hou Z, Gangjee A, Matherly LH. Therapeutic Targeting of Mitochondrial One-Carbon Metabolism in Cancer. *Mol Cancer Ther* (2020) 19(11):2245–55. doi: 10.1158/1535-7163.MCT-20-0423
36. Elnakat H, Ratnam M. Distribution, Functionality and Gene Regulation of Folate Receptor Isoforms: Implications in Targeted Therapy. *Adv Drug Deliv Rev* (2004) 56(8):1067–84. doi: 10.1016/j.addr.2004.01.001
37. Wu M, Gunning W, Ratnam M. Expression of Folate Receptor Type Alpha in Relation to Cell Type, Malignancy, and Differentiation in Ovary, Uterus, and Cervix. *Cancer Epidemiol Biomarkers Prev* (1999) 8(9):775–82.
38. Shen F, Wu M, Ross JF, Miller D, Ratnam M. Folate Receptor Type Gamma Is Primarily a Secretory Protein Due to Lack of an Efficient Signal for Glycosylphosphatidylinositol Modification: Protein Characterization and Cell Type Specificity. *Biochemistry* (1995) 34(16):5660–5. doi: 10.1021/bi00016a042
39. Holm J, Hansen SI. Characterization of Soluble Folate Receptors (Folate Binding Proteins) in Humans. Biological Roles and Clinical Potentials in Infection and Malignancy. *Biochim Biophys Acta Proteins Proteom* (2020) 1868(10):140466. doi: 10.1016/j.bbapap.2020.140466
40. Parker N, Turk MJ, Westrick E, Lewis JD, Low PS, Leamon CP. Folate Receptor Expression in Carcinomas and Normal Tissues Determined by a Quantitative Radioligand Binding Assay. *Anal Biochem* (2005) 338(2):284–93. doi: 10.1016/j.ab.2004.12.026
41. Crozier JA, Necela BM, Thompson EA, Geiger X, Moreno-Aspitia A, McCullough AE, et al. Increased Expression of Folate Receptor-α (FRA) in Triple-Negative Breast Cancer: A Potential Therapeutic Target. *J Clin Oncol* (2013) 31(15_suppl):1037. doi: 10.1200/jco.2013.31.15_suppl.1037
42. Toffoli G, Cernigoi C, Russo A, Gallo A, Bagnoli M, Boiocchi M. Overexpression of Folate Binding Protein in Ovarian Cancers. *Int J Cancer* (1997) 74(2):193–8. doi: 10.1002/(SICI)1097-0215(19970422)74:2<193::AID-IJC10>3.0.CO;2-F
43. Shen J, Hu Y, Putt KS, Singhal S, Han H, Visscher DW, et al. Assessment of Folate Receptor Alpha and Beta Expression in Selection of Lung and Pancreatic Cancer Patients for Receptor Targeted Therapies. *Oncotarget* (2018) 9(4):4485–95. doi: 10.18632/oncotarget.23321
44. Ross JF, Wang H, Behm FG, Mathew P, Wu M, Booth R, et al. Folate Receptor Type Beta Is a Neutrophilic Lineage Marker and Is Differentially Expressed in Myeloid Leukemia. *Cancer* (1999) 85(2):348–57. doi: 10.1002/(SICI)1097-0142(19990115)85:2<348::AID-CNCR12>3.0.CO;2-4
45. Shen J, Hilgenbrink AR, Xia W, Feng Y, Dimitrov DS, Lockwood MB, et al. Folate Receptor-Beta Constitutes a Marker for Human Proinflammatory Monocytes. *J Leukocyte Biol* (2014) 96(4):563–70. doi: 10.1189/jlb.2AB0713-372R
46. Samaniego R, Dominguez-Soto A, Ratnam M, Matsuyama T, Sanchez-Mateos P, Corbi AL, et al. Folate Receptor Beta (FRbeta) Expression in Tissue-Resident and Tumor-Associated Macrophages Associates With and Depends on the Expression of PU.1. *Cells* (2020) 9(6):1445. doi: 10.3390/cells9061445
47. Spiegelstein O, Eudy JD, Finnell RH. Identification of Two Putative Novel Folate Receptor Genes in Humans and Mouse. *Gene* (2000) 258(1-2):117–25. doi: 10.1016/S0378-1119(00)00418-2
48. Low PS, Kularatne SA. Folate-Targeted Therapeutic and Imaging Agents for Cancer. *Curr Opin Chem Biol* (2009) 13(3):256–62. doi: 10.1016/j.cbpa.2009.03.022
49. Tian Y, Wu G, Xing JC, Tang J, Zhang Y, Huang ZM, et al. A Novel Splice Variant of Folate Receptor 4 Predominantly Expressed in Regulatory T Cells. *BMC Immunol* (2012) 13:30. doi: 10.1186/1471-2172-13-30
50. Rodriguez-Garcia A, Lynn RC, Poussin M, Eiva MA, Shaw LC, O'Connor RS, et al. CAR-T Cell-Mediated Depletion of Immunosuppressive Tumor-Associated Macrophages Promotes Endogenous Antitumor Immunity and Augments Adoptive Immunotherapy. *Nat Commun* (2021) 12(1):877. doi: 10.1038/s41467-021-20893-2
51. Roy AG, Robinson JM, Sharma P, Rodriguez-Garcia A, Poussin MA, Nickerson-Nutter C, et al. Folate Receptor Beta as a Direct and Indirect Target for Antibody-Based Cancer Immunotherapy. *Int J Mol Sci* (2021) 22 (11):5572. doi: 10.3390/ijms22115572
52. Wibowo AS, Singh M, Reeder KM, Carter JJ, Kovach AR, Meng W, et al. Structures of Human Folate Receptors Reveal Biological Trafficking States and Diversity in Folate and Antifolate Recognition. *Proc Natl Acad Sci USA* (2013) 110(38):15180–8. doi: 10.1073/pnas.1308827110
53. Brown PM, Pratt AG, Isaacs JD. Mechanism of Action of Methotrexate in Rheumatoid Arthritis, and the Search for Biomarkers. *Nat Rev Rheumatol* (2016) 12(12):731–42. doi: 10.1038/nrrheum.2016.175
54. Nakashima-Matsushita N, Homma T, Yu S, Matsuda T, Sunahara N, Nakamura T, et al. Selective Expression of Folate Receptor Beta and Its Possible Role in Methotrexate Transport in Synovial Macrophages From Patients With Rheumatoid Arthritis. *Arthritis Rheum* (1999) 42(8):1609–16. doi: 10.1002/1529-0131(199908)42:8<1609::AID-ANR7>3.0.CO;2-L
55. Shih C, Chen VJ, Gossett LS, Gates SB, MacKellar WC, Habeck LL, et al. LY231514, A Pyrrolo[2,3-D]Pyrimidine-Based Antifolate That Inhibits Multiple Folate-Requiring Enzymes. *Cancer Res* (1997) 57(6):1116–23.
56. Westerhof GR, Schornagel JH, Kathmann I, Jackman AL, Rosowsky A, Forsch RA, et al. Carrier- and Receptor-Mediated Transport of Folate Antagonists Targeting Folate-Dependent Enzymes: Correlates of Molecular-Structure and Biological Activity. *Mol Pharmacol* (1995) 48(3):459–71.
57. Zhao R, Matherly LH, Goldman ID. Membrane Transporters and Folate Homeostasis: Intestinal Absorption and Transport Into Systemic Compartments and Tissues. *Expert Rev Mol Med* (2009) 11:e4. doi: 10.1017/S1462399409000969
58. Gent YY, Weijers K, Molthoff CF, Windhorst AD, Huisman MC, Smith DE, et al. Evaluation of the Novel Folate Receptor Ligand [18F]Fluoro-PEG-Folate for Macrophage Targeting in a Rat Model of Arthritis. *Arthritis Res Ther* (2013) 15(2):R37. doi: 10.1186/ar4191
59. Kularatne SA, Belanger MJ, Meng X, Connolly BM, Vanko A, Suresch DL, et al. Comparative Analysis of Folate Derived PET Imaging Agents With [(18)F]-2-Fluoro-2-Deoxy-D-Glucose Using a Rodent Inflammatory Paw Model. *Mol Pharm* (2013) 10(8):3103–11. doi: 10.1021/mp4001684
60. Samaniego R, Palacios BS, Domiguez-Soto A, Vidal C, Salas A, Matsuyama T, et al. Macrophage Uptake and Accumulation of Folates Are Polarization-Dependent *In Vitro* and *In Vivo* and Are Regulated by Activin A. *J Leukocyte Biol* (2014) 95(5):797–808. doi: 10.1189/jlb.0613345
61. Verweij NJF, Yaqub M, Bruijnen STG, Pieplenbosch S, Ter Wee MM, Jansen G, et al. First in Man Study of [(18)F]fluoro-PEG-Folate PET: A Novel Macrophage Imaging Technique to Visualize Rheumatoid Arthritis. *Sci Rep* (2020) 10(1):1047. doi: 10.1038/s41598-020-57841-x
62. Chandrupatla D, Jansen G, Vos R, Verlaan M, Chen Q, Low PS, et al. *In-Vivo* Monitoring of Anti-Folate Therapy in Arthritic Rats Using [(18)F]fluoro-PEG-Folate and Positron Emission Tomography. *Arthritis Res Ther* (2017) 19 (1):114. doi: 10.1186/s13075-017-1325-x
63. van der Krogt JMA, van Binsbergen WH, van der Laken CJ, Tas SW. Novel Positron Emission Tomography Tracers for Imaging of Rheumatoid Arthritis. *Autoimmun Rev* (2021) 20(3):102764. doi: 10.1016/j.autrev.2021.102764
64. van Gestel AM, Prevoo ML, van 't Hof MA, van Rijswijk MH, van de Putte LB, van Riel PL. Development and Validation of the European League Against Rheum Response Criteria for Rheumatoid Arthritis. Comparison With the Preliminary American College of Rheumatology and the World Health Organization/International League Against Rheumatism Criteria. *Arthritis Rheumatism* (1996) 39(1):34–40. doi: 10.1002/art.1780390105
65. Paulos CM, Turk MJ, Breur GJ, Low PS. Folate Receptor-Mediated Targeting of Therapeutic and Imaging Agents to Activated Macrophages in Rheumatoid Arthritis. *Adv Drug Deliv Rev* (2004) 56(8):1205–17. doi: 10.1016/j.addr.2004.01.012

66. Turk MJ, Breur GJ, Widmer WR, Paulos CM, Xu LC, Grote LA, et al. Folate-Targeted Imaging of Activated Macrophages in Rats With Adjuvant-Induced Arthritis. *Arthritis Rheum* (2002) 46(7):1947–55. doi: 10.1002/art.10405
67. Matteson EL, Lowe VJ, Prendergast FG, Crowson CS, Moder KG, Morgenstern DE, et al. Assessment of Disease Activity in Rheumatoid Arthritis Using a Novel Folate Targeted Radiopharmaceutical Folatescan. *Clin Exp Rheumatol* (2009) 27(2):253–9.
68. Srinivasarao M, Galliford CV, Low PS. Principles in the Design of Ligand-Targeted Cancer Therapeutics and Imaging Agents. *Nat Rev Drug Discov* (2015) 14(3):203–19. doi: 10.1038/nrd4519
69. Chandrupatla DM, Weijers K, Gent YY, de Greeuw I, Lammertsma AA, Jansen G, et al. Sustained Macrophage Infiltration Upon Multiple Intra-Articular Injections: An Improved Rat Model of Rheumatoid Arthritis for PET Guided Therapy Evaluation. *BioMed Res Int* (2015) 2015:509295. doi: 10.1155/2015/509295
70. Chandrupatla D, Jansen G, Mantel E, Low PS, Matsuyama T, Musters RP, et al. Imaging and Methotrexate Response Monitoring of Systemic Inflammation in Arthritic Rats Employing the Macrophage PET Tracer [(18)F]Fluoro-PEG-Folate. *Contrast Media Mol Imaging* (2018) 2018:8092781. doi: 10.1155/2018/8092781
71. Dijkstra CD, Dopp EA, Vogels IM, Van Noorden CJ. Macrophages and Dendritic Cells in Antigen-Induced Arthritis. An Immunohistochemical Study Using Cryostat Sections of the Whole Knee Joint of Rat. *Scand J Immunol* (1987) 26(5):513–23. doi: 10.1111/j.1365-3083.1987.tb02285.x
72. Richards PJ, Williams AS, Goodfellow RM, Williams BD. Liposomal Clodronate Eliminates Synovial Macrophages, Reduces Inflammation and Ameliorates Joint Destruction in Antigen-Induced Arthritis. *Rheumatology* (1999) 38(9):818–25. doi: 10.1093/rheumatology/38.9.818
73. Figus FA, Piga M, Azzolin I, McConnell R, Iagnocco A. Rheumatoid Arthritis: Extra-Articular Manifestations and Comorbidities. *Autoimmun Rev* (2021) 20 (4):102776. doi: 10.1016/j.autrev.2021.102776
74. Karatas A, Koca SS, Ozgen M, Dagli AF, Erman F, Sahin N, et al. Pemetrexed Ameliorates Experimental Arthritis in Rats. *Inflammation* (2015) 38(1):9–15. doi: 10.1007/s10753-014-0002-3
75. van der Heijden JW, Assaraf YG, Gerards AH, Oerlemans R, Lems WF, Scheper RJ, et al. Methotrexate Analogues Display Enhanced Inhibition of TNF-Alpha Production in Whole Blood From RA Patients. *Scandinavian J Rheumatol* (2014) 43(1):9–16. doi: 10.3109/03009742.2013.797490
76. Gent YY, Ter Wee MM, Voskuyl AE, den Uyl D, Ahmadi N, Dowling C, et al. Subclinical Synovitis Detected by Macrophage PET, But Not MRI, Is Related to Short-Term Flare of Clinical Disease Activity in Early RA Patients: An Exploratory Study. *Arthritis Res Ther* (2015) 17:266. doi: 10.1186/s13075-015-0770-7
77. Gent YY, Voskuyl AE, Kloet RW, van Schaardenburg D, Hoekstra OS, Dijkmans BA, et al. Macrophage Positron Emission Tomography Imaging as a Biomarker for Preclinical Rheumatoid Arthritis: Findings of a Prospective Pilot Study. *Arthritis Rheum* (2012) 64(1):62–6. doi: 10.1002/art.30655
78. Hu Y, Wang B, Shen J, Low SA, Putt KS, Niessen HWM, et al. Depletion of Activated Macrophages With a Folate Receptor-Beta-Specific Antibody Improves Symptoms in Mouse Models of Rheumatoid Arthritis. *Arthritis Res Ther* (2019) 21(1):143. doi: 10.1186/s13075-019-1912-0
79. Schniering J, Benesova M, Brunner M, Haller S, Cohrs S, Frauenfelder T, et al. (18)F-AzaFol for Detection of Folate Receptor-Beta Positive Macrophages in Experimental Interstitial Lung Disease-A Proof-Of-Concept Study. *Front Immunol* (2019) 10:2724. doi: 10.3389/fimmu.2019.02724
80. Esen I, Jiemy WF, van Sleen Y, van der Geest KSM, Sandovici M, Heeringa P, et al. Functionally Heterogenous Macrophage Subsets in the Pathogenesis of Giant Cell Arteritis: Novel Targets for Disease Monitoring and Treatment. *J Clin Med* (2021) 10(21):4958. doi: 10.3390/jcm10214958
81. Jahandideh A, Uotila S, Stahle M, Virta J, Li XG, Kyto V, et al. Folate Receptor Beta-Targeted PET Imaging of Macrophages in Autoimmune Myocarditis. *J Nucl Med* (2020) 61(11):1643–9. doi: 10.2967/jnumed.119.241356
82. Jager NA, Westra J, van Dam GM, Teteloshvili N, Tio RA, Breek JC, et al. Targeted Folate Receptor Beta Fluorescence Imaging as a Measure of Inflammation to Estimate Vulnerability Within Human Atherosclerotic Carotid Plaque. *J Nucl Med* (2012) 53(8):1222–9. doi: 10.2967/jnumed.111.099671
83. Muller C, Schibli R, Maurer B. Can Nuclear Imaging of Activated Macrophages With Folic Acid-Based Radiotracers Serve as a Prognostic Means to Identify COVID-19 Patients at Risk? *Pharmaceut (Basel)* (2020) 13(9):238. doi: 10.3390/ph13090238
84. Chen Q, Meng X, McQuade P, Rubins D, Lin SA, Zeng Z, et al. Synthesis and Preclinical Evaluation of Folate-NOTA-Al(18)F for PET Imaging of Folate-Receptor-Positive Tumors. *Mol Pharm* (2016) 13(5):1520–7. doi: 10.1021/acs.molpharmaceut.5b00989
85. Kelderhouse LE, Mahalingam S, Low PS. Predicting Response to Therapy for Autoimmune and Inflammatory Diseases Using a Folate Receptor-Targeted Near-Infrared Fluorescent Imaging Agent. *Mol Imaging Biol* (2016) 18 (2):201–8. doi: 10.1007/s11307-015-0876-y
86. Boogerd LSF, Hoogstins CES, Gaarenstroom KN, de Kroon CD, Beltman JJ, Bosse T, et al. Folate Receptor-Alpha Targeted Near-Infrared Fluorescence Imaging in High-Risk Endometrial Cancer Patients: A Tissue Microarray and Clinical Feasibility Study. *Oncotarget* (2018) 9(1):791–801. doi: 10.18632/oncotarget.23155

Conflict of Interest: The authors declare that the research was conducted in the absence of any commercial or financial relationships that could be construed as a potential conflict of interest.

Publisher's Note: All claims expressed in this article are solely those of the authors and do not necessarily represent those of their affiliated organizations, or those of the publisher, the editors and the reviewers. Any product that may be evaluated in this article, or claim that may be made by its manufacturer, is not guaranteed or endorsed by the publisher.

frontiers in Immunology

ORIGINAL RESEARCH
published: 10 March 2022
doi: 10.3389/fimmu.2022.837370

PD-L1 Antibody Pharmacokinetics and Tumor Targeting in Mouse Models for Infectious Diseases

Gerwin G. W. Sandker[1], Gosse Adema[2], Janneke Molkenboer-Kuenen[1], Peter Wierstra[1], Johan Bussink[2], Sandra Heskamp[1] and Erik H. J. G. Aarntzen[1]**

[1] Department of Medical Imaging, Radboud Institute for Molecular Life Sciences, Radboud University Medical Center, Nijmegen, Netherlands, [2] Department of Radiation Oncology, Radboud Institute for Molecular Life Sciences, Radboud University Medical Center, Nijmegen, Netherlands

OPEN ACCESS

Edited by:
Nick Devoogdt,
Free University of Brussels, Belgium

Reviewed by:
Sridhar Nimmagadda,
Johns Hopkins University,
United States
Weijun Wei,
University of Wisconsin-Madison,
United States
Danielle J. Vugts,
VU Medical Center, Netherlands

***Correspondence:**
Gerwin G. W. Sandker
Gerwin.Sandker@radboudumc.nl
Erik H. J. G. Aarntzen
Erik.Aarntzen@radboudumc.nl

Specialty section:
This article was submitted to Cancer Immunity and Immunotherapy, a section of the journal Frontiers in Immunology

Received: *16 December 2021*
Accepted: *15 February 2022*
Published: *10 March 2022*

Citation:
Sandker GGW, Adema G, Molkenboer-Kuenen J, Wierstra P, Bussink J, Heskamp S and Aarntzen EHJG (2022) PD-L1 Antibody Pharmacokinetics and Tumor Targeting in Mouse Models for Infectious Diseases. Front. Immunol. 13:837370. doi: 10.3389/fimmu.2022.837370

Background: Programmed death-ligand 1 (PD-L1) regulates immune homeostasis by promoting T-cell exhaustion. It is involved in chronic infections and tumor progression. Nuclear imaging using radiolabeled anti-PD-L1 antibodies can monitor PD-L1 tissue expression and antibody distribution. However, physiological PD-L1 can cause rapid antibody clearance from blood at imaging doses. Therefore, we hypothesized that inflammatory responses, which can induce PD-L1 expression, affect anti-PD-L1 antibody distribution. Here, we investigated the effects of three different infectious stimuli on the pharmacokinetics and tumor targeting of radiolabeled anti-PD-L1 antibodies in tumor-bearing mice.

Materials/Methods: Anti-mouse-PD-L1 and isotype control antibodies were labelled with indium-111 ([^{111}In]In-DTPA-anti-mPD-L1 and [^{111}In]In-DTPA-IgG2a, respectively). We evaluated the effect of inflammatory responses on the pharmacokinetics of [^{111}In]In-DTPA-anti-mPD-L1 in RenCa tumor-bearing BALB/c mice in three conditions: lipopolysaccharide (LPS), local *Staphylococcus aureus*, and heat-killed *Candida albicans*. After intravenous injection of 30 or 100 µg of [^{111}In]In-DTPA-anti-mPD-L1 or [^{111}In]In-DTPA-IgG2a, blood samples were collected 1, 4, and 24 h p.i. followed by microSPECT/CT and *ex vivo* biodistribution analyses. PD-L1 expression, neutrophil, and macrophage infiltration in relevant tissues were evaluated immunohistochemically.

Results: In 30 µg of [^{111}In]In-DTPA-anti-mPD-L1 injected tumor-bearing mice the LPS-challenge significantly increased lymphoid organ uptake compared with vehicle controls (spleen: 49.9 ± 4.4%ID/g versus 21.2 ± 6.9%ID/g, $p < 0.001$), resulting in lower blood levels (3.6 ± 1.6%ID/g versus 11.5 ± 7.2%ID/g; $p < 0.01$) and reduced tumor targeting (8.1 ± 4.5%ID/g versus 25.2 ± 5.2%ID/g, $p < 0.001$). Local *S. aureus* infections showed high PD-L1$^+$ neutrophil influx resulting in significantly increased [^{111}In]In-DTPA-anti-mPD-L1 uptake in affected muscles (8.6 ± 2.6%ID/g versus 1.7 ± 0.8%ID/g, $p < 0.001$). Heat-killed *Candida albicans* (Hk-*C. albicans*) challenge did not affect pharmacokinetics. Increasing [^{111}In]In-DTPA-anti-mPD-L1 dose to 100 µg normalized blood clearance and tumor uptake in LPS-challenged mice, although lymphoid organ uptake remained higher. Infectious stimuli did not affect [^{111}In]In-DTPA-IgG2a pharmacokinetics.

Conclusions: This study shows that anti-PD-L1 antibody pharmacokinetics and tumor targeting can be significantly altered by severe inflammatory responses, which can be compensated for by increasing the tracer dose. This has implications for developing clinical PD-L1 imaging protocols in onco-immunology. We further demonstrate that radiolabeled anti-PD-L1 antibodies can be used to evaluate PD-L1 expression changes in a range of infectious diseases. This supports the exploration of using these techniques to assess hosts' responses to infectious stimuli.

Keywords: PD-L1, *Staphylococcus aureus*, *Candida albicans*, lipopolysaccharide, nuclear imaging (SPECT), antibody, cancer, infectious diseases

INTRODUCTION

Immune checkpoint molecules play a vital role in immune homeostasis; they prevent autoimmune disease and maintain tissue integrity during inflammatory responses. Programmed death-ligand 1 (PD-L1, also CD274) is a key immune checkpoint, with a dynamic expression profile on a broad range of tissues (1). It promotes effector T-cell exhaustion when ligating its receptor programmed death-1 (PD-1), thereby down-tuning the adaptive immune response. In cancer patients, PD-L1 expressed by tumor or activated immune cells promotes immune escape (2, 3). Blocking PD-L1 with therapeutic antibodies results in increased anti-tumor immunity in various cancer types and has revolutionized cancer immunotherapy (4). In response to infection, increased levels of local or systemic proinflammatory cytokines, e.g., IFN-γ and TNF-α, induce the upregulation of PD-1/PD-L1 expression (5–7). Paralleling onco-immunology, T-cell dysfunction and exhaustion mediated by increased PD-1/PD-L1 expression in patients with unresolved chronic infections or sepsis result in ineffective microbial clearing and increased mortality (5, 6, 8). In preclinical sepsis models, PD-1 and PD-L1 blocking monoclonal antibodies (mAb) have been shown to reinvigorate the immune system, thereby enhancing bacterial clearance and improving survival (9, 10). These results prompted clinical studies evaluating the efficacy of PD-1 or PD-L1 targeting mAbs in patients with sepsis (11, 12).

Nuclear imaging using radiolabeled anti-PD-L1 antibodies allows for non-invasive, sensitive, and quantitative assessments of PD-L1 expression on a whole-body scale (13–16). Various preclinical studies in onco-immunology have demonstrated the feasibility of this approach in immunocompetent mouse models (17–19). Moreover, recent clinical studies using a radiolabeled anti-PD-L1 antibody (14, 20), adnectin (15), peptide (21), or nanobody (22) demonstrated that nuclear imaging using PD-L1 targeting tracers can assess PD-L1 expression *in vivo* (18). Accumulation of the radiolabeled anti-PD-L1 antibodies was also observed in tissues with physiological PD-L1 expression (e.g., spleen, lymph nodes, and bone marrow) as well as in inflammatory sites (14). In general, the spleen is the main organ for the accumulation of radiolabeled antibodies (23). During systemic responses to infection, PD-L1 expression in the spleen is upregulated (10). Therefore, we hypothesized that inflammatory responses that induce local or systemic PD-L1 expression can affect anti-PD-L1 antibody biodistributions. Furthermore, no study has performed an in-depth investigation of PD-L1 expression or imaging in infectious disease models.

The aim of our study was to assess changes in PD-L1 expression in response to a range of inflammatory stimuli and how these would influence imaging of PD-L1 expression in the tumor. Severe-to-mild bacterial infection was mimicked by inducing systemic inflammatory responses with lipopolysaccharide (LPS), or local responses with *Staphylococcus aureus* infection or heat-killed *Candida albicans* (Hk-*C. albicans*) in tumor-bearing mice. Analysis of blood clearance and *in vivo* biodistribution of different doses of indium-111-labeled anti-mPD-L1 antibodies showed that inflammatory responses can significantly alter the physiological PD-L1 expression in lymphoid organs, both locally and systemically. This resulted in accelerated blood clearance and decreased tumor targeting of radiolabeled PD-L1 antibodies.

MATERIALS AND METHODS

Study Design

The effect of three clinically relevant infection models on the pharmacokinetics of anti-mPD-L1 antibodies was investigated. For this purpose, RenCa tumor-bearing female BALB/c mice were injected with 1) LPS intraperitoneal, 2) *S. aureus* intramuscular, 3) Hk-*C. albicans* intraperitoneal, 4) vehicle intramuscular, or 5) vehicle intraperitoneal. Subsequently, mice were injected intravenously with 30 μg of [^{111}In]In-DTPA-anti-mPD-L1 mAb (^{111}In-mPD-L1, previously determined as the optimal tracer dose for PD-L1 imaging) (24). Next, the effect of antibody dosing on the pharmacokinetics in these infection

Abbreviations: PD-L1, programmed death-ligand 1; PD-1, programmed cell death protein 1; LPS, lipopolysaccharide; Hk-*C. albicans*, heat-killed *Candida albicans*; *S. aureus*, *Staphylococcus aureus*; IFN-γ, interferon gamma; TNF-α, tumor necrosis factor alpha; ^{111}In-mPD-L1, indium-111-labeled anti-mouse PD-L1 antibody; ^{111}In-rIgG2a, indium-111-labeled rat IgG2a antibody; Ict-DTPA, isothiocyanatobenzyl-diethylenetriaminepentaacetic acid; MBq, megabequerel; A_s, specific activity; EDTA, ethylenediaminetetraacetic; SPECT, single-photon emission CT; iTLC, instant thin-layer chromatography; CFU, colony-forming units; i.v., intravenous; i.p., intraperitoneal; i.m., Intramuscular; Pi, post injection; RT, room temperature; TMDD, target-mediated drug disposition; AR, antigen retrieval; PBS, phosphate-buffered saline; BSA, bovine serum albumin; NrabS, normal rabbit serum; (m)Ab, (monoclonal) antibody; v/v, volume per volume.

models was examined by injecting identical groups with 100 μg of ^{111}In-mPD-L1. Finally, to assess whether uptake was PD-L1 specific, subgroups of mice were injected with 30 or 100 μg of ^{111}In-labeled non-biologically affine IgG2a. For all conditions, the antibody blood concentrations were assessed by collecting blood samples at several time points following tracer injection. Furthermore, the distribution of the radiolabeled antibodies was assessed by single-photon emission CT (SPECT)/CT and *ex vivo* biodistribution analysis. PD-L1 tissue expression was investigated immunohistochemically. All *in vivo* experiments were approved by the Animal Welfare Body of the Radboud University, Nijmegen, and the Central Authority for Scientific Procedures on Animals and were conducted in accordance with the principles laid out by the Dutch Act on Animal Experiments (2014).

Cell Culture

RenCa murine renal cell carcinoma cells (CLS, 400321) were cultured in Roswell Park Memorial Institute (RPMI) 1640 (Gibco, Life Technologies Limited, Paisley, UK), supplemented with 10% fetal calf serum (FCS; Sigma-Aldrich Chemie BV, Zwijndrecht, the Netherlands) and 2 mmol/L glutamine (Gibco, Grand Island, NY, USA) at 37°C in a humidified atmosphere containing 5% CO_2. Cells were tested and found negative for mycoplasma and mouse pathogens. The maximum number of passages between thawing and tumor cell inoculation was five.

Tumor-Bearing Mice

Female BALB/c mice (n = 126, 10–12 weeks, Janvier Labs, Le Genest-Saint-Isle, France) were housed under specific-pathogen-free conditions in individually ventilated cages with a filter top (Blue line IVC, Techniplast, Buguggiate, VA, Italy) in which cage enrichment was present and food and water were available *ad libitum*. Mice (n = 121) were injected subcutaneously (right flank) with 0.5×10^6 RenCa cells in 200 μl of RPMI 1640. Tumor size was measured using a caliper twice weekly. When mean tumor volume reached approximately 0.2 cm^3, mice were block-randomized into the following groups; 1) LPS intraperitoneal, 2) *S. aureus* intramuscular, 3) Hk-*C. albicans* intraperitoneal, 4) vehicle control intraperitoneal, or 5) vehicle control intramuscular. A total of 21 mice were excluded from analysis for the following reasons: no discernable tumor present at the time of dissection (n = 16), a humane endpoint was reached (n = 3), the animal deceased before the end of the experiment (n = 1), or presence of a large concavity in the tumor (n = 1).

Preparation and Administration of Infection Model Agents

Lipopolysaccharide

LPS (L6529, Sigma-Aldrich, St. Louis, MO, USA) was dissolved in physiological saline (0.9% NaCl, Braun Melsungen AG, Melsungen, Germany) and stored at –20°C at a concentration of 1 mg/ml. Solutions were thawed, and physiological saline was added to a final concentration of 0.075 mg/ml. LPS was injected intraperitoneally (0.6 mg/kg body weight) 24 h before radiolabeled antibody injection, the previously determined optimal time point (24).

Staphylococcus aureus

S. aureus (substrain 25923, ATCC, Manassas, VA, USA) were seeded in Columbia III agar containing 5% sheep blood (BD Biosciences, San Jose, CA, USA) and incubated overnight at 37°C. Next, in duplicate, 3 to 5 colonies *S. aureus* were transferred to 4.5 ml of brain heart infusion (BHI) broth (BD) in 15-ml falcon tubes and incubated overnight at 37°C. The following day, the suspension was spun down at 1,000*g*, and the pellet was resuspended in 5 ml of NaCl 0.9% (Laboratoire Aguettant, Lyon, France); subsequently, the content of both tubes were pooled (10 ml, 1×10^9 colony-forming units (CFU)/ml). This suspension was transported at –80°C on dry ice and thawed 1 h later right before use. The bacterial suspension was mixed 1:1 v/v with heparinized homologous blood collected by heart puncture from isoflurane-anesthetized donor mice. The exact CFU count was calculated from a titration series of the sample, which was incubated overnight on agar at 37°C. Mice were anesthetized using isoflurane, and *S. aureus* (50 μl, with CFUs ranging from 0.8×10^7 to 4.5×10^7) was injected in the left calf muscle 48 h before radiolabeled antibody injection for the infection and subsequent inflammatory response to develop sufficiently (25).

Heat-Killed *Candida albicans*

C. albicans (substrain UC 820, ATCC) were incubated overnight in Sabouraud broth at 30°C and subsequently killed by heating at 56°C for 30 min, and the preparation was kindly provided by M. Jaeger and M. Netea, Radboudumc Nijmegen (26). The suspension was diluted with sterile pyrogen-free phosphate-buffered saline (PBS) to a final concentration of 5×10^7 CFU/ml. Hk-*C. albicans* was injected intraperitoneally (0.5×10^7 CFU Hk-*C. albicans* in 100 μl of PBS) 24 h before radiolabeled antibody injection for antifungal immune responses to develop (27).

Vehicle Controls

For the groups receiving intraperitoneal injection, physiological saline (0.9% NaCl) was used as a vehicle control (for the LPS and Hk-*C. albicans* model groups) and injected 24 h before radiolabeled antibody injection. For the intramuscular *S. aureus* group, vehicle control was a mixture of autologous blood: physiological saline 1:1 v/v (prepared according to the protocol for the *S. aureus* infection). The mixture was injected 48 h before radiolabeled antibody injection.

Radiolabeling and Antibody Injection

Rat IgG2b anti-murine PD-L1 (mPD-L1, clone 10F.9G2, Bio X Cell, Lebanon, NH, USA) and rat IgG2a non-biological affine control (IgG2a, clone 2A3, Bio X Cell) antibodies were conjugated with isothiocyanatobenzyl-diethylenetriaminepentaacetic acid (p-SCN-Bn-DTPA, Macrocyclics, Plano, TX, USA), as described previously (13, 24). DTPA-conjugated antibodies were labeled with indium-111 chloride ($^{111}InCl_3$, Curium, Helsinki, Finland) as follows: DTPA-anti-mPD-L1 or DTPA-IgG2a were incubated with $^{111}InCl_3$ in a ratio of 1 MBq per μg antibody in 0.5 M of MES buffer (pH 5.4) at room temperature (RT) for 20 min. Thereafter, unincorporated ^{111}In was chelated by adding 1/10th of the

labeling volume of 50 mM of ethylenediaminetetraacetic (EDTA) in PBS to reach a final concentration of 5 mM of EDTA. The labeling efficiencies were evaluated using instant thin-layer chromatography (iTLC), using silica gel impregnated glass microfiber membrane chromatography strips (SGI0001, Agilent Technologies, Santa Clara, CA, USA) and 0.1 M, pH 6.0, of citrate buffer (Sigma-Aldrich) as a mobile phase. The activity profiles were captured with photosensitive plates (Fuji MS, Cytiva, Marlborough, MA, USA) and analyzed using a phosphor imager (Typhoon FLA 7000, GE, Chicago, IL, USA). When labeling efficiency was ≥92.5%, pH was adjusted by adding 1/10th volume 10× PBS (pH 7.4). When labeling efficiency was below 92.5%, non-labeled ^{111}In was removed using PD10 buffer exchange columns (Cytiva) and PBS as eluant following the manufacturer's protocol. Moreover, to lower the salt concentration of all IgG2a labeling reactions and subsequent injection fluids, buffers were exchanged to PBS using PD10 columns directly after the radiolabeling procedure. Subsequently, the desired concentration of either 30 or 100 µg of antibody per 200 µl was reached by adding the appropriate amount of unlabeled antibody and volume of sterile pyrogen-free PBS. The radiochemical purity of the injected products exceeded 92.5% for all experiments. For each infection model groups, mice were injected in the lateral caudal vein with 200 µl of PBS containing one of the following; a) 30 µg of [^{111}In]In-DTPA-anti-mPD-L1 mAb (^{111}In-mPD-L1, specific activity (A_s): 0.34–0.57 MBq/µg), b) 100 µg of ^{111}In-mPD-L1 (A_s: 0.102–0.172 MBq/µg), c) 30 µg of [^{111}In]In-DTPA-IgG2a (^{111}In-IgG2a, A_s: 0.0063 MBq/µg), or d) 100 µg of ^{111}In-IgG2a (A_s: 0.0055 MBq/µg). Heat lamps warmed the mice prior to i.v. injections. The *in vitro* and *in vivo* characterization of ^{111}In-mPD-L1 and ^{111}In-rIgG2a has been reported previously (13, 24). During all experiments, researchers and biotechnicians were blinded for group allocation.

Pharmacokinetics, *Ex Vivo* Biodistribution, and MicroSPECT/CT Imaging

To assess the blood clearance of ^{111}In-mPD-L1 over time, blood samples of all mice were collected using 25-µl capillary tubes (Hirschmann, Eberstadt, Germany) following lateral caudal venipuncture, at 1, 4, and 24 h post tracer injection. When lateral caudal venipuncture proved unsuccessful, blood samples were obtained by saphenous venipuncture. At 24 h post tracer injection, all mice were euthanized by CO_2/O_2 asphyxiation. In each group, 2 mice were used for SPECT/CT imaging to visualize the *in vivo* biodistribution of ^{111}In-mPD-L1 with SPECT/CT (U-SPECT II/CT, MILabs, Houten, Netherlands) using the following acquisition settings: 25-min acquisition time, 1.0-mm-diameter pinhole mouse high sensitivity collimator, and CT parameters of 160-µm spatial resolution, 615 µA, and 65 kV. Data were reconstructed using the MILabs software (version 2.04) using the following settings: energy windows at 171 keV (range 154 to 188 keV) and 245 keV (range 220 to 270 keV), 1 iteration, 16 subsets, and a 0.4-mm voxel size. The Inveon Research Workplace software package (version 4.1) was used to create maximum intensity projections (MIPs). For all mice, directly following euthanasia or SPECT/CT scanning, tumor and other tissues of interest (spleen, left and right inguinal lymph nodes, brown adipose tissue, bone marrow, thymus, duodenum, liver, kidney, heart, lung, pancreas, stomach, colon, bone, muscle, and when available *S. aureus*-infected or vehicle control-injected muscle) were collected for *ex vivo* biodistribution analysis. Blood and tissue samples were weighed (XPE105DR, Mettler Toledo, Columbus, OH, USA) and measured with a well-type gamma-counter (Wallac 2480 Wizard, Perkin Elmer, Waltham, MA, USA). For reference, aliquots of injection fluid were measured concomitantly. Antibody accumulation was calculated as a fraction of the injected dose and normalized for tissue weight [percentage injected dose per gram tissue (%ID/g)]. Tumor, the spleen, and *S. aureus*-infected and vehicle-injected muscle were stored in 4% formalin in PBS for subsequent immunohistochemical evaluation.

Immunohistochemistry

Formalin-fixed paraffin-embedded tissue sections (5 µm) of tumor and the spleen, and *S. aureus*-infected and vehicle control muscle were evaluated by immunohistochemistry for PD-L1 expression and PD-L1, F4/80, and Ly6G expression respectively. All sections were deparaffinized and rehydrated. For F4/80, sections were post fixated with 4% formalin in PBS for 10 min at RT. Antigen retrieval (AR) was performed in either 10 mM of sodium citrate buffer (pH 6.0) at 96°C for 10 min for both PD-L1 and Ly6G, or at 37°C for 2 h followed by 0.075% trypsin in PBS for 7 min at 37°C for F4/80. Endogenous peroxidases were blocked before AR with 3% H_2O_2 (107209, Merck, Darmstadt, Germany) in methanol for 20 min for F4/80, or after AR with 3% H_2O_2 in PBS for 10 min for both PD-L1 and Ly6G. For PD-L1, endogenous biotin was blocked using a biotin/avidin blocking set (SP-2001, Vector, Burlingame, CA, USA). Next, for PD-L1 and F4/80, blocking was performed with 10% normal rabbit serum (NrabS, BDC-10112, Bodinco, Alkmaar, Netherlands) and for Ly6G with 20% normal goat serum (5095, Bodinco) in PBS for 30 min. Primary antibody incubation was performed with either goat-a-murine PD-L1 (AF1019, R&D Systems, Minneapolis, MN, USA) diluted 1:500 in PBS/1% bovine serum albumin (BSA; Sigma, Darmstadt, Germany) overnight at 4°C, rat-anti-F4/80 (BM8, Invitrogen, Carlsbad, CA, USA) diluted 1:1,000 in PBS/2% NrabS and incubated overnight at 4°C, or rat-anti-mouse-Ly6G (BP0075-1, Bio X Cell) diluted 1:1,000 in PBS+1% BSA and incubated for 2 h at RT. Thereafter, tissues were incubated for 30 min at RT with the following secondary antibodies: biotinylated-rabbit-anti-goat (E0466, DAKO, Glostrup, Denmark) diluted 1:400 in PBS/1% BSA, goat-a-Rat-peroxidase (A9037, Sigma) diluted 1:100 in PBS/1% BSA, or biotinylated rabbit-anti-rat-IgG (BA-4001, Vector) 1:200 dilution in PBS-2% NrabS, for the PD-L1, Ly6G, or F4/80, respectively. Next, for PD-L1 and F4/80, horseradish peroxidase-Biotin/Streptavidin Complex (PK-6100, Vectastain) diluted 1:250 in PBS/1% BSA for 30 min at RT was used. Finally, all tissues were incubated with bright DAB (B-500, Immunologic, Duiven, the Netherlands) for 8 min, followed by nuclei blueing with hematoxylin (4085-9001, Klinipath/VWR, Olen, Belgium), and dehydrated with ethanol (4099-9005, Klinipath/VWR) and xylene (4055-9005, Klinipath/VWR). Sections were mounted with a coverslip using Permount (SP15-500, Fisher, Hampton, NH, USA). Consecutive sections to the PD-L1-, F4/80-, and Ly6G-stained sections were stained for morphological reference with H&E Y (1.15935.0100, Merck).

Statistical Analysis

Differences in tissue uptake and blood concentrations of both doses ^{111}In-mPD-L1 and ^{111}In-IgG2a were tested for significance using two-way ANOVAs with a Bonferroni *post-hoc* test. Values are presented as mean ± SD. Statistical significance was defined as a p-value below 0.05. Statistical analyses were performed using GraphPad Prism version 5.03 for Windows.

RESULTS

Lipopolysaccharide Significantly Changes ^{111}In-mPD-L1 Pharmacokinetics and Tumor Targeting

The effect of LPS on the pharmacokinetics of ^{111}In-mPD-L1 in tumor-bearing mice is presented in **Figures 1** and **2**, and the biodistribution data of all collected organs can be found in **Supplementary Table 1**. Increased PD-L1 antibody clearance from blood was observed in LPS-challenged mice injected with 30 µg of ^{111}In-mPD-L1, compared with control mice (24 h p.i.: 3.6 ± 1.6%ID/g versus 11.5 ± 7.2%ID/g, respectively, $p < 0.01$; see also **Supplementary Table 1**). Furthermore, accumulation of ^{111}In-mPD-L1 in the spleen was more than twofold higher in LPS-challenged compared with control mice (49.9 ± 4.4%ID/g versus 21.2 ± 6.9%ID/g, respectively, $p < 0.001$). Increased PD-L1 antibody uptake was also observed in lymph nodes (33.8 ± 9.6% ID/g versus 17.3 ± 6.1%ID/g, $p < 0.01$), bone marrow (17.8 ± 3.3%ID/g versus 7.4 ± 2.3%ID/g, $p < 0.001$), and, to a lesser extent, other tissues with physiological PD-L1 expression, such as the lungs, heart, duodenum, and brown adipose tissue. The increased uptake of ^{111}In-mPD-L1 in primary and secondary lymphoid organs occurred at the expense of tumor uptake, which was only 8.1 ± 4.5%ID/g in LPS-challenged mice versus 25.2 ± 5.2%ID/g in control mice ($p < 0.001$).

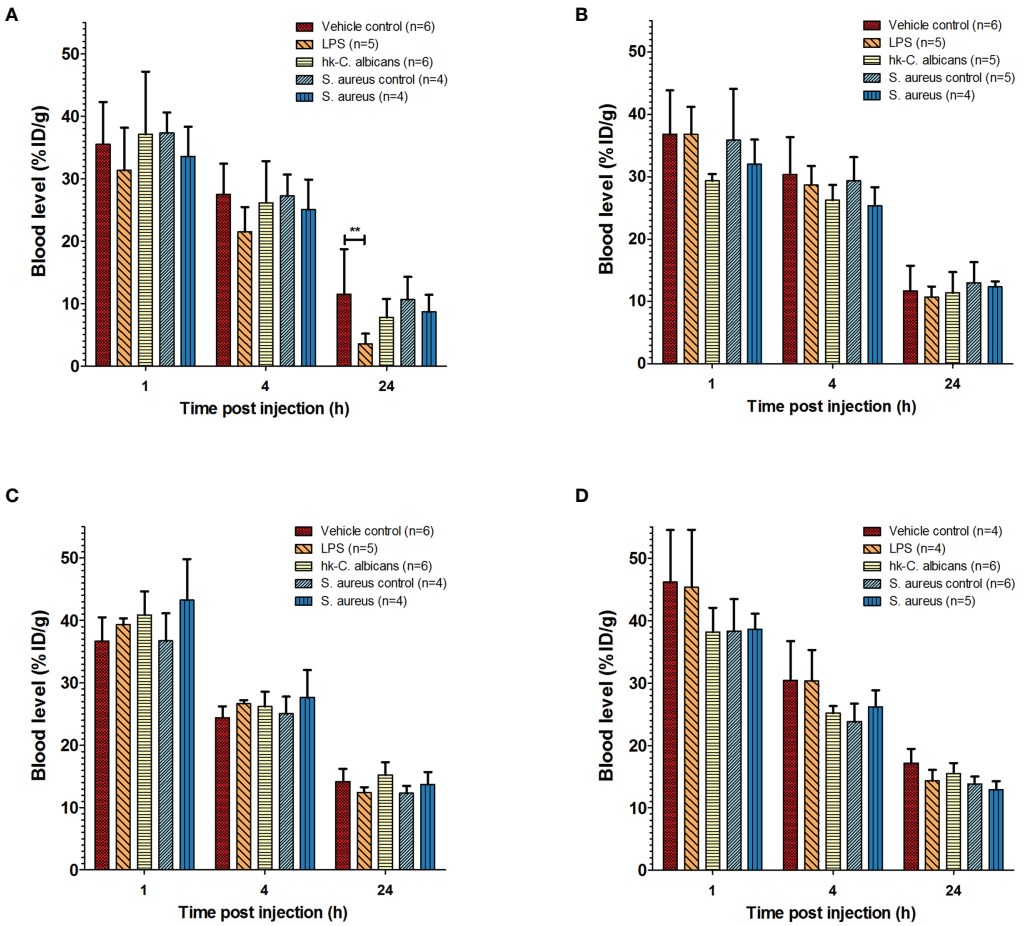

FIGURE 1 | Pharmacokinetics of ^{111}In-mPD-L1 and ^{111}In-IgG2a in a range of infection models. Pharmacokinetics of 30 µg of ^{111}In-mPD-L1 **(A)**, 100 µg of ^{111}In-mPD-L1 **(B)**, 30 µg of ^{111}In-IgG2a **(C)**, and 100 µg of ^{111}In-IgG2a **(D)** in RenCa tumor-bearing BALB/c mice immune stimulated with the following conditions: vehicle control, LPS, Hk-*C. albicans*, *Staphylococcus aureus* i.m. infected, and vehicle i.m. control. ^{111}In-mPD-L1 and ^{111}In-IgG2a blood concentrations 1, 4, and 24 h post antibody injection are given in % injected dose per gram of blood (%ID/g). Differences in blood levels were tested for significance using two-way ANOVAs with a Bonferroni *post-hoc* test (**$p < 0.01$) (see legend in figure for number of animals per group). LPS, lipopolysaccharide; Hk-*C. albicans*, heat-killed *Candida albicans*.

Increasing the antibody dose to 100 μg of ^{111}In-mPD-L1 restored blood levels and tumor uptake in LPS-challenged mice to similar levels as in control mice (**Figures 1A**, **2B** and **Supplementary Table 1**). Accumulation of ^{111}In-mPD-L1 in lymphoid organs remained elevated but was less pronounced as compared with the lower antibody dose. Spleen uptake in mice injected with 100 μg of ^{111}In-mPD-L1 was 21.0 ± 5.0%ID/g versus 12.6 ± 1.9%ID/g ($p < 0.01$), for LPS-challenged versus control mice. SPECT/CT imaging confirmed the *ex vivo* biodistribution analyses for both antibody doses (**Figure 3**), namely, LPS stimulation increased ^{111}In-mPD-L1 uptake in lymphoid organs and decreased tumor uptake. Furthermore, in control and LPS-stimulated mice, ^{111}In-mPD-L1 accumulation in brown adipose tissue and the liver was observed.

To determine whether the LPS-induced changes in the blood clearance and biodistribution reflected changes in PD-L1 expression levels, and not non-specific Fc-receptor-mediated uptake and clearance, separate groups of mice were injected with an isotype control antibody (^{111}In-IgG2a), using the same experimental design. In contrast to ^{111}In-mPD-L1, blood clearance and *in vivo* biodistribution of both the 30 μg and 100 μg dose levels of ^{111}In-IgG2a were not affected by LPS challenge (**Supplementary Table 1**). Furthermore, immunohistochemistry for PD-L1 showed that splenic PD-L1 expression was very high and that LPS stimulation might have increased its expression in the red pulp (**Figure 4**). Finally, immunohistochemical analysis of tumor sections showed that LPS stimulation did not decrease PD-L1 expression on the tumor cell membrane, indicating that the lower ^{111}In-mPD-L1 tumor uptake was not due to decreased PD-L1 expression.

^{111}In-mPD-L1 Detects Locoregional Upregulation of PD-L1 in *Staphylococcus aureus* Infection

Local intramuscular *S. aureus* infection (2.5×10^7 CFU) did not affect blood clearance of ^{111}In-mPD-L1 (**Figure 1**). Furthermore, ^{111}In-mPD-L1 accumulation in tumor and lymphoid organs was unaffected by *S. aureus* infection (**Figure 2**). However, ^{111}In-mPD-L1 uptake in *S. aureus*-infected muscle itself was significantly increased compared with vehicle-injected muscle (30 μg of ^{111}In-mPD-L1: 8.6 ± 2.6%ID/g versus 1.7 ± 0.8%ID/g, respectively $p < 0.001$). SPECT/CT imaging confirmed these results as, apart from the accumulation of ^{111}In-mPD-L1 in the *S. aureus*-infected muscle, no differences in antibody distribution were observed (**Figure 3** and **Supplementary Table 1**).

Whether the ^{111}In-mPD-L1 uptake in *S. aureus* infections was PD-L1 mediated was evaluated by comparing the uptake with that of ^{111}In-IgG2a. Although ^{111}In-IgG2a did show uptake in *S. aureus*-infected muscles, this was twofold lower as compared with ^{111}In-mPD-L1 (5.6 ± 0.6%ID/g versus 10.2 ± 1.8%ID/g, $p < 0.001$), indicating that uptake was predominantly PD-L1 mediated. Similarly, as for ^{111}In-mPD-L1, *S. aureus* infection did not alter blood clearance, and tumor and normal tissue targeting of ^{111}In-IgG2a.

To further demonstrate that the accumulation observed in *S. aureus*-infected muscle was predominantly PD-L1 specific, we performed immunohistochemical analysis of the *S. aureus*-infected muscle. We Observed a high number of PD-L1 positive cells in and around sites of *S. aureus* infections, whereas only a few PD-L1 expressing cells were detected in the control site (**Figure 5**). The PD-L1 positive cells morphologically resembled neutrophils and macrophages, and staining with Ly6G and F4/80 showed that the PD-L1 expression colocalized with sites containing high numbers of neutrophils with macrophages present in fewer numbers. At the injection site of vehicle control, fewer PD-L1-positive macrophages and few to no neutrophils were detected. Both the ^{111}In-IgG2a biodistribution analysis and the immunohistochemical analyses show that the uptake of ^{111}In-mPD-L1 in *S. aureus*-infected muscles was partly PD-L1-mediated.

Heat-Killed *Candida albicans* Stimulation Does Not Affect ^{111}In-mPD-L1 Pharmacokinetics

The blood clearance and *in vivo* biodistribution of ^{111}In-mPD-L1 in mice intraperitoneally injected with Hk-*C. albicans* was comparable to those of vehicle controls for both antibody doses (**Figures 1**, **2**). In this model, no differences in lymphoid tissue or tumor uptake of ^{111}In-mPD-L1 were observed. SPECT/CT imaging confirmed these observations (**Figure 3**). Similarly, no effect on the blood clearance or biodistribution was observed for ^{111}In-IgG2a.

DISCUSSION

PD-L1 is a central immune checkpoint molecule in tissue homeostasis and peripheral tolerance (1). Monoclonal antibodies blocking the interaction between PD-1 and PD-L1 have had a tremendous impact in the field of onco-immunology (3) and are now established treatment options for many cancer types (4). Realizing that immune checkpoint molecules are also involved in immune paralysis following severe systemic inflammatory responses (28), or persistent infections due to sustained local immune suppressions (29), PD-1 or PD-L1 targeting antibodies are currently investigated to overcome immune suppression in prolonged or severe infections (11, 12). Its dynamic and systemic expression in response to infectious stimuli cannot be determined by tissue sampling, but these aspects are relevant when developing novel treatment regimens. Furthermore, assessment of PD-L1 expression on tumor tissue samples is hampered by sampling errors and invasiveness of the procedure. Therefore, molecular imaging techniques using radiolabeled antibodies are of great interest, as they allow for longitudinal assessment of PD-L1 expression on a whole-body scale.

In this study, we demonstrate that inflammatory responses can significantly affect the pharmacokinetics of anti-PD-L1 antibodies. LPS challenge resulted in increased antibody uptake in lymphoid organs and thereby significantly accelerated blood clearance and decreased tumor targeting of ^{111}In-mPD-L1. This effect was most pronounced with a low antibody dose of 30 μg

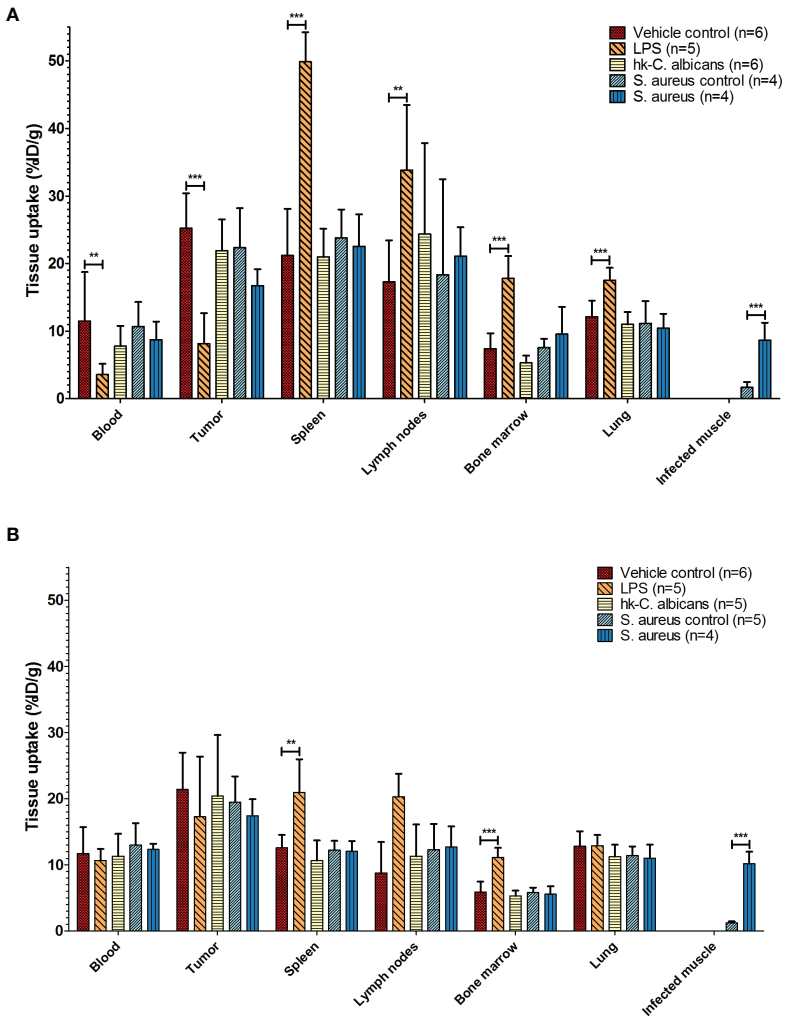

FIGURE 2 | Biodistribution of ^{111}In-mPD-L1 in different infection models. *Ex vivo* biodistribution of 30 µg and 100 µg of ^{111}In-mPD-L1 antibody doses in RenCa tumor-bearing BALB/c mice injected with vehicle control or immune stimulated with LPS, Hk-*C. albicans*, or *Staphylococcus aureus*, at 24 h post injection. Data for tissues not shown can be found in **Supplementary Table 1**. **(A)** In 30 µg of ^{111}In-mPD-L1-injected mice, immune stimulation with LPS significantly affects ^{111}In-mPD-L1 blood clearance, lymphoid, and tumor uptake. In *S. aureus*-infected muscle, significantly increased uptake of ^{111}In-mPD-L1 was observed. **(B)** For 100 µg of ^{111}In-mPD-L1-injected mice, LPS stimulation increased uptake in lymphoid organs, but no effect was observed on blood levels or tumor targeting. Significant uptake of ^{111}In-mPD-L1 can be observed in *S. aureus*-infected muscles. Biodistribution of neither ^{111}In-mPD-L1 dose was affected by Hk-*C. albicans* stimulation. ^{111}In-mPD-L1 tissue uptake is given in % injected dose per gram of tissue (%ID/g), and differences in uptake were tested for significance using two-way ANOVAs with a Bonferroni *post-hoc* test (**$p < 0.01$, and ***$p < 0.001$) (see legend in figure for number of animals per group). LPS, lipopolysaccharide; Hk-*C. albicans*, heat-killed *Candida albicans*.

and could be compensated for by increasing the antibody doses to 100 µg. This dose-dependent clearance from circulation has also been observed in clinical studies (20). Moreover, these results are in line with other studies that show that 10F.9G2 and other anti-PD-L1 antibodies exhibit target-mediated drug disposition (TMDD), meaning that these antibodies show non-linear pharmacokinetics at low doses, while increasing the dose leads to linear pharmacokinetics (30, 31). As a consequence, a saturation of tissues with high antigen levels, which are readily accessible (also described as "sink organs," such as the spleen), is required to achieve effective target tissue uptake (31, 32). Studies with isotype control antibodies did not show LPS-induced changes in pharmacokinetics, which suggest that the changes are PD-L1-mediated and not solely caused by enhanced Fc-receptor-mediated uptake nor by other effects such as increased perfusion. Furthermore, our imaging and *ex vivo* biodistribution results are in accordance with previous flow cytometry studies that showed LPS-induced sepsis increased PD-L1 expression on monocytic and myeloid immune cells in the spleen (24, 33). Concluding, we found that LPS-induced sepsis can substantially alter anti-PD-L1 antibody pharmacokinetics, which can be monitored by PD-L1 imaging. For this purpose, lower antibody doses might be more sensitive to detect changes in PD-L1 expression levels in tissues with readily accessible PD-L1

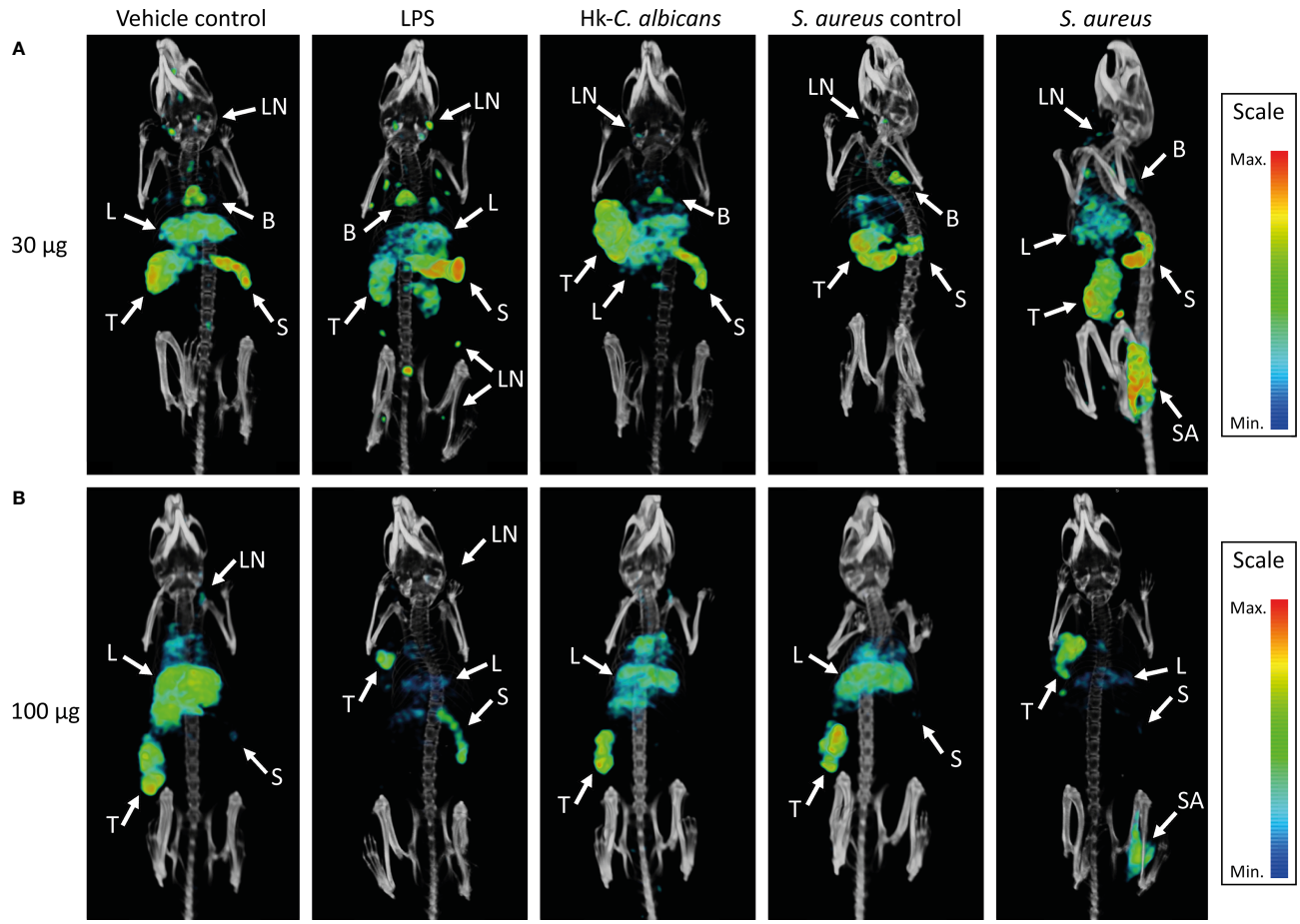

FIGURE 3 | SPECT/CT images showing the *in vivo* distribution of ^{111}In-mPD-L1 in vehicle-injected and LPS-stimulated, *Staphylococcus aureus*-infected, or Hk-*C. albicans*-stimulated RenCa tumor-bearing mice. Representative MIPs of vehicle control, LPS-stimulated, *S. aureus*-infected, and Hk-*C. albicans*-stimulated RenCa tumor-bearing BALB/c mice, 1 day after injection 30 µg of ^{111}In-mPD-L1 **(A)** or 100 µg of ^{111}In-mPD-L1 **(B)**. Tissue uptake of ^{111}In-mPD-L1 is visualized with MIP thresholded microSPECT/CT images; all images were generated using the same MIPs threshold. Uptake of ^{111}In-mPD-L1 can be appreciated in tumor (T), spleen (S), *S. aureus*-infected (SA), lymph nodes (LN), liver (L), and brown adipose tissue B. LPS, lipopolysaccharide; Hk-*C. albicans*, heat-killed *Candida albicans*; SPECT, single-photon emission CT; MIPs, maximum intensity projections.

(e.g., spleen) but might be unable to detect changes in less accessible tissues such as tumors.

In *S. aureus*-infected muscles, high uptake of the radiolabeled anti-PD-L1 antibody was detected by both *ex vivo* biodistribution and SPECT/CT imaging. This is in accordance with clinical studies observing the accumulation of ^{89}Zr-atezolizumab in local inflammatory processes (14). In our study, the isotype control antibody experiment indicates that the uptake was partly non-specific, which can be explained by the enhanced permeability and retention effect caused by both *S. aureus* itself and the host's inflammatory response against this pathogen (34). In this study, inflammatory responses to local *S. aureus* infections did not affect non-local ^{111}In-mPD-L1 uptake or its blood clearance. This indicates that *S. aureus* elicited a localized inflammatory response with little to no systemically acting PD-L1-upregulating cytokines (e.g., IFN-γ) or PD-L1 positive immune cells. Furthermore, we showed that the localized increase in PD-L1 expression is caused by monocytes and high numbers of neutrophils. These data are consistent with the immunological response to local *S. aureus* infections with induction of PD-L1 expression (6, 35) and rapid recruitment of monocytes, macrophages, and high numbers of neutrophils, of which the latter go into apoptosis and are phagocytosed on site after fulfilling their function (25). Importantly, our study shows that PD-L1 expression induced by the *S. aureus* elicited inflammatory response can be detected with nuclear imaging using anti-PD-L1 antibodies and that pharmacokinetics at tracer level were unaffected by local or systemic responses to local *S. aureus* infections.

Intraperitoneal Hk-*C. albicans* injections mimic candidemia, which has been shown to increase immune checkpoints, such as PD-L1, expression levels on peripheral blood mononuclear cells (5, 10). Furthermore, preclinical studies suggest that candidemia seems to respond to PD-1/PD-L1 blocking therapies, indicating

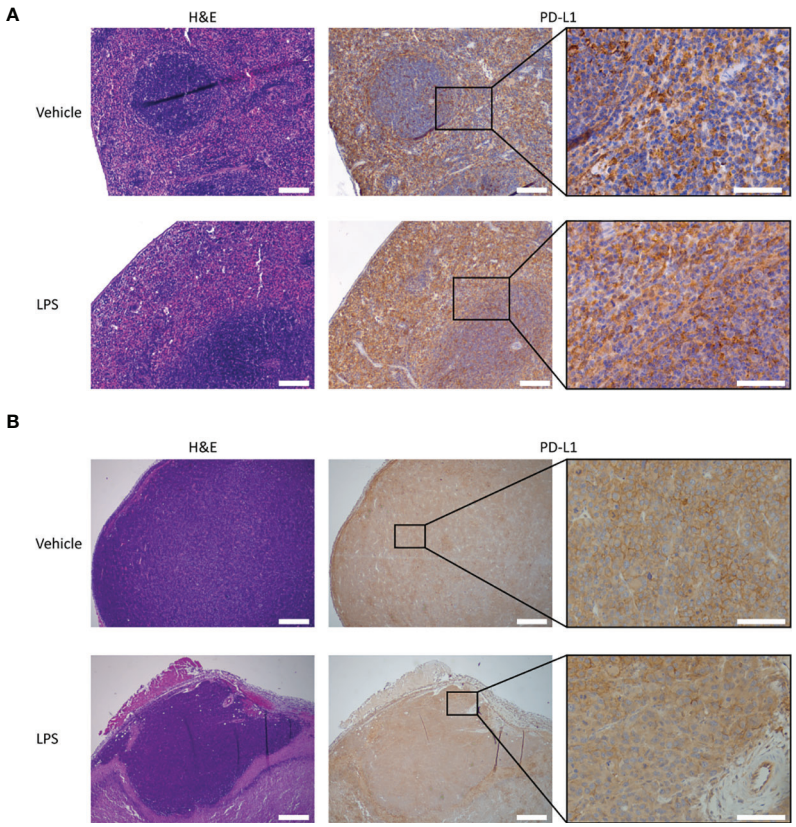

FIGURE 4 | PD-L1 expression and H&E staining of tumor and splenic tissues of LPS- and vehicle-treated mice. Representative images of the immunohistochemical analysis of PD-L1 expression in tumor and spleen tissue of RenCa tumor-bearing BALB/c mice, 2 days after LPS stimulation and vehicle control injection. **(A)** Splenic PD-L1 expression is very high for both vehicle control- and LPS-treated animals. LPS stimulation appears to slightly increase PD-L1 expression in the red pulp. **(B)** Tumor PD-L1 expression is not significantly altered by immune stimulation with LPS. The scale bar represents 500 μm or 100 μm in inset. LPS, lipopolysaccharide.

involvement of these proteins (10). However, in our candidemia model using PD-L1 imaging, we did not observe additional sites of anti-PD-L1 antibody accumulation indicative of local inflammation or altered PD-L1 expression in lymphoid organs. These results seem contrary to findings of another study showing that PD-L1 is upregulated on splenic residing CD4+, NKT, and NK cells (10). However, that study used a two-hit candidemia model consisting of cecal ligation and puncture followed by intravenous injection of live *C. albicans* three days later, thereby conceivably eliciting a more severe inflammatory response than the model used in our study. Moreover, the PD-L1 upregulation in that study as measured by flow cytometry appeared to be modest.

To translate our preclinical findings to the clinical setting, factors should be considered concerning the interspecies differences in physiology, immune biology, age of onset, antibody dosing, localization and severity of infections, and the presence of comorbidities, which can all have differential effects on systemic PD-L1 expression and PD-L1 antibody distribution. Furthermore, for an optimal signal-to-noise ratio, the long circulation time of monoclonal antibodies should be taken into account, as these tracers typically require several days between tracer injection and scanning. In the current study, this interval was 1 day, whereas in clinical practice, 5–7 days is standard; however, shorter intervals of 2–3 days might be sufficient depending on the research question. As the inflammatory effects of cytokines on PD-L1 expression levels can be rapid and/or transient, a short interval between antibody injection and scanning is preferred. Therefore, the use of PD-L1 targeting tracers with shorter circulation times such as peptides or adnectins, which are already being studied clinically, can be used. Finally, PD-L1 imaging cannot differentiate between cell populations. Therefore, complementary tools such as flow cytometry, immunohistochemistry, and RNA-sequencing are necessary to answer more mechanistic questions.

This study opens the door for nuclear imaging to aid in the rational design of studies to advance immune checkpoint inhibition to overcome immune dysfunction in patients with chronic infectious diseases and severe septic responses. For example, clinical imaging can facilitate in determining target tissue antibody uptake in pharmacological studies, thereby supporting and streamlining optimal dose finding and

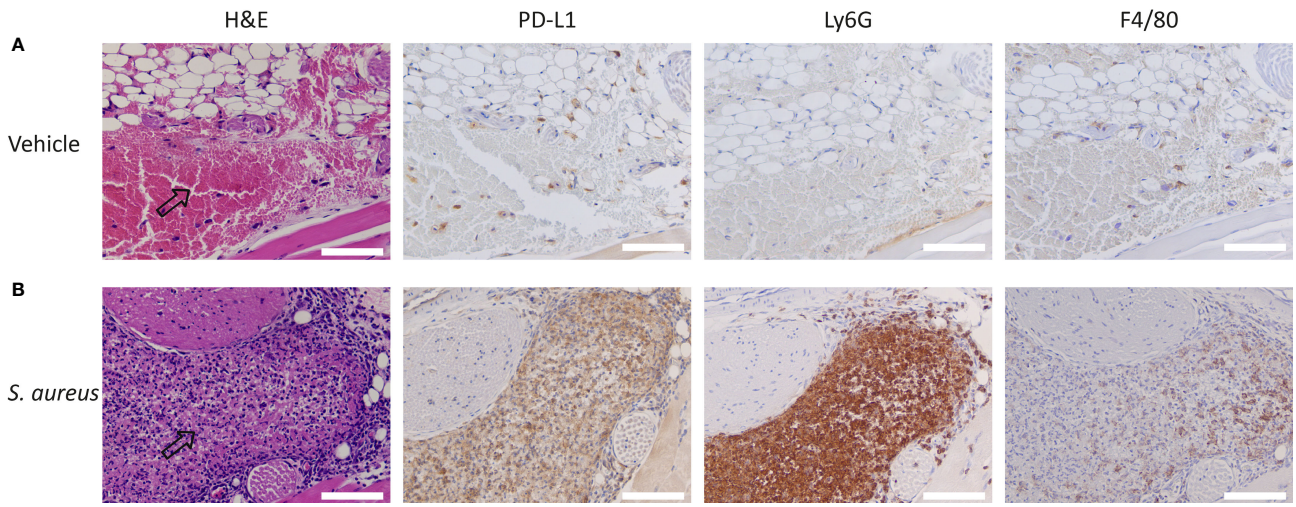

FIGURE 5 | Immunohistochemistry for PD-L1, F4/80, and Ly6G expression and H&E staining of *Staphylococcus aureus*-infected and vehicle control-injected muscles. Representative images of DAB-based (brown color) immunohistochemistry on consecutive tissue sections for PD-L1, Ly6G, and F4/80 of **(A)** vehicle control-injected muscle and **(B)** *S. aureus*-infected muscle tissues of BALB/c mice. Arrows indicate sites where injected autologous blood:*S. aureus* or autologous blood:vehicle mixtures accumulated. *S. aureus* infections attract significantly higher numbers of PD-L1 positive Ly6G$^+$ neutrophils and F4/80$^+$ macrophages when compared with vehicle control-injected muscles. Scale bar represents 100 μm.

development of treatment regimens. Second, it can be used to evaluate possible effects on PD-L1 expression levels and consequently the potential for therapeutic synergy of PD-L1 blockade and current antimicrobial immune-activating therapies such as prednisone, TNF-alpha antagonists, and IL-6 blockers.

In summary, we demonstrate that local and systemic infectious triggers can alter anti-PD-L1 antibody pharmacokinetics using ^{111}In-mPD-L1 SPECT/CT imaging. Increasing the anti-mPD-L1 antibody dose can normalize tumor targeting in mice with septic inflammatory responses. In the future, PD-L1 imaging can be used as a suitable tool to explore host responses in infectious conditions.

DATA AVAILABILITY STATEMENT

The raw data supporting the conclusions of this article will be made available by the authors, without undue reservation.

ETHICS STATEMENT

The animal study was reviewed and approved by the Animal Welfare Body of the Radboud University, Nijmegen, and the Dutch Central Authority for Scientific Procedures on Animals.

AUTHOR CONTRIBUTIONS

GS, SH, GA, JB, and EA contributed to the conception and design of the study. GS and JM performed the experiments. GS organized the database. GS performed the statistical analysis. GS wrote the first draft of the manuscript. SH and EA wrote sections of the manuscript. All authors contributed to manuscript revision and read and approved the submitted version.

FUNDING

This project received funding from the Netherlands Organization for Scientific Research (NWO, project number 91617039) and the Dutch Cancer Society (KWF, project number 10099).

ACKNOWLEDGMENTS

We thank Annemarie Kip, Cathelijne Frielink, Bianca Lemmers-van de Weem, Iris Lamers-Elemans, and Kitty Lemmens-Hermans for technical assistance with the animal experiments.

SUPPLEMENTARY MATERIAL

The Supplementary Material for this article can be found online at: https://www.frontiersin.org/articles/10.3389/fimmu.2022.837370/full#supplementary-material

REFERENCES

1. Sharpe AH, Pauken KE. The Diverse Functions of the PD1 Inhibitory Pathway. *Nat Rev Immunol* (2018) 18(3):153–67. doi: 10.1038/nri.2017.108
2. Ostrand-Rosenberg S, Horn LA, Haile ST. The Programmed Death-1 Immune-Suppressive Pathway: Barrier to Antitumor Immunity. *J Immunol* (2014) 193(8):3835–41. doi: 10.4049/jimmunol.1401572
3. Han Y, Liu D, Li L. PD-1/PD-L1 Pathway: Current Researches in Cancer. *Am J Cancer Res* (2020) 10(3):727–42.
4. Akinleye A, Rasool Z. Immune Checkpoint Inhibitors of PD-L1 as Cancer Therapeutics. *J Hematol Oncol* (2019) 12(1):92. doi: 10.1186/s13045-019-0779-5
5. Spec A, Shindo Y, Burnham CA, Wilson S, Ablordeppey EA, Beiter ER, et al. T Cells From Patients With Candida Sepsis Display a Suppressive Immunophenotype. *Crit Care* (2016) 20:15. doi: 10.1186/s13054-016-1182-z
6. Wang J, Roderiquez G, Norcross MA. Control of Adaptive Immune Responses by Staphylococcus Aureus Through IL-10, PD-L1, and TLR2. *Sci Rep* (2012) 2:606. doi: 10.1038/srep00606
7. Chen S, Crabill GA, Pritchard TS, McMiller TL, Wei P, Pardoll DM, et al. Mechanisms Regulating PD-L1 Expression on Tumor and Immune Cells. *J Immunother Cancer* (2019) 7(1):305. doi: 10.1186/s40425-019-0770-2
8. Patera AC, Drewry AM, Chang K, Beiter ER, Osborne D, Hotchkiss RS. Frontline Science: Defects in Immune Function in Patients With Sepsis Are Associated With PD-1 or PD-L1 Expression and Can Be Restored by Antibodies Targeting PD-1 or PD-L1. *J Leukoc Biol* (2016) 100(6):1239–54. doi: 10.1189/jlb.4HI0616-255R
9. Busch LM, Sun J, Cui X, Eichacker PQ, Torabi-Parizi P. Checkpoint Inhibitor Therapy in Preclinical Sepsis Models: A Systematic Review and Meta-Analysis. *Intensive Care Med Exp* (2020) 8(1):7. doi: 10.1186/s40635-019-0290-x
10. Shindo Y, McDonough JS, Chang KC, Ramachandra M, Sasikumar PG, Hotchkiss RS. Anti-PD-L1 Peptide Improves Survival in Sepsis. *J Surg Res* (2017) 208:33–9. doi: 10.1016/j.jss.2016.08.099
11. Hotchkiss RS, Colston E, Yende S, Angus DC, Moldawer LL, Crouser ED, et al. Immune Checkpoint Inhibition in Sepsis: A Phase 1b Randomized, Placebo-Controlled, Single Ascending Dose Study of Antiprogrammed Cell Death-Ligand 1 Antibody (BMS-936559). *Crit Care Med* (2019) 47(5):632–42. doi: 10.1097/CCM.0000000000003685
12. Hotchkiss RS, Colston E, Yende S, Crouser ED, Martin GS, Albertson T, et al. Immune Checkpoint Inhibition in Sepsis: A Phase 1b Randomized Study to Evaluate the Safety, Tolerability, Pharmacokinetics, and Pharmacodynamics of Nivolumab. *Intensive Care Med* (2019) 45(10):1360–71. doi: 10.1007/s00134-019-05704-z
13. Heskamp S, Hobo W, Molkenboer-Kuenen JD, Olive D, Oyen WJ, Dolstra H, et al. Noninvasive Imaging of Tumor PD-L1 Expression Using Radiolabeled Anti-PD-L1 Antibodies. *Cancer Res* (2015) 75(14):2928–36. doi: 10.1158/0008-5472.CAN-14-3477
14. Bensch F, van der Veen EL, Lub-de Hooge MN, Jorritsma-Smit A, Boellaard R, Kok IC, et al. (89)Zr-Atezolizumab Imaging as a Non-Invasive Approach to Assess Clinical Response to PD-L1 Blockade in Cancer. *Nat Med* (2018) 24 (12):1852–8. doi: 10.1038/s41591-018-0255-8
15. Niemeijer AN, Leung D, Huisman MC, Bahce I, Hoekstra OS, van Dongen G, et al. Whole Body PD-1 and PD-L1 Positron Emission Tomography in Patients With Non-Small-Cell Lung Cancer. *Nat Commun* (2018) 9 (1):4664. doi: 10.1038/s41467-018-07131-y
16. Fruhwirth GO, Kneilling M, de Vries IJM, Weigelin B, Srinivas M, Aarntzen E. The Potential of *In Vivo* Imaging for Optimization of Molecular and Cellular Anti-Cancer Immunotherapies. *Mol Imaging Biol* (2018) 20(5):696–704. doi: 10.1007/s11307-018-1254-3
17. Broos K, Lecocq Q, Raes G, Devoogdt N, Keyaerts M, Breckpot K. Noninvasive Imaging of the PD-1:PD-L1 Immune Checkpoint: Embracing Nuclear Medicine for the Benefit of Personalized Immunotherapy. *Theranostics* (2018) 8(13):3559–70. doi: 10.7150/thno.24762
18. Wierstra P, Sandker G, Aarntzen E, Gotthardt M, Adema G, Bussink J, et al. Tracers for Non-Invasive Radionuclide Imaging of Immune Checkpoint Expression in Cancer. *EJNMMI Radiopharm Chem* (2019) 4(1):29. doi: 10.1186/s41181-019-0078-z
19. Nimmagadda S. Quantifying PD-L1 Expression to Monitor Immune Checkpoint Therapy: Opportunities and Challenges. *Cancers (Basel)* (2020) 12(11):3173. doi: 10.3390/cancers12113173
20. Smit J, Borm FJ, Niemeijer AN, Huisman MC, Hoekstra OS, Boellaard R, et al. PD-L1 PET/CT Imaging With Radiolabeled Durvalumab in Patients With Advanced Stage Non-Small Cell Lung Cancer. *J Nucl Med* (2021) 63(3). doi: 10.2967/jnumed.121.262473
21. Zhou X, Jiang J, Yang X, Liu T, Ding J, Nimmagadda S, et al. First-In-Human Evaluation of a PD-L1-Binding Peptide Radiotracer in Non-Small Cell Lung Cancer Patients With PET. *J Nucl Med* (2021) 63(3). doi: 10.2967/jnumed.121.262045
22. Xing Y, Chand G, Liu C, Cook GJR, O'Doherty J, Zhao L, et al. Early Phase I Study of a (99m)Tc-Labeled Anti-Programmed Death Ligand-1 (PD-L1) Single-Domain Antibody in SPECT/CT Assessment of PD-L1 Expression in Non-Small Cell Lung Cancer. *J Nucl Med* (2019) 60(9):1213–20. doi: 10.2967/jnumed.118.224170
23. Cataldi M, Vigliotti C, Mosca T, Cammarota M, Capone D. Emerging Role of the Spleen in the Pharmacokinetics of Monoclonal Antibodies, Nanoparticles and Exosomes. *Int J Mol Sci* (2017) 18(6):1249. doi: 10.3390/ijms18061249
24. Heskamp S, Wierstra PJ, Molkenboer-Kuenen JDM, Sandker GW, Thordardottir S, Cany J, et al. PD-L1 microSPECT/CT Imaging for Longitudinal Monitoring of PD-L1 Expression in Syngeneic and Humanized Mouse Models for Cancer. *Cancer Immunol Res* (2019) 7 (1):150–61. doi: 10.1158/2326-6066.CIR-18-0280
25. Rigby KM, DeLeo FR. Neutrophils in Innate Host Defense Against Staphylococcus Aureus Infections. *Semin Immunopathol* (2012) 34(2):237–59. doi: 10.1007/s00281-011-0295-3
26. Gow NA, Netea MG, Munro CA, Ferwerda G, Bates S, Mora-Montes HM, et al. Immune Recognition of Candida Albicans Beta-Glucan by Dectin-1. *J Infect Dis* (2007) 196(10):1565–71. doi: 10.1086/523110
27. Lionakis MS, Lim JK, Lee CC, Murphy PM. Organ-Specific Innate Immune Responses in a Mouse Model of Invasive Candidiasis. *J Innate Immun* (2011) 3(2):180–99. doi: 10.1159/000321157
28. Hotchkiss R. Activating Immunity to Fight a Foe — A New Path. *N Engl J Med* (2020) 382:1270–2. doi: 10.1056/NEJMcibr1917242
29. Wykes MN, Lewin SR. Immune Checkpoint Blockade in Infectious Diseases. *Nat Rev Immunol* (2018) 18(2):91–104. doi: 10.1038/nri.2017.112
30. Kurino T, Matsuda R, Terui A, Suzuki H, Kokubo T, Uehara T, et al. Poor Outcome With Anti-Programmed Death-Ligand 1 (PD-L1) Antibody Due to Poor Pharmacokinetic Properties in PD-1/PD-L1 Blockade-Sensitive Mouse Models. *J Immunother Cancer* (2020) 8(1):8. doi: 10.1136/jitc-2019-000400
31. Nedrow JR, Josefsson A, Park S, Ranka S, Roy S, Sgouros G. Imaging of Programmed Cell Death Ligand 1: Impact of Protein Concentration on Distribution of Anti-PD-L1 SPECT Agents in an Immunocompetent Murine Model of Melanoma. *J Nucl Med* (2017) 58(10):1560–6. doi: 10.2967/jnumed.117.193268
32. An G. Concept of Pharmacologic Target-Mediated Drug Disposition in Large-Molecule and Small-Molecule Compounds. *J Clin Pharmacol* (2020) 60 (2):149–63. doi: 10.1002/jcph.1545
33. Langereis JD, Pickkers P, de Kleijn S, Gerretsen J, de Jonge MI, Kox M. Spleen-Derived IFN-Gamma Induces Generation of PD-L1(+)-Suppressive Neutrophils During Endotoxemia. *J Leukoc Biol* (2017) 102(6):1401–9. doi: 10.1189/jlb.3A0217-051RR
34. Azzopardi EA, Ferguson EL, Thomas DW. The Enhanced Permeability Retention Effect: A New Paradigm for Drug Targeting in Infection. *J Antimicrob Chemother* (2013) 68(2):257–74. doi: 10.1093/jac/dks379
35. Curran CS, Busch LM, Li Y, Xizhong C, Sun J, Eichacker PQ, et al. Anti-PD-L1 Therapy Does Not Improve Survival in a Murine Model of Lethal Staphyloccocus Aureus Pneumonia. *J Infect Dis* (2021) 224(12):2073–84. doi: 10.1093/infdis/jiab274

Conflict of Interest: The authors declare that the research was conducted in the absence of any commercial or financial relationships that could be construed as a potential conflict of interest.

the publisher, the editors and the reviewers. Any product that may be evaluated in this article, or claim that may be made by its manufacturer, is not guaranteed or endorsed by the publisher.

Frontiers in Immunology

Explores novel approaches and diagnoses to treat immune disorders.

The official journal of the International Union of Immunological Societies (IUIS) and the most cited in its field, leading the way for research across basic, translational and clinical immunology.

Discover the latest Research Topics

See more →

Frontiers

Avenue du Tribunal-Fédéral 34
1005 Lausanne, Switzerland
frontiersin.org

Contact us

+41 (0)21 510 17 00
frontiersin.org/about/contact